A contribution to high temperature applications using femtosecond laser direct writing in silica-based glasses and optical fibers

Yitao Wang

▶ **To cite this version:**

Yitao Wang. A contribution to high temperature applications using femtosecond laser direct writing in silica-based glasses and optical fibers. Material chemistry. Université Paris-Saclay, 2021. English. NNT : 2021UPASF038 . tel-03836247

HAL Id: tel-03836247
https://theses.hal.science/tel-03836247

Submitted on 2 Nov 2022

HAL is a multi-disciplinary open access archive for the deposit and dissemination of scientific research documents, whether they are published or not. The documents may come from teaching and research institutions in France or abroad, or from public or private research centers.

L'archive ouverte pluridisciplinaire **HAL**, est destinée au dépôt et à la diffusion de documents scientifiques de niveau recherche, publiés ou non, émanant des établissements d'enseignement et de recherche français ou étrangers, des laboratoires publics ou privés.

Thèse de doctorat

NNT : 2021UPASF038

université PARIS-SACLAY

A contribution to high temperature applications using femtosecond laser direct writing in silica-based glasses and optical fibers

Une contribution aux applications à haute température utilisant l'écriture directe par laser femtoseconde dans des verres et des fibres optiques à base de silice

Thèse de doctorat de l'université Paris-Saclay

École doctorale n°571 : 2MIB
(Sciences chimiques : molécules, matériaux, instrumentation et biosystèmes)
Spécialité de doctorat : Chimie
Unité de recherche : Université Paris-Saclay, CNRS, Institut de chimie moléculaire et des matériaux d'Orsay, 91405, Orsay, France.
Référent : Faculté des sciences d'Orsay

Thèse présentée et soutenue à Paris-Saclay, le 18 octobre 2021, par

Yitao WANG

Composition du Jury

Nadège OLLIER Directeur de recherche Institut polytechnique de Paris	Présidente
Wilfried BLANC Directeur de recherche CNRS – Université de Côte d'Azur	Rapporteur & Examinateur
Emmanuel MARIN Professeur des universités Université de Saint-Etienne	Rapporteur & Examinateur
Guillaume LAFFONT Ingénieur de recherche CEA Saclay	Examinateur

Direction de la thèse

Matthieu LANCRY Professeur ICMMO,Université Paris-Saclay	Directeur de thèse

Université Paris-Saclay, CNRS
Institut de chimie moléculaire et des matériaux d'Orsay, 91405, Orsay, France.

Acknowledgements

We are all in the gutter, but some of us are looking at the stars. I am not an enthusiast of Oscar Wilde, but these words have always touched me. Scientific research is a muddy road from beginning to end, which makes everyone in it covered with mud. If you keep struggling with your head down, you will be completely stuck in the quagmire. If you always look up at the sky, countless predecessors are waiting and they will help you to explore the next destination on this road until you find an unknown star in the distance.

I am lucky. Before I set foot on this path, I had not even considered the difficulties. The warnings from the people around me did not obliterate my fighting spirit, and I started this journey without hesitation. I am lucky because I have met the best guide, my supervisor Prof. Matthieu Lancry from the beginning. Under his protection, I can move forward smoothly. He always helps me with his experience and knowledge. His passion for life and scientific research infected me a lot. Whether it's the guidance of experimental operations, the guidance of various academic issues, or the ideas that help me open up in every discussion, his help is like sunshine shining into the gutter, letting me keep moving easily on this supposedly difficult path. I am lucky, along the way, I met only kind people, and their friendly help made my journey without a hitch. Bertrand Poumellec, he is like the big father of the whole team. He is wealthy in knowledge and has a rigorous attitude towards scientific research. He has given me great help in theoretical knowledge; Maxime Cavillon, a guy with strength far beyond his age, he is very helpful to me in experimental operations and article writing. He is always an example I followed; Tian Jing, teaches me a lot about the experiment operations, and also teaches me her own experience; Benjiamin Sapaly, a very friendly engineer, he has rich experience and we have done many experiments together; Que Ruyue, Elisa Muzi, Xie Qiong, Zhang Chanjuan, etc., it is the existence of these fellow travelers that make this journey less lonely. In addition, there are many partners who have cooperated with me, Francois Brisset for SEM measurement, Prof. John Canning and Dr. Kevin Cook from UTS, Prof. Gangding Peng and Dr. Shuen Wei from UNSW, etc. Thanks for all the help they provided me in the experiment.

The path to success requires the brave to have a strong heart. I want to thank my parents. They have always respected and supported every decision I made, which made me strong inside and always maintained the belief in success. I want to thank my girlfriend Alice, her company and encouragement made me fearless of any challenges.

Feel appreciated when life does not forget. I am very grateful to all the people I met on this road. Maybe in the future I will go further on the path of scientific research, to explore and discover more unknowns, but no matter when and where, these three years will be my most precious treasure of all the time, and make me always maintain the passion for life. Thanks all.

Orsay, 7 July, 2021 Yitao WANG

Introduction

The photosensitivity of glass (e.g. in germanosilicates and Boron-doped silica glasses) to ultraviolet (UV) laser radiation (continuous wave or nanosecond pulsed lasers) was perceived in the 1990s as a tool for functionalizing materials. The lasers used at that time, though relatively intense to induce substantial structural modifications of a material, operated by absorption in linear (one-photon) or weakly nonlinear (two-photon) optical domain. The main strategy was to trigger point defects, absorbing in the material optical bandgap range, as an initial step to couple laser energy with the glass network. The absorption is followed by a noticeable modification of the absorption spectrum, i.e., growth of absorption bands and bleaching of others. This is indicative of the migration and retrapping of electrons extracted from ionized atoms or/and ions. Light can also induce the transport of atoms or ions leading to change in the glass structure (permanent volume changes) and stress field. Chemistry quickly took its share within this field, as it was realized that photosensitivity is a function of glass chemical composition as well as its physico-chemical environment (including material thermal history and surrounding environmental conditions). Thus, the physical properties of the material, subsequent to its laser irradiation, originated from photochemistry processes. Usually, the mechanisms can be hypothesized based on a large data set of experimental results coming from various investigation methods.

The development of ultrashort pulse lasers in the femtosecond regime (1-100's fs, with 1 fs = 10^{-15} s), enabling the use of pulses having extremely high peak power, completely transformed this vision. Using these lasers, the peak power intensity is such that the research community moved to nonlinear optics with the possibility of electrons excitation across the silica optical bandgap, using six photons or even eight photons at 800 nm or 1030 nm, respectively. In fact, the use of femtosecond lasers enables to deliver, within a controlled volume and after focusing, high power intensity on the order of $10^{12\text{-}14}$ W/cm^2. These multiphoton excitations lead to photo-induced physico-chemical reactions and various structural modifications [1]: changes of the intrinsic material ordering (through a fictive temperature change), phase changes (re-crystallization, phase separation), chemical migrations. These modifications induce permanent changes of physical properties, including dielectric tensor, second order nonlinear optical properties (frequency doubling, electro-optical effects...). Femtosecond (fs)-lasers are thus attractive candidates for many applications since the photo-induced effects are by nature strongly localized in 3D in a "voxel" volume of a few cubic microns (µm^3). Their impact at the industrial level is recognized this technology generates employment activities. Thus, femtosecond laser direct writing is expected to become a ubiquitous tool of choice for the realization of micro optical devices in 3D.

As a result of the progress in these research fields, "stable" changes in refractive index in excess of 10^{-3} can routinely be obtained in most silica-based fibers, planar waveguides or bulk samples. Such index changes allow for the fabrication of an outstanding number of passive optical devices including in-waveguide grating-based optical components and laser-written planar waveguides [2-4]. Photosensitivity also finds applications in trimming optical path

difference in waveguide interferometers [5]. Advanced methods for the fabrication of these devices and specific applications of Bragg gratings are reviewed in various books and reviews [6-9]. In particular, Ultraviolet (UV) written intracore Fiber Bragg gratings are now routinely used for applications in optical telecommunications but also as sensors in civil engineering. Most applications require a long grating lifetime. For example, in dense wavelength-division multiplexing (DWDM) optical communication systems, the grating-based devices should keep working to an agreed specification for 25 years in the temperature range −40 °C< θ < 80 °C. Since a few years, harsh environmental sensing using Fiber Bragg Gratings (FBGs) technologies has emerged and is a rapidly growing field of research [10, 11]. A new generation of devices that operate in extreme environments (particularly those operating above 600 °C and up to 1500 °C), including environments with additional challenges such as radiation and intense optical fields (e.g. high power lasers), must be capable of withstanding gradual annealing and degradation, or aging, over time while preserving their intrinsic advantages (multiplexing capabilities, electromagnetic immunity, low intrusivity, mechanical reliability) with respect to conventional thermocouples. Of particular local relevance these include live diagnostics with optical sensor(s) embedded into high-temperature composites for aircraft, helicopters and spatial infrastructures [12], monitoring/mapping of temperature distribution at power plants [13], smelter furnaces and chemical reactors, monitoring of fuel combustion machinery [11], regulation of diesel locomotive engine temperature and to assist the structural health assessment of a building post-fire [12]. The oil, gas and geothermal industries are also set to benefit from such sensors as man's quest for fossil fuels and the lure of "free" geothermal power forces bore holes to be drilled ever deeper – a new world record only recently set with a drill depth of almost 5 km [14]. At these depths temperatures in excess of 500 °C, as well as extreme pressures are encountered. For example, some overview of ultrahigh temperature FBG sensors were presented in Refs [13, 15].

One innovating approach to solve the high temperature problem is to take advantage of the selectivity in spatial and time domains that Near-Infrared (IR) femtosecond lasers offer. In particular, the variety of permanent modifications written by a femtosecond laser [15-17] can enable sensing technologies to operate in various harsh environments at elevated temperatures [18-21] (standard type I FBGs are limited to 600 °C). In addition, femtosecond written FBGs can even be regenerated although they own already high temperature performance [22]. Several international teams are working on high temperature FBGs, including ultraviolet regenerated FBGs and/or the use of fs-lasers. However, despite this early success (e.g. demonstration of operation for 200 hours at 1000 °C in SiO_2 [15] or a few 10's minutes at 1745 °C in Sapphire fibers [19]), fs laser direct writing technology is still not mature and requires new innovative developments in material performances. Indeed, meaningful demonstrations, study of erasure mechanisms and modelling of the lifetime prediction are rarely performed and remain limited to standard telecommunication optical fibers i.e. generally lightly doped-SiO_2 based fibers. This is one major shortcoming preventing the deployment of high temperature FBG solutions into industrial applications. In addition, the deployment of such fs-FBG temperature sensors arrays to real life application requires fulfilling stringent requirements from the end-users. Thus efficient solutions have to be developed in order to propose fs-FBGs as a reliable and mature industrial solution with regard to well-established techniques such as thermocouples.

In this PhD thesis, the technology of glass fibers will be applied at a sub-micron scale using fs-laser patterning – "*glass smithing with nanoscale resolution becomes feasible"*. Usually, in fiber-based sensors such as FBGs, glass properties (e.g., refractive index, density, fictive temperature) are altered. This induces a highly localized periodic refractive index change but also significant stress-induced modifications around these irradiated regions. Consequently, during operation at high temperatures the device performance is limited by the thermal response of both the fiber core material and its surrounding regions. So here much of the answer is related to inherent glass structure and properties, particularly viscous flow/chemical migration and stress relaxation. It therefore may be overcome by judicious application of glass preparation, IR femtosecond laser writing and thermal stabilization procedure using either furnace or even a CO_2 laser heating for arbitrary profile [8, 23-25].

In particular, one key breakthrough forms the basis of this PhD thesis. This is the discovery of self-organized nanogratings in SiO_2, which exhibit 200-400 nm periodicity persisting on mm range, including nanolayers as thin as 10-30 nm, which are in fact the smallest structures ever created by light [26]. From the Authors, these nanogratings arise from modulation of the chemical composition (probably oxygen redistribution) and this would be related to stationary density waves in the plasma produced by the coupling between bulk plasmonic waves and light waves. In 2011, our group revealed that nanogratings are in fact an assembly of nanoporous layers due to oxide decomposition [27, 28] likely through a tensile stress assisted nanocavitation process [29]. These structures, also called Type II modifications in the literature, are at the root of other experimental unusual phenomena like high linear birefringence response (up to -10^{-2}), polarized luminescence, anisotropic light scattering, strong linear "dichroism", negative index changes and excellent thermal stability (until a few 10's hours at 1000 °C) [30]. These experimental observations left a number of opened questions that should be addressed to enable reliable applications. Therefore, how is it possible to master such fs-laser induced structures and the resulting properties associated? Furthermore, can we stabilize them for long-time operation in a high temperature regime? Finally, can we predict their erasure kinetics in their operating conditions? This thesis aims to solve these questions, in silicate glasses comprising both optical fiber and bulk forms.

Main PhD Tasks

Harsh environmental sensing technology is a rapidly growing field of research. The purpose of this PhD thesis is to bring a significant contribution to design, develop, and validate fs-3D structured fibers and bulk materials that overcome current thermal stability limitation and operate above 800°C and tentatively up to 1500 °C. Therefore, this project is many-fold as it includes both fundamental investigation of light-matter interactions and practical devices development. This PhD therefore brings together some key tasks that can be summarized as follows:

- Exploiting conventional GeO_2-SiO_2 optical fibers but made using a non-conventional approach i.e. 3D printed fibers;
- Exploiting "sensing dedicated" optical fibers developed by some collaborators (Clemson University in USA and Leibniz institute of photonic technology in Germany) with Al_2O_3-Y_2O_3-SiO_2 and Al_2O_3-SiO_2 cores with high Al concentrations up to > 50%;

- Inscription of FBGs like structures in said fibers and bulk glasses using fs-laser irradiation, mostly within Type II regime. In addition, Rayleigh backscattering will be investigated, as it is also suitable for high temperature monitoring;
- Maximizing the fs-laser induced modifications thermal performance through material control (influence of OH content, influence of GeO_2, Al_2O_3 and YAG content with concentrations up to > 50%) and laser parameters (writing speed, pulse energy);
- Build new physicochemical models and improve current ones for lifetime prediction of fs laser induced modifications in ultrahigh temperature conditions (> 800 °C), including glass composition and property aspects;
- Stabilization procedure to get drift-less modifications (and ultimately FBG sensors) for high Temperature applications.

First of all, the first chapter provides a review of the basic knowledge necessary to fully understand this PhD thesis. We will highlight the structure of silica glass, which is the principal material constituting the investigated glass samples in this thesis. We will discuss ultrashort laser pulse propagation in glass as well. Following this will be summarized the different mechanisms of ultrashort light pulses - glass interaction leading to structural changes, associated with the formation of permanent changes in the glass optical properties with a particular focus on silica glass. Finally, the last part of this chapter will be dedicated on the anisotropic optical properties and nanogratings formation in silica glass, since the later are preponderous in this work. Most specifically, we will focus on their thermal performances both in fiber-form and bulk glasses.

The second chapter is dedicated to the experimental techniques necessary to carry out all of our studies in the next chapters. We describe the femtosecond laser direct writing (FLDW) bench available in our institute (ICMMO at University Paris Saclay) and the experimental conditions tested in this thesis. The predominant non-destructive way to characterize nanogratings is quantitative birefringence measurements and more generally anisotropic optical properties, which provides information on the dependence of laser-induced modifications on the various laser-writing parameters, along with multiple thermal treatments. Finally, the overall characterization methods (Scanning electron microscopy, Raman spectroscopy, etc…) will be quickly described, since they provide the means to measure and probe the key physical quantities of the femtosecond laser written structures with sufficient accuracy to draw meaningful conclusions from the experiments designed in each chapter.

The third chapter is dedicated to the analysis of fs laser induced Type II modifications in bulk glasses. This chapter is made of 3 publications that were published during this PhD work. A deep analysis of birefringent self-organized nanogratings in silica glass is presented first, followed by the description of each laser-induced transformation and its respective contribution to the aggregate birefringence response. Finally, the thermal erasure kinetics from each one of these contributions is investigated and discussed. In the second section, we investigate a set of glass samples with varying laser parameters and glass composition/impurities (OH, Cl). This allows us to investigate the dependence of writing speed, pulse energy, and glass composition on the thermal stability of Type II modifications. Finally, a special focus is dedicated to high alumina (Al_2O_3)-containing silicate glasses made by aero-levitation, which are selected as

potential candidates to improve the glass thermal stability relative to conventional silica bulk and optical fiber glasses.

In chapter 4, we build on the achievements obtained from the previous chapter and focus on high alumina containing fibers fabricated by the molten core method. Two papers are presented here: the first one is about YAG derived and includes a short review of the literature whereas the second one is dedicated to Sapphire derived fibers. Femtosecond laser was used to imprint Type II modifications inside these fibers with a line-by-line FBG-like geometry. Both the writing kinetics and thermal withstanding of the modified regions were investigated. In this work, the fibers are tested under a wide temperature range (20-1250 °C), and compared to a conventional GeO_2-doped silica fiber (SMF28). In addition, we monitored Rayleigh backscattering during the isochronal annealing process to study the decay of the scattering signature related to Type II modifications.

In chapter 5, in order to provide a wide flexibility in terms of both glass materials and fiber design, a novel fiber fabrication method involving 3D silica printing lithography of the glass preform is employed to fabricate a GeO_2 doped fiber. Although great progress has been achieved in this area of research and development, there are still some challenges. This chapter is composed of 3 publications that result from a 3 months' fellowship with Australia (University of Technology Sydney and University of New South Wales) funded by the Partenariat Hubert Curien France-Australia Science Innovation Collaboration (PHC FASIC). In the first section the loss reduction of optical fibers fabricated by the new 3D silica lithography method is achieved by post heat treatment. In the second section, the photosensitivity of silica optical fibers to femtosecond laser light, and fabricated by 3D printing a preform, is investigated and compared to conventional single mode fibers (such as Single mode fiber SMF-28). Finally, in the third section we exploit UV laser photosensitivity to demonstrate the novel production of helical gratings in fibers that exhibit a high form birefringence arising from an initial strong core asymmetry combined with the greater induced index asymmetry from pulsed UV light.

Finally, in chapter 6, we will summarize the obtained results and provide an extensive discussion. The various contributions to the birefringence response related to Type II modifications, along with their thermal stability, will be synthetized. They include defect points, stress fields, self-organized porous nanolayers and densification mechanisms in silica glass. Moreover, simulations using the Rayleigh-Plesset (R-P) equation will be performed to model the erasure kinetic of nanopores in nanogratings during isochronal or isothermal annealing treatments. The simulated results will be compared with the experimental ones. Finally, the master curve formalism will be used to tentatively perform nanogratings lifetime prediction in a reliable approach.

References

1. Stoian, R., *Volume photoinscription of glasses: three-dimensional micro-and nanostructuring with ultrashort laser pulses.* Applied physics. A, Materials science & processing, 2020. **126**(6).
2. Mizrahi, V., et al., *Ultraviolet laser fabrication of ultrastrong optical fiber gratings and of germania-doped channel waveguides.* Applied physics letters, 1993. **63**(13): p. 1727-1729.
3. Svalgaard, M., et al., *Direct UV writing of buried singlemode channel waveguides in Ge-doped silica films.* Electronics Letters, 1994. **30**(17): p. 1401-1403.
4. Maxwell, G. and B. Ainslie, *Demonstration of a directly written directional coupler using UV-induced photosensitivity in a planar silica waveguide.* Electronics Letters, 1995. **31**(2): p. 95-96.
5. Kashyap, R., G. Maxwell, and B. Ainslie, *Laser-trimmed four-port bandpass filter fabricated in single-mode photosensitive Ge-doped planar waveguide.* IEEE photonics technology letters, 1993. **5**(2): p. 191-194.
6. Kashyap, R., *Fiber bragg gratings*. 2009: Academic press.
7. Cusano, A., A. Cutolo, and J. Albert, *Fiber Bragg grating sensors: recent advancements, industrial applications and market exploitation*. 2011: Bentham Science Publishers.
8. Liao, C. and D. Wang, *Review of femtosecond laser fabricated fiber Bragg gratings for high temperature sensing.* Photonic Sensors, 2013. **3**(2): p. 97-101.
9. Majumder, M., et al., *Fibre Bragg gratings in structural health monitoring—Present status and applications.* 2008. **147**(1): p. 150-164.
10. Mihailov, S.J., *Fiber Bragg grating sensors for harsh environments.* Sensors, 2012. **12**(2): p. 1898-1918.
11. Canning, J., *Regeneration, regenerated gratings and composite glass properties: the implications for high temperature micro and nano milling and optical sensing.* Measurement Science Technology, 2016. **79**: p. 236-249.
12. Inaudi, D. and B. Glisic. *Fiber optic sensing for innovative oil & gas production and transport systems*. in *Optical Fiber Sensors*. 2006. Optical Society of America.
13. Desmarchelier, R., et al. *Monitoring of single-mode fiber laser heating using Rayleigh scattering and 1 st order fs-PbP fiber Bragg Grating*. in *2017 25th Optical Fiber Sensors Conference (OFS)*. 2017. IEEE.
14. Gaspar, J., et al., *Surface heat flux estimation with embedded fiber Bragg gratings measurements: Numerical study.* Nuclear Materials Energy, 2017. **12**: p. 1077-1081.
15. Smelser, C.W., S.J. Mihailov, and D. Grobnic, *Formation of Type I-IR and Type II-IR gratings with an ultrafast IR laser and a phase mask.* Optics express, 2005. **13**(14): p. 5377-5386.
16. Martinez, A., et al., *Photoinduced modifications in fiber gratings inscribed directly by infrared femtosecond irradiation.* IEEE Photonics Technology Letters, 2006. **18**(21): p. 2266-2268.
17. Mihailov, S.J., et al., *Bragg grating inscription in various optical fibers with femtosecond infrared lasers and a phase mask.* Optical Materials Express, 2011. **1**(4): p. 754-765.
18. Mihailov, S.J., D. Grobnic, and C.W. Smelser, *High-temperature multiparameter sensor based on sapphire fiber Bragg gratings.* Optics letters, 2010. **35**(16): p. 2810-2812.
19. Busch, M., et al., *Inscription and characterization of Bragg gratings in single-crystal sapphire optical fibres for high-temperature sensor applications.* Measurement Science Technology, 2009. **20**(11): p. 115301.

20. Elsmann, T., et al., *Inscription of first-order sapphire Bragg gratings using 400 nm femtosecond laser radiation.* Optics Express, 2013. **21**(4): p. 4591-4597.
21. Grobnic, D., et al., *Sapphire fiber Bragg grating sensor made using femtosecond laser radiation for ultrahigh temperature applications.* IEEE Photonics Technology Letters, 2004. **16**(11): p. 2505-2507.
22. Cook, K., et al. *Regenerated femtosecond fibre Bragg gratings*. in *Third Asia Pacific Optical Sensors Conference*. 2012. International Society for Optics and Photonics.
23. Gao, S., et al., *All-optical fiber anemometer based on laser heated fiber Bragg gratings.* Optics express, 2011. **19**(11): p. 10124-10130.
24. Li, Y., et al., *Fiber Bragg gratings with enhanced thermal stability by residual stress relaxation.* Optics express, 2009. **17**(22): p. 19785-19790.
25. Ju, S., P.R. Watekar, and W.-T. Han, *Enhanced sensitivity of the FBG temperature sensor based on the PbO-GeO $ _ {2} $-SiO $ _ {2} $ glass optical fiber.* Journal of Lightwave Technology, 2010. **28**(18): p. 2697-2700.
26. Shimotsuma, Y., et al., *Self-organized nanogratings in glass irradiated by ultrashort light pulses.* Physical review letters, 2003. **91**(24): p. 247405.
27. Canning, J., et al., *Anatomy of a femtosecond laser processed silica waveguide [Invited].* Optical Materials Express, 2011. **1**(5): p. 998-1008.
28. Lancry, M., et al., *Ultrafast nanoporous silica formation driven by femtosecond laser irradiation.* Laser and Photonics Reviews, 2013. **7**: p. 953-962.
29. Rudenko, A., J.-P. Colombier, and T.E. Itina, *Nanopore-mediated ultrashort laser-induced formation and erasure of volume nanogratings in glass.* Physical Chemistry Chemical Physics, 2018. **20**(8): p. 5887-5899.
30. Bricchi, E. and P.G. Kazansky, *Extraordinary stability of anisotropic femtosecond direct-written structures embedded in silica glass.* Applied physics letters, 2006. **88**(11): p. 111119.

Chapter 1. State of the art of Femtosecond laser direct writing in glasses

Introduction 11
1.1 Silica Glass 11
1.2 Optical fibers 13
1.2.1 Definition and principle 13
1.3 Femtosecond laser interactions in glasses and different type of permanent modification it caused 16
1.3.1 Ionization and relaxation in intense field 16
1.3.2 Relaxation mechanisms 18
1.4 Damage thresholds and different type of permanent modifications. 19
1.4.1 Isotropic index changes based modifications (Type I) 20
1.4.2 Anisotropic refractive index changes (Type II modifications) 23
1.4.3 Voids (Type III) 24
1.5 On the origin of the anisotropic linear optical properties within Type II regime in fs-irradiated silica glass 24
1.5.1 Form birefringence within Type II regime 25
1.5.2 Stress-induced birefringence within Type II regime 29
1.5.3 Point defects formation and annealing within Type II regime 32
1.5.4 Conclusion on anisotropic linear properties thermal stability 35
1.6 Potential applications based on Femtosecond laser irradiation 36
1.6.1 Long-term data storage 37
1.6.2 General overview of the main fiber optic sensors 38
1.7 Thermal stability of the laser-induced refractive index changes in fibers 40
1.7.1 UV FBGs 40
1.7.2 IR-fs FBGs 42
1.7.3 Physico-chemical methods used for enhancing the thermal stability of BG written in a standard telecommunication fiber 44

1.7.4 Chemical composition influence on the thermal stability of FBG 47
1.7.5 Summary of different types of FBGs 48
Conclusions 49
References 51

Introduction

This chapter provides the basic notions required to understand the work performed in this thesis. First, we will review the main aspects of silica structure and the effect of composition doping. Next, the ultrashort laser pulse propagation in the matter will be described, along with the different processes involved during this light / matter interaction. The structural changes associated with permanent modifications inside the glass will be summarized, as well as their effect on the glass optical properties. Additionally, we will review the potential applications based on ultrafast laser irradiation such as the optical sensors, capable to operate in a high-temperature environment. Finally, the last part of this chapter is specifically is dedicated to the thermal stability of laser-induced refractive index changes.

1.1 Silica Glass

Silica glasses have been extensively studied and especially since the discovery of their photosensitivity to Ultraviolet (UV) radiation at the end of the 70s [1]. Since the 1960s, the effects of electron bombardment on glasses have been studied with high-energy sources in the MeV range [2-4]. As early as the 1980s, some authors began using less energetic electron beams (of the order of keV) in order to study the induced changes in volume and induced optical modifications [5-7]. Irrespective of the type of irradiation, these changes are based on structural changes induced by irradiation. That is why we begin this first chapter with a short description of the structure and optical properties of silica glasses.

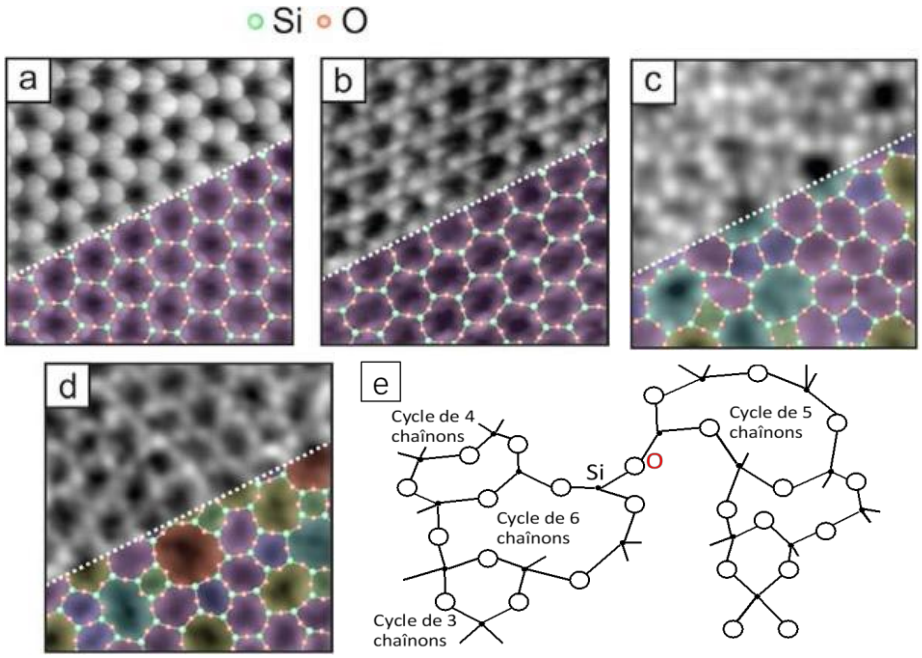

Figure 1-1: Atomic resolution STM images of silica bilayers: crystal structures of α-quartz (a and b) and disordered SiO_2 glass (c and d); scheme of the random network and silica rings (e). Adapted from [8].

Most commercial glasses are silicates and they contain many constituents included in a SiO_2 based matrix. The glass with the simplest composition is pure silica glass, despite its difficulty to

be technically developed with high purity. It is composed of an irregular 3D network consisting of disordered tetrahedral SiO_4 units as shown in *Figure 1-1* using atomic resolution STM of silica bilayers [8]. In this PhD work we will mostly use Type III- silica glasses that are synthetic vitreous silica produced by hydrolysis of $SiCl_4$ when spraying into an oxygen-hydrogen flame. This material is practically free from metallic impurities, but contains a high amount of OH, in the order of 1000 ppm, and because of the starting material, Cl, in quantities of the order of 100 ppm. Trade names are for example Suprasil (from Heraeus), Spectrosil or Corning 7940.

Silica glasses structure

There are various possibilities of assembling SiO_4 tetrahedra in 3D with each other. But the most stable configuration that is established is that for which the Si-Si distance will be longest, which is achieved in an assembly by the vertices. This mode of assembly is found in all forms of silica: quartz, trydimite, cristobalite and coesite. The intermediate bond of the Si-O-Si group gives an average angle of 145° [9], which admits a certain dispersion, corresponding to an Si-Si distance of approximately 3.12 Å. The distance Si-O varies between 1.62 Å and 1.77 Å and the distance O-O is between 2.50 Å and 2.65 Å [10]. The complete assembly of all the tetrahedra in silica glass thus forms a three-dimensional network presenting only a short-range order, but having no order at a long distance. This representation of the structure corresponds to the definition of the disordered or random network in the literature.

At a short distance, the order is governed by the coordination of silicon: a silicon atom is surrounded by 4 oxygen atoms forming a tetrahedron and, each oxygen is shared between 2 tetrahedra, to respect the SiO_2 stoichiometry. Silica glass is a special case of disordered systems because it has a medium range order. The latter is due to molecular connectivity. There are always four tetrahedra surrounding a given tetrahedron. However, there is no Euclidean translational symmetry [11]. The correlation length is defined as the number of successive correctly ordered tetrahedra. The free space in the structure allows tetrahedra to rotate. In this case, the correlation length or the degree of polymerization of the glass may vary according to the method of preparation and especially the cooling rate and more generally the thermal history. The structure of a cooled glass is frozen from a so-called fictive temperature T_f as described in details in Ref. [12]. Silica has the same medium-range order as the crystalline form of tridymite and cristobalite. When silica is elaborated under high pressures [13], its specific volume is lower. It then adopts a denser structure, this new configuration approaching that of quartz or coesite. Silica subjected to a very high pressure can also adopt a rutile structure in the form of SiO_6 octahedra, it is stishovite [14].

A few words on point defects in silica glasses

A glass can be subjected to a multitude of treatments such as heating, high pressure or laser irradiations and their combination. These treatments will locally modify the linkage sequence to form point defects. The definition of a defect in the glass is different from the definition given in a crystal. Indeed, in a crystal, any exception in translational symmetry is considered a defect. In a glass, this symmetry of translation does not exist and this definition cannot apply. The notion of

default is then based on the notion of chemical order. The perfect network of silica glass can be presented as a sequence of SiO_4 tetrahedra interconnected by common oxygen atoms. Thus, each silicon atom is connected to four oxygen atoms and each oxygen atom must have two Si as nearest neighbors. Any exception in this sequence ≡Si-O-Si≡ can be considered as a defect. Each defect has a structure and properties (absorption, fluorescence, magnetism, etc ...) that are unique to it. In order to better understand and subsequently control the impact of point defects on the properties of silica, it is essential to know their atomic structure. This is usually determined by a combination of experimental results from spectroscopy and theoretical calculations of quantum chemistry. The experimental technique that quickly proved to be the most suitable for developing and confirming defect models was the RPE (Electronic Paramagnetic Resonance). Although the RPE is a priori only applicable to paramagnetic defects, the absence of RPE signal in the case of a diamagnetic defect can be important information in the search for models. Rigorously applied, the RPE can thus indicate the orbital composition of the spin functions of the single electron spins, as well as the chemical nature, the size and the steric environment of the atoms. Each defect thus has a signature RPE of its own. If we can thus demonstrate the correlation between the RPE signal and an optical absorption band, we can deduce the origin of this one. A certain number of absorption bands have thus been identified. Begun several decades ago, the study of point defects is far from over. The structure of many defects, the absorption bands associated with them, or the mechanisms that lead to their appearance or disappearance, are still the subject of many disagreements. For more details on the properties of point defects, we can refer to the works of Griscom [15, 16], Garapon [17], Skuja [18, 19] and Trukhin [20].

1.2 Optical fibers

Since the advent of optical fiber in the last century, it has brought essential and revolutionary changes to the fields of information communication, optical sensors, medical and industrial fields. Because the transmission loss of information in optical fibers is much lower than that of electricity in wires, and because the main production material is silicon, which has large reserves and is easier to mine, the price is very cheap, which promotes the use of optical fibers as long-distance information delivery medium.

1.2.1 Definition and principle

Generally, an optical fiber is a long flexible glass wire made of vitreous silica that has the capacity to guide light over long distances, typically several hundred kilometers. More rigorously, an optical fiber is a "waveguide" of cylindrical geometry, which is made up of several regions with the different refractive index, which allows the propagation of only certain modes. The central region (center of the cylinder), called the core, then has a higher refractive index than the region around it (outer layer of the cylinder), called the optical cladding. The radial variation of the refractive index is called the index profile and can be of different nature (gradient, multistep, etc.) depending on the intended application for the fiber. *Figure 1-2* shows a simplified structure of an optical fiber.

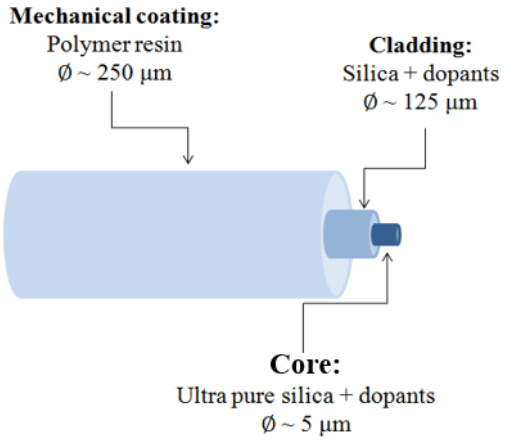

Figure 1-2: Simplified structure of an optical fiber

To obtain the desired index profile, it is necessary to introduce the chemical elements into the silica glass, called "dopants" in the optical telecommunications industry, which is capable to modify the optical properties of the material.

Light propagation in optical fiber

The principle of total reflection explains the operation of light guidance in an optical fiber with the index n_c of the core is different from the index n_g of the cladding. This principle is based on the law Snell-Descartes, described the behavior of a light wave at the diopter separated two media with different refractive index, according to *Equation 1-1*:

$$n_c \times \sin(i) = n_g \times \sin(r) \quad \text{(Equation 1-1)}$$

With i the angle of incidence and r the angle of refraction.

Any light ray in the core would totally be reflected at the interface of the core-cladding diopter when the angle of incidence of the ray is greater than the limit angle i_{lim}, defined by the *Equation 1-2*.

$$i_{lim} = \arcsin\left(\frac{n_g}{n_c}\right) \quad \text{(Equation 1-2)}$$

The reflected angle having the same angle as the incident angle, then the light continues to propagate in the core by total successive reflections at the level of the optical diopter separating the core and the cladding. *Figure 1-3* shows the principle of total internal reflection in an optical fiber.

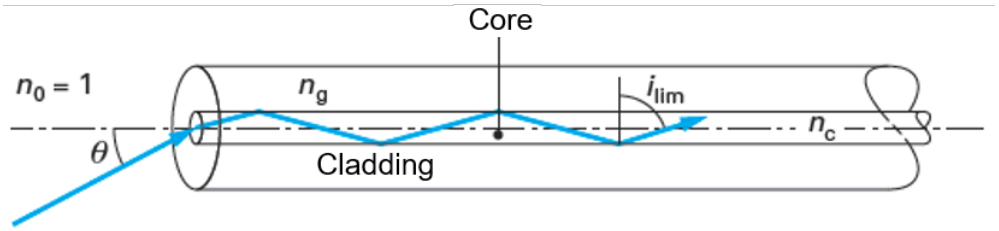

Figure 1-3: Diagram illustrating the principle of total internal reflection in an optical fiber (taken from [21]).

In order to reflect completely the injected light, the injection angle in the core of the fiber (angle of incidence at the entrance of the fiber) must induce a ray respecting the principle of total

internal reflection. In the air, the maximum injection angle θ relative to the axis of the fiber used to guide the light in the fiber is equal to:

$$\theta = \left|arcsin\left(\sqrt{n_c^2 - n_g^2}\right)\right| \qquad \text{(Equation 1-3)}$$

The maximum injection angle makes it possible to define the numerical aperture NA of the fiber according to *Equations 1-4 and 1-5*:

$$\mathrm{NA} = \mathrm{n_0} \times \sin(\theta) \qquad \text{(Equation 1-4)}$$

With n_0 = 1, the refractive index of air

$$\mathrm{NA} = \sqrt{\mathrm{n_c^2} - \mathrm{n_g^2}} \qquad \text{(Equation 1-5)}$$

Thus its digital aperture NA defines each fiber, since the latter depends on the refractive indices of the core and of the cladding (n_c and n_g).

The rays guided in phase in the optical core are called guided modes. The presence of one or more modes depends on the radius of the fiber core r, NA and the wavelength λ of the light. The normalized frequency V of the fiber, defined by *Equation 1-6*, determines the number of guided modes in the fiber.

$$\mathrm{V} = \frac{2\times\pi\times\mathrm{r}}{\lambda} \times \mathrm{NA} \qquad \text{(Equation 1-6)}$$

If the parameter V is less than 2.405, the fiber is defined to be single-mode and guides only one mode: only the propagation of the fundamental mode LP_{01} of Gaussian form is allowed. Beyond that, the fiber is said to be multimode and the number of propagation modes is approximately $V^2/2$. Next, I will introduce the difference between several kinds of optical fibers in more detail.

Different types of optical fibers

Optical fibers are today used in many fields of application, the main one of which is that of optical telecommunications, so-called transmission fibers are used. In other cases, they can also use for optical amplification, fibers called "component fibers" are used. The fibers differ according to the internal structure adopted (core diameter, index profile, ...) which separate into two categories: multi-mode fibers, denoted MMF and single-mode fibers denoted SMF. The propagation modes likely to propagate in the fiber corresponding to the solutions of the electromagnetic field of the propagation equation in a guided environment, that is to say when the refractive index is not uniform in the material. In the case where $n_{core} \approx n_{cladding}$, case corresponding to “weak guidance”, these propagation modes are designated by the two letters LP for “Linearly Polarized”. They are of type LP01 for the fundamental mode and LP11, LP12, etc. ... for the other modes. They are characterized by their cut-off wavelength denoted λ_c, wavelength above which the mode is no longer guided inside the fiber but refracted.

Consequently, a fiber is single-mode at the wavelength λ if it propagates in only one mode (the LP01); opposite of this, the multimode fiber where it propagates several modes simultaneously at the wavelength λ. A fiber is multimode if its core has a large diameter compared to the working wavelength. Typically, the diameters of the MMFs are between 50 and 200 µm for the silica fibers. The two most common types of MMFs are the fibers with the step index and the gradient index. The application range of the former is the short-distance transmission. The

medium distance telecommunications (up to 16km), use for computer applications and video distribution belongs to the latter. SMFs, whose core diameter is much smaller (typically 4 to 10 µm) than that of MMFs, are the most used for long-distance transmissions.

1.3 Femtosecond laser interactions in glasses and different type of permanent modification it caused

1.3.1 Ionization and relaxation in intense field

In order to introduce the interest of femtosecond lasers for the laser-matter interaction, this section briefly presents the mechanisms of interaction in glasses under the influence of an intense and ultra-brief electromagnetic field. Numerous fundamental studies on the physical processes involved have been conducted, allowing significant progress in understanding these mechanisms and leading to a fairly clear vision of the interaction processes shown in *Figure 1-4*.

Figure 1-4 shows the time scale of the interaction mechanisms that can be summarized in three steps: the electronic excitation [22], the thermalization, the different relaxation mechanisms and the permanent modifications. Part of the laser energy absorbed by the electrons is transferred to the network (i.e. to the phonons) over a period of about ten picoseconds in the silica. After a few nanoseconds, a shock wave is emitted. On the time scale from nanosecond to microsecond, heat propagates around the focal zone. For rates that are low enough to prevent heat accumulation build-up [23, 24], the material returns to ambient temperature within a few microseconds in SiO_2. At sufficiently high energy, these processes can also cause non-thermal ionic motion and leave permanent structural changes such as inelastic deformation (densification or expansion depending on the irradiation conditions and the composition of the material), the appearance of an elastic response (stress) [25-29] in and around the irradiated area and the formation of point defects [30] that absorb in UV and VUV, etc ... These mechanisms are developed in the following references [31-35].

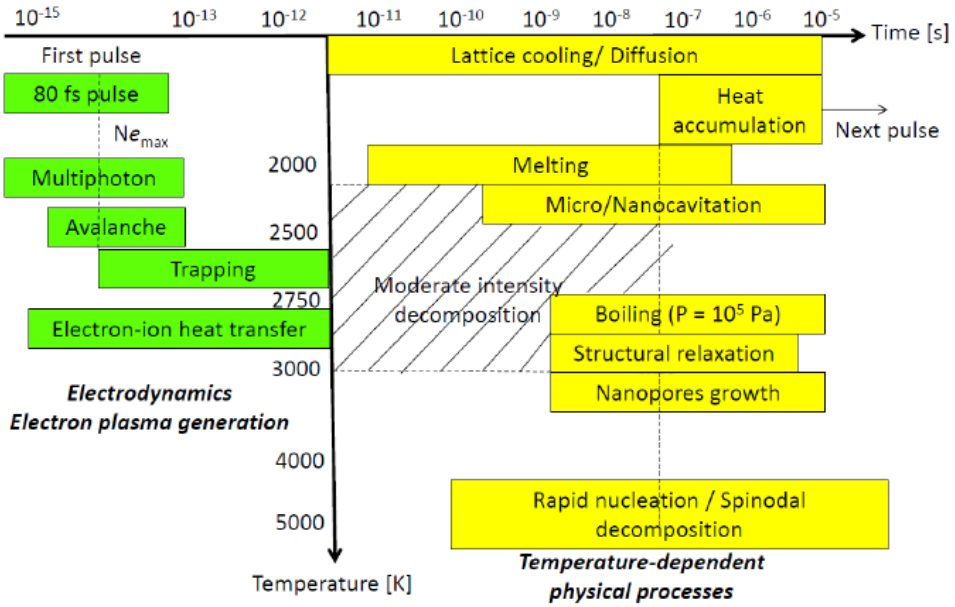

Figure 1-4: Schematics of main physical processes involved in the ultrashort laser processing of silica glass including temperature-dependent processes (taken from [36]).

The solids we have studied in this thesis are essentially dielectric materials with wide bandgap, chosen for their many applications in different fields that may be optics. We studied mostly silica glass (SiO_2). In these materials, the conduction band is empty and the highest populated electronic states are those at the top of the valence band. Between the two, the forbidden band is of the order of 9 eV, and is therefore much higher than the photons energy (1.5 eV for the Ti-Sa laser emitting at 800nm and 1.2 eV for 1030nm laser). Electronic excitation can only occur by a non-linear process such as the simultaneous absorption of several photons. This multi-photon ionization process can only be observed for high laser field amplitude. It has been shown that at these high intensities, there is also a phenomenon of "electron heating" within the conduction band, which continue to absorb a large number of photons after having crossed the forbidden band. Thus, by means of photoemission experiments, the measurement of the kinetic energy of the photoelectrons has made it possible to obtain the energy distribution of the electrons in the conduction band, which ranges between 10 and 40 eV for silica [37] and for conditions similar to the experiments we will performed within this PhD thesis.

Some results show that in our experimental conditions (NA = 0.5 and I = 1-30 TW/cm^2), the main mechanism of ionization happens to be multiphoton ionization: 6 photons in silica and 5 photons in Ge-doped silica. It should be noted that under our experimental conditions, neither tunnel ionization nor the presence of avalanche ionization are detected for pulse durations below 200fs [38, 39]. More recently, under specific conditions, an increase in carrier ionization impact has been shown that in SiO_2 [40]. All these results demonstrate that the avalanche process, which is often invoked in the laser breakdown literature, does not play a dominant role in optical breakdown induced by fs pulses. The relative importance of this phenomenon is always subject to intense discussion. It is now widely accepted that this relative importance depends largely on the experimental parameters [41-45]. In particular, it seems to depend on the pulse duration as well as its illumination or the width of the bandgap of the material.

1.3.2 Relaxation mechanisms

After this phase of electronic excitation, which takes place during the excitatory pulse, the photo-excited charge carriers are "out of equilibrium" and will thermalize with the solid by different mechanisms according to their kinetic energy. If the energy of the electrons is greater than the forbidden band, the inelastic collisions between electrons of the conduction band and the valence band, or the impact ionization, can occur at the attosecond scale (*Figure 1-5 step1*). In this case, the electron loses a significant energy, at least equal to the forbidden band and we end up with two electrons of lower energy at the bottom of the conduction band. For time scales from femtosecond to picosecond (*Figure 1-5 step 2*), lower energy electrons transfer their energy mainly via collisions with the lattice, by acoustic or optical phonon emission leading to heat effects leading permanents change like phase transition, photochemistry... In some materials, the electron-hole or exciton pairs induces local polarization and lattice deformation (*Figure 1-5 step 3*). At this deformation or atomic displacement, defined in the following part, corresponds to the appearance of electronic levels in the forbidden band, on which the charge carriers will be able to locate (*Figure 1-5 step 4*). We talk about trapped excitons (or self-trapped excitons noted STE) but also STH (self-trapped holes). This mechanism has a very short lifetime and occurs for a small percentage of charge carriers. STE has been studied in all alkali halides [46]. It has been demonstrated in silica and doped silica, and constitutes the intermediate step between electronic excitation and the formation of point defects (color centers). Finally, non-trapped electrons will recombine with a hole in the valence band (*Figure 1-5 step 5*).

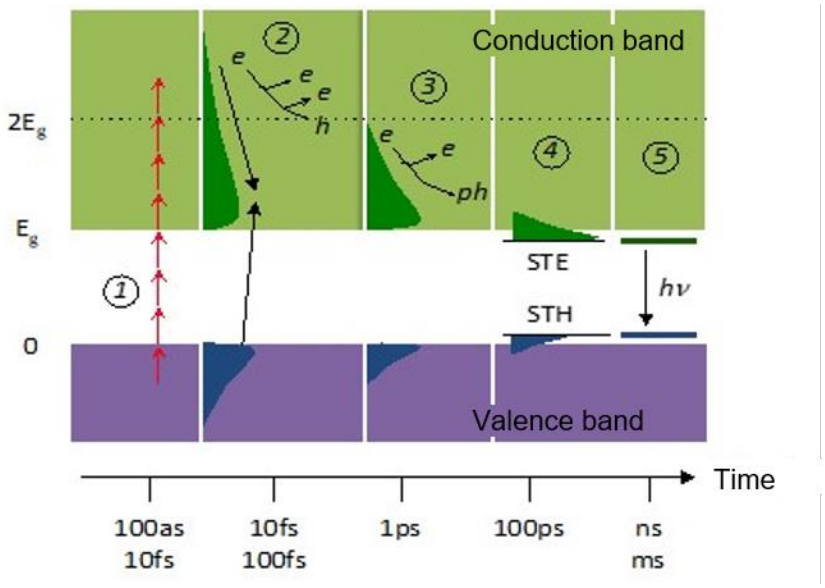

Figure 1-5: Diagram showing the elementary mechanisms involved during and after the interaction between a short pulse and a dielectric sample. 1: electronic excitation: either multiphoton ($h\nu<E_g$) or one photon ($h\nu>E_g$); 2: electronic relaxation: process of inelastic electron-electron collisions or impact ionization; 3: electronic relaxation, continued: thermalization via collisions with the network; 4: trapping and location of charges (self-trapped excitons); 5: radiative recombination of excitons [extracted from HDR of S. Guizard, CEA/LSI].

1.4 Damage thresholds and different type of permanent modifications

The structural modifications of the glass are, of course, dependent on the efficiency of transfer of light energy to the material. As we have said before, in the case of an ultrashort light pulse and sufficiently powerful, interband transitions by multiphoton absorption are possible. They lead to the creation of quasi-free electron plasma, which is followed by electronic relaxations (STE, point defects, network heating). In silica, three structural transformation regimes are observed and correspond to different kind of modifications as shown in *Figure 1-6*: an isotropic modification of the refractive index of the medium [47], anisotropic modification of the refractive index mainly due to form birefringence according to the literature [48-50], and micro-explosions leading to nano/micro-voids formation [51]. These modification regimes depend not only on the laser parameters: energy, pulse duration, laser repetition rate, wavelength, polarization (state and orientation), numerical aperture, depth of focus, writing speed, etc. [52] but also properties of the material: band gap, viscosity, density, heat capacity, thermal conductivity and their dependence with temperature [53-56]. It is possible to identify 4 regimes with 3 "damage" thresholds in SiO_2 glass as Poumellec et al. reviewed according matser parameters (NA, pulse duration, wavelength ...) in [52] :

- Below the first threshold, T1, (e.g. 0.085±0.015 μJ/pulse in pure silica, 800 nm, 160 fs, 0.5 NA, 100 kHz, 100 μm/s), the increase of the index relaxes following third order kinetics. The writing process is two-photon dependent when an absorption band exists at the relevant final energy. The index change decays within a few seconds.
- Between the two damage thresholds, the index change is permanent and nearly isotropic, the thermal stability is increased when compared to UV-induced changes but moderate. The maximum index change is $3\text{-}6\times10^{-3}$ in fused silica [57]. This is very large compared to UV laser-induced one which is limited to 3.10^{-4} using 193 nm excimer laser writing [58].
- Above the second damage threshold, T2, (e.g. 0.31±0.05 μJ/pulse in pure silica, 800 nm, 160 fs, 0.5 NA, 100 kHz), the characteristics are quite different. The index change magnitude can be as large as -10^{-2} and resists to decay during at least two hours at 1000°C [59, 60]. The index change is highly anisotropic [48, 61, 62] and this is the most striking feature. The principal axes are determined by the laser polarization [61]. This is attributed to the formation of self-organized nanogratings [49] made of nanoporous silica [63] as extensively described in the next section.
- Above the third damage threshold, T3 (e.g. 4 μJ/pulse in pure silica, 800nm, 160fs, 0.5 NA, 100 kHz), we can observe voids [60, 64].

These regimes can be clearly distinguished employing laser pulses shorter than 200 fs [45, 50, 65] (*Figure 1-6*). But at longer pulses, the region II narrows a lot which make it difficult to realize Type I modifications in multipulses regime.

As shown in *Figure 1-6*, another important parameter for femtosecond laser direct writing is focusing conditions, which roughly can be arranged into three groups depending on the numerical aperture (NA). The low NA regime is related to lenses with NA < 0.1, this gives a spot size of more than 10 μm. The femtosecond laser beam weakly focused into the bulk of transparent material

turns into filament below damage threshold preventing single-shot permanent structural modification [66, 67]. As a result, low NA lenses are typically used for surface modification, where self-focusing is not playing a crucial role. The lenses with NA from 0.1 to 0.6 can already induce a confined permanent modification inside of transparent material. At these numerical apertures spherical aberration can strongly affect the laser beam propagation. The refractive index of fused silica is higher than air's by roughly 0.45. The light is therefore non-uniformly refracted at the interface between the air and the material. As a result the adjacent part of the beam is focused deeper than the central, the waist is shifted and the focal spot is elongated in the propagation direction whereas the lateral spot size remains the same [68]. The strength of this effect is increasing with numerical aperture. The refractive index mismatch can be compensated by using objectives with spherical aberration correction, immersion optics or adaptive optics methods [69, 70]. Even larger numerical apertures (NA>0.9) can be achieved with immersion oil lenses. The immersion optics not only tightly focuses the laser beam but also compensates refractive index mismatch at the surface of the sample. As a result, tightly focused femtosecond laser beam can modify material even at nanojoule energy level [71, 72], i.e. ultrashort pulse oscillator energy is sufficient to induce the permanent modifications. The characteristics of these different regimes and modifications are detailed below.

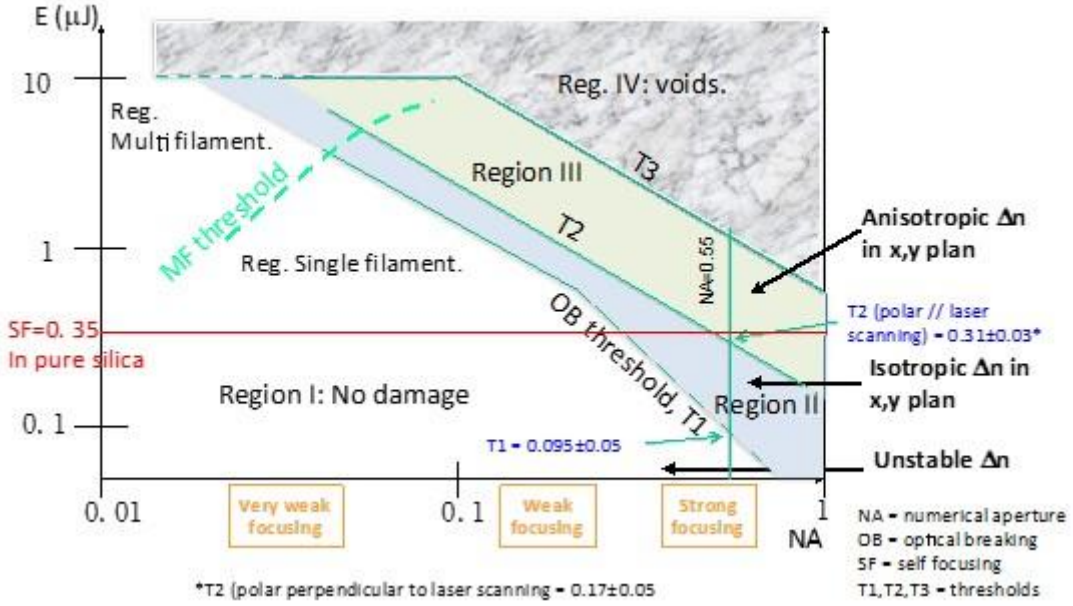

Figure 1-6: Diagram of the different types of damage according to the energy of the laser pulses and the numerical aperture (NA) of the focusing. MF: multi-filamentation; AF: Self-focusing; T1, T2 and T3: thresholds of the different types of damage; * T2 (polarization perpendicular to the direction of laser writing) = 0.17 ± 0.05 µJ. Laser parameters: 800nm; 160fs; 100kHz; 100m / s; parallel configuration; SiO_2. Adapted from Ref. [52].

1.4.1 Isotropic index changes based modifications (Type I)

The first observation of a threshold that we can report under a sufficiently intense irradiation is the reduction of the optical transmission. It is observed over a wide range of wavelengths from infrared to blue [73, 74]. This indicates that the glass is modified in its structure. The corresponding threshold energy has been tentatively defined by Schaffer et al. [34] taking into account the beam propagation effect. For diffraction-limited focusing and taking into account the presence of weak

self-focusing, the energy required to reach the breakdown intensity is related to the NA by using the relation:

$$E_{th} = \frac{I_{th}\Delta t\lambda^2}{\pi(NA)^2 + I_{th}\frac{\lambda^2}{P_{cr}}} \qquad \text{(Equation 1-7)}$$

where I_{th} is the intensity; Δt is the pulse duration; λ is the wavelength; NA is the numerical aperture of the focusing lens and P_{cr} is the critical power defined in the relationship *Equation 1-7*. At low energy, an increase (from 10^{-4} up to 5.10^{-3}) of the refractive index is observed in the silica which is one order magnitude higher than with UV ns laser (193 nm or 157 nm) [58]. It is attributed to a permanent densification due to a rapid cooling of the initially very hot focal volume [76, 77]. In addition, the focusing of the femtosecond laser pulses gives rise to a constraint that plays a role in this densification under certain conditions [78]. Defects centers (also called color centers) induced by femtosecond laser irradiation may be responsible for a portion of the refractive index change through the Kramers-Kronig relationship (a change in absorption leads to a refractive index change since these two quantities are conjugate complexes of the dielectric constant) [79]. Although color centers induced in femtosecond laser irradiated glasses have been observed [80, 81], there has been no experimental evidence so far of a strong link between their formation and induced index change. Waveguides formed in silica with an infrared femtosecond laser [82] showed photo-induced absorption peaks at 213 nm and 260 nm corresponding to the respective center defects E' and NBOHC. However, the two defects were completely erased after annealing at 400 °C, although it retained its guiding properties up to 900 °C. As a result, color centers are unlikely to have played a strong role in the refractive index change [82]. Other results lead to the conclusion that the thermal stability of the colored centers produced in borosilicate and silica glasses is not compatible with that of the change in refractive index [81]. It has recently been shown, in pure silica glasses for the realization of waveguides, that colored centers contribute to the refractive index changes for only 20% [57] whereas the major part has been attributed to defects-assisted densification by the authors.

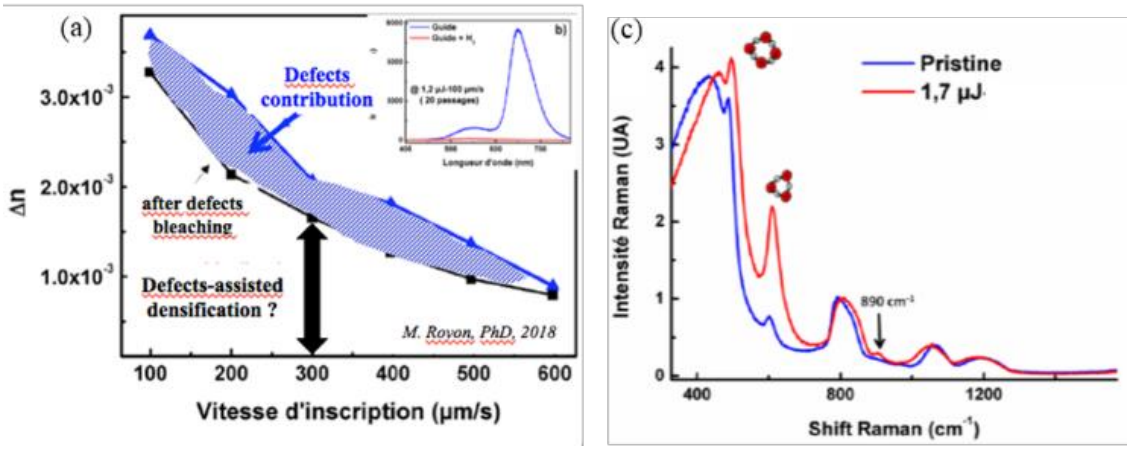

Figure 1-7: (a) Measurements of Δn waveguides in a Corning 7980 fused silica, adapted from Royon et al. [57]. The blue curve represents the change in index after femtosecond irradiation while the black curve shows the index change following hydrogen loading and complete desorption. (b) NBOHC PL emission that is bleached after H_2-loading. (c) Raman spectra of the pristine sample and of a waveguide ($\Delta n = 3.10^{-3}$, Type I regime) photo-inscribed with the following conditions: 1.7 µJ (slit shaping conditions)- 100 µm/s with 8 passes [83].

In an extremely simplistic view of the free electron plasma relaxation created by laser irradiation, it can be said that the transfer of energy from free electrons to the glass network leads to very high local temperature. The temperature can reach several thousand degrees [24] at the focal point limited by thermal conduction [84] (and likely high pressures), up to the local melting of the glass, inducing densification (or expansion as a function of the relationship between the density and the cooling rate i.e. glass fictive temperature) after the fast cooling of the glass [85]. This results, for example, in a lower average Si-O-Si angle and thus some changes in some infrared bands (for example, the antisymmetric elongation vibration centered at 1120 cm^{-1}) and a change in the D_1 and D_2 bands observed in Raman spectroscopy [85, 86], D_1 and D_2 being respectively associated with the vibrations of cycles with 4 and 3 tetrahedra. In silica, these structural modifications are correlated with an increase in the refractive index, of the order of a few 10^{-3} in writing conditions close to ours. The hypothesis of local densification of glass as a contribution to the increase of the refractive index was already advanced during the first publications on this subject [47, 79, 81, 87-91] following atomic force microscopic or phase shift interferometer observation of the depression of the surface (i.e. a valley) by a few tens of nanometers at the level of the irradiated zone.

B. Poumellec and M. Lancry have published a model of an original physico-chemical mechanism to explain these observations for Type I modifications. They proposed that T1 threshold is based on the modification of the fictive temperature T_f of the glass when the duration of the "heat pulse" corresponding to the light energy is greater than the relaxation time $\eta(T)/G(T)$. This one depends on the viscosity η and the shear modulus G of the material, the lower the viscosity, the smaller the relaxation time and globally the larger the T, the smaller the relaxation time. If the increase of the temperature is long enough to transform the glass, this defines T1. For that they have solved the Fourier equation and taken into account the variations of heat capacity, of thermal diffusion, η and G with doping and temperature. The results show that the glass fictive temperature increases (several hundred degrees higher than the original temperature) and then does not change significantly. We have also described the dependence on the chemical composition of glass in the germanium, phosphorus, F-doped silica family [84].

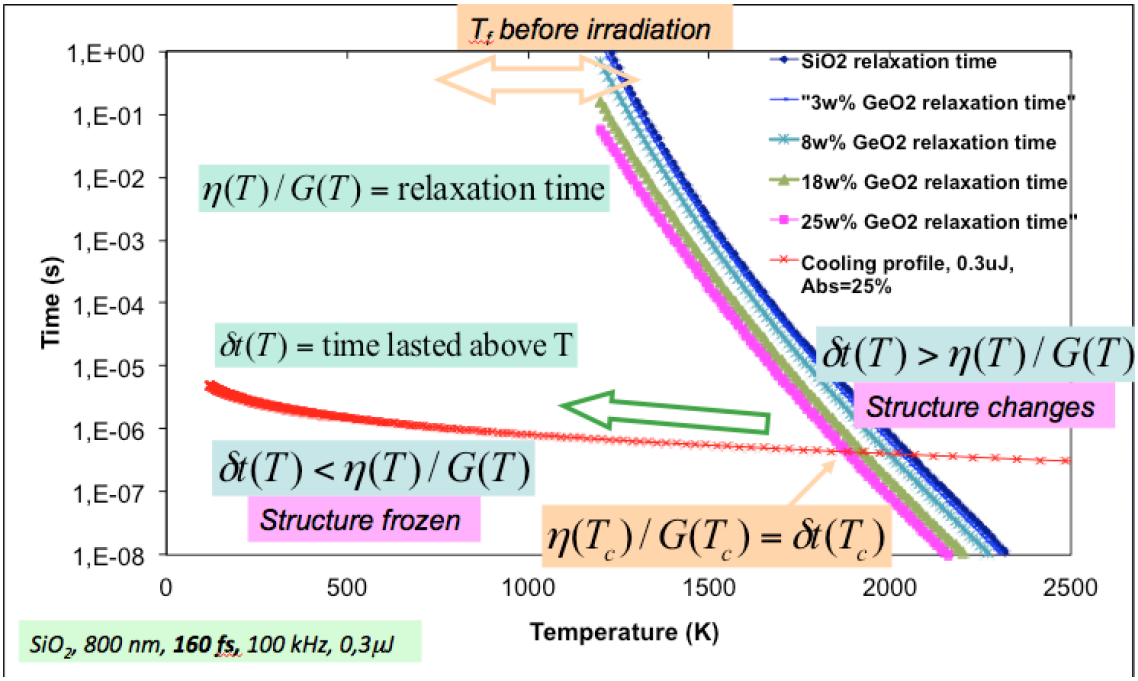

Figure 1-8: This graph compares the glass relaxation time and the cooling profile after single pulse femtosecond laser irradiation for pure and GeO_2-doped silica. The heat cooling profile is for pure silica only. Graph adapted from our group work in Ref. [84].

1.4.2 Anisotropic refractive index changes (Type II modifications)

For higher energy pulses, a second threshold is observed which is based on the appearance of nanostructures (see *Figure 1-9*) caused for example by the interference between the laser field and the electron plasma wave (a bulk Plasmon) according to the first model that was proposed in 2003 [49]. Y. Shimotsuma and P. Kazansky made this discovery in 2003. It remained to determine the nature of these nanoplanes. Some saw fractures, others oxygen depletions [49]. In 2011 we finally revealed that nanogratings are formed by a decomposition of silica (nanoporous silica formation [92]) as confirmed in 2013 [63]. At the nanoscale the free-electron density (or electronic temperature) modulation is imprinted in the matter by decomposition of SiO_2, revealing a high plasma temperature T_e (or plasma density n_e) that is higher than a "decomposition" limit. This decomposition of silica into nanoporous layers can be done, contrary to the fictive temperature modification, only by a pulse-to-pulse accumulation. As the material cooled down completely between pulses, we initially proposed an accumulation of point defects. We then explain the variations with doping by production of defects that vary greatly. This production is favored by the addition of germanium or conversely, it can be inhibited to observe only isotropic index change by adding fluorine in silica, which provide interesting results depending on the type of application envisaged [84].

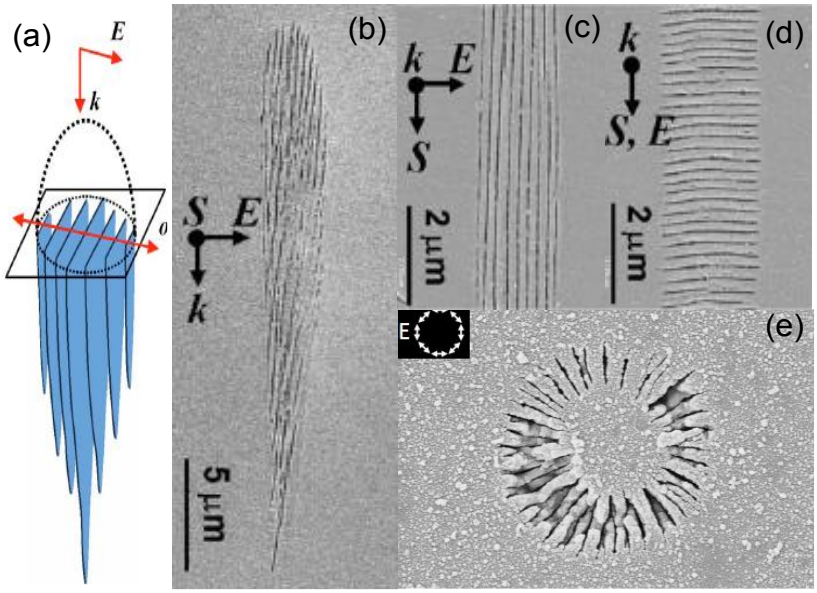

Figure 1-9: Nanogratings scheme within a laser track cross-section (a). Scanning electron microscopy (SEM) image of the nanogratings inscribed at 65 µm from the surface with a linear polarization perpendicular (b, c) and parallel (d) to the writing direction and azimuthal polarization (e). Laser parameters: 125 fs, 0,65 NA, 0,3 µJ, 100 kHz, 30 µm/s. Images extracted from Ref. [93].

1.4.3 Voids (Type III)

For even higher energy pulses giving rise to peak intensities greater than 10^{14} W/cm^2, holes in volume (so-called voids) are achievable by femtosecond laser irradiation. They are at the origin of a mechanism called the micro-explosion. A first model was proposed by Fleischer's team [94] and also reported later by Schaffer [95]. The mechanism at the base of void formation was initially suggested to be a Coulombian explosion i.e. when the density of excitations at a point in the material is very large, the Coulombian force between ions can overcome their binding energy. In this case, ions are also moved to interstitial positions around the starting point. However, this is unlikely to happen in the mentioned irradiation conditions so the mechanism was then revisited as follows: the energy is absorbed in a small volume producing a pressure which subsequently drives a shock wave and stress exceeding the Young modulus of the material. The strong spherical shock wave starts to propagate outside the center of symmetry of the absorbed energy region compressing the material [96-100]. At the same time, a rarefaction wave propagates to the center of symmetry decreasing the density in the area of the energy deposition. The shock wave stops when the pressure behind the shock front becomes comparable with the Young modulus. The corresponding threshold is noted T3 in our threshold diagram in *Figure 1-6*. Such voids can be exploited for 3D storage of information [101].

1.5 On the origin of the anisotropic linear optical properties within Type II regime in fs-irradiated silica glass

The key characteristic feature of Type II modifications in SiO_2 is the formation of porous nanogratings that can easily be detected through linear birefringence measurements (polarization

dependent). These nanogratings can also be directly imaged using SEM and TEM techniques. However, the measured linear birefringence arises from the aggregate contribution of several factors, including form birefringence, stress-induced birefringence, as well as the formation of point defects and Type I-densified area (e.g. in between the porous nanolayers). In this section, we will shortly review these different linear contributions in pure silica and we will also be discussed their respective thermal stability since it provides a way to estimate the contribution of each mechanism and their potential link with the original chiral-optical properties we observed in this thesis.

1.5.1 Form birefringence within Type II regime

Briefly, in 2003, a new type of self-organized structures was observed inside SiO_2 glass after irradiation with an ultrafast femtosecond laser [102]. Such structuration of the glass was found to be strongly anisotropic [48, 103, 104]. These highly ordered sub-wavelength structures with lamellae-like oxygen-deficient regions were oriented perpendicular to the incident beam polarization [102, 105]. A decade ago, Bricchi et al. demonstrated that such thermally stable nanostructures [59], due to their sub-wavelength periodicity, behave as a negative uniaxial birefringent material where the fast axis (slow axis) is parallel (perpendicular) to the orientation of the writing laser polarization [106]. Unlike intrinsic birefringence, which is due to the anisotropy of oriented molecules or atomic arrangements in uniaxial or biaxial crystals, the effect of form birefringence manifests itself due to the alignment of submicroscopic rodlets or platelets [61, 107]. The light polarized parallel to the interfaces experiences a larger refractive index and as a result, a phase difference for two perpendicular polarizations is acquired. The strength of the form birefringence can be controlled by the filling factor and the materials refractive indices (and thus the chemical composition) of the microstructure

Recently our group has demonstrated that the form birefringence is related to the formation of nanoporous silica [92] and is quantitatively correlated to the porosity-filling factor ff_{porous} of the nanolayers [108]. Control of the porosity was achieved by adjusting the pulse energy and the number of pulses/µm i.e. the overlapping rate [108] but also through the chemical composition [109-112]. In strongly Ge-doped SiO_2 (a "normal" glass [111]), we found that the matter surrounding the nanopores exhibited significant Δn decrease that is likely due to a fictive temperature increase (corresponding to a Δn increase in SiO_2). A second possibility may be that this matter in-between nanopores could be composed of silica with a significant amount of Frenkel oxygen defects $O_0^x \rightarrow V_0^{\cdot\cdot} + O_I$ (an interstitial oxygen and a vacancy) resulting in a Δn decrease as suggested in Ref. [108]. Furthermore, a densification in between these porous nanolayers has been indirectly suggested in [59], where the authors estimated a Δn increase by measuring the form-birefringence

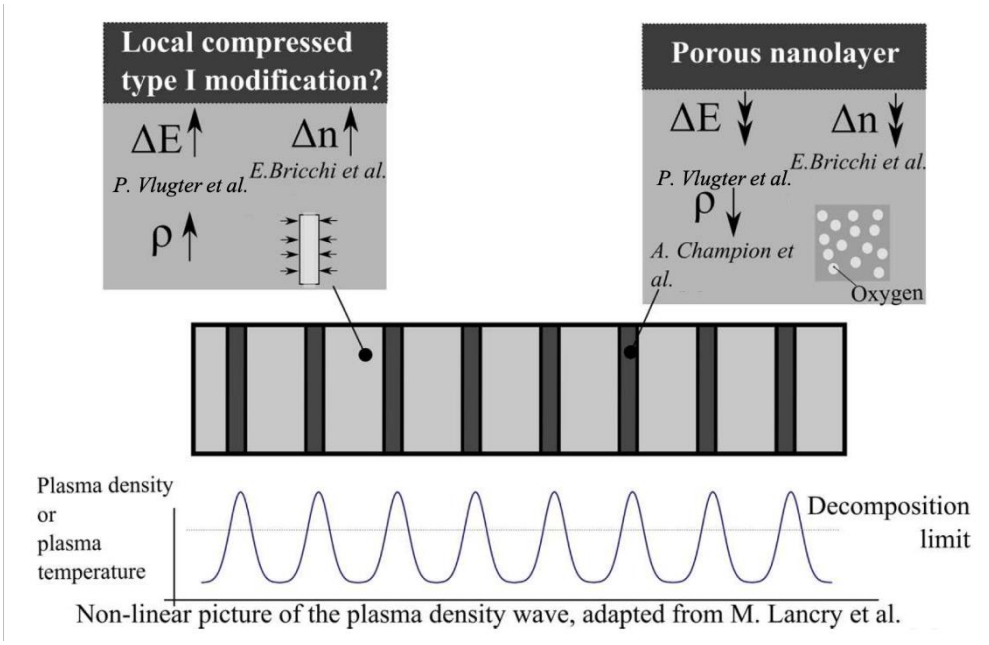

Figure 1-10 Middle: an illustrative summary of the nanogratings structure. Top-right: an illustration of the predicted material properties and chemical composition signature of a porous layer - the refractive index change estimated by [61], the oxygen filled pores [63] and elastic modulus [113]. In the top-left, a refractive index increase [61] and the elastic modulus increase [113]. Below the spatial distribution of plasma density, with peaks exceeding the decomposition limit. Schemes are adapted from Ref. [63].

The increase of the Young's modulus [113], refractive index, and possible densification, is like a Type I modifications [25, 87, 114], which exhibit similar characteristics. Previous works [31, 63] made similar observations. Lancry et al. [63] proposed a plasma density profile where, in the non-porous layers, the glass met the thermo-mechanical conditions for a modification of Type I, while in the position of the porous nanolayers, a decomposition threshold for SiO_2 molecules would be exceeded. Therefore, the local Young's modulus increases [113] and its corresponding Δn response also increases as measured in [61] and going from $2x10^{-2}$ to $5x10^{-2}$. This value is significantly higher than the one found for regime I modifications, where a Δn increase up to a few 10^{-3} is expected [57, 115, 116]. For completeness, the formation of color centers is expected to decrease the glass Young's modulus, as it will lower the connectivity of the 3D glass network. Therefore it is more likely that a mechanism based on the occurrence of fast compressive stress combined with thermal quenching is responsible for the noticeable Δn increase observed in [113]. The aforementioned mechanisms and their contributions to properties (density, Young's modulus, refractive index) are schematically summarized in *Figure 1-10*.

Form birefringence model

The birefringent properties of materials are usually explained in terms of the anisotropic electrical properties of molecules they are made of. We start the discussion from a classical wave propagation approach; the medium being in two dimensions, there are two modes of propagation according to whether the field oscillates in the plane or perpendicular to the plane of the medium. If the electric field is parallel to the nanolayers, the mode is TE (ordinary index). If the field is perpendicular to the nanolayers, the mode is TM (extraordinary index). The proper modes of propagation are:

$\vec{E} = \vec{E}_k(z) * \exp(i(\omega t - \beta x - Kz))$, with nanolayers along x, y, and perpendicular to z. So the x here represents any component in the x, y plane, K is the longitudinal propagation constant. In the case of nanogratings, they are used in such a way that there is always a component β, but K = 0. There are two branches in the dispersion relationships, one for TE and the other for TM. They are given by the solutions of Maxwell's equations and boundary conditions. Note here $\frac{\omega}{c} = \frac{2\pi}{\lambda}$. We have:

$$\cos(\mathrm{K}\,\Lambda) = \cos(\mathrm{k_{1z}a})\cos(\mathrm{k_{2z}b}) - \frac{1}{2}\left(\frac{\mathrm{k_{2z}}}{\mathrm{k_{1z}}} + \frac{\mathrm{k_{1z}}}{\mathrm{k_{2z}}}\right) \times \sin(\mathrm{k_{1z}a})\sin(\mathrm{k_{2z}b}) \quad (\mathrm{TE}) \qquad \text{(Equation 1-8)}$$

$$\cos(\mathrm{K}\,\Lambda) = \cos(\mathrm{k_{1z}a})\cos(\mathrm{k_{2z}b}) - \frac{1}{2}\left(\frac{\mathrm{n_2^2 k_{1z}}}{\mathrm{n_1^2 k_{2z}}} + \frac{\mathrm{n_1^2 k_{2z}}}{\mathrm{n_2^2 k_{1z}}}\right) \times \sin(\mathrm{k_{1z}a})\sin(\mathrm{k_{2z}b}) \quad (\mathrm{TM}) \qquad \text{(Equation 1-9)}$$

With: $\mathrm{k_{1z}^2} = (\frac{\mathrm{n_1}\omega}{\mathrm{c}})^2 - \beta^2$ and $\mathrm{k_{2z}^2} = (\frac{\mathrm{n_2}\omega}{\mathrm{c}})^2 - \beta^2$

As shown in *Figure 1-11*, $\Lambda = t_1 + t_2$, the grating period with t_1 and t_2 the two thicknesses, n_1 and n_2 the refractive indices of the two materials which are assumed to be isotropic. If the linear dimensions of the faces of the plates are assumed to be large but the thickness t_1 and t_2 are small compared to the wavelength, we can get $\Lambda \ll \lambda$ and developed until $(\frac{\Lambda}{\lambda})^2$, the field in the plates and in the spaces may be considered uniform so that we can drive to the equation [117]:

$$\frac{\mathrm{K}^2}{\mathrm{n_0^2}} + \frac{\beta^2}{\mathrm{n_0^2}} = (\frac{\omega}{\mathrm{c}})^2 \quad (\mathrm{TE}) \qquad \text{(Equation1-10)}$$

$$\frac{K^2}{n_0^2} + \frac{\beta^2}{n_e^2} = (\frac{\omega}{c})^2 \quad (TM) \qquad \text{(Equation 1-11)}$$

With: $n_0^2 = \frac{t_1}{\Lambda} n_1^2 + \frac{t_2}{\Lambda} n_2^2$ and $\frac{1}{n_e^2} = \frac{t_1}{\Lambda}\frac{1}{n_1^2} + \frac{t_2}{\Lambda}\frac{1}{n_2^2}$

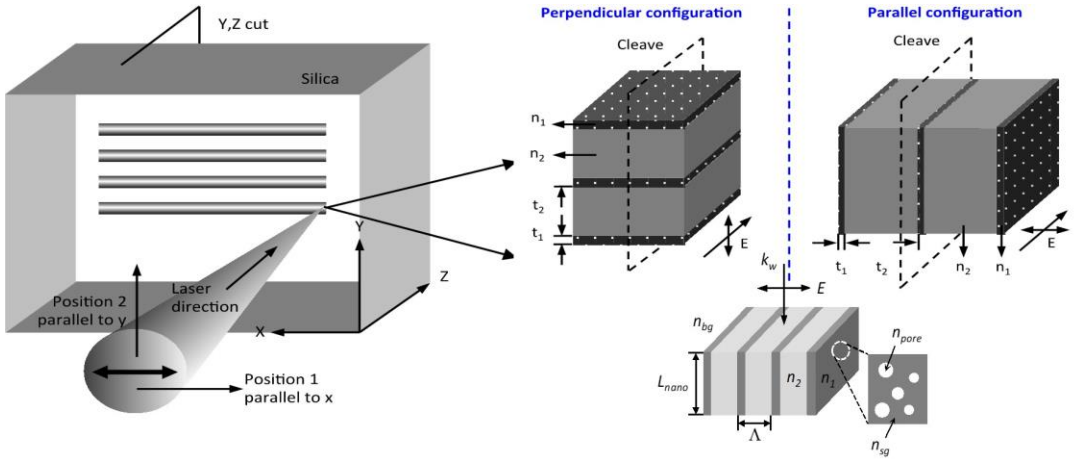

Figure 1-11: Experimental scheme for writing configuration and schematic of nanogratings formed in cross-section of the irradiated region. n_1 et n_2: local refractive indices of the nanolayers; t_1 and t_2, are their respective thicknesses. Right bottom: Schematic of sub-wavelength periodic structure formed in cross-section of the irradiated region. n_{pore} (=1) and n_{sg}: local refractive index for nanopores and for surrounding oxygen defect regions, respectively; $\Lambda = t_1 + t_2$: period of nanogratings and n_{bg}: refractive index of the surrounding material, L_{nano}: thickness of nanogratings. Schemes are adapted from Ref. [108].

As a result, we see that a layered material with a period much less than the wavelength is uniaxial. Birefringence is also negative with $n_e < n_o$. Note that the indices depend on the ratio $\frac{t_1}{t_2}$,

that the dispersion in λ is only in the dispersion of n_1 and n_2. As we would have K = 0 in our case, in TE polarization (field parallel to the layers), the dispersion relation expressed in wavelength is:

$$\beta_{TE}^2(\lambda) = n_o^2(\lambda)\left(\frac{\omega}{c}\right)^2 = n_o^2(\lambda)\left(\frac{2\pi}{\lambda}\right)^2 \qquad \text{(Equation 1-12)}$$

and in TM polarization (field perpendicular to the layers), the relation is

$$\beta_{TM}^2(\lambda) = n_e^2(\lambda)\left(\frac{\omega}{c}\right)^2 = n_e^2(\lambda)\left(\frac{2\pi}{\lambda}\right)^2 \qquad \text{(Equation 1-13)}$$

For an irradiated area larger than the probe beam, it is well known that the strength of form birefringence depends on the thickness of the nanolayers (t_1 and t_2) and their respective refractive indices (n_1 and n_2). If the materials are not isotropic (a textured microstructure, aligned ellipsoid nanopores for example), and when $\Lambda \ll \lambda$, the uniaxial birefringence Δn due to the nanogratings can be written as a refractive index difference between ordinary (n_o) and extraordinary (n_e) wave:

$$\Delta n = n_e - n_0 = \underbrace{\frac{n_1 n_2}{\sqrt{f_\perp n_2^2 + (1-f_\perp)n_1^2}}}_{n_e} - \underbrace{\sqrt{f_\perp n_1^2 + (1-f_\perp)n_2^2}}_{n_0} \qquad \text{(Equation 1-14)}$$

where $f_\perp = t_1/(t_1+t_2) = t_1/\Lambda$ is the 1D nanogratings filling factor $f_\perp$ and Λ is the nanoplanes spacing, n_1, n_2, t_1 and t_2 are defined in *Figure 1-11*. This relation, valid for nanogratings, can be generalized for any anisotropic structures like series of nanoplanes, in the case where the probe beam diameter w is larger than nanoplanes area:

$$\Delta n = \frac{\Lambda - \sqrt{(t_1 n_1^2 + t_2 n_2^2)\left(\frac{t_1}{n_1^2} + \frac{t_2}{n_2^2}\right)}}{\Lambda\left(\frac{t_1}{n_1^2} + \frac{t_2}{n_2^2}\right)} \qquad \text{(Equation1-15)}$$

and, in the case where w is smaller than nanoplane area:

$$\frac{w - \sqrt{\left[l_t n_2^2 + N_p(t_1 n_1^2 + t_2 n_2^2)\right]\left[\frac{l_t}{n_2^2} + N_p\left(\frac{t_1}{n_1^2} + \frac{t_2}{n_2^2}\right)\right]}}{\sqrt{w\left[\frac{l_t}{n_2^2} + N_p\left(\frac{t_1}{n_1^2} + \frac{t_2}{n_2^2}\right)\right]}} \qquad \text{(Equation1-16)}$$

where N_p is the number of period Λ and w is probe beam diameter and l_t is defined by $l_t = w - N_p\Lambda$.

This results into a strong birefringence response for wavelengths longer than the nanogratings periodicity (λ >> Λ). On the other hand, for λ ≈ Λ, this response is strongly decreased to a level that is no more exploitable for most optical applications [117].

Let's go back to the general case. The next consideration is therefore the value of $n_1(\lambda)$ and $n_2(\lambda)$. The material should be unchanged between the nanolayers as a first approximation (whereas a densification up to 10^{-2} has been reported [61]), so we know roughly its dispersion. For the other, it consists of nanopores, possibly ellipsoidal, more or less aligned, immersed in a material whose index has decreased compared to that of silica. If we know the refractive index of nanopores n_{pore} considering that it is a gas, it could be assigned a constant dispersion and a value equal to 1, whereas the index of the surrounding n_{sg} reduced silica [108] will have to be hypothesized for a complete description of the problem. To obtain the index of the composite

material of the nanoplanes, it is necessary to apply the theory of the effective medium whose application to the permittivity is due to Maxwell-Garnett [64, 118].

For spheres distributed randomly, we have:

$$\frac{\varepsilon_{\mathrm{eff}}-\varepsilon_{\mathrm{m}}}{\varepsilon_{\mathrm{eff}}+2\varepsilon_{\mathrm{m}}} = \mathrm{ff}_{\mathrm{porous}}\left(\frac{\varepsilon_{\mathrm{i}}-\varepsilon_{\mathrm{m}}}{\varepsilon_{\mathrm{i}}+2\varepsilon_{\mathrm{m}}}\right) \qquad \text{(Equation1-17)}$$

With ε_{eff} for the composite, ε_i for the inclusion, ε_m for the medium, and ff_{porous} for volume fraction taken by the nanopores. For a material made up of ellipsoid inclusions randomly oriented to each other, there is no birefringence, but a correction in the following formulas [119, 120].

$$(1-\mathrm{ff}_{\mathrm{porous}})\frac{\varepsilon_{\mathrm{eff}}-\varepsilon_{\mathrm{m}}}{\varepsilon_{\mathrm{eff}}+2\varepsilon_{\mathrm{m}}} = \mathrm{ff}_{\mathrm{porous}}\left(\frac{\varepsilon_{\mathrm{i}}-\varepsilon_{\mathrm{m}}}{\varepsilon_{\mathrm{i}}+2\varepsilon_{\mathrm{m}}}\right) \qquad \text{(Equation1-18)}$$

On the other hand, for a textured and therefore anisotropic material, with two axes such as collectively aligned ellipsoid nanopores, there would be two values of permittivity $\varepsilon_{\parallel}$ and $\varepsilon_{\perp}$ according to the polarization plane aligned parallel or perpendicular to the direction of the ellipses. However, we will not further consider this case in this PhD thesis.

1.5.2 Stress-induced birefringence within Type II regime

Generalities

Stress-induced birefringence can result from different conditions such as applied external pressure, process-induced temperature gradients, manufacturing processes (thermal expansion coefficient mismatch in optical fibers manufacturing, etc…) but also laser writing (due to permanent volume changes ε^p leading to elastic strain ε^e and thus stress σ). Therefore, the glass refractive index also becomes locally anisotropic through photoelastic effects. The plane-polarized wave will propagate through the stressed part of the glass at different speeds according to its polarization direction. For electromagnetic radiation with a polarization parallel and/or perpendicular to the direction of the mechanical stress the refractive indices can be rewritten as $n_{\parallel} = n_0 + \Delta n_{\parallel}\ and\ n_{\perp} = n_0 + \Delta n_{\perp}$. Whereby n_0 is the refractive index of the isotropic medium. For the small mechanical stress σ, the refractive index changes $\Delta n_{\parallel}$ and $\Delta n_{\perp}$ are proportional to the mechanical stress σ where $\Delta n_{\parallel}$ ($\Delta n_{\perp}$) is the refractive index change for oscillating light parallel (perpendicular) to the stress direction. The appropriate differential quotients are called the stress optical coefficients: $K_{\parallel} = \frac{dn_{\parallel}}{d\sigma}, K_{\perp} = \frac{dn_{\perp}}{d\sigma}$ with $K = (K_{\parallel} - K_{\perp})$ (3.55 × 10^{-12} Pa^{-1} for fused silica at 546 nm). The difference in the optical path length, also called the retardance R, can be easily measured and is proportional to the stress-induced birefringence $n_{\parallel} - n_{\perp}$ and the birefringent layer thickness *d*. As a simple view, for a single axis stress state, R can be directly related to the principal stress components and the stress optic coefficient K by the following equation: $R = (n_{\parallel} - n_{\perp}).d = (K_{\parallel} - K_{\perp}).d.\sigma = K.d.\sigma$. The orientation and the amount of birefringence is thus related to the amount of stress applied in a given point via the photoelastic tensor.

Femtosecond laser direct writing and stress field

As mentioned earlier, femtosecond laser exposure of SiO_2 leads to various structural modifications including the appearance of stress-fields for different reasons. As the laser pulse energy increases, there are two types of structural modifications of interest here. First, the Type I modifications where homogeneous optical changes occur, it leads to an increase of refractive index in SiO_2 (albeit negative in most other glasses) mostly attributed to a permanent glass densification. Moreover, a tensile stress field and a minor contribution of point defects centers (typ. 25%, see chapter 3) are also contributing to the observed Δn. In contrast Type II modifications correspond to the formation of porous nanogratings [63, 92]. During the decomposition of SiO_2, many nanopores or nanocavities are created within these hot plasma nanolayers leading to a net glass volume expansion [121, 122], which correlates with the formation of nanogratings. The specific glass volume is expanded inside the Type II irradiated zone, and corresponds to the appearance of a permanent strain $\varepsilon^p > 0$ (whereas it is negative for a densification e.g. Type I in SiO_2). The later results into elastic strain $\varepsilon^e < 0$ as a direct response of the material, and therefore a compressive stress σ within and around the laser-modified region. According to the photoelastic effect, when a stress is applied to a material, the latter develops a form of linear birefringence. In addition, dealing with the stress profile measurements, Champion et al. have used a laser-written pattern, which enlarges the span of the stressed region, and derived an equation to model the stress field accordingly [121]. Their results indicate that the stress surrounding the irradiated area should depend on the nanolayers orientation with respect to the writing direction. Thus depending on the laser exposure conditions including polarization, the overall stress can be enhanced or minimized [122] leading to tunable birefringence values from 10^{-5} up to ~10^{-3} [123-125] but what about the neutral axis orientation?

Neutral axis orientation of the stress-induced birefringence around a laser written line

In the following we provide a simple qualitative model to illustrate the properties of the stress-induced birefringence in the proximity of a line written with series of femtosecond laser pulses. Here we discussed the following writing conditions: a single line with a length of around several hundreds of microns along x-axis, a width of a few microns (typ. 1-5 µm) along y-axis and a thickness of around 50-100 µm in the z-direction (the typical length of a laser track), which induces a field of displacement u_z mainly perpendicular to the widest face of the sample namely (x,y) plane.

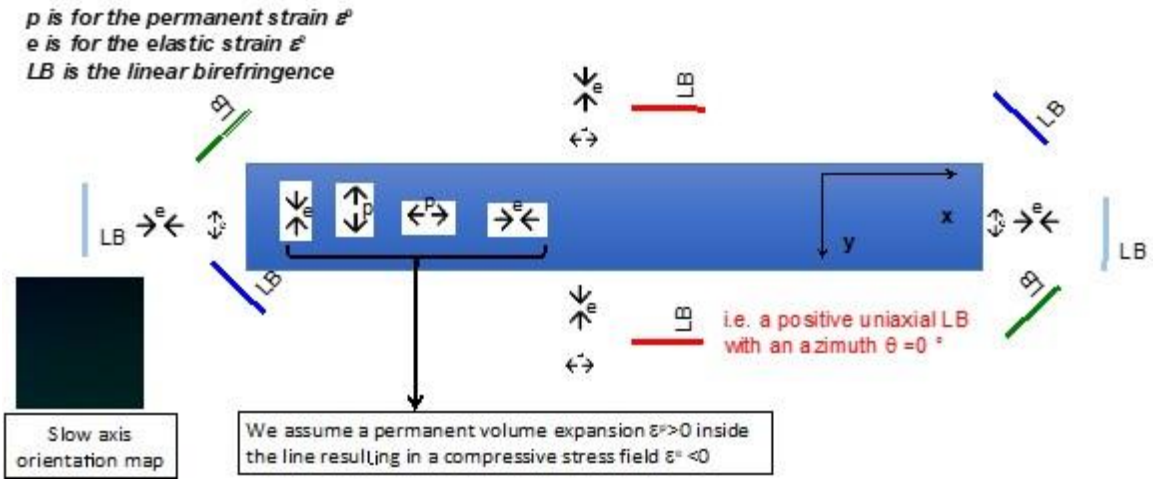

Figure 1-12: Scheme of laser line represents together with permanent strain (volume expansion) and related elastic strain within Type II regime. The slow axis orientation of the resulting stress-induced birefringence (notes LB) is shown out of the laser line and is code in color following the orientation map shown in the bottom left.

Within the line, nanogratings consist of planar structures i.e. lamellas made of nanoporous SiO_2 that are in expansion. Thus nanogratings formation implies a net volume expansion within the line: it is a positive permanent strain ${\varepsilon^p}_{Type\ II} > 0$ (inside the laser irradiated zone), therefore the response of the material leads to a negative elastic strain ${\varepsilon^e}_{Type\ II} < 0$ and the related stress field σ being in compression. Consequently, the Δn decreases (within porous nanolayers but also in the overall Type II affected volume in agreement with the observed net volume expansion) and *the slow axis direction of the stress-induced birefringence is parallel to the written line* (the red line in the *Figure 1-12*). Here the slow axis orientation is only determined by the geometry and does not depend on the laser writing polarization as a first approximation (except at the two extremities of the written line where the slow axis is azimuthally distributed). In other words, whether the laser writing polarization is aligned along x or y, the slow axis orientation remains unchanged. However, stress-induced birefringence amplitude will be different [26]. Next, if we consider an irradiated area like a rectangular or a square with the dimensions around 100x100 μm^2, such as a stressor, it can be considered as the superposition of lines (as a first approximation) and therefore the slow axis of the stress-induced birefringence results to be parallel to the lines.

Form birefringence vs Stress-induced birefringence

In the framework of this work, stress-induced birefringence can be induced by the presence of Type I or Type II modifications but also by their co-existence. On the one hand, if we consider a "pure Type II" modification (so associated Type I), the combination the form birefringence and stress-induced birefringence will have either an additive or subtractive superposition of the two components. For parallel (Xx) writing configuration we will have a subtractive superposition, whereas it is an additive superposition for perpendicular (Xy) writing configuration. Moreover, under thermal treatment (annealing) a part of the stress is expected to relax when approaching a temperature around $0.8T_g$ (T_g = glass transition temperature) for a few hours or $0.9T_g$ for a few tens of minutes as we will observe in the chapter 3. On the other hand, the formation of Type I modifications can happen along the laser track like in its tail but also likely occur inside Type II regions as suggested initially by Bricchi [61] and later by Bellouard [126] and Poumellec [127]:

- In the first case, the measured retardance corresponds to two "additive" contributions $R_{Type\ I} + R_{Type\ II}$ but one needs to consider different problems including overlapping and the respective neutral axis orientation of these contributions (which can lead to additive or subtractive effects).
- In the second case, Type I modifications might be present either between the nanolayers (refractive index n_2) as suggested in the literature [61] but also in the material (refractive index n_{sg}) surrounding the nanopores inside the nanolayers (refractive index n_1).

Stress-induced birefringence and annealing treatments

For going a step further, we can exploit the thermal annealing treatments. Indeed in the literature it has been demonstrated that Type I modifications (and its stress-induced birefringence) will be erased at a lower temperature than the nanogratings themselves (i.e. porous nanolayers) during the thermal treatments [60, 128, 129]. Thus depending on the location of Type I modifications and on the laser writing configuration, the relaxation of the permanent densification (and also point defects but to less extent) under annealing will impact the overall retardance measurements in different ways:

- Optically: by affecting the refractive index difference $|n_2 - n_1|$).
- Mechanically: by increasing the average volume expansion $\varepsilon^p{}_{\text{Type II}}$ in the affected volume.

However, the erasure of Type I densified zones has another collateral mechanical effect that appears to be dominating. The relaxation of the glass densification ($\varepsilon^p{}_{\text{Type I}} < 0$) is thus accompanied by an increase of the net volume expansion ($\varepsilon^p{}_{\text{Type I I}} > 0$) within Type II regions since there are two contributions to the total permanent strain that exhibit opposite signs i.e. $\varepsilon^p{}_{\text{Type II}} = \varepsilon^p{}_{\text{Type I}} + \varepsilon^p{}_{\text{porous}}$, where $\varepsilon^p{}_{\text{porous}} > 0$ is related to the porous nanolayers. This could explain the unexpected increase of the retardance or index modulation in FBG (Fiber Bragg Gratings) observed in the literature [60, 130, 131] but also our observation in chapter 3, 4, 5 where the stress-induced birefringence (measured between two stress bars) is first increasing (600-1000 °C) before to relax at higher temperature (typ. above 1000 °C).

1.5.3 Point defects formation and annealing within Type II regime

In addition to the form birefringence and stress-induced birefringence we mentioned above, the nanogratings also contains a variety of point defects. Through their optical absorption bands, mostly located in the UV range, they are contributing to the observed refractive index changes through the Kramer-Kronig (KK) relationship. Generally, most defects are absorbing in the UV-VUV range and they are contributing positively to the refractive index changes measured in the Vis, near IR range. Once these defects are bleached under thermal treatment, the refractive index is therefore found to decrease. Consequently, the existence of such point defects could affect the measured birefringence (more accurately the measured retardance) that is usually too simply attributed to the nanogratings form birefringence. *However, and according to most of the literature, the contribution of point defects to the nanogratings refractive index difference n_2-n_1 (and thus birefringence) remains minor as described below in a short review.*

Point defects generate within type II regime

In the literature the main part of the losses observed for Type II modifications has been attributed to the Rayleigh scattering due to the inhomogeneous nanostructure, which has a $1/\lambda^4$ dependence for spherical inclusions much smaller than the probing wavelength. Additionally, two absorption bands can be distinguished at short wavelengths that are attributed to SiE' centers at 210 nm, (≡Si·, an unpaired electron in a silicon atom bound to three oxygen atoms), and ODC(II) at 245 nm, (≡Si-Si≡, a divalent silicon atom) [132]. For comparison, structures exhibiting isotropic refractive index increase showed negligible scattering and only absorption band related to E' centers could be observed at short wavelengths. The E' centers, together with NBOHC (non-bridging oxygen hole centers), are produced as a result of self-trapped exciton decay [133, 134]. Indeed, recently an absorption peak at 244 nm was attributed to the NBOHC [134]. However, the absorption of NBOHC normally peaks at 260 nm and has much wider width of the peak, which extends to almost 300 nm [18]. The NBOHC can react with E' centers when some critical concentration is reached forming ODC(II) as it is sketched below [52, 84, 135].

$$STE \left| \begin{array}{l} \xrightarrow{\text{radiative or non-radiative recombination}} \varnothing \\ \qquad\qquad\qquad\qquad \text{structural modification} \\ \qquad\qquad\qquad\qquad \text{like glass densification} \\ \longrightarrow SiE' + NbOHC \longrightarrow SiODC(II) + O_2 \end{array} \right.$$

Figure1-13:The reaction of the defects.

Point defects and annealing treatments

The study on the thermal stability of the nanogratings is of great significance to understand not only the mechanisms of erasure but the writing ones as well and the contribution of each mechanism to the measured birefringence. Indeed, in 2006, Bricchi et al. [59] reported the first experiments related to the annealing of fs-laser written Type II modifications (Laser conditions: λ = 800 nm, 100 kHz, 0.06 mm/s, pulse duration = 200 fs), which showed extraordinary thermal stability: such modifications can withstand at least 2 hours at 1000 °C without any degradation. The unexpected behaviour displayed by these structures, namely a slight growth of the absolute value of the ordinary and extraordinary refractive index difference as the temperature progressively increased in the 200-500 °C range, was suggested to come from the erasure of point defects centers like SiODC and SiE' defects generated in the irradiated volume.

This was followed by a few studies as summarized here. In 2012, Richter et al. [136] confirmed that nanogratings exhibit an extremely large temperature stability, i.e., up to 1150 °C for 30 minutes (Laser conditions: λ=1030-515 nm, 9.4 MHz, average power = 5 W, NA = 0.55, pulse duration = 450 fs). Investigations of the thermal stability of nanogratings showed that E' centers vanished upon annealing, whereas NBOHCs remained stable up to 900°C after initial hydrogen-recombination. In addition the signature of free O_2 is detected up to ~600 °C using Raman spectroscopy (see Figure 3.14 of Ref. [137]), and agrees well with the aforementioned defect bleaching. Thus, they proposed that nanogratings based components could be rendered truly thermally stable by a thermal annealing in order to erase the unstable part mostly related to point defects.

Krol et al. [138] have subsequently investigated the thermal stability of femtosecond laser modification inside fused silica (Laser conditions: λ=800 nm, 1 kHz, NA = 0.25, 0.05 mm/s, pulse duration = 150 fs). Raman and photo-luminescence spectroscopy showed that fs-laser induced NBOHC defects completely disappeared at 300 °C (for a 10 hours annealing), whereas changes in Si-O ring structures only anneal out after heat treatment at 800-900 °C (for a 10 hours annealing). After annealing at 900 °C optical waveguides written inside the glass had completely disappeared whereas more significant damages induced in the glass remained.

In 2014, Qiu et al. [139] highlighted that the linear birefringence response of the nanogratings experiences a slight increase with increasing annealing temperature up to 900 °C (Laser conditions: λ=800 nm, 1 kHz, NA = 0.55, 0.01 mm/s, pulse energy = 2 µJ, pulse duration = 150 fs, laser polarization = 45°） in agreement with Bricchi et al. [59]. But after annealing at 1100 °C for 1 h, the birefringence sharply decreased by a factor of 4. They also monitored the so-called "defects" lines (labelled D_1 and D_2) using Raman spectroscopy as a function of temperature. These lines are related to 3 and 4-membered rings in the silica network.

In chapter 3, in the paper "An overview of the thermal erasure mechanisms of Femtosecond laser-induced nanogratings in silica glass", some silica samples were annealed for 30min at 600 °C. The absorption bands attributed to E' and ODC(II) defects were annealed for Type II modifications as it can be seen in *Figure 1-14*. Note that all point defects generated within Type I modifications were also completely erased in similar conditions (2 hours at 450 °C) [140]. As a result, significantly lower losses were measured from 200 to 350 nm. In the visible range, however, no major improvement in optical quality was observed.

The retardance variation of Type II structures was also measured from 200 nm to 2100 nm in the same samples [140] as shown in *Figure 1-14 (b)*. The retardance dependence with the wavelength shows a steady rise in the spectral region from 200 to 680 nm and when asymptotically decreases to a plateau extending to at least 2.1 µm. A long plateau tail is expected as at longer wavelengths the retardance approaches asymptotically to the value predicted by the effective medium. The annealing for 2hours at 450 °C decreased the overall retardance value only by than 5% whereas all defects were bleached. This indicates that defects centers exhibit only a minor contribution to the observed birefringence for the chosen writing conditions.

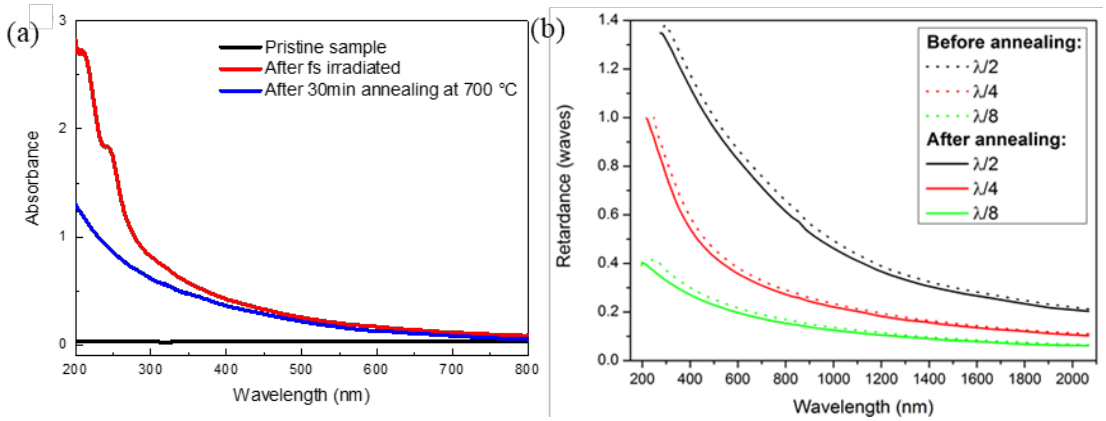

Figure 1-14: (a) Spectral absorbance of pristine, irradiated sample (at 1.5 µJ/pulse) and after 30 min annealing at 600 °C. (b) Spectral retardance dependence before and after annealing (2 hours at 450 °C) measured with

the ellipsometer. The target retardance values were half, quarter and eighth of 1030 nm. Graph extracted from Ref. [140]. The laser parameters were: 1030 nm, 250 fs, 0.6 NA, 100kHz, 0,1 mm/s.

To sum up on point defects, it is still not fully clear how the point defects are contributing to the observed birefringence but this appears quantitatively small. We can think about two main cases: 1) the anisotropic/oriented defects and 2) isotropic defects but spatially distributed in an anisotropic way, both of them can create small amount of birefringence.

- The first possibility would be the formation of anisotropic and oriented defects that would create a linear dichroism and thus a linear birefringence through KK relationship. However, we did not detect any LD band in the UV-Vis range in the PhD work of Jing Tian. LD bands were observed recently but only around 1.2-1.4 µm. The apparent linear dichroism in the UV-Vis range has been attributed to polarization dependent light scattering. Indeed, the arrangement of porous nanolayers creates anisotropic light scattering resulting in a linear diattenuation [117] (rather than linear dichroism) tail observed in the UV-Vis range. Because the impact of anisotropic/oriented defects appears no significant (no linear dichroic bands have been observed), we chose to ignore it in the following.
- The second possibility about distributed isotropic defects can separate itself into two branches. On the one hand, defects are present between the nanolayers (area of index n_2 in *Figure 1-11*). When they are bleached under thermal treatment, n_2 decreases and therefore the retardance R (proportional to $\mathrm{n}_2 - \mathrm{n}_1$) decreases. On the other hand, we expect the formation of defects inside the nanolayers (area of index n_1 in *Figure 1-11)* especially in the material surrounding the nanopores (n_{sg}). When they disappear during the heat treatment, the refractive index n_{sg} (and n_1) decreases and thus the refractive index difference $|\mathrm{n}_2 - \mathrm{n}_1|$ increases resulting in an increase of the retardance deduced from the form birefringence model.

Compared with the form birefringence and the stress-induced birefringence, although the defects induce a minor effect to the nanogratings refractive index difference $|\mathrm{n}_2 - \mathrm{n}_1|$ (and thus on the measured birefringence or retardance), they have still to be considered as a part that cannot be ignored. This is especially the case when considering their sensitivity to the thermal stability that will impact the response of photonic objects such as Fiber Bragg Gratings, or the measured retardance R when we study the erasure of nanogratings written in a bulk glass sample. Another example is their contribution to the reduction (typ. 40%) of the coefficient of thermal expansion (CTE) observed by Y. Bellouard's group within Type I regime [141], which was attributed to the presence of point defects. Note after an annealing of 10 hours at 300°C most defects were erased and CTE recovers its initial value like the pristine glass.

1.5.4 Conclusion on anisotropic linear properties thermal stability

In this section, we summarized the different contributions of the total birefringence response in silica glasses induced by femtosecond laser irradiation, as well as their corresponding erasure mechanism during a high temperature annealing process as summarized in *Figure 1-15*. Those events are not necessarily characterized in our work but have been synthetized both from literature and from our observations.

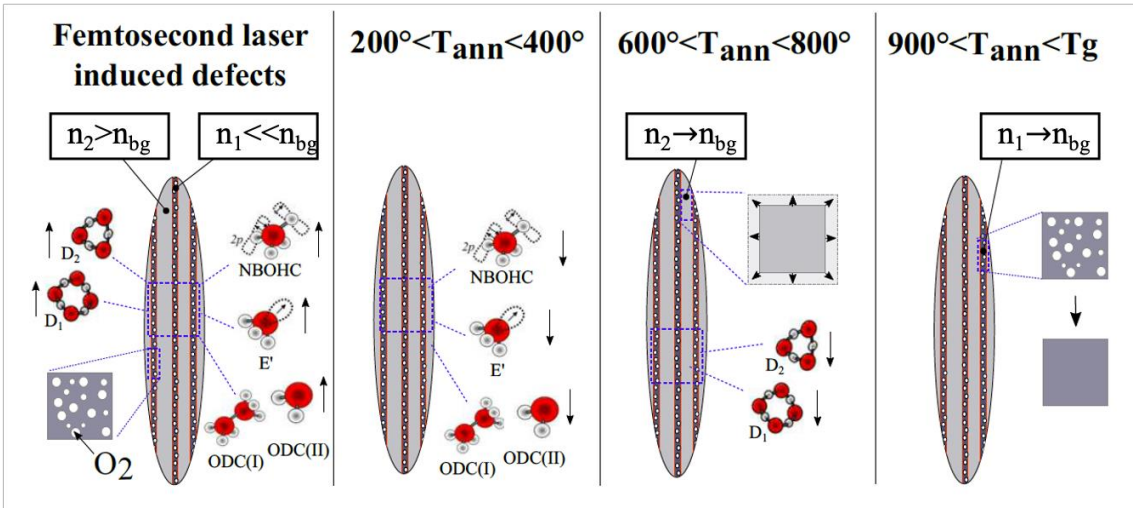

Figure 1-15: An illustrative summary of laser induced defects and changes for the nanogratings modifications under step isochronal thermal annealing at T_{ann}. n_2, n_1 and n_{bg} are the densities of the non-porous layer, nanoporous layer and pristine substrate, respectively. T_g is the glass transition temperature of SiO_2 (typ. T_g is around 1120°C for SuprasilCG) (taken from [142]).

The results of Raman and UV absorption spectroscopies had revealed the effect of defects on nanogratings structural modifications. However, it should be pointed out that they induce a minor effect to the nanogratings refractive index difference $|n_2 - n_1|$ (and thus on the measured birefringence or retardance). The point defects centers are bleached under a fairly low temperature thermal treatment (< 600 °C) and only minor changes (typ. < 5%) in the retardance value can be found in this temperature range. The subsequent unexpected rise from 600 °C - 1000 °C is attributed to the co-existence of Type I (densification) and Type II modifications, the erasure of the former occurred at this stage and likely caused an unexpected increase of both the overall retardance R but also the stress-induced birefringence (as shown in chapter 3). Then, through monitoring the anisotropic optical properties of the irradiated area and the surrounding stress-induced birefringence area during the annealing process, it is determined that stress relaxation (typ. around 30 min at 1100 °C) is an important factor leading to full erasure of circular optical properties associated with a slight decrease (typ. 20%) of the linear birefringence [143]. Finally, at high temperature the last contribution is related the nanopores size and their filling factor (ff_{porous}), which have been determined by the SEM micrographs. In a recent work our group has revealed that the evolution of the pore size can be calculated by the Rayleigh-Plesset (R-P) equation under a viscoelastic regime revealing the key role of the glass viscosity behavior at high temperatures [144]. More details will be presented in Chapter 3, and discussed in Chapter 6.

1.6 Potential applications based on Femtosecond laser irradiation

Femtosecond laser pulses provide a powerful electric field, which can exceed the binding ability of valence band electrons, and thus can make tremendous changes in the electronic system of molecules or atoms. During the interaction between laser and matter, femtosecond laser pulses show different properties from picosecond and nanosecond pulses, such as a small heat-

affected area, a strong effect can break the optical diffraction limit and good spatial selectivity, etc. These characteristics have important application value in many fields. Such as ultra-fine processing, micro photonic device manufacturing, medical precision surgery, long-term data storage, optical sensors, etc.

1.6.1 Long-term data storage

Through the spatial arrangement of the above mentioned 3D localized modifications high-density optical storage can be realized. In this view one can use different “support” from isotropic index changes (Type I) to the formation of the voids resulting in a microvoids (Type III).

A decade ago, the results of a joint project “300-million-year data-storage” which launched by Hitachi (Japanese company) and Prof. Kiyotaka Miura’s group had proved the possibility of this application [145, 146]. Using a femtosecond pulse laser with the High-speed high-density recording technology, when the laser pulse is irradiated inside the silica glass, dots with different refractive indices are formed. Digital data is recorded with this dot as "1" and the part without dot as "0". In order to increase the recording capacity, a multilayer recording technology has been developed that optimizes the laser power, the interval between dots to be formed, and the interval in the depth direction, enabling high-density recording. High recording density can be obtained by forming multiple recording layers inside the silica glass by changing the focus position of the Femtosecond laser. By making four recording layers, a data recording density equal to 1.5 GB/inch² was achieved. A batch recording technology has been also developed that records 100 dots at a time using a spatial phase modulator (A device that two-dimensionally modulates the amplitude and phase of light) that can modulate the amplitude and phase of light in a two-dimensional manner to improve the recording speed. In addition, accelerated ageing test in which heating was performed at 1000 ° C for 2 hours confirmed that data can survive to such “deterioration”. This indicates that the long-term storage of data for hundreds of years (or potentially more) is possible and this laser direct writing technology could be expected as a new long-term information preservation technology.

In recent research results, Prof. Kazansky from “Optoelectronics Research Centre” from the University of Southampton has further develop the recording and retrieval processes using five-dimensional (5D) digital data by femtosecond laser writing [147]. In traditional optical storage such as DVD and CD, people usually only use three spatial dimensions to burn and etch one or more layers in the “plastic disk”, causing many tiny pits in it, so as to achieve the purpose of storing data. However, through the role of the femtosecond laser, two new dimensions will be introduced. When the femtosecond laser irradiates the silica glass, it produces also thousands of tiny pits but with “dots made of nanogratings”. The birefringence from the nanograting will bring two additional parameters: the slow-axis orientation was defined as the fourth dimension and the strength of retardance was the fifth, which defined as a product of the birefringence and the length of the structure. These two additional dimensions were introduced to the three spatial coordinates and manipulate them by modifying the polarization and light intensity, the 5D optical data storage can be achieved as shown in *Figure 1-16*.

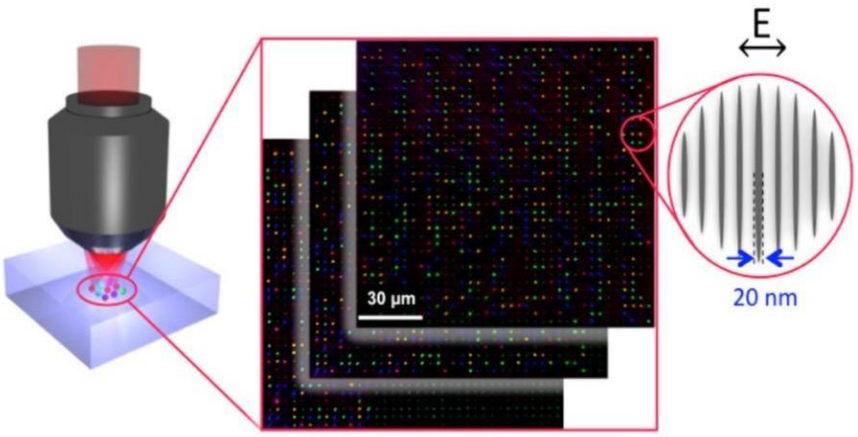

Figure 1-16: 5D optical data storage, written in fused quartz using a femtosecond laser. Three spatial dimensions and two optical ones (the slow axis orientation and the retardance) are exploited (taken from [148]).

The storage manufactured by this technology has 360 TB/disc data capacity. It has also passed the thermal stability test up to 1000 °C for a few hours, so it can be deduced from a simple Arrhenius law that it can maintain 13.8 billion years in a 190 °C environment and can maintain a virtually unlimited lifetime at room temperature. Note this a simple view here and this lifetime prediction is neither accurate nor reliable since glasses have configurational and chemical disorder that must be considered when performing such kind of predictions. Anyway this reveals that femtosecond laser irradiation has brought huge progress to Long-term data storage.

1.6.2 General overview of the main fiber optic sensors

Fiber optic sensors are used to take advantage of their compactness (<250 µm in diameter), their resistance to electromagnetic waves and the possibility of working on a long length of fiber to make or transmit the measurements. In addition, some of these sensors can be linearly multiplexed: several sensors can be used on the same optical fiber. This characteristic then makes it possible to reduce the number of fibers to be used to measure the temperature at several positions relative to the thermocouples, which can only make a measurement at a single point. There are many fiber optic sensor technologies that exploit different optical properties of the fiber. These technologies can be generally classified into three types:

- ***Gratings-based sensors:*** based on the presence of modifications in the optical fiber with a periodicity defined as required, such as:
    - Bragg grating sensors
    - Long pitch array sensors
    - The inclined line sensors such tilted fiber Bragg gratings
- ***Interferometric sensors****:* based on an intrinsic or extrinsic interferometric cavity; such as:
    - SOFO sensors (a French acronym for Surveillance d'Ouvrages par Fibres Optiques)
    - Fabry–Perot sensors
    - Mach-Zehnder interferometer sensors
    - Sagnac interferometer sensors
    - Sensors based on micro-bend losses

- ***Distributed sensors:*** based on the scattering of light in the material (scattering occurring in the optical core of the fiber).
    - Distributed sensors based on Rayleigh scattering
    - Distributed sensors based on Raman scattering
    - Distributed sensors based on Brillouin scattering

Some of the sensors are commercial sensors that have been used in industry, the following *Table 1-1* will specifically introduce their characteristics. A presentation about the characteristics of various sensors and more details will be shown in Appendix 2.

Table 1-1: Characteristics of optical fiber sensors used industrially (taken from [149]).

	Bragg grating sensors	**SOFO sensors**	**Fabry Perot sensor**	**ROTDR (Raman)**	**BOTDR (Brillouin)**	**OFDR (Rayleigh)**
Type	- Point - Distributed	Long gauge (> 10 cm)	Point	Distributed	Distributed	Distributed
Measurable parameters	-Temperature -Deformation -Rotation -Pressure	Deformation	-Temperature -Deformation -Rotation -Pressure	Temperature	-Temperature -Deformation	-Temperature -Deformation -Rotation
Multiplexing	- Distributed - Spectral multiplexing	- Parallel - Time multiplexing	- Parallel - Time multiplexing	Distributed	Distributed	Distributed
Measuring range or number of sensors	1000 sensors per fiber (over 10 km)	1 sensor per fiber	1 sensor per fiber	10 km (possible for 30 km)	20-50 km	30-70 m (possible for 2 km)
Spatial resolution	2 mm	Ø	1 mm	?	?	22 µm
Minimum gauge length	Ø	Ø	Ø	1 m	1 m	1 mm
Temperature resolution	0.01 °C	Ø	0.1 °C	0.1 °C	0.2 °C	0.1 °C (2 cm gauge)
Strain resolution	0.1 µε	1 µε	0.15 µε	Ø	10 µε	1 µε (2 cm gauge)
Maximum operating temperature	1000 °C (even 1200 °C on heat-treated fibers)	?	Usually 250 °C (1100 °C if the cavity is microstructured fiberglass)	700 °C (depending on the fiber)	700 °C (depending on the fiber)	775 °C on SMF-28 fiber (850 °C on fibers with a gold coating)
Advantages	- Accurate - High resolution	- Long gauge - High spatial resolution	- High sensitivity - Accurate	- Very high spatial resolution	- Very high spatial resolution	- Very high spatial resolution
Drawback	Sensitivities of	Low	Single	- Only	Sensitivities of	- Low speed

	the various related parameters	measuremen t speed (~ 10 s)	measuring point	temperature measurement - High cost	the various related parameters	(~ 10 s) - Sensitivities of the various related parameters

1.7 Thermal stability of the laser-induced refractive index changes in fibers

On the one hand, full knowledge of the thermal stability of photo-induced refractive index changes has both scientific and practical interest. For example, it can help to identify the chemical species responsible for the index changes by looking for any correlation between temperature-induced decays of these species concentrations and that of the index change. On the other hand, most applications require a long device lifetime and, at least, the possibility of forecasting possible spontaneous degradation of the photo-induced index change. In the case of optical fibers, there is an extensive literature about the thermal stability of fiber Bragg gratings (FBGs). Here it is necessary to take a closer look at the mechanisms that lead to a modification of the refractive index because as long as these changes in the fiber persist, an FBG is also "thermal stable". Which mechanisms play a role here depends heavily on the laser writing conditions. As this topic has been reviewed in recent papers [150-155], in the following, we only present a quick overview of the different types of gratings, their mechanisms of formation and the temperature stability.

1.7.1 UV FBGs

Let us consider UV-laser writing of FBGs mostly within germano-silicate fibers. A number of BG types have been distinguished over the last three decades and these have been characterized by markedly different spectral and thermal behaviors.

Type I and Type In FBGs

So-called Type I gratings are mainly based on VUV-UV absorption changes, which arise when exposed to low-intensity ultraviolet (UV) light, without any "damages" of the glass. Usually, there is a linear relationship between the reflectivity and the fluency of the laser (energy density accumulated at the location of the fiber overall pulses used for writing) for low-reflectivity gratings. For highly reflective gratings, the reflectivity gradually saturates as the fluency grows. Typical changes in the refractive index are usually in the range from a few 10^{-5} to a few 10^{-3} depending on the chosen laser wavelength and the regime (typ. cw or ns). The spectra of type I gratings are mostly very narrow-band and symmetrical, which is why they are often used for applications in sensor technology.

When exposed to UV radiation, there are two main mechanisms that lead to a change in the refractive index. On the one hand, there is the formation (or transformation) of defect centers and their related absorption bands. The change in the refractive index is usually described by the Kramers-Kronig relationship, according to which an absorption band in the visible (VIS) and UV-

VUV range can cause changes in the refractive index up to the near-infrared range (NIR) [156]. On the other hand, there is also a mechanism that leads to compaction (a permanent negative strain) of the glass matrix accompanied by the formation of an elastic strain field (and thus a tensile stress field), which have a direct influence on the refractive index via the photo-elastic effect [157, 158]. Both mechanisms (defect centers and compaction) can be the cause of type I gratings.

Type In FBGs (also called Type IIA and negative index gratings), are formed in hydrogen-free silica fibers after a kind of regeneration [159-162]. This regeneration is thermally induced but through an extended laser exposure times using CW or pulsed UV lasers. Similar results may also be achieved through annealing in a furnace [163]. Type In gratings likely forms due to the relaxation of internal stresses that are induced from the UV radiation.

Type II FBGs

Type II gratings are the result of optical damages within silica glass bulk. They can be inscribed by nanosecond UV lasers or shorter pulsed, femtosecond lasers with no constraints on the laser wavelength by the way. These are damage gratings inscribed by multiphoton excitation with higher intensity lasers that exceed the bulk damage threshold of the glass. The lasers employed are usually pulsed in order to reach these intensities. As early as 1993, UV nanosecond lasers were used for the imprinting of Type II "100% "reflective FBG using a single pulse [164], paving the way for laser direct writing on the fiber draw tower [165]. Type II gratings are extremely stable in extreme temperature environment (at least 2 hours, above 1000 °C). However, the "mechanical defects" generated light scattering and the FBG spectra are wide and distorted, which further limits their capacity for wavelength multiplexing. Femtosecond pulses produce much better type II gratings, but their very low coherence length remains an important practical limitation. It will be developed in more detail in Section 1.7.2.

Thermal Stability

Perhaps the most common kind of FBGs used for "high-temperature operation" are stabilized Type I FBGs. Generally, Type I gratings are stabilized to meet telecommunication specifications (-20 °C ≤ T ≤ +80 °C for time, t > 25 years) but can be processed to operate at much higher temperatures for short, but still useful, timeframes depending on the application. For example, a Type I FBG can be thermally annealed at 700 °C, strongly reducing the FBG "strength" (refractive index contrast and thus reflectivity) but allowing operation for finite time periods up to 600 °C [166]. Other approaches to stabilize Type I gratings involve some photosensitization techniques [167] to "partly remove" the unstable component generated during grating inscription.

The Type In FBGs are capable of operating up to T ~ 500 °C before decaying [159, 160]; however, by using higher intensity exposures, generating higher local temperature, the functionality may be extended to T ~ 700 – 800 °C in step-index [161, 162] and photonic crystal fibers [168]. Thermal properties strongly depend on the dopant nature (mostly Ge but also Boron that is usually detrimental for thermal stability) and doping concentration, e.g. 1 hour at 500 °C in highly (30 mol%) Ge-doped fiber; or 1 hour at 700 °C in a Ge-B co-doped fiber [161, 162].

Using a single 40mJ UV pulse of 20ns duration at 248 nm, Archambault et al. exhibited the thermal stability of Type II gratings [164]. No significant modifications can be observed in the grating reflectivity below 800 °C after 24h heat treatment. Then if we increased the temperature to 900 °C, we could found out a very slow decrease and finally most of the gratings had disappeared after 4h at 1000 °C. Notice that the thermal stability of such gratings could be higher with using multiphoton laser writing and especially femtosecond laser inscription.

Dependence on pulse duration

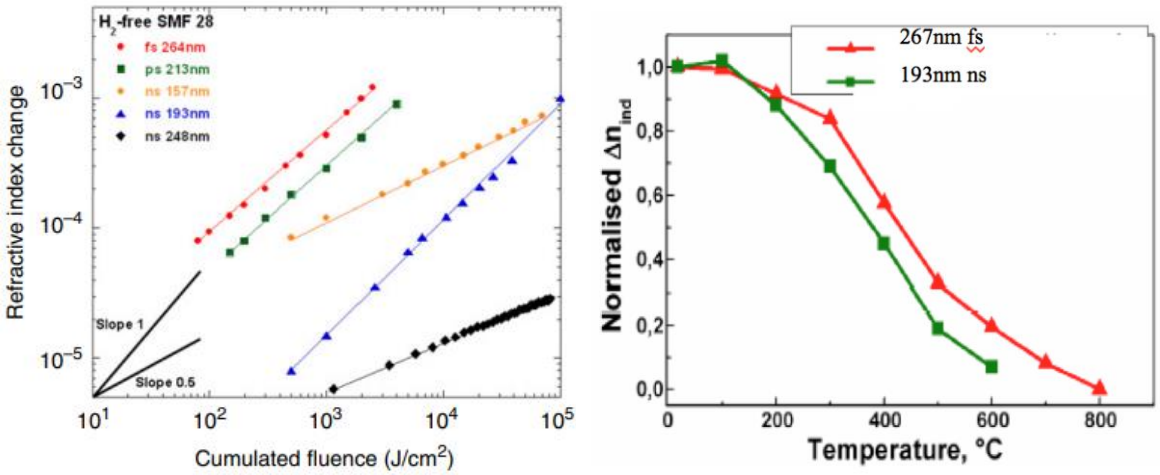

Figure 1-17. (a) UV-induced refractive index change kinetics in pristine SMF 28 fiber using UV lasers for various pulse durations (from ns up to fs) (taken from [58]). (b) the refractive index changes as a function of annealing temperature for 267nm femtosecond and 193nm nanosecond pulse duration.

Lancry et al, summarized the impact of laser pulse duration on the amplitude of the refractive index changes [58]. The results showed in *Figure 1-17* allow comparing UV nanosecond laser writing with UV picosecond/femtosecond pulse duration that may include specific advantages [169]. For example, the use of short wavelength (e.g. 213 nm) ps radiation may trigger two-photon processes (more efficiently than ns pulses) in the fiber core and cladding that are not directly dependent on highly absorbing dopants and defects. Furthermore, picosecond laser pulses can easily interfere through phase mask elements without the penalty of extreme spatial dispersion [169]; while interference pattern formation is straightforward using open interferometers without strict alignment requirements due to a limited coherence length as that holds for femtosecond pulses. In addition, picosecond pulses lead to significantly higher intensities compared with nanosecond duration, accelerating the growth kinetics.

Compaction driven index changes usually associated with bond breaking (defects accumulation) in the Ge-doped glass matrix due to two-photon absorption is usually more significant for the case of UV fs/ps radiation. The superposition of two photons in the UV range provides energy “quantum” that lies well above the band gaps of pure silica and germanosilicate glasses. Thus index changes due to UV induced compaction can steadily grow due to the short pulse duration and extremely high intensity, which promote non-linear interactions namely two or even three photons absorption processes.

1.7.2 IR-fs FBGs

Fabrication techniques, involving UV-photosensitivity, are, for the most part, limited to the production of one-or two-dimensional structures [170]. The pulse duration of a femtosecond

laser is on the order of ≈ 50-200 femtoseconds, making it easy to produce high peak power densities such as ≈ 100 TW/cm^2 after focusing the laser spot. As a result, the development of this type of near infrared ($\lambda_p \approx 820$ nm) laser has prompted the investigation of multiphotons reaction-induced photosensitivity in glasses that does not linearly absorb efficiently at the laser wavelength. Accordingly, it results in highly localized laser-induced effects including ablation, photo-structural changes and consequently changes in the refractive index and even birefringence or voids. As the process exhibits a highly non-linear dependence on the laser power density, it allows for the fabrication of three-dimensional photonic devices. As a result, the focusing conditions have to be carefully adjusted so that to avoid damages within the glass and to keep the exposure-induced propagation loss at a low-level [171, 172]. By so doing, good quality uniform devices can be written in various glasses including silica and Ge-doped fibers [173] without the need for any photosensitization process such as H_2-loading or others variants (OH-flooding, hypersensitization, etc…) [58].

Since nearly two decades, Ultrafast lasers are used to write FBGs (thereby known as femtosecond FBGs or fs-FBGs) either by using a phase mask [174] or by inscribing each grating plane point-by-point [175]. The use of visible or near infrared femtosecond laser light presents an inherent advantage of writing an FBG through the protective coating such as acrylate or polyimide [176]. Even if this coating does not usually withstand temperature beyond 350 °C, it is particularly useful to get a preserved polymer coating for packaging and deployment issues. The use of NIR radiation means the excitation of the silica band edge is a multiphoton process and therefore highly localized, leading to much finer gratings than those achieved using two-photon absorption with 193 nm light [177, 178]. Unlike the gratings inscribed using UV lasers, the mechanism responsible for index change does not necessarily depend (or much less) on core chemical composition, does not require hydrogen and leads to higher refractive index change in “non photosensitive materials” like SiO_2. Gratings written using fs radiation may be classed as either being above or below the above-mentioned modifications thresholds in section 1.4.

In SiO_2 or slightly doped SiO_2, **Type I IR-fs** are based on isotropic index changes are due to permanent densification (sometimes attributed to an increase of glass fictive temperature T_f [84]) with a partial contribution (typically 20%) of point defects [57]. However, Type I IR-fs FBGs can be completely erased by annealing at temperatures exceeding 800 °C (e.g. full erasure after 30 min at 1000 °C). **Type II IR-fs** gratings are attributed to the formation of self-organized nanogratings due to highly localized plasma ionization and oxide decomposition [63]. Due to their inherent “oriented phase separation”, these Type II fs-FBGs demonstrate remarkable thermal stability since no drift was observed up to ~ 1000 °C for 150 hours but after a stabilization for 1 hour at 1000 °C [60]. Going further, operating for 100 hours at 1050 °C reveals a slight (5%) decay of the reflectivity and a + 0.2 nm Bragg wavelength drift. This is likely associated with thermal relaxation of the net volume expansion (associated to nanoporous layers formation) at these temperatures. As relates to applications, fs-FBGs have recently been tested as temperature sensors for monitoring fluidized bed combustors, as well as for radiation resistant temperature sensors [179]. Refractive index modifications are highly localized and involve significant stress-induced changes in and around the irradiated regions. For this reason, the higher temperature regime is limited by the thermal response of both the surrounding regions and the fiber itself, which has not been relaxed prior to application. However when the fiber is pre-annealed (before FBG writing) at high temperature (typ. 5 hours at 1100 °C), Type II fs-IR FBGs are stable up to 1200 °C during 20 hours

[180]. Following this view, regeneration can also improve fs-FBG performance to some extent [181, 182]. In conventional single mode fibers (SMFs, Ge-doped silica glass), the point-to-point voids FBG (so called **type III fs-IR FBGs**) have slight loss of reflectivity (typically 20% of its initial strength) in less than 20 hours at 1000 °C, before stabilizing [183]. At 1050 °C, the reflectivity of point-by-point Bragg grating rapidly decreases to less than 20% after a few hours. Recently it was demonstrated that fs-FBGs fabricated via laser ablation in suspended-core microstructure fiber gratings can be operated at 1300 °C for 5 minutes [184].

Femtosecond FBGs are now commercially available [185, 186]. The main shortcomings are related to the lack of reliable lifetime prediction for long term operation above 800-1000 °C where many processes occur, including not only residual stress relaxation of both the fiber and the laser-induced modifications, but also plastic deformation and glass structural relaxation leading to changes of the glass disorder (and thus fictive temperature changes).

1.7.3 Physico-chemical methods used for enhancing the thermal stability of BG written in a standard telecommunication fiber

A widespread method used for increasing the stability of a BG after its inscription consists in post-annealing the BG for a time t_{anneal} at a temperature T_{anneal} above T_{use}. A coherent rationale of this method is formulated from the VAREPA approach (Variable Reaction Pathways framework) in ref. [151]. Basically the treatment wipes out the portion of the index change that would normally decay over the lifetime of the device and keeps only the stable portion of the index change [151]. This method proves to be effective for enhancing the stability of index changes in both H_2-Loaded and non-hydrogenated germano-silicate fibers. In general, the higher the desired temperature of operation of any grating, the higher the local annealing temperature required to stabilize it, a general consequence arising from the relaxation continuum of an amorphous system.

An alternative method for enhancing the stability of Bragg grating reflectivity consists in pre- or post-exposing the BG to uniform UV light [153, 154]. The assumption according to which the stability depends on the writing conditions can be put forwards to explain this observation as a blanket irradiation increases the proportion of large-barrier energy sites at the grating place [154]. Yet, due to a large mean index level of the mean index induced by the post-exposure, the stabilization method increases the thermal stability of the grating reflectivity at the expense of a larger Bragg wavelength shift [155]. The hydrogen treatments (OH flooding, UV hyper-sensitization, low-temperature hyper-sensitization) also increase the stability of Normalized Integrated Coupling Constant (NICC) and Bragg wavelength shift compared to those in the pristine counterpart [187]. Yet, as the above-mentioned treatments induce a large mean index level, the absolute shifts in the Bragg wavelength are also larger in the treated fiber, which is one key drawback of these methods.

Enhanced thermal stability by a pre-anneal and pre-stress treatment

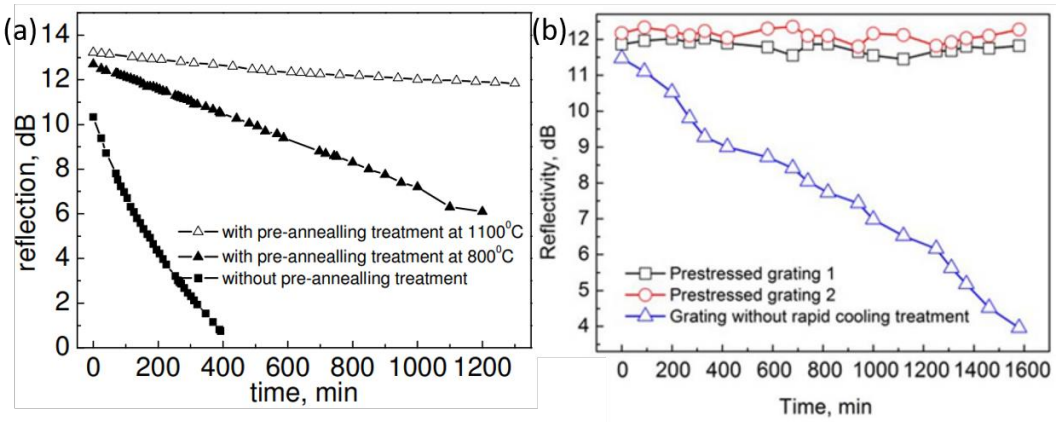

Figure 1-18: Change in the reflectivity of the type II-IR FBGs inscribed in (a): normal and pre-annealed fibers over a 1300 min period and (b): normal and pre-stressed FBGs (fabricated using 550 µJ pulse energy) over more than 26h at an annealing temperature of 1200 °C. (taken from [180, 188]).

It is well known that conventional optical fibers own residual stress that would have a negative effect on the thermal stability at high temperature e.g. when the working temperature approach $0,8T_a$ (T_a being the glass annealing temperature) for a few hours. Thus the residual stress can be released theoretically by high-temperature annealing to improve the thermal stability of the fibers themselves as shown recently by Li et al. [180]. The SMF-28 fibers were chosen and pre-annealed at 800 °C and 1100 °C respectively for about 5 hours to relax the residual stress prior any laser irradiation. Then, the Type II IR-fs FBGs inscription was performed on three fiber samples (without pre-annealing, pre-annealing at 800 ºC and pre-annealing at 1100 °C) by femtosecond laser for fixed writing conditions. Heating the gratings to 1200 ºC and holding them for 20 hours was then implemented to evaluate the thermal stability. The change in the grating reflectivity was monitored and exhibited in *Figure 1-18 (a)*. As we can observe, the FBGs on the pre-annealed fibers demonstrated significantly a better performance. After exposure of about 400 min at 1200 °C, the FBGs on the non-annealed fiber were almost erased, whereas type II FBGs written in the pre-annealed fibers revealed an ultra-high thermal stability. More specifically, the gratings written in the pre-annealed fibers at 800 °C have a slow decay rate and the reflectivity decreases by only ~2.44 dB after 700 min (about 0.21 dB/hour). The type II IR-fs gratings written in the pre-annealed fibers at 1100 °C show even better behavior, they were almost unaffected (10% decrease over 20hours) in the high-temperature environment at 1200 °C. *The thermal stability of the FBG can thus be improved by relaxing the residual stress in the fiber before any grating inscription. The background material, its residual stress and likely it fictive temperature are thus some key parameters to develop drift less fiber based sensors for high temperature operation.*

However, the fiber after high-temperature annealing treatment becomes brittle, which makes the grating manufacturing process more difficult. Another solution is proposed by Li et al. [188]. Firstly, use a laser to write the grating in the optical fiber, relax the residual stress in the optical fiber through high-temperature annealing treatment, and then perform rapid air quenching treatment to introduce reverse-compression stress into the optical fiber. Balance the tension caused by high temperature treatment. This treatment method similar to glass annealing will further improve the high temperature stability of FBG. The experimental results shown in

Figure 1-18 (b) successfully proved this proposition, compare with the pristine sample, the pre-stressed gratings exhibit clearly enhanced thermal stability, which is almost unaffected by thermal exposure at temperatures up to 1200 °C, and there is only a slight fluctuation of the grating strength during the 26 h test. Therefore, the thermal stability of the FBG can be improved by pre-stress the fiber after the grating inscription as well.

Chemical composition Gratings (CCG) and Regenerated FBGs

Another variant with superior temperature stability is "chemical composition grating (CCG)" [189] where a periodic index modulation can be "regenerated" after erasure of the UV induced Type I grating written in H_2-loaded germanosilicate fiber (also containing fluorine), if annealed ~1000 °C. The prediction was a local reduction, or increase, of fluorine in the UV-exposed zones at that high temperature through diffusion of HF. A subsequent study on annealing of type-I gratings at high temperature, however, has shown that the presence of fluorine is not necessary for this regeneration of index modulation [190]. So-called chemical composition gratings (CCG) are found in Er-doped fiber with other dopants such as Ge, Al and Sn – as the number of possible diffusing materials increased, a number of researchers settled on oxygen diffusion (through OH) leading to stoichiometric changes. Finally, these CCG are included in a more general category called Regenerated FBGs (RFBGs).

The general phenomenon of regeneration has been found in simple H_2-loaded germanosilicate fiber [191]. *In its simplest recognizable expression, regeneration involves the annealing and resurrection of a structure patterned into a glass through optical or thermal treatment. This pattern, or seed structure, has changed the thermal or optical history of the glass so that whilst the annealing is identical in all areas, the local response is different, equivalent to a local variation in quenching*. Regeneration is thus a way to achieve FBG operation above 800 °C mostly in Ge, B doped silica. Regenerated FBGs are fabricated by annealing a so-called seed grating, typically (but not always) a Type I grating. Hydrogen is often used (but not necessary) to further increase strain in processed regions versus those that are unprocessed. The hydrogen can be added to the fiber prior to seed formation or later before the regeneration process. The ability to introduce hydrogen after the seed grating fabrication is key for making possible the regeneration of draw tower gratings [192]. Thus a seed grating is fabricated in a hydrogen-loaded doped-silica fiber using a UV laser [193, 194] and subsequently regenerated at temperatures in the range of T ~ 800 – 900 °C. Note it is possible to also use femtosecond (Vis or IR-fs) lasers to inscribe the seed [181]. Since these fibers are mostly made of silica, these gratings can survive at T ~ 1295 °C [195] or even T ~ 1450 °C for 20 to 30 minutes [196]. Regenerated gratings have also been demonstrated to continuously operate at T ~ 890 °C for an impressive 9000 hours [197], also revealing ere some complex and non monotonous drift of the Bragg wavelength. In contrast to thermal stabilization of Type I and Type In FBGs, the high temperatures involved in the regeneration leads to the "complete" relaxation of stresses in the fiber. Regenerated gratings have, over the last years, proven to be a viable sensing technology in a range of areas, for example in the profiling of high temperature manufacturing equipment [198], dual pressure/temperature sensing for gas turbines [199], sodium cooled nuclear reactors [200], high temperature air flow meters for internal combustion engines [201] and train engine temperature regulation [202]. Regenerated gratings have also been utilized to make the first accurate measurements of fiber viscosity [203]. Complex RFBG structures such as phase-shifted gratings [204], chirped gratings [205]

and even final Bragg wavelength controlling [206] have been fabricated. Multiplexed distributed sensing also is possible [198, 207].

Regenerated FBGs are commercially available (e.g., [176]). However, this comes along with few shortcomings: devices are limited to only few fiber compositions (e.g. regeneration efficiency is low in pure silica core fibers), the thermal engineering process leads to brittle fibers, multiplexing FBGs in same fibers is possible [207] but difficult, and there is no available model to perform a reliable prediction of long term operation.

1.7.4 Chemical composition influence on the thermal stability of FBG

Sapphire FBGs

To achieve even higher temperature operation FBGs can be inscribed in materials with higher melting points oxide than SiO_2. Single crystalline aluminum oxide (sapphire, melting point > 2000 °C) optical fibers have been used with femtosecond laser fabrication [208-213]. Sapphire FBGs demonstrate remarkable thermal stability up to ~ 1600 °C for 6 hours after a stabilization for 20 minutes at 1745 °C [214]. Sapphire FBGs boast the highest temperature performance to date, operable up to 1800 °C. However, sapphire optical fibers presently are highly multimode to their having an air cladding. Moreover, they are crystalline, leading to both short lengths and a lack of flexibility given their fairly large diameters and to date they are closer to thin rods than real optical fibers. The next generation of fibers that may overcome this involves hybrid mixes of silica with aluminosilicate cores [215], provided their alumina concentration is sufficiently high to bring significant interest like imprinted oriented nanoscale phase separation or local nanocrystals (like Mullite $3Al_2O_3$-$2SiO_2$ or maybe even sapphire nanocrystals) with high melting temperature.

Aluminosilicate glass optical fibers with a high Al_2O_3 content

Highly “doped” aluminosilicate fibers (also called AS fibers in this PhD) have first been fabricated and reported in 2012 [216] by our project partner Prof. John Ballato at Clemson University (USA). In these non-conventional fibers, concentrations ranging from 25 to 55 mole% of Al_2O_3 (the rest being silica) were realized thanks to the molten core technique. In 2014, another group (IPHT Jena, Germany) fabricated fibers with 50 mole% of Al_2O_3 [215]. Fibers (and canes) with 15 to 55 mole% of Y_2O_3-Al_2O_3 into the fiber core were also fabricated [217] in 2009, again in the group of Prof. John Ballato. In 2014 and 2015, FBGs were inscribed in Al_2O_3-SiO_2 fibers (4%, 30%, 49% of Al_2O_3) [215, 218]. If the FBGs inscribed in the 4% and 30% Al_2O_3-doped fibers had lower thermal stability relative to conventional single mode fibers (like SMF28), on the contrary, 49% Al_2O_3 fiber exhibited superior thermal stability. Recent work from our group Ref. [219]) on a fiber containing 30 mole% of Al_2O_3-Y_2O_3 demonstrated that IR-fs Type II nanostructures in the fiber core had improved thermal stability with respect to its silica cladding. These recent results indicate that high Al content fibers have the potential to exceed the limit imposed by conventional silica fibers. Additionally, very recent modeling work has suggested ways to fabricate optical fibers with even higher concentrations (> 60 mol% Y_2O_3-Al_2O_3) by controlling fiber draw parameters [220]. More details about how the chemical composition influence on the thermal stability of FBGs will be discussed in this PhD.

1.7.5 Summary of different types of FBGs

Finally, to help the reader to understand better the different type of Bragg gratings and find the information more convenient, we summarize several key informations in *Table 1-2*, such as the main characteristics, fabrication techniques, maximum temperature of operation and wavelength shift as a function of temperature ($^{d\lambda}/_{dT}$) for the various types of fiber Bragg gratings we have discussed above.

Table 1-2:Typical grating specifications for high temperature operation.

Grating type	Characteristics	Fabrication techniques	Maximum temperature of operation (°C)	$^{d\lambda}/_{dT}$ ($pm\ °C^{-1}$)	Ref.
UV-Type I	Simple grating writing in photosensitive doped fibers, mainly germanosilicate, including doped photonic crystal fibers. Contributions from defect polarizability changes and structural changes like densification. Latent sensitization behavior, crucial for grating growth, observed. Stresses usually increase with irradiation.	Phase mask/point by point	~300 (~60h) reduce 70% reflectivity Full erasure after few hours at 600	Typ. 12	[221-224]
UV-Type In	Characteristic curve usually onsets after type I grating growth rolls over. Onset determined by fiber drawing history, composition, presence of H_2, optical intensity, applied stresses and hyper sensitization. Partial stress relief through anisotropic "equilibration"/relaxation of stresses. Under continued exposure at high intensities, increased strain that can lead to eventual fracturing and type II-like damage.	Phase mask	Full erasureafter ~700 (~1h)	12.8	[162, 224]
UV-Type II	Gratings produced with intensity exceeding damage threshold of the glass leading to damages, fracturing or void formation. Can also be done using ultrashort UV pulses with high peak intensity (cascade ionization and plasma generation leading to permanent damages and strong light scattering)	Phase mask/point by point	~1000 (~3h) reduce 80% reflectivity		[164, 224]
Regenerated or Chemical composition gratings	Gratings produced after annealing out type I gratings, usually regenerated at temperatures > 500°C and to 1100°C. This method has significant potential for optimization. Similarities with type II gratings although reflectivity is weak and therefore comparable losses and scattering not observed. Can be repeatedly cycled to very high temperatures with no degradation.	Annealing seed grating (usually a type I FBG)	Full erasure after ~1295 (~20min)	16.3	[194, 224]
fs-IR-Type I	Type I IR-fs modifications is featured by an isotropic growth of the refractive index with respect to the non-irradiated regime. They mostly are based on a glass fictive temperature T_f increase when the duration of the heat pulse corresponding to the light energy is greater than the glass relaxation time η(T)/G(T) (shear viscosity / shear modulus) with a partial contribution (typically 20%) of point defects.	Phase mask/point by point	Strong decay at 600 Full erasure after ~1000 (~20min)	Typ. 12	[182]
fs-IR-Type II	Type II IR-fs modifications are attributed to the formation of self-organized nanogratings made of oxide decomposition. They characterized by a high level of anisotropic index change and resulting birefringence.	Phase mask/point by point	~1000 (~150h): no sign of erasure	16	[60, 61]
Sapphire fs-FBG	Sapphire FBGs boast the highest thermal stability but lack the flexibility (short length fibers, high loss, multimode, low mechanical resistance)	Phase mask/point by point	Full erasure after ~1600 (~6h)	23 at RT 35 at 1500	[208]

Sapphire derived (or AS) fs-FBG	IR-fs Type II in the AS fiber core had improved thermal stability with respect to its silica cladding and have the potential to exceed the limit imposed by conventional silica fibers.	Phase mask/point by point	Full erasure after ~1200 (~1h)	[225]

An obvious conclusion of this section is that some care must be taken in analyzing the stability of the laser-induced index changes. Indeed, the stability of laser induced refractive index changes is defined by parameters such as the material composition, the optical power density, the characteristics of the laser used to illuminate the glass, the index changes strength etc… We note it is even more complex for Bragg grating because mainly two quantities, index modulation (proportional to reflectivity) and mean index (proportional to Bragg wavelength drift), define it. These quantities can exhibit different stability if they are based on different decay reactions or if the decay reaction (even if unique) is related to the writing one (e.g. stability depends on grating strength).

Conclusions

In this chapter, we first briefly introduce basic characteristics and relevant phenomena. The short-term vision of femtosecond laser direct writing (FLDW) is to make the ultrafast photonics manufacturing available within the next years to many fields of application, part of which being already known (e.g. integrated optics, microfluidics) and a majority being new applications (e.g. sensing, fully integrated nonlinear devices, optical components with specifically tailored properties in a wide range of transparent materials, micro-reactor for asymmetric synthesis, local piezoelectricity, multiferroic domain orientation). As recognized in Photonics community, lithography and laser material micro-processing are complementary at the mid/long term. The advantages of the fs laser manufacturing are tightly linked to the unique properties of the photon:

- Due to small photon energy (≈ 1eV) when compared to the bandgap energy (≈ 9eV in silica) and ultrashort pulse duration (minimized heat diffusion, delivering a finite quantity of energy in very short time, multiphoton ionization/absorption), the dose can be tailored precisely to the process resulting in very high 3D precision.
- Contact-less processing is possible opening up the way to completely novel processes.
- The ability to precisely alter the material properties in the volume of a transparent medium uniquely enables the generation of photonic devices both in the bulk and in fibers. Furthermore, the generation of linear and potentially circular anisotropic optical properties in amorphous media, but also 2nd order non-linear susceptibility opens up new exciting possibilities.
- Variable parameters such as wavelength, power, polarization and especially their spatio-temporal distribution along the beam propagation and in the beam cross-section, make it a very flexible tool, which can be controlled very precisely and automated to a large extend.

Of particular interest is the formation of nanogratings structures within the so-called Type II regime. Then, several important hypotheses and models that explain the mechanism of nanogratings formation are summarized. Important controlling parameters and the processes

involved in the nanogratings formation, and its thermal stability are then discussed. Considering the fast development of nanogratings based applications, some representative demonstrations for potential applications were reported by many research groups around the world as described in the following references [123, 128, 226-235]. Among them, long lifetime optical data storage and optical sensing is the core of the thesis. This optical sensing technology used in harsh environments is a rapidly growing field of research. A new generation of devices that operate in extreme environments (particularly those operating above 700 °C and ideally up to 1500 °C), including environments with additional challenges such as radiation and intense optical fields (e.g. high power lasers), must be capable of withstanding gradual annealing and degradation, or aging, over time. Of particular local relevance these include live diagnostics with optical sensor embedded composites for aircraft, helicopters and space infrastructure, temperature and pressure sensing in increasingly deeper and hotter oil bores, and the monitoring and mapping of temperature distribution at power plants, furnaces and chemical reactors. Femtosecond lasers written devices in glasses (bulk and fibers) take advantage of the selectivity in spatial and time domains that near IR femtosecond lasers offer. Or put in another way, the technology of glass taken for granted in the macro scale can be applied on a sub-micron scale with a degree of unheralded finesse using laser patterning - glass smithing with nanoscale resolution becomes feasible.

In the end, the different types of fiber Bragg gratings induced by laser and their thermal stability are shortly reviewed As it is proposed in this PhD, femtosecond laser written devices (e.g. FBGs) form an excellent test-bed for understanding and optimizing the behavior of glass substrates foreseen to instrument structures operating in extreme environments; their centrality to a new generation of sensors that can be integrated with relatively low loss into coming intelligent optical SmartGrids means they are of immense practical importance as well. Despite this early success, the general feedback is that the writing technologies are still too early and requires improvement in material performance. Indeed, deployment of such fs-FBG temperature/strain sensors arrays to real-life applications requires fulfilling stringent requirements from the end-users. Moreover, efficient solutions have to be developed in order to propose these innovative FBGs as a reliable and mature industrial solution with regard to well-established techniques such as thermocouples. Among the key expected advances and results that will allow the deployment of calibrated arrays of fs-FBGs, let mention: i) the availability of collective and standardized temperature calibration/stabilization methods, ii) the limitation of thermal stability brings by the optical fiber material at extremely high temperatures (>1200 °C), iii) increased and qualified mechanical reliability for high T strain measurements, iv) high-temperature coatings able to protect and package this high T resistant FBGs and also v) lifetime prediction models and tools.

In the following chapters, we will focus on Femtosecond laser writing in glasses using a line-by-line writing geometry that is close to the design of Bragg gratings. From the bulk glass to the optical fiber, increase the thermal stability of the nanogratings (IR-fs type II modifications) and construct a reliable lifetime prediction model will be the core objective of the research.

References

1. Hill, K.O., et al., *Photosensitivity in optical fiber waveguides: Application to reflection filter fabrication.* Applied Physics Letters, 1978. **32**(10): p. 647-649.
2. Arnold, G.W. and W.D. Compton, *Radiation effects in silica at low temperatures.* Phys. Rev., 1959. **116**(4): p. 802-811.
3. Primak, W. and R. Kampwirth, *The radiation compaction of vitreous silica.* Journal of Applied Physics, 1968. **39**(12): p. 5651-5658.
4. Rajaram, M., T.-E. Tsai, and E.J. Friebele, *Radiation-Induced Surface Deformation in Low-Thermal-Expansion Glasses and Glass-Ceramics.* Advanced Ceramic Materials, 1988. **3**(6): p. 598-600.
5. Barbier, D., M. Green, and S.J. Madden, *Waveguide fabrication for integrated optics by electron beam irradiation of silica.* Journal of Lightwave Technology, 1991. **9**(6): p. 715-720.
6. Dellin, T.A., D.A. Tichenor, and E.H. Barsis, *Volume, index-of-refraction, and stress changes in electron-irradiation vitreous silica.* Applied Physics, 1977. **48**(3): p. 1131.
7. Syms, R.R.A., T.J. Tate, and M.F. Grant, *Reduction of propagation loss in silica-on-silicon channel waveguides formed by electron beam irradiation.* Electronics Letters, 1994. **30**(18): p. 1480-1481.
8. Lichtenstein, L., M. Heyde, and H.-J. Freund, *Atomic arrangement in two-dimensional silica: from crystalline to vitreous structures.* The Journal of Physical Chemistry C, 2012. **116**(38): p. 20426-20432.
9. Warren, B.E., *Summary of work on atomic arrangement in glass.* American Ceramic Society, 1941. **24**(8): p. 256-261.
10. Liebau, F., *Structural chemistry of silicates.* 1985.
11. Wright, A.C., *The structure of vitreous silica: what have we learned from 60 years of diffraction studies?* Journal of Non-Crystalline Solids, 1994. **179**: p. 84-115.
12. Lancry, M., E. Régnier, and B. Poumellec, *Fictive temperature in silica-based glasses and its application to optical fiber manufacturing.* Progress in Materials Science, 2012. **57**(1): p. 63-94.
13. Arndt, J., Physics and Chemistry of Glasses, 1983. **24**: p. 104-10.
14. Stishov, S.M. and S.V. Popova, *New dense polymorphic modification of silica.* Geokhimiya, 1961. **10**: p. 837-839.
15. Griscom, D.L., *The natures of point defects in amorphous silicon dioxide*, in *Defects in SiO2 and Related Dielectrics: Science and Technology*, L.S.a.D.L.G. G. Pacchioni, Editor. 2000. p. 117-159.
16. Griscom, D.L., *Optical Properties and Structure of Defects in Silica Glass: Optical Materials.* Journal of the Ceramic Society of Japan, 1 October 1991. **99**(1154): p. 923-942.
17. Garapon, J., *Etude théorique des défauts déficients en oxygène dans la silice pure ou dopée.* 2001, Université de Paris Sud.
18. Skuja, L.N., *Optically active oxygen-deficiency-related centers in amorphous silicon dioxide.* Journal of Non-Crystalline Solids, 1998. **239**(Section 1. Defect studies in vitreous silica and related materials): p. 16-48.
19. Skuja, L., *Optical properties of defects in silica*. Pacchioni, G., Skuja, L., Griscom, D. ed. Defect in SiO2 and related dielectrics : Science and Technology, ed. P.a.C. Mathematics. 2000, Dirdrecht, Netherlands: Kluwer Academic.
20. Trukhin, A.N., et al., *Cathodoluminescence and IR absorption of oxygen deficient silica - influence of hydrogen treatment.* Radiation effects and defects in solids., 1999. **149**: p. 61-68.

21. Ferdinand, P., *Capteurs à fibres optiques à réseaux de Bragg.* Techniques de l'ingénieur, 1999. **6735**: p. 1-24.
22. Mao, S., et al., *Dynamics of femtosecond laser interactions with dielectrics.* Applied Physics A, 2004. **79**(7): p. 1695-1709.
23. Schaffer, C., J. García, and E. Mazur, *Bulk heating of transparent materials using a high-repetition-rate femtosecond laser.* Applied Physics A: Materials Science & Processing, 2003. **76**(3): p. 351-354.
24. Eaton, S.M., et al., *Heat accumulation effects in femtosecond laser-written waveguides with variable repetition rate.* Optics Express, 2005. **13**(12): p. 4708-4716.
25. Bellouard, Y., et al., *Stress-state manipulation in fused silica via femtosecond laser irradiation.* Optica, 2016. **3**(12): p. 1285-1293.
26. Champion, A., et al., *Stress distribution around femtosecond laser affected zones: effect of nanogratings orientation.* Optics Express, 2013. **21**(21): p. 24942-24951.
27. Dürr, F., et al., *Tomographic measurement of femtosecond-laser induced stress changes in optical fibers.* Applied Physics Letters, 2004. **84**(24): p. 4983-4985.
28. Bhardwaj, V., et al., *Stress in femtosecond-laser-written waveguides in fused silica.* Optics Letters, 2004. **29**(12): p. 1312-1314.
29. Poumellec, B., et al., *Femtosecond laser irradiation stress induced in pure silica.* Optics Express, 2003. **11**(9): p. 1070-1079.
30. Guizard, S., et al., *Time-resolved study of laser-induced colour centres in.* Journal of Physics: Condensed Matter, 1996. **8**(9): p. 1281.
31. Mishchik, K., et al., *Ultrafast laser induced electronic and structural modifications in bulk fused silica.* Journal of Applied Physics, 2013. **114**(13): p. 133502.
32. Mishchik, K., *Ultrafast laser-induced modification of optical glasses: a spectroscopy insight into the microscopic mechanisms*. 2012.
33. Itoh, K., et al., *Ultrafast processes for bulk modification of transparent materials.* MRS Bulletin, 2006. **31**: p. 620-625.
34. Schaffer, C.B., A. Brodeur, and M. E., *Laser-induced breakdown and damage in bulk transparent materials induced by tighly focused femtosecond laser pulses.* Measurement Science Technology, 2001. **12**: p. 1784-1794.
35. Stoian, R., *Volume photoinscription of glasses: three-dimensional micro-and nanostructuring with ultrashort laser pulses.* Applied physics. A, Materials science & processing, 2020. **126**(6).
36. Rudenko, A., *Numerical study of ultrashort laser-induced periodic nanostructure formation in dielectric materials*. 2017, Université de Lyon.
37. Quéré, F., S. Guizard, and P. Martin, *Time-resolved study of laser-induced breakdown in dielectrics.* EPL (Europhysics Letters), 2001. **56**(1): p. 138.
38. Mao, S.S., et al., *Dynamics of femtosecond laser interactions with dielectrics.* Applied Physics a-Materials Science & Processing, 2004. **79**(7): p. 1695-1709.
39. Lancry, M., et al., *Time-resolved plasma measurements in Ge-doped silica exposed to infrared femtosecond laser.* Physical Review B, 2011. **84**(24): p. 245103.
40. Mouskeftaras, A., et al., *Mechanisms of femtosecond laser ablation of dielectrics revealed by double pump–probe experiment.* Applied Physics A, 2013. **110**(3): p. 709-715.
41. Lenzner, M., et al., *Femtosecond optical breakdown in dielectrics.* Physical review letters, 1998. **80**(18): p. 4076.
42. Stuart, B.C., et al., *Nanosecond-to-femtosecond laser-induced breakdown in dielectrics.* Physical review B, 1996. **53**(4): p. 1749.
43. Itina, T.E. and N. Shcheblanov, *Electronic excitation in femtosecond laser interactions with wide-band-gap materials.* Applied Physics A, 2010. **98**(4): p. 769-775.

44. Schaffer, C.B., A. Brodeur, and E. Mazur, *Laser-induced breakdown and damage in bulk transparent materials induced by tightly focused femtosecond laser pulses.* Measurement Science and Technology, 2001. **12**(11): p. 1784.
45. Rajeev, P., et al., *Field dependent avalanche ionization rates in dielectrics.* Physical Review Letters, 2009. **102**(8): p. 83001.
46. Wasiela, A., G. Ascarelli, and Y. Merle d'Aubigné, *Détection optique de la résonance électronique de l'exciton autopiégé dans les halogénures alcalins ; observation d'un croisement de niveaux.* J. Phys. France, 1974. **35**(5): p. 466.
47. Miura, K., et al., *Photowritten optical waveguides in various glasses with ultrashort pulse laser.* Applied Physics Letters, 1997. **71**(23): p. 3329-3331.
48. Sudrie, L., et al., *Writing of permanent birefringent microlayers in bulk fused silica with femtosecond laser pulses.* Optics Communications, 1999. **171**(4-6): p. 279-284.
49. Shimotsuma, Y., et al., *Self-organized nanogratings in glass irradiated by ultrashort light pulses.* Physical Review Letters, 2003. **91**(24): p. 247405.
50. Hnatovsky, C., et al., *Pulse duration dependence of femtosecond-laser fabricated nanogratings in fused silica.* Applied Physics Letters, 2005. **87**: p. 14104-1/3.
51. Juodkazis, S., et al., *Laser-induced microexplosion confined in the bulk of a sapphire crystal: evidence of multimegabar pressures.* Phys Rev Lett, 2006. **96**(16): p. 166101-166101.
52. Poumellec, B., et al., *Modification thresholds in femtosecond laser processing of pure silica: review of dependencies on laser parameters [Invited].* Optical Materials Express, 2011. **1**(4): p. 766-782.
53. Chan, J.W., et al., *Waveguide fabrication in phosphate glasses using femtosecond laser pulses.* Applied Physics Letters, 2003. **82**(15): p. 2371-2373.
54. Siegel, J., et al., *Waveguide structures in heavy metal oxide glass written with femtosecond laser pulses above the critical self-focusing threshold.* Applied Physics Letters, 2005. **86**: p. 121109.
55. Vega, F., et al., *Mechanisms of refractive index modification during femtosecond laser writing of waveguides in alkaline lead-oxide silicate glass.* Applied Physics Letters, 2005. **87**(2): p. 021109.
56. Zoubir, A., et al., *Femtosecond laser fabrication of tubular waveguides in poly(methyl methacrylate).* Opt. Lett., 2004. **29**(16): p. 1840-1842.
57. Royon, M., et al., *X-ray preconditioning for enhancing refractive index contrast in femtosecond laser photoinscription of embedded waveguides in pure silica.* Optical Materials Express, 2019. **9**(1): p. 65-74.
58. Lancry, M. and B. Poumellec, *UV laser processing and multiphoton absorption processes in optical telecommunication fiber materials.* Physics Reports, 2013. **523**(4): p. 207-229.
59. Bricchi, E. and P.G. Kazansky, *Extraordinary stability of anisotropic femtosecond direct-written structures embedded in silica glass.* Applied Physics Letters, 2006. **88**(11): p. 2-4.
60. Grobnic, D., et al., *Long-term thermal stability tests at 1000°C of silica fibre Bragg gratings made with ultrafast laser radiation.* Measurement Science and Technology, 2006. **17**(5): p. 1009.
61. Bricchi, E., B.G. Klappauf, and P.G. Kazansky, *Form birefringence and negative index change created by femtosecond direct writing in transparent materials.* Optics Letters, 2004. **29**(1): p. 119-121.
62. Bricchi, E., et al., *Birefringent Fresnel zone plates in silica fabricated by femtosecond laser machining.* Opt. Lett., 2002. **27**(24): p. 2200-2202.
63. Lancry, M., et al., *Ultrafast nanoporous silica formation driven by femtosecond laser irradiation.* Laser and Photonics Reviews, 2013. **7**: p. 953-962.

64. Glezer, E.N., et al., *3-D Optical Storage Inside Transparent Materials.* Optics Letters, 1996. **21**: p. 2023-2026.
65. Onda, S., et al., *Study of filamentary damage in synthesized silica induced by chirped femtosecond laser pulses.* JOSA B, 2005. **22**(11): p. 2437-2443.
66. Ashcom, J.B., et al., *Numerical aperture dependence of damage and supercontinuum generation from femtosecond laser pulses in bulk fused silica.* Journal of Optical Society of America B, 2006. **23**(11): p. 2317-2322.
67. Von der Linde, D. and H. Schüler, *Breakdown threshold and plasma formation in femtosecond laser–solid interaction.* JOSA B, 1996. **13**(1): p. 216-222.
68. Nemoto, S., *Waist shift of a Gaussian beam by plane dielectric interfaces.* Applied optics, 1988. **27**(9): p. 1833-1839.
69. Marcinkevičius, A., et al., *Effect of refractive index-mismatch on laser microfabrication in silica glass.* Applied Physics A, 2003. **76**(2): p. 257-260.
70. Simmonds, R.D., et al., *Three dimensional laser microfabrication in diamond using a dual adaptive optics system.* Optics express, 2011. **19**(24): p. 24122-24128.
71. Streltsov, A.M. and N.F. Borelli, *Fabrication and analysis of a directional coupler written in glass by nanojoule femtosecond laser pulses.* Optics Letters, 2001. **26**(1): p. 42-43.
72. Schaffer, C. and E. Mazur, *Micromachining using ultrashort pulses from a laser oscillator.* Optics & Photonics News, 2001. **12**(4): p. 20-23.
73. Sudrie, L., *Propagation non-linéaire des impulsions laser femtosecondes dans la silice.* 2002, Université de Paris Sud XI Orsay.
74. Schaffer, C.B. and E. Mazur, *Micromachining using ultrashort pulses from a laser oscillator.* Optics Photonics news, 2001. **12**(4): p. 20-23.
75. Couairon, A., et al., *Filamentation and damage in fused silica induced by tightly focused femtosecond laser pulses.* Physical Review B, 2005. **71**(12): p. 125435.
76. Chan, J.W., et al., *Modification of the fused silica glass network associated with waveguide fabrication using femtosecond laser pulses.* Applied Physics a-Materials Science & Processing, 2003. **76**(3): p. 367-372.
77. Brückner, R., *Properties and structure of vitreous silica. I.* Journal of Non-Crystalline Solids, 1970. **5**(2): p. 123-175.
78. Sakakura, M., et al., *Temperature distribution and modification mechanism inside glass with heat accumulation during 250kHz irradiation of femtosecond laser pulses.* Applied Physics Letters, 2008. **93**(23): p. 231112-231112-3.
79. Hirao, K. and K. Miura, *Writing waveguides and gratings in silica and related materials by a femtosecond laser.* Journal of Non-Crystalline Solids, 1998. **239**(1): p. 91-95.
80. Chan, J.W., et al., *Modification of the fused silica glass network associated with waveguide fabrication using femtosecond laser pulses.* Applied Physics A, 2003. **76**(3): p. 367-372.
81. Streltsov, A.M. and N.F. Borrelli, *Study of femtosecond-laser-written waveguides in glasses.* J. Opt. Soc. Am. B, 2002. **19**(10): p. 2496-2504.
82. Saliminia, A., R. Vallée, and S.L. Chin, *Waveguide writing in silica glass with femtosecond pulses from an optical parametric amplifier at 1.5um.* Optics Communications, 2005. **256**(4-6): p. 422-427.
83. Royon, M., *Ingénierie de verres de silice: influence de pré-traitements sur la variation d'indice de réfraction de guides d'ondes photo-inscrits par laser femtoseconde.* 2018.
84. Lancry, M., et al., *Dependence of the femtosecond laser refractive index change thresholds on the chemical composition of doped-silica glasses.* Optical Materials Express, 2011. **1**(4): p. 711-723.
85. Bressel, L., et al., *Femtosecond laser induced density changes in GeO2 and SiO2 glasses: fictive temperature effect*.

86. Chan, J.W., et al., *Structural changes in fused silica after exposure to focused femtosecond laser pulses.* Opt. Lett., 2001. **26**(21): p. 1726-1728.
87. Davis, K.M., et al., *Writing waveguides in glass with a femtosecond laser.* Optics Letters, 1996. **21**(21): p. 1729-1731.
88. Bernasconi, M., *Ab-initio molecular dynamics simulation of amorphous silica surface.*, in *Defects in $Si0_2$ and related dielectrics: Science and Technology.*, L.S.a.D.L.G. G. Pacchioni, Editor. 2000, Kluwer: Dordrecht.
89. Nolte, S., et al., *Waveguides produced by ultrashort laser pulses inside glasses and crystals.* 2002: p. 188-196.
90. Efimov, O., et al., *Waveguide writing in chalcogenide glasses by a train of femtosecond laser pulses.* Optical Materials, 2001. **17**(3): p. 379-386.
91. Petite, G., et al., *Ultrafast processes in laser irradiated wide bandgap insulators.* Applied Surface Science, 1997. **109–110**(0): p. 36-42.
92. Canning, J., et al., *Anatomy of a femtosecond laser processed silica waveguide [Invited].* Optical Materials Express, 2011. **1**(5): p. 998-1008.
93. Hnatovsky, C., et al., *Fabrication of microchannels in glass using focused femtosecond laser radiation and selective chemical etching.* Applied Physics A, 2006. **84**(1-2): p. 47-61.
94. Fleischer, R., P. Price, and R. Walker, *Solid-state track detectors: Applications to nuclear science and geophysics.* Annual Review of Nuclear Science, 1965. **15**(1): p. 1-28.
95. Schaffer, C., et al., *Laser-induced microexplosions in transparent materials: microstructuring with nanojoules.* Proceedings of SPIE, 1999. **3616**: p. 143.
96. Stoian, R., et al., *Investigation and control of ultrafast laser-induced isotropic and anisotropic nanoscale-modulated index patterns in bulk fused silica.* Optical Materials Express, 2013. **3**(10): p. 1755-1768.
97. Glezer, E.N. and E. Mazur, *Ultrafast-laser driven micro-explosions in transparent materials.* Applied physics letters, 1997. **71**(7): p. 882-884.
98. Juodkazis, S., et al., *Laser-induced microexplosion confined in a bulk of silica: Formation of nanovoids.* Applied Physics Letters, 2006. **88**(20): p. 201909.
99. Mermillod-Blondin, A., et al., *Dynamics of femtosecond laser induced voidlike structures in fused silica.* Applied Physics Letters, 2009. **94**(4): p. 041911.
100. Juodkazis, S., et al., *Laser-induced microexplosion confined in the bulk of a sapphire crystal: evidence of multimegabar pressures.* Physical review letters, 2006. **96**(16): p. 166101.
101. Glezer, E.N., et al., *Three-dimensional optical storage inside transparentmaterials.* Optics Letters, 1996. **21**(24): p. 2023-2025.
102. Shimotsuma, Y., et al., *Self-organized nanogratings in glass irradiated by ultrashort light pulses.* Physical review letters, 2003. **91**(24): p. 247405.
103. Kazansky, P.G., et al., *Anomalous anisotropic light scattering in Ge-doped silica glass.* Physical Review Letters, 1999. **82**(10): p. 2199-2202.
104. Bricchi, E., et al., *Birefringent Fresnel zone plates in silica fabricated by femtosecond laser machining.* Optics Letters, 2002. **27**(24): p. 2200-2202.
105. Hnatovsky, C., et al., *Polarization-selective etching in femtosecond laser-assisted microfluidic channel fabrication in fused silica.* Optics Letters, 2005. **30**(14): p. 1867-1869.
106. Bricchi, E., B.G. Klappauf, and P.G. Kazansky, *Form birefringence and negative index change created by femtosecond direct writing in transparent materials.* Optics Letters, 2004. **29**: p. 119-121.
107. Yu, N., et al., *AlPO 4 in Silica Glass Optical Fibers : Deduction AlPO 4 in Silica Glass Optical Fibers :.* IEEE Photonics Journal, 2019. **11**: p. 1-13.

108. Desmarchelier, R., et al., *In the Heart of Femtosecond Laser Induced Nanogratings: From Porous Nanoplanes to Form Birefringence.* World Journal of Nano Science and Engineering, 2015. **5**(04): p. 115.
109. Simmons, K.D., et al., *Photosensitivity of solgel-derived germanosilicate planar waveguides.* J Optics letters, 1993. **18**(1): p. 25-27.
110. Zimmermann, F., et al., *Femtosecond laser written nanostructures in Ge-doped glasses.* Optics letters, 2016. **41**(6): p. 1161-1164.
111. Lancry, M., et al., *Nanoscale femtosecond laser milling and control of nanoporosity in the normal and anomalous regimes of GeO2-SiO2 glasses.* Optical Materials Express, 2016. **6**(2): p. 321-330.
112. Stanczyk, T., et al., *Influence of high temperatures on optical fibers coated with multilayer protective coatings*, in *Proc. SPIE 9816, Optical Fibers and Their Applications 2015*. 2015. p. 98160F.
113. Vlugter, P. and Y. Bellouard, *Elastic properties of self-organized nanogratings produced by femtosecond laser exposure of fused silica.* Physical Review Materials, 2020. **4**(2): p. 023607.
114. Bellouard, Y., et al., *Nanoindentation and birefringence measurements on fused silica specimen exposed to low-energy femtosecond pulses.* Optics express, 2006. **14**(18): p. 8360-8366.
115. Mishchik, K., et al., *Nanosize structural modifications with polarization functions in ultrafast laser irradiated bulk fused silica.* Optics express, 2010. **18**(24): p. 24809-24824.
116. Hernandez-Rueda, J., et al., *The influence of femtosecond laser wavelength on waveguide fabrication inside fused silica.* Applied Physics Letters, 2017. **110**(16): p. 161109.
117. Born, M. and E. Wolf, *Principles of optics: electromagnetic theory of propagation, interference and diffraction of light*. 2013: Elsevier.
118. Holmberg, P., F. Laurell, and M. Fokine, *Influence of pre-annealing on the thermal regeneration of fiber Bragg gratings in standard optical fibers.* Optics Express, 2015. **23**: p. 27520.
119. Rosales-sosa, G.A., et al., *Crack-resistant Al 2 O 3 – SiO 2 glasses.* 2016: p. 1-7.
120. Zhang, B., X. Liu, and J. Qiu, *Single femtosecond laser beam induced nanogratings in transparent media - Mechanisms and applications.* Journal of Materiomics, 2019. **5**: p. 1-14.
121. Champion, A. and Y. Bellouard, *Direct volume variation measurements in fused silica specimens exposed to femtosecond laser.* Optical Materials Express, 2012. **2**(6): p. 789-798.
122. Thomson, R.R., et al., *Stress-state manipulation in fused silica via femtosecond laser irradiation.* Optica, 2016. **3**: p. 1285.
123. Yuan, L., et al., *Stress-induced birefringence and fabrication of in-fiber polarization devices by controlled femtosecond laser irradiations.* Optics Express, 2016. **24**(2): p. 1062-1071.
124. Fernandes, L.A., et al., *Stress induced birefringence tuning in femtosecond laser fabricated waveguides in fused silica.* Optics Express, 2012. **20**(22): p. 24103-24114.
125. Fernandes, L.A., et al., *Strong birefringence tuning of optical waveguides with femtosecond laser irradiation of bulk fused silica and single mode fibers.* Journal of Lightwave Technology, 2013. **31**(22): p. 3563-3569.
126. Curien, L.H., et al., *X-ray preconditioning for enhancing refractive index contrast in femtosecond laser photoinscription of embedded waveguides in pure silica.* Optical Materials Express, 2019. **9**: p. 65-74.

127. Poumellec, B. and M. Lancry, *Damage Thresholds in Femtosecond Laser Processing of Silica: A Review.* Bragg Gratings, Photosensitivity, and Poling in Glass Waveguides, OSA Technical Digest (CD), 2010.
128. Mihailov, S.J., et al., *Extreme Environment Sensing Using Femtosecond Laser-Inscribed Fiber Bragg Gratings.* Sensors, 2017. **17**.
129. Smelser, C., S. Mihailov, and D. Grobnic, *Formation of Type I-IR and Type II-IR gratings with an ultrafast IR laser and a phase mask.* Optics Express, 2005. **13**(14): p. 5377-5386.
130. Bricchi, E. and P.G. Kazansky, *Extraordinary stability of anisotropic femtosecond direct-written structures embedded in silica glass.* Applied Physics Letters, 2006. **88**(11).
131. Biriukov, A.S., et al., *Strength and Reliability of Metal-Coated Optical Fibers at High Temperatures*, in *MRS Proc.* 1998. p. 297-300.
132. Zoubir, A., et al., *Laser-induced defects in fused silica by femtosecond IR irradiation.* Physical Review B, 2006. **73**(22): p. 224117.
133. Saeta, P.N. and B.I. Greene, *Primary relaxation processes at the band edge of SiO 2.* Physical review letters, 1993. **70**(23): p. 3588.
134. Richter, S., et al., *The role of self-trapped excitons and defects in the formation of nanogratings in fused silica.* Optics letters, 2012. **37**(4): p. 482-484.
135. Martinez, A., I.Y. Khrushchev, and I. Bennion, *Thermal properties of fibre Bragg gratings inscribed point-by-point by infrared femtosecond laser.* Electronics Letters, 2005. **41**: p. 176-178.
136. Richter, S., et al., *Nanogratings in fused silica: Formation, control, and applications.* Journal of Laser Applications, 2012. **24**(4): p. 042008.
137. Zimmermann, F., *Ultrashort pulse induced nanostructures in transparent materials*. 2017.
138. Witcher, J.J., et al., *Thermal annealing of femtosecond laser written structures in silica glass.* Optical Materials Express, 2013. **3**(4): p. 502-510.
139. Zhang, F., et al., *Wavelength response and thermal stability of embedded nanograting structure light attenuator fabricated by direct femtosecond laser writing.* Applied Physics B, 2014. **117**(1): p. 53-58.
140. Beresna, M., et al., *Broadband anisotropy of femtosecond laser induced nanogratings in fused silica.* Applied Physics Letters, 2013. **103**(13): p. 131903.
141. Vlugter, P., E. Block, and Y. Bellouard, *Local tuning of fused silica thermal expansion coefficient using femtosecond laser.* Physical Review Materials, 2019. **3**(5): p. 053802.
142. Vlugter, P., *Investigation of femtosecond laser-tuned thermomechanical properties of fused silica*. 2020, EPFL.
143. Tian, J., et al., *Spectral dependence of femtosecond laser induced circular optical properties in silica.* OSA Continuum, 2019. **2**(4): p. 1233-1241.
144. Cavillon, M., et al., *Erasure of nanopores in silicate glasses induced by femtosecond laser irradiation in the Type II regime.* Applied Physics A 2020.
145. Yin, Z.Y. and B. Garside, *Low-loss GeO 2 optical waveguide fabrication using low deposition rate rf sputtering.* J Applied optics, 1982. **21**(23): p. 4324-4328.
146. *Developed technology to record and reproduce digital data with the same capacity as a CD inside quartz glass* Available from: https://www.hitachi.co.jp/New/cnews/month/2012/09/0924.html.
147. Kazansky, P., et al., *Eternal 5D data storage via ultrafast-laser writing in glass.* SPIE Optoelectronics Communications, 2016.
148. Kazansky, P., et al., *Virtually eternal 5D data storage in quartz glass*, in *ASCEND 2020*. 2020. p. 4044.
149. Bulot, P., *Étude et réalisation sur tour de fibrage de capteurs à fibre optique pour environnements extrêmes*. 2019, Lille 1.

150. Åslund, M., J. Canning, and G. Yoffe, *Locking in photosensitivity within optical fiber and planar waveguides by ultraviolet preexposure.* Optics Letters, 1999. **24**(24): p. 1826-1828.
151. Erdogan, T., et al., *Decay of ultraviolet-induced fiber Bragg gratings.* Journal of applied physics, 1994. **76**(1): p. 73-80.
152. Kannan, S., J.Z. Guo, and P.J. Lemaire, *Thermal stability analysis of UV-induced fiber Bragg gratings.* Journal of lightwave technology, 1997. **15**(8): p. 1478-1483.
153. Poumellec, B. *Tutorial lecture at summer school on Photosensitivity in Optical Waveguides and Glasses (POWAG 2000)*. 2000.
154. E. Salik, D.S.S., V. Grubsky, J. Feinberg,. in *Dig of Optical Fiber Communication Conference (OFC 99), 56*. 1999.
155. Wang, Q., et al., *Influence of blanket postexposure on the thermal stability of the spectral characteristics of gratings written in a telecommunication fiber using light at 193 nm.* Journal of Lightwave Technology, 2000. **18**(8): p. 1078.
156. Hand, D. and P.S. Russell, *Photoinduced refractive-index changes in germanosilicate fibers.* Optics letters, 1990. **15**(2): p. 102-104.
157. Douay, M., et al., *Densification involved in the UV-based photosensitivity of silica glasses and optical fibers.* Journal of Lightwave technology, 1997. **15**(8): p. 1329-1342.
158. Limberger, H., et al., *Compaction-and photoelastic-induced index changes in fiber Bragg gratings.* Applied Physics Letters, 1996. **68**(22): p. 3069-3071.
159. Dong, L. and W. Liu, *Thermal decay of fiber Bragg gratings of positive and negative index changes formed at 193 nm in a boron-codoped germanosilicate fiber.* Applied optics, 1997. **36**(31): p. 8222-8226.
160. Dong, L., W. Liu, and L. Reekie, *Negative-index gratings formed by a 193-nm excimer laser.* Optics letters, 1996. **21**(24): p. 2032-2034.
161. Groothoff, N. and J. Canning, *Enhanced type IIA gratings for high-temperature operation.* Optics letters, 2004. **29**(20): p. 2360-2362.
162. Frazao, O., M. Lima, and J. Santos, *Simultaneous measurement of strain and temperature using type I and type IIA fibre Bragg gratings.* Journal of Optics A: Pure Applied Optics, 2003. **5**(3): p. 183.
163. Lindner, E., et al., *Thermal regenerated type IIa fiber Bragg gratings for ultra-high temperature operation.* Optics communications, 2011. **284**(1): p. 183-185.
164. Archambault, J., L. Reekie, and P.S.J. Russell, *100% reflectivity Bragg reflectors produced in optical fibres by single excimer laser pulses.* Electronics Letters, 1993. **29**(5): p. 453-455.
165. Askins, C., et al., *Stepped-wavelength optical-fiber Bragg grating arrays fabricated in line on a draw tower.* Optics letters, 1994. **19**(2): p. 147-149.
166. Åslund, M.L., et al., *Thermal stabilization of Type I fiber Bragg gratings for operation up to 600° C.* Optics letters, 2010. **35**(4): p. 586-588.
167. Canning, J., *Photosensitization and photostabilization of laser-induced index changes in optical fibers.* Optical Fiber Technology, 2000. **6**(3): p. 275-289.
168. Cook, K., A. Pohl, and J. Canning, *High-temperature type IIa gratings in 12-ring photonic crystal fibre with germanosilicate core.* Journal of the European Optical Society-Rapid publications, 2008. **3**.
169. Pissadakis, S. and M. Konstantaki, *Photosensitivity of germanosilicate fibers using 213nm, picosecond Nd: YAG radiation.* Optics express, 2005. **13**(7): p. 2605-2610.
170. Homoelle, D., et al., *Infrared photosensitivity in silica glasses exposed to femtosecond laser pulses.* Optics Letters, 1999. **24**(18): p. 1311-1313.
171. K. Sakuma, S.I., T. Shikata, T. Fukuda, H. Hosoya,. in *Optical Fiber Communication Conference (OFC 2003)*. 2003. Optical Society of America.

172. K.P. Chen, P.R.H., R. Tam, , *2001*, in *roceedings on Bragg Grating, Photosensitivity and Poling in Glass Waveguides, , Stresa, paper BthA5*.
173. Davis, K.M., et al., *Writing waveguides in glass with a femtosecond laser.* Optics letters, 1996. **21**(21): p. 1729-1731.
174. Mihailov, S.J., et al., *Review of femtosecond infrared laser-induced fibre Bragg grating sensors made with a phase mask.* Sensor Review, 2011.
175. Martinez, A., et al., *Direct writing of fibre Bragg gratings by femtosecond laser.* Electronics Letters, 2004. **40**(19): p. 1170-1172.
176. SANDHAGE, K.H. and G.J. YUREK, *Indirect dissolution of sapphire into silicate melts.* J Journal of the American Ceramic Society, 1988. **71**(6): p. 478-489.
177. Albert, J., M. Fokine, and W. Margulis, *Grating formation in pure silica-core fibers.* Optics letters, 2002. **27**(10): p. 809-811.
178. Groothoff, N., et al., *Bragg gratings in air–silica structured fibers.* Optics Letters, 2003. **28**(4): p. 233-235.
179. Morana, A., et al., *Radiation tolerant fiber Bragg gratings for high temperature monitoring at MGy dose levels.* Optics letters, 2014. **39**(18): p. 5313-5316.
180. Li, Y., et al., *Fiber Bragg gratings with enhanced thermal stability by residual stress relaxation.* Optics express, 2009. **17**(22): p. 19785-19790.
181. Cook, K., et al. *Regenerated femtosecond fibre Bragg gratings*. in *Third Asia Pacific Optical Sensors Conference*. 2012. International Society for Optics and Photonics.
182. Grobnic, D., C. Hnatovsky, and S.J. Mihailov, *Low loss Type II regenerative Bragg gratings made with ultrafast radiation.* Optics express, 2016. **24**(25): p. 28704-28712.
183. Martinez, A., I. Khrushchev, and I. Bennion, *Thermal properties of fibre Bragg gratings inscribed point-by-point by infrared femtosecond laser.* Electronics letters, 2005. **41**(4): p. 176-178.
184. Warren-Smith, S.C., et al., *Temperature sensing up to 1300 C using suspended-core microstructured optical fibers.* Optics express, 2016. **24**(4): p. 3714-3719.
185. Landron, C., L. Hennet, and D. Thiaudiere. *Combining measurements of synchrotron radiation and neutrons from liquids at high temperature*. in *Analytical Sciences/Supplements Proceedings of IUPAC International Congress on Analytical Sciences 2001 (ICAS 2001)*. 2002. The Japan Society for Analytical Chemistry.
186. Glorieux, B., et al., *Density of superheated and undercooled liquid alumina by a contactless method.* J International journal of Thermophysics, 1999. **20**(4): p. 1085-1094.
187. M. Lancry, P.N., M. Douay, P. Cordier, C. Depecker, I. Riant, P, in *roceedings of BGPP 2003, BraggGratings, Photosensitivity and Poling in Glass Waveguides, paper MC2, 40*. 2003.
188. Li, Y., et al., *Prestressed fiber Bragg grating with high temperature stability.* Journal of Lightwave Technology, 2011. **29**(10): p. 1555-1559.
189. Fokine, M., *Formation of thermally stable chemical composition gratings in optical fibers.* JOSA B, 2002. **19**(8): p. 1759-1765.
190. Trpkovski, S., et al., *High-temperature-resistant chemical composition Bragg gratings in Er 3+-doped optical fiber.* Optics letters, 2005. **30**(6): p. 607-609.
191. Zhang, B. and M. Kahrizi, *High-temperature resistance fiber Bragg grating temperature sensor fabrication.* IEEE sensors journal, 2007. **7**(4): p. 586-591.
192. Lindner, E., et al., *Post-hydrogen-loaded draw tower fiber Bragg gratings and their thermal regeneration.* Applied optics, 2011. **50**(17): p. 2519-2522.
193. Bandyopadhyay, S., et al., *Ultrahigh-temperature regenerated gratings in boron-codoped germanosilicate optical fiber using 193 nm.* Optics letters, 2008. **33**(16): p. 1917-1919.
194. Wang, T., et al., *Temperature and strain characterization of regenerated gratings.* Optics letters, 2013. **38**(3): p. 247-249.

195. Canning, J., et al., *Extreme silica optical fibre gratings.* Sensors, 2008. **8**(10): p. 6448-6452.
196. Åslund, M.L., et al. *Rapid disappearance of regenerated fibre Bragg gratings at temperatures approaching 1500 ºC in boron-codoped germanosilicate optical fibre*. in *Fourth European Workshop on Optical Fibre Sensors*. 2010. International Society for Optics and Photonics.
197. Laffont, G., R. Cotillard, and P. Ferdinand. *9000 hours-long high temperature annealing of regenerated fiber Bragg gratings*. in *Fifth European Workshop on Optical Fibre Sensors*. 2013. International Society for Optics and Photonics.
198. Åslund, M.L., et al., *Mapping the thermal distribution within a silica preform tube using regenerated fibre Bragg gratings.* International journal of heat mass transfer, 2012. **55**(11-12): p. 3288-3294.
199. Chen, T., et al., *Regenerated gratings in air-hole microstructured fibers for high-temperature pressure sensing.* Optics letters, 2011. **36**(18): p. 3542-3544.
200. Laffont, G., et al., *Temperature resistant fiber Bragg gratings for on-line and structural health monitoring of the next-generation of nuclear reactors.* Sensors, 2018. **18**(6): p. 1791.
201. Chen, R., A. Yan, and K.P. Chen. *High-temperature flow sensing using regenerated gratings in self-heated high attenuation fibers*. in *CLEO: Science and Innovations*. 2014. Optical Society of America.
202. Mezzadri, F., *Monitoramento de temperatura em turbina de motordiesel de locomotiva com sensor a fibra ótica*. 2012, Universidade Tecnológica Federal do Paraná.
203. Shao, L.-Y., et al., *Viscosity of silica optical fibres characterized using regenerated gratings.* Acta materialia, 2013. **61**(16): p. 6071-6081.
204. Canning, J., et al., *Regenerated gratings.* Journal of the European Optical Society-Rapid publications, 2009. **4**.
205. Gao, S., J. Canning, and K. Cook, *Ultra-high temperature chirped fiber Bragg gratings produced by gradient stretching of viscoelastic silica.* Optics letters, 2013. **38**(24): p. 5397-5400.
206. Wang, T., et al., *Regeneration of fiber Bragg gratings under strain.* Applied optics, 2013. **52**(10): p. 2080-2085.
207. Laffont, G., R. Cotillard, and P. Ferdinand, *Multiplexed regenerated fiber Bragg gratings for high-temperature measurement.* Measurement Science Technology, 2013. **24**(9): p. 094010.
208. Habisreuther, T., et al., *Sapphire fiber Bragg gratings for high temperature and dynamic temperature diagnostics.* Applied Thermal Engineering, 2015. **91**: p. 860-865.
209. Grobnic, D., et al., *Sapphire fiber Bragg grating sensor made using femtosecond laser radiation for ultrahigh temperature applications.* IEEE Photonics Technology Letters, 2004. **16**(11): p. 2505-2507.
210. Mihailov, S.J., D. Grobnic, and C.W. Smelser, *High-temperature multiparameter sensor based on sapphire fiber Bragg gratings.* Optics letters, 2010. **35**(16): p. 2810-2812.
211. Xu, X., et al., *Sapphire fiber Bragg gratings inscribed with a femtosecond laser line-by-line scanning technique.* Optics letters, 2018. **43**(19): p. 4562-4565.
212. Chen, C., et al., *Femtosecond laser-inscribed high-order Bragg gratings in large-diameter sapphire fibers for high-temperature and strain sensing.* Journal of Lightwave Technology, 2018. **36**(16): p. 3302-3308.
213. Yang, S., et al., *Fiber Bragg grating fabricated in micro-single-crystal sapphire fiber.* Optics letters, 2018. **43**(1): p. 62-65.

214. Busch, M., et al., *Inscription and characterization of Bragg gratings in single-crystal sapphire optical fibres for high-temperature sensor applications.* Measurement Science Technology, 2009. **20**(11): p. 115301.
215. Elsmann, T., et al., *High temperature sensing with fiber Bragg gratings in sapphire-derived all-glass optical fibers.* Optics express, 2014. **22**(22): p. 26825-26833.
216. Dragic, P., et al., *Sapphire-derived all-glass optical fibres.* Nature Photonics, 2012. **6**(9): p. 627-633.
217. Dragic, P., et al., *Brillouin spectroscopy of YAG-derived optical fibers.* Optics express, 2010. **18**(10): p. 10055-10067.
218. Grobnic, D., et al., *Type I and II Bragg gratings made with infrared femtosecond radiation in high and low alumina content aluminosilicate optical fibers.* Optica, 2015. **2**(4): p. 313-322.
219. Cavillon, M., et al., *Overview of high temperature fibre Bragg gratings and potential improvement using highly doped aluminosilicate glass optical fibres.* Journal of Physics: Photonics, 2019. **1**(4): p. 042001.
220. Cavillon, M., et al., *Insights and aspects to the modeling of the molten core method for optical fiber fabrication.* Materials, 2019. **12**(18): p. 2898.
221. Baker, S.R., et al., *Thermal decay of fiber Bragg gratings written in boron and germanium codoped silica fiber.* Journal of Lightwave Technology, 1997. **15**(8): p. 1470-1477.
222. Eggleton, B., et al., *Grating resonances in air–silica microstructured optical fibers.* Optics Letters, 1999. **24**(21): p. 1460-1462.
223. Dyer, P., et al., *Amplification of fibre Bragg grating reflectivity by post-writing exposure with a 193 nm ArF laser.* Electronics Letters, 1994. **30**(14): p. 1133-1134.
224. Canning, J., *Fibre gratings and devices for sensors and lasers.* Laser Photonics Reviews, 2008. **2**(4): p. 275-289.
225. Wang, Y., et al., *Femtosecond laser direct writing in SiO2-Al2O3 binary glasses and thermal stability of Type II permanent modifications.* Journal of the American Ceramic Society, 2020. **103**(8): p. 4286-4294.
226. Della Valle, G., R. Osellame, and P. Laporta, *Micromachining of photonic devices by femtosecond laser pulses.* Journal of Optics A: Pure and Applied Optics, 2008. **11**(1): p. 013001.
227. Cheng, G., et al., *Ultrafast laser photoinscription of polarization sensitive devices in bulk silica glass.* Optics Express, 2009. **17**(12): p. 9515-9525.
228. Osellame, R., G. Cerullo, and R. Ramponi, *Femtosecond Laser Micromachining: Photonic and Microfluidic Devices in Transparent Materials*. Vol. 123. 2012: Springer Science & Business Media.
229. Beresna, M., M. Gecevičius, and P.G. Kazansky, *Polarization sensitive elements fabricated by femtosecond laser nanostructuring of glass [Invited].* Optical Materials Express, 2011. **1**(4): p. 783-795.
230. Beresna, M., *Polarization engineering with ultrafast laser writing in transparent media*. 2012, Southampton.
231. Zhang, J., et al., *Seemingly unlimited lifetime data storage in nanostructured glass.* Physical Review Letters, 2014. **112**(3): p. 033901.
232. Beresna, M., M. Gecevičius, and P.G. Kazansky, *Harnessing Ultrafast Laser Induced Nanostructures in Transparent Materials*, in *Progress in Nonlinear Nano-Optics*. 2015, Springer. p. 31-46.
233. Desmarchelier, R., et al., *Achromatic polarization rotator imprinted by ultrafast laser nanostructuring in glass.* Applied Physics Letters, 2015. **107**(18): p. 181111.

234. Drevinskas, R., et al., *Ultrafast laser-induced metasurfaces for geometric phase manipulation.* Advanced Optical Materials, 2017. **5**(1): p. 1600575.
235. Sun, Q., et al. *Control of Laser Induced Stress for Diffractive Optics in Transparent Media*. in *The European Conference on Lasers and Electro-Optics*. 2019. Optical Society of America.

Chapter 2. Experimental details

Introduction 65
2.1 Sample production 66
2.1.1 Silica-based glasses manufacturing processes 67
2.1.2 Optical fiber fabrication 69
2.2 Characterization techniques 79
2.2.1 Density measurement 79
2.2.2 Chemical composition analysis 79
2.2.3 Spectroscopic characterization 81
2.3 Laser irradiation 88
2.3.1 Femtosecond laser direct writing (FLDW) system 88
2.3.2 Fs-laser irradiation in optical fibers 92
2.4 Microscopic characterization after laser irradiation 95
2.4.1 The “de Sénarmont” compensator 95
2.4.2 Full wave retardation plate 97
2.4.3 Scanning electron microscope (SEM) 98
Conclusions 102
References 103

Introduction

This chapter describes the methods used for the fabrication of the bulk glass and optical fibers. Then the technique used for characterizing the microstructures produced using femtosecond laser exposure on these silica-based samples will also be reported. Most of the contents of this thesis rely on these experimental procedures.

In Section 2.1, we will first introduce the fabrication methods of all samples involved in this PhD thesis. The different methods for silica based glasses and optical fibers will be discussed separately. Next, in order to understand the various properties of different samples, a series of characterization methods will be presented in Section 2.2. The measurements based on the Archimedes principle will be implied to detect the density of our sample; SEM coupled to energy dispersive X-ray spectroscopy (SEM/EDS) is used to determine the chemical composition of the samples and finally, several spectroscopic characterization techniques as Fourier-transform infrared spectroscopy (FTIR), Raman scattering microspectroscopy and UV-Vis-NearIR absorption will also be presented in details. The femtosecond laser described in Section 2.3 has characteristics, like pulse duration and energy per pulse, ideal to produce nonlinear absorption in glasses and therefore to produce the required permanent changes in the substrate. Additional components in the laser delivery system, also described in Section 2.3, further allow for the manipulation of the femtosecond laser beam to facilitate the fabrication of segmented lines and to obtain the desired nano/micro-structures such as gratings or waveguides like structures. After irradiation, the predominant way of characterizing nanogratings is the analysis of the nanostructures under a scanning electron microscope. Despite its straightforwardness, the method restricts characterization of the femtosecond laser induced anisotropy to the measurements of the nanogratings period, nanopores size and the porosity-filling factor. The alternative, nondestructive way of characterizing the anisotropic structure is quantitative birefringence measurements (associated to slow/fast axis detection) and more generally anisotropic optical properties. This provides information on the dependence of induced modification on writing parameters such as fluence per pulse, repetition rate, numerical aperture, etc… The overall characterization methods described in Section 2.4 provide the means to measure the key physical quantities of the femtosecond laser written structures with sufficient accuracy to draw meaningful conclusions from the experiments designed in each chapter.

2.1 Sample production

Table 2-1. The sample summary for bulk glass.

Sample	Composition (mole %)	Density	Refractive index	Fabrication method	Impurities OH (ppm)	Annealing temperature (°C)
Type I silica (Infrasil 301)	100 SiO_2	2.201	1.458	Melting nature quartz	830	1180
Type III silica (Suprasil CG)	100 SiO_2	2.201	1.458	Burning $SiCl_4$	8	1100
Germanosilicate glass	$xGeO_2$-(1-x)SiO_2, x=1.9, 5, 11.8, 16.9	2.245-2.348	1.436-1.474	PECVD	< 0.1	990-1090
Aluminosilicate glass	xAl_2O_3-(1-x)SiO_2, x=10, 20, 30, 40, 50, 60	2.475-2.772	1.534-1.588	Aerodynamic levitation	N.A	859.6-821.2

*The ULE Corning (93SiO_2-7TiO_2) and Borofloat 33 (81SiO_2-13B_2O_3-4Na_2O/K_2O-2Al_2O_3) are also researched in the thesis for a sake of comparison.

Table 2-2. The sample summary for optical fiber.

Sample	Composition (mole %)	Density	Refractive index	Diameter (Core/Cladding, μm)	Fabrication method	Annealing temperature (°C)
SMF 28	$xGeO_2$-(1-x)SiO_2, x ≈ 5-6	2.275	1.4676(1310nm)	8.2/125	MCVD, PCVD	887.6
YAG fiber	71%SiO_2-20%Al_2O_3-9%Y_2O_3		1.5559	~20/125	Molten core	
Aluminosilicate fiber	xAl_2O_3-(1-x)SiO_2, x=42.5, 51.5	2.575-2.674	1.554-1.572	21/125	Molten core	843.5-832.1
3D printed fiber	$xGeO_2$-(1-x)SiO_2, x ≈ 10			~8/128	3D printed preform	

2.1.1 Silica-based glasses manufacturing processes

Due to excellent physical and chemical properties, vitreous silica-based (v-SiO_2-based) glasses prove to be key materials in optical waveguides, metal-oxide semiconductors and other optical elements. Thus, numerous elaboration methods are used to produce v-silica-based devices. For example, the technique of vapor phase deposition (e. g.: Flame Hydrolysis Deposition (FHD), Modified Chemical Vapor Deposition (MCVD), Plasma Enhanced Chemical Vapor Deposition (PECVD)) is common in the fabrication of most standard telecommunication silica fibers or planar waveguides[1-4]. Moreover, planar waveguides or thin films can be produced from silica containing solid source by physical vapor deposition techniques such as reactive sputtering deposition [5, 6] or Helicon Activated Reactive Evaporation (HARE)[7]. Waveguides can also be fabricated by means of electron [8]or ion (Si, Ge, Se, O, B, P or H) implantation in pure silica[9-13] . Furthermore, other processes including sol-gel synthesis [14, 15] or conventional melting of raw materials are routinely used to manufacture sol-gel fiber; glassy thin films or multicomponent glass in which waveguides are realized by means of technique such as ion exchange[16, 17]. As a result of the large variety of elaboration processes, all the v-SiO_2-based glasses are different in terms of chemical composition and structural disorder [18]. Nonetheless, they share two properties, leading to important practical consequences. On one hand, v-SiO_2 based glass exhibits **macroscopic inversion symmetry** and should not exhibit any even-order optical nonlinear effect ($\chi^{(2n)}$) such as Pockels (n=1) effect unless it had been prepared by a poling technique that breaks the inversion symmetry[19-23]. On the other hand, all these glasses (and others such as chalcogenide or fluoride glasses) prove to be **photosensitive**, depending on both the exposure conditions of the glass to laser light and on their composition.

Classical 4 types of silica glass

Fused quartz is a glass obtained by melting quartz or sand with very high silica content, without the addition of flux. In order to obtain high purity, it can also be produced from synthetic quartz or silica, it is then called silica glass. In the past half-century, the research about the melting processes of silica has been still in vigorous progress, several methods are submitted to be used to make quartz glass. Based on the classification proposed by Brückner in 1970 [24], we categorized the mechanism of manufacture into four types.

Type I Silica glass is produced by induction melting natural quartz in a vacuum or an inert gas atmosphere. It contains comparatively high metallic impurities of the order of 4 ppm Na and 30-100 ppm Al but nearly no OH-groups about less than 5 ppm. It is commercially known by the name Infrasil.

Type II Silica glass is produced by fusing quartz crystal powder in a high-temperature

flam (Verneuille process). Its metallic impurities are less than the Type I silica glass because of the nonappearance of any crucible material during the fabrication process and the partial volatilization. But the atmosphere of the hydrogen-oxygen flame brings a higher OH-content of about 150-400 ppm. The commercial name is known as Herasil or Homosil. Also, there is a particular catalog called Ultrasil which is especially thermal treated in an oxygen atmosphere and obtain good optical transparency in the ultraviolet range.

Type III Silica glass is synthetic vitreous silica produced by burning $SiCl_4$ in a Hydrogen-Oxygen flame. The starting material brings a high quantity of Cl in the order of 100 ppm. It also contains a high amount of OH in order of 1000 ppm. On the contrary, this kind of glass is practically free from metallic impurities. Its trade names are Suprasil and Spectrosil for example.

Type IV Silica glass is produced by burning $SiCl_4$ in a water vapor free plasma flame. It is also synthetic vitreous silica. This type of glass is quite similar to the Type III glass but contains a much lower OH of about 0.4 ppm and higher Cl of about 200 ppm. Cl content could rise up to 1000-2000 ppm for MCVD or PCVD silica dedicated to optical fibers but at the expense of a lower OH content (Typ. <10ppb). The trade names are similar too, as Suprasil W and Spectrosil WF. There exists another type of glass that is produced for the laboratory only. The raw material is the silicon of semiconductor-quality which was oxidized in pure oxygen high-frequency plasma flame. Its impurity is extremely high and contains nearly no OH-groups[24].

Aerodynamic levitation

The term aerodynamic levitation is a technique, in which solids or liquids are freely floated on top of a vertical gas stream. It is the use of gas pressure to levitate materials so that they are no longer in physical contact with any container. Therefore, aerodynamic levitation allows the conduction of high-temperature experiments while avoiding problems related to the chemical interaction between sample and container walls [25] (e.g., corrosion of oxide crucibles by silicate melts [26, 27], gain or loss of siderophile elements, and Fe in Pt crucibles [28, 29]).

This method has been used extensively to study metal oxides and to a lesser extent metals, alloys, and semiconductors [30]. The small size of the aerodynamic levitation components enables them to be integrated with a wide variety of non-contact diagnostic methods. Because aerodynamic levitation requires a gaseous environment, it allows the use of process gases to adjust the chemistry of a sample in situ. For example, adjustment of the $p(O_2)$ using a redox mixture can be used to change the oxidation state of cations in a melt [31, 32]. In the case of metallic samples that may be prone to oxidation, levitation gas can be purified to parts per billion (ppb) levels of oxidizing impurities by using an oxygen getter[33]. The use of ppb purity gas is equivalent to using a total pressure of 10^{-9} atmospheres and it

avoids the need for use of an ultrahigh vacuum system. The presence of gas suppresses evaporation of the sample and reduces the coating of the windows and other components by the evaporated material.

Aerodynamic levitation has been used for studies of the physical properties of solids [34] and liquids [35-39] at high temperatures. Oxides and silicates can be heated and melted with a CO_2 gas laser [34], a mirror furnace [40], or a solar furnace [41], while they are floating on top of the gas stream. Depending on the supplied energy, temperatures >3000°C can be reached [42]. It has also been used to investigate the crystallization behavior of oxides [43]and silicates [44-46]. Due to the absence of heterogeneous nucleation sites, aerodynamic levitation was also used for the preparation of glasses from substances that otherwise crystallize during cooling [47-49].

In this thesis, we use the aerodynamic levitation technique to fabricate the SiO_2-Al_2O_3 binary glasses (fabricated in Miura Lab, Kyoto university). Aluminum oxide (alumina, Al_2O_3) and silicon dioxide (silica, SiO2) ultrapure raw powders based on the stoichiometry $xSiO_2$ – (1 − x) Al_2O_3 (x = 50, 60, 70, 80) were mixed in alumina mortar and pressed into pellets. The pellets were sintered for 12 hours at 1100 °C in air, and crushed, and used as a preform for aerodynamic levitation with CO_2 laser melting. The calcined preforms were levitated using a flow of dry air (N_2: 79%, O_2: 21%) and melted through the focusing of 100 W CO_2 laser via a ZnSe lens (f = 254 mm). To ensure homogeneity of the melt, the temperature was kept above the melting point for tens of seconds. Then, turning off the laser power while gas levitating rapidly cooled the melt. Colorless and transparent spherical samples with a diameter of approximately 1-2 mm were obtained.

2.1.2 Optical fiber fabrication

The conventional way to fabricate an optical fiber can be decomposed into a two-step process. The first one consists into making a long glass rod called a fiber preform, which already has the desired structure of the final fiber (typically 2 elements: a core and a cladding part). The second step is called “drawing”, and the preform is elongated to form the fiber.

A. Conventional fiber fabrication methods: Modified Chemical Vapor Deposition (MCVD) and Plasma Chemical Vapor Deposition (PCVD)

Chemical vapor deposition (CVD) is a vapor deposition method for the manufacturing of high-performance optical fibers preforms guide. Plasma Chemical Vapor Deposition (PCVD), which appeared in the 1970s, is a process that involves depositing thin layers of silica soot inside a hollow substrate tube made of high purity vitreous silica. Before the implementation of the PCVD method, the Modified Chemical Vapor Deposition (MCVD)

technology was used for a long time and still used a lot today. The latter is identical to PCVD except that the heat necessary for the formation of soot is obtained by the presence of an H_2/O_2 torch moving along the tube and reaching temperatures between 1400 and 1600 °C. Although the PCVD technology is more expensive than the MCVD, it allows working with a wider range of compositions with high doping levels, while the deposited layers are thinner (up to 1000 for the primary preform). These characteristics enable the realization of complex index profiles with fine index modulation tuning. Moreover, whatever the CVD process considered, the high purity of the raw materials used is essential and the high purity of the precursor comes from the process itself where the vapor phase is carefully selected. More details could be found in [50].

Modified Chemical Vapor Deposition (MCVD)

In order to introduce these two technologies in more detail, first, we first cover the most established method, which is Modified Chemical Vapor Deposition (MCVD). The preform is fabricated by using the MCVD method to bubble oxygen through solutions of silicon chloride ($SiCl_4$), germanium chloride ($GeCl_4$), phosphorous oxychloride ($POCl_3$) and or other various materials to create silicon dioxide with a specific amount of intentional dopants (germanium or phosphorous)[51] .

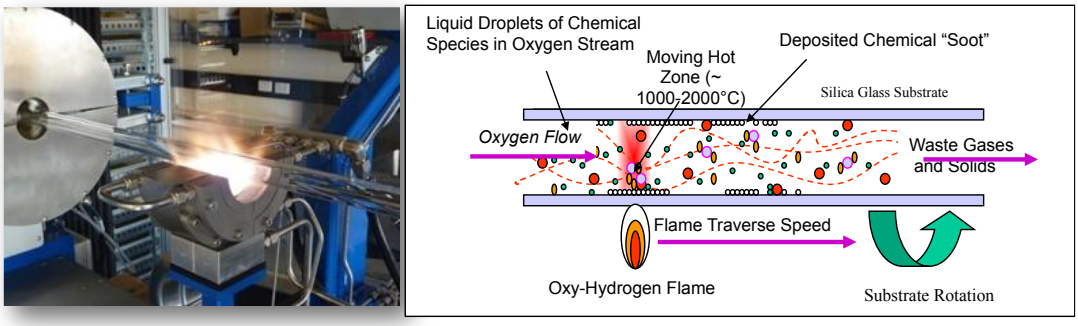

Figure 2-1. The schema of the modified chemical deposition procedure.

As shown in *Figure 2-1*, the gas vapors are then injected into a cylindrical fused silica tube that is placed on a high-temperature lathe. As the silica glass tube rotates, a heat source is applied along tube to create a reaction that forms large soot particles that deposit on the inside of the tube[52] . As the heat source is moved along the tube, the soot particles fuse together to form a silica glass. After the glass is built up to the desired thickness (forming a layer), the tip of the preform is heated and pulled out as a long thread (the preform). The preform is then placed on a draw tower and subsequently drawn into a fiber. A laser interferometer is used to measure the thickness of the optical fiber as it is being drawn as the thickness of the fiber can be controlled by the tension applied during the

drawing process[53]. The silicon dioxide was deposited inside the quartz tube to form the cladding while the doped silica glass (e.g. doped by GeO_2 in the inner layers to increase the refractive index and make the fiber optically waveguiding) forms the core of the fiber as it is being drawn. The intentional doping in the SiO_2 (germanium, phosphorous, etc.) that make up the core of the fiber create an index of refraction that is just slightly higher (typ. a few 10^{-3} in single mode fibers like SMF28) than that of the pure SiO_2 that forms the cladding surrounding the core. The refractive index difference Δn between the two fiber elements (i.e., core and cladding) allows the fiber to exhibit Total Internal Reflection (TIR) within a specific solid angle called the numerical aperture NA. Δn can be controlled through the amount of dopants that are added to the glass during the preform fabrication, and standard processes allow a maximum of typically 30 mol% GeO_2 (the rest being SiO_2). The higher the levels of dopants, the higher the difference in the refractive index will be. As the fiber is pulled from the preform, it is also coated with polymers to strengthen the fiber that would otherwise be very brittle. A selection of coatings, depending of specifications, is reported in the table below.

Table 2-3. Different fiber coatings used in MCVD.

Type of coating	Standard acrylate	High temperature acrylate	Silicone	Polyimide coating
Permanent temperature of operation	$\leq 85\ °C$	$\leq 180\ °C$	$\leq 200\ °C$	$\leq 300\ °C$ $(350\ °C\ short\ term)$
Coating diameter (optional jacket)	Up to 400 µm (900 µm)	Up to 400 µm (900 µm)	Up to 400 µm (900 µm)	Up to 155 µm

Typically, there are two different types of coating, UV-cured urethane acrylate or polyimide composite. Also, a few companies are developing metal or ceramic-based coatings for optical fibers operating in radiative environment or high temperature applications. More classically, the purpose of the coating on the optical fiber is to protect the glass from scratches, micro bends, and moisture. Scratches and moisture lead to diminished strength of the optical fiber, while micro bends can cause light attenuation in the fiber due to sharp angles in the fiber core that reflect light at an angle that is less than that of the critical angle [54]. The fiber is usually considered structurally compromised when the coating is removed or burned off at high temperatures. Polyimide coatings can survive temperatures up to 300 °C, while the acrylate coating is only rated up to 180 °C.

Plasma Chemical Vapor Deposition (PCVD)

The PCVD process uses a starting tube and, very much like the MCVD process, the silica soot deposition takes place inside the tube. Here, the tube is either stationary or oscillating and the pressure is kept at 10–15 torr[55]. Reactants are fed inside the tube, and the reaction is accomplished by traveling microwave plasma inside the tube. The entire tube is maintained at approximately 1200 °C. The plasma causes heterogeneous depositions of glass on the tube wall, significantly increasing the deposition efficiency. After the required depositions of the cladding and core are complete, the tube is taken out and collapsed on a separated equipment. Extreme care is required to prevent impurities from getting into the tube during the transport and collapse procedure. The PCVD process has the advantages of high-efficiency, no-tube distortion because of the lower temperature and very accurate profile control because of the large number of layers deposited in a short time. However, going to higher flow rates can be challenging due to the need to maintain a low pressure.

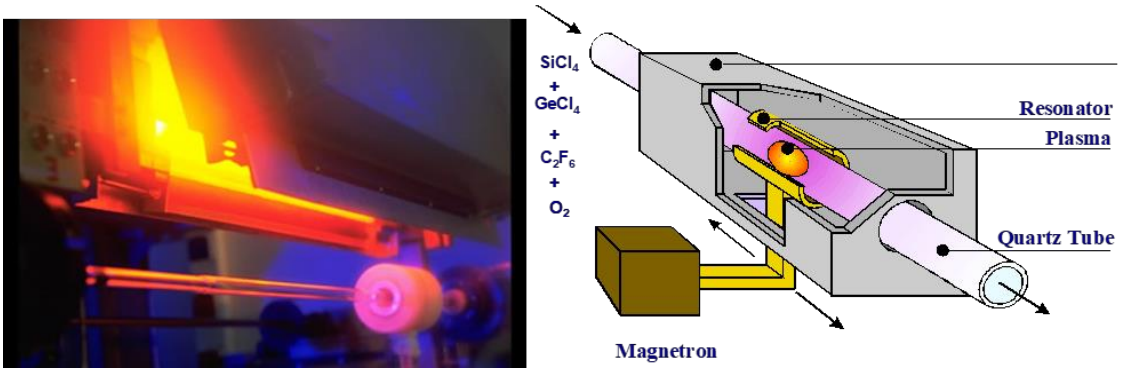

Figure 2-2: Scheme of the PCVD apparatus. [56]

The operation principle of PCVD is also described in *Figure 2-2*, showing a sketch of a PCVD apparatus for optical fiber preform preparation. The main constituents of the experimental setup are: the gas supply system, the reactor, and the exhaust pumping system. In the gas supply system, the starting materials are metered and mixed in the gas phase. The resulting gases, normally mixtures of $SiCl_4$, O_2 with varying contents of e.g., C_2F_6 and/or $GeCl_4$, are then fed into a silica tube with an inner diameter between 18 and 26 mm. In a moving non-isothermal plasma, which traverses along the tube, molecular reactions are stimulated and deposition of the desired glass components on the inner wall of the tube occurs. If desired, the tube can be rotated continuously or in discrete steps. In each pass of the plasma zone a compact glass layer can be deposited. Normally, the plasma is generated in a microwave cavity which operates at a frequency of 2.45 GHz. Typical values used area plasma power of 200-6000 W, traverse speeds of the microwave cavity of 6-10 m/min, and deposition lengths of 50-100 cm. A pumping system downstream maintains a pressure of 10-20 mbar inside the tube and removes the reaction products such as chlorine or excess oxygen.

The features inherent to the PCVD process can be summarized as follows.

1) The reaction and deposition rates do not markedly depend on the ambient gas temperature and the plasma activation turns out to be highly effective. This implies both high reaction yields and similar deposition behavior of silica and dopants.

2) The deposition takes place heterogeneously on the inner wall of the substrate tube at relatively low temperatures, resulting in compact pure or doped silica. This implies no soot formation and subsequently no doping with phosphorus is necessary to lower sintering temperatures. This also means that substrate tube deformation during deposition can be neglected.

3) The energy required to maintain the plasma and to stimulate the reactions is coupled directly into the gas phase. This means that the depositions is not influenced by heat capacity and conductivity problems of the deposited core and cladding glass material. This implies that the desired profiles can be approximated with high radial resolution, accuracy, and reproducibility by multilayered structures of up to some 1000 layers for a primary preform.

B. Molten core method (MCM)

Although optical fibers fabricated using conventional CVD techniques present unquestionable advantages and remarkable performances, such as extremely low impurity levels (< ppb), they suffer from being fairly restrictive in terms of the glass compositions they permit[57], and silica is somewhat limited in terms of its transmission window (up to the near-infrared wavelength region), and properties including nonlinear coefficients (either too high or too low depending on the application), or their lack of electronic functionality. In order to overcome the aforementioned limitations arising from the intrinsic nature of silica, new materials, that can be fabricated and shaped into optical fibers, are required. One interesting fabrication technique, employed to fabricate some fibers investigated in these thesis, is the Molten Core Method (MCM). This versatile technique enables the production of a wide variety of novel multicomponent all-glass optical fibers as well as practical crystalline core semiconductor optical fibers. These novel core fibers are expected to find application in a wide range of areas, such as high power fiber laser development, high temperature operating devices, surgical probes, or again terahertz waveguides.

This method somewhat differs from the conventional CVD technique. In general, a precursor core phase (powder, crystal rod, glass etc…) is inserted inside a tube (most of the time being pure silica glass), which serves as the cladding glass (*Figure 2-3*)[58]. The tube (called the preform) is set on a draw tower and the furnace temperature is increased until it reaches the temperature where the cladding glass tube draws into fiber. At this temperature, the core precursor phase is already in a molten state. The whole assembly (precursor and preform tube) is then drawn into a fiber, and the fluent core melt goes “along

for the ride" and ultimately solidifies as the fiber cools. Originally developed as a means to make all-glass fiber with core compositions not stable enough to form into rods and draw directly, [59] the molten-core method enables making long lengths of fiber directly from a simple preform and from a range of common materials such as silicon, germanium, YAG ($Y_3Al_5O_{12}$), and alumina. [60-62].

It must be pointed out that there is a degree of mixing between the core and cladding materials during the fiber drawing. The melt (core) contacts the softened glass (cladding) at the interface, and the two necessarily interact via dissolution and subsequent diffusion; the precursor and cladding nature, as well as the process itself impact these effects.

The fabrication of an optical fiber using the MCM is fundamentally different, and in many ways opposite, from the conventional approach to making fiber compositions where the silica host is doped with the modifying additives either in the vapor phase or in the solution phase. With the molten core method, the molten core dissolves some of the glass cladding and brings its constituents into the resulting core phase. Thus, a wider range of core compositions is possible. (Paragraph picked up from[58, 63]).

From practical considerations, there are some limitations in the precursors that can be employed, including materials with high vapor pressures at the temperature of drawing, which can blow out the softened glass cladding tube during the draw. In the case of powders, bubbles in the melt resulting from the porosity of the powder can be a concern. Finally, the impurity levels (from the precursors) is a limiting factor to produce low losses optical fibers (state of the art results are 0.1 dB/m, which is still 3 order of magnitude higher than silica based telecom fibers fabricated using CVD techniques).

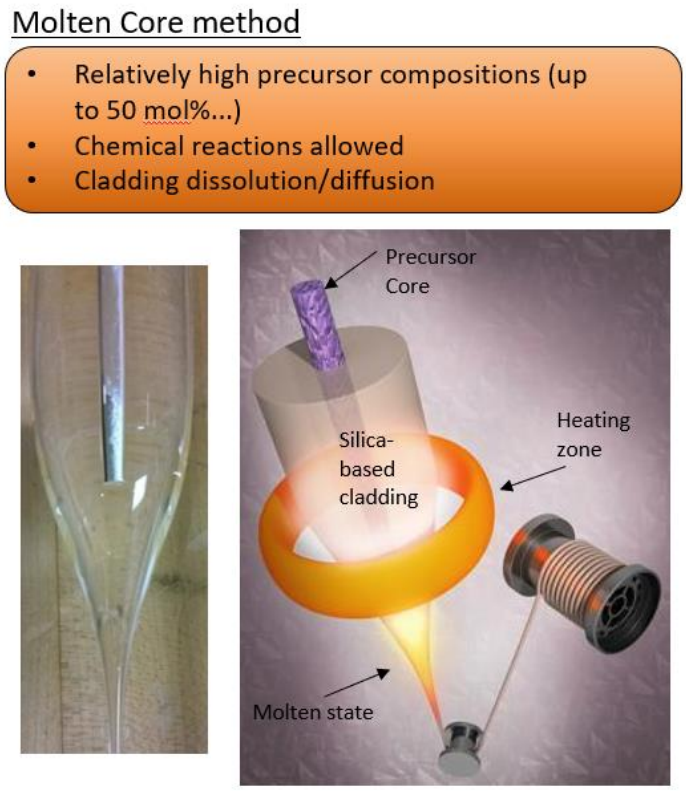

Figure 2-3: Schematic representation of the molten core method. [58]

An advantage of starting with crystalline core phases is the ability to use phases that cannot otherwise be made into glass. Two examples of this are YAG-derived [62, 64] and sapphire-derived [61] optical fibers fabricated using the molten core method. Interaction between the core precursor and the silica cladding can cause Liquid–liquid immiscibility (e.g., in Y_2O_3–SiO_2 and Al_2O_3–SiO_2 melts), which further restrict the range of compositions. The resultant core glasses contain much higher yttrium and alumina concentrations than would otherwise be possible, opening the door to "novel fibers from common materials" (just not common when it comes to optical fibers).

In this thesis, the YAG-derived and sapphire-derived fibers are fabricated with molten core method by our partner COMSET lab, Clemson university and IPHT lab, Jena university. For example, the sapphire-derived fibers have alumina concentrations up to about 54 mol% [58], which is the highest alumina concentration reported for a silicate glass not made using more extreme methods, such as melt levitation. By comparison, given the immiscibility and time–temperature requirement on conventional CVD optical fiber preforms, the typical limit to alumina content is about 8 mol%. It is worth mentioning that in the following chapters, we will conduct further exploration and research on the high Al_2O_3 content (typ. 50mol%) aluminosilicate fiber fabricated by MCM [65].

C. Optical Fibers Drawn from a 3D printed preform

As mentioned earlier, with the development of optical fiber technology, the focus has gradually included increasing specialization of the fiber for components such as fiber Bragg grating (FBG) sensors, lasers, and amplifiers. Ideally optical fiber fabrication has to remain compatible with standard low-loss fiber as well as opening the door to novel functionalities. Nevertheless, for the two optical fiber fabrication methods described above chemical vapor deposition (CVD) and molten core method (MCM), the former have limitation in the choice of material and the latter is limited more or less by the structure flexibility, neither of them can satisfy the diverse and custom-designed functionalities[66-68]. To address these limitations a new alternative is the use of additive manufacturing in the fabrication of preforms from which fiber is drawn[69, 70].

The early work in this field was on 3D printing plastic fibers [69], followed by 3D printed silica-based fiber preform fabrication[70]. 3D silica printing allows greater freedom in both structure and material design and choice. This fabrication process will be a major disruption more broadly because it reduces the skill requirements typically required in CVD processes and reduces overall costs whilst enabling newer designs.

One of the challenges with 3D printed fibers is the ultra-high temperatures required, often exceeding T = 1900 °C. The practical issue of developing technology that can handle such temperatures when melting the glass and moving it around on an xyz stage has impeded development in this area. Nonetheless, glass printing has been reported, including a brute force approach using fused deposition modeling (FDM) with high temperature zirconate nozzles to pump through molten silica [71]. Unfortunately, this approach was also stymied by the high viscosity of the glass, limiting practical printing at this stage to a resolution of ~ 4 mm, ten times worse than common plastic based FDM. To circumvent the extraordinarily high temperatures required, hybrid or composite material using a lower melting polymer with either organic encapsulated silica[72, 73] or nano or micro particles of glass has been reported[74]. The first 3D printed transparent fused silica glass extending several millimeters but with micron resolution, was achieved using ultraviolet (UV) sensitive monomer suspended with silica and direct light project (DLP) 3D printing or direct laser writing [75, 76]. Similar methods were used based on direct ink writing (DIW) to obtain several centimeter-long samples with sub-millimeter resolution [77, 78]. These latter methods used sol-gel silica suspended in an aqueous organic solution. Overall the main processes are similar involving material formulation to reduce thermal temperatures, photo- or thermal-polymerization to solidify the liquid state and subsequent polymer annealing. Debinding and the removal of the polymer and impurities before fusing the silica through sintering at higher temperatures followed this.

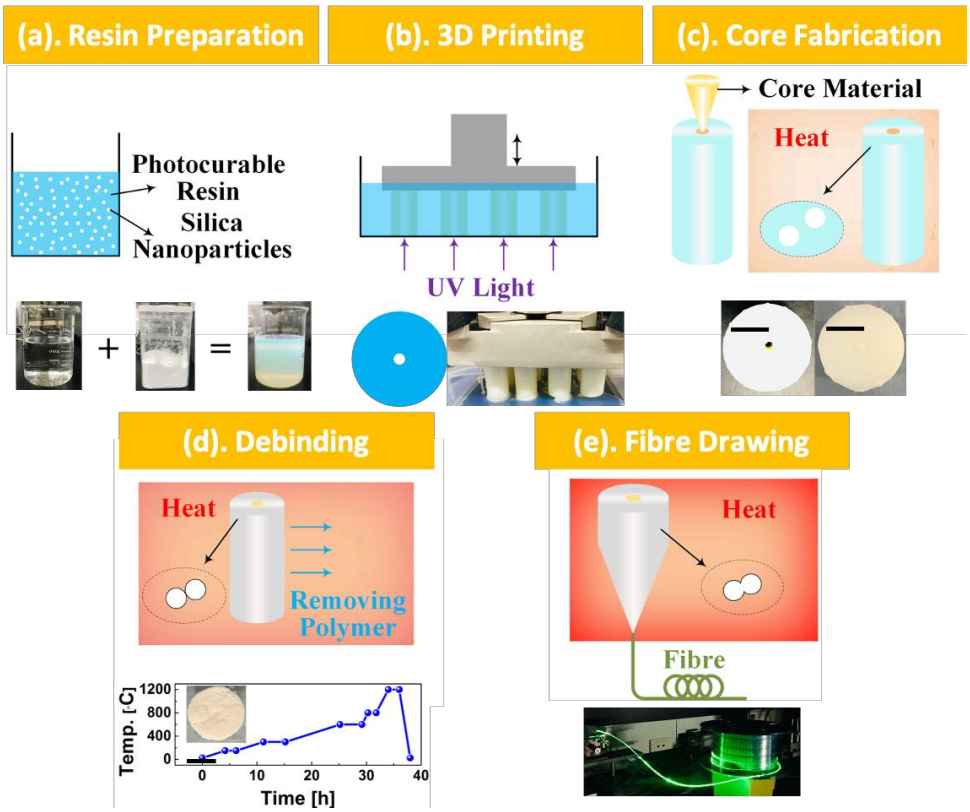

Figure 2-4: Fabrication of the step-index optical fiber using 3Dprinting: (a) dispersion of silica nanoparticle into ultraviolet curable resin;(b) DLP3D printing with UV light at 385 nm; (c) core material was poured into printed preform and undertaken a further thermal curing; (d) debinding process to remove organic binder; and finally (e) fibre drawing. All scale bars shown are 10 mm. [70]

A summary of the printing method used for step-index optical fibers is shown in *Figure 2-4*. The steps involve photocurable resin preparation, 3D printing of preforms, core fabrication, thermal debinding and final fibre drawing. Amorphous silica nanoparticles (ϕ ~ 40 nm, Aerosil OX50, Supplier: Evonik, Australia) were dispersed in photocurable resin, shown in *Figure 2-4(a).* The photocurable resin was fabricated by mixing 2-hydroxyethyl methacrylate (HEMA), 2-phenoxyethanol (POE), tetra(ethylenglycol) diacrylate (TEGDA), diphenyl (2,4,6- trimethylbenzoyl) phosphine oxide (DPO) and hydroquinone (Hyd). All of which were purchased from Sigma-Aldrich, Australia. The composition of the combined printing resin was 37.4 wt% SiO_2, 36.9 wt % HEMA, 19.0 wt % POE, 6.36 wt% TEGDA, 0.2 wt% DPO, and 0.1 wt% Hyd. This mixed resin was polymerized with the DLP 3D printer using λ = 385 nm (Asiga Freeform Pro 2 75 UV; x,y pixel resolution ~ 75 µm). By avoiding traditional optical fiber preform fabrication using a centre-spun lathe, it is possible to produce arbitrary structures.

The preform structure was designed on Inventor CAD (inner/outer diameter ratio, ϕinner/ ϕouter = 3/25 mm and length, L = 20 - 100 mm). The preform was printed layer-by-

layer using UV light traversed in the vertical direction - see *Figure 2-4(b)* (IUV = 5.8 mW/cm^2, tcuring =3.5s, layer thickness τ=75µm).

The step-index core was fabricated by inserting a prepared resin into the centre hole of the printed cladding preform, illustrated in *Figure 2-4(c).* GeO_2, TiO_2 and 2,2-azobis (2-methylpropionitrile) or AIBN (all from Sigma-Aldrich) were added to increase the refractive index. The final core resin composition contained 32.6 wt% SiO_2, 38.6 wt% HEMA, 19.9 wt% POE, 6.65 wt% TEGDA, 0.2 wt% DPO, 0.1 wt% Hyd, 0.5 wt% AIBN, 1.2 wt% GeO_2, and 0.84 wt% TiO_2. The core resin was poured into the cladding hole and cured at T=600C for t=2hrs and T=900C fort=0.5hrs, similar to[79, 80].

The fabricated preform was subsequently subjected to thermal debinding, where the polymer and other impurities are removed, illustrated in *Figure 2-4(d).* During debinding, the organic components were removed. Five temperature stages were employed: 150, 300, 600, 800 and 1200 °C for 2, 4, 4, 1.5 and 2 h respectively, with heating rate dT/dt = 0.5 °C/min up to T = 600 °C and dT/dt = 3 °C/min after 600 °C. The corresponding shrinkage and weight loss with polymer removal leaves behind an inorganic solid glass held together primarily by van der Waals force and perhaps some partial sintering. The size of preforms reduced predictably after debinding, consistent with their concentrations: the outer diameter, inner diameter and height decreased 30%, 34% and 23% respectively. These are important parameters for integrating this shrinkage into the fiber design of single and multicore fibers generally.

After debinding, the preform was inserted into a Heraeus F300 quartz tube for support and drawn directly into fiber on a commercial drawing tower *Figure 2-4(e)*. The drawing temperature (T ~ 1855 °C) was slightly lower than normal MCVD processing to help remove air, water and residual polymer gradually. The inner pressure of the preform was kept as low as possible (P ~ 50 mbar). Finally, fibers of length L ~ 2.3 km were readily drawn, shown in *Figure 2-4(e).* During this process, the change in the silica nanoparticles is illustrated by the dashed ellipses shown in *Figure 2-4(c), (d), (e).* Those enlarged white dots represented silica nanoparticles whilst the blue background represents the polymer binder. As the temperature gradually increased, the polymer is ablated leaving behind the silica nanoparticles, which come closer together leading to preform shrinkage. Sintering at higher temperatures fuses them together. Similarly, this type of fiber will also be studied in the chapter 5.

It is worth to mention that I fabricated the 3D printed fibers by myself with the help of our partners from University of technology Sydney and University of new south wales during the 3 months' research project in Sydney Australia. These fibers own an asymmetry core and remains a high loss ~9dB/m, we will investigate them in Chapter 5.

2.2 Characterization techniques

2.2.1 Density measurement

The density measurements have been carried out at the "Institut de Physique du Globe de Paris" (IPGP) in the team of Daniel Neuville. These measurements are based on the Archimedes principle, which implies that anybody immersed in a fluid receives from this fluid a force equal to the weight of the volume of fluid displaced. To know the density of a solid, it is then a question of accurately evaluating the mass of the body and that of the same volume of liquid. In our case, the fluid used is toluene. Because of its greater wettability than water, it offers better measurement accuracy, thus avoiding the generation of air bubbles around the sample. The density of an unknown sample is estimated by measuring its mass in air and then in toluene, by applying *Equation 2-1*:

$$\rho_{sample} = \rho_{toluene} + \frac{m_{air}}{m_{air} - m_{toluene}} \quad \text{(Equation 2-1)}$$

ρ_{sample} : density of the sample analyzed;

m_{air} : mass of the sample in air;

$m_{toluene}$: mass of the sample immersed in toluene;

$\rho_{toluene}$: density of toluene.

However, the volume of a liquid varies with temperature, so does its density. The measurement then also takes into account the temperature of the toluene. The relation between the density of toluene and the temperature is known and given by the *Equation 2-2*.

$$\rho_{toluene} = 0.8845 - 0.9159 \times 10^{-3} T + 0.368 \times 10^{-6} T^2 \quad \text{(Equation 2-2)}$$

The samples weighed must have a mass between 10 and 10,000 mg. Finally, ten to twenty measurements are taken for each different series of samples in order to reduce the error due to handling.

2.2.2 Chemical composition analysis

In this PhD thesis SEM coupled to energy-dispersive X-ray spectroscopy (SEM/EDS) is used to determine the distribution of atoms in and around the laser-modified areas. It was conducted in a field-emission gun scanning electron microscope (FEG-SEM ZEISS SUPRA 55 VP).

Energy-dispersive X-ray spectroscopy (EDS, EDX, EDXS or XEDS), sometimes called energy dispersive X-ray analysis (EDXA) or energy dispersive X-ray microanalysis (EDXMA), is an analytical technique used for the elemental analysis or chemical characterization of a sample. In fact, EDS is a kind of X-ray spectrometer. This uses a high-energy focused beam of electrons to generate X-rays characteristic of the elements within a sample from volumes as small as 1 micrometer (10^{-6} m) across. Low-energy thermionic electrons are produced from a tungsten filament and accelerated by a positively biased anode plate to 10-30 thousand electron volts (keV). The anode plate has a hole in its center and the electrons pass through it and are collimated and focused by a series of magnetic lenses and apertures. The interaction of incident electron beams with atoms in the sample can cause inter-shell electron transitions, resulting in X-ray emission. The incident electrons kick out an electron located around the atomic nucleus. Then, an electron from an outer shell comes down to take the place of the previously ejected electron. Each element produces a unique set of characteristics X-rays (i.e. an energy and wavelength characteristic of the element).

The X-rays resulting from beam interaction with the sample are sent to the X-ray detector. Usually silicon or germanium doped with lithium (Si(Li) or Ge(Li)) semiconductor detectors are used. X-ray photons are converted to electron-hole pairs in the semiconductor and are collected to detect the X-rays. When the temperature is low enough (the detector is cooled by Peltier effect or even cooler liquid nitrogen), it is thus possible to directly determine the X-ray energy spectrum; this method is called energy-dispersive X-ray spectroscopy (EDX or EDS). Finally, the energy-dispersive software sorts the X-rays depending on their energy, producing an output in the profile of a plot of intensity as a function of X-ray photon energy. Chemical composition is determining by comparing the intensity of X-rays from standards (known composition) with those from unknown materials and correcting for the effects of absorption and fluorescence in the sample.

The system is designed specifically for detecting and measuring characteristic X-rays. It uses an electron beam current from 10 to 200 nanoamps (nA), roughly 1000 times greater than that in a scanning-electron microscope (SEM). Note that high beam currents produce more X-rays from the sample and improve both the detection limits and accuracy of the resulting analysis but at the expense of a lower spatial resolution (higher probe volume). Analysis locations are selected using the SEM and line profile or 2D cartography can be done. The resulting data yield quantitative chemical information in a textural context. Variations in chemical composition within a material, such as a mineral grain or metal, can be readily determined. The electron microprobe can quantitatively analyze elements from fluorine (Z=9) to uranium (Z=92) at routine levels as low as 100 ppm.

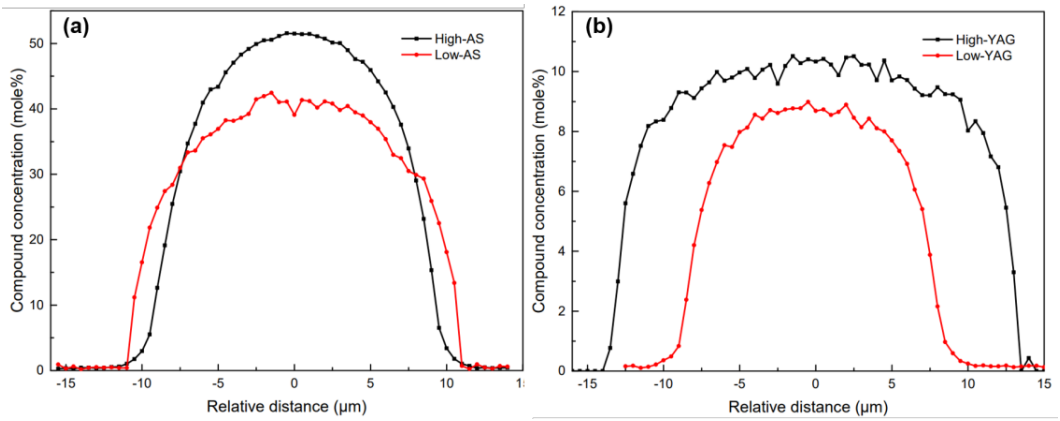

Figure 2-5. Concentration profile of the fiber core somposition for (a) Aluminosilicate fiber; (b) YAG fiber.

Figure 2-5 shows two examples of the chemical composition analysis for our fibers. The parabolic profiles explain the content of the Al_2O_3 or Y_2O_3 continue to increase until the center of the fiber core because of the diffusion and convective mixing between the core and the cladding during fiber drawing. More discussion about the results will be presented in the following chapters.

2.2.3 Spectroscopic characterization

Since spectroscopy (UV, Vis, IR) was discovered, it has been recognized as an important analytical tool with high potential, due to its non-destructive nature and its ability to provide information in a wide variety of fields like physics, chemistry, earth sciences and biology. In the framework of this PhD thesis, over the last two decades laser-induced Δn profiling in SiO_2 glasses was widely used for production of in-fiber/waveguide Bragg grating-based (BG) optical devices for photonics industry [81]. Irrespective of the type of irradiation, these changes are based on point defects (observed in VUV-UV-Vis absorption and EPS spectroscopy) and structural changes (observed in vibrational spectroscopy and in particular Raman spectroscopy) induced by irradiation. As a result, many authors consider that the Raman or FTIR bands record matter densification/expansion in glass.

In particular, a phenomenon observed from the first studies received a lot of attention because of its quasi-universal nature (under laser irradiation or radiative environment, under hydrostatic loading, under shock, etc.) but also its potential in the field of optics for light guidance or the manufacture of integrated optical functions. This is a phenomenon of permanent densification of silica (but also sometimes expansion in other glass compositions). In particular silica glasses densification is commonly observed under various kinds of irradiations employing neutrons, ions, electrons, X rays, γ rays with energies ranging from keV to MeV [82-87]. Such kind of modification occurs also after sub-bandgap irradiations with UV ns or Vis-IR femtosecond lasers. The experimental fact that fused silica undergoes

densification upon prolonged exposure to high-energy radiation is well documented in the literature.

A. Raman spectroscopy

The so-called Raman effect describes the changes in the radiation frequency when a monochromatic light interacts with a substance. When monochromatic radiation ν_o, is incident on a system (in any physical state) most of the radiation is transmitted through the system without interacting with it. Only some of the radiation is scattered. This light mostly has the same frequency as the incident light. Only a small amount presents a change in the frequency. The frequency of the scattered radiation corresponds to $\nu' = \nu_o \pm \nu_m$. In molecular systems, the frequency of the Raman-active vibration (ν_m) is found to lie principally in the range associated with transitions between vibrational, rotational and electronic energy levels[88].

The principle of Raman spectroscopy is the illumination of a material (either bulk, powder, or fiber) with a beam of monochromatic light (laser) in the visible spectral range followed by the interaction of the incident photons with the molecular vibrations or crystal phonons, which induces a slight shift in the wavelength of the scattered photons. Scattering can occur with a change in vibrational, rotational or electronic energy of a molecule. When the scattered radiation has the same frequency as the incident light, the scattering is elastic (Rayleigh scattering) and this is the predominant interaction. In contrast, the scattering is called inelastic when the scattered photons have a different frequency (Raman scattering) and the scattered photons exhibit a shift in energy called the Raman shift. However, the Raman shift only occurs when the electron cloud, between the vibrating atoms involved in the interaction with the incident light, can be deformed. This deformation is described as the polarizability of the molecule or bond. A change in the degree of polarization potential or polarizability with respect to the vibrational coordinates of the system being studied is required for a molecule to exhibit the Raman effect. The frequency or energy shift can then be measured by a spectrometer. The spectral shift or Raman shift (given in cm^{-1} $\Delta\nu = (1/\lambda_0 - 1/\lambda_m)$: ν is the Raman shift expressed in wavenumber, λ_0 is the laser wavelength and λ_m the Raman spectrum wavelength) corresponds to the vibrational frequency of the vibrational source (molecule, molecular/atomic group) and is characteristic of the atoms undergoing vibration. The relative intensity of the Raman peaks or bands depends upon the nature of the scattering material and the type and concentration of the atoms undergoing vibration (specifically to the molecule or bond polarizability).

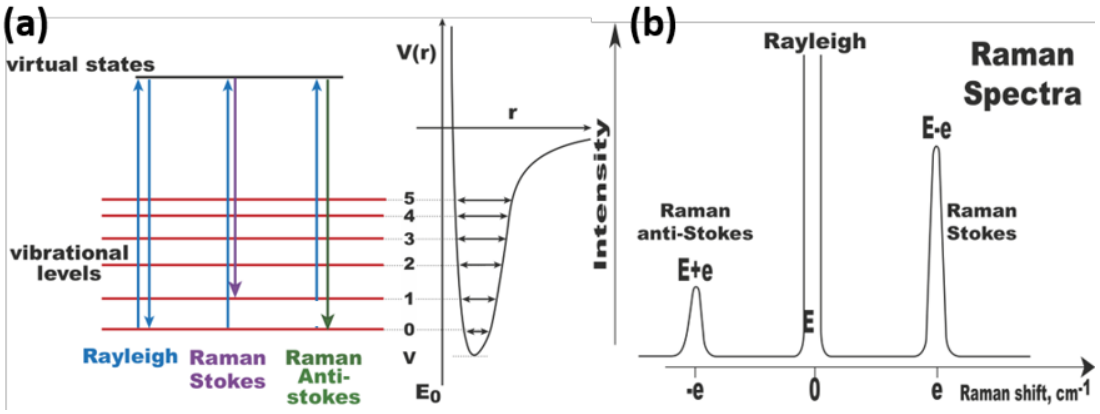

Figure 2-6*: (a) Virtual states versus vibrational levels.* (b) Schematic of the exciting line, at 0 cm^{-1}, and the Raman scattering on the left and right, Stokes and Anti-stokes Raman frequencies, respectively.

In other words, monochromatic laser light with frequency ν_o excites molecules and transforms them into oscillating dipoles the magnitude of which is related to the degree of polarizability. Such oscillating dipoles cause the interacting photons to be scattered with three different frequencies (schematically represented in *Figure 2-6 (a):*

- A molecule with no Raman-active modes (vibrations) interacts with a photon with frequency ν_o. The excited molecule returns back to the same basic vibrational state and scatters light with the same frequency ν_o as the excitation source. This type of interaction is elastic Rayleigh scattering.
- A photon with frequency ν_o interacts with a Raman-active molecule, which, at the time of interaction, is already in the excited vibrational state. Excessive energy of excited Raman-active mode is released, molecule returns to the basic vibrational state and the resulting frequency of scattered light goes up to $\nu_o + \nu_m$. This Raman frequency is called “Anti-Stokes”.
- A photon with frequency ν_o interacts with a molecule, which at the time of interaction is in the basic vibrational state. Part of the photon’s energy is transferred to the Raman-active vibration with frequency ν_m and the resulting frequency of scattered light is reduced to $\nu_o - \nu_m$. This Raman frequency is called Stokes frequency, or just “Stokes”.

If the investigated material is illuminated by monochromatic light, for example with a laser, the spectrum of the scattered light consists of a strong line (the exciting line see *Figure 2-6 (b)* of the same frequency as the incident illumination together with much weaker lines on either side shifted from the strong line by frequencies ranging from a few to about 4000 cm^{-1}. The higher the frequencies, lighter are the atoms involved in the molecular vibration.

In a classical theory, Raman scattering occurs when monochromatic light interacts with

molecular vibrations or crystal phonons (vibrations propagating along the crystallographic axis). To a first approximation (the so-called harmonic approximation), the vibration can be modeled by a spring binding two masses (m_1 and m_2) with a force constant k. The vibrational frequency, corresponding to the eigen mode of vibration of the spring, can be calculated as $\nu = 1/2\pi(k/\mu)^{1/2}$ with, the reduced mass ($\mu = m_1.m_2/(m_1+m_2)$).

The vibrational frequency depends on several physical and chemical parameters: the chemical nature of the atoms involved in the bond, the nature of the bond (modeled by the force constant, k) and the symmetry of the molecule or molecular group undergoing the vibration. Thus, the vibrational frequency can be considered as a characteristic signature of the material being studied. Indeed, each specific molecule or crystal has its own vibrational frequencies and can be characterized and identified by using these frequencies. Raman spectroscopy enables one to measure these fundamental vibrations resulting in sharp, well-resolved bands visible in a Raman spectrum of a gas or crystalline material. Several books are available on the subject from theory to applications [89-94].

In the framework of this PhD thesis, Raman microspectroscopy will be used to detect the vibrational structure of different samples, especially to observe their changes after femtosecond laser irradiation. One common way is to follow the structural changes that indicate a density change using Raman spectroscopy and particularly the so-called 'defect' bands that are quite sensitive. Historically, the D_1 and D_2 bands, located at 490 and 605 cm^{-1} respectively, have been first interpreted by [95, 96] as being 'breathing' vibration modes of four and three-membered rings respectively in the material. Both the relative intensities and the peak position shift of the D_1 and D_2 defect lines at 490 cm^{-1} and 606 cm^{-1} respectively, can be used to determine permanent volume changes. As a first approximation, and for a given composition, a change in the intensity (or the area) but also the peak position (a more reliable indicator) of these bands indicates a modification in the rings statistics. The Raman spectra of SiO_2-based glasses show the 440 cm^{-1} band, the maximum of which is characteristic of the maximum of the distribution of the T–O–T (T = Si or Ge) intertetrahedral angles θ. The shift of this band towards high energy and narrowing corresponds to a decrease of θ [97-99] indicating a densification. Here an example is exhibited in the *Figure 2-7*, we demonstrate the Raman spectra of SiO_2-Al_2O_3 samples with different concentrations. The evolution of the bands can be easily observed as the concentration of Al_2O_3 increases, especially the D_1 and D_2 defect lines.

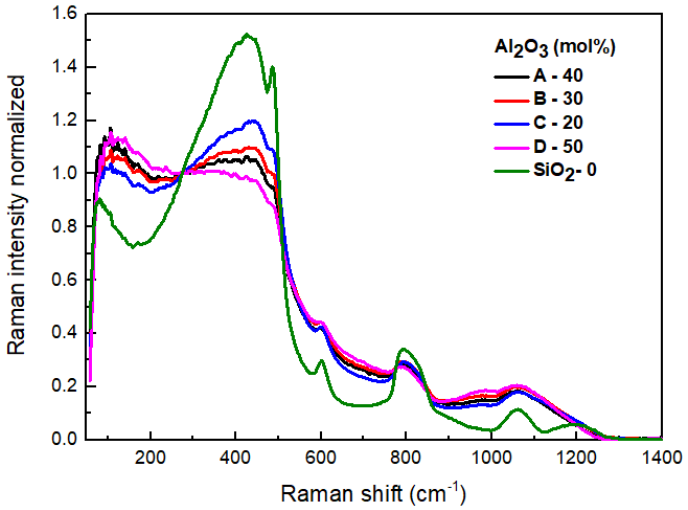

Figure 2-7. Raman spectra of SiO_2-Al_2O_3 samples, the phase SiO_2 is also inserted for a sake of comparison.

B. Fourier-transform infrared spectroscopy (FTIR)

Infrared spectroscopy is a non-destructive characterization technique based on the absorption of an infrared beam by a sample. It allows, via the detection of characteristic vibrations of the bonds of molecules, to know the chemical functions present in the compound. Relatively simple to implement, it does not require any special preparation of the sample, except in the case where the measurement result is correlated with the surface quality of the latter (typically polishing). It is therefore used in many fields relating to research and development, both for qualitative and quantitative analysis.

Fourier transform infrared spectrometers are instruments that acquire a broadband absorption spectrum from near infrared to far infrared. First collecting and digitizing the interferogram of a signal from a sample using a Michelson interferometer, and then applying a Fourier transform obtain the infrared spectrum. Many advantages are attributed to FTIR spectrometers, compared to dispersive spectrometers, such as monochromators:

- FTIR spectrometers simultaneously collect all working wavelengths, which ensures particularly fast acquisitions. This characteristic is called the Felgett advantage or multiplexing. The signal-to-noise ratio is also improved by using an average of several scans (typ 100's within a few minutes), which provides a better sensitivity.
- The wavenumbers σ (in cm^{-1}) are calculated relative to the precisely known frequency of the laser. The reproducibility of the measurements is significantly

improved compared to a dispersive spectrometer, which requires a grating position adjustment by a mechanical arm like a rotation stage.

- There is a larger optical aperture at the input of an interferometer, allowing the flux emitted by the source to be used at a larger solid angle. The luminosity arriving on the sample is then much higher which allows also using small diaphragm especially coupled to a microscope resulting in a spatial resolution down to 10microns in the best case.
- Finally, the amount of stray light, which is unexpected radiation reaching the detector, remains low in an interferometer.

The schematic diagram of the FTIR spectrometry technique is shown in *Figure 2-8*. The sample is first excited by incident radiation, the energy of which is close to the vibrational energy of the molecules. Part of the incident beam is absorbed by the sample while the rest is transmitted and collected by the detector. Comparison of the spectrum acquired with a reference spectrum, called a "background", makes it possible to deduce the absorption of the molecules present. This requires two major components, the one is the Michelson interferometer that is essential for generating the interferogram, and the other is the Fourier transform processing for "deciphering" information.

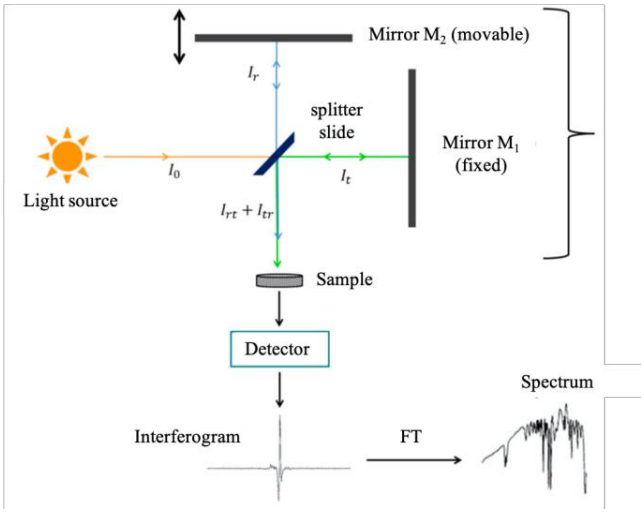

Figure 2-8: Schematic diagram of the FTIR spectrometer [100].

The FTIR spectrometers are based on a Michelson interferometer shown schematically in *Figure 2-8*. The interferometer consists of a separator and two orthogonal plane mirrors M1 and M2, one fixed (M1) and the other movable (M2), which can be translated very precisely. The splitter is inclined at 45 ° concerning the direction of propagation of the beam and is placed in the center of the optical assembly. It is actually a glass slide treated to be semi-reflective, which allows half of the incident beam to be transmitted and the other half

to be reflected. Incident radiation from source (I_o) is separated into two beams, one transmitted (I_t) to M1 and the other reflected (I_r) to M2. The two mirrors in turn reflect the beam towards the splitter, which again splits it. When the two beams recombine, it appears, according to Fresnel's laws, constructive or destructive interference depending on the position of the mobile mirror. In the end, two beams result from this optical assembly, one directed towards the source which is therefore unusable, and the other I_{rt} + I_{tr} which is led towards the detector, used for acquisitions.

In the framework of this PhD thesis: In silica-based glasses, it has been shown that the IR absorption band located near 1120 cm^{-1} (or its overtone around 2260 cm^{-1}) and that corresponds to the fundamental asymmetric stretching vibration of the Si–O–Si structure, is very sensitive to structural changes and thus to permanent volume changes. This IR vibrational structural band is related to the Si–O–Si bond angle [101, 102], which provides an accurate way to probe permanent volume changes.

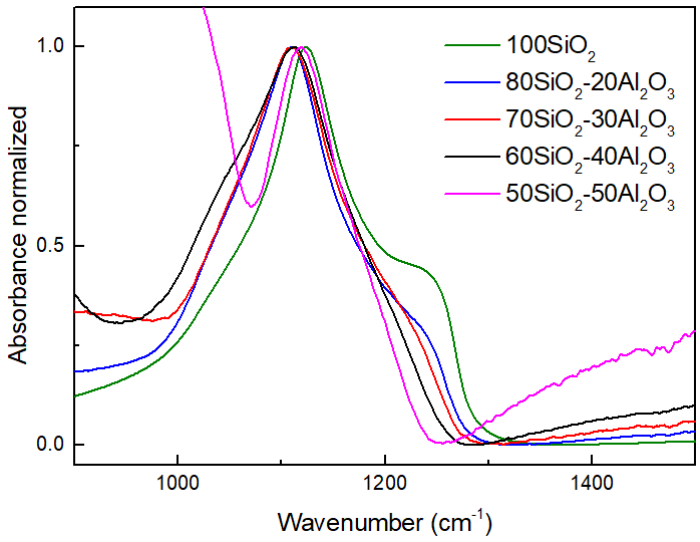

Figure 2-9. FTIR spectra of SiO_2-Al_2O_3 samples, the phase SiO_2 is also inserted for a sake of comparison.

Figure 2-9 shows an example of the FTIR spectra, which is the test for our SiO_2-Al_2O_3 samples with different concentrations. The spectra were carried out in reflection mode on the samples. We especially note a band with a shoulder around 1100-1200 cm^{-1} which is attributed to the TO (Optical Transversal) and LO (Optical Longitudinal) Modes of the antisymmetric elongation vibration of the Si-OT bonds (T = Si or Al). We note in *Figure 2-9* that this band around 1100 cm^{-1} shifts towards the low frequencies when we add Alumina to SiO_2. We also notice that the LO Mode around 1200 cm^{-1} is less intense when we add alumina and a shoulder appears around 1050 cm^{-1} which would be linked to the appearance of Si-O-Al bonds. What needs special attention is the spectrum of sample which has 50%

Alumina where we can clearly see a band around 900-1000 cm^{-1} attributable to the formation of Al-O-Al bonds (bending).

C. Ultraviolet Visible Absorption Spectroscopy

Ultraviolet Visible Absorption Spectroscopy (UV-Vis-NIR absorption spectra), referred to as ultraviolet spectroscopy (belonging to molecular spectroscopy), is the absorption spectrum produced by the transition of electrons when the molecules of a substance absorb electromagnetic waves in the ultraviolet-visible region. Generally speaking, the wavelength range of the ultraviolet spectrum is mainly 200-600nm (10-200nm is the vacuum ultraviolet region. Because air has strong absorption of electromagnetic waves in the deep-ultraviolet region, the VUV spectrum is less studied. Because the molecules of different substances have different compositions and structures, they have different characteristic energy levels, and their energy level differences are different. Each substance can only absorb light radiation equivalent to the energy level difference within their molecules. Therefore, different substances respond to different wavelengths of light. We can thus analyze, determine, and infer the composition, content and structure of the material through the ultraviolet-visible spectrum and the degree of absorption of electromagnetic waves in the ultraviolet-visible region. We use the UV-Vis absorption spectroscopy to monitor the thermal stability of the point defects in the femtosecond laser induced Type II modification area.

2.3 Laser irradiation

2.3.1 Femtosecond laser direct writing (FLDW) system

For the work described in this thesis, we mostly used a femtosecond fiber laser writing system. The femtosecond fiber laser system used for fabrication of our samples in bulk fused silica consists of a directly diode-pumped Ytterbium fiber laser (Satsuma HP from Amplitude Systèmes), with a center wavelength of 1030 nm and variable repetition rates from 200 kHz to 2 MHz. The key characteristics of this system are summarized in *Figure 2-10*. It is equipped with a pulse picker (acousto-optic modulator), which allows to reduce the repetition rate down to a single pulse if need. The average power is fixed to 10 W that allows reaching up to 25 µJ/pulse at 400 kHz or 10 µJ/pulse at 1 MHz.

	Laser Parameters		Unit	Target		Measurement	
				400 kHz	2000 kHz	400 kHz	2000 kHz
IR	Energy per pulse		µJ	≥ 25	≥ 5	26.5	27
	Average power		W	≥ 10	≥ 10	11.1	11.3
	Center wavelength		nm	1030 +/- 5		1032.1	1032.2
	Bandwidth FWHM			≤ 10		8.6	8.9
	Pulse duration		fs	< 500		220	240
	Pulse energy over 12h	Average	µJ	> 25	> 5	27.8	-
		RMS	%	< 2		0.08	
	Polarization ratio		-	> 100:1		625:1	
	M^2	M^2x	-	< 1.30		1.10	
		M^2y				1.07	
	Beam diameter	W_0x	mm	2 +/- 0.5		1.53	
		W_0y				1.50	
	Beam ellipticity		%	< 13%		1.9	
	Astigmatism			< 50%		27.8	
	Waist ellipticity			< 13%		0.1	

Figure 2-10: Certificate of Conformance (CoC) of the Satsuma HP Laser used in this PhD work.

After amplification and compression, the pulse width is typ. 250 fs full width at half maximum (FWHM). Note that the intra-cavity distance between the chirped gratings is adjustable using a motorized translation stage in order to optimize the compression of the pulses according to the repetition rate provided by the laser.

The laser is linearly polarized horizontally (parallel to the optical table) and perpendicular to the z-axis (as defined in *Figure 2-11*). The computer controlled half waveplate (Newport SR50CC rotation stage) and the Glan-Laser polarizer provides a way of tuning the beam power while guaranteeing the linear polarization of the laser, which is fixed horizontal at this point (along x-axis, and thus parallel the ideal plane of the laser compressor). The laser path can then be selected between two alternatives, the acousto-optic modulator (AOM) path and non-AOM path.

The AOM is also computer controlled by a digital RF driver signal, and is optimized to create one first order diffraction beam with an adjustable diffraction efficiency from 0 up to 100% of the total power of the input beam. In some cases, this configuration serves as a fast on/off switch for the laser beam and can reliably operate at frequencies up to 2 MHz with the current setup. For example, the ability to modulate the laser beam with the AOM allows the direct fabrication of Bragg grating waveguides (BGWs) [103-105], by creating a waveguide composed of periodic segments, or volumetric pixels (voxels), of refractive index higher than that of the background refractive index of fused silica. At this point in the fabrication setup of *Figure 2-11*, the laser wavelength is 1030 nm and the pulse width is typ. 250 fs with a variable repetition rate ranging from 400 kHz to 2 MHz and the possibility of AOM modulation (typ. 100 kHz and down to single pulse) and an additional shutter for synchronization.

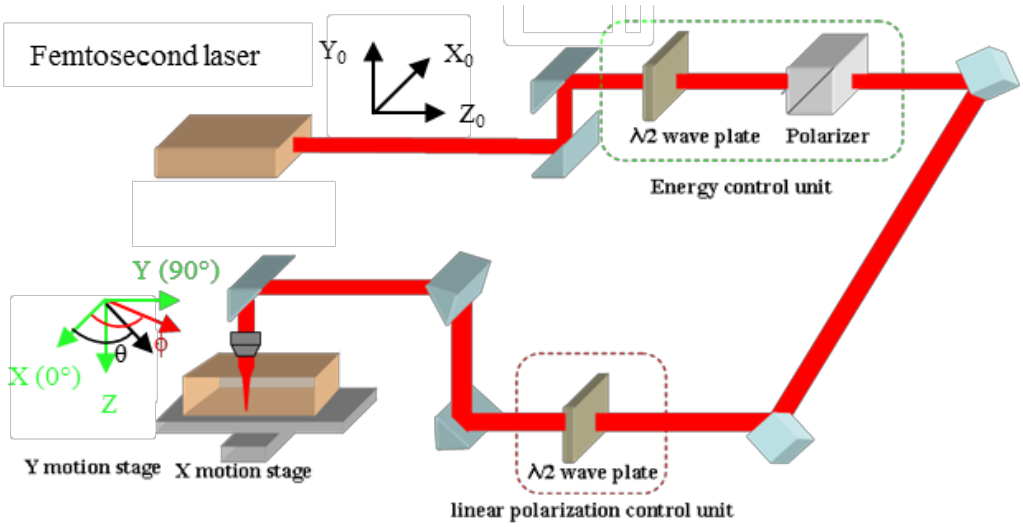

Figure 2-11: Schematic diagram of the femtosecond laser direct writing (FLDW) setup used at ICMMO laboratory.

The laser beam is then aligned inside the target delivery system described *Figure 2-12* and focused into the silica glass sample that is mounted in the computer controlled motion XY-stages (one-XY200HA from Newport) having a minimum resolution of 50 nm, a bi-directional repeatability of 90 nm and a speed up to 200mm/s. The computer controlled Z-stage (Newport UTS100CC) positions the laser spot typically at 300 µm below the surface of the glass substrate. Aspheric lenses with numerical apertures (NAs) ranging from 0.16 NA to 0.65 NA were used to create spot sizes with diameters ranging from 4,5 µm to 1,1 µm (e.g. 1,3 µm for 0.55 NA). The diameter is calculated at $1/e^2$ of the maximum intensity with *Equation 2-3*, where ω_0 is the spot radius for the infrared 1030 nm wavelength, considering a typical beam quality of $M^2 < 1.1$, and assuming a Gaussian distribution.

$$\omega_0 = \frac{M^2 \lambda}{\pi \mathrm{NA}} \quad \text{(Equation 2-3)}$$

The additional motorized half-waveplate pictured in the diagram of *Figure 2-13* further permits the control of the laser beam polarization state to be linear along the y-axis, linear along the x-axis or any linear polarization state in between at the sample position. This waveplate is mounted on a fast belt driven rotation stage (Newport URB100CC) with a typical speed of 720°/s. Using this freedom to control the laser polarization, the laser power together with the XYZ motion control, it is possible to have the polarization of the laser beam oriented parallel or perpendicular, or, even oriented at an arbitrary azimuth with respect to the laser scanning direction in the glass sample.

Figure 2-12 illustrates the laser being focused into a fused silica sample and a laser written line (like a waveguide for example in [106]) being formed by scanning the sample through the laser spot. The geometry also illustrates the orientation of the birefringence

proper polarization axis of the waveguide modes, or polarization eigenmodes, which are formed by the orthogonal directions: Vertical, V, and Horizontal, H, defined with respect to the optical table.

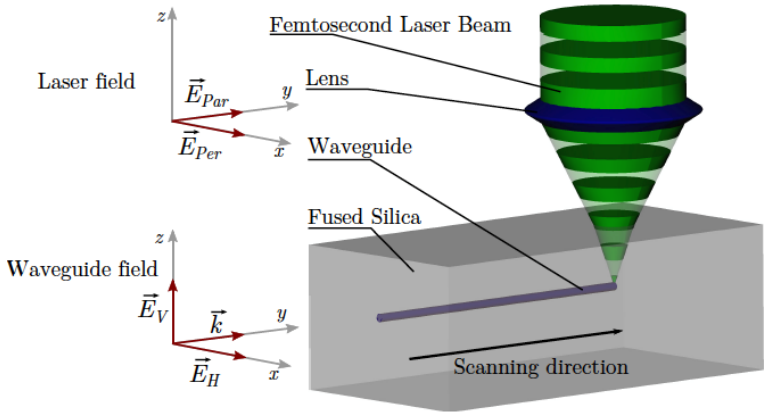

Figure 2-12: Schematic diagram of the laser lines (waveguide like) fabrication where Epar and Eper represent the parallel and perpendicular polarizations of the writing laser. The scanning direction was fixed along Y-axis. For Epar (Yy writing configuration), we have the nanogratings form birefringence optical fast axis along y whereas slow axis is along x. For Eper case (Yx writing configuration), we have optical fast axis along x whereas slow axis is along y. Graph adapted from [107].

All motorized components are connected to a computer via an XPS - 8-axis controller from Newport. The control interface is made from the GOL3D software whose schematic description is shown in *Figure 2-13*. This software is designed to centralize the control of the elements of the assembly, but also to control the translation plates where the sample is positioned. This makes it possible to perform complex writing paths at a constant speed such as a spiral or sets of objects in 3D. The write speed is an important parameter to take into account because it influences the pulse accumulation on the laser trace. It is therefore necessary that it remains identical throughout the trajectory by optimization of the writing algorithm and the writing synchronization with the shutter.

Throughout this work, the first type of substrates used were Infrasil or SuprasilCG fused silica with a typical dimension of 75 mm length, 25 mm width, and 1 mm thickness, with double side optically polished. Then, the second type of substrates used were the different type of fibers as the SMF 28, Aluminosilicate fiber and 3d printed fiber with a typical dimension of 25 µm core diameter and 125 µm cladding diameter. The length chosen in each case depended on the minimum length required for each particular experimental device.

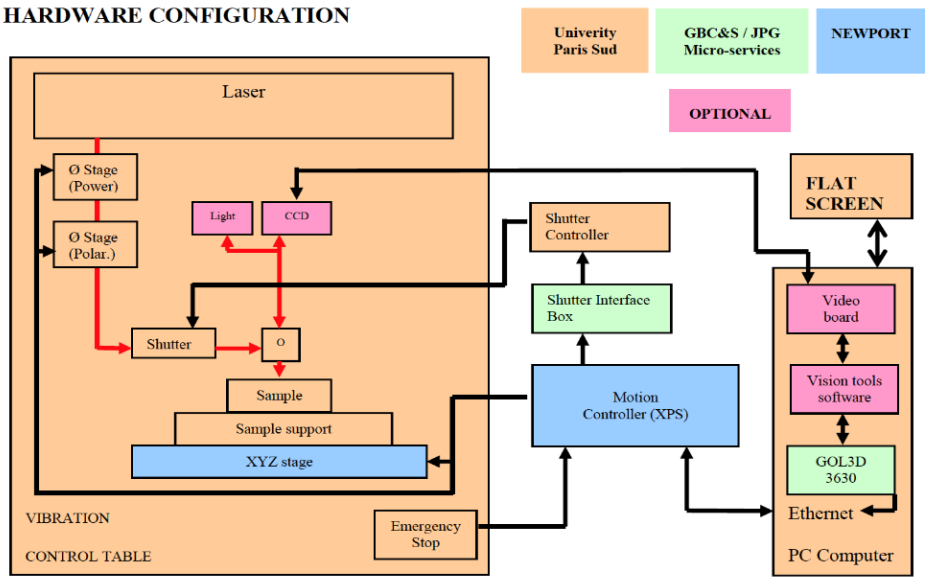

Figure 2-13: Schematic diagram of the hardware configuration related to our direct writing software "GOL3D".

2.3.2 Fs-laser irradiation in optical fibers

Fiber Bragg gratings can be photo-inscribed or written in optical fibers using a laser source such as a UV laser (as done in chapter 5 in UTS, Sydney) but also Vis-IR femtosecond laser since 2006 [108]. Generally, photosensitive fibers such as germanium-doped silica fiber or a hydrogenated fiber (usually pre-soaked in hydrogen) are used in the manufacture of fiber Bragg gratings. In our case, we also use the Aluminosilicate fibers both sapphire derivated or YAG derivated fibers made by the molten core technique. In the literature, different methods are used to inscribe or write these gratings in the core of photosensitive fibers. The two main processes or techniques used are interference phase masking technique and point-to-point inscription techniques have been briefly presented above.

However, in this PhD thesis, we are focusing our attention on fundamental processes and we are targeting to realize local measurements in contrast to non-local measurements such as the ones based on Bragg reflectivity and Bragg wavelength. In the following we will thus write gratings like structure using a line-by-line technique as described in the scheme *Figure 2-14 (a)*.

On the one hand we will write some set of lines in a transversal geometry. The similar to line-by-line FBG writing was inscribed by Femtosecond laser irradiation (λ = 1030 nm, 250 fs) with different pulse energy on the samples. Place the prepared sample on a XYZ motorized translation stage, as shown in *Figure 2-14*, series of lines along the x-axis with a

linear laser polarization oriented either parallel (Yy configuration) or perpendicular (Yx configuration) to writing direction are drawn by the femtosecond laser. For the case of the fiber sample, normally a 5cm length fiber segment with coating removed is taken before the irradiation and fixed on a fused silica glass slide. A few drops of index-matching oil (GN Nettest, n_D=1.4580 at 25 °C) are injected on the fiber and then cover by a borosilicate glass (~170 µm thin) on the top for an easier observation. Finally, the sample will be characterized by using Sénarmont method (Birefringence-Retardancy), slow axis imaging, QPm, and eventually learned the thermal stability by the heat treatment. It should be point out here that for each target sample, we processed laser irradiation generally with two polarizations (Xx and Xy) and a series of different energies for a sake of comparison, then birefringence measurement was launched 3-5 times for each irradiated area, and finally the results were presented by the average value.

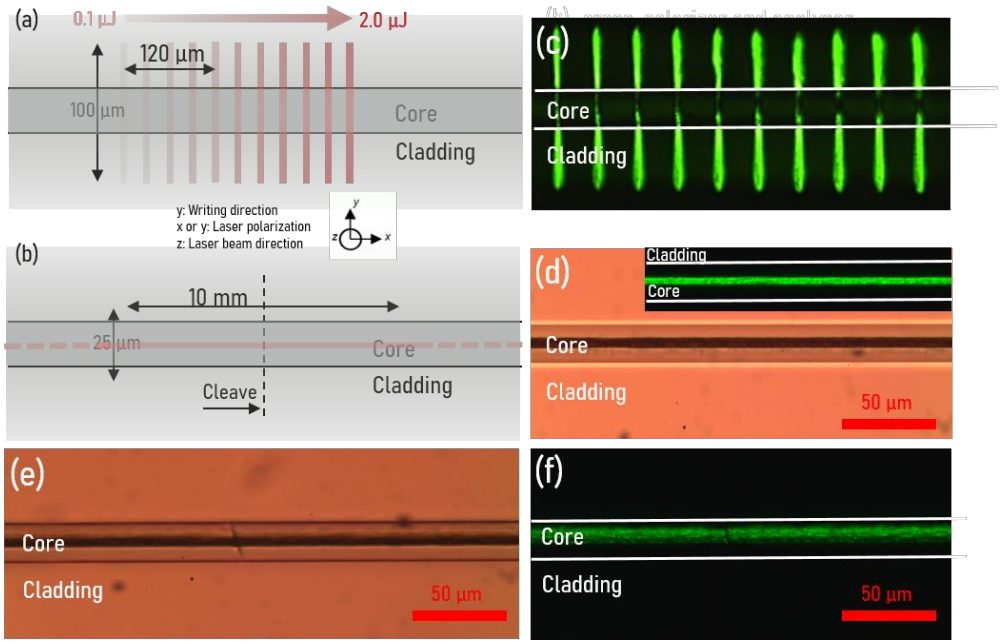

Figure 2-14.(a) Irradiation of fs laser inside fiber core and cladding of an optical fiber at different pulse energies; (c) Longitudinal (along with x) irradiation at constant pulse energy (1.0 µJ) using different laser polarization conditions: parallel (//, along with x) and perpendicular (⊥, along y) to the writing direction; (b) and (d) optical microscope (bottom light illumination) image of the High-AS fiber take from (a), (b) respectively. (b) and (d) insert are taken with a crossed polarizer and analyzer, and (d) is taken with natural bottom light illumination; (e) and (f) are the lateral view of (d) and (d) insert respectively. laser conditions: λ = 1030 nm, 100 kHz, 100 µm/s, 10^3 pulses/µm, NA = 0.6, pulse duration = 250 fs.

On the other hand, we will also write some longitudinal lines along the fiber axis (*Figure 2-14 (c)*) in such a way we can then cleave the fibers to observe its cross section (*Figure 2-15 (b)*) using SEM. This will allow to image the written texturation such as nanopores formation

(using Xx writing configuration, *Figure 2-15 (c)*) and nanogratings (using Xy writing configuration, *Figure 2-15 (d)*). For example, as shown in the *Figure 2-14(d),* a single line of 10 mm lengths parallel to the light propagation axis of the fiber was performed. With a stable type II nanogratings regime pulse energy was selected, we demonstrate here the *Figure 2-14 (d), (d) insert, (e) and (f),* which present vertical and lateral view of the fiber after irradiation. The photos taken from both angle of view, with or without crossed polarizer and analyzer, prove that the Type II nanogratings are well inscribed in the center of fiber core. Then, the fibers were cleaved and analyzed their cross sections by the SEM. We exhibit the SEM micrographs in *Figure 2-15 (c) and (d)*, according to the laser polarization orientations, the nanopores can be found in the laser-induced nanoplanes with the parallel configuration (Xx) and the nanolayers (sideways visualization of nanoplanes) with a regular spacing appeared when the polarization orientation perpendicular to the writing direction (Xy). Finally, the porosity of the nanopore region and the period of the nanolayer will be studied base on the results obtained from the SEM micrographs.

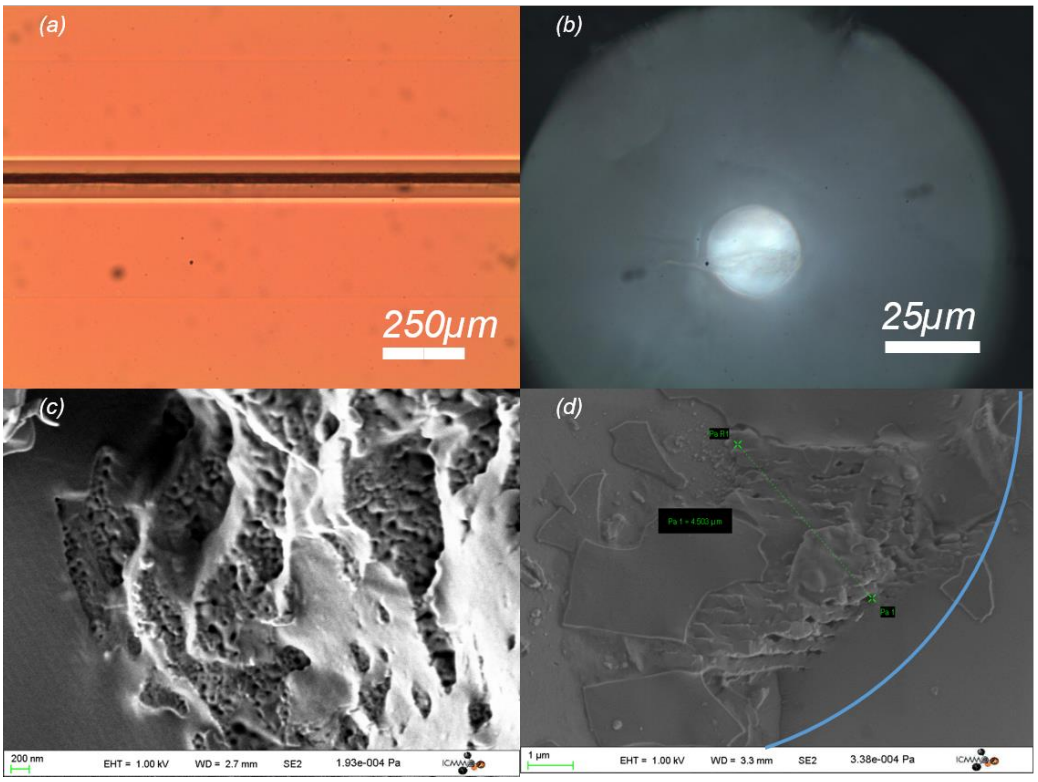

Figure 2-15. (a) and (b) optical microscope (bottom light illumination) image of the optical fiber for the side view and cross section view respectively; Scanning electron micrographs in the optical fiber, for parallel (c) and orthogonal (d) laser polarization direction with respect to the writing direction.

2.4 Microscopic characterization after laser irradiation

2.4.1 The “de Sénarmont” compensator

The “de Sénarmont” compensator couples a highly precise quarter wave birefringent quartz or mica crystalline plate with a 180-degree rotating analyzer to provide retardation measurements having an accuracy that approaches one thousandth of a wavelength or less. The device is utilized for retardation measurements over an optical path difference range of approximately 550 nanometers (one wavelength in the green region) for the quantitative analysis of crystals, fibers, and birefringence in living organisms, as well as investigations of optical strain. In addition, “de Sénarmont” compensators are useful for emphasizing contrast in weakly birefringent specimens that ordinarily are difficult to examine under crossed polarized illumination.

As described by the Olympus ressource centers, the principle behind the “de Sénarmont” compensation technique rests on the fact that the elliptically (or circularly) polarized light electric vector emerging from the specimen is superimposed upon the circular polarization vector introduced by the quarter waveplate to yield plane (linearly) polarized light having a vibration azimuth different from that of the polarizer (see *Figure 2-16*). The effect occurs because the quarter waveplate produces linearly polarized light from elliptically or circular polarized light that is incident on the crystal surface. The azimuth of the linear polarized light emerging from the compensator is a direct function of the optical path difference induced by the specimen. By rotating the analyzer until the specimen is extinct (dark), the azimuth of the vibration produced by the compensator can be ascertained along with the optical path difference introduced by the specimen.

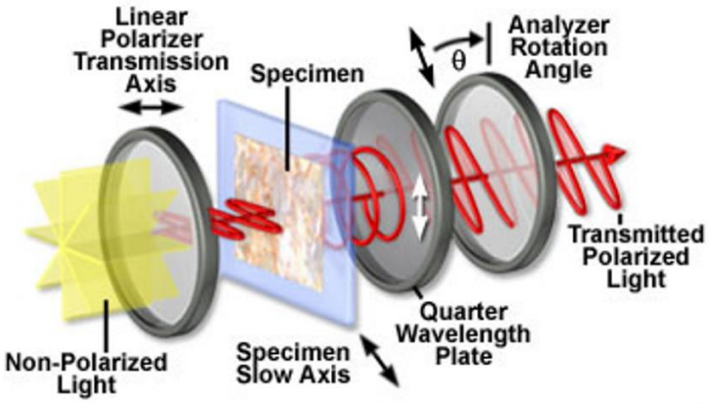

Figure 2-16: Diagram of the “de Sénarmont” compensator configuration with the (OXY) benchmarks related to the assembly reference and (Oxy) linked to the reference frame of the irradiated sample [source: http://www.olympusmicro.com/]

In order to obtain a measurement of specimen birefringence (and the related optical path difference), the "de Sénarmont" compensator is placed into the microscope optical train after the sign of birefringence and orientation of the specimen slow axis has been established with a first-order retardation plate (describe in the next section).

The rotation angle θ of the analyzer at extinction is equal to one-half of the full phase shift $(\theta = \frac{\phi_l}{2})$ between the orthogonal (ordinary and extraordinary) wavefronts passing through the specimen. Therefore, the relative retardation R (in nanometers) is described by the following equation:

$$R = \Delta n\, l = \theta \frac{\lambda}{\pi} \quad \text{or} \quad R = \Delta n\, l = \theta \frac{\lambda}{180} \; if \; \theta \text{ is in degree} \qquad \text{(Equation 2-4)}$$

In the case of the femtosecond laser written lines illustrated in *Figure 2-17*, the green interference filter has a narrow bandpass centered at 546 nm (i.e. around 3 nm per degree), and the analyzer rotation angle was 78,7 degrees. Therefore, the measured retardation value R for these lines is approximately 239 nm for a 546 nm probe. For highly accurate measurements of relative retardation, several trials should be conducted. In addition, the specimen can be rotated by 90-degrees and the analyzer rotated to the opposite side of the crossed position to obtain extinction for additional measurements (and better accuracy).

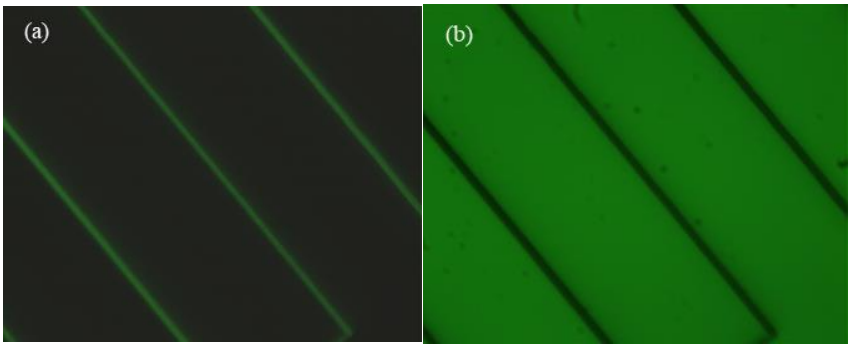

Figure 2-17: Image through the microscope eyepiece in the "de Senarmont" compensator configuration of laser irradiation traces (parallel fine lines) in a silica slide. (a): for crossed polarizers (θ = 0 °), the isotropic bottom appears black; (b): for a positioning of the analyzer minimizing the transmission of light through the irradiated areas (here some lines).

Determining the impact of errors: The error on the determination of the delay δR is defined by the following equation, which has been deduced from the theoretical relation of the delay:

$$\delta R^2 = \left(\frac{\partial R}{\partial \theta}\right)^2 \delta\theta^2 + \left(\frac{\partial R}{\partial \lambda}\right)^2 \delta\lambda^2 = \left(\frac{\lambda}{\pi}\right)^2 \delta\theta^2 + \left(\frac{\theta}{\pi}\right)^2 \delta\lambda^2 \qquad \text{(Equation 2-5)}$$

where δθ is the error on the analyzer defined by the angle measured experimentally θ_{exp} to regain the extinction of transmitted light subtracts from the initial angle θ_0 crossed

with the polarizer. So we can deduce $\delta\theta^2 = \left(\frac{\partial\theta}{\partial\theta_{exp}}\right)^2 {\delta\theta_{exp}}^2 + \left(\frac{\partial\theta}{\partial\theta_0}\right)^2 {\delta\theta_0}^2 = {\delta\theta_{exp}}^2 + {\delta\theta_0}^2$; $\delta\lambda$ is the error on the wavelength defined by the interference filter. For a filter at 546nm, we determine a θ_{exp} error of 1,52° over 40 measurements, $\delta\theta_0 = 0{,}1°$ and considering $\theta_{exp} = 80°$, we get an error on the delay of $\delta R = \sqrt{\left(\frac{\lambda}{\pi}\right)^2 \delta\theta^2 + \left(\frac{\theta}{\pi}\right)^2 \delta\lambda^2} = 4{,}9$ nm.

Polarizer error: a polarizer positioning error does not change the extinction angle of the transmitted intensity but only the amplitude of the transmitted intensity.

Sample orientation error: In the case of a sample positioning angular error γ, it has been modeled in the thesis of R. Desmarchelier [109] that this error relates to the measurement of θ. So for an error:

- $\gamma = 5°$, $\theta_\gamma = 44{,}1°$ (instead of 45°) corresponding to an error of 4,1 nm on the retardance.
- $\gamma = 1°$, $\theta_\gamma = 44{,}9°$ corresponding to an error of 3,1 nm on the retardance.

Conclusion: After developing the measurement of birefringence by the "de Sénarmont" method, we have seen how to measure Δn through the angle of the analyzer for which a minimum of transmitted intensity is observed. But when the sample has several anisotropic optical properties (linear or circular), we observe changes in the intensity transmitted but also a variation in the measured angle of the birefringence, especially when the sample has circular dichroism or circular birefringence. In the simulations of R. Desmarchelier [109] related the linear birefringence measurement, he has shown that when circular properties are small ($CB = {}^{\pi}/_{160}$ and $CD = {}^{\pi}/_{320}$), the errors on the retardance are then less than 4 nm which is relatively low.

2.4.2 Full wave retardation plate

Without prior knowledge of the birefringent characteristics (positive or negative sign) of a specimen, it may be difficult to ascertain the correct extinction angle for the analyzer during de Sénarmont compensation measurements. For example, in some cases the same rotation angle of the analyzer can produce extinction for a positively birefringent specimen that retards the wavefronts and a negatively birefringent specimen that advances the wavefronts. When a first-order (full wavelength) compensator or retardation plate is substituted for the de Sénarmont compensator in the optical train between the objective rear aperture and the analyzer, a known optical path difference of 530 (the exact wavelength depends on the manufacturer) will be added to the entire wavefront field. This technique can be used to determine the orientation of the index ellipse for birefringent specimens

before undertaking relative retardation measurements using the de Sénarmont technique.

The full wave retardation plate is generally made of optically anisotropic thin quartz with a precise thickness. It is located above the nosepiece and between the polarizer and analyzer (diagonally between crossed polarizers). It produces a specific optical path length difference of mutually perpendicular plane-polarized light waves (i.e. entire wavelength for the green one). The slow axis direction of the full wave plate is marked with "λ" accompanied with a double-headed arrow. It is at 45° from the analyzer or polarizer.

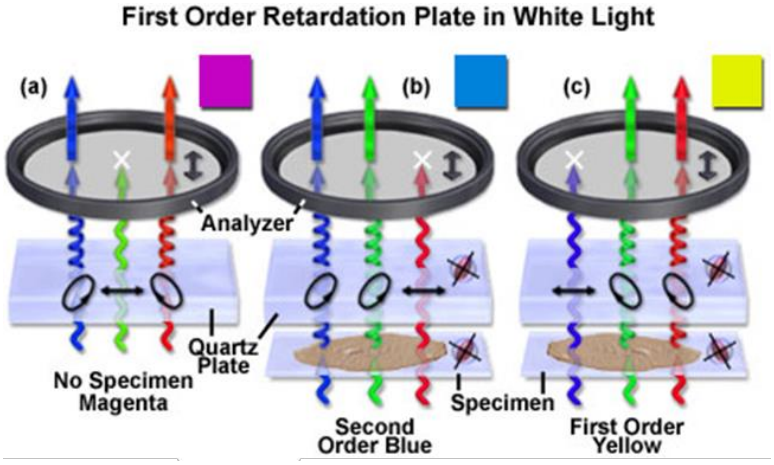

Figure 2-18: Working mechanism of first order retardation plate measuring slow axis of sample (cited from [110])

The polarized white light is symbolized by three wave fronts: blue, green, and red. As illustrated in *Figure 2-18(a)*, the background is magenta (i.e. the green wavelength is missing) when light passes through the full wave retardation plate and after an isotropic or without sample. When the slow axis of sample is placed parallel to the slow axis of the first order plate, the full wave retardation plate retardance is added to the sample retardance (i.e. the relative retardation of the orthogonal wave fronts increase). In that case, the red light is linear polarized and blocked by the analyser, resulting in second-order blue (*Figure 2-18(b)*). When the fast axis of sample is parallel to the slow axis of the full wave retardation plate, first-order yellow occurs because blue color is blocked (*Figure 2-18(c)*).

2.4.3 Scanning electron microscope (SEM)

Scanning electron microscopy (SEM) was used for the observation of microstructure of laser-modified area. SEM measures were conducted in a field-emission a gun scanning electron microscope (FEG-SEM ZEISS SUPRA 55 VP). Electron backscatter diffraction (EBSD), an accessory of SEM, was performed to determine the microstructure heterogeneities such as grain size, texture of the laser-modified area.

The schematic diagram of a SEM is shown in *Figure 2-19(a)*. The electron source may be from thermionic emission (e.g. LaB_6) or field emission. The magnetic lenses guide and focus the electron beam (with a spot of few nm). By using scanning coils, the focused electron beam scans across the specimen surface.

There is an interaction between the specimen and electron beam. *Figure 2-19(b)* illustrates the schematic representation of processes resulting from electron bombardment and interaction with specimen. Electrons penetrate inside and generate various signals [111].

The common used detectors in SEM are the ones for secondary electrons and the backscattered electrons. Secondary electrons are emitted from the top surface, which can be used for topographic imaging. The backscattered electrons are from a deeper zone in the specimen. Their intensity is depending on atomic number (Z), which can be used to provide information about the chemical composition (i.e. the higher the Z, the brighter the image contrast). Finally, by the imaging system, image is formed. The resolution of the method is depending on the measured specimen volume (i.e. the detected electron), the accelerating voltage, working distance, and the probe size.

Because the laser-modified area is embedded in the glass matrix (i.e. several hundred µm below the glass surface), it is necessary to expose the irradiated area for morphology, crystallization observations, and chemical analysis by electron microscopy. One way is to cut the irradiated line along the plane perpendicular to the scanning direction, polished. Characterizations were thus performed on the cross section of the irradiated lines. The other way is to polish along the plane perpendicular to the laser propagation direction until to have the laser-modified part at the surface. In addition, hydrofluoric acid (HF) was sometimes used to increase the contrast in SEM measurement.

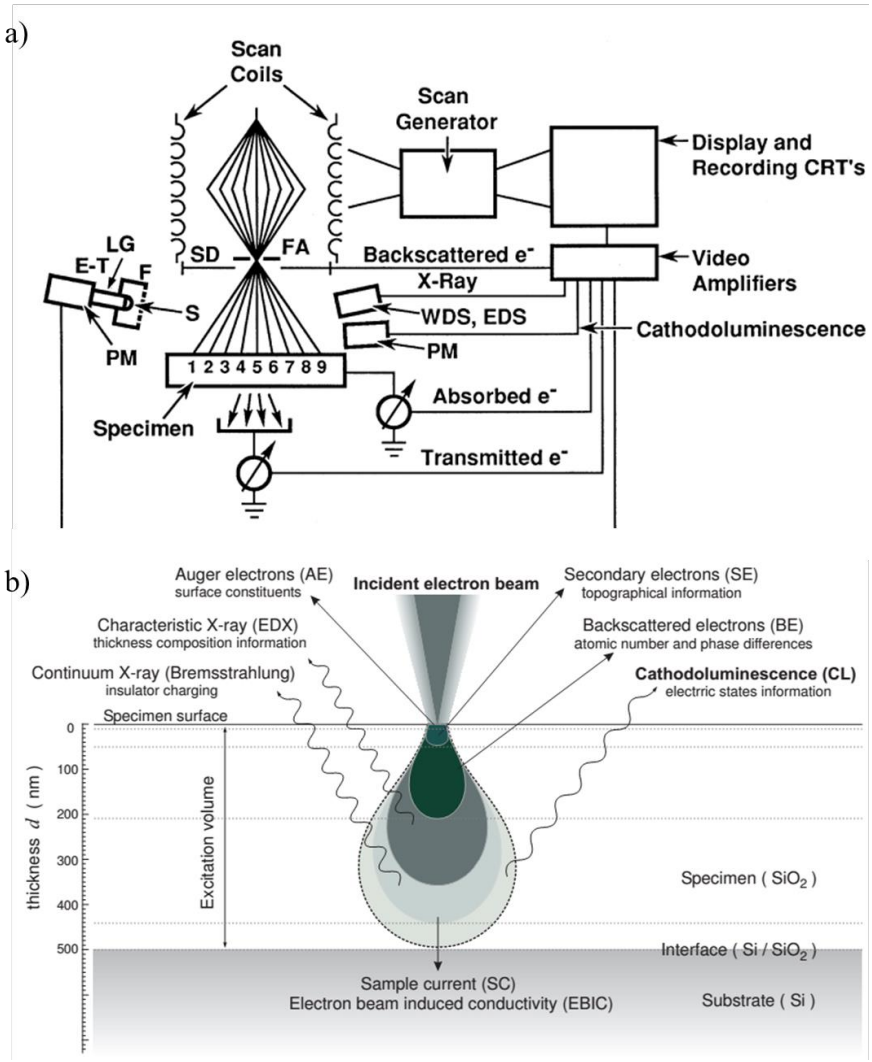

Figure 2-19: a) Schematic representations of scanning electron microscopy. FA: final aperture; SD: solid state backscattered electron detector; EDS: energy-dispersive X-ray spectrometer; WDS: wavelength-dispersive X-ray spectrometer; CRT: cathode ray tube; E-T: Everhart-Thornley secondary/backscattered electron detector, consisting of F: Faraday cage; S: scintillator; LG: light guide; and PM: photomultiplier (cited from [112]), b) processes resulting from electron bombardment (cited from [111]).

In our case, we use the scanning electron microscopy to investigate the morphology and the texturing of fs laser-induced glass modifications. In this view, two sets of textures are written using two different laser polarization orientations: parallel (labeled Xx) and perpendicular (labeled Xy) to the laser scanning direction (X axis) and the pulse energy was fixed to a stable Type II nanograting regime pulse energy depends on different samples. Then, in order to probe the matter within the nanolayers and its, the sample was cleaved perpendicularly to the writing direction as shown in *Figure 2-20*.

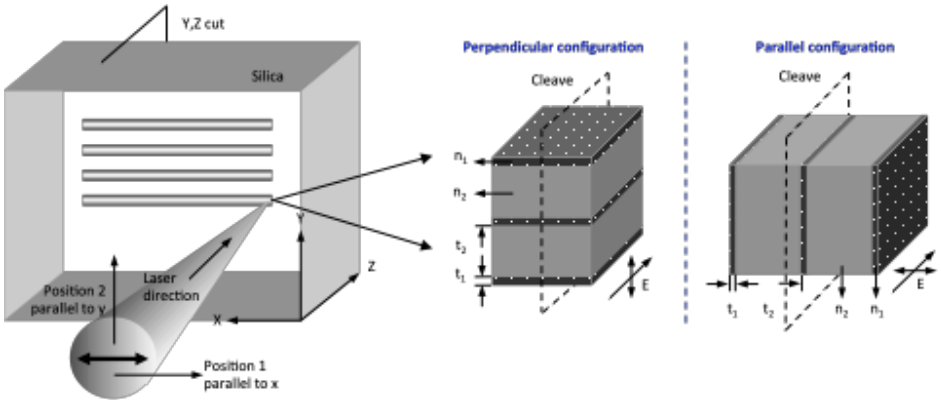

Figure 2-20. Experimental setup scheme for configuration for writing (from the left to the right top) and schematic of sub-wavelength periodic structure formed in cross-section of the irradiated region. n_1 et n_2: local refractive indices of the nanoplates; t_1 and t_2, are their respective thicknesses. Right: Schematic of sub-wavelength periodic structure formed in cross-section of the irradiated region.

Such cleaving scheme allowed the laser track cross-sections to be observed by SEM (Field-Emission Gun Scanning Electron Microscope, ZEISS SUPRA 55 VP, 1 kV accelerating voltage). Depending on the laser polarization orientations along Xx or Xy, the nanopores can be found in the laser-induced nanoplanes from the former (*Figure 2-21 (a)*) and the nanolayers (sideways visualization of nanoplanes) with a regular spacing would appear as shown in *Figure 2-21 (b)*.

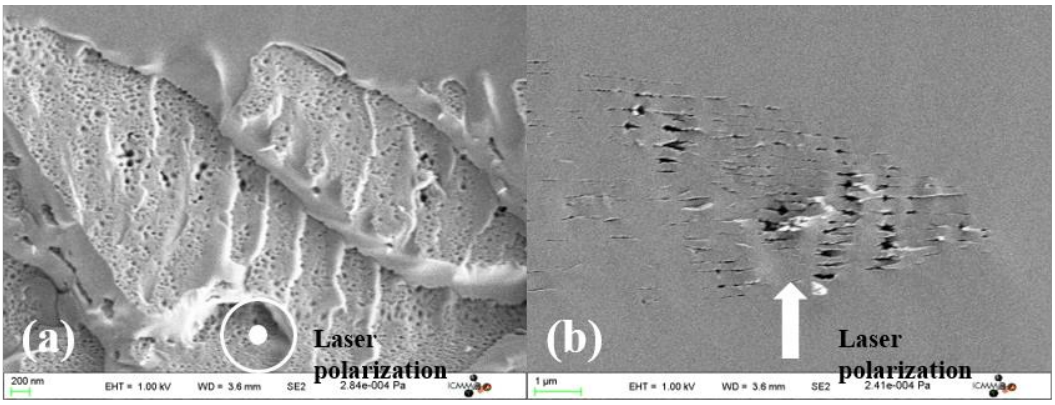

Figure 2-21. Scanning electron micrographs of Type II modification areas in silica glass, for parallel (a) and orthogonal (b) laser polarization direction with respect to the writing direction.

Conclusions

In this chapter, we first introduce the fabrication methods of various samples used in this thesis. Several characterization methods for studying the properties of samples are discussed. Next, we describe in detail the principle and method of the femtosecond laser direct writing experiment and how to use this technology to manufacture fiber Bragg gratings (FBGs). The microscopic characterization method such as the "de Sénarmont method" was presented in the end to help us detect the sample after laser irradiation. It should point out that each irradiated areas are measured several times and calculate the average as the final value, all the results are available for different laser polarizations (Xx and Xy) and laser pulse energies. Finally, these kinds of measurement can help us effectively quantify the modifications brought by the femtosecond laser to the sample, and they will be used repeatedly in each of the next chapters.

References

1. Bazylenko, M., et al., Pure and fluorine-doped silica films deposited in a hollow cathode reactor for integrated optic applications. Journal of Vacuum Science & Technology A, 1996. 14(2): p. 336-345.
2. Dianov, E.M., et al., Low-hydrogen silicon oxynitride optical fibers prepared by SPCVD. Journal of Lightwave Technology, 1995. 13(7): p. 1471-1474.
3. Poulsen, C.V., et al. Novel type of highly photosensitive germanium-doped silica glass: codoping with nitrogen. in Photosensitive Optical Materials and Devices. 1997. International Society for Optics and Photonics.
4. W.G. French, R.E.J., J.B. Mac Chesney, S.R. Nagel, K Nassau, A.D. Pearson Optical Fiber Telecommunications. S.E. Miller, A.G. Chynoweth Eds. Academic Press, 1979. 233.
5. Nishii, J., et al., Preparation of Bragg gratings in sputter-deposited GeO 2–SiO 2 glasses by excimer-laser irradiation. J Optics letters, 1996. 21(17): p. 1360-1362.
6. Yin, Z.Y. and B. Garside, Low-loss GeO 2 optical waveguide fabrication using low deposition rate rf sputtering. J Applied optics, 1982. 21(23): p. 4324-4328.
7. Durandet, A., R. Boswell, and D. McKenzie, New plasma-assisted deposition technique using helicon activated reactive evaporation. J Review of scientific instruments, 1995. 66(4): p. 2908-2913.
8. Madden, S., M. Green, and D. Barbier, Optical channel waveguide fabrication based on electron beam irradiation of silica. J Applied physics letters, 1990. 57(27): p. 2902-2903.
9. Albert, J., et al., Refractive-index changes in fused silica produced by heavy-ion implantation followed by photobleaching. J Optics letters, 1992. 17(23): p. 1652-1654.
10. Brebner, J.L., et al. Modification of the properties of silica glasses by ion implantation. in Photosensitive Optical Materials and Devices. 1997. International Society for Optics and Photonics.
11. H. Hosono, J.N., H. Kawazoe, Technical Digest of the Topical Meeting on Photosensitivity and non linearity in glass waveguides 1995 O.S.A Technical Digest 1995. series 22, 61
12. Hughes, P., et al., Optical characteristics of photosensitive Ge-doped SiO/sub 2/planar waveguides implanted with protons at 800/spl deg/C. J Electronics Letters, 2000. 36(5): p. 427-428.
13. Magruder III, R., et al., Formation and photosensitivity of defects in Se implanted silica. J Journal of non-crystalline solids, 1998. 239(1-3): p. 78-83.
14. E.A. Mendoza, D.J.F., R.A. Lieberman, Proc. SPIE 1994. 62: p. 2288.

15. Simmons, K.D., et al., Photosensitivity of solgel-derived germanosilicate planar waveguides. J Optics letters, 1993. 18(1): p. 25-27.
16. M. Ferraris, G.M., F. Ortenzio, G. Perrone, D. Pîrcàlàboiu, I. Montrosset, L. Cognolato., Proceedings of the European Conference on Integrated Optics. ECIO, Stockholm, 1997: p. 334/ Eth 10-1.
17. Roman, J. and K. Winick, Photowritten gratings in ion-exchanged glass waveguides. J Optics letters, 1993. 18(10): p. 808-810.
18. Hosono, H., et al., Physical disorder and optical properties in the vacuum ultraviolet region of amorphous SiO 2. J Physical review letters, 2001. 87(17): p. 175501.
19. Sasaki, Y. and Y. Ohmori, Phase-matched sum-frequency light generation in optical fibers. J Applied Physics Letters, 1981. 39(6): p. 466-468.
20. Österberg, U. and W. Margulis, Dye laser pumped by Nd: YAG laser pulses frequency doubled in a glass optical fiber. J Optics letters, 1986. 11(8): p. 516-518.
21. Myers, R., N. Mukherjee, and S.R. Brueck, Large second-order nonlinearity in poled fused silica. J Optics letters, 1991. 16(22): p. 1732-1734.
22. Ikushima, A., T. Fujiwara, and K. Saito, Silica glass: A material for photonics. J Journal of Applied Physics, 2000. 88(3): p. 1201-1213.
23. Agrawal, G., Optics and photonics. J Nonlinear Fiber Optics, edited by G. Agrawal, 5th ed., 1995: p. 397-456.
24. Brueckner, R., Properties and structure of vitreous silica. I. J Journal of non-crystalline solids, 1970. 5(2): p. 123-175.
25. Pack, A., et al., Description of an aerodynamic levitation apparatus with applications in Earth sciences. J Geochemical transactions, 2010. 11(1): p. 1-16.
26. SANDHAGE, K.H. and G.J. YUREK, Indirect dissolution of sapphire into silicate melts. J Journal of the American Ceramic Society, 1988. 71(6): p. 478-489.
27. Malvin, D.J., Silica-glass containers for high-temperature experiments. J American Mineralogist, 1988. 73(9-10): p. 1198-1200.
28. Grove, T., Use of FePt alloys to eliminate the iron loss problem in 1 atmosphere gas mixing experiments: Theoretical and practical considerations. J Contributions to Mineralogy Petrology, 1982. 78(3): p. 298-304.
29. Johannes, W. and B. Bode, Loss of iron to the Pt-container in melting experiments with basalts and a method to reduce it. J Contributions to Mineralogy Petrology, 1978. 67(2): p. 221-225.
30. Price, D.L., High-temperature levitated materials. 2010: Cambridge University Press.
31. Alderman, O., et al., Local structural variation with oxygen fugacity in Fe2SiO4+ x fayalitic iron silicate melts. J Geochimica et Cosmochimica Acta, 2017. 203: p. 15-36.
32. Alderman, O., et al., Iron K-edge X-ray absorption near-edge structure spectroscopy of aerodynamically levitated silicate melts and glasses. J Chemical Geology, 2017. 453: p. 169-185.

33. Benmore, C.J. and J. Weber, Aerodynamic levitation, supercooled liquids and glass formation. J Advances in Physics: X, 2017. 2(3): p. 717-736.
34. Nordine, P.C. and R.M. Atkins, Aerodynamic levitation of laser-heated solids in gas jets. J Review of Scientific Instruments, 1982. 53(9): p. 1456-1464.
35. Landron, C., L. Hennet, and D. Thiaudiere. Combining measurements of synchrotron radiation and neutrons from liquids at high temperature. in Analytical Sciences/Supplements Proceedings of IUPAC International Congress on Analytical Sciences 2001 (ICAS 2001). 2002. The Japan Society for Analytical Chemistry.
36. Nordine, P.C., J.R. Weber, and J.G. Abadie, Properties of high-temperature melts using levitation. J Pure applied chemistry
2000. 72(11): p. 2127-2136.
37. Glorieux, B., et al., Density of superheated and undercooled liquid alumina by a contactless method. J International journal of Thermophysics, 1999. 20(4): p. 1085-1094.
38. Weber, J., et al., Structure of binary CaO–Al2O3 and SrO–Al2O3 liquids by combined levitation-neutron diffraction. J Journal of Neutron Research, 2003. 11(3): p. 113-121.
39. Glorieux, B., F. Millot, and J. Rifflet, Surface tension of liquid alumina from contactless techniques. J International Journal of Thermophysics, 2002. 23(5): p. 1249-1257.
40. Oran, W. and L. Berge, Containerless melting and solidification of materials with an aerodynamic levitation system. Review of Scientific Instruments, 1982. 53(6): p. 851-853.
41. Ouaida, M., O. MB, and B. JM, Dispositif de levitation aerodynamique associe a un concentrateur solaire pour l'etude de materiaux liquides. 1982.
42. Landron, C., et al., Structure of liquid oxides at very high temperatures. Nuclear Instruments Methods in Physics Research Section B: Beam Interactions with Materials Atoms, 2003. 199: p. 481-488.
43. Arai, Y., T. Aoyama, and S. Yoda, Spherical sapphire single-crystal synthesis by aerodynamic levitation with high growth rate. Review of scientific instruments, 2004. 75(7): p. 2262-2265.
44. Blander, M., et al., Non-equilibrium concepts lead to a unified explanation of the formation of chondrules and chondrites. Meteoritics Planetary Science, 2004. 39(12): p. 1897-1910.
45. Nagashima, K., et al., Critical cooling rates for glass formation in levitated Mg2SiO4-MgSiO3 chondrule melts. Journal of Mineralogical Petrological Sciences, 2008. 103(3): p. 204-208.
46. Nagashima, K., et al., Reproduction of chondrules from levitated, hypercooled melts. Journal of crystal growth, 2006. 293(1): p. 193-197.

47. Weber, J.R., et al., Novel synthesis of calcium oxide–aluminum oxide glasses. Japanese journal of applied physics, 2002. 41(5R): p. 3029.
48. Skinner, L., A. Barnes, and W. Crichton, Novel behaviour and structure of new glasses of the type Ba–Al–O and Ba–Al–Ti–O produced by aerodynamic levitation and laser heating. Journal of Physics: Condensed Matter, 2006. 18(32): p. L407.
49. Tangeman, J.A., et al., Vitreous forsterite (Mg2SiO4): Synthesis, structure, and thermochemistry. Geophysical research letters, 2001. 28(13): p. 2517-2520.
50. Li, T., Optical fiber communications: fiber fabrication. 2012: Elsevier.
51. Gowar, J., Optical communication systems (2d ed.). 1993, Hempstead, UK: Prentice-Hall.
52. Jungbluth, E.D., HOW DO THEY MAKE THOSE MARVELOUS FIBERS. Laser Focus World, 1992. 28(3): p. 165.
53. Ketron, L., Fiber optics: the ultimate communications media. Am. Ceram. Soc. Bull., 1987. 66(11): p. 1571-1578.
54. Kurkjian, C.R., P.G. Simpkins, and D. Inniss, Strength, degradation, and coating of silica lightguides. Journal of the American Ceramic Society, 1993. 76(5): p. 1106-1112.
55. Tariyal, B. and A. Cherin, Optical Fiber Communications. 2003.
56. Lydtin, H., PCVD: A technique suitable for large-scale fabrication of optical fibers. Journal of lightwave technology, 1986. 4(8): p. 1034-1038.
57. Ballato, J. and P. Dragic, Rethinking optical fiber: new demands, old glasses. Journal of the American Ceramic Society, 2013. 96(9): p. 2675-2692.
58. Morris, S. and J. Ballato, Molten-core fabrication of novel optical fibers. Bull. Am. Ceram. Soc, 2013. 92(4): p. 24-29.
59. Ballato, J. and E. Snitzer, Fabrication of fibers with high rare-earth concentrations for Faraday isolator applications. Applied optics, 1995. 34(30): p. 6848-6854.
60. Ballato, J., et al., Advancements in semiconductor core optical fiber. Optical Fiber Technology, 2010. 16(6): p. 399-408.
61. Dragic, P., et al., Sapphire-derived all-glass optical fibres. Nature Photonics, 2012. 6(9): p. 627-633.
62. Ballato, J., et al., On the fabrication of all-glass optical fibers from crystals. Journal of Applied Physics, 2009. 105(5): p. 053110.
63. Ballato, J. and A. Peacock, Perspective: Molten core optical fiber fabrication—A route to new materials and applications. APL Photonics, 2018. 3(12): p. 120903.
64. Dragic, P., et al., Brillouin spectroscopy of YAG-derived optical fibers. Optics express, 2010. 18(10): p. 10055-10067.
65. Grobnic, D., et al., Type I and II Bragg gratings made with infrared femtosecond radiation in high and low alumina content aluminosilicate optical fibers. Optica, 2015. 2(4): p. 313-322.

66. Andreone, A., Selected topics in photonic crystals and metamaterials. 2011: World Scientific.
67. Luo, Y., et al., Bismuth and erbium codoped optical fiber with ultrabroadband luminescence across O-, E-, S-, C-, and L-bands. Optics letters, 2012. 37(16): p. 3447-3449.
68. Michie, A., et al., Spun elliptically birefringent photonic crystal fibre. Optics Express, 2007. 15(4): p. 1811-1816.
69. Cook, K., et al. Air-structured optical fibre drawn from a 3D-printed preform. in 24th International Conference on Optical Fibre Sensors. 2015. International Society for Optics and Photonics.
70. Chu, Y., et al., Silica optical fiber drawn from 3D printed preforms. Optics letters, 2019. 44(21): p. 5358-5361.
71. Bikas, H., P. Stavropoulos, and G. Chryssolouris, Additive manufacturing methods and modelling approaches: a critical review. The International Journal of Advanced Manufacturing Technology, 2016. 83(1-4): p. 389-405.
72. Yang, Y., et al., Recent progress in biomimetic additive manufacturing technology: from materials to functional structures. Advanced Materials, 2018. 30(36): p. 1706539.
73. Camposeo, A., et al., Additive manufacturing: applications and directions in photonics and optoelectronics. Advanced optical materials, 2019. 7(1): p. 1800419.
74. Klein, J., et al., Additive manufacturing of optically transparent glass. 3D Printing Additive Manufacturing, 2015. 2(3): p. 92-105.
75. Kotz, F., et al., Three-dimensional printing of transparent fused silica glass. Nature, 2017. 544(7650): p. 337-339.
76. Kotz, F., et al., Fabrication of arbitrary three-dimensional suspended hollow microstructures in transparent fused silica glass. Nature communications, 2019. 10(1): p. 1-7.
77. Nguyen, D.T., et al., 3D-printed transparent glass. Advanced Materials, 2017. 29(26): p. 1701181.
78. Destino, J.F., et al., 3D printed optical quality silica and silica–titania glasses from sol–gel feedstocks. Advanced Materials Technologies, 2018. 3(6): p. 1700323.
79. Kotz, F., et al., Liquid glass: a facile soft replication method for structuring glass. Advanced Materials, 2016. 28(23): p. 4646-4650.
80. Kotz, F., et al., Glassomer—processing fused silica glass like a polymer. Advanced Materials, 2018. 30(22): p. 1707100.
81. Lancry, M., et al., Ultrafast nanoporous silica formation driven by femtosecond laser irradiation. Laser Photonics Reviews, 2013. 7(6): p. 953-962.
82. Primak, W., Fast-neutron-induced changes in quartz and vitreous silica. 1958. 110(6): p. 1240.

83. Vanelstraete, A. and C. Laermans, Saturation of the density of states of tunneling systems in defective crystalline neutron-irradiated quartz. Physical Review B, 1988. 38(9): p. 6312.
84. Primak, W. and R. Kampwirth, The radiation compaction of vitreous silica. Journal of Applied Physics, 1968. 39(12): p. 5651-5658.
85. Borrelli, N., et al., Densification of fused silica under 193-nm excitation. JOSA B, 1997. 14(7): p. 1606-1615.
86. Devine, R., Macroscopic and microscopic effects of radiation in amorphous SiO2. Nuclear Instruments Methods in Physics Research Section B: Beam Interactions with Materials Atoms
1994. 91(1-4): p. 378-390.
87. Barbier, D., M. Green, and S. Madden, Waveguide fabrication for integrated optics by electron beam irradiation of silica. Journal of lightwave technology, 1991. 9(6): p. 715-720.
88. Neuville, D.R., D. de Ligny, and G.S. Henderson, Advances in Raman spectroscopy applied to earth and material sciences. Reviews in Mineralogy Geochemistry, 2014. 78(1): p. 509-541.
89. Herzberg, G., Molecular spectra and molecular structure. Vol. 2: Infrared and Raman spectra of polyatomic molecules. 1945.
90. Wilson, E.B., J.C. Decius, and P.C. Cross, Molecular vibrations: the theory of infrared and Raman vibrational spectra. 1980: Courier Corporation.
91. Sherwood, P.M.A., Vibrational spectroscopy of solids. 1972: CUP Archive.
92. Lazarev, A., Vibrational Spectra and Structure of Silicates, Consultants Bureau. 1972.
93. Long, D., Raman Spectroscopy. vol. 2. 1977, McGraw-Hill.
94. Harris, D.C. and M.D. Bertolucci, Symmetry and spectroscopy: an introduction to vibrational and electronic spectroscopy. 1989: Courier Corporation.
95. Sharma, S.K., J.F. Mammone, and M. Nicol, Raman investigation of ring configurations in vitreous silica. Nature, 1981. 292(5819): p. 140-141.
96. Galeener, F.L., Planar rings in vitreous silica. Journal of Non-Crystalline Solids, 1982. 49(1-3): p. 53-62.
97. Geissberger, A. and F.L. Galeener, Raman studies of vitreous Si O 2 versus fictive temperature. Physical Review B, 1983. 28(6): p. 3266.
98. Martinez, V., et al., Structural studies of germanium doped silica glasses: the role of the fictive temperature. Optical Materials, 2003. 24(1-2): p. 59-62.
99. Uchino, T., Y. Tokuda, and T. Yoko, Vibrational dynamics of defect modes in vitreous silica. Physical Review B, 1998. 58(9): p. 5322.
100. Heili, M., Influence de l'histoire thermique sur la diffusion optique dans les préformes et les fibres optiques GeO2-SiO2: F. 2013, Paris Sud.

101. Bell, R., N. Bird, and P. Dean, The vibrational spectra of vitreous silica, germania and beryllium fluoride. Journal of Physics C: Solid State Physics, 1968. 1(2): p. 299.
102. Galeener, F.L., Band limits and the vibrational spectra of tetrahedral glasses. Physical Review B, 1979. 19(8): p. 4292.
103. Zhang, H., et al., Type II high-strength Bragg grating waveguides photowritten with ultrashort laser pulses. Optics Express, 2007. 15(7): p. 4182-4191.
104. Zhang, H., S.M. Eaton, and P.R. Herman, Single-step writing of Bragg grating waveguides in fused silica with an externally modulated femtosecond fiber laser. Optics letters, 2007. 32(17): p. 2559-2561.
105. Marshall, G.D., M. Ams, and M.J. Withford, Direct laser written waveguide-Bragg gratings in bulk fused silica. Optics Letters, 2006. 31(18): p. 2690-2691.
106. Nemoto, S., Waist shift of a Gaussian beam by plane dielectric interfaces. Applied optics, 1988. 27(9): p. 1833-1839.
107. Fernandes, L.A., et al., Femtosecond laser writing of waveguide retarders in fused silica for polarization control in optical circuits. Optics express, 2011. 19(19): p. 18294-18301.
108. Grobnic, D., S.J. Mihailov, and C.W. Smelser, Femtosecond IR laser inscription of Bragg gratings in single-and multimode fluoride fibers. IEEE Photonics Technology Letters, 2006. 18(24): p. 2686-2688.
109. Desmarchelier, R., Analyses des forces photo-induites par le laser femtoseconde dans les verres à base de silice. 2014, Paris 11.
110. Davidson, M., The first order (full wave) retardation plate. 2019.
111. Salh, R., Defect related luminescence in silicon dioxide network: a review. 2011: InTech Rijeka.
112. Goldstein, J.I., et al., Scanning electron microscopy and X-ray microanalysis. 2017: Springer.

Chapter 3. Thermal stability of fs-laser induced type II modifications in bulk glasses

Introduction 113
3.1 Overview of the thermal erasure mechanisms of femtosecond laser-induced nanogratings in silica glass 114
3.2 Thermal stability of type II modifications by IR femtosecond laser in silica-based glasses 130
3.3 Femtosecond laser direct writing in SiO_2-$Al2O_3$ binary glasses and thermal stability of Type II permanent modifications 145
Conclusions 155

Introduction

Investigate the silica based glasses and optical fibers for harsh environment operation using FLDW, and further fabricate the laser written sensors (such as FBGs) is a key objective, which goes beyond this PhD work. In this realm, we have previously addressed the benefit that femtosecond laser written FBGs, and more generally, IR-fs-induced refractive index transformations, could offer. In this PhD chapter, we will therefore focus on the fs-laser-induced Type II modifications (also called nanogratings) in bulk glasses and investigate their thermal stability according to chemical composition, manufacturing process and laser writing parameters. For the following studies, we employ bulk glasses since they facilitate controlled and systematic laser irradiation experiments, as well as thermal facility measurements. Although most of optical devices are fiber-based, they usually present small core sizes, composition gradients, and a variety of fabrication processes, which would complicate the interpretation.

In the first part, we will study the Type II modifications induced by IR femtosecond laser pulses in a chosen silica glass, namely Suprasil CG. These modifications are characterized by birefringent self-organized nanogratings, and present excellent thermal stability at high temperatures (typically > 800 °C). The aggregate birefringence response of these structures arises from multiple contributions, including form birefringence, stress-induced birefringence, densification, and point defects. This part tentatively quantifies and discriminates the effect of each contribution on the overall nanogratings thermal erasure kinetics in SiO_2.

Following this, in the second part, we investigate the impact of both laser writing parameters and glass composition on the overall thermal stability of these fs-laser induced transformation. This includes investigation of thermal stability of Type II modifications in various conventional glass systems (including pure silica glasses with various Cl and OH contents, GeO_2-SiO_2 binary glasses, TiO_2- and B_2O_3-doped commercial glasses) and with varying laser parameters (writing speed, pulse energy). In order to monitor and characterized the thermal stability, isochronal annealing experiments (Δt and ΔT typically of 30 min, and 50 °C, respectively) from room temperature up to 1400 °C were performed on the irradiated samples, along with quantitative retardance measurements. Among the findings to highlight, it was established that ppm levels of Cl and OH can drastically reduce thermal stability (by about 200 °C in this study). Moreover, GeO_2-doped PCVD SiO_2 (up to 17 mol%) only has a minor impact on the thermal stability. Finally, relationships between glass viscosity, dopants/impurities, and thermal stability, are established and discussed.

Finally, in the last part of this chapter, and based on the apparent relationship between glass viscosity and the thermal stability of nanogratings, we discuss on the potential of Al_2O_3 addition into silica as an attractive way to improve the thermal stability of fs-laser induced modifications. We thus studied a range of SiO_2-Al_2O_3 glasses by aerodynamic levitation method, characterized (density and Raman) and investigated their optical response after being irradiated by IR-fs laser. The formation of nanogratings in such glasses is confirmed through electron microscopy imaging and quantified using quantitative birefringence measurements. Their thermal stability is then investigated through 30 minutes step isochronal annealing up to 1250 °C. Finally, the results show that a $50SiO_2$-$50Al_2O_3$ glass (molar composition) effectively exhibit a high thermal stability of nanogratings similar to the one of SiO_2 Suprasil glass.

3.1 Overview of the thermal erasure mechanisms of femtosecond laser-induced nanogratings in silica glass

RESEARCH ARTICLE

physica status solidi a

www.pss-a.com

An Overview of the Thermal Erasure Mechanisms of Femtosecond Laser-Induced Nanogratings in Silica Glass

*Yitao Wang, Maxime Cavillon, Nadège Ollier, Bertrand Poumellec, and Matthieu Lancry**

Type II modifications induced by infrared (IR) femtosecond (fs) lasers are used in many optical devices due to their excellent thermal stability at high temperatures (typically >800 °C). The characteristic feature of type II modifications is the formation of nanogratings, which are easily detected through birefringence measurements. However, the measured birefringence is an aggregate value of multiple contributions including form birefringence, stress-induced birefringence due to permanent volume changes, and point defects. This work investigates the thermal erasure kinetics of each one of these contributions in silica glass. Firstly, samples are irradiated with a fs-laser using different conditions (polarization, energy). Secondly, accelerated aging experiments are conducted to evaluate the stability of the laser-induced modifications, including defects, densification, stress field, and porous nanogratings. Finally, the aforementioned contributions to the thermal stability of the nanogratings are identified using spectroscopic techniques (Raman, Rayleigh scattering, UV–vis absorption) and electron microscopy. Moreover, porous nanogratings erasure kinetics are simulated using the Rayleigh–Plesset equation. Herein, a valuable framework in the realization of silica glass-based optical devices operating at high temperatures (≫800 °) is provided by 1) evidencing the effect of annealing on each erasure mechanism and 2) providing information on the optical response (mainly birefringence) upon annealing.

1. Introduction

Over the past two decades, significant progress has been made to identify different types of material modifications occurring upon infrared (IR) or visible (vis) femtosecond laser (fs laser) light focused inside transparent dielectrics.[1] Fs light pulses, with laser fluence above the multiphoton ionization threshold, can deposit their energy homogeneously and in volume in transparent dielectrics producing moderate-density plasmas.[2] In 1999, anomalous anisotropic scattering of light[3] in Ge-doped silica glass was observed, and then the memorized polarization-dependent light scattering[4] was reported in 2000. Following this, in 2001, there was the first experimental observation of strong linear birefringence (LB)[5] in fused silica from fs-modified zones. These works provided the first clues of nanogratings formation in the glass volume. The first direct evidence for periodic nanogratings came in 2003 using a stationary and fixed focused fs laser beam.[6] Later our group revealed that these self-organized subwavelength nanolayers are based on glass decomposition that resolidifies into a nanoporous, usually silicon-rich structure, creating a strong and highly stable refractive index contrast.[7] Since then, studies have been conducted to improve the control of nanogratings fabrication, leading to many novel applications mostly based on birefringent devices. For example, the fabrication of these nanogratings has found applications in 2D- and 3D-based space-variant birefringence objects (such as waveplates,[8] micropatterned waveplates, polarization converters), high-temperature Fiber–Bragg gratings (FBG)[9] for structural health monitoring (SHM), or again 5D optical data storage[10,11] with virtually "unlimited lifetime" at room temperature (RT). For most of these optical devices, thermal stability is an important factor to be considered to ensure reliable functionality during their lifetime, e.g., to prevent any drift in the device optical response over time. Therefore, a study on the thermal stability of the fs type II modifications (i.e., nanogratings regime) is of great significance to understand the mechanisms of erasure before being able to perform a reliable lifetime prediction.

Bricchi et al.[12] reported the first results related to the annealing of fs laser written type II modifications (laser conditions: $\lambda = 800$ nm, 100 kHz, NA = 0.55, 0.06 mm s^{-1}, pulse duration = 200 fs), which showed extraordinary thermal stability: such modifications can withstand at least 2 h at 1000 °C without

Y. Wang, Dr. M. Cavillon, Prof. B. Poumellec, Dr. M. Lancry
Institut de Chimie Moléculaire et des Matériaux d'Orsay (ICMMO/SP2M/MAP)
Université Paris-Saclay
CNRS
91405 Orsay Cedex, France
E-mail: matthieu.lancry@universite-paris-saclay.fr

Dr. N. Ollier
LSI
CEA/DRF/IRAMIS
Ecole Polytechnique
CNRS
Institut Polytechnique de Paris
91128 Palaiseau, France

The ORCID identification number(s) for the author(s) of this article can be found under https://doi.org/10.1002/pssa.202100023.

DOI: 10.1002/pssa.202100023

© 2021 Wiley-VCH GmbH

any degradation. The unexpected behavior displayed by these structures, namely, a slight growth of the absolute value of the ordinary and extraordinary refractive index difference as the temperature progressively increased in the 200–500 °C range, was suggested to come from the erasure of point defects centers like SiODC and SiE' defects generated in the irradiated volume.

This was followed by a few studies, as summarized here. Richter et al.[13] confirmed that nanogratings exhibit an extremely high temperature stability, i.e., up to 1150 °C for 30 min (laser conditions: $\lambda = 1030-515$ nm, 9.4 MHz, average power = 5 W, NA = 0.55, pulse duration = 450 fs). Investigations of the thermal stability of nanogratings showed that E' centers vanished upon annealing, whereas nonbridging oxygen hole centers (NBOHCs) remained stable up to 900 °C for 2 h. Thus, they proposed that nanogratings-based components could be rendered truly thermally stable by thermal annealing to erase the unstable part mostly related to point defects.

Krol and coworkers[14] subsequently investigated the thermal stability of fs laser modification inside fused silica (laser conditions: $\lambda = 800$ nm, 1 kHz, NA = 0.25, 0.05 mm s^{-1}, pulse duration = 150 fs). Raman and photoluminescence spectroscopies showed that fs-laser induced NBOHC defects completely disappeared at 300 °C (for a 10 h annealing), whereas changes in Si−O ring structures only annealed after heat treatment at 800–900 °C (for a 10 h annealing). After annealing at 900 °C for 10 h, optical waveguides written inside the glass completely disappeared, whereas more significant damages induced in the glass remained.

Zhang et al.[15] highlighted that the LB response of the nanogratings experiences a slight increase with increasing annealing temperature up to 900 °C (laser conditions: $\lambda = 800$ nm, 1 kHz, NA = 0.55, 0.01 mm s^{-1}, pulse energy = 2 μJ, pulse duration =150 fs, laser polarization at 45° off the writing direction), in agreement with Bricchi et al.[12] However, after annealing at 1100 °C for 1 h, the birefringence sharply decreased by a factor of 4. They also monitored the so-called "defect lines" (labeled D1 and D2) using Raman spectroscopy as a function of temperature. These lines are related to three- and four-membered rings in the silica network. In this study, the authors found no correlations between the evolution of the lines and the overall birefringence response. Furthermore, in this study, the authors also conducted scanning electron microscopy experiments in which the width of nanoplane period (nanogratings etched by HF acid) decreased from 120 nm to 50 nm after annealing at 1100 °C for 1 h, but again they do not reveal any direct correlation with the quantitative birefringence measurements.

There are numerous studies on the thermal stability of optical properties within the type II regime, i.e., retardance in bulk samples,[10,12,13,15–19] but also Bragg wavelength shift[20] and/or reflectivity of FBGs.[21–29] However, there are only few studies on the erasure kinetics of the underlying mechanisms supporting these optical properties as we have summarized in the previous paragraphs. In addition, the measured birefringence within the nanogratings regime is composed of multiple contributions including the well-known form birefringence but also stress-induced birefringence, point defects, and densification. As these modifications are intrinsically different from each other, they likely present a different thermal behavior as well. Following this view, we propose here a comprehensive overview of these erasure mechanisms, associated with an extensive set of data in silica glass. The strategy is to investigate in detail the overall erasure mechanisms of type II IR fs laser modifications by comparing the thermal stability of the measured linear retardance with the one of 1) defect centers (i.e., SiODC(II) and SiE'), 2) Rayleigh scattering signature, 3) densification through Raman microspectroscopy, 4) stress-induced birefringence using a dedicated stress-engineered waveplate, and 5) nanogratings texturing (period, porosity filling factor [FF], nanopores size).

In addition, in this work, we quantify, within our working conditions, the amplitude that each mechanism has on the "aggregate" measured retardance and provide some elements about the densification nature within the type II regime. Finally, with this article, we frame under which annealing conditions each one of the aforementioned contributions will be active and to what extent the optical response, especially retardance or birefringence herein, is expected to change. With this in mind, this work paves the way for the complete description of the thermally affected mechanisms that impact glass-based devices under high-temperature operation. It will provide guidelines for future glass formulation development and the use of adequate laser parameters depending on priorities (low losses, high-temperature operation, high birefringence values, etc.)

2. Experimental Section

2.1. Fs Laser Writing

The experimental setup of the infrared fs laser direct writing procedure is shown in **Figure 1** and has been described accurately in previous works.[7,8,17] In this study, briefly, the commercial Suprasil CG glass from Heraeus (a synthetic type III pure SiO_2 glass[30]) plates, 3 mm thick, were used for these investigations. Suprasil CG glass exhibited 400−1000 ppm OH concentration, a high Cl content (typ. 2500 ppm), and a minor amount of additional impurities (<10 ppb).

The laser beam was produced by a fs laser system operating at $\lambda = 1030$ nm and delivering 250–300 fs pulses at a repetition rate of 100 kHz with a maximum available power of 10 W. The beam was focused to a depth of 500 μm (in glass) below the front face of 3 mm-thick silica glass plates using a 0.16 NA aspheric lens (estimated beam diameter of ≈4.1 μm). Based on preliminary experiments,[17] the laser energy and the scanning speed were chosen, so that the irradiated region fell within the type II regime (typ. 1.75 μJ pulse^{-1} and 0.5 mm s^{-1} scanning speed), corresponding to the formation of nanogratings in silica glass. In addition, some type I modifications were written at 0.15 μJ pulse^{-1} for the sake of comparison.

The sample was placed on an *XYZ*-motorized translation stage and the first experiment included a series of squares (3 mm × 3 mm in the *XY* plane). The squares were composed of 3000 parallel lines with a 1 μm line gap to have a uniform anisotropic area and avoid any diffraction effects. Note that such a design (array of lines) is representative of various optical components such as polarization converters, waveplates, and

© 2021 Wiley-VCH GmbH

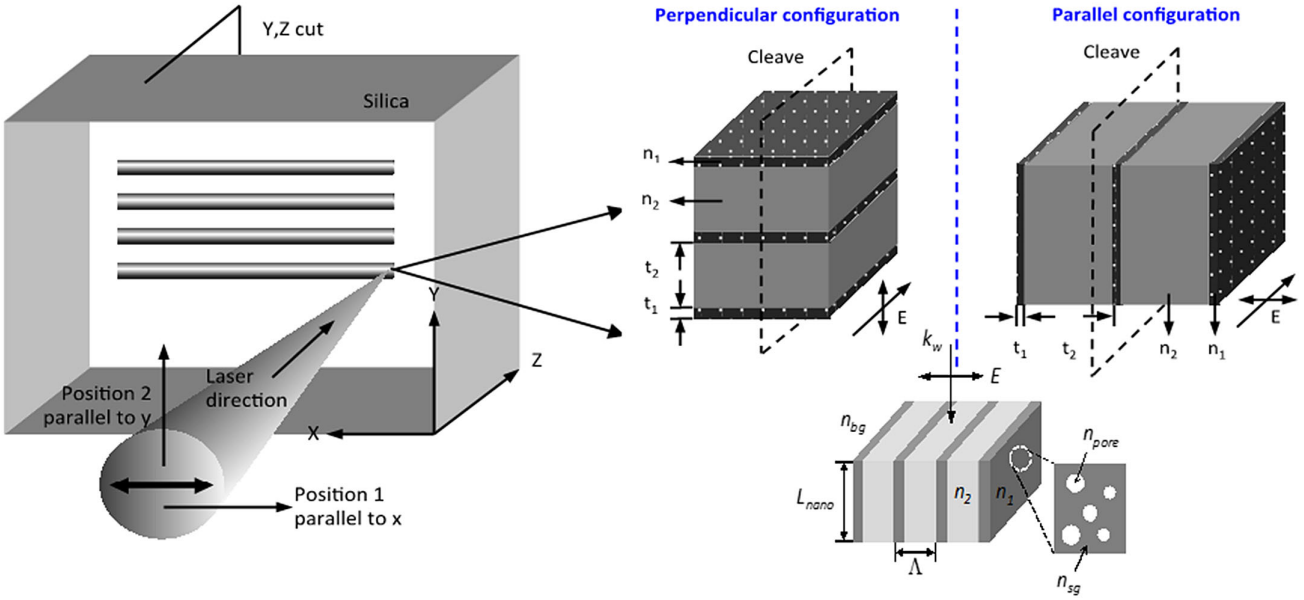

Figure 1. Experimental setup scheme for configuration of writing (from the left to the right top) and schematic of subwavelength periodic structure formed in the cross section of the irradiated region. n_1 and n_2: local refractive indices of the nanoplates; t_1 and t_2 are their respective thicknesses. Bottom right: Schematic of subwavelength periodic structure formed in the cross section of the irradiated region. n_{pore} and n_{sg}: local refractive indices of nanopores ($n_{pore} = 1$) and for surrounding oxygen defect regions, respectively; $\Lambda = t_1 + t_2$: period of nanogratings; n_{bg}: refractive index of the surrounding material; L_{nano}: thickness of nanogratings.

waveplates array for polarimetric imaging, stress-engineered waveplates, or microlenses. The laser beam was scanned along the *X*-axis and the linear polarization was set at 90° (i.e., along the *Y*-axis), 45°, and 22.5° relative to the scanning direction, so we labeled the samples Xy, X45, and X22.5.

2.2. Accelerated Aging

Usually accelerated aging measurements are required to evaluate the stability of nanogratings in their future working conditions. In this work, the decay rate was evaluated using step isochronal annealing experiments in the 100−1250 °C temperature range and with a fixed step time ($\Delta t = 30$ min) at each temperature. After the step, during which the samples were kept at a temperature for time Δt, the samples were cooled down to RT to record the photo-induced birefringence, Raman spectra, and the UV−vis−NIR absorption spectra. Thus, any temperature-induced reversible effects that may occur above RT does not spoil the measurements.

2.3. Characterization Techniques

Optical retardance of the laser-induced modifications, defined as the product of LB by the thickness (l) of the birefringent object, i.e., $R = LB \times l$, was measured using an Olympus BX51 polarizing optical microscope equipped with a "de Sénarmont" compensator. The "de Sénarmont" compensator coupled a high-precision quarter waveplate with a 180° rotating analyzer to provide retardation measurements in the visible range. Such a setup had an accuracy that approached a few nm when used in our conditions. In addition, UV−vis−NIR absorption spectra were conducted using a Cary5000 spectrophotometer in nonpolarized light with a data interval of 0.5 nm.

The irradiated zone was also analyzed using Raman microspectroscopy to track the glass densification signature and compare it with various silica samples densified under various conditions (thermal, electron irradiation, high pressure−high temperature). Raman spectra were recorded in MONARIS Lab (Paris 6) using a Labram HR microspectrometer (from Horiba Jobin-Yvon) equipped with a 458 nm Argon laser (6 mW on the sample) and a x100 microscope objective. All measurements were carried out at RT.

The second set of experiments was conducted to investigate the morphology and the texturing of fs laser-induced glass modifications.[31] In this view, two sets of single lines were written using two different laser polarization orientations: parallel (labeled Xx) and perpendicular (labeled Xy) to the laser scanning direction (*X*-axis), and the pulse energy was fixed to 1.2 μJ pulse^{-1}. Then, to probe the matter within the nanolayers and its transformation after step isochronal annealing, the sample was cleaved perpendicularly to the writing direction. Such a cleaving scheme allowed the laser track cross sections to be observed by an SEM (Field-Emission Gun Scanning Electron Microscope, ZEISS SUPRA 55 VP, 1 kV accelerating voltage) at 1000, 1100, and 1200 °C. Depending on the laser polarization orientations along Xx or Xy, the nanopores were found in the laser-induced nanoplanes from the former, and the nanolayers (sideways visualization of nanoplanes) with regular spacing would appear in the latter.

© 2021 Wiley-VCH GmbH

3. Results

3.1. Study of the Retardance during Step Isochronal Annealing

Figure 2 shows the retardance $R_{norm}(T)$ of the fs-irradiated regions, which is the retardance (T) normalized with respect to the retardance value from the as-irradiated glass at RT, as a function of isochronal annealing temperature. Here, we selected two kinds of irradiated areas, namely, type II modifications written at 1.75 μJ pulse^{-1} using different writing configurations and an additional low-energy (0.85 μJ pulse^{-1}; X45°) type II for sake of comparison. Note that the neutral axis did not show any significant rotation during the stage of annealing although the results are characteristic of different decay rates, indicative of distinct erasure mechanisms that will be discussed in the next section.

We first focus on the stress-induced birefringence, i.e., the green line in Figure 2a. Based on the results published by McMillen et al.,[32] the design has been tailored, so that we could reach a high optical retardance R of 200 nm (i.e., a half waveplate at 400 nm) within a 0.1 × 0.1 mm^2 area[33] that is free from any laser direct modifications. Here we created twin columns of lines (defined as "stress bar") spaced by 0.1 mm, which defines the clear aperture. Each stress bar is made up of an assembly of five layers written with a spacing Δz of 50 μm. The pulse energy was fixed to 2 μJ pulse^{-1}. In this simple arrangement,[32,33] the stress-induced birefringence was detected in between the two irradiated zones (see Figure 2b), along with monitoring of its thermal stability and its contribution to the overall retardance. The $R_{norm}(T)$ of the stress-induced birefringence remained rather stable from RT up to 800 °C. However, beyond 900 °C, its value drastically diminishes until it reaches zero at 1150 °C and is associated with stress relaxation of the silica glass around its glass transition temperature T_g.[34] We note here that the stress field produced by the nanoporous layers does not disappear with the annihilation of the nanopores themselves, which takes place at a higher temperature.

Now, we turn to the evolutionof $R_{norm}(T)$ values for the other samples, as shown in Figure 2a. They exhibit a slight increase of 10% up to 450–500 °C, which could be attributed to the erasure of the defects. Then, the modified area corresponding to type II modifications within low pulse energy (0.85 μJ pulse^{-1}) declines from 500 to 1150 °C progressively. However, an opposite trend on the evolution of $R_{norm}(T)$ is observed for a higher energy of 1.75 μJ pulse^{-1} in our writing conditions. Indeed, a rather large increase in $R_{norm}(T)$ of about 40% from RT up to 1000 °C is observed. According to the literature, it could be related to the coexistence of type I modifications (defects and densification) within nanogratings,[12,23] and more details will be given in the end part of the Discussion Section. Above 1000 °C, $R_{norm}(T)$ decreases abruptly and no measurable birefringence can be found after 30 min at 1250 °C. It should be pointed out that each irradiated area experiences a different path down to $R_{norm}(T) = 0$, and more specifically within the 1000–1100 °C range, where a kind of two-step decay is observed. As discussed earlier, the stress-induced birefringence was found to rapidly decay in this 1000–1100 °C range. Consequently, we ascribe the observed "first steep decay" of $R_{norm}(T)$ from its highest value as a stress relaxation mechanism. The final decay is attributed to the erasure of the nanoporous layers as we modeled recently using the Rayleigh Plesset (R–P) equation.[35] The various observed trends of $R_{norm}(T)$, in relationship with different erasure mechanisms, will be investigated in great detail in the Discussion Section.

3.2. Study of Point Defects Stability Using UV−vis Absorption Spectroscopy

UV−absorption spectra were collected at RT after each annealing step to monitor the absorbance of type II modifications.

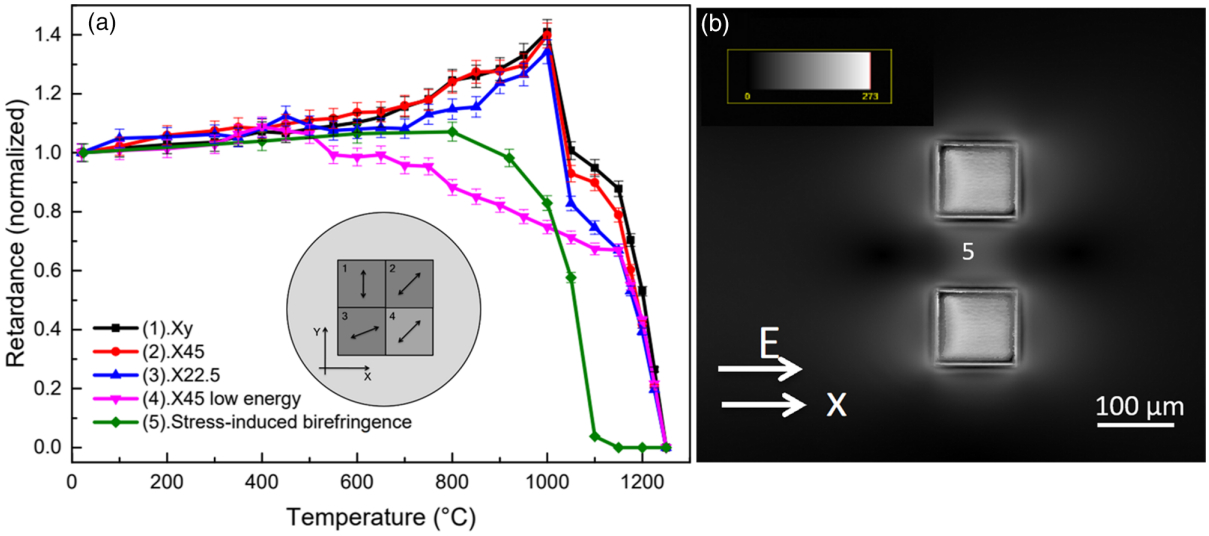

Figure 2. a) Normalized retardance as a function of temperature using isochronal step ($\Delta t = 30$ min) and for four "nanogratings" samples, as well as stress-induced birefringence (green curve). The measurements were carried out at RT. The inset shows the experimental laser writing designs. Four squares (3 mm × 3 mm) were written using $\lambda = 1030$ nm, 250–300 fs, 0.16 NA, 100 kHz, 0.5 mm s^{-1}, 0.85 or 1.75 μJ, laser polarization = 22.5°, 45°, and 90°. b) An example of stress-induced birefringence area that could be observed around and between the 0.1 × 0.1 mm^2 squares. The image was taken using an optical microscope with crossed polarizers. The thermal stability of the position marked by "5" is also shown (green curve in a).

© 2021 Wiley-VCH GmbH

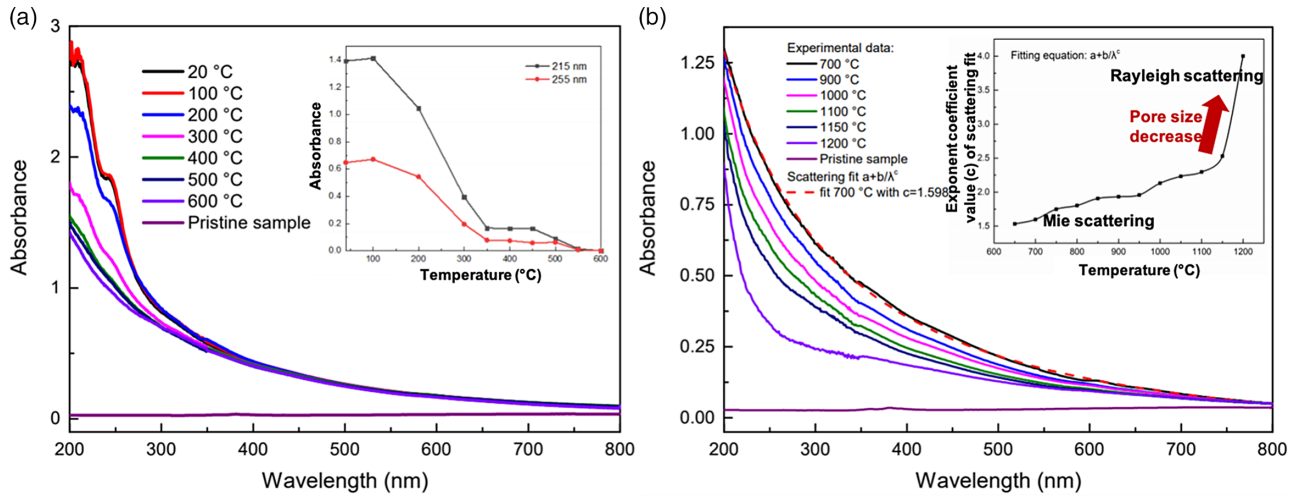

Figure 3. UV–vis absorption spectra of type II modification area (square 3 from Figure 2a), as a function of isochronal ($\Delta t = 30$ min) annealing temperature: a) 40–600 °C range and b) 650–1200 °C range. The spectra of a nonirradiated region (pristine silica) taken at RT were added as a reference. In (b) the absorption curve at 700 °C was fit by an equation of the form $a + b/\lambda^c$, typically relevant to study scattering losses. Inset graph in (a): absorbance as a function of temperature for the specific wavelengths (215 and 255 nm) and Inset graph in (b): exponent coefficient value (c) of the scattering fit and as a function of annealing temperature.

The results are shown in **Figure 3**. Several contributions are aggregated in the absorbance spectra: 1) the intrinsic absorption losses and 2) the light scattering caused by nanostructure.[15] As the pristine silica sample, taken as a reference, shows in Figure 3, the nonirradiated glass exhibits a quite flat absorption curve with nearly no absorption from the visible-to-the-near-IR region. In contrast, the absorbance of type II modifications significantly increases as one moves along the curve from the Vis side to the UV side of the spectrum.

In Figure 3a, the typical band features are clearly annealed away as the temperature progressively increases from RT up to 600 °C. The evolution of these features is attributed to the bleaching of defects. The band peaking at 255 nm (5.08 eV) corresponds to SiODC(II) whereas the band peaking at 215 nm (around 5.8 eV) was attributed to SiE' centers. Upon annealing up to 600 °C, we observe a significant impact on both bands at 5.08 and 5.8 eV. This is in accordance with the temperature-dependent decay of SiE' centers reported by Messina and Cannas.[36] After thermal treatment at 400 °C, most of these defects were bleached.

For the annealing treatments in the 600–1100 °C range (see Figure 3b), there is a slight continuous decrease in the UV tail. This "UV tail" is the signature of light scattering and is attributed to the nanoporosity inside the nanoplanes that we have fitted as follows: absorbance $(\lambda,T) = a + b(T)/\lambda^{c(T)}$. The exponent "$c(T)$" of the fitted equation increases from 1.5 (at 600 °C) up to 2.5 (at 1100 °C), indicating a Mie scattering regime. However, for temperature higher than 1100 °C, the exponent "c" exhibits a steep increase up to the value of 4, revealing a Rayleigh scattering regime and indicating a decrease in the nanopore size. The "$b(T)$" coefficient decreases with T indicating a decrease in the nanopores FF in agreement with the SEM observations. In addition, the polarization dependence of scattered light[37] reveals higher losses for a probe polarization oriented perpendicular to the nanolayers, which indicate that the scattering centers might be inside the nanogratings. This agrees with a layered medium made of alternating layers of two different isotropic materials with complex refractive indices, exhibiting a linear dichroism,[38] or more accurately here some polarization-dependent scattering losses due to the intrinsic nanoporous nature of the nanogratings.[7]

3.3. Study of Densification Stability Using Micro-Raman Spectroscopy

In this paragraph, we analyze the densification of fs-irradiated silica within the type II regime. The principal Raman features of silica glass, peaking at around 440, 490 (D1), and 606 cm^{-1} (D2), are well observed. The D1 and D2 peaks, attributed to four-member and three-member siloxane rings, respectively, are generally (but not always[39]) characteristics of a "dense" silica glass, and the latter is monitored as a function of temperature, as shown in **Figure 4**a. The magnitude of the D2 peak intensity is increased for the irradiated samples with respect to the pristine glass. This phenomenon could be attributed to some changes in ring statistics, where the dominant five- and sixfold rings were transformed by the laser irradiation to threefold and fourfold rings. This transformation would have the effect of a reduction of the average Si—O—Si bond angle distribution and would eventually lead to an increase in the glass density[40] in agreement with the shift and the width reduction of the main band at 440 cm^{-1}.

In Figure 4a, as the annealing temperature increases (as for various conditions), the strength of the D2 line with different laser parameters decreases beyond 500–600 °C. Raman intensities are previously normalized with respect to the value of the irradiated samples at room temperature (the D2 strength of the pristine sample was taken as zero here). Through further observation, according to the different annealing time and laser

© 2021 Wiley-VCH GmbH

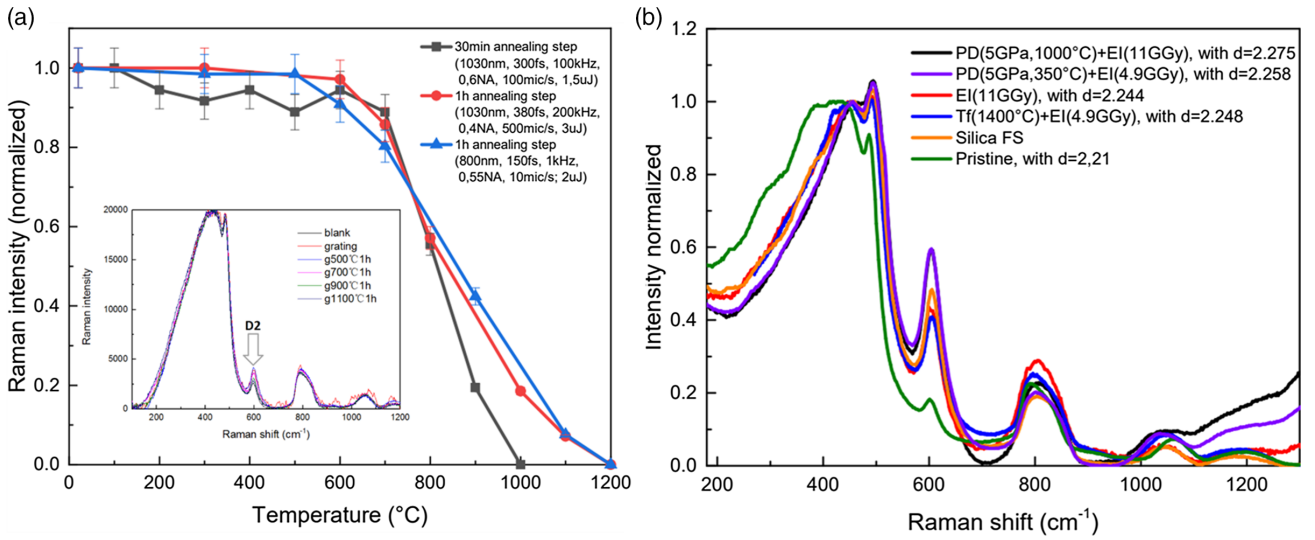

Figure 4. a) Raman spectra and the evolution as a function of temperature of D2 peak intensity for fs laser-irradiated silica glass. The data extracted from the literature for different annealing times (red[41] and blue[15]) are also inserted for comparison. Inset graph: Raman spectra of the area before and after laser irradiation and subsequent annealing during 1 h.[41] b) Raman spectra of silica with the following conditions: black, predensified (PD), (5 GPa, 1000 °C) + electron irradiation (EI), (11 GGy); purple, predensified (5 GPa, 350 °C) + electron irradiation (4.9 GGy); red, electron irradiation (11 GGy); and blue, fictive temperature treated (1400 °C) + electron irradiation (4.9 GGy); the data are extracted from the literature.[39,42] Silica irradiated by fs laser (orange) and the pristine sample (green) is also added for comparison.

parameters, the intensity went back to zero at around 1000– 1200 °C. As a side note, the thermal stability of type II modifications, being the function of laser writing conditions, may explain the subtle differences between each curve.[16]

In the following paragraphs, we compare the Raman signature of fs type II with the one of various silica samples studied in various studies,[39,42] for which we have measured their macroscopic density. More specifically, Figure 4b shows the Raman spectra of fs type II in comparison with high-energy electron-irradiated predensified silica glasses obtained either from high pressure–high temperature (HP–HT) or from thermal treatment increasing their initial fictive temperature (T_f).[39] From there, we can see that the Raman signature of fs type II mimics the one of HP–HT or high-T_f samples that have been irradiated to high electron doses (5–11 GGy range). In particular, the Raman spectrum of fs type II silica is quite close to both T_f 1400 °C silica irradiated at 5 GGy and the sample irradiated at 11 GGy. The densities of latter samples are 2.248 and 2.244, respectively. This further confirms that the material between porous layers exhibits similar characteristics as type I modification, i.e., a denser structure accompanied by a higher Young's modulus[43] compared with pristine silica.

To better quantify the observed variations to previously densified glasses (T_f and HP–HT) under irradiation (electrons vs fs), the full width at half maximum (FWHM) of the 440 cm^{-1} band and the D2 intensity from the study by Ollier et al.[39] as a function of density are shown in **Figure 5**. We can notice in Figure 5a that for density values lower than 2.3, the D2 band intensity increases linearly with the density and then decreases for higher density, and we place here the D2 amplitude related to fs type II spectrum with the red line. Now, we compare this observation with the 440 cm^{-1} FWHM versus the glass density shown in Figure 5b. It can be seen that the FWHM (i.e., the Si–O–Si angle dispersion) decreases when the silica glass density increases for all irradiated samples. This calibration curve leads to a rough estimate of the average density to be around 2.25–2.27 after fs irradiation. This corresponds to a refractive index change of around $+10^{-2}$[39] in agreement with some anisotropic refractive index measurements made by Bricchi et al.[12] However, this is difficult to give a more reliable value at this step due to the composite nature of the probe volume that is made of an assembly of porous thin nanolayers (typ. 30 nm thickness) with densified interlayers (typ. 200–300 nm thickness) and some potential volume changes occurring around the nanopores as well. Given the nature of the densification process, a pure thermal mechanism, i.e., melting followed by fast quenching, can be excluded as it would not relax at temperatures below T_g for such a short (30 min) annealing time, as shown in Figure 4a. Interestingly, the estimated elastic properties of the densified interlayers are higher compared with a type I modification.[43] This suggests that the densification mechanism is more complex than the regime I modification. However, it is still unclear if the densification is due do defects accumulation (such as for electrons irradiation, for instance) or from a more likely mechanism based on a HP–HT that develops during the nanogratings formation.[44]

3.4. Observation of Nanostructure Thermal Stability Using Scanning Electron Microscope

To further investigate the impact of annealing on the nanostructure changes, the samples were cleaved and observed by a scanning electron microscope (SEM). **Figure 6** shows SEM

© 2021 Wiley-VCH GmbH

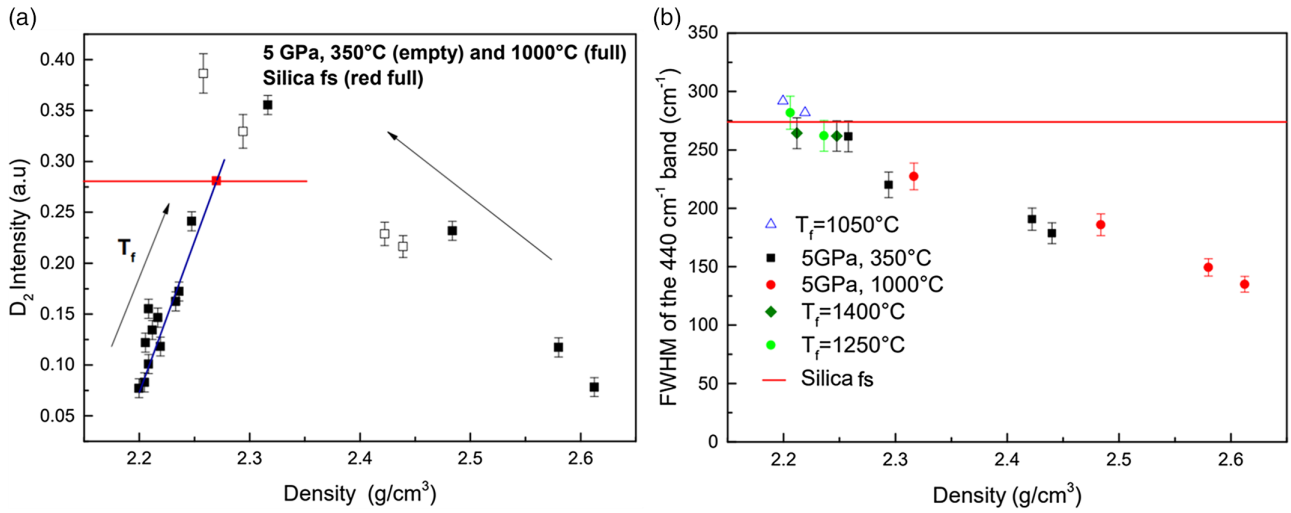

Figure 5. a) Raman D2 band intensity as a function of density for HP–HT and T_f samples. b) FWHM of the R-band as a function of density for HP–HT and T_f samples. Both figures were extracted from the study by Oillier et al.,[39] and the results of the silica irradiated by fs laser were inserted. Laser parameters: $\lambda = 1030$ nm, 100 kHz, 100 µm s^{-1}, 10^3 pulses µm^{-1}, NA = 0.16, pulse duration = 250–300 fs, and $E = 1.5$ µJ pulse^{-1}.

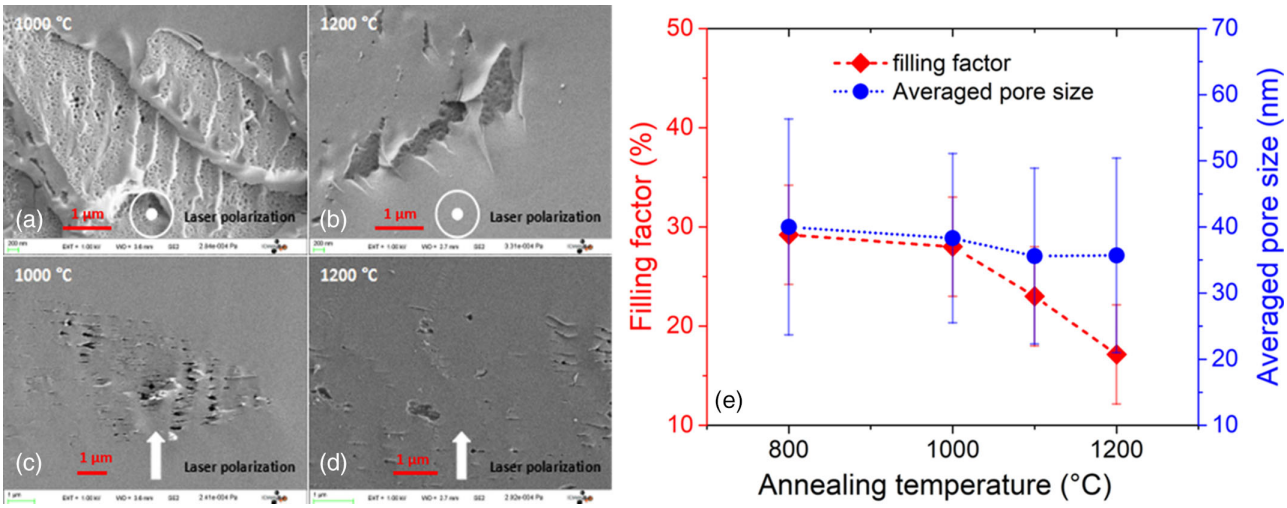

Figure 6. Scanning electron micrographs of type II modification areas in silica glass annealed at 1000 and 1200 °C, for a,b) parallel and c,d) orthogonal laser polarization directions with respect to the writing direction. e) Evolution of the 2D porosity FF in the nanolayers and the average pore size diameter as a function of annealing temperature. The lines serve here only as guide to the eye. Laser parameters: $\lambda = 1030$ nm, 100 kHz, 100 µm s^{-1}, 10^3 pulses µm^{-1}, NA = 0.16, pulse duration = 250–300 fs, $E = 1.2$ µJ pulse^{-1}.

micrographs for different annealing temperatures and laser polarization directions. First, and from Figure 6c, some well-defined nanolayers could be observed at 1000 °C. This observation is consistent with the results shown in Figure 2, where retardance (hence birefringence) can easily be detected. When the temperature is further increased to 1200 °C, as shown in Figure 6d, we observed the disappearance of several layers. From Figure 6a–c, we make the observation that upon an increase in temperature, the irradiated glass morphology evolves such that 1) the 2D porosity FF in the nanolayers decreases, 2) the average pore size slightly decreases, and 3) the number of nanolayers decreases (the side nanolayers are less stable than the middle ones). These observations can be explained on the basis of the R–P equation,[35] where we observe that small pores are erased more quickly than larger ones. To help the reader, the main equations from the aforementioned reference are added in Appendix A. As a result, the ongoing erasure of the small pores population is no more included in counting (due to the limited resolution of the SEM) to determine the average pore size diameter. This has an effect of "shifting up" the average pore size distribution to larger values. However, the FF still decreases as pores are progressively erased, which is in agreement with both the scattering measurements and the observation of a decrease in retardance upon temperature increase.

© 2021 Wiley-VCH GmbH

4. Discussion

4.1. Summary and Tentative Decomposition of the Measured Retardance $R_{norm}(T)$

In this work, we have highlighted the dependency of fs laser modifications (including defects centers, densification, stress, and distributed nanopores) with temperature. In the following section, we only consider birefringence contributions which only have proper axes along x or y, i.e., $\delta LB = \delta n_x - \delta n_y$ that can be >0 or <0. If this is not the case (e.g., X22 or X45 writing or the occurrence of shear−stress for instance), one needs to extract (e.g., using Mueller's formalism) the contributions along both x- and y-axis before to do summation. Under this restrictive hypothesis, we can consider that the total measured birefringence is composed of additive/subtractive but not independent (e.g., stress is related to the permanent volume changes) contributions. In addition, they all present different erasure kinetics based on their thermal stabilities, as shown in **Figure 7**.

These contributions are divided into three categories. 1) First the birefringence of the type I-like modification can be considered as the combination of the defect, the densification, and the proportional stress-induced birefringence to the previous two. 2) Then, type II modification contains stresses from two different origins, the one of type I modification that disappears with the erasure of type I modification at temperatures below plastic relaxation and the second one coming from nanoporous layers that will relax plastically (a plastic deformation around nanopores occurs) because nanopores are more stable and will ultimately erase at higher temperature. 3) The third contribution is form birefringence related to the nanopores arranged within nanolayers' so-called nanogratings.

Following this view, we conducted a decomposition of the normalized retardance $R_{norm}(T, \delta t = 30\ min)$ for Xy sample (data are taken from Figure 2a) using a three-component model: type I modification (black), stress that relaxes into plastic deformation (green) and nanopores themselves (orange), as shown in Figure 7b. In the following paragraphs, we assume that the erasure kinetics of each component follows a sigmoidal evolution.

$$R_{norm}(t, T) = a\left(\frac{1}{1 + \exp(-2\ln(3)T_0/\Delta_T^{\delta t})(3)^{\frac{2T}{\Delta_T^{\delta t}}}}\right) \quad (1)$$

In this equation, "a" represents the relative contribution to R_{norm}, "T_0" is the temperature where the curve falls, and $\Delta_T^{\delta t}$ (in K) regulates the slope of decay. Due to the numerous fitting parameters, we have chosen to initiate the coefficients "T_0" based on the results shown in Figure 7a. The fitted values of a, T_0, and $\Delta_T^{\delta t}$ are shown in **Table 1**. Note that in the VAREPA framework developed by Poumellec et al.,[45] we can tentatively give a physical meaning to these parameters. Some details of the framework are described in Appendix B. T_o is related to the center of activation energy distribution $E_0 = k_B T_0 \ln(k_o t)$ and $\Delta_T^{\delta t}$ to the FWHM ΔE of the distribution that can be rewritten as $\Delta_E = k_B \Delta_T^{\delta t} \ln(k_o t)$.

Now by comparing the three components to Figure 7a and in particular T_0 values with the inflexion point of the curves in Figure 7a, we can tentatively assimilate each function to a mechanism and its relative "weight" to the overall measured retardance. The first function represents the major contribution ($a = 0.94$) of the nanopores, which should be erased at around 1250 °C. Then, the second function can account for the stress-induced birefringence contribution ($a = 0.48$), which can last until 1100 °C. Finally, we can subtract the third function that

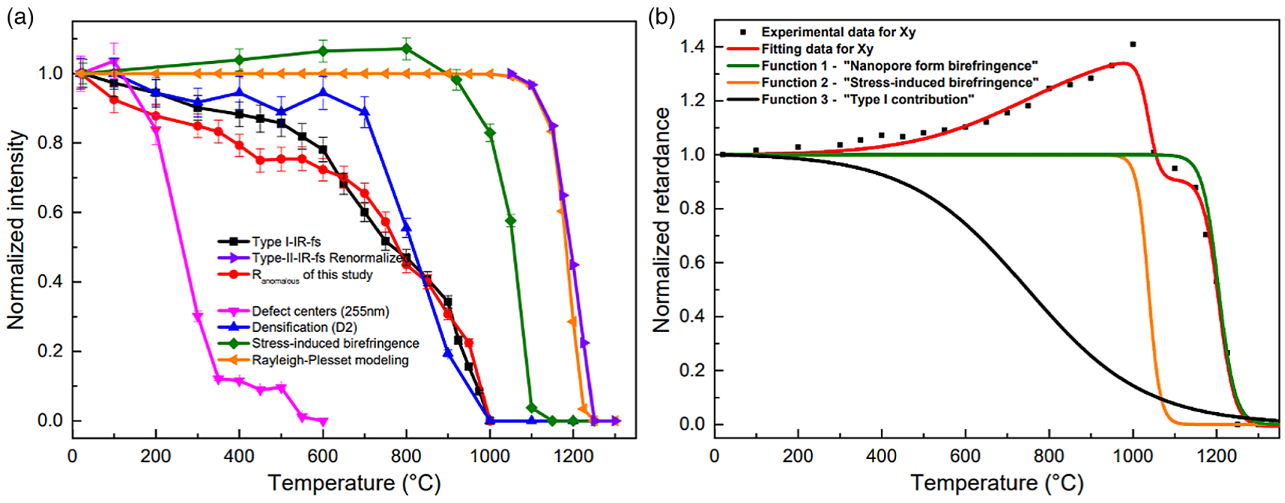

Figure 7. a) Normalized index change $\Delta n_{TypeI}(T)$ of type I modification by IR fs laser (black); $R_{anomalous}(T)$ (red) is the renormalized "anomalous part" of the type II (see Equation (1)) (i.e., the 40% increment in Figure 2a). We also add D2 peak intensity (blue) and the SiODC defect (255 nm) UV absorption intensity (pink) and the stress-induced birefringence (green). In the highest T range, we have the simulation of the nanopores' erasure using the R−P equation (orange, simulation conditions: the surface energy $S = 0.3\ J\ m^{-2}$; pore size diameter = 70 nm) and the normalized retardance (at 1050 °C) of type II (purple, X45° taken from Figure 2), as a function of the isochronal annealing temperature. b) Decomposition of the normalized retardance $R_{norm}(T, \delta t = 30\ min)$ for Xy sample using three components. The fitting curve (red) is composed of three sigmoidal functions that could be assimilated to "nanopores " (orange), "stress-induced birefringence" relaxing into a plastic deformation around nanopores (green), and "type I like contribution" (black, the curve has been inverted for the purpose of the layout).

© 2021 Wiley-VCH GmbH

Table 1. Coefficients values of the fitting using Equation (1) for each of the three contributions.

Coefficient	Nanopore form birefringence [δLB_{form}]	Stress-induced birefringence [δLB_{stress}]	"Type I-like" contribution
a	0.941 ± 0.022	0.476 ± 0.026	-0.417 ± 0.024
T_0 [in K]	1478.3 ± 2.1	1310.4 ± 4.7	1020.3 ± 37.0
$\Delta_T^{\delta t}$ [in K]	42.29 ± 4.0	30.01 ± 2.50	310.81 ± 29.16

we attributed to type I-like modification ($a = -0.42$) to fit the anomalous increase in the retardance in the RT−1000 °C range.

In **Table 2**, we classified and summarized the different categories of mechanisms (labeled A, B, and C in Table 2) that can induce birefringence within the nanogratings formation regime along with their contribution to the total birefringence and thermal stability. We focus our analysis upon two major modification aspects, which are refractive index changes (δn) and δLB, that may be due to either form birefringence or stress-induced birefringence. These contributions (from Figure 7 and Table 2) are discussed in the next sections.

4.2. Overview of the Different Contributions to the Measured Birefringence

4.2.1. Case A: Contribution of Nanopores Formation Within Type II Regime

At this point, it is worth pointing out that the main contribution to the aggregate birefringence is usually attributed to the nanogratings form birefringence LB_{form} in close relationship with the formation of nanopores in aligned nanoplanes and related volume expansion, as summarized in the cases A1 and A3 in Table 1. For more details on these contributions, we recommend the reader the following studies.[35,44,50] Note that recent study by Sakakura et al.[46] has reported some low-loss birefringent modifications qualified by type X modifications. As described shortly in case A2 of Table 1, form birefringence was attributed to the formation of oblate and oriented nanopores (case A2b) with a slow axis parallel to the long axis of the nanopores.

Case A1: From the SEM micrographs shown in Figure 5, we can deduce the changes in morphology (e.g., porosity, FF) with respect to the annealing thermal treatment. Very recently, Cavillon et al.[35] have shown the correlation between the thermal stability of anisotropic optical properties and the erasure of the nanopores present in the nanogratings. Briefly, in the perpendicular configuration Xy, although several nanolayers gradually dissolved, we noticed that the average spacing between the remaining nanolayers does not change with the annealing temperature.

In contrast, in the parallel configuration Xx, the number of nanopores and the average pore size for each laser track are found to decrease as the temperature increases. In addition, these results indicate that all nanopores tend to become smaller by the same quantity (in agreement with the scattering signature in Figure 3); thus, the smallest pores (e.g., 20−30 nm long) disappear (typ. of diameter around 70−90 nm) for thermal treatments above 1000 °C and up to 1200 °C in silica. As a result, the average pore size does not decrease so much than with a proportional size decrease and the porosity FF decreases as the annealing temperature increases.

Using the R−P equation to simulate the erasure of the pores (see details in Appendix A), the evolution of the normalized retardance R_{norm} could be calculated for a given pore size diameter and glass material. In Figure 7 (SuprasilCG modeled curve, the orange solid line), the nanopore erasure is displayed using the R−P equation, and the evolution of the normalized retardance was also calculated. Then, the curve presents the experimental results (SuprasilCG curve X45°, the purple solid line) is used to compare, the measured data obtained by following the same experimental condition as the R–P simulation and removing the anomalous increase. Then, it is normalized relative to the sharp retardance decrease at the highest annealing temperature values that we hypothesized here to be characteristic of the nanopore erasure. These two curves show quite similar trends in Figure 7. More details can be found in the study by Cavillon et al.,[35] and this leads to the conclusion that the porosity can play an extremely important role in the erasure of nanogratings and their associated birefringence in a high-temperature regime. In particular, the R−P equation sheds light on the major role played by the temperature dependence of the glass viscosity on the thermal stability of fs-induced type II modifications. The viscous behavior of glass, at high temperatures, is the major parameter that drives the nanogratings erasure and related form birefringence. Current research efforts are ongoing to better understand the role played by the nanopores, within the nanoporous regions, on the overall thermal stability of the laser-induced type II modifications.

4.2.2. Case A3: Contribution of the Stress-Induced Birefringence Within Type II Regime

Usually when conducting step isochronal annealing, within the last decade, a few research groups have shown the presence of a zone of mechanical stress,[51–53] possibly associated with birefringence properties in the irradiated zone, related to the polarization of the writing laser beam.[47] Within the type II regime, the nanolayers are made of porous material, and our group suggested that they are created by glass decomposition during the laser interaction within the hot plasma nanolayers.[7] During the decomposition of SiO_2, many nanopores or nanocavities are created within these layers, leading to a net glass volume expansion,[44,54] which correlates with the formation of porous nanogratings.[7,55] This corresponds to the appearance of a permanent strain $\varepsilon^p > 0$ within type II zones (whereas it is negative for glass densification within the type I regime) and thus $\Delta n < 0$ in the laser-affected volume. The latter results into a negative elastic strain $\varepsilon^e < 0$ as a direct elastic response of the material and therefore a compressive elastic strain field within and around the laser-modified region. Finally based on the photoelasticity theory, stress-induced birefringence LB_{stress} has been observed, which finally participates to the total measured birefringence LB, as summarized in case A3 in Table 2. Depending on the laser exposure conditions, the overall stress can be enhanced or minimized,[44] leading to tunable birefringence values from 10^{-5} up to $\approx 10^{-3}$.[56–58]

© 2021 Wiley-VCH GmbH

Table 2. Summary of the different potential contributions of total birefringence within nanogratings regime.

Primary mechanism	Subcases	Index contribution δn_i	Birefringence contribution[a]: $\delta LB = \delta n_x - \delta n_y$ Note that δLB can be >0 or <0.	Contribution quantity/thermal stability
A Fs Type II Birefringence (due to nanopores formation)	Case A1: Spherical nanopores distributed uniformly in the nanolayers of refractive index *n1*	$(1-\mathrm{FF})\left(\frac{\varepsilon_{\mathrm{eff}}-\varepsilon_m}{\varepsilon_m+2\varepsilon_{\mathrm{eff}}}\right)=\mathrm{FF}\left(\frac{\varepsilon_i-\varepsilon_{\mathrm{eff}}}{\varepsilon_i+2\varepsilon_{\mathrm{eff}}}\right)$[c] $n_1=\sqrt{\varepsilon_{\mathrm{eff}}}=\sqrt{n_m^2\frac{n_m^2+\frac{(1+2\mathrm{FF})}{3}(n_i^2-n_m^2)}{n_m^2+\frac{(1-\mathrm{FF})}{3}(n_i^2-n_m^2)}}$, n_2[d]	Form birefringence $\delta\mathrm{LB}_{\mathrm{form}}$ (negative uniaxial) Slow axis is along nanolayers, i.e., perpendicular to the laser polarization orientation *E*	Contribution: Main contribution to the measured LB or Retardance Range of thermal erasure: (>T_a)[f]
	Case A2a: Oblate or cylindrical nanopores randomly oriented in the probe volume	Same as above	None due to the random orientation	
	Case A2b: Oriented oblate or cylindrical nanopores (without layers)—like type X low-loss modification[46]	$\varepsilon_{\mathrm{eff}\parallel}=\varepsilon_m+\mathrm{FF}(\varepsilon_i-\varepsilon_m)$[b] $\varepsilon_{\mathrm{eff}\perp}=\varepsilon_m+\frac{\mathrm{FF}(\varepsilon_i-\varepsilon_m)}{1+(1-\mathrm{FF})(\varepsilon_i-\varepsilon_m)/2\varepsilon_m}$	Form birefringence $\delta\mathrm{LB}_{\mathrm{form}}$ Slow axis is parallel to the long axis of nanopores [46]	
	Case A3: Permanent volume expansion and compressive elastic strain [47] [e]	Refractive index n_1 decreases (Lorentz−Lorenz + Pockels)	Stress birefringence $\delta\mathrm{LB}_{\mathrm{stress}}$; Slow axis parallel to the scanning direction (for lines) $\delta\mathrm{LB}_{\mathrm{stress}}$ (>0 for X writing)	Contribution: e.g. $\varepsilon^p=0.005$ leads to $\delta\mathrm{LB}_{\mathrm{stress}}=0.0012$ Range of thermal erasure: (800 °C−T_a)
B Point defects	Case B1: Anisotropic and oriented defects uniformly distributed in the laser track	Δn_{ii} increases, higher Δn_{ii} along the high absorption axis	$\delta\mathrm{LB}_{\mathrm{defects}}>0$ (α_{high} along *x*), <0 (α_{high} along *y*) Slow axis is along high-absorption α_{high} direction	Contribution: LB or Retardance contribution usually limited to less than 5%[37] Range of thermal erasure: (200 °C–500 °C)
	Case B2a: Isotropic defect (or anisotropic defects randomly oriented) distributed between the nanolayers (n_2)	n_2 increases (KK)	$\mathrm{LB}_{\mathrm{form}}$ increases	
	Case B2b: Isotropic defect (or anisotropic defects randomly oriented) distributed inside the porous nanolayers (n_1)	n_1 increases (KK)	$\mathrm{LB}_{\mathrm{form}}$ decreases	
C Densification	Permanent densification and associated tensile strain	Refractive index Δn increases (Lorentz−Lorenz + Pockels)		Contribution: e.g. $\varepsilon^p=-0.0053$ leads to $\delta\mathrm{LB}_{\mathrm{stress}}=0.00125$ and $\Delta n=+10^{-2}$ between layers. Range of thermal erasure: (600–900 °C)
	Case C1: Uniform along the laser track as a "separate layer"	n_1 and n_2 increase	Stress birefringence $\delta\mathrm{LB}_{\mathrm{stress}}$; Slow axis perpendicular to the scanning direction (for lines geometry) $\delta\mathrm{LB}_{\mathrm{stress}}$ (<0 for X writing and >0 for Y writing)	
	Case C2a: Within the porous nanolayers	n_1 increases	$\mathrm{LB}_{\mathrm{form}}$ decreases	
	Case C2b: Between the nanolayers	n_2 increases	$\mathrm{LB}_{\mathrm{form}}$ increases	

[a] We only consider contributions which only have proper axes along *x* or *y*. If this is not the case (e.g., X22 or X45 writing), we need to extract the contributions along *x* and *y* axes (e.g., using Mueller formalism); [b] Formulae are valid for infinite cylinder[48,49] ∥ and ⊥ are relative to the major axis of the cylindrical nanopores. [c] $\varepsilon_{\mathrm{eff}}$ is the dielectric constant for the composite (e.g., nanoporous layers), ε_i for the inclusion (here nanopores), and ε_m for the surrounding medium (e.g., silica, understoichiometric silica, densified silica). [d] *n* represents the refractive index. n_1 : refractive index of the composite medium (porous nanolayers); n_2: index of the material in between nanolayers (likely densified silica); and n_i: the local refractive index for inclusions (nanopores). FF = porosity 3D filling factor; n_m: index for the surrounding medium (between the nanopores in the nanoplanes:); [e] ε^p represents the permanent strain due to specific volume changes; ε^e is for elastic strain due to the material response, whereas σ represents the stress. [f] T_a = glass annealing point (temperature where the glass viscosity is set at $\eta=10^{12}$ Pa s).

Note that the slow axis direction is mostly determined by the geometry of the irradiated regions and does not depend on the laser writing polarization as a first approximation (except at the edges of the written line).[47] For single lines or superposition of lines, there is quasiuniaxial loading, and the slow axis direction of the stress-induced birefringence is parallel to the lines for volume expansion[33] and perpendicular to the lines for densification. As a first approximation, considering a "pure type II" modification (without any associated type I, nor densified volume), if we combine the $\mathrm{LB}_{\mathrm{form}}$ and the $\mathrm{LB}_{\mathrm{stress}}$, we will have

© 2021 Wiley-VCH GmbH

either additive or subtractive superposition of these two components. For Xx writing configuration (the slow axes from two components are perpendicular), we will have a subtractive superposition, whereas it is an additive superposition for Xy (the slow axes of the two components are parallel) writing configuration. For intermediate configurations (e.g., X22°), there is a need to extract (e.g., using Mueller formalism) the LB components before to calculate the results of the superposition. Then under thermal treatment, a part of the stress is expected to relax when approaching a temperature around $0.8 \times T_g$ for a few hours or $0.9 \times T_g$ for a few tens of minutes (T_g is the glass transition temperature). In our experiments, this starts from 800 °C, as shown in Figure 7 (stress curve, the green solid line), which correlates with the "first-component" decay of $R_{norm}(T)$ in the 1000−1000 °C range, as shown in Figure 2a. We note here that the compressive stress field produced by nanoporous layers does not disappear with the annihilation of the nanopores themselves (which takes place at a higher temperature) but by plastic deformation of the glass around the nanopores. This is not the case with the tensile stress field associated with the densification for which it disappears because the "producer" disappears.

4.2.3. Case B: Contribution of Point Defects Which Remains Quite Limited

In addition to the well-known existence of both form birefringence and stress-induced birefringence, type II modifications in silica glass also contain a variety of point defects. Through their optical absorption bands, they contribute to the observed refractive index changes Δn, as usually described by the Kramer−Kronig (KK) relationship. Generally, most defects absorb in the UV−VUV range and they contribute positively to Δn measured in the vis−near-IR range. This contribution decreases when the defects are bleached under thermal treatment. Therefore, their existence may also affect (n_1, n_2) the form birefringence LB_{form} (and thus the measured retardance R) that is mostly attributed to the nanogratings form birefringence in the literature.[12] Different cases are shown in Table 1 but we can think about two main cases: 1) anisotropic and oriented defects and 2) isotropic defects but uniformly distributed only inside nanolayers (not in between). Both (1) and (2) can create some small amount of birefringence.

Case B1: The first possibility would be the formation of anisotropic and oriented defects that create linear dichroism and thus LB through the KK relationship. Linear dichroism was observed recently but only at wavelengths of around 1.2–1.4 μm.[33] In addition, there is apparent linear dichroism in the UV−vis range, which has been attributed to polarization-dependent light scattering.[33] Indeed, the arrangement of porous nanolayers creates anisotropic light scattering, resulting in a linear diattenuation (rather than linear dichroism) tail observed in the UV−vis range,[33] but no dichroic bands have been observed in this range.[33]

Case B2: The second possibility is about the spatial distribution of isotropic defects absorbing in the UV range. There are two subcases. Case B2a: On the one hand, the defects are preferentially located between the nanolayers (region of index n_2 in Figure 1). When they are bleached under thermal treatment, n_2 decreases and therefore LB_{form} (proportional to n_2-n_1 and with $n_1 < n_2$, initially) decreases. Case B2b: On the other hand, the defects are formed inside the nanolayers (area of index n_1 in Figure 1) especially in the material surrounding n_{sg} the nanopores. When they disappear during heat treatment, the refractive index n_{sg} (and n_1) decreases and thus LB_{form} increases, resulting in an increase in R.

Correlating Figure 2 and 3, most defects were bleached at around 400 °C, whereas there is no significant effect or maybe a slight increase in the measured retardance within this range of temperature (see Figure 2a). In summary, compared with the form birefringence and the stress-induced birefringence, the defects play a minor role in the total retardance response induced within the nanogratings regime. This is in agreement with previous works, where silica samples were annealed for 2 h at 450 °C. All point defects generated within type I modifications were completely erased[37] whereas the overall retardance value was observed to decrease only by less than 5%.[37]

4.2.4. Case C: Contribution of Permanent Densification Within Type II Regime

Now, considering that densification annealed out at lower temperatures than nanopores themselves, this could impact the measured birefringence through two different mechanisms: 1) by affecting the nanogratings refractive index changes n_1 and n_2 and thus LB_{form} and/or 2) through the direct contribution of stress-induced birefringence (δLB_{stress}) to the measured total LB. In addition, as shown in Table 1, one has to consider different possibilities for densification to happen: Case C1, along the laser track (e.g., in the tail) bringing an additional stress-birefringence contribution and/or Case C2, within type II regions, as suggested by Bellouard[59] and Poumellec.[60] About the second case and considering the periodical structure of the nanogratings, densification might be mostly present either between the nanolayers (n_2) or in the material surrounding the nanopores n_{sg} within the nanolayers themselves (n_1).

Case C2a: We can first assume that densification is present in the material surrounding the nanopores (of refractive index n_{sg} in Figure 1). From our data and the literature[23] we expect that densification will be erased at a much lower temperature than the nanopores themselves. Hence, as the annealing temperature increases, densified regions will gradually anneal away, causing a decrease in the refractive index n_{sg} and thus n_1 within the porous nanolayers (see Figure 1). Consequently, LB_{form} increases and therefore we have an increase in the measured LB (or retardance R).

Case C2b: Now, if we assume that that densification is preferentially located in between the nanolayers, this should result in a decrease in the LB_{form} under thermal treatment. This agrees with early results of Bricchi et al.,[12] showing n_2 increase up to a few 10^{-2}, whereas Vlugter et al.[43] recently revealed an increase in the Young's modulus in the silica material between porous nanolayers associated with an increase in material density also suggested by Raman spectroscopy. Assuming a densification contribution of $\Delta n_2 = 10^{-2}$[12] and some typical values of n_1 (1.3) and n_2 (1.46), one can calculate the LB_{form} changes.

© 2021 Wiley-VCH GmbH

When this contribution vanishes under thermal treatment, one finds a decrease of around 20–30 nm for a total retardance of 270 nm so < 10%.

Now taking into account the stress contribution in the aforementioned cases, the LB (or retardance) measurements correspond to two "additive" contributions $LB_{stress} + LB_{form}$. But one needs to consider several difficulties, including spatial distribution in depth (overlapping or not like case C1) and the respective neutral axis orientation of these contributions, which can lead to additive or subtractive effects depending on the respective slow axis orientation.

4.2.5. The Origin of the Unexpected Increase in the Retardance Within RT–1000 °C

Usually when conducting step isochronal annealing, we observe a monotonous decay of the laser-induced refractive index changes,[16] as is also the case here for the low-energy type II (0.85 μJ pulse^{-1}) or type I modifications. However, as shown in Figure 2a for the three "high-energy" samples, we observed an unexpected behavior, namely, a slight increase (a few%) in $R_{norm}(T)$ in the 100–500 °C range followed by a strong one (up to 40%!) from 550 to 1000 °C. Such behavior was already observed, although less pronounced, in both bulk silica and Ge-doped optical fibers.[12,23] It was suggested that the coexistence of type I modifications (defects and densification) within nanogratings can explain this behavior.[12,23] More precisely, it was suggested that the slight increase observed below 500 °C is attributed to point defects bleaching, whereas at higher temperature it is rather related to the relaxation of permanent densification. Now by comparing and analyzing the characteristic curves shown in Figure 7, we can tentatively explore the relationship between this unexpected increase[23] and the different erasure mechanisms. In this view, we have first renormalized the $R_{norm}(T)$ "anomalous increase" of type II curve (the red solid line in Figure 7) as follows.

$$R_{anomalous}(T) = \frac{R(1000\,°C) - R(T)}{R(1000\,°C) - 1} \text{ for } T < 1000\,°C \quad (2)$$

Then, for sake of comparison, we inserted in Figure 7 the normalized refractive index changes of type I modifications (black solid line), labeled $\Delta n_{Type\ I\text{-}IR\text{-}fs}(T)$, as a function of annealing temperature. Both curves $R_{anomalous}$(T) and $\Delta n_{Type\ I\text{-}IR\text{-}fs}(T)$ follow similar trends, i.e., a slow decay from RT up to 500 °C, a steeper decrease starting at around 600 °C, and a full erasure at 1000 °C. The initial decay of $\Delta n_{Type\ I\text{-}IR\text{-}fs}(T)$ is usually related to point defects erasure (up to 400 °C), whereas the main part might be attributed to the relaxation of glass densification. In silica, this is usually supported by micro-Raman spectroscopy as the D2 band intensity shows a significant decay starting from 600 °C up to 1000 °C (see the blue curve in Figure 7).

Before going further in the tentative explanation, let us focus on the Case C2b. LB_{stress} contains two components: a positive contribution (tensile stress) in response to the permanent densification $\varepsilon^{P}_{densification}$ between the nanolayers but the main component is negative (compressive stress) due to nanolayers volume expansion $\varepsilon^{P}_{expansion}$.[44] Therefore, the thermal relaxation of the densification ($\varepsilon^{P}_{densification}$ vanishes within the 600–900 °C range) will result in a higher net volume expansion. Thus, the compressive stress and LB_{stress} will become higher in agreement with the green curve in Figure 7. We note that the tensile stress associated with densification relaxes but the compressive one related to the volume expansion still remains until higher temperatures. Quantitatively, LB_{stress} amplitude usually remains quite low[59] but it cumulates from pulse to pulse and lines to lines, considering our writing geometry that favors stress accumulation.[33] A rough estimate of LB_{stress} changes when relaxing permanent strain $\varepsilon^{P}_{densification}$ (<0) can be done. Assuming an initial $\Delta n_2 = 10^{-2}$, we calculated ε^{P} using the Lorentz–Lorenz equation and an estimate of elastic strain ε^{e} based on our writing geometry. Finally, we found from photoelastic equations LB_{stress} that could reach 60–100 nm (for a total of 270 nm), which agrees rather well with the unexpected increase (up to 40%) of the measured retardance $R_{norm}(T)$ in Figure 2a.

4.3. Influence of the Laser Parameters on fs Type II (Nanogratings) Thermal Stability

Laser parameters can impact the thermal stability of the laser-induced refractive index changes,[16] included within the type II regime. In the particular framework of this article, both the relative contribution of each mechanism and the final steep decay (attributed to the erasure of the nanopores[35]) will be altered by the different laser writing parameters.

For instance, laser-writing speed has been proved to be one of the key factors. Our previous work has revealed that higher speed (e.g., 10 mm s^{-1} instead of 1 or 0.1 mm s^{-1}, 2 μJ pulse^{-1}, 1030 nm, 250 fs, 100 kHz, NA = 0.6) leads to higher thermal stability in SiO_2 that can be attributed to larger nanopores generated during fs irradiation, as confirmed by SEM.[31] High pulse energy also leads to higher thermal stability modifications with the erasure constant k_0 of the nanogratings that increases from 2.10^5 (1 μJ pulse^{-1}) to 7.10^5 s^{-1} for 1.75 μJ pulse^{-1} (800 nm 700 fs, 0.16 NA, 200 kHz, 1 mm s^{-1}, Xy configuration).[18] As shown in Figure 2, we found as well that the square written a low energy (0.8 μJ pulse^{-1}) exhibits lower thermal stability than for 1.75 μJ pulse^{-1}, especially in the intermediate temperature range (500–1000 °C). The key difference here seems relegated to the relative contribution of type I-like modifications (like interlayers densification) within the type II regime. Such thermal stability that depends on the writing pulse energy was also observed in Ge-doped SiO_2 optical fibers (SMF28 and 3D-printed fibers),[61] where the final steep decay is shifted toward high T at high pulse energy. Again we likely could attribute this effect to the larger size of the nanopores generated by the higher pulse energy in agreement with SEM observations.[35]

Something may be less expected; the writing configuration has a significant impact on thermal stability. Indeed lines[62] or squares[18] written using Xx configuration exhibit higher thermal stability (k_0 = a few 10^7 s^{-1}) than Xy (k_0 = a few 10^5 s^{-1}) but the reasons are still unclear. In this work, some significant differences could be observed between the three investigated configurations in the intermediate temperature range (500–1000 °C). In particular, the stress-induced birefringence contribution is quite different according to the polarization orientation (higher

© 2021 Wiley-VCH GmbH

for Xy writing, in agreement with the study by Champion et al.,[47] whereas the final steep decay remains quite similar).

In contrast, the relative contributions of each mechanism will indeed vary according to pulse energy, scanning speed, numerical aperture, and pulse duration but with the writing geometry as well (dots, single lines, array of lines, etc.). First, based on the results demonstrated in most publications (bulk or fibers), it can be deduced that the defect centers exhibit a minor contribution (typ. below 5%) to the measured LB, which is in line with what we discussed earlier. Note that the defects can be bleached without affecting the other contributions. The typical densification contribution can be roughly estimated from results of the study by Bellouard et al.[44] that measures the volume changes according to the total deposited dose in various experimental conditions. In contrast, it is more complicated for the situation of stress-induced birefringence as it cumulated from pulses to pulses and with the energy. In addition to this, it also depends on the geometry (single lines or lines array, line-to-line distance), and[33,44] it can vary from 5 to 10% of the total linear birefringence for a single line writing and up to a few 10% for squares writing, where stress cumulates when writing lines array (as reported in the present article). Finally, provided we remain within the type II regime, the "ultimate and key contribution" (i.e., final erasure of the nanopores) is always related to the viscosity(T) of the glass and the nanopores size (laser parameters dependent).

5. Conclusion

In this work, we discussed the different contributions of the total LB response in silica glass induced by fs laser irradiation within the nanogratings regime, as well as their corresponding erasure mechanisms during a high-temperature annealing process. The results of UV absorption spectra revealed that point defects induce a minor effect to the nanogratings refractive indices n_1 and n_2 (and thus on the measured birefringence or retardance). Raman spectroscopy pointed out that an increase in glass density (likely induced by a HP–HT mechanism) between the nanolayers and density was estimated to be around 2.25–2.27 in agreement with refractive index changes on the order of $+10^{-2}$.

The point defects centers are bleached under a fairly low-temperature thermal treatment ($< 600\,^{\circ}$C), and no significant change in the retardance value can be found in this temperature range. The subsequent unexpected increase from 60 to 1000 °C is attributed to the coexistence of "type I-like" modifications with the ones specific to type II, i.e., nanogratings structuration with porous nanolayers. The progressive erasure of the former occurred at this stage and eventually caused an "abnormal" increase in the retardance R. Then, through monitoring the retardance R of the irradiated area and the surrounding stress-induced birefringence area during the annealing process, it is determined that stress relaxation is an important factor contributing to the measured birefringence. We note here that the compressive stress field produced by the nanoporous layers disappears before the annihilation of the nanopores themselves, likely by plastic deformation around the nanopores.

Finally, the porosity FF, which is determined by the SEM micrographs, and then the evolution of the pore size by the R–P equation under a viscoelastic regime, is also found to play a key role in the ultimate thermal stability of the fs laser-induced nanogratings. This research is expected to provide a comprehensive view of the different mechanisms involved during thermal annealing of type II modifications in glass, which can be valuable for reliable optical components' lifetime adjustment for many applications including 5D optical data storage[10,11] and sensing applications[20,23] in harsh environments.

Appendix A

The form birefringence related to so-called nanogratings is quantitatively correlated with the porosity–FF of these nanostructures and was demonstrated by our group recently. The R–P equation was used to simulate the erasure of pores in the nanostructure during the annealing process. The equation describes the evolution of a spherical bubble inside an incompressible Newtonian fluid, and it can be expressed as follows

$$\frac{\Delta P}{\rho} = R_{\text{pore}}\frac{\mathrm{d}^2 R_{\text{pore}}}{\mathrm{d}t^2} + \frac{3}{2}\left(\frac{\mathrm{d}R_{\text{pore}}}{\mathrm{d}t}\right)^2 + \frac{4\eta(T)}{\rho R_{\text{pore}}}\frac{\mathrm{d}R_{\text{pore}}}{\mathrm{d}t} + \frac{2S}{\rho R_{\text{pore}}} \quad \text{(A1)}$$

Here, ΔP is the pressure difference (in Pa) between the inside of the nanopore (supposedly spherical) and far away from it, ρ is the glass density (in kg m^{-3}), R_{pore} the radius (in m) of the spherical nanopore, t the time (in s), $\eta(T)$ the viscosity (in Pa.s), and S is the surface energy (in J m^{-2}). The viscosity and its dependence with respect to temperature can be injected into the model using Vogel–Tammann–Fulcher's (VTF) law in the form $\log(\eta) = A + B/(T - T_0)$. Initial conditions are R_{pore} (at $t = 0$) $= R_0$ and $\mathrm{d}R_{\text{pore}}/\mathrm{d}t$ (at $t = 0$) $= 0$. The nanopore size diameter from the R–P equation needs to be converted into a normalized retardance (R) value. The Maxwell–Garnet equation is first used to calculate the average refractive index of the porous nanolayer (n_{pl}).

$$n_{\text{pl}} = \sqrt{n_{\text{G}}^2\frac{n_{\text{G}}^2 + \frac{(1+2\text{FF})}{3}(n_{\text{pore}}^2 - n_{\text{G}}^2)}{n_{\text{G}}^2 + \frac{(1-\text{FF})}{3}(n_{\text{pore}}^2 - n_{\text{G}}^2)}} \quad \text{(A2)}$$

n_{G} is the fiber refractive index (taken as $n_{\text{G}} = 1.484$, estimated from the chemical composition of the fiber) and n_{pore} is the nanopore refractive index (taken equal to 1). Another important factor is the FF, which is defined as the proportion of the nanopores' volume taken in a unit volume of the porous nanolayer (V), so it is obviously related to the number of nanopores (N) with an averaged nanopore radius (R_{pore}) and can be calculated using

$$FF = N\frac{4\pi R_{\text{pore}}^3}{3V} \quad \text{(A3)}$$

The birefringence B can be determined by the difference between the refractive indices of the ordinary axis (n_{o}) and the extraordinary axis (n_{e}). It takes the following form

$$B = n_{\text{o}} - n_{\text{e}} = \sqrt{\left[1 - \frac{\delta}{\Lambda}\right]n_{\text{G}}^2 + \frac{\delta}{\Lambda}n_{\text{pl}}^2} - \left[\sqrt{\frac{\left[1 - \frac{\delta}{\Lambda}\right]}{n_{\text{G}}^2} + \frac{\frac{\delta}{\Lambda}}{n_{\text{pl}}^2}}\right]^{-1} \quad \text{(A4)}$$

© 2021 Wiley-VCH GmbH

n_G represents the refractive index between the porous nanolayers, Λ is the average spacing between nanolayers, δ is the porous nanolayer thickness, and $(\Lambda - \delta)$ is the interlayer thickness. With the birefringence B calculated, the retardance R can be worked out by the expression $R = B \times L$, where B is the birefringence and L is the length of the birefringent object being measured. Finally, we take into account the same conditions for a direct comparison of the retardance evolution during annealing between the experiment and simulation and to further explore the relationship between the form birefringence and the porosity−FF of the nanostructures.

Appendix A2

In ref fibers,[45] we find that if the erasure kinetics is Arrhenius type with distributed activation energy, and if this distribution is according to a sigmoidal derivative with the following expression.

$$[B](t,T) = B_0\left(\frac{1}{1+\exp(-\frac{2\ln(3)E_D}{\Delta_E})(k_0 t)^{\frac{2\ln(3)k_B T}{\Delta_E}}}\right) \quad \text{(A5)}$$

B_0 is just an initial value of the followed quantity (for example the optical retardance).

k_B the Boltzmann constant: $8.617333262 \times 10^{-5}$, eV K^{-1}.

k_0 the attempt to escape frequency in s^{-1}.

ΔE the FWHM of the activation energy distribution that can be rewritten as $\Delta_E = k_B \Delta_T^{\delta t} \ln(k_o \delta t)$. Here ΔT is a T deviation of which corresponds to the fall of $[B](t,T)$ around T_0 and δt being the isochronal annealing time.

"a" is a coefficient equal to $\exp(-2\ln(3)E_0/\Delta_E)$ (where E_0 is the center of distribution). Thus it is worth to note that Δ_E and E_0 define the distribution.

Then, we have $E_0 = k_B T_0 \ln(k_o \delta t)$ and T_0 is this the inflection point of the falling curve (isochronal annealing), so $a = \exp(-2\ln(3)T_0/\Delta_T^{\delta t})$.

Finally, we can rewrite Equation (A1) as follows.

$$R_{norm}(t,T) = a\left(\frac{1}{1+\exp(-2\ln(3)T_0/\Delta_T^{\delta t})(3)^{\frac{2T}{\Delta_T^{\delta t}}}}\right) \quad \text{(A6)}$$

or

$$R_{norm}(t,T) = a\left(\frac{1}{1+(9)^{\frac{T-T_0}{\Delta_T^{\delta t}}}}\right) \quad (1)$$

Acknowledgements

This research was funded by Agence Nationale pour la Recherche, FLAG/IR project, grant number ANR-18-CE08-0004-01, CNRS Défi Instrumentation aux Limites, UltraBragg project and International Emerging Actions (IEA), INC 2020-2021.

Conflict of Interest

The authors declare no conflict of interest.

Data Availability Statement

Data sharing is not applicable to this article as no new data were created or analyzed in this study.

Keywords

birefringence, femtosecond lasers, nanogratings, silica glasses

Received: January 15, 2021
Revised: March 5, 2021
Published online:

[1] R. Taylor, C. Hnatovsky, E. Simova, *Laser Photonics Rev.* **2008**, *2*, 26.
[2] D. Rayner, A. Naumov, P. Corkum, *Opt. Express.* **2005**, *13*, 3208.
[3] P. Kazansky, H. Inouye, T. Mitsuyu, K. Miura, J. Qiu, K. Hirao, F. Starrost, *Rev. Lett.* **1999**, *82*, 2199.
[4] J. Qiu, P. Kazanski, J. Si, K. Miura, T. Mitsuyu, K. Hirao, A. L. Gaeta, *Appl. Phys. Lett.* **2000**, *77*, 1940.
[5] L. Sudrie, M. Franco, B. Prade, A. Mysyrowicz, *Opt. Commun.* **2001**, *191*, 333.
[6] Y. Shimotsuma, P. G. Kazansky, J. Qiu, K. Hirao, *Phy. Rev. Lett.* **2003**, *91*, 247405.
[7] M. Lancry, B. Poumellec, J. Canning, K. Cook, J. C. Poulin, F. Brisset, *Laser Photonics Rev.* **2013**, *7*, 953.
[8] M. Lancry, B. Poumellec, A. Chahid-Erraji, M. Beresna, P. Kazansky, *Opt. Mater. Express.* **2011**, *1*, 711-723.
[9] G. C. Kahandawa, J. Epaarachchi, H. Wang, K. Lau, *Photonic Sens.* **2012**, *2*, 203.
[10] J. Zhang, M. Gecevičius, M. Beresna, P. G. Kazansky, *Phy. Rev. Lett.* **2014**, *112*, 033901.
[11] Y. Shimotsuma, M. Sakakura, P. G. Kazansky, M. Beresna, J. Qiu, K. Miura, K. Hirao, *Adv. Mater.* **2010**, *22*, 4039.
[12] E. Bricchi, P. G. Kazansky, *Appl. Phys. Lett.* **2006**, *88*, 111119.
[13] S. Richter, M. Heinrich, S. Döring, A. Tünnermann, S. Nolte, U. Peschel, *J. Laser Appl.* **2012**, *24*, 042008.
[14] J. J. Witcher, W. J. Reichman, L. B. Fletcher, N. W. Troy, D. M. Krol, *Opt. Mater. Express.* **2013**, *3*, 502.
[15] F. Zhang, Y. Yu, C. Cheng, Y. Dai, H. Zhang, J. Qiu, *Appl. Phys. B* **2014**, *117*, 53.
[16] S.-E. Wei, Y. Wang, H. Yao, M. Cavillon, B. Poumellec, G.-D. Peng, M. Lancry, *Sensors* **2020**, *20*, 762.
[17] Y. Wang, S. Wei, M. R. Cicconi, Y. Tsuji, M. Shimizu, Y. Shimotsuma, K. Miura, G. D. Peng, D. R. Neuville, B. Poumellec, *J. Am. Ceram. Soc.* **2020**, *8*, 4286.
[18] M. Gecevičius, *Polarization Sensitive Optical Elements by Ultrafast Laser Nanostructuring of Glass*, University of Southampton, Southampton **2015**.
[19] T. Asai, Y. Shimotsuma, T. Kurita, A. Murata, S. Kubota, M. Sakakura, K. Miura, F. Brisset, B. Poumellec, M. Lancry, *J. Am. Ceram. Soc.* **2015**, *98*, 1471.
[20] D. Grobnic, C. Hnatovsky, S. Dedyulin, R. B. Walker, H. Ding, S. J. Mihailov, *Sensors* **2021**, *21*, 1454.
[21] M. Cavillon, M. Lancry, B. Poumellec, Y. Wang, J. Canning, K. Cook, T. Hawkins, P. Dragic, J. Ballato, *J. Phys.: Photonics* **2019**, *1*, 042001.
[22] C. W. Smelser, S. J. Mihailov, D. Grobnic, *Opt. Express.* **2005**, *13*, 5377.
[23] S. J. Mihailov, D. Grobnic, C. Hnatovsky, R. B. Walker, P. Lu, D. Coulas, H. Ding, *Sensors* **2017**, *17*, 2909.
[24] D. Grobnic, C. Hnatovsky, S. J. Mihailov, *Opt. Express* **2016**, *24*, 28704.
[25] D. Grobnic, C. W. Smelser, S. J. Mihailov, R. B. Walker, *Meas. Sci. Technol.* **2006**, *17*, 1009.

© 2021 Wiley-VCH GmbH

[26] Y. Li, C. Liao, D. Wang, T. Sun, K. T. Grattan, *Opt. Express.* **2008**, *16*, 21239.
[27] C. Hnatovsky, D. Grobnic, S. J. Mihailov, *Opt. Express.* **2018**, *26*, 23550.
[28] Y. Li, M. Yang, D. Wang, J. Lu, T. Sun, K. T. Grattan, *Opt. Express.* **2009**, *17*, 19785.
[29] Y. Li, M. Yang, C. Liao, D. Wang, J. Lu, P. Lu, *J. Lightwave Technol.* **2011**, *29*, 1555.
[30] R. Brueckner, *J. Non-Cryst. Solids* **1970**, *5*, 123.
[31] R. Desmarchelier, B. Poumellec, F. Brisset, S. Mazerat, M. Lancry, *World J. Nano Sci. Eng.* **2015**, *5*, 115.
[32] B. McMillen, C. Athanasiou, Y. Bellouard, *Opt. Express.* **2016**, *24*, 27239.
[33] J. Tian, H. Yao, M. Cavillon, E. Garcia-Caurel, R. Ossikovski, M. Stchakovsky, C. Eypert, B. Poumellec, M. Lancry, *Micromachines* **2020**, *11*, 131.
[34] J. D. Musgraves, J. Hu, L. Calvez, *Springer Handbook of Glass*, Springer Nature, Basel, Switzerland **2019**.
[35] M. Cavillon, Y. Wang, B. Poumellec, F. Brisset, M. Lancry, *Appl. Phys. A*, **2020**, *126*, 1.
[36] F. Messina, M. Cannas, *J. Non-Cryst. Solids* **2007**, *353*, 522.
[37] M. Beresna, M. Gecevičius, M. Lancry, B. Poumellec, P. Kazansky, *Appl. Phys. Lett.* **2013**, *103*, 131903.
[38] P. Yeh, *Opt. Commun.* **1978**, *26*, 289.
[39] N. Ollier, M. Lancry, C. Martinet, V. Martinez, S. Le Floch, D. Neuville, *Sci. Rep.* **2019**, *9*, 1.
[40] J. W. Chan, T. Huser, S. Risbud, D. Krol, *Opt. Lett.* **2001**, *26*, 1726.
[41] F. Zimmermann, Dissertation, **2017**.
[42] I. Reghioua, M. Lancry, O. Cavani, S. L. Floch, D. R. Neuville, N. Ollier, *Appl. Phys. Lett.* **2019**, *115*, 251101.
[43] P. Vlugter, E. Block, Y. Bellouard, *Phys. Rev. Mater.* **2019**, *3*, 053802.
[44] Y. Bellouard, A. Champion, B. McMillen, S. Mukherjee, R. R. Thomson, C. Pépin, P. Gillet, Y. Cheng, *Optica* **2016**, *3*, 1285.
[45] B. Poumellec, M. Lancry, *Fibers* **2015**, *3*, 206.
[46] M. Sakakura, Y. Lei, L. Wang, Y.-H. Yu, P. G. Kazansky, *Light-Sci. Appl.* **2020**, *9*, 1.
[47] A. Champion, M. Beresna, P. Kazansky, Y. Bellouard, *Opt. Express.* **2013**, *21*, 24942.
[48] R. Oldenbourg, E. Salmon, P. Tran, *Biophys. J.* **1998**, *74*, 645.
[49] W. L. Bragg, A. B. Pippard, *Acta Crystallogr.* **1953**, *6*, 865.
[50] E. Bricchi, B. G. Klappauf, P. G. Kazansky, *Opt. Lett.* **2004**, *29*, 119.
[51] V. Bhardwaj, P. Corkum, D. Rayner, C. Hnatovsky, E. Simova, R. Taylor, *Opt. Lett.* **2004**, *29*, 1312.
[52] F. Dürr, H. Limberger, R. Salathe, F. Hindle, M. Douay, E. Fertein, C. Przygodzki, *Appl. Phys. Lett.* **2004**, *84*, 4983.
[53] B. Poumellec, L. Sudrie, M. Franco, B. Prade, A. Mysyrowicz, *Opt. Express.* **2003**, *11*, 1070.
[54] A. Champion, Y. Bellouard, *Opt. Mater. Express.* **2012**, *2*, 789.
[55] J. Canning, M. Lancry, K. Cook, A. Weickman, F. Brisset, B. Poumellec, *Opt. Mater. Express.* **2011**, *1*, 998.
[56] L. Yuan, B. Cheng, J. Huang, J. Liu, H. Wang, X. Lan, H. Xiao, *Opt. Express.* **2016**, *24*, 1062.
[57] L. A. Fernandes, J. R. Grenier, P. R. Herman, J. S. Aitchison, P. V. Marques, *Opt. Express.* **2012**, *20*, 24103.
[58] L. A. Fernandes, J. R. Grenier, P. V. Marques, J. S. Aitchison, P. R. Herman, *J. Lightwave Technol.* **2013**, *31*, 3563.
[59] Y. Bellouard, E. Barthel, A. Said, M. Dugan, P. Bado, *Opt. Express.* **2008**, *16*, 19520.
[60] B. Poumellec, M. Lancry, A. Chahid-Erraji, P. G. Kazansky, *Opt. Mater. Express.* **2011**, *1*, 766.
[61] Y. Wang, S. Wei, M. Cavillon, B. Sapaly, B. Poumellec, G.-D. Peng, J. Canning, M. Lancry, *Appl. Sci.* **2021**, *11*, 600.
[62] M. Lancry, in *Int. Conf. on Laser Ablation*, **2017**.

© 2021 Wiley-VCH GmbH

3.2 Thermal stability of type II modifications by IR femtosecond laser in silica-based glasses

sensors

MDPI

Article

Thermal Stability of *Type II* Modifications by IR Femtosecond Laser in Silica-based Glasses

Shu-En Wei [1], Yitao Wang [2,*], Heng Yao [2], Maxime Cavillon [2], Bertrand Poumellec [2], Gang-Ding Peng [1] and Matthieu Lancry [2,*]

[1] Photonics and Optical Communications Group, School of Electrical Engineering, University of New South Wales, Sydney, NSW 2052, Australia; shuen.wei@unsw.edu.au (S.-E.W.); g.peng@unsw.edu.au (G.-D.P.)
[2] Institut de Chimie Moléculaire et des Matériaux d'Orsay, Université Paris Saclay, 91400 Orsay, France; heng.yao22021992@gmail.com (H.Y.); maxime.cavillon@u-psud.fr (M.C.); bertrand.poumellec@u-psud.fr (B.P.)
* Correspondence: yitao.wang@u-psud.fr (Y.W.); matthieu.lancry@u-psud.fr (M.L.); Tel.: +33-169156218

Received: 9 January 2020; Accepted: 27 January 2020; Published: 30 January 2020

Abstract: Femtosecond (fs) laser written fiber Bragg gratings (FBGs) are excellent candidates for ultra-high temperature (>800 °C) monitoring. More specifically, *Type II* modifications in silicate glass fibers, characterized by the formation of self-organized birefringent nanostructures, are known to exhibit remarkable thermal stability around 1000 °C for several hours. However, to date there is no clear understanding on how both laser writing parameters and glass composition impact the overall thermal stability of these fiber-based sensors. In this context, this work investigates thermal stability of *Type II* modifications in various conventional glass systems (including pure silica glasses with various Cl and OH contents, GeO_2-SiO_2 binary glasses, TiO_2- and B_2O_3-doped commercial glasses) and with varying laser parameters (writing speed, pulse energy). In order to monitor thermal stability, isochronal annealing experiments (Δt~30 min, ΔT~50 °C) up to 1400 °C were performed on the irradiated samples, along with quantitative retardance measurements. Among the findings to highlight, it was established that ppm levels of Cl and OH can drastically reduce thermal stability (by about 200 °C in this study). Moreover, GeO_2 doping up to 17 mole% only has a limited impact on thermal stability. Finally, the relationships between glass viscosity, dopants/impurities, and thermal stability, are discussed.

Keywords: fiber Bragg gratings (FBGs); thermal stability; *Type II* modification; femtosecond laser; silica-based glasses

1. Introduction

Over the past 10 years, development of high temperature optical fiber-based sensors, such as fiber Bragg gratings (FBGs), has drawn great attention due to their wide range of applications, including temperature profiling of equipment in manufacturing industry like smelters or laser additive manufacturing [1], monitoring temperature and strain in oil, gas and geothermal industries [2], or again temperature and pressure monitoring in next generation sodium cooled nuclear reactors, airplanes engines, etc.

Conventional FBGs typically are inscribed into fibers composed of germanium-doped silica cores, due to their photosensitivity under intense ultraviolet (UV) light irradiation [3]. Under such irradiation, point defects are created inside the glass core, yielding changes in the glass macroscopic properties such as density and refractive index. These refractive index changes are positive with respect to the pristine (i.e., non-irradiated) glass and are often referred to as *Type I* index change [4]. When UV-induced refractive index changes are chosen as a way to inscribe photonic devices (i.e., *Type I* Bragg

grating sensors), the later can only be used up to ~450 °C. Above this temperature, the imprinted object would progressively be thermally erased, making *Type I* Bragg grating sensors no longer suitable for temperature monitoring [5]. To go beyond the thermal limitations imposed by the technology described above, it is possible to imprint other kinds of modifications in the glass that can withstand higher temperature operation. One possibility is to make femtosecond *Type II* fiber Bragg gratings (also referred to *Type II* fs-FBGs) [5,6]. As opposed to *Type I* refractive index change, the *Type II* modification corresponds to the formation of nanostructures in most silica-based glasses associated with a high level of anisotropic index change [7]. It has been demonstrated that *Type II* fs-FBGs exhibited thermal stability at ~1000 °C for at least several hours in silica [8,9] and up to 150 h provided the FBGs have been stabilized [5,6].

Additionally, it is important to point out that both the structural characteristics of the fs-*Type II* modification and its thermal stability are both dependent on the fiber core glass composition. In fiber fabrication processes, germanium oxide (GeO_2, typically up to 30 mole percent) is arguably the most common fiber core dopant and is used to increase the refractive index of the core relative to the one of the cladding material (being silica, SiO_2) in order to form a guiding core [10]. In addition to GeO_2, other common dopants such as fluorine (F), aluminum oxide (Al_2O_3), boron oxide (B_2O_3), and titanium dioxide (TiO_2) also are incorporated into the fiber, and this for different purposes [11–13]. For example, we recently investigated "high temperature fibers" composed of aluminosilicate cores made by the molten core method [4]. For the Y_2O_3-Al_2O_3-SiO_2 core composition, the measured birefringence does not decrease when tested up to 1000 °C for 30 min, while for the SiO_2 F300 cladding it decreased by ~30%. These results suggest that inscription of "*Type II fs-IR*" modifications in such fibers could be employed to make FBGs with high thermal stability and to potentially overcome the current performances of pure silica core or Ge-doped SiO_2 fibers. During the incorporation of dopants or along the fabrication process, impurities such as chlorine (Cl) and hydroxyl groups (OH) are also inevitably introduced [14,15]. All these intended incorporated elements or unintended contaminations would influence the formation of fs-*Type II* modifications and their thermal stability. To date, the relevant research on the impact of these incorporated elements/impurities on the formation of fs-*Type II* modification and thermal stability is sparse and not systematic [4,16–20].

In addition to the material, laser-writing process has been proved to be another important factor influencing the thermal performance of FBGs. It has been theoretically shown that thermal stability of FBGs can be enhanced by increasing the writing time [21], while the effect of pulse intensity and repetition rate on the thermal performance of FBGs has been investigated elsewhere (Reference [22]). However, to date there is no clear understanding on how both laser writing parameters and glass composition impact the overall thermal stability of these fiber-based sensors. Consequently, it prevents reliable lifetime and performance predictions of the fabricated objects, as the underlying mechanisms of erasure at high temperatures are not well identified.

It is not convenient to carry out a controlled and systematic research work by directly using fibers, because of their (usually) small core sizes along with the variety of their fabrication processes. In addition, to ensure a good quality of the irradiations and accuracy of measurements, homogeneous glass samples, rather than fiber samples, which have gradient distributed dopants concentration in their cores, are preferred in the present study. Consequently, in this work, the formation of fs-*Type II* modifications and their thermal stability in silica-based bulk glasses, instead of fibers, are investigated. More specifically, the impact of the writing conditions, especially writing speed, on fs-*Type II* modification thermal stability, is studied. Furthermore, we investigate the impact of impurities (Cl and OH) and dopants (GeO_2, TiO_2 and B_2O_3) on fs-*Type II* modification thermal stability. This work is expected to help in the future high temperature fiber sensor designs based on investigated oxide glass compositions.

2. Materials and Methods

In order to investigate the impact of the laser writing speed on thermal stability of fs-*Type II* modifications, a standard grade fused silica sample from Heraeus (Suprasil CG®) was chosen.

To study the impact of composition on thermal stability, several sets of optical glasses are investigated. The samples are silica glasses with different Cl and OH concentrations in them (which are considered impurities as mentioned above). More specifically, we investigated Type I (Infrasil 301®), Type II (Homosil®), Type III (Suprasil CG® and Spectrosil 2000®), and Type IV (Suprasil F300®) silica glasses. The second set of samples is composed of 4 germanosilicate (SiO_2-GeO_2) glasses with GeO_2 concentration ranging from 1.9 to 16.9 mole%. These SiO_2-GeO_2 glasses, all with low OH content (<0.1 ppm) and high Cl content (typ. 2000 ppm), were manufactured by chemical vapor deposition (CVD) method. Finally, the last set of samples includes four silicate glasses doped with different oxide components (among which TiO_2, GeO_2, B_2O_3) and one fused silica glass for sake of comparison. More specifically, these samples are Infrasil 301® for the silica one, two germanosilicate glasses, one TiO_2-doped silica (ULE®, Corning), and one alumino-borosilicate glass (Schott Borofloat33®).

To help the reader, Table 1 summarizes the glass samples investigated in this study, along with their compositions, impurity types and concentrations, and annealing temperature (T_a, defined as the temperature at which the viscosity is 10^{13} dPa·s). The latter will be helpful during the discussion of the results.

Table 1. Designations, compositions, impurities [1], and T_a [2] of samples for each section.

Section	Designations	Compositions(mole%)	Impurities [1] (ppm)		T_a [2] (°C)
			OH	Cl	
3.1 Speed	Suprasil CG®	100 SiO_2	830	< 2500	1100
3.2 OH; Cl	Type I (Infrasil 301®)	100 SiO_2	8	< 0.15	1180
	Type II (Homosil®)		380	< 1	1180
	Type III (Suprasil CG®)		830	< 2500	1100
	Type III (Spectrosil 2000®)		800–1200	< 0.15	1025
	Type IV (Suprasil F300®)		0.1	2500	1110
3.3 GeO_2	Germanosilicate	$x$$GeO_2$-(1-$x$) SiO_2, x = 1.9, 5, 11.8, 16.9	< 0.1	~2000	990–1090
3.4 Dopants	Infrasil 301®	100 SiO_2	8	< 0.15	1180
	Germanosilicate	1.9 GeO_2-98.1 SiO_2	< 0.1	~2000	1090
	Germanosilicate	16.9 GeO_2-83.1 SiO_2	< 0.1	~2000	990
	ULE corning®	7 TiO_2-93 SiO_2	—	—	900
	Borofloat33®	81 SiO_2-13 B_2O_3-4 Na_2O/K_2O -2 Al_2O_3	—	—	663.6

[1] Impurities: Impurity concentrations were obtained from the manufacturers, Fourier transform infrared spectroscopy (FTIR), or electron probe micro-analysis (EPMA). [2] T_a: Annealing temperature of samples was obtained from the manufacturers or from measurements. T_a is defined as the temperature at which the viscosity is 10^{13} dPa·s.

The laser used in this study was a commercial Yb-doped fiber amplifier femtosecond laser (Satsuma, Amplitude Systèmes Ltd. Pessac, France.), and the experimental conditions of laser inscriptions were the following: laser operating at 1030 nm, 250 fs delivering pulses, and 100 kHz repetition rate. The laser beam was focused at a depth of 200 μm using a 0.6 NA aspheric lens (estimated beam waist w ~1.5 μm) with the incident beam set perpendicular to the surface of the sample. The samples are affixed to a translation stage, which can be moved in the three dimensions of space, and the direction of the linear polarization was controlled using a λ/2 waveplate mounted on a rotation stage.

To understand how glass composition influences laser-induced modifications and thermal stability, a series of squares were inscribed with a femtosecond laser in glass samples mentioned above. For each inscribed square, the laser writing direction is set to be the X axis, and the laser light polarization is oriented either parallel (Xx configuration, //) or perpendicular (Xy configuration, ⊥) to it. Then, using a scanning speed v, we created several squares 0.1 × 0.1 mm^2, made up of a set of lines with a line spacing Δy = 1 µm to have a uniform anisotropic area and avoiding any diffraction effects. Scheme about the laser writing procedure is shown in Figure 1 and more details can be found in Reference [23].

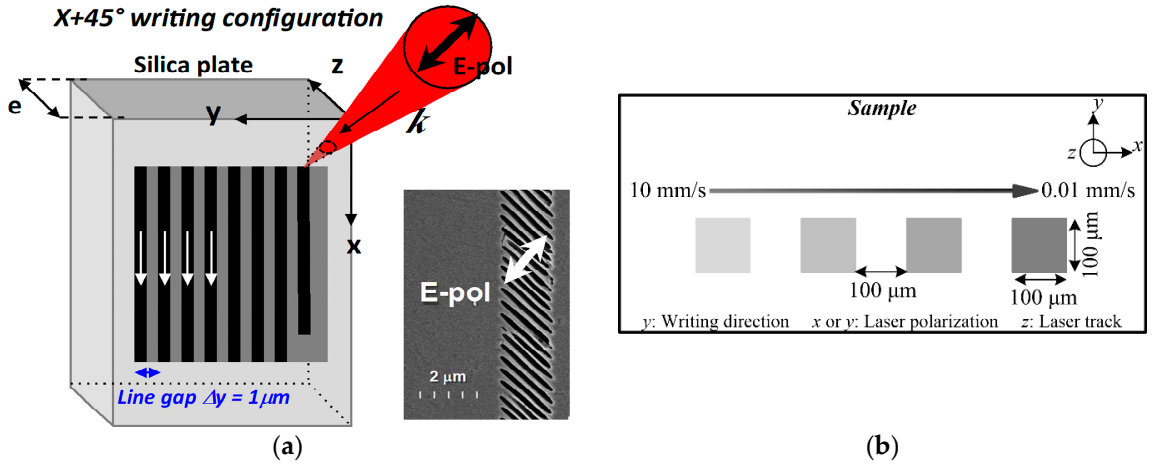

Figure 1. (**a**) Experimental setup scheme for X + 45° writing configuration and SEM image of sub-wavelength periodic structure formed along a single irradiated line. Original image is courtesy of Dr. Cyril Hnatovsky. (**b**) Experimental laser writing design.

As pulse energy used during laser irradiation is set to be above the fs-*Type II* modification threshold (T2), the index change of irradiated regions is highly anisotropic, and its magnitude can be as large as 10^{-2} [16]. Such index change demonstrates thermal stability at 1000 °C for a few hours [9], which is a critical advantage for its high temperature application. According to previous research, fs-*Type II* modifications of SiO_2 (Suprasil CG®) happen above an energy threshold of 0.4 µJ for laser polarization parallel to the laser scanning (λ = 1030 nm, Δt_p = 300 fs, RR = 100 kHz, and NA = 0.6) [24]. Therefore, in order to study the writing kinetic of *type-II* modifications, we performed the experiments by varying pulse energy from 0.3 µJ to 4 µJ. In order to study the impact of the writing speed on thermal stability, the scanning speed v was adjusted from 0.1 to 10 mm/s.

After femtosecond laser irradiation, the amount of optical retardance (R), induced by laser irradiation, was measured with an Olympus BX51 polarizing optical microscope equipped with a "De Sénarmont" compensator. The compensator couples a high precision quarter waveplate (made of quartz) with a 180-degree rotating analyzer to provide retardation measurements, yielding an accuracy of retardation measurements that approaches one thousandth of the wavelength [25]. The retardance is defined as $R = B \times l$, where B is the linear birefringence (typ. n_e-n_o) and l is the thickness of the birefringent layer inscribed by the laser (and often corresponds to the laser track length expressed in nm). Hence, when a laser irradiates a sample and a birefringent object is formed, the measured R value corresponds to the amount of B integrated over the laser track length (in the z direction from Figure 1).

Moreover, the sample cross sections were investigated using a Scanning Electron Microscope (FEG-SEM, Field-Emission Gun Scanning Electron Microscope, ZEISS SUPRA 55 VP, 1 kV accelerating voltage, Oberkochen, Germany) after cleaving the samples using a diamond pen.

To investigate the thermal stability of the written fs-*Type II* modifications, the samples were isochronally (δt = 30 min step) heat treated with an incremental increase (typ. ΔT = 50 °C) of temperature T up to 1400 °C. After each annealing step, retardance R of the squares was measured at

room temperature after natural cooling and normalized with respect to the retardance value from the as-irradiated glass.

3. Results

3.1. Impact of the Writing Speed

Figure 2a displays the normalized retardance (R_{norm}) as a function of isochronal annealing temperature for a SiO_2 sample from Heraeus (Suprasil CG®), with different writing speeds, namely: 0.01 mm/s, 0.1 mm/s, 1 mm/s, and 10 mm/s. In this experiment, the pulse energy was set to 2.0 µJ/pulse. In addition, retardance values as a function of writing speed for the non-heat-treated samples were measured and are reported in the inset graph of Figure 2a. It shows that with the higher writing speed, the lower retardance value would be achieved, and agrees well with the tendency reported in Reference [26]. From Figure 2a, some common features can be found. First, there is a slight decrease in the normalized retardance value from 400 °C to 600 °C corresponding approximately to 10% decay of the retardance strength. This feature might be attributed, according to the literature, to the erasure of point defects centers (E′, ODC, NBOHC) [27]. In the 800–1000 °C temperature range, the faster decay of normalized retardance was found for low writing speeds (0.01 mm/s and 0.1 mm/s). This decline might be related to the erasure of Si-O three and four-fold rings at 800–900 °C [4,27] related to the relaxation of glass densification (*Type I* contribution) or of the strong compressive stress. Finally, for annealing temperature above 1000 °C, a very steep decrease of the birefringence is observed. $R_{norm}(T)$ reaches zero at ~1175 °C for all samples.

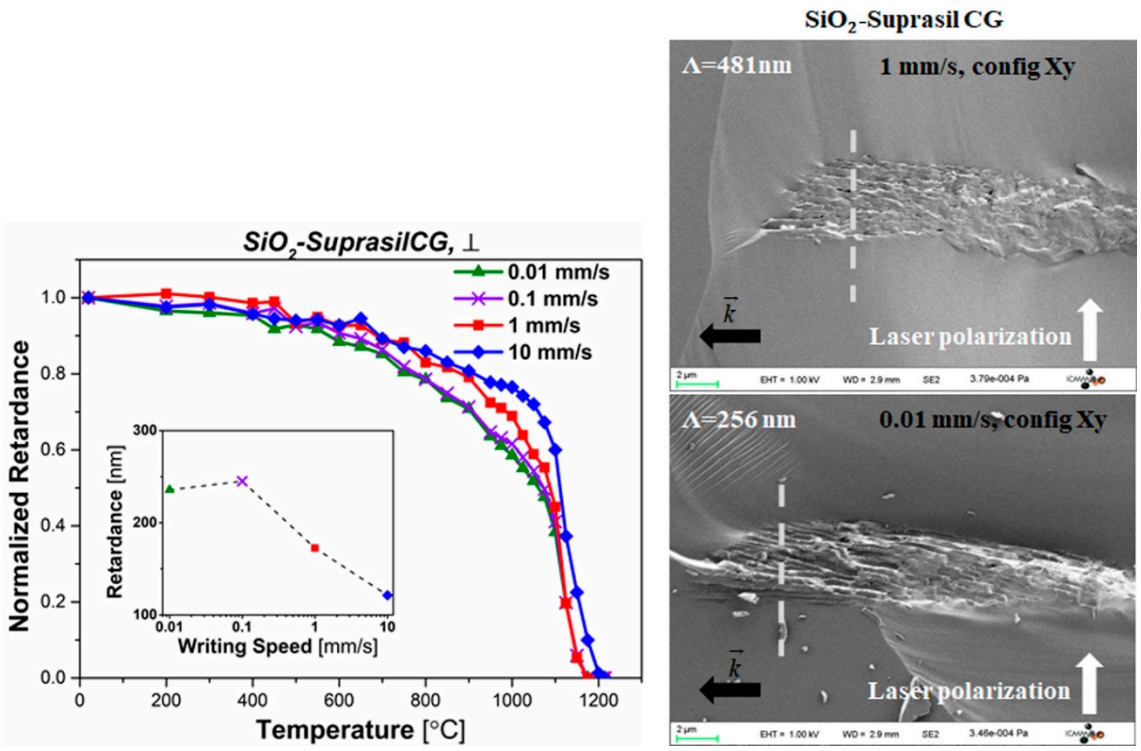

(**a**) (**b**)

Figure 2. (**a**) Normalized retardance (R_{norm}) as a function of temperature for SiO_2 (Suprasil CG®) samples inscribed by different writing speed (0.01 mm/s, 0.1 mm/s, 1 mm/s, and 10 mm/s). The other laser parameters are: 2 µJ/pulse, 1030 nm, 250 fs, 100 kHz, NA = 0.6, laser polarization ⊥ to the writing direction. Measurements were performed at room temperature. **Inset**: initial retardance, measured before any annealing, according to the writing speed. (**b**) FEG-SEM, Secondary electron micrographs of the cross section of laser tracks for v = 1 mm/s (upper) and 0.01 mm/s (lower speed).

Writing speed v is a key factor for formation of nanogratings, as it directly relates to the overlap between two subsequent pulses. In general, it can be estimated by the formula *1-v/(f*D)*, where v is the writing speed, f is the repetition rate and D is the laser beam diameter [26]. According to previous results, a decrease in writing speed yields to a higher overlap rate, which further creates a higher number of nanogratings with shorter average spacing [28]. The results shown in Figure 2b are in agreement with these results. Indeed, the spacing of nanogratings (Λ) is decreased from ~481 ± 10 nm to ~256 ± 10 nm as the writing speed v is decreased from 1 mm/s to 0.01 mm/s. At the same time, by comparing the thermal behavior of all samples with different writing speeds in Figure 2a, the sample inscribed by fast writing speed (v = 10 mm/s) demonstrates the highest thermal stability, accompanied with a sharp decay at 1100 °C. It completely annealed out after 30 min at ~1210 °C. This temperature is slightly higher than other samples inscribed at lower writing speeds. However, in view of Figure 2a,b, whether there is a correlation between thermal stability of fs-*Type II* nanogratings and nanogratings spacing still need further investigations and in particular a thorough analysis on the impact of nanolayers porosity (filling factor, core size). These results are shortly commented in the last section of the discussion.

3.2. Impact of Cl and OH Impurities

To reveal the impact of Cl and OH impurities on writing kinetics of fs-*Type II* modifications and their thermal behavior, five silica glass samples fabricated by different processes were studied. Based on the classification proposed by Brückner in 1970 [29], we categorized samples into four types as shown in the inset of Figure 3a: Type I silica is fused from natural quartz by electrical melting and its commercial name is Infrasil 301® (OH < 8 ppm; Cl < 0.15 ppm). Type II silica is fused from natural quartz by plasma flame fusion and contains 380 ppm OH and <1 ppm Cl. Type III (Suprasil CG®; Spectrosil 2000®) and Type IV silica (Suprasil F300®) were synthetic and were prepared respectively, by electrical melting, or plasma-activated chemical vapor deposition (PCVD). The main similar point between types III and IV silica is the Cl content, on the order of 100 ppm [29], while the most significant difference is the OH content: which is 400–1000 pm in the former (wet sample) and <3 ppm in the later (dry sample) [30]. In addition, due to different raw materials used for silica glass production, that is natural quartz for Type I and II silica and synthetic precursors for Type III and IV silica, the latter are expected to be purer than the formers in terms of trace impurities, such as Al, etc. while containing higher level of Cl. Again, impurity contents for the various silica types are summarized in Table 1.

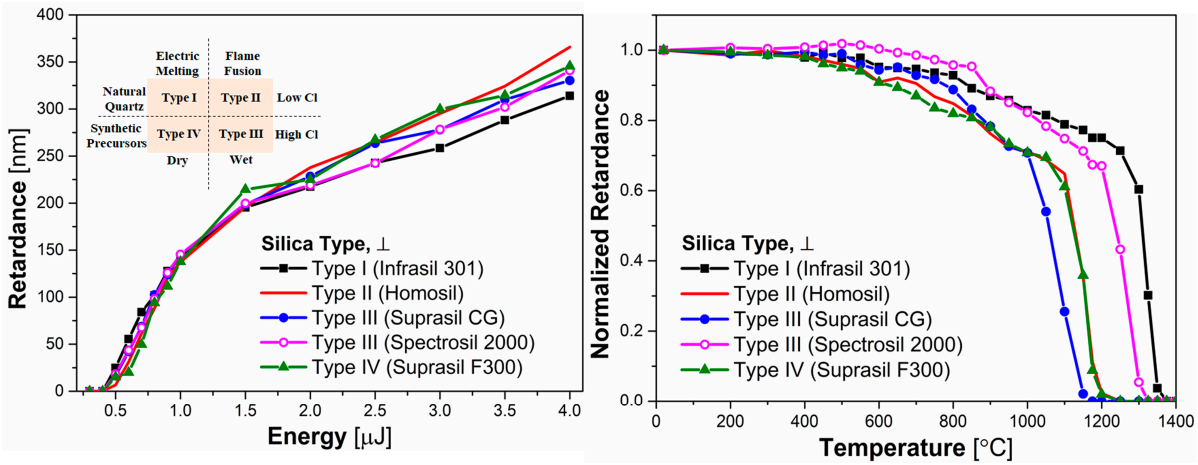

Figure 3. (**a**) Retardance as a function of pulse energy for SiO_2 glasses: Type I (Infrasil 301®), II (Homosil®), III (Suprasil CG® and Spectrosil 2000®), and IV (Suprasil F300®). Laser parameters are: 1030 nm, 250 fs, 100 kHz, 100 μm/s, NA = 0.6, laser polarization ⊥ to writing direction. Inset: category and characteristics of sample; (**b**) Normalized retardance (R_{norm}) as a function of temperature for all SiO_2 glasses. Pulse energy is 2 μJ/pulse and other laser conditions are same mentioned above. The measurements were performed at room temperature.

Figure 3a shows the retardance values measured for all investigated silica glasses, manufactured by the different techniques explained above, as a function of the laser pulse energy. The first interesting result is that there was no variation of the T2 threshold (0.4 μJ/pulse) with respect to the glass manufacturing technique used. Each sample exhibited a similar trend in their writing kinetics (i.e., retardance versus pulse energy). In all cases the retardance *R* was found to increase sharply from 0 nm to 200 nm in the 0.4–1.5 μJ/pulse energy domain. However, for higher pulse energies, up to 4 μJ/pulse the retardance increased more slowly. From the results of Figure 3a, it can be stated that the origin of increasing R for all samples is similar, i.e., the formation of a periodic array of porous nanoplanes isolated by non-porous glass [4,7], cooperating to form birefringence [4,31]. Furthermore, it is also reasonable to conclude that the impact of fabrication techniques and impurities content on the writing kinetics of fs-*Type II* modifications for all silica samples is not significant, which agrees well with results reported in Reference [16].

Figure 3b displays the evolution of the normalized retardance (R_{norm}) of all silica glasses as a function of the annealing temperature. In this Figure, it can be found that retardance values for all samples started to decay at 400 °C. After the step at which the silica samples were kept at 1025 °C for 30 min, the decay of normalized retardance was ~32% for Types II, III (Suprasil CG®), and IV silica, while only ~19% for Types I and III (Spectrosil 2000®) silica. After this step, a sudden drop of retardance is observed. For type III silica (Suprasil CG®), which is the sample to exhibit this feature at the lowest temperature, no retardance could be detected after 1175 °C. For Type II and IV silica, normalized retardance started to diminish drastically at 1075 °C and became hard to measure at 1225 °C, which was 50 °C higher than Type III. Compared with Type II, III (Suprasil CG®) and IV, Type I and III (Spectrosil 2000®) glass exhibited a better thermal stability and a similar decreasing trend. The normalized retardance kept decreasing slowly to ~75% until ~1300 °C and there is a very sharp erasure process after that. Finally, the normalized retardance of Type III (Spectrosil 2000®) and I silica could not be detected after 1320 °C and 1400 °C respectively, indicating that the fs-*Type II* modifications of these two samples were completely erased. It is worth pointing out that these values are beyond the estimated glass transition temperature of 1260 °C for Type I fused quartz with low OH and aluminum contents [32].

Now, from Figure 3b and by looking at the evolution of R_{norm} as a function of temperature, some typical characteristics can be revealed. At the same OH levels, by comparing Type I (Infrasil 301®, Cl < 0.15 ppm) with Type IV (Suprasil F300®, Cl ~2500 ppm) silica or Type II (Homosil®, Cl < 1 ppm) with Type III (Spectrosil 2000®, Cl < 0.15 ppm; Suprasil CG®, Cl ~2500 ppm) silica, we can find that silica glasses produced by less pure natural quartz with the lower level of Cl all demonstrate the better thermal stability than the ones made from synthetics precursor. This indicates that high level of Cl would be one factor to deteriorate the overall thermal stability of fs-*Type II* modifications. Similarly, by comparing Type I (Infrasil 301®, OH < 8 ppm) with Type II (Homosil®, OH ~380 ppm) silica or Type IV (Suprasil F300®, OH ~0.1 ppm) with Type III (Suprasil CG®, OH ~830 ppm) silica, it is found that dry glasses demonstrate a higher thermal stability than wet glasses when produced by the same precursor material. From these observations, one first conclusion to be drawn is that fs-*Type II* modifications in dry silica glass with lower levels of Cl, such as Type I silica (Infrasil®) in this study, would exhibit a better thermal stability. We note also that Cl has a stronger impact than OH (for a fixed concentration) on the thermal stability.

3.3. Influence of GeO_2 Content

To study the influence of GeO_2 content on writing kinetics and thermal stability of fs-*Type II* modifications, several *x* GeO_2- (1-*x*) SiO_2 glasses with various GeO_2 concentrations ranging from 1.9 mole% to 16.9 mole% were studied in this work. This concentration range is typical for standard optical fibers from single mode fibers like SMF28 (typ. 4 mole% GeO_2) to multimode fibers. These samples are optical fiber preforms. They were all manufactured by plasma chemical vapor deposition (PCVD) with low OH contents (<0.1 ppm) and high level of Cl (~2000 ppm).

Figure 4a displays the retardance values as a function of pulse energy for the four germanosilicate glasses investigated. Results of pure SiO_2 (Suprasil CG®) is added to serve as a reference. Insets are two microscope images taken between crossed polarizers that reveal the formation of birefringence. The left inset was made using a full order waveplate and highlights the slow axis orientation which flips of 90° (from yellow to blue color) when the writing laser polarization was changes from x to y orientation. This signature of polarization dependent birefringence confirms indirectly the formation of nanogratings, which have been previously confirmed by SEM [17]. As it can be seen, the threshold T2 [7], related to formation of nanogratings with form birefringence, is about 0.4 μJ for all tested samples in our experimental conditions, which is the same value of the T2 threshold of pure silica samples shown in Figure 3a. It should also be noted that we did not observe any variation of T2 with the increasing content of GeO_2 in the investigated range. From 0.4 μJ to 1 μJ, the evolution of *R* as a function of pulse energy for all samples nearly is identical. For higher pulse energies, the slower growth of retardance of all samples can be found. In addition, from 1 μJ to 4 μJ, it has been reported that overall magnitude of *x* GeO_2-(1-*x*) SiO_2 binary glasses is higher than retardance values of pure SiO_2 sample due to a higher amount of glass decomposition within nanolayers. Such higher form birefringence is also observed in GeO_2 glass [20] or GeO_2 doped glasses [19] and is explained by smaller pore size of GeO_2 but a higher decomposition level (resulting in a higher porosity filling factor) in SiO_2-GeO_2 [17] and thus stronger birefringence response [20]. However, opposite trend of writing kinetics has also been observed, showing that the higher the GeO_2 content [17], the lower the retardance could be obtained when nanogratings were inscribed by the higher repetition rate (500 kHz), writing speed (0.5 mm/s), and higher pulse duration (300 fs). Further systematic study is needed to reveal the impact of writing parameters on fs-*Type II* modifications in germanosilicate glasses.

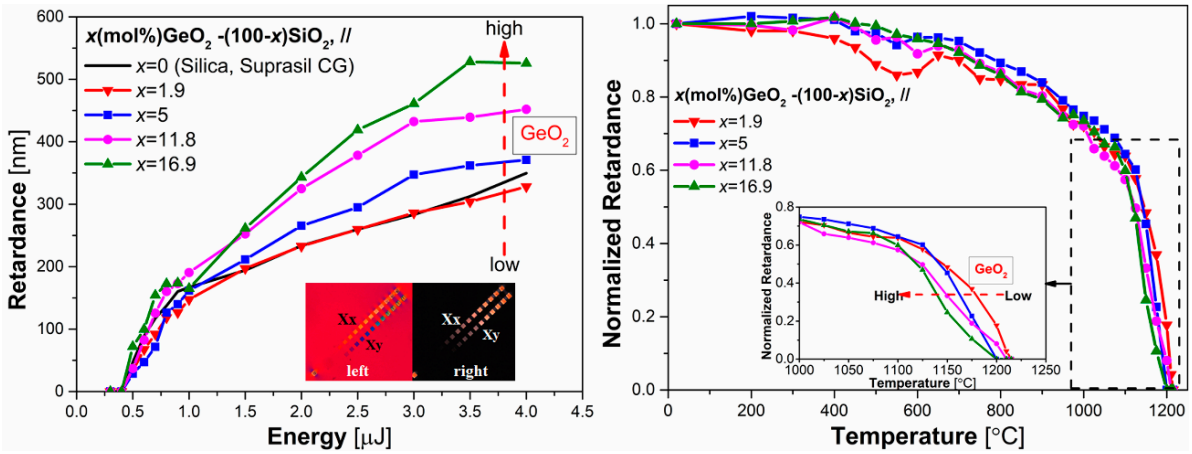

(**a**) (**b**)

Figure 4. (**a**) Retardance as a function of pulse energy for x GeO_2-(1-x) SiO_2 glasses (x = 1.9 to 16.9 mole%). Inset graph of the sample 16.9 GeO_2-83.1 SiO_2 glass: **left:** optical microscope (bottom light illumination) cross a full-wave plate, polarizer, and analyzer; **right:** optical microscope (bottom light illumination) cross polarizer and analyzer; (**b**) Normalized retardance (R_{norm}) as a function of temperature for x GeO_2-(1-x) SiO_2 glasses (x = 1.9 to 16.9 mole%). Pulse energy is 2 μJ/pulse. Laser parameters are: 1030 nm, 250 fs, 100 kHz, 100 μm/s, NA = 0.6, polarization // to writing direction.

Figure 4b displays the normalized retardance R_{norm} of germanosilicate glasses as a function of annealing temperature and shows some characteristic features. In this experiment, we also thermally treated samples written at 2.0 μJ/pulse, to induce fs-*Type II* modifications. As we can see, at the beginning, there is a slight increase of the retardance value from 600 °C to 800 °C, and it is more obvious for germanosilicate glasses with less GeO_2 content. Similar behavior of the birefringence has been observed in SiO_2 [9,24], 50SiO_2-50Al_2O_3 pellet [24] and slightly Ge-doped optical fibers [8]. Briefly, it is assumed that this observed unexpected increase is related to some contribution of residual part of *Type I* (defects, densification, and related stress), which erased at low temperature, resulting in a higher birefringence response [24]. As the annealing temperature increases, the induced stress relaxes gradually, lessening the refractive index and further decreasing retardance. Finally, above 1100 °C, retardance diminishes dramatically, and no birefringence can be found after ~1200°C annealing. From the inset of Figure 4b, it should be also noted that the "erasing slope" is inversely dependent on the GeO_2 concentration and increases from 1150 °C to 1200 °C as GeO_2 decreases from 16.9 mole% to 1.9 mole%. Such result matches with the estimated glass transition temperature (T_g) for germanosilicate glasses fabricated by Sol-gel technique with different GeO_2 content [33]. In addition, it is also generally accepted that viscosity of glass is reduced by the high level of OH concentration, which further reduces the glass transition temperature (T_g) [33]. Therefore, due to the very fact that samples in our case were fabricated with less OH content and the fact that germanosilicate glasses are composed of an interpenetrated and interconnected structure of SiO_4 and GeO_4 tetrahedral units [34], viscosity of glass is expected to change slowly as the concentration of GeO_2 varies from 1.9 mole% to 16.9 mole%. This is confirmed by our viscosity measurements made in two of these samples shown in Figure 4b (red and blue curves). It explained why incorporating GeO_2 has less impact on overall thermal behavior of all germanosilicate glasses in comparison with pure silica glasses (especially, Type II and IV silica) presented Figure 3b.

3.4. Impact of Dopants

In this part, the impact of dopants on thermal stabilities of fs-*Type II* modifications is discussed. In addition to the thermal behavior of the pure silica (Infrasil 301®) and the germanosilicate glasses presented in this work, results of titania-silicate glass (ULE®; 7 mole% TiO_2) and aluminoborosilicate

(Borofloat33®; 81 mole% SiO_2, 13 mole% B_2O_3, 4 mole% Na_2O/K_2O, 2 mole% Al_2O_3) are also collected and compared.

Figure 5a shows the normalized retardance (R_{norm}) as a function of temperature. The thermal stability was studied through an annealing experiment of isochronal (δt = 30 min) annealing steps (ΔT = 50 °C or 25 °C). Note that the thermal stability is related to a couple (t,T) and thus related to a thermal energy often called demarcation energy that is usually written as $k_B.T.\ln(k_0.T)$ for simple cases [35] where k_0 is the pre-exponential factor in the Arrhenius rate constant of the erasure reaction and k_B is the Boltzmann constant. If you determine the k_0 value using multiple isothermal or isochronal annealing experiments both isothermal and isochronal accelerated ageing are equivalent and bring similar information's allowing also the possibility to perform reliable lifetime prediction. In our case, the curves in Figure 5a represents the "stability curve" provided that the criterion $(\delta t.k_0)^{-(\Delta T/Tmax)} \ll 1$ is fulfilled [35] where k_0 is the pre-exponential factor in the Arrhenius rate constant of the erasure reaction. For nanogratings written in silica, k_0 has been estimated to be around de $5 \times 10^5 - 5 \times 10^7$ s^{-1} [36] depending on the laser writing parameters. So, when this criterion is respected, each point can be considered independent of each other. If the criterion is not fulfilled this means that our measurements are slightly under-estimating the real thermal stability.

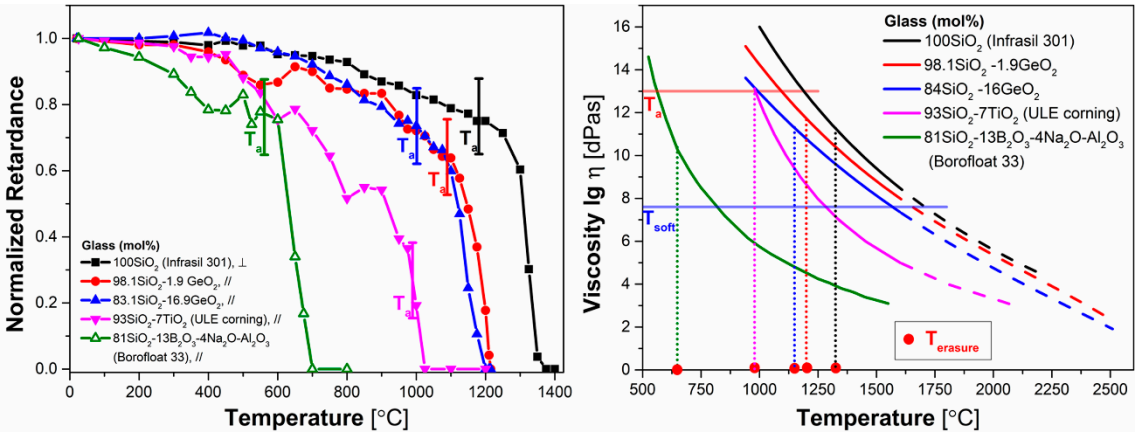

(**a**) (**b**)

Figure 5. (**a**) Normalized retardance (R_{norm}) as a function of annealing temperature T for SiO_2 (Infrasil 301®), $1.9GeO_2$-$98.1SiO_2$, $16.9GeO_2$-$83.1SiO_2$, $93SiO_2$-$7TiO_2$ (ULE®), and $81SiO_2$-$13B_2O_3$-$4Na_2O/K_2O$-$2Al_2O_3$ (Borofloat33®). (**b**) Viscosities of glasses with different compositions as a function of temperature (dash line: extrapolated part). Annealing temperature (T_a) is defined when log(η) = 13 dPa·s. Softening temperature (T_{soft}) is defined when log(η) = 7.6 dPa·s. Erasure temperature ($T_{erasure}$) is defined at half-amplitude of the final erasure slope of $R_{norm}(T)$.

As can be seen from Figure 5a, R_{norm} of ULE® and Borofloat33® first decreases smoothly until 600 °C, leading to a 20% decrease for both two samples. At higher temperatures, the decrease in R_{norm}(T) is accelerated and neither retardance nor refractive index contrast can be found at 650 °C for Borofloat33® and at 1025 °C for ULE®, respectively. The studies of mechanisms leading to decay in retardance at high temperature is exemplified in Reference [24] and is attributed to the erasure of point defects below 500 °C. Then there are at least two additional contributions: the first one (intermediate temperature range, typ. $0.8T_a$ to T_a) is related to the stress-induced birefringence generated inside and outside the nanolayers; the second one (sharp final decay above T_a) is related to the nanotexturation itself (porosity and periodicity) leading to form birefringence. For germanosilicate glasses, the sharp decay process starts to take place at 1100 °C and retardance cannot be measured at ~1200 °C, showing a better thermal stability than ULE® and Borofloat33®. For pure silica (Infrasil 301®), from ~1300 °C and above, a steep decrease of R_{norm} occurs up to 1400 °C for 30 min. To sum up, thermal stability of fs-*Type II* modifications on the various samples can be classified as follow (from higher to lower

thermal stability): 100 SiO_2 > 1.9 GeO_2 - 98.1 SiO_2 > 16.9 GeO_2-83.1 SiO_2 > 93 SiO_2-7 TiO_2 > 81 SiO_2-13 B_2O_3-4 Na_2O/K_2O-2 Al_2O_3.

Viscosities η of glasses with dopants were plotted as a function of temperature (Figure 5b). The viscosities of Infrasil 301®, ULE®, and Borofloat33® were obtained from the commercial data. The viscosity of germanosilicate glasses was measured and extrapolated above 1500 °C. The annealing temperature (T_a) of the glasses, related to the glass structural relaxation, were determined from the curves when the log(η) reaches 13 dPa·s. From the Figure 5b, it is evident that viscosities η(T) of all the samples decrease when temperature increases. In addition, it is clear that pure silica (Infrasil 301®) has the highest viscosities and T_a (1180 °C) compared with other silicate glasses. Furthermore, compared with pure silica, the viscosity and T_a of GeO_2-doped glass samples only slightly decreases with the increase of GeO_2 content, indicating that there are minor changes of the glass network structure after doping with GeO_2. However, when it comes to titania-silicate glass and aluminoborosilicate, the viscosities and T_a decreases drastically, showing that high doping levels of titania oxide (TiO_2) or boron trioxide (B_2O_3) would significantly modify the initial silica glass network structure. Combined with the results shown in Figure 5a, we found that a steep decay always starts to take place after T_a, typ. around $T_{erasure}$ (reported in Figure 5b), and is always fully erased for a temperature slightly lower than T_{soft}. So, the thermal stability of fs-*Type II* modifications seems to be correlated qualitatively but not quantitatively to their T_a. A more accurate view might be related to the temperature corresponding to a glass structural relaxation time τ(T) of 30 min, usually defined by τ(T) = η(T)/G(T), with G being the glass shear modulus.

4. Discussion

In agreement with Reference [37], fs-*Type II* modifications or nanogratings formation in silica or glass is limited by internal structural relaxation of glass when using high pulse energy or high repetition rate. In our studies, the thermal stability or nanogratings erasure, also might be related to the glass structural relaxation τ(T) but this is likely more complex due to the multiple steps' erasure mechanism. Indeed, the nanogratings erasure relates to oxide decomposition/formation in SiO_2, nanoscale phase separation in other glasses, oxygen chemical migration/reaction, all taking time. However, they do not depend only on the viscosity e.g., the viscous flow but also mostly the surface tension, are especially important for voids and pores erasure. Especially, at high temperature, chemical migration coefficient and viscosity are strongly interconnected with each other. It explains why "thermal stability" of fs-*Type II* modifications in silicate glasses is in the same order as their annealing temperature (T_a): the higher T_a, the most stable behavior at high temperature of fs-*Type II* modifications can be found and expected.

It has been shown that doping titania oxide (TiO_2) or boron trioxide (B_2O_3) into silicate glasses would significantly affect the silicate network structure. For instance, complex silicate sheets can be depolymerized into simpler silicate structures by doping with TiO_2 [38] and can yield to weak B-O bonds with low bond energies when the glass is doped with B_2O_3 [39]. As a result, viscosity and T_a decrease, making fs-*Type II* modifications easier to be erased at high temperature as shown in Figure 5a. In addition to that, impurities, such as hydroxyl (OH) and chloride (Cl), are also proven to be another factor influencing the thermal stability of fs-*Type II* modifications as we shown in Section 3.2. For OH impurities, it has generally been agreed that water incorporated in glass structure is in the form of hydroxyl ions (SiOH) and the presence of SiOH in glasses therefore increases the concentration of non-bridging anions, which further decrease the viscosity of glass and thus T_a [40]. It explains why fs-*Type II* modifications in dry glasses (Type I and IV silica) in our study shows better thermal performance than wet glasses (Type II and III silica). Similarly, Cl as another impurity that relies to the manufacturing process would decrease the viscosity, T_a and relaxation time of the glass [41], making fs-*Type II* modifications in Type III and IV silica in our study become less stable.

When it comes to the influence of germanium dioxide (GeO_2) in Figure 4b, we can see that by doping with GeO_2 up to approximately 17 mole%, the thermal behavior of fs-*Type II* modifications is somewhat similar. It is attributed to the fact that GeO_2 and SiO_2, when mixed, form a continuous

random mixture, and the two networks are strongly connected or "interpenetrated" [34]. That is why adding a few mole% of GeO_2 does not change so much viscosity, T_a and thus thermal stability. However, we also observed, at high temperature, the steep decay to be weakly dependent of GeO_2 concentration (inset of Figure 4b) in agreement with our viscosity measurements.

For the impact of writing speed on thermal stability of fs-*Type II* modifications, it is not easy to draw a conclusion at this step. For example, we cannot say that higher nanogratings spacing induced by slow writing would lead to a better thermal performance of fs-*Type II* modifications, because of some counter-examples. From the perspective of porosity erasure, at the same level of viscosity and by the same annealing procedures, it would take more time to erase the larger pores rather than the small ones. However, this may not directly be related to porosity or periodicity. It is true that we observed a large difference in thermal stability in the 900–1100 °C temperature range from Figure 2a, but this difference reduces when the erasure is total, around 1200 °C. This significant difference in retardance we observed might be rather related to stress effects, contributing to our retardance measurements (stress-induced birefringence), which usually relax during a thermal treatment at 0.8–0.9.T_a. Based on Reference [42], higher deposited energy dose (i.e., lower speed) leads to higher cumulative stress: each nanolayer undergoes a net volume expansion [43], which results in some residual compressive stress. Consequently, slow writing speed resulting in more nanolayers per unit of length (i.e., shorter periods) would yield to higher cumulative residual stress and thus stress birefringence values. So following this view, from Figure 2a, we can estimate that low speed writing leads to a high stress induced birefringence, contributing to 40% of the total retardance, instead of 20% for high writing speed at ~1100 °C.

5. Conclusions

In this work, we mainly investigated the impacts of writing speed, impurities (Cl and OH), and GeO_2, TiO_2 dopants on thermal stability of *Type II* modifications and their writing kinetics by IR femtosecond laser in silica-based glasses. From this study, we found that the impact of writing speed on *fs-Type II* modifications thermal stability is not intuitive in pure silica. High level of OH and Cl impurities would reduce the *Type II* modifications thermal stability, while causing negligible impact on their writing kinetics. We observed that by adding GeO_2 into SiO_2 up to ~17 mole%, the thermal stability is only slightly influenced, while the magnitude of the retardance is found to be dependent on GeO_2 concentration. By comparing the thermal behavior and viscosity of Borofloat33®, ULE®, GeO_2-SiO_2 and SiO_2 (Infrasil 301®) glasses, we found that the thermal stability of *Type II* modifications is partly related to the glass structural relaxation or viscosity but not solely due to additional mechanisms involving nanopores erasure, oxide decomposition/formation, and chemical migration. It also explains the variation of thermal behavior induced by GeO_2 and impurities. These results provide a reference work for writing such "*Type II* fs-IR" modifications on multicomponent silicate fibers to make fiber Bragg gratings with high thermal stability.

Author Contributions: Conceptualization, S.-E.W. and M.L.; data curation, Y.W., H.Y. and M.L.; formal analysis, S.-E.W., M.L., B.P. and M.C.; funding acquisition, M.L.; investigation, S.-E.W., M.C. and M.L.; methodology, M.L., H.Y. and Y.W.; project administration, M.L.; supervision, M.L. and G.-D.P.; Validation, Y.W., M.C., M.L., B.P. and G.-D.P.; visualization, M.L. and S.-E.W.; writing—original draft, S.-E.W.; writing—review and editing, S.-E.W., Y.W., M.C., B.P., M.L. and G.-D.P. All authors have read and agreed to the published version of the manuscript.

Funding: This research was funded by Agence Nationale pour la Recherche, FLAG-IR project, grant number ANR-18-CE08-0004-01 and by CNRS Défi "Instrumentation aux Limites", Ultrabragg project.

Conflicts of Interest: The authors declare no conflict of interest.

References

1. Åslund, M.L.; Canning, J.; Canagasabey, A.; De Oliveira, R.A.; Liu, Y.; Cook, K.; Peng, G.-D. Mapping the thermal distribution within a silica preform tube using regenerated fibre Bragg gratings. *Int. J. Heat Mass Transf.* **2012**, *55*, 3288–3294. [CrossRef]
2. Baldwin, C.S. Brief history of fiber optic sensing in the oil field industry. In *Fiber Optic Sensors and Applications XI*; SPIE: Baltimore, MD, USA, 2014.
3. Hill, K.O.; Meltz, G. Fiber bragg grating technology fundamentals and overview. *J. Light. Technol.* **1997**, *15*, 1263–1276. [CrossRef]
4. Cavillon, M.; Lancry, M.; Poumellec, B.; Wang, Y.T.; Canning, J.; Cook, K.; Hawkins, T.; Dragic, P.; Ballato, J. Overview of high temperature fibre Bragg gratings and potential improvement using highly doped aluminosilicate glass optical fibres. *J. Phys. Photonics.* **2019**, *1*, 042001. [CrossRef]
5. Mihailov, S.J.; Grobnic, D.; Hnatovsky, C.; Walker, R.B.; Lu, P.; Coulas, D.; Ding, H. Extreme environment sensing using femtosecond laser-inscribed fiber Bragg gratings. *Sensors* **2009**, *17*, 2909. [CrossRef]
6. Mihailov, S.J. Fiber bragg grating sensors for harsh environments. *Sensors* **2012**, *12*, 1898–1918. [CrossRef]
7. Lancry, M.; Poumellec, B.; Canning, J.; Cook, K.; Poulin, J.C.; Brisset, F. Ultrafast nanoporous silica formation driven by femtosecond laser irradiation. *Laser Photonics Rev.* **2013**, *7*, 953–962. [CrossRef]
8. Grobnic, D.; Smelser, C.W.; Mihailov, S.J.; Walker, R.B. Long-term thermal stability tests at 1000 °C of silica fibre bragg gratings made with ultrafast laser radiation. *Meas. Sci. Technol.* **2006**, *17*, 1009–1013. [CrossRef]
9. Bricchi, E.; Kazansky, P.G. Extraordinary stability of anisotropic femtosecond direct-written structures embedded in silica glass. *Appl. Phys. Lett.* **2006**, *88*, 111119. [CrossRef]
10. Wood, D.; Walker, K.; MacChesney, J.; Simpson, J.; Csencsits, R. Germanium chemistry in the MCVD process for optical fiber fabrication. *J. Light. Technol.* **1987**, *5*, 277–285. [CrossRef]
11. Van Uitert, L.G.; Pinnow, D.A.; Williams, J.C.; Rich, T.C.; Jaeger, R.E.; Grodkiewicz, W.H. Borosilicate glasses for fiber optical waveguides. *MRS Bull.* **1973**, *8*, 469–476. [CrossRef]
12. Simpson, J.R.; MacChesney, J.B. Optical fibres with an Al_2O_3-doped silicate core composition. *Electron. Lett.* **1983**, *19*, 261–262. [CrossRef]
13. Reddy, P.H.; Rahman, M.F.A.; Paul, M.C.; Latiff, A.A.; Rosol, A.H.A.; Das, S.; Dhar, A.; Bhadra, S.K.; Dimyati, K.; Harun, S.W. Titanium dioxide doped fiber as a new saturable absorber for generating mode-locked erbium doped fiber laser. *Optik.* **2018**, *158*, 1327–1333. [CrossRef]
14. Shibata, S.; Nakahara, M. Fluorine and chlorine effects on radiation-induced loss for GeO_2-doped silica optical fibers. *J. Light. Technol.* **1985**, *3*, 860–863. [CrossRef]
15. Ainslie, B.J.; France, P.W.; Newns, G.R. Water impurity in low-loss silica fibre. *MRS Bull.* **1977**, *12*, 481–487. [CrossRef]
16. Lancry, M.; Groothoff, N.; Guizard, S.; Yang, W.; Poumellec, B.; Kazansky, P.G.; Canning, J. Femtosecond laser direct processing in wet and dry silica glass. *J. Non-Cryst. Solids.* **2009**, *355*, 1057–1061. [CrossRef]
17. Lancry, M.; Canning, J.; Cook, K.; Heili, M.; Neuville, D.R.; Poumellec, B. Nanoscale femtosecond laser milling and control of nanoporosity in the normal and anomalous regimes of GeO_2-SiO_2 glasses. *Opt. Mater. Express.* **2016**, *6*, 321–330. [CrossRef]
18. Lancry, M.; Desmarchelier, R.; Guth, N.; Zimmerman, F.; Brisset, F.O.; Nolte, S.; Poumellec, B. Porous Nanogratings and Related Form Birefringence in Silicate and Germanate Glasses. In Proceedings of the Bragg Gratings, Photosensitivity, and Poling in Glass Waveguides, Barcelona, Spain, 27–31 July 2014.
19. Lancry, M.; Poumellec, B.; Chahid-Erraji, A.; Beresna, M.; Kazansky, P.G. Dependence of the femtosecond laser refractive index change thresholds on the chemical composition of doped-silica glasses. *Opt. Mater. Express.* **2011**, *1*, 711–723. [CrossRef]
20. Lancry, M.; Zimmerman, F.; Desmarchelier, R.; Tian, J.; Brisset, F.; Nolte, S.; Poumellec, B. Nanogratings formation in multicomponent silicate glasses. *Appl. Phys. B.* **2016**, *122*, 66. [CrossRef]
21. Poumellec, B. Links between writing and erasure (or stability) of bragg gratings in disordered media. *J. Non-Cryst. Solids.* **1998**, *239*, 108–115. [CrossRef]
22. Grobnic, D.; Hnatovsky, C.; Mihailov, S.J. Low loss type II regenerative bragg gratings made with ultrafast radiation. *Opt. Express.* **2016**, *24*, 28704–28712. [CrossRef]

23. Desmarchelier, R.; Poumellec, B.; Brisset, F.; Mazerat, S.; Lancry, M. In the heart of femtosecond laser induced nanogratings: From porous nanoplanes to form birefringence. *World J. Nano Sci. Eng.* **2015**, *5*, 115–125. [CrossRef]
24. Wang, Y.; Wei, S.; Cicconi, M.R.; Tsuji, Y.; Shimizu, M.; Shimotsuma, Y.; Miura, K.; Peng, G.-D.; Neuville, D.R.; Poumellec, B.; et al. Femtosecond Laser Direct Writing in SiO_2-Al_2O_3 Binary Glasses and Thermal Stability of Type II Permanent Modifications. *J. Am. Ceram. Soc.*. (under review).
25. The de Sénarmont Compensator. Available online: https://www.olympus-lifescience.com.cn/fr/microscope-resource/primer/techniques/polarized/desenarmontcompensator/ (accessed on 24 January 2020).
26. Fan, C.; Poumellec, B.; Zeng, H.; Lancry, M.; Yang, W.; Bourguignon, B.; Chen, G. Directional writing dependence of birefringence in multicomponent silica-based glasses with ultrashort laser irradiation. *J. Laser Micro/Nanoeng.* **2011**, *6*, 158–163. [CrossRef]
27. Witcher, J.J.; Reichman, W.J.; Fletcher, L.B.; Troy, N.W.; Krol, D.M. Thermal annealing of femtosecond laser written structures in silica glass. *Opt. Mater. Express.* **2013**, *3*, 502–510. [CrossRef]
28. Dogan, Y.; Madsen, C.K. Optimization of ultrafast laser parameters for 3D micromachining of fused silica. *Opt Laser Technol.* **2019**, *123*, 105933. [CrossRef]
29. Brueckner, R. Properties and structure of vitreous silica. I. *J. Non-Cryst. Solids.* **1970**, *5*, 123–175. [CrossRef]
30. Bennett, H.E.; Guenther, A.H.; Newnam, B.E.; Soileau, M.J. *Laser Induced Damage in Optical Materials: 1988*; NIST: Gaithersburg, MD, USA, 1989; pp. 89–90.
31. Bricchi, E.; Klappauf, B.G.; Kazansky, P.G. Form birefringence and negative index change created by femtosecond direct writing in transparent materials. *Opt. Lett.* **2004**, *29*, 119–121. [CrossRef]
32. Champagnon, B.; Le Parc, R.; Guenot, P. Relaxation of silica above and below T_g: Light scattering studies. *Philos. Mag. B.* **2002**, *82*, 251–255. [CrossRef]
33. Ho, C.K.; Djie, H.S.; Pita, K.; Ngo, N.Q.; Kam, C.H. Sintering and porosity control of (x) GeO_2:(1−x) SiO_2 sol-gel derived films for optoelectronic applications. *Electrochem. Solid-State Lett.* **2004**, *7*, F96–F98. [CrossRef]
34. Huang, Y.Y.; Sarkar, A.; Schultz, P.C. Relationship between composition, density and refractive index for germania silica glasses. *J. Non-Cryst. Solids.* **1978**, *27*, 29–37. [CrossRef]
35. Poumellec, B.; Lancry, M. Kinetics of thermally activated physical processes in disordered media. *Fibers* **2015**, *3*, 206–252. [CrossRef]
36. Cerkauskaite, A. Ultrafast Laser Nanostructuring for Photonics and Information Technology. Doctoral Dissertation, University of Southampton, England, UK, 2018.
37. Rudenko, A.; Colombier, J.P.; Itina, T.E. Nanopore-mediated ultrashort laser-induced formation and erasure of volume nanogratings in glass. *Phys. Chem. Chem. Phys.* **2018**, *20*, 5887–5899. [CrossRef] [PubMed]
38. Park, H.; Park, J.Y.; Kim, G.H.; Sohn, I. Effect of TiO_2 on the viscosity and slag structure in blast furnace type slags. *Steel Res. Int.* **2012**, *83*, 150–153. [CrossRef]
39. Cai, Z.; Song, B.; Li, L.; Liu, Z.; Cui, X. Effects of B_2O_3 on viscosity, structure, and crystallization of mold fluxes for casting rare earth alloyed steels. *Metals* **2018**, *8*, 2018. [CrossRef]
40. McMillan, P.W.; Chlebik, A. The effect of hydroxyl ion content on the mechanical and other properties of soda-lime-silica glass. *J. Non-Cryst. Solids.* **1980**, *38*, 509–514. [CrossRef]
41. Haken, U.; Humbach, O.; Ortner, S.; Fabian, H. Refractive index of silica glass: Influence of fictive temperature. *J. Non-Cryst. Solids.* **2000**, *265*, 9–18. [CrossRef]
42. Rajesh, S.; Bellouard, Y. Towards fast femtosecond laser micromachining of fused silica: The effect of deposited energy. *Opt. Express* **2010**, *18*, 21490–21497. [CrossRef]
43. Champion, A.; Bellouard, Y. Direct volume variation measurements in fused silica specimens exposed to femtosecond laser. *Opt. Mater. Express.* **2012**, *2*, 789–798. [CrossRef]

© 2020 by the authors. Licensee MDPI, Basel, Switzerland. This article is an open access article distributed under the terms and conditions of the Creative Commons Attribution (CC BY) license (http://creativecommons.org/licenses/by/4.0/).

3.3 Femtosecond laser direct writing in SiO_2-$Al2O_3$ binary glasses and thermal stability of Type II permanent modifications

Received: 6 December 2019 | Revised: 7 March 2020 | Accepted: 2 April 2020

DOI: 10.1111/jace.17164

Check for updates

Journal of the American Ceramic Society

ORIGINAL ARTICLE

Femtosecond laser direct writing in SiO_2-Al_2O_3 binary glasses and thermal stability of *Type II* permanent modifications

Yitao Wang[1] | **Shuen Wei**[2] | **Miss R. Cicconi**[3] | **Yuta Tsuji**[4] | **Masahiro Shimizu**[4] | **Yasuhiko Shimotsuma**[4] | **Kiyotaka Miura**[4] | **Gang-Ding Peng**[2] | **Daniel R. Neuville**[3] | **Bertrand Poumellec**[1] | **Matthieu Lancry**[1]

[1]Institut de Chimie Moléculaire et des Matériaux d'Orsay, CNRS, Université Paris Sud, Université Paris Saclay, Orsay, France

[2]School of Electrical Engineering & Telecommunications, University of New South Wales, Sydney, NSW, Australia

[3]CNRS-IPGP, Paris, France

[4]Graduate School of Engineering, Kyoto University, Kyoto, Japan

Correspondence
Shuen Wei, School of Electrical Engineering & Telecommunications, University of New South Wales, Sydney, NSW 2052, Australia.
Email: shuen.wei@unsw.edu.au

Funding information
Centre National de la Recherche Scientifique

Abstract

We investigate the potential of fabricating thermally stable refractive index contrasts using femtosecond (fs) near-infrared (IR) radiation in aluminosilicate glasses. A set of pure SiO_2-Al_2O_3 glasses are manufactured, characterized (density and Raman), and investigated after being irradiated by fs laser within the *Type II* regime. The formation of nanogratings is identified and studied using quantitative birefringence measurements. Their thermal stability is then investigated through 30 minutes step isochronal annealing (up to 1250°C). For both SiO_2 and $50SiO_2$-$50Al_2O_3$ compositions, the normalized birefringence does not decrease when tested up to 1100°C, while for the 4,6 mol% GeO_2-SiO_2 erased for 20% at 1000°C.

1 | INTRODUCTION

Since the discovery of the laser-induced periodic surface structure (LIPSS) by Birnbaum nearly a half-century ago,[1] many interesting researches have been carried out from the experimental and theoretical perspectives.[2] One of the intriguing phenomena induced by the femtosecond (fs) laser pulses is the formation of the polarization-dependent sub-wavelength nanostructures.[3] As opposed to the LIPSS written onto the surface of various materials (eg metals, semi-conductors, dielectrics), formation of nanogratings within the bulk has been observed mostly in silicate and germanates glasses with a limited alkali content.[4-9] In the case of SiO_2 or GeO_2 glasses, self-organized nanogratings, which are composed of stripe-like regions with oxygen deficiencies including nanovoids,[10,11] are perpendicularly aligned to the laser polarization.

The very high intensity fields achievable using femtosecond laser pulses can lead to highly localized plasma ionization and deoxygenation, resulting in strong sub-diffraction interference effects between the plasma and the optical field, generating complex condensed structures such as nanogratings. These are based on glass decomposition that resolidifies into a nanoporous,[10] usually silicon-rich, structure, creating a strong and highly stable refractive index contrast.[12] Based on such photo-induced structures showing localized birefringence in glass, various applications ranging from embedded micro-reflectors, retardation plates, microfluidic channels, to rewritable 5D optical storage, polarization imaging have been investigated as review in References 13 and 14.

Besides these applications mentioned above, nanogratings in SiO_2 due to its remarkable thermal stability up to ~1200°C,[12,15] they are now extensively studied for applications like long lifetime optical data storage and for sensing applications in extreme environments. For example, *Type II fs-IR* modifications which are attributed to the formation

 © 2020 The American Ceramic Society

of self-organized nanogratings made of oxide decomposition,[10,11] demonstrate remarkable thermal stability up to ~1000°C for 150 hours after a stabilization for 1 hour at 1000°C,[16] while operating for 100 hours at 1050°C reveals a slight (5%) intensity decay. This is likely associated with thermal relaxation of the bulk glass at these temperatures. It should be noted that, in this work, we categorize the type of modifications from the perspective of the nature of refractive index modifications induced by IR femtosecond laser irradiation. More specifically, *Type I IR-fs* modification is featured by an isotropic growth of the refractive index with respect to the non-irradiated regime. The *Type II* IR-*fs* modification, characterized by a high level of anisotropic index change [8] and resulting birefringence, is typically induced by the presence of nanogratings. As relates to applications, fs-FBGs have recently been tested as temperature sensors for monitoring fluidized bed combustors,[17] as well as for radiation resistant temperature sensors.[18,19] The refractive change is 3D localized and involves significant stress-induced changes around the irradiated regions. For this reason, the higher temperature regime is limited by the thermal response of both the surrounding regions and the fiber itself, which has not been relaxed prior to application. Recent results indicate the need of >30 mol% Al_2O_3[20] to improve FBG thermal stability above standard fibers like SMF28 from Corning. To go beyond the thermal stability limit[16] imposed by standard SiO_2-based optical fibers, FBGs can be inscribed in SiO_2-Al_2O_3 optical fibers using femtosecond laser direct writing.[20-22] The doping that determines the optical fiber core soften the glass far too much and so are not directly involved in the high temperature processing that allows gratings to operate at higher temperatures. The usual dopants like Germanium (Ge), Fluorine (F) or Boron (B) in the fiber core determine the high-temperature processing. Therefore, most commercial fibers will be unlikely to be designed for long-term operation above 1000°C.[16] However, if one examines the softening point (T at which $\log(\eta) = 7{,}1$ with η in dPa.s) or the melting point (T at which $\log(\eta) = 1$), it is suggested that the introduction of a high melting point compatible oxide with SiO_2 like Al_2O_3 (which melts above 2000°C) could overcome to above-mentioned thermal stability limits imposed by silica-based optical fibers.

This paper mainly explores how the substitution of SiO_2 by Al_2O_3 up to 50 mol% in the glass impacts the formation and thermal properties of *Type II* modifications[23] written by IR femtosecond laser. The binary SiO_2-Al_2O_3 glass system was chosen because (a) pure aluminosilicate glasses are known to exhibit high melting temperatures[24] and (b) aluminosilicate glasses containing high Al_2O_3 concentrations typically present an increase in Al coordination number (namely 5- and 6-fold coordination[25-28]), increasing glass network cross-linking density and bond strength. SiO_2-Al_2O_3 glasses are therefore expected to be a good glass candidate for applications in high-temperature environments. In this view, we prepared a set of aluminosilicate glasses using aerodynamic levitation with CO_2 laser heating. To further investigate the impact of dopants on thermal stability of *Type II* modification, Suprasil® CG silica, GeO_2-doped SiO_2, TiO_2-doped SiO_2 (ULE® 7972, Corning) and borosilicate (Borofloat® 33, Schott) were also investigated. Then we irradiated them by femtosecond laser and we studied the *Type II fs-IR* modifications by isochronal heat-treatments up to 1250°C, in order to determine the effect of different dopants on the "thermal stability" of silicate glass.

2 | EXPERIMENTAL DETAILS

Aluminum oxide (alumina, Al_2O_3) and silicon dioxide (silica, SiO_2) ultrapure raw powders based on the stoichiometry $x.SiO_2 - (1 - x).Al_2O_3$ (x = 50, 60, 70, 80) were mixed in alumina mortar and pressed into pellets. The pellets were sintered for 12 hours at 1100°C in air, and crushed and used as a preform for aerodynamic levitation with CO_2 laser melting. The calcined preforms were levitated using a flow of dry air (N_2: 79%, O_2: 21%) and melted through focusing of 100 W CO_2 laser via a ZnSe lens (f = 254 mm). To ensure homogeneity of the melt, the temperature was kept above the melting point for tens of seconds. Then, the melt was rapidly cooled by turning off the laser power while gas levitating. Colorless and transparent spherical samples with a diameter of approximately 1-2 mm were obtained. Imperfections, such as bubbles, would interrupt laser propagation, thus, hot fully homogeneous sphere were melted again. The glass phases of all prepared samples were verified by Cu K X-ray diffraction (XRD, Rigaku; RINT-2500HFK/PC) and SEM-EDS chemical analysis. Volumetric mass density (which will be referred to as density for short) of all samples was measured at room temperature by Archimedean method, using toluene as an immersion liquid. The relation between these weights and density and temperature of toluene is well known. For each composition, measurements were performed on five different samples.

Raman spectra of the samples were recorded at room temperature with a T64000 Jobin-Yvon-Horiba® spectrometer equipped with an Olympus® microscope. A confocal system and a 1024 Charge-Coupled Detector cooled by nitrogen were used, allowing a spatial resolution of 1-2 μm^2 with a ×100 objective. The spectral resolution is ~0.7 cm^{-1}. A Coherent® Argon laser is used with an excitation wavelength of 488,1 nm with 50 mW on the sample. A commercial Suprasil® CG glass from Heraeus (a synthetic Type III pure SiO_2 glass[29]) has been chosen to serve as a reference to calibrate the sample spectra. All sample spectra were acquired in the frequency range 17-1400 cm^{-1} with the same

experimental conditions in order to minimize experimental errors. The intensities of the spectra have been normalized over the total integrated area.

Femtosecond laser irradiation (λ = 1030 nm, 250 fs) was performed on the SiO_2-Al_2O_3 samples to investigate the writing kinetics of *Type II* modifications. To irradiate with a specific depth, and to make testing easier, samples were glued on a glass slide with a transparent resin, then polished using diamond lapping film (ø = 6, 3, 1, 0.25, 0.1 μm) until reaching optical quality. The polished surface was then placed on a xyz motorized translation stages and irradiated. Laser experiments include writing series of lines along the x-axis with a linear laser polarization oriented either parallel (Xx configuration) or perpendicular (Xy configuration) to the scanning direction. The laser pulse repetition rate was fixed to 100 kHz and the scanning speed to 100 μm/s. The laser beam was focused 300 μm below the surface using a 0.6 NA aspheric lens. The pulse energy was varied by step in different range of energy: ranging from 0.1 to 0.5 μJ with step of 0.1 μJ; ranging from 0.6 to 1 μJ with step of 0.2 μJ; ranging from 1.5 to 4 μJ with step of 0.5 μJ. The gap between two consecutive lines was fixed to 25 μm. Then in order to measure the optical retardance *R*, we use an Olympus BX51 polarizing optical microscope equipped with a de Sénarmont compensator. The retardance *R* is defined as $R = B\,L$, where *B* is the linear birefringence ($n_e - n_o$) and *L* is the length of the birefringent object being measured. The de Sénarmont compensator couples a highly precise quarter wavelength birefringent quartz plate with a 180° rotating analyzer to provide retardation measurements having an accuracy that approaches one thousandth of a wavelength.

3 | RESULTS

3.1 | Density measurement of SiO_2-Al_2O_3 samples

Figure 1 shows the evolution of the density of the SiO_2-Al_2O_3 samples for different Al_2O_3 contents. Data from the literature[30-32] are reported for the sake of comparison. There

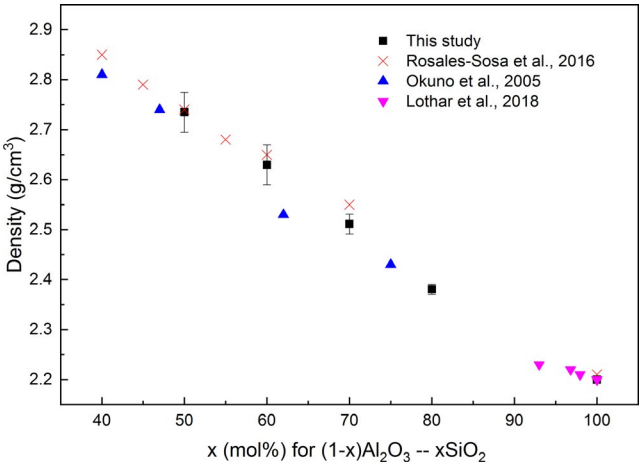

FIGURE 1 Density of the SiO_2-Al_2O_3 samples compared with the results extracted from the literature[30,31,32]

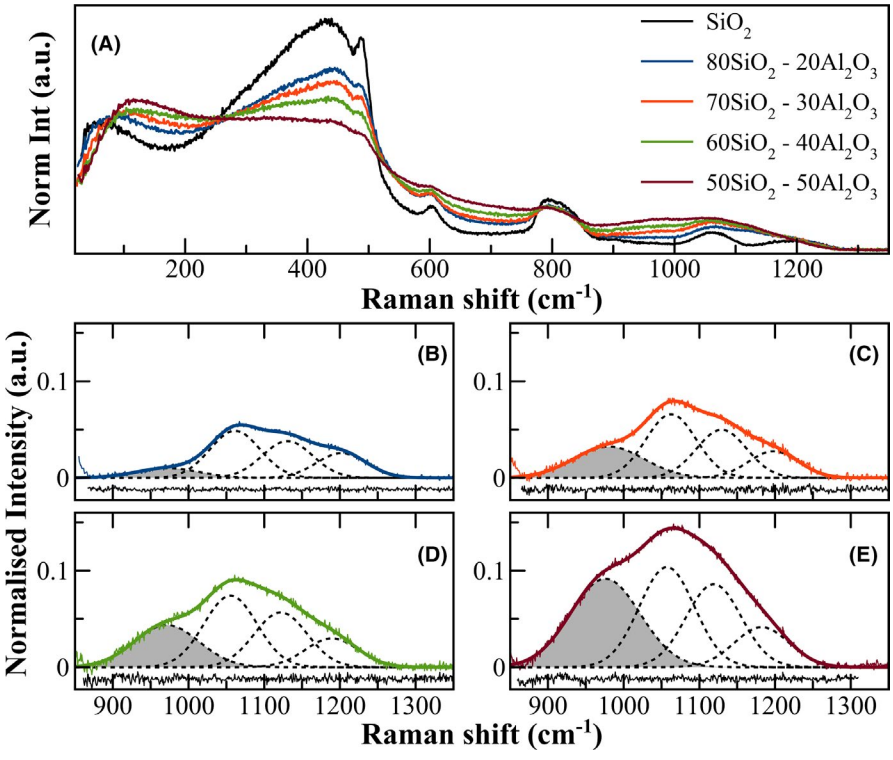

FIGURE 2 (A) Raman spectra of SiO_2-Al_2O_3 samples + phase SiO_2 for sake of comparison (B) Sample $80SiO_2$-$20Al_2O_3$; (C) Sample $70SiO_2$-$30Al_2O_3$; (D) Sample $60SiO_2$-$40Al_2O_3$; (E) Sample $50SiO_2$-$50Al_2O_3$

is a clear trend where density increases as alumina content increases. From this graph, it is intuitive that the densities of our home-made SiO_2-Al_2O_3 samples are consistent with the literature. The standard deviations shown in Figure 1 result from the measurements for five pellets (10 measurements for each pellet) with the same target composition. It can be seen that deviation becomes gradually stronger when the pellet contains more alumina. It might be related to the increasing difficulty to vitrify the glass, which likely results in nanoscale phase separation and voids in the high-alumina-containing samples.

3.2 | Raman spectra of SiO_2-Al_2O_3 samples

Raman spectra of SiO_2-Al_2O_3 samples with different concentrations of aluminum oxide (namely 20%, 30%, 40%, and 50% mole of Al_2O_3) are reported in Figure 2, along with the spectrum of Suprasil® CG glass, used as reference. The most intense contribution is located around 430 cm^{-1} (R band) and is associated to T–O–T symmetric stretching modes (T represents the centered tetrahedron cation).[33] By increasing the Al_2O_3 content, there is a clear intensity decrease of this band, related to both variations of the number of SiO_4 tetrahedra as well as to variations of T-O-T inter-tetrahedral angles and T-O average distances.[30] The sharp peaks, also called D_1 and D_2 defect lines, at around 490 and 600 cm^{-1}, are ascribed to the breathing modes of 4- and 3-membered rings, respectively.[34] According to Figure 2, both peak intensities relatively decrease with a higher content of alumina, which indicates that the addition of alumina causes modifications of the ring statistic in the silica glass network.[30,31] In the mid-frequency area, the asymmetric band near 800 cm^{-1} results from the motion of Si atoms in their tetrahedral oxygen cage,[35] and slightly decreases in intensity and move toward lower wavenumbers upon addition of Al_2O_3. This decrease could be associated to a decrease of Si-BO (Silicon-bridging oxygen).

The high frequency region (HF: 850-1300 cm^{-1}) shows bands related to the Si-O asymmetric stretching vibrations. The HF envelop can be studied by using mathematical function, and in the case of pure SiO_2 glass, three Gaussians can be used to represents the Si-centered tetrahedra connected with four bridging oxygens (at ~1060 cm^{-1}, ~1155 cm^{-1} and ~1200 cm^{-1}). The HF region of the SiO_2-Al_2O_3 samples has been studied as well using mathematical functions, and Figure 2B-E show the Gaussian decomposition of the 850-1300 cm^{-1} frequency region, and the necessity of four components in order to reproduce the envelope. Indeed, besides the three high frequency bands described for SiO_2, the addition of alumina in the silica glass leads to the rise of an additional contribution at ~975 cm^{-1}, which increases in intensity by increasing Al_2O_3. Furthermore, the band at ~1155 cm^{-1} shifts toward lower frequencies and increases in intensity upon addition of alumina, and this can be related to the stabilization of 4-fold or 5-fold coordinated Al^{3+} units, and the formation of Si-O-Al bonds. Indeed because of the high amount of Al_2O_3, besides the presence of AlO_4 tetrahedra, it is expected the presence of higher coordinated species (Al^{3+} 5-fold and/or 6-fold coordinated), which would cause the formation of non-bridging oxygens, and strong modifications in the glass connectivity. In particular based on the literature,[25,26] we expect that around 50% of Al are 5-fold coordinated in these glasses. This results in a depolymerization of the silica network (in agreement with the changes of the Boson peak at low

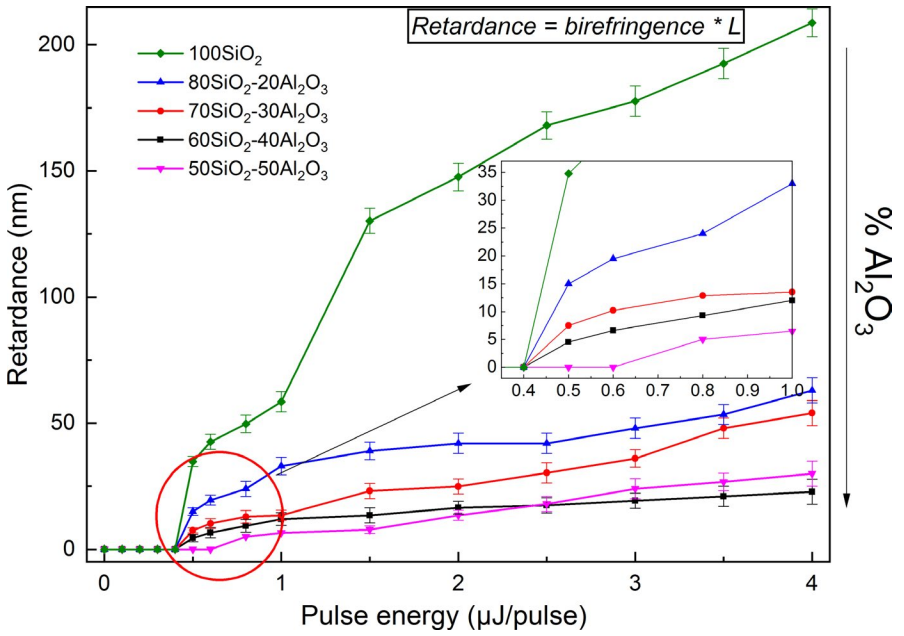

FIGURE 3 Retardance *R* as a function of pulse energy for SiO_2-Al_2O_3 glasses (20%, 30%, 40%, and 50% mole of Al_2O_3). Blue arrow (right scale) indicates the decreasing content of Al_2O_3. Laser parameters are: 1030 nm, 300 fs, 100 kHz, 100 µm/s, NA = 0.6, polarization parallel to the scanning direction ie Xx writing configuration. Inset: Retardance R as a function of pulse energy from 0.3 to 1 µJ. Arrows in inset indicate the advent of *Type II* modifications of pure silica (green), low Al_2O_3 glasses (red) and 50 SiO_2-50 Al_2O_3 glass (pink)

frequency) and to the creation of Q_{n-1} species in agreement with the low frequency shift.

3.3 | Writing kinetics of *Type-II* modifications in SiO_2-Al_2O_3 samples

Figure 3 shows the measurements of the retardance *R* for all investigated pellets with different compositions as a function of the laser pulse energy in μJ/pulse. Note we added the results obtained in Suprasil® CG glass (SiO_2) as a reference here. Above the *Type II* threshold, optical properties of the irradiated regions are modified. The average refractive index usually decreases, and the refractive index contrast continues to maintain even after a high temperature processing (typically an annealing for a few hours at 1000°C) in SiO_2.[12] Moreover a strong linear birefringence (mostly attributed to a form birefringence) is observed and can be easily detected using any birefringence imaging system.

Analysis of the curves shown in Figure 3 indicates that all samples exhibit a similar trend in their writing kinetics. Note that the threshold T1,[23] related to the formation of permanent index changes without form birefringence, is about 0.3 μJ as we can observe a contrast in natural light but not between crossed polarizers. We did not observe any variation of T1 with the increasing content of Al_2O_3 in the investigated range. For higher pulse energy, occurrence of form birefringence was revealed using the full order waveplate technique, which allows detecting the slow/fast axis orientation of the photo-induced birefringence. Since we observed a 90° rotation of the slow axis orientation when switching from Xx to Xy writing configuration, we can attest the formation of orientable birefringence that is usually related to the formation of nanogratings.[6,8] Therefore, it was observed that the threshold T2,[23] which is related to the *Type II* modifications, appears around 0.4 μJ in SiO_2 for our experimental conditions. It depends slightly on the Al_2O_3 concentration and increases up to 0.6 uJ for 50 mole% Al_2O_3. Typically, a strong retardance increase appears above T2 for short pulse energy increment and plateaus around 0.8-1 μJ (1.5 uJ for Suprasil® CG glass). Observing the trends in Figure 3, it is possible to notice two features: as the Al_2O_3 concentration increases both the slope at the origin and the maximum retardance gradually decrease. With respect to silica, SiO_2-Al_2O_3 samples exhibit much lower retardance values by a factor 4 for the $80SiO_2$-$20Al_2O_3$ sample and by a factor of 10 for the $50SiO_2$-$50Al_2O_3$ one.

3.4 | Thermal stability of *Type-II* IR-fs modifications in SiO_2-Al_2O_3 samples

To investigate the thermal stability of the written *Type II* modifications, the samples were heat-treated following Δt = 30 minutes step isochronal annealing up to extreme temperatures to observe the evolution in their birefringence. In this context, we have thus monitored retardance *R* (which is related to the birefringence through the length of the object) at room temperature after each annealing step. The retardance was normalized relative to its initial value at room T, that is, $R_{norm}(\Delta t, T) = R(\Delta t, T)/R(0, 25°C)$. Figure 4 displays the normalized retardance $R_{norm}(\Delta t, T)$ as a function of temperature. Here we have chosen to perform annealing of samples written at 2.0 μJ/pulse, which corresponds to the stable range of *Type II* modifications (in term of writing kinetics) and can facilitate the reliable measurements of the retardance. The thermal stability of $70SiO_2$-$30Al_2O_3$ and $50SiO_2$-$50Al_2O_3$ samples were displayed in Figure 4 together with some additional samples namely SiO_2 (Suprasil® CG, T_a ~1150°C), GeO_2-SiO_2 (4.6 mole% GeO_2; T_a ~1070°C), and TiO_2-SiO_2 (ULE® 7972; 7 mole% TiO_2; T_a ~900°C) and Alumino-borosilicate (Borofloat® 33; 81 mole% SiO_2, 13 mole% B_2O_3, 4 mole% Na_2O/K2O, 2 mole% Al_2O_3; T_a ~652°C). The glass viscosity at 10^{13} dPa.s defines here the annealing point T_a values.

Some typical characteristics of normalized $R_{norm}(\Delta t, T)$ can be observed from the Figure 4, which typically reveals at least three different erasure mechanisms, which are hypothesized and discussed in the next section. However, they have different trends and contributions for each chemical composition. For both Borofloat® 33 and ULE®, the decay starts after the heat-treatment at 300°C. Typically R_{norm} decreases smoothly until 600°C corresponding to a 20% decay. Then the decline is accelerated for higher temperatures until the laser tracks are not visible under polarizing optical microscope. This corresponds to full erasure after a 30 minutes thermal treatment at 650°C in Borofloat® 33 and 1025°C in ULE® glass. These values are quite close to their respective annealing points T_a: 652°C for Borofloat® 33 and 1000°C for ULE®. Note the temperatures mentioned here are dependent on the duration of the isochronal plateau and a longer duration will shift down this "full erasure" temperature, which is somehow at the image of the glass transition temperature range, and revealing in such a way that the erasure mechanisms are in fact distributed.[36]

On the contrary, the R_{norm} of both GeO_2-doped SiO_2 and $70SiO_2$-$30Al_2O_3$ exhibit a higher thermal stability and quite similar trends. The decay starts slowly at 650°C leading to 10% erasure at 850°C in $70SiO_2$-$30Al_2O_3$. Then it begins to fall within 850-1000°C range and there is a very sharp erasure process above 1000°C. Finally, the *Type II* modifications disappear completely at 1075°C in 4.6 mole% GeO_2-doped SiO_2 whereas it survives up to 1175°C in $70SiO_2$-$30Al_2O_3$. Note this value is much higher than the reported glass transition temperature of 865°C (determined from thermal expansion curve) for a 5 wt.% Eu_2O_3-doped $70SiO_2$-$30Al_2O_3$ glass melted within a gold image furnace and quenched using twin roller technique.[37]

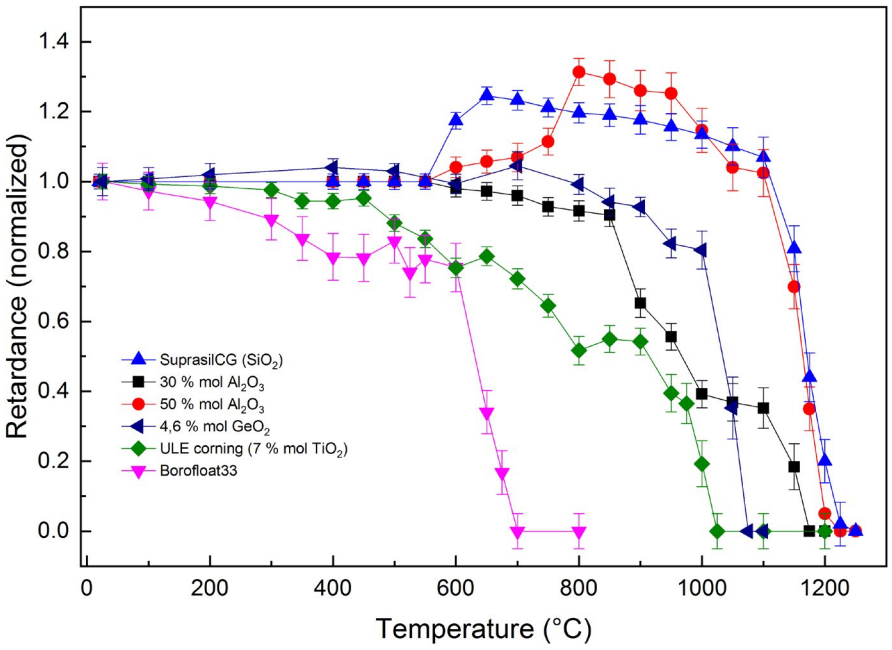

FIGURE 4 Normalized retardance $R_{norm}(\Delta t, T)$ as a function of temperature for Suprasil® CG (SiO_2), 70SiO_2-30Al_2O_3 and 50SiO_2-50Al_2O_3. GeO_2-SiO_2 (4.6 mole% GeO_2), ULE® (7 mole% TiO_2) and Borofloat® 33 glasses are also shown for sake of comparison. Laser conditions are: 1030 nm, 300 fs, 100 kHz, 100 μm/s, NA = 0.6, Xx writing configuration ie laser polarization wad parallel to the writing direction

Finally, the highest temperature resistance can be found for 50SiO_2-50Al_2O_3 pellet and SiO_2 glasses. They show similar trends, and initially the R_{norm} value increases significantly (typ. 30%) above 550°C to reach a maximum around 650°C in SiO_2 and 800°C in 50SiO_2-50Al_2O_3. Then, similarly to the other samples, the R_{norm} value starts to decrease slowly for temperature higher than 800°C. In SiO_2, this feature is well correlated with the structural relaxation of densified silica formed within the nanograting regime[38] that as confirmed by the three and four-folds rings anneal out at the range of 700-900°C.[39,40] Finally, the further increase in the isochronal annealing temperature above 1100°C leads to a very steep decrease of the birefringence, and the R_{norm} value drops to zero at about 1225°C in both SiO_2 and 50SiO_2-50Al_2O_3 samples.

4 | DISCUSSION

Typically, $R_{norm}(\Delta t, T)$ decreases smoothly until 600°C corresponding to a 20% decay in Borofloat® 33 and ULE® glasses whereas it does not change significant in SiO_2, GeO_2-SiO_2, and SiO_2-Al_2O_3 samples This indicates that the contribution of point defects centers (E', ODC, NBOHC) to the refractive index contrast of the nanogratings themselves remain quite limited. As another example waveguide formed in silica with an infrared femtosecond laser[41] showed photo-induced absorption peaks at 213 and 260 nm corresponding to the respective center defects E' and NBOHC. However, most of these two defects were completely erased after annealing at 400°C, although the waveguide retained its guiding properties up to 900°C. As a result, color centers are unlikely to have played a strong role in the refractive index change.[41] Other results lead to the conclusion that the thermal stability of colored centers produced in borosilicate and silica glasses is not compatible with that of the change in refractive index.[42] Their contribution might explain the slight erasure of the measured retardance that is observed below 600°C especially in Borofloat® 33 and ULE® glasses but point defects cannot account for the observed "abnormal" increase of $R_{norm}(\Delta t, T)$ within 600-800°C in both SiO_2 and 50SiO_2-50Al_2O_3 samples.

The next point is the abnormal behavior that is observed in the intermediate temperature range (600-800°C). Bricchi et al[12] and Grobnic[16] have already observed such unusual behavior within *Type II* regime, respectively, in SiO_2 or in slightly Ge-doped optical fibers. We suggest this could be related to some changes in the strain field resulting in an additional stress-induced birefringence, but this hypothesis needs to be further investigated. More specifically, this hypothesis is based on the imposed sequence of step isochronal annealing associated with quenching to room temperature (after each step), which leads to the occurrence of an additional stress field. This suggestion is supported by a recent publication of Y. Bellouard group.[43] In this recent work the authors report that while densified zones (so-called *Type I* regime) display a decrease of thermal expansion coefficient, nanogratings (*Type II* regime) show the opposite trend, with respect to the pristine material. In addition, the authors highlight that an annealing treatment of 10 hours at 300°C leads to a significant increase in the coefficient of expansion α within *Type II* affected zone. In the framework of our step isochronal annealing experiments, this should lead to an increase in the residual stresses and thus traditional stress-induced birefringence resulting in the observed increase of the overall retardance in the 600-800°C range.

The last point is the contribution to the birefringence that exhibits a very high thermal stability in SiO_2 and SiO_2-Al_2O_3.

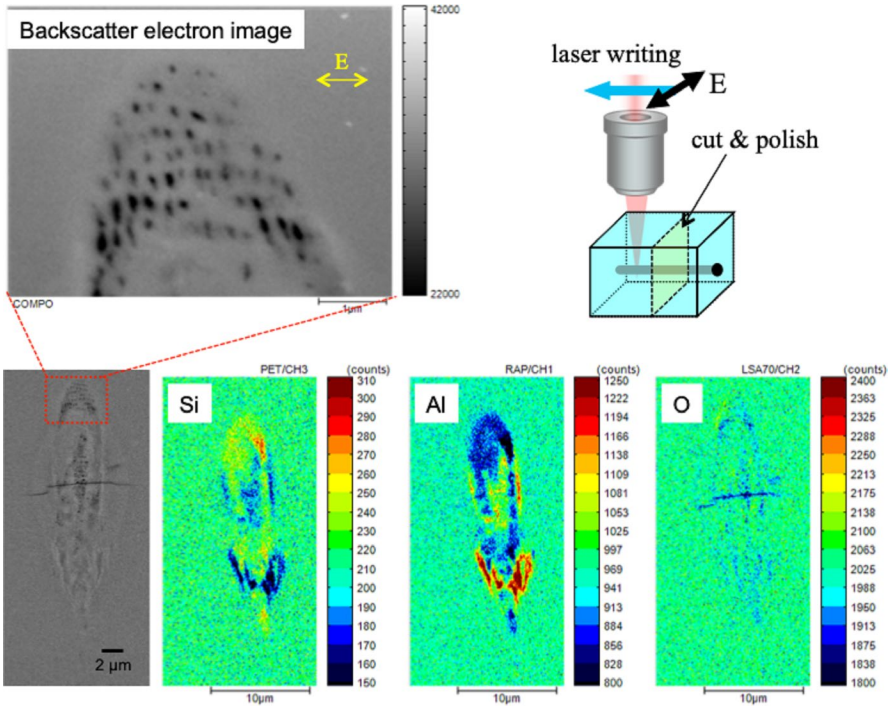

FIGURE 5 Backscattered electron image and element distribution maps obtained by an electron probe micro analyzer (EPMA) equipped with a Schottky field emission (FE) electron gun (JXA-8530F, JEOL). Glass: $50SiO_2$-$50Al_2O_3$. Laser conditions: 1030 nm, 1 ps, 1 µm/s and 2,5 µJ/pulse, Xy writing configuration

This part, typically above 1000°C in Figure 4, is attributed to the nanogratings internal structure itself (eg nanoporous silica in SiO_2). A first comment about Figure 4 is that the $50SiO_2$-$50Al_2O_3$ glass shows similar high temperature stability as the pure silica glass (Suprasil). However, Type II modifications erase at much lower temperature in $70SiO_2$-$30Al_2O_3$. We think that the problem here can mostly be seen in term of glass viscosity and glass structure relaxation. Indeed the limiting factor at high temperature is related the stability of the nanogratings and in particular the "nanopores" within the nanolayers themselves. In a simple view, the thermal stability of these nanopores can be described by the Rayeigh-Plesset equation as suggested by Rudenko et al.[44] Assuming a constant surface tension with T, the key term of this equation is thus related to the glass viscosity η at high T. We suggested that the observe difference is mostly related to η(T) that is likely higher for 50% Al_2O_3 than for 30 mol% Al_2O_3 in agreement with the reported values of glass melting T_m temperatures. This could be attributed to an increase in Al coordination number (4, 5, and 6 fold-coordination[25,26,27,28]), increasing glass network cross-linking density and bond strength. Note that additional measurements of the viscosity-temperature dependence would be nice to validate this view.

In addition based on nanogratings chemical changes observed in other multicomponent oxide glasses,[9,45,46] we suggest that nanogratings in our aluminosilicate samples are made of Al_2O_3-rich phase that separates from the SiO_2-rich matrix phase. Backscattered electron image and element distribution maps shown in Figure 5 have confirmed this view. In particular the high thermal stability of laser-induced phase separation could be related to immiscibility, which has been reported for example in annealed sol-gel glasses containing >10 mol% Al_2O_3 and this immiscibility appears to increase with Al_2O_3 content as reported in References 47 and 48. This immiscibility can be ascribed to the difference in the coordination number between oxygen ions bonded to Si and those bonded to Al. Indeed, when one Al^{3+} ions replaces Si^{4+} in a tetrahedral coordination site, one oxygen ion must ideally tri-bridge three tetrahedra to maintain the charge balance, leading to a densification of the glass network. This could lead to nanoscale separation between Si and Al-rich glassy phases. Based on literature the Al-rich phase would have a typical composition ranging from $3Al_2O_3$-$2SiO_2$ to $2Al_2O_3$-SiO_2,[49] for which the edge-shared AlO_6 octahedral chains are interconnected by AlO_4 or SiO_4 tetrahedra.[50,51] Thus, immiscibility increases the structural connectivity in the "residual" Si-rich matrix. Furthermore, the separation of Al-rich phase likely favors the formation of Mullite nuclei,[49] and it is not excluding that nanolayers are partly nano-crystallized in the form of Mullite, which would need further investigations.

5 | CONCLUSION

Here, femtosecond laser direct writing in a set of binary SiO_2-Al_2O_3 glasses (no alkali) up to 50 mol% Al_2O_3 was investigated. It was shown that *Type II* (ie nanogratings likely made of phase separation) can be photo-induced in these aluminosilicate glasses. Additionally, 30 minutes step

isochronal thermal annealing of $50SiO_2$-$50Al_2O_3$ shows a similar thermal stability of *Type II* modifications compared to SiO_2 and improved compared to Ge-doped SiO_2. Indeed, the normalized retardance shows no decrease in magnitude at temperatures lower than 1100°C. In contrast, in the GeO_2-SiO_2 glass, the retardance has already decreased by ~20% after 30 minutes at 1000°C. More generally there is a trend indicating that *Type II* thermal erasure is strongly related to the glass transition temperature range as suggested by our comparison involving Borofloat® 33, ULE®, GeO_2-SiO_2 and SiO_2 glasses. These results suggest that inscription of such "*Type II fs-IR*" modifications in SiO_2-Al_2O_3 could be employed to make fiber Bragg gratings with high thermal stability. This opens the door toward the fabrication of a new range of "fiber Bragg gratings host fibres" (Al_2O_3 but also ZrO_2 or YAG-derivated[22]) suitable for ultra-high temperature operation.

ACKNOWLEDGMENTS

The DEFI CNRS "Instrumentation aux Limites", UltraBragg project, supported this work. The authors thank Ecole doctorale 2MIB from Paris Saclay University for the financial support provided to Yitao Wang for his doctorate.

CONFLICT OF INTEREST

We declare that we do not have any commercial or associative interest that represents a conflict of interest in connection with the work submitted.

ORCID

Miss R. Cicconi https://orcid.org/0000-0002-4106-4057
Masahiro Shimizu https://orcid.org/0000-0002-9948-891X
Yasuhiko Shimotsuma https://orcid.org/0000-0003-0588-3167
Daniel R. Neuville https://orcid.org/0000-0002-8487-5001
Matthieu Lancry https://orcid.org/0000-0003-2007-7438

REFERENCES

1. Birnbaum M. Semiconductor surface damage produced by ruby lasers. J Appl Phys. 1965;36:3688.
2. Buividas R, Mikutis M, Juodkazis S. Surface and bulk structuring of materials by ripples with long and short laser pulses: recent advances. Prog Quantum Electron. 2014;38(3):119–56.
3. Shimotsuma Y, Kazansky P, Qiu J, Hirao K. Self-organized nanogratings in glass irradiated by ultrashort light pulses. Phys Rev Lett. 2003;91(24):247405.
4. Asai T, Shimotsuma Y, Kurita T, Murata A, Kubota S, Sakakura M, et al. Systematic control of structural changes in GeO2 glass induced by femtosecond laser direct writing. J Am Ceram Soc. 2015;98(5):1471–7.
5. Richter S, Miese C, Döring S, Zimmermann F, Withford MJ, Tünnermann A, et al. Laser induced nanogratings beyond fused silica-periodic nanostructures in borosilicate glasses and ULE™. Optical Materials Express. 2013;3(8):1161–6.
6. Fedotov SS, Drevinskas R, Lotarev SV, Lipatiev AS, Beresna M, Čerkauskaitė A, et al. Direct writing of birefringent elements by ultrafast laser nanostructuring in multicomponent glass. Appl Phys Lett. 2016;108(7):071905.
7. Lancry M, Zimmerman F, Desmarchelier R, Tian J, Brisset F, Nolte S, et al. Nanogratings formation in multicomponent silicate glasses. Appl Phys B. 2016;122(3):66.
8. Bricchi E, Klappauf BG, Kazansky PG. Form birefringence and negative index change created by femtosecond direct writing in transparent materials. Opt Lett. 2004;29:119–21.
9. Lotarev S, Fedotov S, Lipatiev A, Presnyakov M, Kazansky P, Sigaev V. Light-driven nanoperiodical modulation of alkaline cation distribution inside sodium silicate glass. J Non-Cryst Solids. 2018;479:49–54.
10. Lancry M, Poumellec B, Canning J, Cook K, Poulin JÄ, Brisset F. Ultrafast nanoporous silica formation driven by femtosecond laser irradiation. Laser Photonics Rev. 2013;7(6):953–62.
11. Lancry M, Canning J, Cook K, Heili M, Neuville D, Poumellec B. Nanoscale femtosecond laser milling and control of nanoporosity in the normal and anomalous regimes of GeO_2-SiO_2 glasses. Optical Materials Express. 2016;6(2):321–30.
12. Bricchi E, Kazansky PG. Extraordinary stability of anisotropic femtosecond direct-written structures embedded in silica glass. Applied Physics Letters. 2006;88(11):111119.
13. Beresna M, Gecevičius M, Kazansky PG. Ultrafast laser direct writing and nanostructuring in transparent materials. Adv Opt Photonics. 2014;6(3):293–339.
14. Zhang B, Liu X, Qiu J. Single femtosecond laser beam induced nanogratings in transparent media-Mechanisms and applications. J Materiomics. 2019;5(1):1–14.
15. Li Y, Yang M, Wang D, Lu J, Sun T, Grattan KT. Fiber Bragg gratings with enhanced thermal stability by residual stress relaxation. Opt Express. 2009;17(22):19785–90.
16. Grobnic D, Smelser CW, Mihailov SJ, Walker RB. Long-term thermal stability tests at 1000°C of silica fibre Bragg gratings made with ultrafast laser radiation. Meas Sci Technol. 2006;17(5):1009–13.
17. Walker RB, Ding H, Coulas D, Grobnic D, Mihailov SJ, Duchesne MA, et al. eds. Entrained-flow gasifier and fluidized-bed combustor temperature monitoring using arrays of fs-IR written fiber Bragg gratings. 24th International Conference on Optical Fibre Sensors; 2015: International Society for Optics and Photonics.
18. Morana A, Girard S, Marin E, Marcandella C, Paillet P, Périsse J, et al. Radiation tolerant fiber Bragg gratings for high temperature monitoring at MGy dose levels. Opt Lett. 2014;39(18):5313–6.
19. Morana A, Girard S, Marin E, Lancry M, Grelin J, Marcandella C, et al. Dependence of the voids-fiber bragg grating radiation response on temperature, dose, and dose rate. IEEE Trans Nucl Sci. 2017;65(8):1619–23.
20. Grobnic D, Mihailov SJ, Ballato J, Dragic PD. Type I and II Bragg gratings made with infrared femtosecond radiation in high and low alumina content aluminosilicate optical fibers. Optica. 2015;2(4):313–22.
21. Elsmann T, Lorenz A, Yazd NS, Habisreuther T, Dellith J, Schwuchow A, et al. High temperature sensing with fiber Bragg gratings in sapphire-derived all-glass optical fibers. Opt Express. 2014;22(22):26825–33.
22. Cavillon M, Lancry M, Poumellec B, Wang Y, Canning J, Cook K, et al. Overview of high temperature fibre Bragg gratings and potential improvement using highly doped aluminosilicate glass optical fibres. J Physics: Photonics. 2019;1(4):042001.

23. Poumellec B, Lancry M, Chahid-Erraji A, Kazansky P. Modification thresholds in femtosecond laser processing of pure silica: review of dependencies on laser parameters [Invited]. Optical Materials Express. 2011;1(4):766–82.
24. Bowen N, Greig, . uJ. The system: Al_2O_3-SiO_2. J Am Ceram Soc. 1924;7(4):238–54.
25. McMillan PF, Wolf GH, Poe BT. Vibrational spectroscopy of silicate liquids and glasses. Chem Geol. 1992;96(3–4):351–66.
26. Neuville DR, Cormier L, Montouillout V, Florian P, Millot F, Rifflet J-C, et al. Structure of Mg-and Mg/Ca aluminosilicate glasses: 27Al NMR and Raman spectroscopy investigations. Am Miner. 2008;93(11–12):1721–31.
27. Weber R, Sen S, Youngman RE, Hart RT, Benmore CJ. Structure of high alumina content Al_2O_3– SiO_2 composition glasses. J Phys Chem B. 2008;112(51):16726–33.
28. Schaller T, Stebbins JF. The structural role of lanthanum and yttrium in aluminosilicate glasses: A 27Al and 17O MAS NMR study. J Phys Chem B. 1998;102(52):10690–7.
29. Brückner R. Properties and structure of vitreous silica I. J Non-Cryst Solids. 1970;5:123–75.
30. Okuno M, Zotov N, Schmücker M, Schneider H. Structure of SiO_2–Al_2O_3 glasses: combined X-ray diffraction, IR and Raman studies. J Non-Cryst Solids. 2005;351(12–13):1032–8.
31. Ando MF, Benzine O, Pan Z, Garden J-L, Wondraczek K, Grimm S, et al. Boson peak, heterogeneity and intermediate-range order in binary SiO_2-Al_2O_3 glasses. Sci Rep. 2018;8(1):5394.
32. Rosales-Sosa GA, Masuno A, Higo Y, Inoue H. Crack-resistant Al_2O_3–SiO_2 glasses. Sci Rep. 2016;6:23620.
33. Le Losq C, Neuville DR, Florian P, Henderson GS, Massiot D. The role of Al^{3+} on rheology and structural changes in sodium silicate and aluminosilicate glasses and melts. Geochim Cosmochim Acta. 2014;126:495–517.
34. Galeener FL. Planar rings in glasses. Solid State Commun. 1982;44(7):1040.
35. McMillan P. Structural studies of silicate glasses and melts—applications and limitations of Raman spectroscopy. Am Miner. 1984;69(7–8):622–44.
36. Poumellec B, Lancry M. Kinetics of thermally activated physical processes in disordered media. Fibers. 2015;3(3):206–52.
37. Nogami M, Watanabe K, Ito Y, Ito H, Nakano H. Hydrogen gas reaction with Eu^{3+}-doped Al_2O_3–SiO_2 glasses. J Am Ceram Soc. 2010;93(6):1663–7.
38. Bellouard Y, Barthel E, Said A, Dugan M, Bado P. Scanning thermal microscopy and Raman analysis of bulk fused silica exposed to low-energy femtosecond laser pulses. Opt Express. 2008;16(24):19520–34.
39. Zhang F, Yu Y, Cheng C, Dai Y, Zhang H, Qiu J. Wavelength response and thermal stability of embedded nanograting structure light attenuator fabricated by direct femtosecond laser writing. Appl Phys B. 2014;117(1):53–8.
40. Witcher JJ, Reichman WJ, Fletcher LB, Troy NW, Krol DM. Thermal annealing of femtosecond laser written structures in silica glass. Optical Materials Express. 2013;3(4):502–10.
41. Saliminia A, Vallée R, Chin S. Waveguide writing in silica glass with femtosecond pulses from an optical parametric amplifier at 1.5 μm. Opt Comm. 2005;256(4):422–7.
42. Streltsov A, Borrelli N. Study of femtosecond-laser-written waveguides in glasses. J Opt Soc Am B. 2002;19(10):2496–504.
43. Vlugter P, Block E, Bellouard Y. Local tuning of fused silica thermal expansion coefficient using femtosecond laser. Phys Rev Mat. 2019;3(5):053802.
44. Rudenko A, Colombier J-P, Itina TE. Nanopore-mediated ultrashort laser-induced formation and erasure of volume nanogratings in glass. Physical Chemis Chem Phys. 2018;20(8):5887–99.
45. Mori S, Kurita T, Shimotsuma Y, Sakakura M, Miura K. Nanogratings embedded in Al_2O_3-Dy_2O_3 glass by femtosecond laser irradiation. J Laser Micro Nanoeng. 2016;11(1):87.
46. Lotarev S, Fedotov S, Kurina A, Lipatiev A, Sigaev V. Ultrafast laser-induced nanogratings in sodium germanate glasses. Opt Lett. 2019;44(7):1564–7.
47. Liu S, Boffa V, Yang D, Fan Z, Meng F, Yue Y. Clarifying the gel-to-glass transformation in Al_2O_3-SiO_2 systems. J Non-Cryst Solids. 2018;492:77–83.
48. MacDowell J, Beall G. Immiscibility and crystallization in Al_2O_3-SiO_2 glasses. J Am Ceram Soc. 1969;52(1):17–25.
49. Gonzalez-Carreno T, Sobrados I, Sanz J. Formation of mullite and spinel phases from SiO_2–Al_2O_3 gels prepared by a spray pyrolysis technique. A ^{29}Si and ^{27}Al MAS NMR study. Chem Mater. 2007;19(15):3694–703.
50. McConnell JDC, Heine V. Incommensurate structure and stability of mullite. Physical Review B. 1985;31(9):6140.
51. Sadanaga R, Tokonami M, Takeuchi Y. The structure of mullite, $2Al_2O_3.SiO_2$, and relationship with the structures of sillimanite and andalusite. Acta Crystallogr A. 1962;15(1):65–8.

How to cite this article: Wang Y, Wei S, Cicconi MR, et al. Femtosecond laser direct writing in SiO_2-Al_2O_3 binary glasses and thermal stability of *Type II* permanent modifications. *J Am Ceram Soc*. 2020;00:1–9. https://doi.org/10.1111/jace.17164

Conclusions

This chapter presented an overall study of the thermal stability of IR-fs Type II modifications in bulk silicate glasses, which included the different contributions of the nanogratings and their erasure mechanisms, the impact of laser parameters, glass impurities (OH, Cl) and glass composition to some extend (mostly GeO_2, Al_2O_3). To summarize the key observations of this chapter:

I. In "pure" silica glass:

- Nanogratings contributions and their thermal erasure mechanisms:
  - The point defects centers are bleached under a fairly low-temperature thermal treatment (200-500 °C), and exhibit only a minor contribution, to the measured retardance.
  - The subsequent unexpected increase from 600 °C to 900 °C is attributed to the presence of densification. The progressive erasure of the former and related compressive stress can eventually cause an "abnormal" increase in the retardance R.
  - We note here that the compressive stress field produced by the nanoporous layers disappears before the annihilation of the nanopores themselves, likely by plastic deformation around the nanopores, range of thermal erasure: 800 °C – T_a.
  - Finally, the form birefringence due to nanopores formations is found to play a key role in the ultimate thermal stability of the fs laser-induced nanogratings, range of thermal erasure: >T_a; (described by R-P equation under a viscoelastic regime).
- Thermal stability of nanogratings depends on Cl and OH impurities: the lower the impurities (both Cl and OH), the higher the thermal stability.
- Thermal stability of nanogratings depends on laser writing conditions:
  - Writing speed: the highest writing speed demonstrates the highest thermal stability.
  - Laser pulse energy: the higher energy shows better thermal stability.

II. Other glass compositions

- Impact of dopants (e.g. TiO_2, B_2O_3) in SiO_2: the viscosity (T) and T_a appears strongly related to the thermal stability of Type II modifications, i.e., higher viscosity leads to higher thermal stability.
- SiO_2-GeO_2 glass: Influence of GeO_2 content: the incorporation of GeO_2 (at least up to 17 mol%) only has a limited impact on the overall thermal behavior of germanosilicate glasses.
- SiO_2-Al_2O_3 glass:
  - The Type II modifications (nanogratings) can effectively occur in SiO_2-Al_2O_3 glasses (no alkali) but exhibit a much lower birefringence (optical retardance) than in silica glass;
  - Isochronal thermal annealing of 50SiO_2-50Al_2O_3 demonstrated a similar thermal stability of Type II modifications compared to SiO_2 and improved compared to Ge-doped SiO_2.
  - The high thermal stability could be related to nanoscale separation between Si

and Al-rich glassy phases. Furthermore, it is not excluding that nanolayers are partly nano-crystallized in the form of Mullite, which would need further investigations.

In conclusion, we have investigated in details the performances and the mechanisms of type II thermal stability in bulk silica-based glasses. These results suggest that inscription of such "Type II fs-IR" modifications in SiO_2-Al_2O_3 could be employed to make fiber Bragg gratings or others laser written devices with high thermal stability in optical fibers. This might open the door toward the fabrication of a new range of "sensing host fibers" (e.g., aluminosilicates, yttrium aluminosilicates, or zirconium-based glass optical fibers) suitable for ultra-high temperature operation.

Chapter 4. Thermal stability of type II modifications by IR fs laser in aluminosilicate fibers

Introduction 159
4.1 Overview of high temperature fibre Bragg gratings and potential improvement using highly doped aluminosilicate glass optical fibres 160
4.2 3D laser engineering of molten core fibers: towards a new generation of harsh environment sensing devices 173
Conclusions 189
References 190

Introduction

Applying a new generation of fibers for sensing technologies in the industrial processes that take place under extreme physical conditions (down-hole oil/gas exploration, monitoring of fuel combustion machinery, and temperature regulation of engines, etc.) constantly require improved thermal stability of the optical sensors and fibers themselves [1, 2]. In this chapter a short introductory review of high temperature laser induced modifications is presented in the first publication. This overview highlights the fact that the ultimate thermal stability of laser written devices (like Fiber Bragg Gratings FBGs) is closely linked to intrinsic nature (structure and properties) of the core-cladding materials and the laser-induced modifications that constitute the device (e.g., a FBG). This includes dynamics of viscous flow, chemical migration, and stress relaxation. The conventional fiber manufacturing methods are usually based on chemical vapor deposition ("CVD", land such as MCVD, PCVD or OVD). These processes bring significant advantages, including ultra-low attenuation losses, but remain limited in terms of dopants (e.g., Ge, Al, B, P) and respective concentrations that can possibly be incorporated into the final glass fiber form (typically few mol%). If we consider the situation of fs-laser modifications inscribed in conventional telecom GeO_2-doped fibers (such as a SMF-28), thermal stability of Type II FBGs was demonstrated up to 1000 °C for 150 hours after a stabilization for 1 hour at 1000 °C [3]. Another class of optical materials, such as sapphire crystals, exhibits better thermal performance compared to silica glass, and single crystalline sapphire fiber has been investigated and demonstrated stability up to 1850 °C as a grating sensor [4-7]. Unfortunately, these sapphire optical fibers come along with significant drawbacks such as high rigidity fragility, attenuation lossy, and they are highly multimoded.

To go beyond the limitations imposed by conventional techniques, in this work we investigate a new route in investigating fibers fabricated by the Molten Core Method (MCM), which can be classified as a "non-conventional" technique [8]. The later enables a large flexibility in the choice of fiber composition and eventually manufacture fibers with "unstable" core compositions [9], such as the silica-based novel fibers from precursors like sapphire (Al_2O_3) or Yttrium Aluminum Garnet (YAG) crystals. Based on the work performed in bulk glasses and presented in Chapter 3, we decided to focus our attention on Al_2O_3-SiO_2 glass systems but now in the fiber form. Thus, in this chapter, four aluminosilicate fibers that are fabricated with a circular core/cladding geometry comprising an aluminosilicate glass core and a pure silica cladding will be investigated. The 1st paper is dedicated to YAG-derived fibers whereas the 2nd paper is dedicated to sapphire-derived fibers.

Femtosecond laser irradiations were performed on these fibers within the Type II regime (characteristic of the formation of nanogratings) and the induced modifications were characterized using both birefringence measurements and scanning electron microscopy. Thermal stability of the aforementioned modifications was thus studied by step isochronal annealing experiments and further compared to conventional SMF-28 fiber and F300 silica (which is the material composing the cladding of the fibers fabricated by the MCM). To validate our approach, we tested the performance of these fibers by prototyping a distributed fiber sensor based on optical frequency-domain reflectometry, which utilizes the intrinsic Rayleigh scattering from the laser-induced irradiated area inside the fiber core.

4.1 Overview of high temperature fibre Bragg gratings and potential improvement using highly doped aluminosilicate glass optical fibres

JPhys Photonics

TOPICAL REVIEW

Overview of high temperature fibre Bragg gratings and potential improvement using highly doped aluminosilicate glass optical fibres

Maxime Cavillon[1,2], **Matthieu Lancry**[1], **Bertrand Poumellec**[1], **Yitao Wang**[1], **John Canning**[3], **Kevin Cook**[3], **Thomas Hawkins**[2], **Peter Dragic**[4] and **John Ballato**[2]

[1] Institut de Chimie Moléculaire et des Matériaux d'Orsay (ICMMO), Université Paris-Sud, Université Paris Saclay, CNRS, Orsay, France
[2] Center for Optical Materials Science and Engineering Technologies (COMSET) and the Department of Materials Science and Engineering, Clemson University, Clemson, SC, United States of America
[3] Interdisciplinary Photonics Laboratories (iPL), School of Electrical & Data Engineering, University of Technology Sydney, Sydney, NSW, Australia
[4] Department of Electrical and Computer Engineering, University of Illinois at Urbana-Champaign, Urbana, IL, United States of America

E-mail: maxime.cavillon@u-psud.fr

Keywords: fibre Bragg gratings (FBGs), high temperature sensing, molten core method, yttrium aluminosilicates

OPEN ACCESS

RECEIVED
8 April 2019

REVISED
5 July 2019

ACCEPTED FOR PUBLICATION
2 August 2019

PUBLISHED
23 August 2019

Original content from this work may be used under the terms of the Creative Commons Attribution 3.0 licence.

Any further distribution of this work must maintain attribution to the author(s) and the title of the work, journal citation and DOI.

Abstract

In this paper, various types of high temperature fibre Bragg gratings (FBGs) are reviewed, including recent results and advancements in the field. The main motivation of this review is to highlight the potential of fabricating thermally stable refractive index contrasts using femtosecond (fs) near-infrared radiation in fibres fabricated with non-conventional techniques, such as the molten core method. As a demonstration of this, an yttrium aluminosilicate (YAS) core and pure silica cladding glass optical fibre is fabricated and investigated after being irradiated by an fs laser within the Type II regime. The familiar formation of nanogratings inside both core and cladding regions are identified and studied using birefringence measurements and scanning electron microscopy. The thermal stability of the Type II modifications is then investigated through isochronal annealing experiments (up to $T = 1100$ °C; time steps, $\Delta t = 30$ min). For the YAS core composition, the measured birefringence does not decrease when tested up to 1000 °C, while for the SiO_2 cladding under the same conditions, its value decreased by ~30%. These results suggest that inscription of such '*Type II fs-IR*' modifications in YAS fibres could be employed to make FBGs with high thermal stability. This opens the door toward the fabrication of a new range of 'FBG host fibres' suitable for ultra-high temperature operation.

1. Introduction

Over the past decade, research in the field of high temperature fibre Bragg gratings (FBGs) has continued at a steady pace, with a continuous increase of emerging applications. For example, such fibre technology is now employed in diverse areas such as the temperature profiling of high temperature manufacturing equipment [1], monitoring of fuel combustion machinery [2], temperature regulation of large diesel engines in trains [3], and to assess the structural integrity of a building post fire [4]. Oil and gas industries also benefit from such technology, as well as geothermal industries, as they continue to drill ever-deeper into the earth, with exploration depths now reaching 5 km [5]. At these kind of depths the temperatures can exceed 500 °C and extreme pressures are also encountered. In this paper, a short introductory review of high and ultra-high temperature FBG sensors is first presented, following past reviews [6–8]. The prefixes 'high' and 'ultra-high' are defined herein for FBG operating temperature conditions below and above 800 °C, respectively. This overview highlights the fact that the ultimate FBG thermal stability is closely linked to the intrinsic thermal stability of the core-cladding materials from which it is made. Therefore, the potential of nonconventional fibre fabrication techniques, such as the molten core method (MCM), for the fabrication of laser-induced structures with higher thermal resistance is discussed. As an example of this, a circular core/cladding glass fibre comprising a yttrium-doped aluminosilicate core (YAS) and

© 2019 The Author(s). Published by IOP Publishing Ltd

a silica cladding is fabricated using the MCM. This system was chosen since (a) aluminosilicate glasses such as YAS glasses are known to exhibit high glass transition temperatures ($T_g \sim 900$ °C in [9, 10]); and (b) aluminosilicate and YAS glasses containing high Al_2O_3 concentrations typically present an increase in Al coordination number (4, 5, and 6 fold-coordination [11, 12]), increasing the glass network cross-linking density and bond strength. A YAS glass core optical fibre is therefore expected to be a good glass candidate for high temperature applications.

The fibre core and cladding regions are subsequently irradiated by a femtosecond laser with varying laser parameters, such as laser pulse energy and the laser-induced glass modifications, which are characterized through retardance (R) measurements and scanning electron microscopy imaging. R measurements enable the detection of birefringent structures, such as nanogratings (which are defined and discussed later), formed during laser irradiation. Finally, a fibre segment is heat-treated up to 1100°C and the thermal stability of the laser induced modifications in its core glass, compared to its silica cladding which serves as a reference, is investigated. R measurements during these annealing experiments provide a direct mesurement of their thermal stability.

For completeness, if in the overview we principally discuss the various advancements in the field of FBGs operating at very high temperatures, it must be pointed out that other challenges are of prime importance. One of them is the necessity to find coatings, packaging and attachment procedures that can withstand such high temperature regimes. This includes the development of specialty coatings (silicone based coatings like polyimide up to 350 °C (e.g., [13, 14]) in continuous, metallic coatings like Al [15], Cu [16, 17], Mo-Cu to 800 °C [18], Au to 750 °C [19], and packaging in metallic capillaries such as Inconel 600 [20] or steel to 1000 °C [19]. An approach to attach these FBG sensors, especially to metallic substrates, is to bond them using high temperature resistant adhesives. More sophisticated approaches may be to directly embed the FBGs into a metallic substrate thanks to additive layer manufacturing processes [21, 22] or to use metal-coated FBGs and to braze them to the metallic structure. Although of extreme importance, these topics are vast and go beyond the scope of this overview. An interested reader is directed to the aformentioned references for more information.

2. Types of FBGs

In this section, the different 'types' of fabricated FBGs and their respective thermal stabilities are discussed. In this work, FBG 'types' refer to the nature of refractive index modifications induced by laser irradiation rather than the growth kinetics, even if some types exhibit specific kinetics, such as Type I*n*. Type I corresponds to a laser irradiation regime that induces an isotropic increase of the refractive index. This is typically achieved by laser radiation (continuous wave (CW), nanosecond, femtosecond (fs)) that causes defect center formation and glass densification [23, 24]. The Type II regime relates to the formation of an anisotropic index change upon irradiation, typically induced by the presence of nanogratings, and results in the observation of form birefringence [25]. The laser-irradiated region has a lower refractive index than its surrounding (i.e., non-irradiated) medium. Finally, a Type III regime corresponds to the formation of voids/microcavities (due to Coulombic micro-explosion) [26] usually using single pulse fs irradiation and likely accompanied by a densified shell [27].

2.1. Type I and Type In FBGs

Perhaps the most common kind of FBGs used for high-temperature operation are stabilized Type I FBGs. Generally, Type I gratings are stabilised to meet telecommunication specifications ($-20°C \leqslant T \leqslant +80$ °C for time, $t > 25$ years) but can be processed to operate at much higher temperatures for short, but still usefull, timeframes depending on the application. For example, a Type I FBG can be thermally annealed at 700 °C, reducing the FBG strength but allowing operation for finite time periods up to 600 °C [28]. Other approaches to stabilize Type I gratings involve photosensitisation [29] to remove the unstable component generated during grating inscription.

Type I*n* FBGs, also called Type IIA and negative index gratings [30], are formed in hydrogen-free silica fibres after a kind of regeneration [31–34]. This regeneration is thermally-induced through extended laser exposure times using, typically, quasi-CW, CW or pulsed UV lasers. Similar results may also be achieved through annealing in a furnace [35]. Type I*n* gratings form due to the relaxation of internal stresses that are induced from the UV radiation when the FBG is made, in particular the radial and axial stresses. The first Type I*n* FBGs were capable of operating up to $T \sim 500$ °C before decaying [31, 32]; however, by using higher intensity exposures, generating higher local temperature, the functionallity may be extended to $T \sim 700$–800 °C in step-index [33, 34] and photonic crystal fibres [36]. Thermal properties strongly depend on the dopant nature (mostly Ge and B) and doping level, e.g. 1 h at 500 °C in highly (30 mole %) Ge-doped fibre; or 1 h at 700 °C in a Ge-B co-doped fibre [33, 34].

2.2. Ultra-high temperature regenerated FBGs

In order to achieve FBG operation above 800 °C in silica fibres, the process of regeneration is required. Regenerated FBGs (RFBGs) are fabricated by annealing a so-called seed grating, typically (but not always) a Type I grating. Hydrogen is used to further increase strain in processed regions versus those that are unprocessed. The hydrogen can be added to the fibre prior to seed formation or later before the regeneration process. The ability to introduce hydrogen after the seed grating fabrication is key to making possible the regneration of draw tower gratings [37]. A seed grating is fabricated in a hydrogen-loaded silicate fibre using (typically but not always) a UV laser [38, 39] and subsequently regenerated at temperatures in the range of $T \sim$ 800–900 °C. It is possible to also use fs lasers to inscribe the seed [40]. Since these fibres are made of silica, these gratings can survive at $T \sim$ 1295 °C [41] or $T \sim$ 1450 °C for 20 to 30 min [42]. Regenerated gratings have also been demonstrated to continuously operate at $T \sim$ 890 °C for an impressive 9000 h [43]. In contrast to thermal stabilization of Type I and Type I*n* FBGs, the high temperatures involved in the regeneration leads to the complete relaxation of stresses in the fibre. Regenerated gratings have, over the years, proven to be a viable sensing technology in a range of areas, for example in the profiling of high temperature manufacturing equipment [1], dual pressure/temperature sensing for gas turbines [44], sodium cooled nuclear reactors [20], high temperature air flow meters for internal combustion engines [45] and train engine temperature regulation [3]. Regenerated gratings have also been utilised to make the first accurate measurements of fibre viscosity [46]. Complex RFBG structures such as phase-shifted gratings [47], chirped gratings [48] and even final Bragg wavelength controlling [49] have been fabricated. Multiplexed distributed sensing also is possible [1, 50].

Regenerated FBGs are commercially available (e.g., [19]). However, this comes along with few shortcomings: devices are limited to only few fibre compositions (e.g. regeneration efficiency is low in pure silica core fibres), the thermal engineering process leads to brittle fibres, mutiplexing FBGs in same fibres is possible [50] but difficult, and there is no available model to perform a reliable predition of long term operation.

2.3. Femtosecond FBGs (Type II and III FBGs)

Ultrafast lasers, typically in the near infrared (NIR) spectral range, are used to write FBGs (thereby known as femtosecond FBGs or fs-FBGs) either by using a phase mask [51] or by inscribing each grating plane point-by-point [52]. The use of visible or near infrared femtosecond laser light presents an inherent advantage of writing an FBG through the protective coating such as acrylate or polyimide [19]. Even if this coating does not withstand temperature beyond 350 °C, it is particularly useful to get a preserved polymer coating for packaging and deployment issues. The use of NIR radiation means the excitation of the silica band edge is a multiphoton process and therefore highly localised, leading to much finer gratings than those achieved using two-photon absorption with 193 nm light [53, 54]. Unlike the gratings inscribed using UV lasers, the mechanism responsible for index change does not necessarily depend on core chemical composition and does not require hydrogen in a lot of fibres. Gratings written using fs radiation may be classed as either being above or below the damage threshold of the glass. Because of the very high intensity fields achievable with these systems, highly localized plasma ionization and deoxygenation can lead to strong sub-diffraction interference effects between the plasma and the optical field, generating complex condensed structures such as nanogratings. These are based on glass decomposition that resolidifies into a nanoporous, usually silicon-rich structure, creating a strong and highly stable refractive index contrast [55].

Type I fs-FBGs mostly are based on a glass fictive temperature T_f increase [56] when the duration of the heat pulse corresponding to the light energy is greater than the glass relaxation time $\eta(T)/G(T)$ (shear viscosity / shear modulus) with a partial contribution (typically 20%) of point defects [57]. However Type I fs-FBGs can be completely erased by annealing at temperatures exceeding 800 °C. Type II gratings are attributed to the formation of self-organized nanogratings made of oxide decomposition [55]. Type II fs-FBGs demonstrate remarkable thermal stability up to ~1000 °C for 150 h after a stabilization for 1 h at 1000 °C [58], while operating for 100 h at 1050 °C reveals a slight (5%) intensity decay and a +0.2 nm Bragg wavelength drift. This is likely associated with thermal relaxation of the bulk glass at these temperatures. As relates to applications, fs-FBGs have recently been tested as temperature sensors for monitoring fluidized bed combustors [2], as well as for radiation resistant temperature sensors [59]. Refractive index modifications are highly localized and involve significant stress-induced changes around the irradiated regions. For this reason, the higher temperature regime is limited by the thermal response of both the surrounding regions and the fibre itself which has not been relaxed prior to application. When the fibre is pre-annealed (before FBG writing) at high temperature (5 h at 1100 °C), Type II fs-infrared (IR) FBGs are stable up to 1200 °C during 20 h [60]. Following this view, regeneration can also improve fs-FBG performance to some extent [40, 61]. In conventional single mode fibres (SMFs, Ge-doped silica glass), the point-to-point voids FBG (Type III fs-FBGs) have slight loss of reflectivity (typically 20% of its initial strength) in less than 20 h at 1000 °C, before stabilizing [62]. At 1050 °C, the reflectivity of point-by-point Bragg grating rapidly decreases to less than 20% after a few hours. Recently it was demonstrated that fs-FBGs

Table 1. Typical grating specifications for high temperature operation.

Grating type	Maximum temperature of operation (°C)	$d\lambda/dT$ (pm °C^{-1})	References
Type I*n*	~700 (~1 h)	~12[a]	[33]
		12.8	[34]
Regenerated	~1295 (10 min)	16.3	[39]
Femtosecond Type II *fs-IR*	~1000 (150 h)	~16[b]	[58]
Sapphire	~1600 (~6 h)	23.0 at room temperature	[66]
fs—FBG		31.0 at 1000 °C	
		31.0 at 1500 °C	

[a] Estimated from figure 3 of [33].
[b] Estimated from figure 4 of [58].

fabricated via laser ablation in suspended-core microstructure fibre gratings can be operated at 1300 °C for 5 min [63].

Types II and III femtosecond FBGs are now commercially available [64, 65]. The main shortcomings are related to the lack of reliable lifetime prediction for long term operation above 800–1000 °C where many processes occur, including not only residual stress relaxation of both the fibre and the laser-induced modifications, but also glass structural relaxation leading to changes of the glass disorder (fictive temperature changes).

2.4. Sapphire FBGs

To achieve even higher temperature operation FBGs can be inscribed in materials with higher melting points. Single crystalline aluminium oxide (sapphire) optical fibres have been used with femtosecond laser fabrication [66]. Sapphire FBGs demonstrate remarkable thermal stability up to ~1600 °C for 6 h after a stabilization for 20 min at 1745 °C [67]. Sapphire FBGs boast the highest temperature performance to date, operable up to 1800 °C. However, sapphire optical fibres presently are highly multimoded due to their having an air cladding. Moreover, they are crystalline, leading to both short lengths and a lack of flexibility given their fairly large diameters. To date they are closer to thin rods than fibres. The next generation of fibres that may overcome this involves hybrid mixes of silica with aluminosilicate cores [68], provided their alumina concentration is sufficiently high to increase glass transition temperature.

Table 1 summarizes both maximum temperature of operation and wavelength shift as a function of temperature ($d\lambda/dT$) for the various types of gratings discussed above.

3. Molten core fabrication of high-temperature resistant structures

As seen from the previous overview, there is significant interest for waveguides and fibre sensors that can withstand high temperatures. Clearly, even if sapphire fibres/rods can withstand extremely high temperatures, they lack flexibility compared to a 125 μm cladding diameter conventional fibre, and are highly multimode. Nonconventional techniques like the MCM, as opposed to conventional chemical vapor deposition (CVD) techniques, enable the fabrication of silicate glass optical fibres with high concentration of dopants (i.e., other than silica components) in their fibre cores. As an example of this, glass aluminosilicates with aluminium oxide (or alumina) concentrations as high as [Al_2O_3] ~55 mole % at the core center were fabricated using this technique [69]. Subsequent to this, FBGs with varying content of alumina (4% and 30% [70], and 50% [68]) have been successfully fabricated. For the highest fibre concentration ([Al_2O_3] = 50 mole %), good thermal stability up to 1000 °C was reported.

3.1. Experimental procedure

The fibre investigated in this study, which is refered as 'YAG-derived fibre,' was fabricated using the molten core method. More details regarding the fabrication process can be found in [71]. In short, a rod-shaped yttrium aluminium garnet (YAG) crystal of 2.75 mm diameter and 60 mm length was inserted inside a F300 pure silica glass capillary tube (3 mm and 30 mm inner and outer diameters, respectively). The ensemble was placed inside a high temperature graphite furnace and brought to T ~ 2000 °C. At this temperature, the YAG precursor melts, and silica from the capillary tube preform partially is dissolved into the precursor molten core, yielding a SiO_2-Y_2O_3-Al_2O_3 (yttrium aluminosilicate, YAS) core glass. The preform is subsequently drawn into an optical fibre with a targeted cladding diameter of 125 μm, and a conventional acrylate polymer coating was deposited

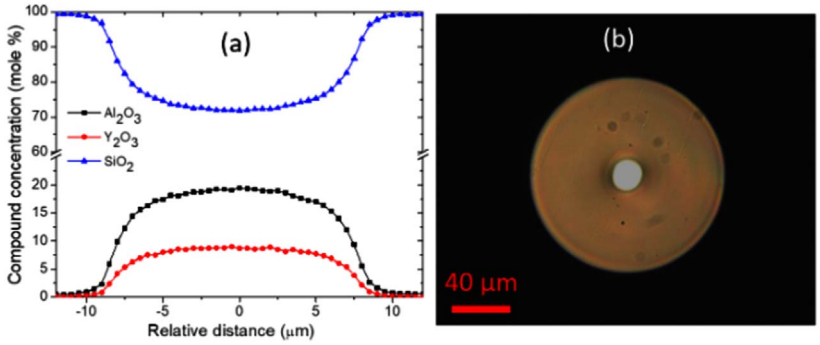

Figure 1. (a) Concentration profile of the fibre core composition and (b) optical microscope (bottom light illumination) image of the fibre cross section.

on-line during the draw. A total fibre length of ~800 m was collected, and a few meters were selected for this work. In figure 1(a) the compound concentration profile across the fibre core is displayed.

Figure 1(b) shows the fibre cross section under an optical microscope. The fibre core concentration profile was measured by Energy Dispersive X-ray (EDX) with a ZEISS SUPRA 55 VP scanning electron microscope (SEM). Additional information regarding specific fibre properties for these YAG-derived fibres fabricated using the MCM can be found in [72, 73]. Typical background losses at 1.55 μm and numerical aperture values in these fibre systems are ~0.5 dB m^{-1} and ~0.5, respectively. However, these values can be adjusted depending on the precursor purity used (for losses) and the amount of dopants incorporated into the core (for numerical aperture). For completeness, it is worth mentioning that these fibre segments can easily be spliced to conventional single mode fibres.

The refractive index profile (RIP) measurement of the glass fibre was performed at 550 nm with an IFA-100 Multiwavelength Optical Fibre Analyzer (Interfiber Analysis). The refractive index at the fibre core center will be used for calculations to determine glass properties in next section (section 3.2). Femtosecond laser irradiation ($\lambda = 1030$ nm) was performed on the YAG-derived fibre, in both core and cladding regions. In order to irradiate the fibres, each selected fibre segment (~5 cm length) had its coating removed, then was sandwiched between a fused silica glass slide (bottom) and a borosilicate glass cover-slip (top, ~170 μm thin), with some index matching oil (GN Nettest, $n_D = 1.4580$ at 25 °C) in between. Additionally, to ensure the fibre segments were properly affixed to the substrate during the heat-treatment analysis described below, both ends of each segment were adhered to the bottom silica substract using high temperature adhesive. Finally, the ensemble was placed on a translation stage, carefully aligned with respect to the fs laser beam, then irradiated. More information regarding the laser setup can be found in [74].

Following a geometry similar to line-by-line FBG writing, a first experiment consisted in drawing 60 μm lines, perpendicular to the direction of fibre longitudinal axis, enabling irradiation in both core and cladding, as shown in figure 2(a). The spacing between each line is 5 μm, and the pulse energy varies by step of 0.1 μJ, ranging from 0.1 to 1.0 μJ. Other lasers parameters are: 1030 nm laser wavelength, 100 kHz laser pulse repetition rate; 100 μm/s speed (resulting in a pulse overlap rate of 1000 pulses/μm); NA (writing objective) $= 0.6$; and laser polarization perpendicular ($\perp$) or parallel ($//$) to the writing direction (figure 2(a)). The R (in nm) of the irradiated regions was mesured at room temperature, using the Senarmont compensator technique on a Olympus BX51 optical microscope. R is defined as $R = B \times d$, with B being the linear birefringence (dimensionless) and d the thickness of the birefringent object (in nm). Hence, when a fibre segment is irradiated by a laser and a birefringent object is formed, the measured R value corresponds to the amount of B integrated over the laser track length (in the z direction from figure 2). For completeness, the fibre segment is immersed in the index matching oil for each retardance measurement, which removes curvature effects from circular fibre geometry during analysis.

A second experiment was performed to investigate the morphology of fs laser induced glass modifications in the YAG-derived fibre (both in core and cladding). In this experiment, a total of 6 lines of 10 mm lengths (5 μm interval between them) parallel to the light propagation axis of the fibre were irradiated, as represented in figure 2(b). The pulse energy was set to 0.8 μJ/pulse, based on the previous set of experiments, was found to be within the Type II regime. Next, the fibre segment was cleaved and the fibre cross sectional area was investigated using an SEM (Field-Emission Gun Scanning Electron Microscope, ZEISS SUPRA 55 VP, 1 kV accelerating voltage). This experiment was repeated using two different laser polarization orientations: parallel ($//$) and perpendicular ($\perp$) to the laser writing inscription. The former condition enables the observation of the inside

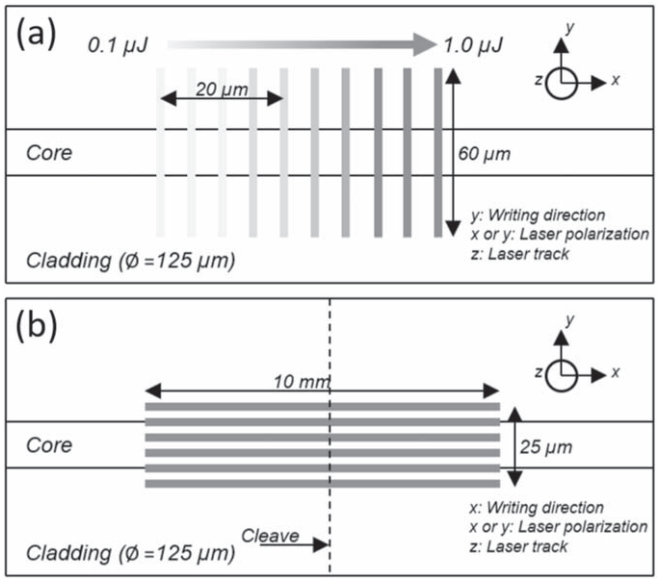

Figure 2. Experimental laser writing designs. a) Irradiation of fs laser inside fibre core and cladding of an optical fibre at different pulse energies ($\lambda = 1030$ nm, 100 kHz, 100 μm s^{-1}, 10^3 pulses/μm, NA $= 0.6$, pulse duration $= 160$ fs). (b) Longitudinal (along x) irradiation at constant pulse energy (0.8 μJ) using different laser polarization conditions: parallel (//, along x) and perpendicular ($\perp$, along y) to the writing direction.

(which are porous in bulk SiO_2 [55]) of the laser-induced nanoplanes, while the latter permits sideways visualization of these nanoplanes, including their spacing [74].

Finally, a fibre segment was irradiated according to figure 2(a) and was subsequently heat-treated up to 1100 °C by incremental temperature steps (400 °C, 500 °C, 600 °C, 700 °C, 800 °C, 850 °C, 900 °C, 950 °C, 1000 °C, 1050 °C, 1075 °C, and 1100 °C) and with a constant heat-treament time (30 min) for each temperature step. R was measured at room temperature between each isochronal annealing step.

3.2. Experimental results

3.2.1. Laser irradiation

Measuremements of retardance (R) as a function pulse energy and under different polarization ($\perp$ and //) conditions are shown in figure 3, for both SiO_2 (taken in the fibre cladding) and the YAS glass core, taken at the core center. Both the YAS and SiO_2 glasses exhibit a very similar behavior, that is, a threshold situated at 0.35 ± 0.03 μJ, above which a strong retardance appears whose slow axis is set by the laser polarization. This is characteristic of the formation of nanogratings in silica [56, 74], and is associated with a local decrease of refractive index within the irradiated region. For the YAS composition, R appears to plateau above 0.6 μJ/pulse, and its overall magnitude is lower than for SiO_2. R values are lower for the $\perp$ configuration relative to the // configuration. Such polarization dependence is explained by the boundary conditions [75] and spatial-temporal properties of the ultrashort pulse laser beam quantified by the pulse front tilt leading to anisotropic photosensitivity phenomena [76].

To better understand the dissimilarities observed from figure 3 between the YAG-derived YAS glass core and the silica cladding, an electron micrograph analysis is carried out as described in section 3.1. In figure 4, SEM micrographs of the fibre cross sections with the laser polarization direction either // (figures 4(a) and (b)) or $\perp$ (figures 4(c) and (d)) to the writing direction are reported. First, from figures 4(a) and (b), the formation of porous nanogratings is clearly identified in both cladding (silica) and core (YAS) regions, which demonstrates the feasibility of inscribing nanogratings inside this glass composition family (within the range of compositions and laser parameters studied herein). Second, by comparing figures 4(c) with (d), one can observe that at core center a less dense network of nanoplanes are visible compared to the irradiated pure silica cladding region. If only two nanoplanes are easily identified (labeled as 1 and 4 in figure 4(c)), two other ones (labeled as '2?' and '3?') seem to be on the verge of formation. This is in agreement with the reduction of the interplanar distance when increasing pulse numbers in SiO_2 [77].

Based on the results of figures 3 and 4, it can be stated that the increase of R for YAG-derived YAS glass fibre core is expected to be of the same origin as for SiO_2, i.e., formation of a periodic array of porous nanoplanes separated by non-porous glass [55], cooperating to form birefringence [25]. The various parameters that factor into the total R value are identified, measured, and summarized in table 2, and more details can be found in [74].

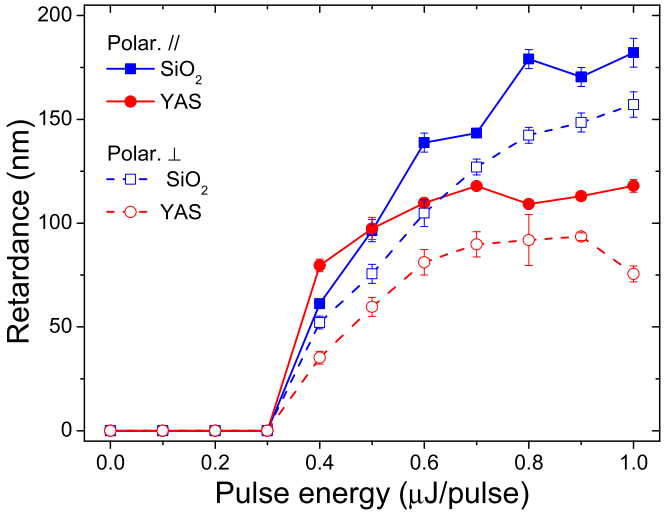

Figure 3. Retardance (R) as a function of pulse energy for: YAG-derived fibre both at the core center (YAS, in red) and in its cladding (silica, in blue). Experimental conditions are: $\lambda = 1030$ nm, 100 kHz, 100 μm s^{-1}, 10^3 pulses/μm, NA $= 0.6$, pulse duration $= 160$ fs, laser polarization $\perp$ and // to writing direction.

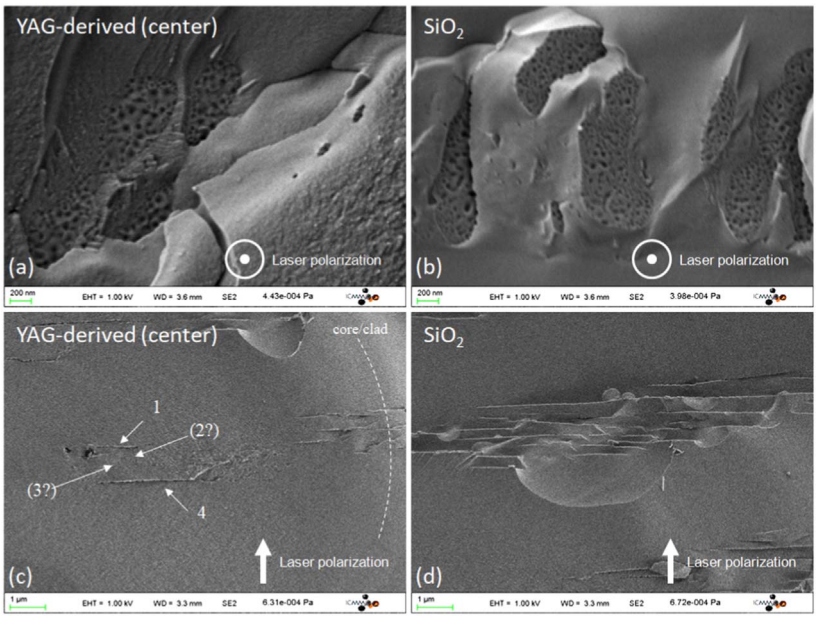

Figure 4. Scanning electron micrographs in the YAG-derived fibre, both at the core center (YAS) and in the cladding (SiO_2), for parallel (a), (b) and orthogonal (c), (d) laser polarization direction with respect to the writing direction. // configuration enables observation of the inside of the nanogratings revealing their nanoporosity (a), (b), while $\perp$ configuration permits sideways visualization of the nanogratings. Laser parameters: $\lambda = 1030$ nm, 100 kHz, 100 μm s^{-1}, 10^3 pulses/μm, NA $= 0.6$, pulse duration $= 160$ fs, E $= 0.8$ μJ/pulse.

The porosity filling factor (ff), which account for the volume of pores per unit glass volume, is found to be slightly higher at the core center than in the silica cladding, while the thickness of its nanoplanes is consequently higher (~45% increase). Now looking at the nanoplane periodicity (Λ), at first, it appears that it is much larger at the core center if we only consider the two well-formed planes (1015 nm versus 330 nm for silica). However, if 4 planes are considered, which includes planes 1, 2, 3, and 4 from figure 4(c), then $\Lambda = 338$ nm, which is close to the value for silica.

Finally, the laser track length (d) is found to be shorter at the core center than in the cladding (13.5 μm versus 19.95 μm). Since d is known and the birefringence can be calculated based on the parameters in table 2 (see [74] for more details), R can be calculated as well ($R = B \times d$) for both cladding and core laser tracks. In the latter case, the nanoplanes throughout the laser track are assumed identical to those at the very core center (i.e., having the same properties), which is certainly not true in reality as the fibre has a graded index profile associated with

Table 2. Comparison between typical nanoplanes' parameters for the YAG-derived fibre at both core center (YAS) and in the cladding (SiO_2).

Materials	SiO_2	YAS
Porosity filling factor, ff. (%)	41.3 ± 0.9	44.5 ± 2.6
Period of the nanoplanes, Λ (nm)	330 ± 7	∼1015 or ∼338[d]
Thickness of porous layer, δ (nm)	42.2 ± 5.5	61.2 ± 11
Laser track length, d (μm)	19.95 ± 1.0	∼13.5
Measured Retardance, R (nm) (at 551 nm)	142 ± 3.8	92 ± 12.2
Index glass background, n_{BG} (550 nm)	1.4599	1.5559[a]
Index porous regions[b], n_{PR} (550 nm)	1.269	1.308
Birefringence, B ($\lvert n_e\text{-}n_o \rvert$)[c]	$\sim 6.3 \times 10^{-3}$	$\sim 5.3 \times 10^{-3}$
Calculated retardance, R_c (nm)[c]	∼125	∼71[e]

[a] Determined from Refractive Index Profile.

[b] Calculated using the Maxwell-Garnett approximation (equation 18 in [78]).

[c] $n_0 = \{[(\Lambda\text{-}\delta)/\Lambda] \times n_{BG}{}^2 + [\delta/\Lambda] \times n_{PR}{}^2]\}^{1/2}$, $n_e = \{[(\Lambda/(\Lambda\text{-}\delta)] \times n_{BG}{}^2 + [\Lambda/\delta] \times n_{PR}{}^2]\}^{1/2}$, in [74, 79], and $R_c = B \times d$.

[d] In figure 4 only two planes are clearly visible in the magnified region. However, the reader should be informed that two additional planes 'in formation' have been identified between the already existing two, which would bring the nanograting periodicity to ∼338 nm.

[e] Calculated with $\Lambda = 1015$ nm.

its composition gradient (see figure 1). However, this assumption is made because the aim of this calculation is to provide a semi-quantitative calculation of what R value can be expected when parameters in table 2 are employed. The calculated R values (R_c) for cladding and core materials were ∼125 nm and ∼71 nm, respectively. These values are in fairly good agreement with the measured values (∼142 nm and ∼72 nm, respectively), although a bit lower in magnitude for SiO_2. This can be attributed to the stress field contribution associated with the formed nanoplanes [80]. Moreover, it appears that the R values between core and cladding principally differ due to their different laser track lengths, but the calculated form birefringence values from the nanostructures opto-geometrical parameters (see table 2) are somewhat similar ($\sim 6.3 \times 10^{-3}$ in SiO_2 versus $\sim 5.3 \times 10^{-3}$ in YAS).

3.2.2. Thermal stability

The YAG-derived fibre segment was heat-treated to 1100 °C after inscription following figure 2(a). R as a function of temperature, R(T), was measured for each energy. The R(T) profile was found to be independent of the pulse energy, although its magnitude is changed (lower pulse energy results in lower R values, as shown in figure 3). Consequently, for each temperature the retardance was averaged over the whole energy range investigated (from 0.1 μJ to 1 μJ). The latter was thus normalized relative to its initial (at T = 25 °C) value, and this operation was repeated for SiO_2 and YAS both in // and ⊥ writing conditions. The results are displayed in figure 5.

From figure 5, the evolution of R as a function of temperature shows some characteristic features, commonly found in both the YAG-derived fibre core center and cladding. First, there is a slight increase in the R value up to 700 °C, more pronounced for both the core center and the SMF samples. Such a feature is attributed to the annealing of point defects formed mostly within nanoplanes [79], promoting an increase of nanogratings index contrast, thus B and, in our case, R. From [81], defects such as non-bridging oxygen hole-centers relax between 300 °C–600 °C, and this within a few minutes at 600 °C. This also is the case for SiE' defects. In other words, this is attribued in the literature to the co-existence of both Type I and Type II index changes [82]. In contrast, changes in Si-O three and four-fold rings anneal out at higher temperatures (typically 700 °C–900 °C range) [81].

As the heat-treatment temperature is increased, induced stress relaxes and consequently to this the refractive index contrast further lessens, and so does R. Finally, above 1000 °C, R diminishes dramatically, and no birefringence is detected after 1075 °C (and the laser tracks are not visible under optical microscope). Beyond 1100 °C both glasses (YAS and SiO_2) converge to R = 0.

By comparing thermal behavior for both SiO_2 and YAS glasses, the former (SiO_2) exhibits a decrease in R values starting roughly around 700 °C. On the other hand, the latter (YAS) shows no decrease in R up to 1000 °C. At this temperature, R value for SiO_2 has already decreased by ∼30%, and suggests that femtosecond-written nanogratings (or so called Type II regime) in YAG-derived fibres may present advantages for high temperature operations over conventional silicate-based fibres. In particular it should be noted that pure silica core fibres have a F-doped cladding, whereas common fibres like SMF-28 have a Ge-doped core, which impacts the high temperature performances of such FBGs.

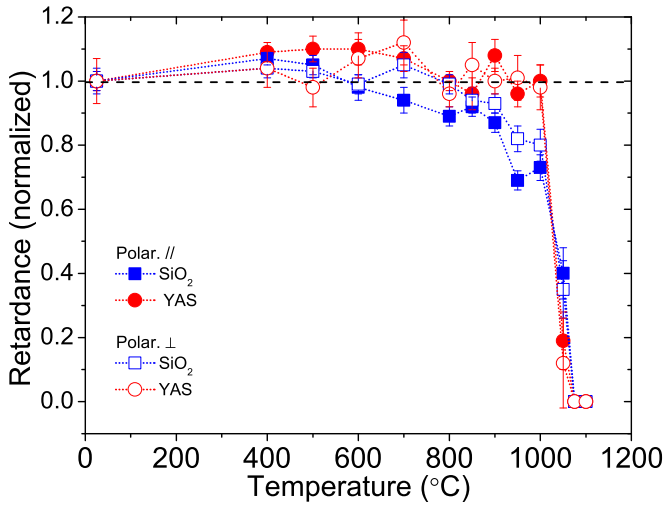

Figure 5. Normalized retardance (averaged over the 0.1 to 1.0 μJ pulse energy range) as a function of temperature for YAG-derived fibre at the core center (YAS) and in the cladding (SiO_2), for both // and ⊥ configurations. The measurements were performed at room temperature.

4. Conclusions

An overview of FBGs for high and ultra-high temperature applications was presented and, in particular, the ability of Type II and Type III femtosecond-laser induced nanostructures to withstand ultra-high temperatures was discussed.

Here, femtosecond-inscription on a yttrium aluminosilicate core—silica cladding glass optical fibre was investigated. It was shown that Type II (nanograting structures) can be photo-induced in this glass composition, and that the laser parameters investigated (pulse energy range, polarization orientation) show that the yttrium aluminosilicate core material response to fs laser irradiation globally resembles that of SiO_2. Additionally, isochronal thermal annealing show an improved thermal stability of Type II modifications written in the core material compared to its SiO_2 cladding. Indeed, the measured retardance in the core shows no decrease in magnitude at temperatures lower than 1000 °C. In contrast, in the F300 SiO_2 cladding, the retardance lowers after 700 °C–800 °C, and has already decreased by ~30% at 1000 °C. Fabrication of fibres with lower SiO_2 concentration in the core (i.e., higher Y_2O_3 and Al_2O_3 dopant concentration) may permit fabrication of fs-laser structures with even higher thermal stability. Further work is underway to characterize nanogratings inscribed in fibre core segments with higher Y_2O_3 and Al_2O_3 content, as well as writing FBGs in these fibre families for lifetime prediction analysis.

Finally, in this paper the Authors advocate an approach based on the development of new fibres with high melting points conjugated to femtosecond direct writing. Non-conventional fibre fabrication techniques, such as the MCM, allow a different route, relative to conventional CVD techniques, to fabricating such fibres. These 'high temperature fibres' could be composed of aluminosilicate cores such as Al_2O_3-SiO_2 (>50 mole% of Al_2O_3), Y_2O_3-Al_2O_3-SiO_2 (as reported in this paper) and potentially fibres with other compositions like in binary SiO_2-ZrO_2 or ternary SiO_2-ZrO_2-Al_2O_3 glass systems. This fibre fabrication method to develop a new range of host fibres suitable for writing ultra-high temperature FBGs and overcoming the current performances of pure silica core or Ge-doped SiO_2 fibres appears promising.

Acknowledgments

The Authors would like to acknowledge Francois Brisset (ICMMO, Université Paris-Sud) for his support in electron microscopy. The Author's (JB and PD) acknowledge financial support from the US Department of Defense High Energy Laser Joint Technology Office (HEL JTO). M L and B P would like to thank CNRS Défi Instrumention aux limites—UltraBragg—for financing this work.

ORCID iDs

Maxime Cavillon https://orcid.org/0000-0003-1341-6294
Peter Dragic https://orcid.org/0000-0002-4413-9130

John Ballato https://orcid.org/0000-0001-5910-3504

References

[1] Åslund M L, Canning J, Canagasabey A, Assis de Oliveira R, Liu Y, Cook K and Peng G 2012 Mapping the thermal distribution within a silica preform tube using regenerated fibre Bragg gratings *Int. J. Heat Mass Transf.* **55** 3288–94

[2] Walker R B, Ding H, Coulas D, Grobnic D, Mihailov S J, Duchesne M A, Hughes R W, McCalden D J and Burchat R 2015 Entrained-flow gasifier and fluidized-bed combustor temperature monitoring using arrays of fs-IR written fiber Bragg gratings *24th Int. Conf. in Optical Fibre Sensors (OFS24)* p 96343X

[3] Mezzadri F, Janzen F C, Martelli C, Canning J and Cook K 2012 Monitoramento de temperatura em turbina de motor diesel de locomotiva com sensor a fibra optica *15th Brazilian Symp. for Microwaves and Optoelectronics (SBMO) and the 10th Brazilian Congress for Electromagnetics (CBMag)*

[4] Rinaudo P, Torres B, Paya-Zaforteza I, Calderón P A and Sales S 2015 Evaluation of new regenerated fiber Bragg grating high-temperature sensors in an ISO 834 fire test *Fire Saf. J.* **71** 332–9

[5] Unnikrishnan K 2017 Iceland is drilling the world's deepest geothermal well *Digit. J.* **2017** 484178

[6] Canning J *et al* 2009 Optical fibre Bragg gratings for high temperature sensing *20th Int. Conf. on Optical Fibre Sensors* p 75032N

[7] Mihailov S J, Grobnic D, Hnatovsky C, Walker R B, Lu P, Coulas D and Ding H 2017 Extreme environment sensing using femtosecond laser-inscribed fiber bragg gratings *Sensors* **17** 2909

[8] Liao C R and Wang D N 2013 Review of femtosecond laser fabricated fiber Bragg gratings for high temperature sensing *Photonic Sens.* **3** 97–101

[9] Johnson J, Weber R and Grimsditch M 2005 Thermal and mechanical properties of rare earth aluminate and low-silica aluminosilicate optical glasses *J. Non. Cryst. Solids* **351** 650–5

[10] Lago D C and Prado M O 2013 Crystallization of yttrium and samarium aluminosilicate glasses *Phys. Procedia* **48** 10–6

[11] Weber R, Sen S, Youngman R E, Hart R T and Benmore C J 2008 Structure of high alumina content Al_2O_3-SiO_2 composition glasses *J. Phys. Chem.* B **112** 16726–33

[12] Schaller T and Stebbins J F 1998 The structural role of lanthanum and yttrium in aluminosilicate glasses: A ^{27}Al and ^{17}O MAS NMR study *J. Phys. Chem.* B **102** 10690–7

[13] Betz D, Trutzel M N, Staudigel L, Martin W and Krumpholz O 2000 Fiberoptic smart sensing of component deformations in adaptive wings *ICAS 2000 Congress* pp 1–495

[14] Huang L, Dyer R S, Lago R J, Stolov A A and Li J 2016 Mechanical properties of polyimide coated optical fibers at elevated temperatures *Optical Fibers and Sensors for Medical Diagnostics and Treatment Applications XVI* **9702** 97020Y

[15] Semjonov S L, Bubnov M M, Dianov E M and Shchebunyaev A G 1994 Reliability of aluminum-coated fibers at high temperature *Proc. SPIE 2074, Fiber Optics Reliability and Testing: Benign and Adverse Environments* ed D K Paul and H H Yuce

[16] Biriukov A S, Bogatyrjov V A, Lebedev V F, Sysolyatin A A and Khitun A G 1998 Strength and reliability of metal-coated optical fibers at high temperatures *MRS Proc.* **531** 297–300

[17] Stanczyk T *et al* 2015 Influence of high temperatures on optical fibers coated with multilayer protective coatings *Proc. SPIE 9816, Optical Fibers and Their Applications* **2015** 98160F

[18] He J, Ding L, Cai J, Zhu W and Dai J 2019 A novel high temperature resistant Mo-Cu functional gradient coating for optic fiber Bragg grating *Results Phys.* **14** 102456 (2–10)

[19] Technica https://technicasa.com/

[20] Laffont G, Cotillard R, Roussel N, Desmarchelier R and Rougeault S 2018 Temperature resistant fiber bragg gratings for on-line and structural health monitoring of the next-generation of nuclear reactors *Sensors* **18** 1791

[21] Jinesh M, MacPherson W N, Hand D P and Maier R R J 2016 Stainless steel component with compressed fiber Bragg grating for high temperature sensing applications *Proc. SPIE 9916, Sixth European Workshop on Optical Fibre Sensors* p 99160J

[22] Tu Y, Ye L, Zhou S P and Tu S T 2017 An improved metal-packaged strain sensor based on a regenerated fiber bragg grating in hydrogen-loaded boron–germanium co-doped photosensitive fiber for high-temperature applications *Sensors* **17** 1–18

[23] Kashyap R 2010 *Fiber Bragg Gratings* (Amsterdam: Elsevier)

[24] Chan J W, Huser T, Risbud S and Krol D M 2001 Structural changes in fused silica after exposure to focused femtosecond laser pulses *Opt. Lett.* **26** 1726–8

[25] Bricchi E, Klappauf B G and Kazansky P G 2004 Form birefringence and negative index change created by femtosecond direct writing in transparent materials *Opt. Lett.* **29** 119–21

[26] Glezer E N, Milosavljevic M, Huang L, Finlay R J, Her T-H, Callan J P and Mazur E 1996 3D optical storage inside transparent materials *Opt. Lett.* **21** 2023–6

[27] Martinez A, Dubov M, Khrushchev I and Bennion I 2006 Photoinduced modifications in fiber gratings inscribed directly by infrared femtosecond irradiation *IEEE Photonics Technol. Lett.* **18** 2266–8

[28] Åslund M L, Canning J, Stevenson M and Cook K 2010 Thermal stabilization of Type I fiber Bragg gratings for operation up to 600 °C *Opt. Lett.* **35** 586–8

[29] Canning J 2000 Photosensitization and photostabilization of laser-induced index changes in optical fibers *Opt. Fiber Technol.* **6** 275–89

[30] Canning J 2008 Fibre gratings and devices for sensors and lasers *Laser Photonics Rev.* **2** 275–89

[31] Dong L and Liu W F 1997 Thermal decay of fiber Bragg gratings of positive and negative index changes formed at 193 nm in a boron-codoped germanosilicate fiber *Appl. Opt.* **36** 8222–6

[32] Dong L, Liu W F and Reekie L 1996 Negative-index gratings formed by a 193-nm excimer laser *Opt. Lett.* **21** 2032–4

[33] Groothoff N and Canning J 2004 Enhanced type IIA gratings for high-temperature operation *Opt. Lett.* **29** 2360–2

[34] Frazão O, Lima M J N and Santos J L 2003 Simultaneous measurement of strain and temperature using type I and type IIA fibre Bragg gratings *J. Opt. A: Pure Appl. Opt.* **5** 183–5

[35] Lindner E, Canning J, Chojetzki C, Brückner S, Becker M, Rothhardt M and Bartelt H 2011 Thermal regenerated type IIa fiber Bragg gratings for ultra-high temperature operation *Opt. Commun.* **284** 183–5

[36] Cook K and Canning J 2008 High-temperature type IIa gratings in 12-ring photonic crystal fibre with germanosilicate core *J. Eur. Opt. Soc.—Rapid Publ.* **3** 08031 (1–5)

[37] Lindner E, Canning J, Chojetzki C, Brückner S, Becker M, Rothhardt M and Bartelt H 2011 Post-hydrogen-loaded draw tower fiber Bragg gratings and their thermal regeneration *Appl. Opt.* **50** 2519–22

[38] Bandyopadhyay S, Canning J, Stevenson M and Cook K 2008 Ultrahigh-temperature regenerated gratings in boron-codoped germanosilicate optical fiber using 193 nm *Opt. Lett.* **33** 1917–9
[39] Wang T, Shao L-Y, Canning J and Cook K 2013 Temperature and strain characterization of regenerated gratings *Opt. Lett.* **38** 247–9
[40] Cook K, Smelser C, Canning J, le Garff G, Lancry M and Mihailov S 2012 Regenerated femtosecond fibre Bragg gratings *Third Asia Pacific Optical Sensors Conf.* p 835111
[41] Canning J, Stevenson M, Bandyopadhyay S and Cook K 2008 Extreme silica optical fibre gratings *Sensors* **8** 6448–52
[42] Åslund M L, Canning J, Fu H and Tam H 2010 Rapid disappearance of regenerated fibre Bragg gratings at temperatures approaching 1500 °C in boron-codoped germanosilicate optical fibre *Fourth European Workshop on Optical Fibre Sensors (EWOFS'10)* p 76530Q
[43] Laffont G, Cotillard R and Ferdinand P 2013 9000 h-long high temperature annealing of regenerated Fiber Bragg 9000 hours-long high temperature annealing of regenerated Fiber Bragg gratings *Proc. SPIE 8794, Fifth European Workshop on Optical Fibre Sensors* p 87941X
[44] Chen T, Chen R, Jewart C, Zhang B, Cook K, Canning J and Chen K P 2011 Regenerated gratings in air-hole microstructured fibers for high-temperature pressure sensing *Opt. Lett.* **36** 3542–4
[45] Chen R, Yan A and Chen K P 2014 High-temperature flow sensing using regenerated gratings in self-heated high attenuation fibers *CLEO:2014, OSA Technical Digest* p paper SF2I.2
[46] Shao L, Canning J, Wang T, Cook K and Tam H-Y 2013 Viscosity of silica optical fibres characterized using regenerated gratings *Acta Mater.* **61** 6071–81
[47] Canning J, Stevenson M and Fenton J 2009 Regenerated gratings *J. Eur. Opt. Soc.—Rapid Publ.* **4** 09052 (2–7)
[48] Gao S, Canning J and Cook K 2013 Ultra-high temperature chirped fiber Bragg gratings produced by gradient stretching of viscoelastic silica *Opt. Lett.* **38** 5397–400
[49] Wang T, Shao L, Canning J and Cook K 2013 Regeneration of fiber Bragg gratings under strain *Appl. Opt.* **52** 2080–5
[50] Laffont G, Cotillard R and Ferdinand P 2013 Multiplexed regenerated Fiber Bragg Gratings for high temperature measurement *Meas. Sci. Technol.* **24** 094010
[51] Mihailov S J, Grobnic D, Smelser C W, Walker R B, Lu P and Ding H 2011 Review of femtosecond infrared laser-induced fibre Bragg grating sensors made with a phase mask *Sens. Rev.* **31** 321–7
[52] Martinez A, Dubov M, Khrushchev I and Bennion I 2004 Direct writing of fibre Bragg gratings by femtosecond laser *Electron. Lett* **40** 1–2
[53] Albert J, Fokine M and Margulis W 2002 Grating formation in pure silica-core fibers *Opt. Lett.* **27** 809–11
[54] Groothoff N, Canning J, Buckley E, Lyttikainen K and Zagari J 2003 Bragg gratings in air-silica structured fibers *Opt. Lett.* **28** 233–5
[55] Lancry M, Poumellec B, Canning J, Cook K, Poulin J-C and Brisset F 2013 Ultrafast nanoporous silica formation driven by femtosecond laser irradiation *Laser Photonics Rev.* **7** 953–62
[56] Lancry M, Poumellec B, Chahid-Erraji A, Beresna M and Kazansky P G 2011 Dependence of the femtosecond laser refractive index change thresholds on the chemical composition of doped-silica glasses *Opt. Mater. Express* **1** 711
[57] Royon M, Marin E, Girard S, Boukenter A, Ouerdane Y and Stoian R 2019 X-ray preconditioning for enhancing refractive index contrast in femtosecond laser photoinscription of embedded waveguides in pure silica *Opt. Mater. Express* **9** 65–74
[58] Grobnic D, Smelser C W, Mihailov S J and Walker R B 2006 Long-term thermal stability tests at 1000 °C of silica fibre Bragg gratings made with ultrafast laser radiation *Meas. Sci. Technol.* **17** 1009–13
[59] Morana A, Girard S, Marin E, Marcandella C, Paillet P, Périsse J, Macé J-R, Boukenter A, Cannas M and Ouerdane Y 2014 Radiation tolerant fiber Bragg gratings for high temperature monitoring at MGy dose levels *Opt. Lett.* **39** 5313–6
[60] Lu J, Yang M, Wang D N, Grattan K T, Sun T and Li Y 2009 Fiber Bragg gratings with enhanced thermal stability by residual stress relaxation *Opt. Express* **17** 19785–90
[61] Robnic D A N G, Natovsky C Y H and Ihailov S T J M 2016 Low loss Type II regenerative Bragg gratings made with ultrafast radiation *Opt. Express* **24** 28704–12
[62] Martinez A, Khrushchev I Y and Bennion I 2005 Thermal properties of fibre Bragg gratings inscribed point-by-point by infrared femtosecond laser *Electron. Lett* **41** 176–8
[63] Warren-Smith S C, Nguyen L V, Ebendorff-Heidepriem H, Lang C and Monro T M 2016 Temperature sensing up to 1300 °C using suspended-core microstructured optical fibers *Opt. Express* **24** 3714–9
[64] ANFF—OptoFab NODE http://optofab.org.au/uli.html
[65] Femto Fiber Tec https://femtofibertec.de/de/#home
[66] Habisreuther T, Elsmann T, Pan Z, Graf A, Willsch R and Schmidt M A 2015 Sapphire fiber Bragg gratings for high temperature and dynamic temperature diagnostics *Appl. Therm. Eng.* **91** 860–5
[67] Busch M, Ecke W, Latka I, Fischer D, Willsch R and Bartelt H 2009 Inscription and characterization of Bragg gratings in single-crystal sapphire optical fibres for high-temperature sensor applications *Meas. Sci. Technol.* **20** 1–6
[68] Elsmann T *et al* 2014 High temperature sensing with fiber Bragg gratings in sapphire-derived all-glass optical fibers *Opt. Express* **22** 26825–33
[69] Dragic P, Hawkins T, Foy P, Morris S and Ballato J 2012 Sapphire-derived all-glass optical fibres *Nat. Photonics* **6** 627–33
[70] Grobnic D, Mihailov S J, Ballato J and Dragic P D 2015 Type I and II Bragg gratings made with infrared femtosecond radiation in high and low alumina content aluminosilicate optical fibers *Optica* **2** 313–22
[71] Ballato J and Peacock A C 2018 Perspective: Molten core optical fiber fabrication—a route to new materials and applications *APL Photonics* **3** 120903(1)-120903(14)
[72] Dragic P, Law P-C, Ballato J, Hawkins T and Foy P 2010 Brillouin spectroscopy of YAG-derived optical fibers *Opt. Express* **18** 10055–67
[73] Sanamyan T *et al* 2009 On the fabrication of all-glass optical fibers from crystals *J. Appl. Phys.* **105** 053110
[74] Desmarchelier R, Poumellec B, Brisset F, Mazerat S and Lancry M 2015 In the heart of femtosecond laser induced nanogratings: from porous nanoplanes to form birefringence *World J. Nano Sci. Eng.* **5** 115–25
[75] Nesterov A V and Niziev V G 1999 Influence of beam polarization on laser cutting efficiency *J. Phys. D: Appl. Phys.* **32** 1455–61
[76] Kazansky P G, Shimotsuma Y, Sakakura M, Beresna M, Gecevi M, Svirko Y, Akturk S, Qiu J, Miura K and Hirao K 2011 Photosensitivity control of an isotropic medium through polarization of light pulses with tilted intensity front *Opt. Express* **19** 20657–64
[77] Richter S, Heinrich M, Döring S, Tünnermann A, Nolte S and Peschel U 2012 Nanogratings in fused silica: formation, control, and applications *J. Laser Appl.* **24** 042008(1)-042008(8)
[78] Markel V A 2016 Introduction to the Maxwell Garnett approximation: tutorial *J. Opt. Soc. Am.* A **33** 1244–56
[79] Bricchi E and Kazansky P G 2006 Extraordinary stability of anisotropic femtosecond direct-written structures embedded in silica glass *Appl. Phys. Lett.* **88** 2–4

[80] Thomson R R, Gillet P, Mukherjee S, Cheng Y, Bellouard Y, Pépin C, McMillen B and Champion A 2016 Stress-state manipulation in fused silica via femtosecond laser irradiation *Optica* **3** 1285
[81] Witcher J J, Reichman W J, Fletcher L B, Troy N W and Krol D M 2013 Thermal annealing of femtosecond laser written structures in silica glass *Opt. Mater. Express* **3** 502–10
[82] Smelser C W, Mihailov S J and Grobnic D 2005 Formation of Type I-IR and Type II-IR gratings with an ultrafast IR laser and a phase mask *Opt. Express* **13** 5377–86

4.2 3D laser engineering of molten core fibers: towards a new generation of harsh environment sensing devices

Title: 3D laser engineering of molten core fibers: towards a new generation of harsh environment sensing devices

*Yitao Wang, Maxime Cavillon, John Ballato, Tino Elsmann, Manfred Rothhardt, Rudy Desmarchelier, Guillaume Laffont, Bertrand Poumellec, and Matthieu Lancry**

Yitao.Wang, Dr. Cavillon, Prof. Poumellec, Prof. Lancry
Institut de Chimie Moléculaire et des Matériaux d'Orsay (ICMMO/SP2M/MAP), Université Paris-Saclay, CNRS, 91405 Orsay Cedex, France
E-mail: matthieu.lancry@universite-paris-saclay.fr

Prof. Ballato
Center of Optical Materials Science and Engineering Technologies (COMSET), Clemson University, Clemson, USA

Dr. Elsmann, Mr. Rothhardt
Leibniz Institute of Photonic Technology, Albert-Einstein-Str. 9, 07745 Jena, Germany

Dr. Desmarchelier, Dr. Laffont
CEA, LIST, Laboratoire Capteurs et Architectures Electroniques, F-91191 Gif-sur-Yvette, France

Keywords: fiber sensor, birefringence, femtosecond laser, Rayleigh backscattering, eutectic

Abstract text: We highlight here that aluminosilicate glasses exhibit a huge potential as host for a new generation harsh environment optical devices. As a demonstration, we exploit here a non-conventional manufacturing process, i.e. the molten core method, that enables to manufacture Sapphire (Al_2O_3) or YAG (Yttrium Aluminum Garnet) derived silicate optical fibers. Femtosecond (fs) laser nanostructuring was used to imprint oriented phase separation inside these fibers. Both the writing kinetics and thermal withstanding of the modified regions were investigated under a wide temperature range (20-1200 °C). The laser-imprinted changes in these aluminosilicate fibers own better thermal stability even compared to SiO_2 and SMF28 commercial GeO_2-doped silica fibers. In addition, taking profit of the "amplified" Rayleigh backscattering also revealed the high temperature sensitivity of these non-conventional fibers. This suggests that the 3D functionalization of aluminosilicate fibers by femtosecond laser direct writing open the door to a new generation of optical devices suitable for high temperature operation.

1. Introduction

There is an increasing broad demand for high-temperature (HT) materials for a wide range of industries and applications, such as aviation / space (aeronautical turbine engine, launcher), manufacturing (3D laser additive manufacturing of metal or ceramics parts, steel industry), Nuclear (instrumentation of future reactors and tokamaks), or again in photonics (high power lasers, long-term optical data storage, etc) and optical sensing (structural health monitoring, …). In most applications operating in a HT environment, refractory crystalline oxide materials such as Alumina (Al_2O_3) or zirconia (ZrO_2) are excellent candidates, due to their high melting points and good resistance to oxidation and abrasion. Furthermore, directionally solidified eutectic ceramics (e.g., unidirectionally solidified Al_2O_3/Oxide eutectic composite made of perovskite or garnet phase) also can improve the thermal stability

efficiency, as demonstrated for instance in aircraft gas turbines and of thermal power generation systems (e.g., operation for 1000 h at 1700 °C [1]).

However, many HT applications such as eternal data storage or optical sensors (down-hole oil/gas exploration, monitoring of structure health, and temperature regulation of engines, etc.) require using glass materials that can be functionalized and shaped into chips, disks, planar waveguides or optical fibers. Both the materials and geometry design bring mandatory requisites for these applications, such as compactness and lightness, flexibility, high-transparency, fast and complex manufacturing shaping, again chemical/radioactive/electromagnetic resistance, and even the low cost. For these reasons, glass optical materials have been extensively used and functionalized over the past three decades [2-4].

From now, concomitant advances in materials chemistry, glass manufacturing methods, and ultrafast laser nanostructuring of transparent materials (i.e., to functionalize the material), open the door to develop such sensing devices but also optical data storage systems that could withstand harsh environments, such as thermo-mechanical solicitations much beyond the 800 °C limit [3, 5, 6]. Thus developing a new generation of reliable and robust sensing technologies for industrial processes that take place under extreme physical conditions require improved thermal stability of the optical devices [7, 8]. The bottleneck to this continuous enhancement of HT stability is related to *intrinsic nature of glass and the laser-induced structural changes* that constitute the optical device. This includes considering HT dynamics of viscous flow, chemical migration, and stress relaxation [9].

Up to now the current material limitation is mostly related to the use of conventional manufacturing method such as Chemical Vapor Deposition and mostly exploiting "golden standard" glasses such as SiO_2 and GeO_2-SiO_2. To go beyond the limitations imposed by conventional techniques, in this work with investigate a new route, through the use of a non-conventional (i.e., as opposed to CVD) fabrication technique mostly dedicated to optical fibers, the Molten Core Method (MCM) [10]. The later enables a large flexibility in the choice of composition (both its nature and composition) and even manufacture fibers with "unstable" core compositions, such as the silica-based novel fibers from precursors like Sapphire (Al_2O_3), YAG (Yttrium Aluminium Garnet) or ZrO_2 crystals.

Now starting from these dedicated glass materials for HT operation, ***femtosecond laser direct writing*** offers a new advantage, partly in a non-conventional way: it allows restructuring of our most important optical materials, to enable the imprinting of permanent optical properties for HT operation. Here some aspects of the light-matter interaction are fundamentally new e.g. solid and plasma coexist for a fraction of picoseconds. In this operation, the solid is restructured by the force field created during the laser irradiation. This is a new physics but new chemistry too since the processes involved are performed in highly excited states, and largely off equilibrium. This open the door towards the 3D writing of oriented structural modifications like self-organized nanostructures (so-called nanogratings), directionally solidified oxide decomposition or oriented nanocrystals with outstanding thermal stability.

In this paper, being somehow inspired by these unidirectionally solidified Al_2O_3 based eutectics, we decided to investigate both Sapphire and YAG-derived glass optical fibers that will pave the way to the future development of a new generation of oxide glasses or glass-ceramics dedicated to ultrahigh temperature applications. Femtosecond laser direct writing was performed to imprint an oriented phase separation taking the form of nanogratings (ref) as seen by scanning electron microscopy (SEM). Kinetics and thermal stability of the aforementioned modifications was thus studied and further compared to key optical materials like SiO_2 and GeO_2-SiO_2. To validate our approach, we also demonstrate the HT performance of these materials by making a distributed fiber sensor based on optical frequency-domain

reflectometry (OFDR); which utilizes the intrinsic Rayleigh scattering inherent to these fs-laser induced phase separation.

2. Results and Disscussion

Writing Kinetic of Type-II Modification in Aluminosilicate Fibers

Measurements of retardance, *R*, as a function of the laser pulse energy are exhibited in Fig. 1 for all investigated fibers. Data recorded in the pure silica cladding are also shown for comparison. The laser energy above the Type II threshold modified the optical properties of the irradiated regions.

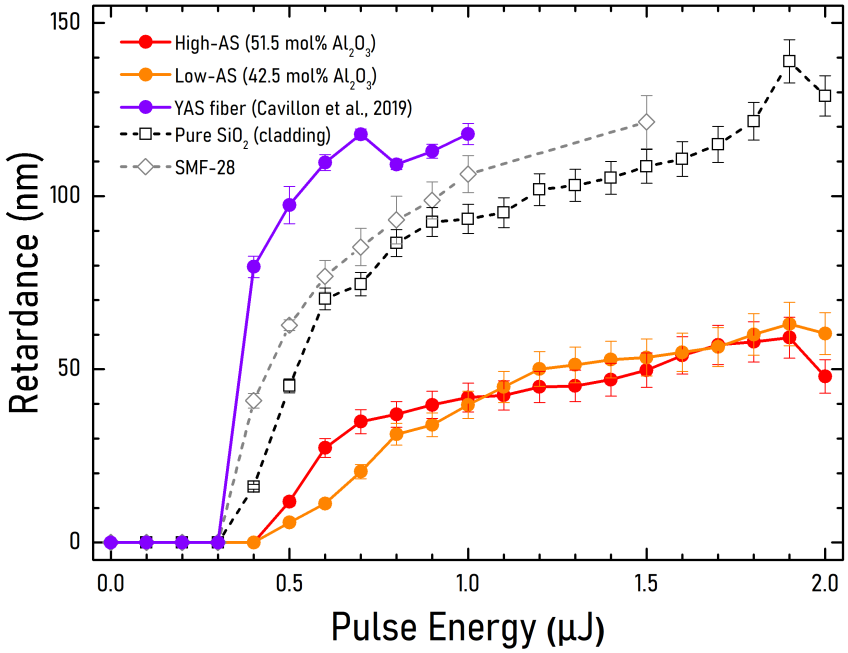

Figure 1. Retardance (R) as a function of pulse energy for aluminosilicate fibers: High-AS (red) and Low-AS (orange) and pure silica taken from the cladding (black). The yttrium aluminosilicate fiber, YAS (purple) and the SMF-28 fiber (grey) are also shown for comparison. Experimental conditions are: λ = 1030 nm, 100 kHz, 100 µm/s, 1000 pulses/µm, NA = 0.6, pulse duration = 160 fs, laser polarization parallel to the writing direction.

The lowest energy at which a non-zero R value is detected corresponds to the IR-fs-Type II threshold, and where polarization dependent anisotropic optical properties start to appear in the irradiated lines (formation of nanogratings). As we illustrated in Fig. 7(c), a strong linear birefringence can be detected under polarized optical microscope between crossed polarizers when the energy exceeds this threshold. This is likely originating from the formation of nanogratings [11] as it is well known in silica or slightly doped silica [12, 13]. In our experimental conditions, the Type II thresholds are located in the range of 0.3 - 0.4 uJ and is composition dependent [12]. Here, the threshold slightly depends on the Al_2O_3 concentration and can increase up to 0.44 +/- 0.05 uJ for both aluminosilicate fibers. In contrast, the other samples exhibit very similar behavior with the threshold situated at 0.35 µJ. Above Type II threshold, the retardance generally follows a monotonous increase with the pulse energy. Observing the trends in Fig. 1, the pure silica cladding and the SMF 28 fiber (96 mol% silica) display a similar trend with the low pulse energy (< 1 uJ). Interestingly, the two aluminosilicate fibers exhibit much lower retardance values relative to the silica-rich glasses. We also observe that the progressive increase of R rapidly reaches a plateau around E_p = 0.75

μJ for all glass compositions. The R values for the aluminosilicate fibers are approximately half the values of pure silica (50 nm and 100 nm at E_p = 1.5 μJ, respectively).

Scanning Electron Micrographs in the Aluminosilicate Fibers

To investigate the observed differences and trends in the retardance measurement, and to comprehend the effect of high Al_2O_3 addition into the final morphology of the modified regions, we performed a Scanning Electron Microscope analysis. It enabled us to confirm the existence of nanogratings in both the aluminosilicate fiber core and the silica cladding of the sapphire derivate fibers. This is exemplified with Fig. 2, where SEM micrographs of the High-AS fiber cross-sections are selected and reported, using both the laser polarization direction oriented perpendicular (Fig. 2(a) and (b)) or parallel (Fig. 2(c)) to the writing direction.

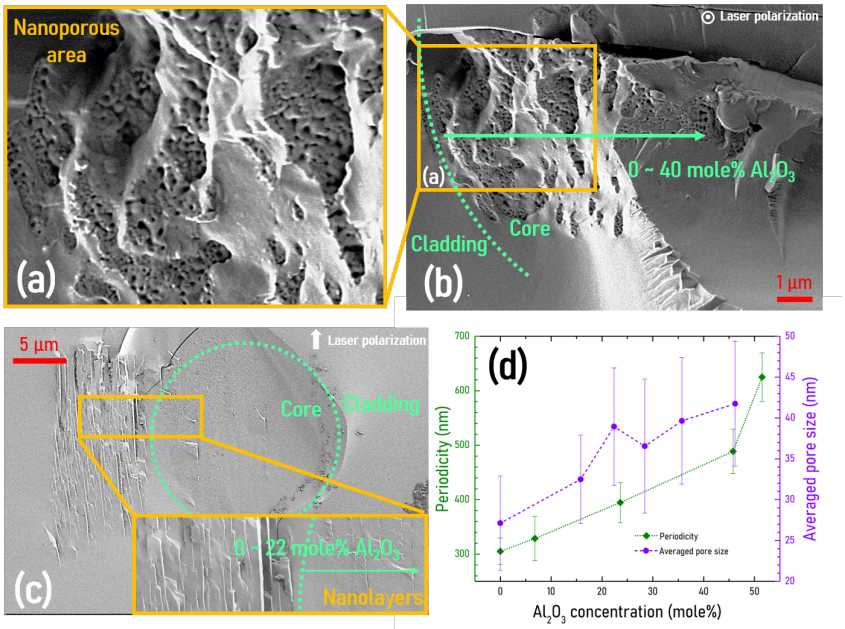

Figure 2. Scanning electron micrographs in the High-AS fiber, for parallel **(a)** and **(b)**, and orthogonal **(c)** laser polarization direction with respect to the writing direction. Experimental conditions are: λ = 1030 nm, 100 kHz, 100 μm/s, 1000 pulses/μm, NA = 0.6, E=1.0 μJ/pulse. **(d)** averaged nanopore size and periodicity of nanoporous planes as a function of the Al_2O_3 content in the fiber core, results measured from **(c)**.

Investigating the Fig. 2(a) and (b) in the perpendicular configuration, and moving from the core/cladding interface nearly to the core center, a periodic nanolayers structure could be easily observed. Similarly, in Fig. 2(c), using a polarization orientation parallel to the writing direction (Xx configuration), we observe that the formation of nanoporous structure throughout the compositional range. Fig. 2(d) summarizes the evolution of the averaged pore size and periodicity in the nanoporous and nanolayers structure respectively, as the function of Al_2O_3 concentration. First, the average spacing (periodicity) gradually decreases with the increase of the Al_2O_3 concentration can be observed. The periodicity for silica cladding is estimated around 305 nm that is quite similar to our previous investigation [14]. Then as the Al_2O_3 concentration increases, we observe an average spacing up to 630 nm for 51.5 mol% Al_2O_3, which is close to two times of the value for silica. We can also see that the nanopores size follows the same trends since it increases around 50% from 27 nm in the fiber cladding up to 42 nm near the center of the core.

For completeness, we point out that the existence of nanogratings can still be observed up to the core center in agreement with recent work published in bulk samples [15]. All these results suggest that the measured retardance in aluminosilicate fibers is of the same origin as for SiO_2, i.e., production of a periodic array of porous nanoplanes separated by non-porous glass [16], resulting in a form birefringence [17].

Thermal Stability of Type II Modification in Aluminosilicate Fibers

Step isochronal annealing (Δt = 30 minutes) is carried out in order to investigate the thermal stability of Type II modifications in High-AS fiber. The fiber was irradiated at different pulse energies in order to investigate the dependence of the thermal stability with the writing conditions. Fig. 3 shows the evolution of normalized retardance (R_{norm}) as a function of the heat treatment temperature.

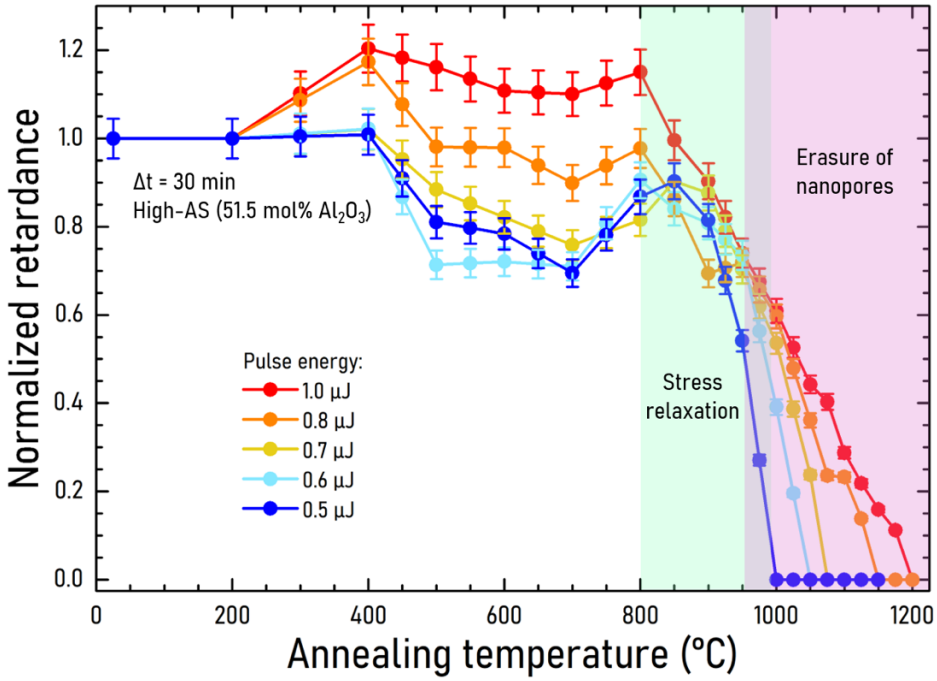

Figure 3. Normalized retardance $R_{norm}(\Delta t,T)$ as a function of annealing temperature for High-AS fiber irradiated with different pulse energies. Experimental conditions are: λ = 1030 nm, 100 kHz, 100 µm/s, 1000 pulses/µm, NA=0.6, laser polarization ⊥ to writing direction (Yx). All measurements were performed at room temperature.

Several features in the normalized retardance $R_{norm}(\Delta t,T)$ can be distinguished according to the annealing temperature and depending on the pulse energy considered.

Within Type II regime and for pulse energy smaller than 0.7 µJ: the retardance exhibits a monotonous decrease immediately after the heat treatment from 400°C to 700 °C. Depending on the pulse energy, the largest decay of R_{norm} can reach about 35% for the lowest writing pulse energy (E = 0.5 µJ). Then there is a slight "recovery", namely an increase of the measured $R_{norm}(\Delta t,T)$ within the 600 – 800 °C temperature range, and which appears around $0.9T_a$ (T_a is the glass annealing temperature). This agrees well with the glass annealing temperature of $50Al_2O_3:50SiO_2$ that is estimated to be around 830-850 °C [18].

For pulse energy greater than 0.65 µJ: the $R_{norm}(\Delta t,T)$ unfold a different thermal behavior. It increases from the beginning of the heat treatments at 200 °C and up to 400 °C. Then, some ups and downs of R_{norm} appear between 400 °C - 800 °C. However, for the line written at 1 uJ, it always keeps a R_{norm} growth of about 15% - 20% compare with its initial value. This is in agreement with the results related to Type II Fiber Bragg gratings reported by

Mihailov group in aluminosilicate fibers with Al_2O_3 content up to 30 mol% and in silica fibers as well [19].

Then as the annealing temperature increases, $R_{norm}(\Delta t,T)$ starts to diminish dramatically at 800 °C – 950 °C. At first all curves exhibit a steep decay of about 30 - 35% after the heat-treatment around 850 °C – 950 °C. Following that, the complete erasure is then observed from 1000 °C to 1200 °C and no measurable birefringence can be found after 30 minutes at 1200 °C.

The final decay is attributed to the erasure of the nanoporous layers as we modeled recently using Rayleigh-Plesset equation [20]. In addition, it can be obviously told that the higher the laser pulse energy, the higher the annealing temperature required to completely erase this last contribution. This can be explained as follow: as the energy increases, the deposited dose increases. This is a typical case described in Ref. [21] when there is a link between writing and erasure. When we use a higher energy in the laser writing process, the demarcation energy increases and more stable species or larger size nanopores are produced [20]. The subsequent modifications become more stable. The process is reflective of the distribution of energies possible within amorphous materials; i.e., distribution of local structures or atomic configurations.

Discussing the Thermal Performance of Different Fibers

We further compare the annealing results of aluminosilicate fibers to SMF 28 standard fibers and previous work performed in YAS fibers exposed to similar experimental condition.

To interpret the difference erasure kinetics, we can consider that the total measured birefringence is composed by additive/subtractive but not independent (e.g. stress is related to the permanent volume changes) contributions. In a recent publication the various observed trends of $R_{norm}(T)$, in relationship with different erasure mechanisms, has been investigated in great details in silica [11]. These contributions are divided into three categories:

First the birefringence of the Type I-like modification can be considered as the combination of the defect, the densification and the proportional stress-induced birefringence to the previous two. Usually the point defect centers are bleached under a fairly low temperature thermal treatment (<600 °C) [11] whereas there is no significant effect or maybe a slight increase of the measured retardance within this range of temperatures.

Then Type II modification contains stresses from two different origins, the one of Type I modification that disappears with the erasure of type I modification at temperatures below plastic relaxation, and the second one coming from nanoporous layers will relax plastically (a plastic deformation around nanopores occurs) because nanopores are more stable and will ultimately erase at higher temperature.

- The subsequent unexpected rise from 600 °C - 950 °C is attributed to the co-existence of “Type I like” modifications with the ones specific of Type II i.e. nanogratings structuration with porous nanolayers. The progressive erasure of the former occurred at this stage and eventually caused an “abnormal” increase of the retardance R.
- Then under thermal treatment a part of the stress is expected to relax when approaching a temperature around $0.9\times T_g$ for a few tens of minutes (T_g is the glass annealing temperature). In our experiments, this relaxation starts from 800 °C, which correlates with the “1st component” decay of $R_{norm}(T)$ in the 800-950 °C range seen in Figure 5. We note here that the compressive stress field produced by the nanoporous layers does not disappear with the annihilation of the nanopores themselves (which takes place at a higher temperature) but by plastic deformation of the glass around the nanopores.

The third contribution is the form birefringence related to the nanopores arrangement within nanolayers so-called nanogratings as confirmed by SEM micrographs. More details

can be found in [20], and leads to the conclusion that the porosity plays a key role in the erasure of nanogratings and their associated birefringence in a high temperature regime. In particular, the R-P equation sheds light on the major role played by the viscous behavior of the glass, at high temperature, that is the major parameter that drives the nanogratings erasure and related form birefringence.

The "ultimate and key contribution" (i.e., final erasure of the nanopores) is always related to the viscosity(T) of the glass and the nanopores size (laser parameters dependent).

In this work we have highlighted that a large incorporation of Al_2O_3 can improve the thermal stability of optical fibers. In order to prove this point of view, several kinds of optical fibers are selected and compared such as SMF 28, YAG-derived fiber (YAS) and two sapphire-derived fibers (High-AS and Low-AS). Fig. 4 displays an aggregate of annealing results and monitoring the normalized retardance R_{norm} (Δt, T) as a function of temperature. Note that here we have chosen to perform annealing of samples written at 1.0 µJ/ pulse, which corresponds to the stable range of Type II modifications for each sample (in term of writing kinetics) and can facilitate the reliable measurements of the retardance.

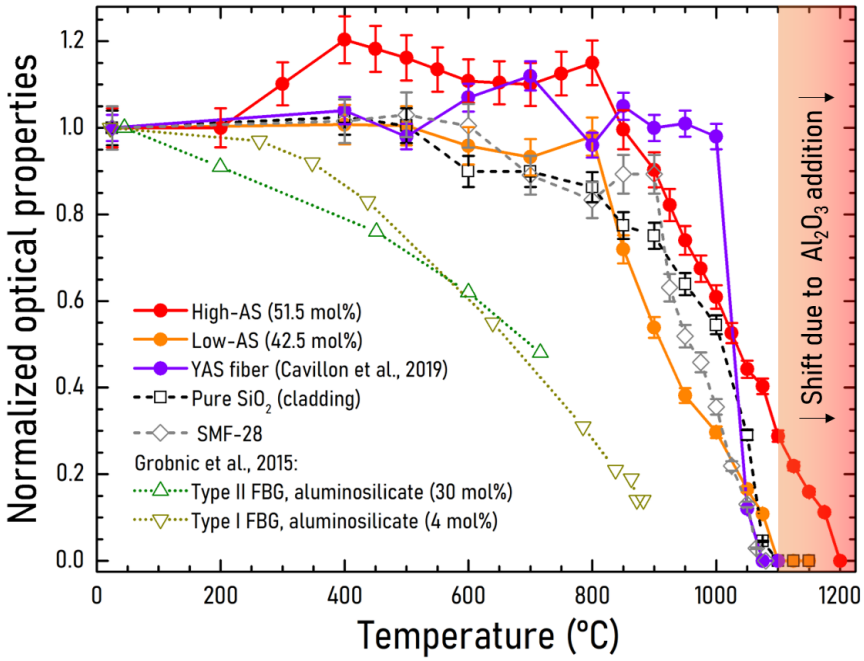

Figure 4. The normalized retardance of irradiated regions as a function of temperature for aluminosilicate fibers High-AS (red), Low-AS (orange) and Fiber cladding (black). The SMF-28 fiber (grey) and the yttrium aluminosilicate fiber YAS (purple) and are also shown for sake of comparison. Experimental conditions are: Pulse energy = 1µJ, λ = 1030 nm, 100 kHz, 100 µm/s, 10^3 pulses/µm, NA=0.6, laser polarization ⊥ to writing direction (Yx). The measurements were performed at room temperature. The results of Type I FBG in low content aluminosilicate fiber (4 mol%, olive) and Type II FBG in high content aluminosilicate fiber (30 mol%, green) are extracted from [19] and inserted for comparison

From Fig. 4, the evolution of R as a function of temperature shows some characteristic features, which typically reveals different erasure mechanisms, they have different trends and contributions for each samples.

The R_{norm} value starts to decrease slowly for temperatures higher than 800 °C. The changes in Si-O three and four-fold rings anneal out in the 700 °C – 900 °C range, and are well correlated with the structural relaxation of densified silica formed within the nanograting regime [21]. However, another increase can be observed around 800 °C for both AS, SMF 28

and YAS fiber. This significant change could be related to some changes in the stress field, which creates an extra stress-induced birefringence. Since in the isochronous annealing process, the measurement of each steps were proceeded until the sample returned to room temperature, this would induce an additional residual stress and slightly increase the stress-induced birefringence [22], thus result in the increase of the overall retardance.

As the heat-treatment temperature is increased, induced stress relaxes and consequently to this the stress-induced birefringence further lessens. Finally, the erasure of nanopores in the nanogratings leads to a very steep decrease of the form birefringence induced by themselves, and the R_{norm} value drops to zero in the range of 1075 °C - 1200 °C depends on the chemical composition and structure of the different fibers. By comparing thermal behavior for both SMF 28 fiber and YAS fiber, the former exhibits a decrease in R values starting roughly around 900 °C and fully disappear at 1080 °C. On the other hand, the latter YAS fiber demonstrates a better thermal stability between 800 °C -1000 °C when compares with the other fibers, it had been proven to be an excellent choice of fibers which used in high temperature environment in Ref. [14]. Its R_{norm} however diminishes dramatically above 1000 °C, in contrast, the AS fibers reveals the better performance at the higher temperature until 1175 °C.

The AS fibers exhibit the best thermal stability among all of the samples when the temperature reaches 1100 °C or higher. We have reported in our previous work that the formation of the nanogratings in the aluminosilicate glass is led by the separation of Al_2O_3-rich phase from SiO_2-rich matrix phase. The high thermal stability of laser-induced nanograting could be related to the phase immiscibility, Ref. [23, 24] also confirmed this immiscibility could be increased with a higher Al_2O_3 content. As shown in Figure 4, the High-AS fiber performs better than the Low-AS during the annealing, which could be attributed to the increase in aluminum coordination (4,5,6 times coordination [25, 26]), thus, improve the glass network cross-linking density and bond strength.

Studying Laser-induced Modification Using Rayleigh Backscattering

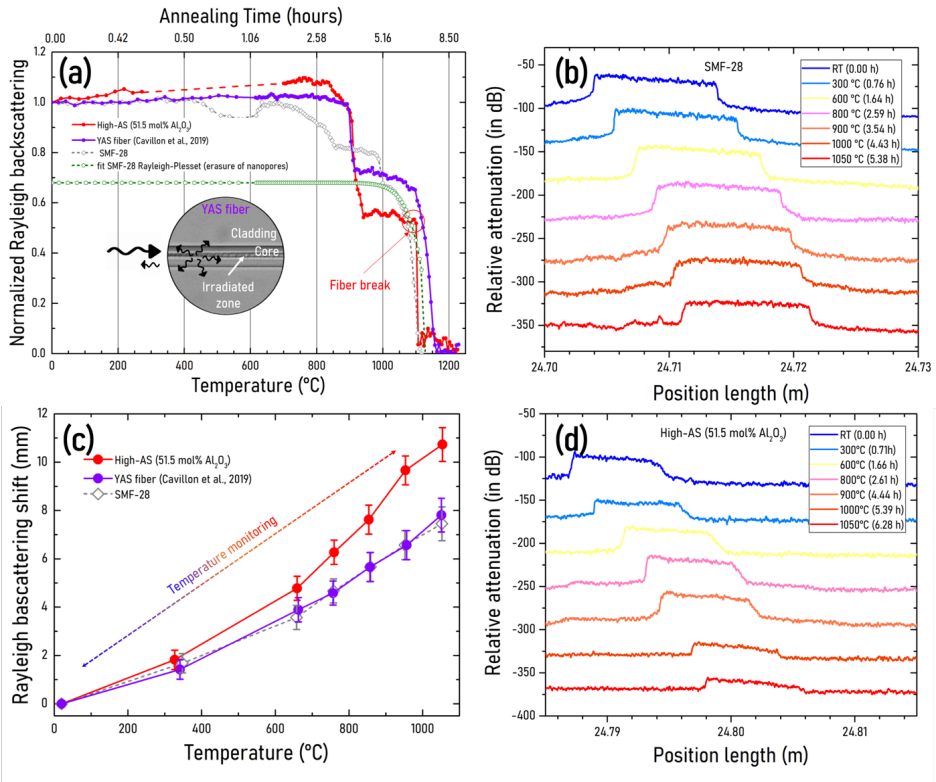

Figure 5. (a): The Rayleigh scattering amplitude of irradiated zones as a function of temperature for High-AS fiber (red), YAS fiber (purple), and SMF 28 fiber (grey). we did the simulation of the nanopores' erasure in SMF 28 fiber using the Rayleigh-Plesset (R-P) equation (blue, simulation conditions: the surface energy S = 0.3 J.m-2; pore size diameter = 15 nm) and the normalized amplitude (at 1000 °C) of SMF 28 fiber (red), as a function of the isochronal annealing temperature. The result (green) is also inserted in (a). Experimental conditions are: Pulse energy = 0.8 μJ, λ = 1030 nm, 100 kHz, 100 μm/s, 1000 pulses/μm, NA= 0.6, laser polarization $\perp$ to writing direction (Yx). The measurements were performed during the annealing. **(b) and (d)**: The sensing position length at different temperature for SMF 28 fiber and High-AS fiber respectively **(c)**: The summarize of the Rayleigh backscattering shift as a function of temperature for High-AS fiber, YAS fiber and SMF 28 fiber.

To effectively verify the capability of molten core fiber to operate as the sensing devices, the distributed sensors based on Rayleigh scattering are fabricated with the Aluminosilicate fibers and YAS fibers. By monitoring Rayleigh backscattering during the fiber annealing process, we can compare the results with retardance (R) evolution during the annealing and study the thermal stability of the fs-laser induced modification as well. Rayleigh scattering is an elastic scattering of light by localized density fluctuations. The effect is used for measurements distributed by frequency reflectometry, which called optical frequency-domain reflectometry (OFDR). As the Fig. 5(a) inset graph illustrates, a fluctuating polarization-induced light emission in all directions can be observed once the light signal induced to the irradiated zone in the fiber core, some of the scattered Rayleigh light is re-captured by the waveguide and sent in the backward direction. This backward propagating Rayleigh scattered light has a time delay that can be used for distributed sensing[27].

Using OFDR algorithm to extract the distributed sensing information, determine the shift of the correlation peak, thus define the accurate temperature change [28]. A 10 mm line is irradiated on the High-AS fiber, YAS fiber and also SMF 28 fiber as reference, Fig. 5(a) demonstrates the progression of their Rayleigh scattering amplitude during the annealing, notice that the results are the average of measurement values over entire length of the irradiated area. The changes of the scattering amplitude happen in the similar temperature range as the change of the R value in Fig. 4. First, the amplitude of all three fibers show varying degrees of decline from 800 °C to 1000 °C, which could be attributed to the structural relaxation of the laser modification regime. Then, a dramatically decrease of the scattering amplitude is observed following the increase of the annealing temperature, YAS fiber shows slightly better thermal stability than SMF 28 fiber. Unfortunately, the High-AS fiber broke around 1100 °C, and we need further experiment to investigate its performance at higher temperature.

Cavillon et al. [20] have recently proven the quantitative correlation between the form birefringence and porosity of the nanostructures. Using Rayleigh-Plesset equation to simulate the evolution of the pore size diameter for a given material during the annealing, and thus calculate the normalized retardance R. Fig. 5(a) compares as well the performance in the heat treatment between Rayleigh-Plesset simulation of nanopore erasure process and the Rayleigh scattering experimental results for SMF 28 fiber. The latter is taken from the Figure 4 and normalized relative to the sharp retardance decrease around 1000 °C that we hypothesized here to be characteristic of the nanopore erasure. Both curves start their strong decrease around the same temperature (1000 °C) and show the quite similar trend after, which prove the Rayleigh scattering is highly sensitive to the temperature as the nanogratings, and open up a different choice for the temperature sensor else than FBGs.

The temperature change induced phase differences via refractive index variation, the OFDR can be used to monitor the change of temperature by observing the shift of sensing

position length relative to the fixed reference length of local oscillator[27]. Fig. 5 (b) and (d) demonstrate the sensing position length at different annealing temperatures in the case of SMF 28 fiber and High-AS fiber respectively, the length shift towards a higher value as the increase of temperature can be observed obviously in both fibers. Fig. 5 (c) summarizes the Rayleigh backscattering shift as a function of heat treatment temperature. The performance of YAS fiber and SMF 28 fiber is considered to be very similar, while the curve representing High-AS fiber exhibits a higher slope, which means that compared with other fibers, the High-AS fiber which performs as a distributed sensor based on Rayleigh scattering, owns a higher sensitivity to temperature.

3. Conclusions

In this work, a high potentiality to apply aluminosilicate fiber as the harsh environment sensor is demonstrated. This technology is fully based on the molten core method which provides great flexibility in the selection of the materials during optical fiber manufacturing and allows the fabrication of unstable core composition (Sapphire, YAG, etc.). Using the femtosecond laser to achieve the high-intensity fields and leads to the generation of nanogratings inside of the investigated fiber core, the High-AS fiber eventually exhibited better thermal stability than the conventional SMF 28 fiber. Moreover, the former owns higher temperature sensitivity as well when it was performed as Rayleigh scattering-based distributed sensors (DOFS). We believe this technique presents an ideal large-scale platform for the next generation of the harsh environment sensing device, further work is underway to characterize the FBGs inscribed in these fiber families for lifetime prediction analysis and to explore further applications.

4. Experimental Section

EMA and Raman Spectroscopy Studies

Table 1. Labels and compositions of the Investigated optical fibers

Label	Core center composition (molar percentage)
High-AS	51.5%Al_2O_3 – 48.5%SiO_2
Low-AS	42.5%Al_2O_3 – 57.5%SiO_2
SMF-28	4%GeO_2 – 96% SiO_2
YAS	19.5%Al_2O_3 – 8.7%Y_2O_3-71.8%SiO_2

The investigated fibers are labeled as High-AS, Low-AS, SMF-28 (Corning conventional fiber) and YAS [14]. Table 1 reports the fiber core center compositions for each of them. The molten core method is used to fabricate the Aluminosilicate fibers [10, 29], resulting in a graded-index profile [30, 31]. The compound concentration profiles across the fiber core are measured by electron microprobe analysis (EMA) and showed a typical parabolic profile in Fig.6(a) (for High-AS and Low-AS). The graded-index profile is related to dissolution of the glass cladding into the core and chemical diffusion during fiber drawing [32]

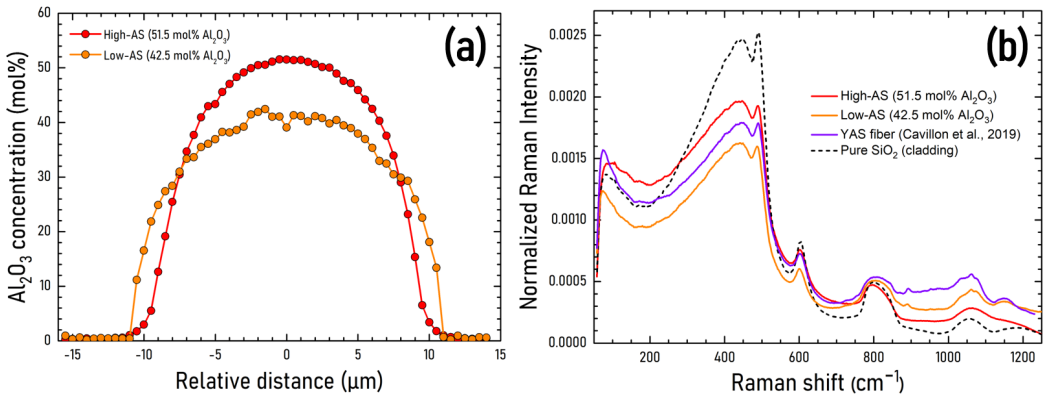

Figure 6. (a): Concentration profile of two fibers core composition. **(b):** Raman spectra of Aluminosilicate fiber cores. The spectrum of the SiO_2 fiber cladding and YAS fiber are also inserted for sake of comparison.

Raman spectra of both aluminosilicate and YAS fiber cores are reported in Fig. 6(b), along with the spectrum of low-AS fiber cladding (SiO_2), used as reference. The sharp peaks located around 490 and 600 cm^{-1}, also called D1 and D2 defect lines, are ascribed to the breathing modes of 4- and 3-membered rings, respectively. By increasing the Al_2O_3 content, both peaks demonstrate a clear intensity decrease, which indicates that the addition of alumina causes modifications of the ring statistic in the silica glass network [33, 34]. The band near 800 cm^{-1} results from the motion of Si atoms in their tetrahedral oxygen cage [35], and the intensity of this band relatively decreases and is shifted toward lower wavenumbers when alumina content increases. This could be associated to a decrease in the number of Silicon - bridging oxygen bonds. Finally, the high frequency bands at about 850-1300 cm^{-1} are usually related to the Si-O asymmetric stretching vibrations. The bands at around ~1060 cm^{-1}, ~1150 cm^{-1} are observed in the spectra of cladding (pure SiO_2), which represent tetrahedral SiO_4 group. In contrast, the formed interconnected Si-O-Al network [33, 34, 36] could be found in the case of the aluminosilicates because of the high amount of Al_2O_3. Notice there is no evidence that crystallization has occurred in the center of the fiber core and all the band shifts is similar to previously reported work, such as in Ref. [25, 37].

Laser Writing Experiments and Post-irradiation Characterization

All fibers are inscribed by Femtosecond laser irradiation (λ = 1030 nm, 250 fs) following a pattern similar to a line-by-line or point-by-point FBG writing. A 5 cm long fiber segment with coating removed is taken before the irradiation and fixed on a fused silica glass slide. A borosilicate cover slip (~170 µm thin) is then placed on top of the fiber segment, and an index-matching oil (GN Nettest, n=1.4580 at 25 °C) is used to ensure a refractive index continuity of the setup for both optical microscope observation and irradiation. In addition, for the subsequent heat treatment, the ends of each fiber segments are fixed to Infrasil silica glass substrate by using high temperature adhesive.

The prepared samples are then positioned on a XYZ motorized translation stage, and a series of 100 µm length lines are inscribed along the x-axis with a linear laser polarization oriented either parallel (Yy configuration) or perpendicular (Yx configuration) to writing direction. The spacing between each line is 30 µm, and the pulse energy varies by step of 0.1 µJ, ranging from 0.1 to 2.0 µJ. This is schematized in Fig. 7(a). The laser pulse repetition rate is fixed to 100 kHz, the scanning speed to 100 µm/s and the laser beam is focused using a 0.6

NA aspheric lens. The laser parameters setting are chosen based on previous work [15] which is known to induce Type II permanent modifications in SiO_2-Al_2O_3 binary glasses.

To measure the optical retardance (R) induced by the fabricated nanogratings, we use an Olympus BX51 polarizing optical microscope equipped with a de Sénarmont compensator. The retardance is defined as R = B*d, with B is the linear birefringence and d the thickness of the birefringent object (generally expressed in nm). The "de Sénarmont" method couples a highly precise quarter wavelength birefringent quartz or mica crystalline plate with a 180-degree rotating analyzer to provide retardation measurements having an accuracy that approaches one-thousandth of a wavelength.

A complementary experiment is set to investigate the irradiated fibers by using a Scanning Electron Microscope (SEM, Field-Emission Gun Scanning Electron Microscope, ZEISS SUPRA 55 VP, 1 kV accelerating voltage). The writing geometry is sketched in Fig. 7(b): a single line of 10 mm length, parallel to the light propagation axis of the fiber, was written. Based on the previous experiment, the pulse energy is fixed at 1.0 uJ. Then, the fiber is cleaved within the irradiated zone and its cross section is brought under the SEM. According to the laser polarization orientations, the nanopores can be found with the parallel configuration (Xx) and the nanolayers (sideways visualization of nanoplanes) with a regular spacing appeared when the polarization orientation is perpendicular to the writing direction (Xy). Finally, Fig. 7(c) and (d) exhibit the strong birefringence in the High-AS fiber which follow the laser inscription setup (a) and (b) respectively.

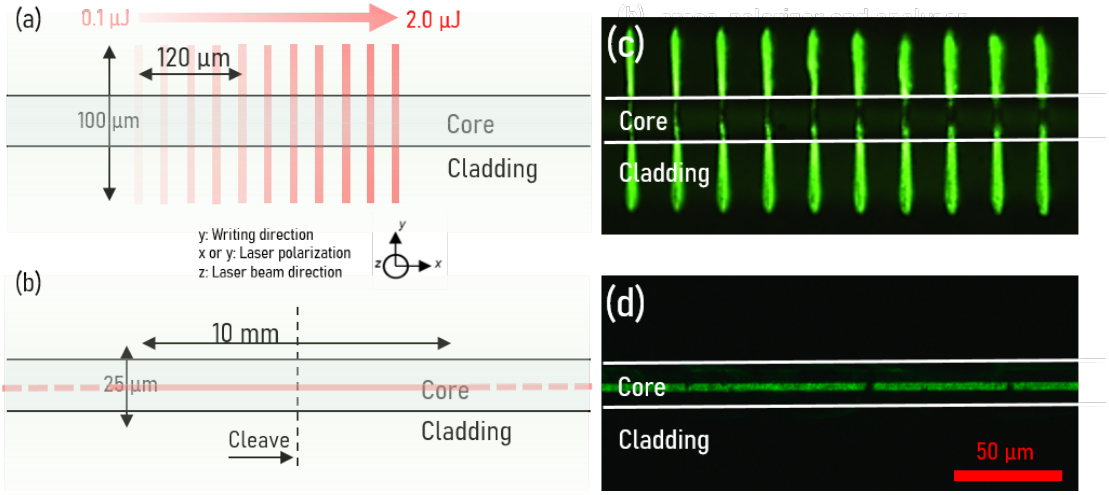

Figure 7. (a) Irradiation of fs laser inside fiber core and cladding of an optical fiber at different pulse energies (λ = 1030 nm, 100 kHz, 100 µm/s, 103 pulses/µm, NA = 0.6, pulse duration = 160 fs). (b) Longitudinal (along with x) irradiation at constant pulse energy (1.0 µJ) using different laser polarization conditions: parallel (//, along with x) and perpendicular (⊥, along y) to the writing direction. (c) and (d) optical microscope (bottom light illumination) image of the High-AS fiber with a cross polarizer and analyzer taken from (a), (b) respectively.

Accelerated Ageing Experiments

Finally, the samples that followed the line-by-line inscription (Fig.7(a)) are isochronally (Δt = 30 min per temperature step) heat-treated with an incremental temperature increase (Typ. ΔT = 50K) up to 1200 ºC. After each annealing step, the retardance of each line is measured at room temperature after quenching the samples in air. The reported values, $R_{norm}(\Delta t,T)$, are all normalized to the initial value prior to any annealing R (Δt, 20 °C).

Meanwhile, the thermal stability of "amplified" Rayleigh scattering is investigated at the Optic Fiber Sensors Laboratory (LCFO) of CEA France. In this view, different fiber

segments are uniformly irradiated by IR femtosecond laser namely High AS, SMF 28, and YAS. Laser parameters are chosen to produce nanogratings inside the fiber core resulting in a strong increase of the light scattering along this segment. Then, these fibers are spliced to single mode fiber pigtails. Each sample is put inside a silica glass tube then inserted into the center of the horizontal tubular furnace. Type N thermocouple is used to monitor the temperature. During the step isochronal annealing process (Δt = 30 min per temperature step, from 600 ºC – 1000 ºC, ΔT = 100K; from 1000 ºC – 1250 ºC, ΔT = 50K), Rayleigh backscattering level is measured during annealing using an OBR4600 from Luna based on optical frequency-domain reflectometry (OFDR) technique. Coupled to an optical switch, the setup allows interrogating each fiber sequentially. Once the annealing process is completed, the OBR measurements are analyzed in post-processing to obtain the intensity of Rayleigh backscattered light propagating through of the different fiber optics.

Reference

1]. Y. Waku, N. Nakagawa, T. Wakamoto, H. Ohtsubo, K. Shimizu and Y. Kohtoku, *Journal of Materials Science*, 1998, **33**, 1217-1225.
2]. J. Zhang, A. Čerkauskaitė, R. Drevinskas, A. Patel, M. Beresna and P. G. Kazansky, 2016.
3]. S. J. Mihailov, *Sensors*, 2012, **12**, 1898-1918.
4]. S. Musikant, *Optical materials: an introduction to selection and application*, CRC Press, 2020.
5]. S. J. Mihailov, D. Grobnic, C. Hnatovsky, R. B. Walker, P. Lu, D. Coulas and H. Ding, *Sensors*, 2017, **17**, 2909.
6]. C. Zhan, Y. Zhu, S. Yin and P. Ruffin, *Optical Fiber Technology*, 2007, **13**, 98-107.
7]. R. B. Walker, H. Ding, D. Coulas, D. Grobnic, S. J. Mihailov, M. A. Duchesne, R. W. Hughes, D. J. McCalden and R. Burchat, 2015.
8]. F. Mezzadri, Universidade Tecnológica Federal do Paraná, 2012.
9]. D. Grobnic, C. W. Smelser, S. J. Mihailov and R. B. Walker, *Measurement Science and Technology*, 2006, **17**, 1009.
10]. J. Ballato and A. Peacock, *APL Photonics*, 2018, **3**, 120903.
11]. Y. Wang, M. Cavillon, N. Ollier, B. Poumellec and M. Lancry, *physica status solidi (a)*, 2100023.
12]. M. Lancry, B. Poumellec, A. Chahid-Erraji, M. Beresna and P. Kazansky, *Optical Materials Express*, 2011, **1**, 711-723.
13]. R. Desmarchelier, B. Poumellec, F. Brisset, S. Mazerat and M. Lancry, *World Journal of Nano Science and Engineering*, 2015, **5**, 115.
14]. M. Cavillon, M. Lancry, B. Poumellec, Y. Wang, J. Canning, K. Cook, T. Hawkins, P. Dragic and J. Ballato, *Journal of Physics: Photonics*, 2019, **1**, 042001.
15]. Y. Wang, S. Wei, M. R. Cicconi, Y. Tsuji, M. Shimizu, Y. Shimotsuma, K. Miura, G. D. Peng, D. R. Neuville and B. Poumellec, *Journal of the American Ceramic Society*, 2020, **103**, 4286-4294.
16]. M. Lancry, B. Poumellec, J. Canning, K. Cook, J. C. Poulin and F. Brisset, *Laser & Photonics Reviews*, 2013, **7**, 953-962.
17]. E. Bricchi, B. G. Klappauf and P. G. Kazansky, *Optics letters*, 2004, **29**, 119-121.
18]. M. Nogami, K. Watanabe, Y. Ito, H. Ito and H. Nakano, *Journal of the American Ceramic Society*, 2010, **93**, 1663-1667.
19]. D. Grobnic, S. J. Mihailov, J. Ballato and P. D. Dragic, *Optica*, 2015, **2**, 313-322.
20]. M. Cavillon, Y. Wang, B. Poumellec, F. Brisset and M. Lancry, *Applied Physics A*, 2020, **126**, 1-9.
21]. B. Poumellec and M. Lancry, *Fibers*, 2015, **3**, 206-252.
22]. P. Vlugter, E. Block and Y. Bellouard, *Physical Review Materials*, 2019, **3**, 053802.
23]. J. MacDowell and G. Beall, *Journal of the American Ceramic Society*, 1969, **52**, 17-25.
24]. S. Liu, V. Boffa, D. Yang, Z. Fan, F. Meng and Y. Yue, *Journal of Non-Crystalline Solids*, 2018, **492**, 77-83.
25]. D. R. Neuville, L. Cormier, V. Montouillout, P. Florian, F. Millot, J.-C. Rifflet and D. Massiot, *American Mineralogist*, 2008, **93**, 1721-1731.
26]. R. Weber, S. Sen, R. E. Youngman, R. T. Hart and C. J. Benmore, *The Journal of Physical Chemistry B*, 2008, **112**, 16726-16733.
27]. X. Bao and L. Chen, *sensors*, 2012, **12**, 8601-8639.
28]. M. Wang, K. Zhao, J. Wu, Y. Li, Y. Yang, S. Huang, J. Zhao, T. Tweedle, D. Carpenter and G. Zheng, *International Journal of Extreme Manufacturing*, 2021, **3**, 025401.
29]. S. Morris and J. Ballato, *Bull. Am. Ceram. Soc*, 2013, **92**, 24-29.

30]. T. Elsmann, A. Lorenz, N. S. Yazd, T. Habisreuther, J. Dellith, A. Schwuchow, J. Bierlich, K. Schuster, M. Rothhardt and L. Kido, *Optics express*, 2014, **22**, 26825-26833.
31]. P. Dragic, T. Hawkins, P. Foy, S. Morris and J. Ballato, *Nature Photonics*, 2012, **6**, 627-633.
32]. M. Cavillon, P. Dragic, B. Faugas, T. W. Hawkins and J. Ballato, *Materials*, 2019, **12**, 2898.
33]. M. Okuno, N. Zotov, M. Schmücker and H. Schneider, *Journal of Non-Crystalline Solids*, 2005, **351**, 1032-1038.
34]. M. F. Ando, O. Benzine, Z. Pan, J.-L. Garden, K. Wondraczek, S. Grimm, K. Schuster and L. Wondraczek, *Scientific reports*, 2018, **8**, 1-14.
35]. P. McMillan, *American Mineralogist*, 1984, **69**, 622-644.
36]. M. Busch, W. Ecke, I. Latka, D. Fischer, R. Willsch and H. Bartelt, *Measurement Science and Technology*, 2009, **20**, 115301.
37]. P. F. McMillan, G. H. Wolf and B. T. Poe, *Chemical Geology*, 1992, **96**, 351-366.

Conclusions

In this chapter we studied the photosensitivity of a range of “high temperature sensing candidates”, namely aluminosilicate fibers, under femtosecond laser irradiation. A femtosecond laser was used to imprint IR-fs-Type II modifications (nanogratings) inside these fibers, and both the writing kinetics and thermal withstanding of the birefringent modified regions were investigated. The fibers were tested under a wide temperature range (from room temperature to -1250 °C), and compared to both conventional GeO_2-doped silica fiber (SMF-28) and F300 pure silica cladding.

Below are summarized and highlighted some key results learned from this chapter:

- The YAG derived fiber core (yttrium aluminosilicate glass) response to fs laser irradiation globally resembles that of SiO_2, or slightly Ge-doped SiO_2 (SMF-28) in terms of Type II modifications thresholds or writing kinetics. In contrast sapphire derived fibers exhibit significantly lower birefringence amplitude.
- Higher nanogratings periodicity and higher average nanopore sizes can be observed by SEM when increasing Al_2O_3 concentration in the fiber core in both types of fibers.
- The thermal stability depends on the laser writing conditions: the higher the laser pulse energy, the higher the thermal stability (both in SMF-28 and sapphire-derived fibers). This could be tentatively attributed to the larger size of the nanopores at high energies.
- Compared with SMF-28 fiber or F300 pure silica cladding, the YAG derived fiber has an improved thermal stability around 800 °C – 1000 °C whereas sapphire derived fiber (Al_2O_3 > 50 mole%) shows enhanced performance in the 1000 °C – 1200 °C temperature range.
- The Rayleigh-scattering signature of the sapphire-derived fiber containing the highest concentration of Al_2O_3 (51.5 mol%) is found to be more temperature-sensitive compared to the SMF-28 or fibers with lower Al_2O_3-concentrations.

Finally, in this chapter we propose an approach based on the development of new fibers conjugated to femtosecond direct writing for high temperature operation. These “high temperature fibers” could be composed of aluminosilicate cores such as Al_2O_3-SiO_2 (>50 mole% of Al_2O_3), Y_2O_3-Al_2O_3-SiO_2 (as reported in these two papers) and potentially fibers with other compositions including high melting temperatures oxides such as ZrO_2 or Gd_2O_3. The MCM method is an attractive approach to develop a new range of host fibers photosensitive to fs-laser writing, and suitable for fabricating ultra-high temperature resistant devices (e.g., FBGs), to ultimately overcome the current performances of commercial fibers. Further work consists to characterize nanogratings inscribed in these fiber core segments as well as to write FBGs in these fiber families for lifetime prediction analysis.

References

1. Walker, R.B., et al. *Entrained-flow gasifier and fluidized-bed combustor temperature monitoring using arrays of fs-IR written fiber Bragg gratings*. in *24th International Conference on Optical Fibre Sensors*. 2015. International Society for Optics and Photonics.
2. Mezzadri, F., *Monitoramento de temperatura em turbina de motordiesel de locomotiva com sensor a fibra ótica*. 2012, Universidade Tecnológica Federal do Paraná.
3. Grobnic, D., et al., *Long-term thermal stability tests at 1000 C of silica fibre Bragg gratings made with ultrafast laser radiation.* Measurement Science Technology, 2006. **17**(5): p. 1009.
4. Grobnic, D., et al., *Sapphire fiber Bragg grating sensor made using femtosecond laser radiation for ultrahigh temperature applications.* IEEE Photonics Technology Letters, 2004. **16**(11): p. 2505-2507.
5. Elsmann, T., et al., *Inscription of first-order sapphire Bragg gratings using 400 nm femtosecond laser radiation.* Optics Express, 2013. **21**(4): p. 4591-4597.
6. Busch, M., et al., *Inscription and characterization of Bragg gratings in single-crystal sapphire optical fibres for high-temperature sensor applications.* Measurement Science and Technology, 2009. **20**(11): p. 115301.
7. Elsmann, T., et al., *High temperature sensing with fiber Bragg gratings in sapphire-derived all-glass optical fibers.* Optics express, 2014. **22**(22): p. 26825-26833.
8. Ballato, J. and A. Peacock, *Perspective: Molten core optical fiber fabrication—A route to new materials and applications.* APL Photonics, 2018. **3**(12): p. 120903.
9. Dragic, P., et al., *Sapphire-derived all-glass optical fibres.* Nature Photonics, 2012. **6**(9): p. 627-633.

Chapter 5. 3D printed perform optical fibers

Introduction 193

5.1 Loss reduction of 3D silica lithography fiber by post heat treatment 194

5.2 Thermal Stability of Type II Modifications Inscribed by Femtosecond Laser in a Fiber Drawn from a 3D Printed Preform 199

5.3 Helical distributed feedback fiber Bragg gratings and rocking filters in a 3D printed preform-drawn fiber 211

Conclusions 216

Introduction

In this chapter, we will introduce a recent fiber fabrication method, which is the fiber drawn from a 3D printed preform. This method has attracted considerable attention over the past decade; since compare with the conventional CVD methods, 3D printing of fiber preforms offers a wider choice for both structure (including photonic crystals fibers) and materials. More importantly, it will reduce the skills required by the CVD processes and effectively reduce overall costs whilst enabling new and flexible designs. Therefore, in this chapter we investigate the optical and thermal performances of fs-laser written structures in these optical fibers. This chapter is composed of three publications and is the result of a 3 months visit in Australia under the supervision of Prof. Gang Ding Peng (UNSW) and Prof. John Canning (UTS).

In the first publication, we try to reduce the attenuation losses of a 3D printed germano-silicate fiber by post heat treatment. The loss reduction is observed through measuring the evolution of transmission spectra of “3D silica lithography fiber” from 900 to 1350 nm during multiple heat treatment cycles performed at 800 °C. A 30% loss decrease is observed at 1300 nm after heat treatment. The mechanisms of temperature-induced reversible loss and loss reduction by post heat treatment are also discussed.

In the second publication, the photosensitivity of Ge-doped silica optical fibers to femtosecond laser light and drawn from a 3D printed preform is investigated. By varying the laser pulse energy and investigating the birefringence response of femtosecond laser written structures, we study the writing kinetics and the thermal performances of Type II modifications. In addition, we compare these results to conventional telecom single mode fiber (SMF28) to identify the thermal performance of such fiber.

In the last publication, an asymmetric core optical fiber was drawn from a 3D printed preform. First, linear fiber Bragg gratings were produced on one side of the core by using UV-induced attenuation across the twisted asymmetric fiber core. Then, we balanced and matched optical losses of each polarization eigenstate to create an effective zero birefringence by pre-twisting the fiber. Finally, removing the twist can produce a helical grating with a period matching the twist rate.

5.1 Loss reduction of 3D silica lithography fiber by post heat treatment

Loss reduction of 3D silica lithography fiber by post-draw annealing

Shuen Wei, Ming Lu*, Yanhua Luo, Bowen Zhang, Yitao Wang, Matthieu Lancry, John Canning, and Gang-Ding Peng

***Abstract*—The loss reduction of optical fiber fabricated by 3D silica lithography is achieved by post-draw annealing. The loss reduction is observed through measuring the evolution of transmission spectra from 900 to 1350 nm during multiple 800 ºC post-draw annealing cycles. The loss coefficient at 1300 nm (α_{1300nm} ~ 9.5 dB/m) could decrease by ~ 3 dB/m after post-draw annealing. By comparing Raman spectroscopy of pristine with annealed sample, the post-draw annealing induced fiber core structure densification is found and could be associated with the annealing induced loss reduction.**

***Index Terms*—3D silica lithography fiber, Loss reduction, post-draw annealing**

I. Introduction

Silica optical fiber is the most important part in fiber-optic communications, where they permit transmission over long distances at high bandwidth. To achieve low-loss silica telecom fibers, since 1970s, many fabrication processes were tried and employed to make the bulk preforms from which optical fibers subsequently are drawn [1]. The most common and successful process could be modified chemical vapor deposition (MCVD) [2], which has been utilized for fabricating various commercial silica fibers. With the development of fiber-optics technology, the development focus has gradually moved from transmission medium to multifunctional hosts, such as fiber-based sensors, lasers, and amplifiers. For this development trend, optical fibers of diversified materials and sophisticated structures are highly demanded. Nevertheless, the traditional fabrication method, including MCVD and rod-and tube stacking, has limited capability in both material and structure flexibility for diverse and custom-designed functionalities. Fortunately, the recent research and development of 3D printing technologies create a new way to eliminate these limits [3-6].

So far, several advanced 3D printing manufacturing methods, such as fused deposition modeling (FDM), filament feed, direct ink writing (DIW), and direct light project (DLP) have been employed for fabricating dense, transparent, homogeneous, and complex silica-based glass structures [7]. The overall process of these techniques is quite similar, involving material formulation to reduce thermal temperatures, photo- or thermal-polymerization to solidify the liquid state, and subsequent thermal processing. Among these steps, the thermal processing is quite important for complete glass densification, which finally determine the transparence of 3D printed glass [8-10].

Among these techniques, due to the enormous potential in fabricating silica with greater freedom in both structure and material formation, the 3D silica printing lithography was first employed by DLP for optical fiber fabrication (3D fibers) in 2019 [11], and these 3D fibers have been successfully applied in fabricating sensors [12, 13]. Like 3D printed glasses, a complete densified, homogeneous, and transparent glass structure is also important for 3D fibers to achieve a low-loss light guide structure.

Although great progress has been achieved, there is still large space to develop the performance of 3D fibers. More specially, as the thermal processing procedure of 3D fiber perform is not systemically investigated and optimized, the 3D fibers could be insufficient densified, leading to the background losses. Due to this fact, in this letter, we mainly investigate whether post-draw annealing could be applied to further densify the 3D printed glass structure and further reduce the background loss of 3D fibers. Through this study, 3D silica lithography fiber fabrication optimization is further proposed.

II. Sample and Experimental Setup

The 3D fibers in this work were drawn from the silica preform fabricated by 3D lithography printing. The detailed fabrication process can be found in [11]. In short, the preform was prepared by 3D printing a mixture of high purity silica glass nanoparticles and photocurable resin, subsequent core formation using direct light projection (DLP) printing. It was followed by thermal debinding to remove the polymer resin leaving only a silica structure. No evidence of polymer or water from the preform was detected using Fourier-transform infrared spectroscopy (FTIR) spectroscopy [13]. Finally, the preform was inserted into a supporting silica tube, placed inside a draw tower, and drawn into fiber at ~ 1855 ºC.

Manuscript received ---- --, ----; revised ---- --, ----; accepted ---- --, ----. Date of publication ---- --, ----; date of current version ---- --, ----. This work was supported by two ARC LIEF grants (LE0883038 and LE100100098) on the national fiber facility at UNSW, Sydney, and the support from NSFC (61520106014 and 61675032), and STCSM (SKLSFO2018-02).

Shuen Wei, Ming Lu, Yanhua Luo, Bowen Zhang and Gang-Ding Peng are with Photonics and Optical Communication Group, School of Electrical Engineering and Telecommunications, University of New South Wales, Kensington, NSW 2052, Australia. (*Corresponding author: Ming Lu*, e-mail: ming.lu2@unswalumni.com)

John Canning, Ming Lu, School of Electrical and Data Engineering, University of Technology Sydney.

Yitao Wang and Matthieu Lancry are with Institut de Chimie Moléculaire et des Matériaux d'Orsay, Université Paris-Sud 11, Orsay 91405, France.

Color versions of one or more of the figures in this letter are available online at http://ieeexplore.ieee.org.

Digital Object Identifier

There are two 3D fiber samples selected for this study. One is single mode fiber (3D-SMF), the other is fiber doped with bismuth and erbium (3D-BEDF). The core of these two samples demonstrates an elliptical shape and might be caused by core distortion during the drawing process. These two samples were fabricated in the same way while there is a difference in their fiber core compositions. Based on the results of energy dispersive x-ray analysis (EDX), the concentration of GeO_2 in the 3D-SMF core region is estimated to be ~ 10 mol%. The TiO_2 (~ 2 mol%) and GeO_2 (~ 2 mol%) co-doping of 3D-BEDF is for improving the refractive index. The concentration of Bi/Er/Al of 3D-BEDF is estimated to be less than 1 mol%. The detailed core glass compositions, diameter, and cutoff wavelength (λ_{co}) of these two fibers is listed in Table 1. In this study, we mainly investigate the performance of 3D-SMF. The results of 3D-BEDF are used to verify the observed effects.

TABLE 1. Characteristics of the 3D silica lithography fibers

Abbr.	Composition	D_f, μm	Irregular elliptical shape core, μm	λ_{co}, μm	Ref
3D-SMF	SiO_2, GeO_2	128.2	$\Phi_{max/min}$~ 6.4/ 3.2	0.78	[11]
3D-BEDF	SiO_2, GeO_2, TiO_2, Al_2O_3, Bi/Er	121.8	$\Phi_{max/min}$~ 6.2/ 3.2	0.72	[14]

Fig. 1 (a) below shows the optical loss spectrum of the 3D-SMF in the spectral region from 900 to 1700 nm measured by the traditional cutback method. The sharp decay of observed from 1050 to 1200 nm is caused by the higher order modes leakage of pigtail SMF that is used in the cutback method. The high absorption peak at ~ 1380 nm is caused by OH overtone. The loss at 1300 nm (α_{1300nm}) is ~ 9.50 dB/m.

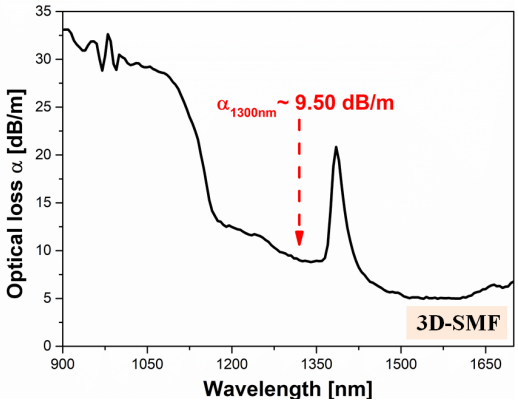

Fig. 1. (a) The optical loss spectrum of 3D-SMF using the cutback method.

To investigate the variation of transmission spectrum during the process of annealing and further reveal the variation of loss, a section of bared 3D-SMF (~ 40 cm) was connected and put into furnace as shown in Fig. 2. In this experiment, we used a halogen lamp as white light source. For the whole experiment, the temperature was monitored by the thermometer, and the transmission spectrum was recorded through a GPIB-USB cable from an optical spectrum analyzer (OSA) to the PC every minute. We selected 800 ºC as an annealing temperature due to two main reasons: (1) 800 ºC is one of the main stages used for debinding and sintering [11] , (2) 800 ºC is not high enough that could lead to strong loss caused by devitrification for a long-time experiment [15]. Due to the practical lab safety reasons, the annealing dwell time for each cycle was controlled to be 10 hrs. Then the fiber was slowly cooled down to room temperature. The loss variation ($\Delta\alpha$) was obtained by regarding the transmission spectrum of un-treated 3D-SMF at room temperature as the reference. To make a comparison, a similar experiment was conducted by annealing SMF 1550 at 800 ºC.

To further verify the observed effect, a section of a 3D-BEDF (~ 48 cm) was measured and treated in the similar way. In this case, the white light source was replaced by 830 nm laser source with the fixed power, and the OSA was replaced by power meter. The variation of 830 nm loss ($\Delta\alpha_{830nm}$) was obtained by comparing the residual 830 nm pump power measured during annealing process, with the value obtained before annealing. The 830 nm loss ($\alpha_{830\ nm}$) of this 3D-BEDF is ~ 30.76 dB/m.

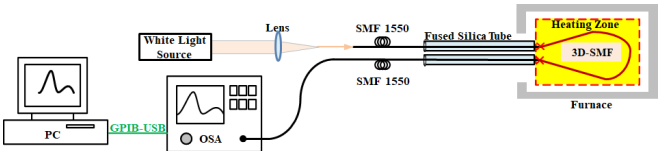

Fig. 2. Experiment setup for measuring the transmission spectrum of 3D-SMF during the process of heat treatment.

Besides, to measure the dimension variation before and after annealing, a batch of 3D-SMF (~ 2 cm) were put into furnace and processed at 800 ºC for 10 hr. Their cross-sections dimensions were measured by an optical microscope.

III. Results

A. 3D fiber loss reduction

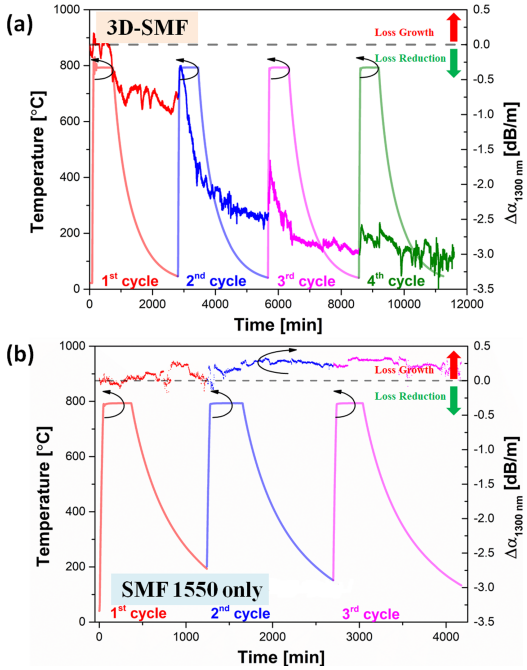

Fig. 3. Variation of 1300 nm loss ($\Delta\alpha_{1300nm}$) of (a) 3D-SMF and (b) SMF 1550 during 800 ºC annealing cycles.

Fig. 3 (a) shows the variation of 1300 nm loss ($\Delta\alpha_{1300nm}$) of 3D-SMF during the process of 800 ºC annealing cycles. The loss reduction starts to take place at the end of annealing in the

1st treatment cycle. Then as fiber slowly cooled down to room temperature, the loss reduction continues gradually. A sharp decay of loss reduction at 1300 nm could be observed in the annealing process of the 2nd and 3rd treatment cycles. In the 4th treatment cycle, the observed loss reduction seems to slowly reach saturation at -3 dB/m. To eliminate the impact of splice points, such observed loss reduction was confirmed when repeating similar experiment by intentionally putting splice points between SMF 1550 and 3D-SMF out of the furnace (~ 55 cm 3D-SMF in the furnace, ~ 1.1 m in total length). Similar loss reduction was also verified in 800 ºC annealed 3D-BEDF. The 830 nm loss ($\alpha_{830\ nm}$) of this 3D-BEDF is reduced by ~ 6 dB/m after 10 hr annealing.

To make a comparison, a section of SMF 1550 was also post treated in the same furnace for three times at 800 ºC. The annealing dwell time was set to 5 hrs for each cycle. The variation of 1300 nm loss ($\Delta\alpha_{1300nm}$) of this fiber is demonstrated in Fig. 3 (b). Different from 3D-SMF, we could only observe the irreversible growth of loss increasing about 0.25 dB/m after a total of 15 hrs annealing time. The observed irreversible growth of loss could be caused by fiber devitrification [15]. This result also indicates that the observed loss reduction shown in Fig. 3 (a) is completely caused by 3D fibers.

Besides the 1300 nm loss reduction observed from Fig. 3 (a), the loss reduction of the whole measured spectrum from 900 to 1350 nm after each heat treatment cycle could also be achieved as demonstrated in Fig. 4 (a). The most distinct loss reduction could be observed after 2nd heat treatment cycle. Then, such loss reduction became less significant after 3rd heat treatment cycle. After the 4th treatment cycle, it should be noted that the loss reduction can no longer continue while the growth of loss starts to take place especially for short wavelength range. The significant loss dips at the wavelength around 1100 nm are caused by the variation of cut-off wavelength (λ_{co} ~ 1100 nm) of the pigtail fiber SMF 1550 nm that also annealed in the furnace. In the case that annealing 3D-SMF by intentionally putting splice points between SMF 1550 and 3D-SMF out of the furnace, there is no significant loss dip at 1100 nm in the loss variation spectra.

It becomes clearer as we plot the variation of loss of specific wavelength against treatment cycles, as demonstrated in Fig. 4 (b). The observed loss reduction by post heat treatment is more pronounced for short wavelength, e.g., $\Delta\alpha_{900\ nm}$ compared to $\Delta\alpha_{1300\ nm}$ after 2nd and 3rd treatment cycle. Then after 4th treatment cycle, the growth of loss starts to take place and is also pronounced for short wavelength, e.g., $\Delta\alpha_{900\ nm}$ and $\Delta\alpha_{1100\ nm}$ compared to $\Delta\alpha_{1300\ nm}$. Meanwhile, no significant dimension changes were observed as comparing the untreated sample with 800 ºC 10 hr annealed sample.

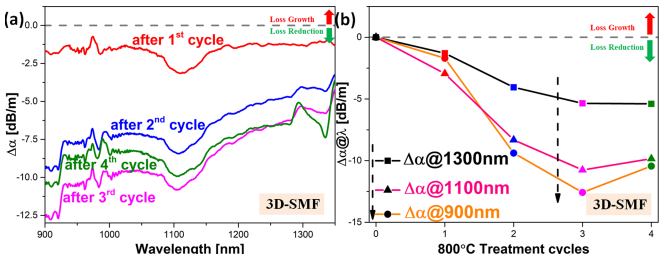

Fig. 4. (a) The variation of loss (Δα) from 900 nm to 1350 nm after 4 times 10 hr 800 ºC heat treatment cycles. (b) The variation of loss at 900 nm, 1100 nm, and 1300 nm of 3D-SMF as a function treatment cycles.

B. 3D fiber loss at high temperature

In addition to the loss reduction observed after 800 ºC annealing, in Fig. 3 (a), another notable feature is a sharp tip of loss growth observed as furnace temperature initially raised to the target temperature of 800 ºC. A similar phenomenon is also observed in 3D-BEDF as temperature elevated to high temperature. We assume that the observed the sharp tip of loss growth could be caused by the high temperature. To verify this assumption, in the 5th treatment cycle, the 3D-SMF was heated to 700 ºC step by step and then slowly cooled down to room temperature. To avoid the long-time high temperature annealing caused permanent loss changes as demonstrates in Fig. 3 (a), the annealing temperature was selected as 700 ºC instead of 800 ºC, and the annealing dwell time for each annealing temperature stage was controlled to be only 1hr. Meanwhile, the variation of intensity at 1300 nm ($I_{1300\ nm}$) was recorded by the experimental set-up depicted in Fig. 2 (a).

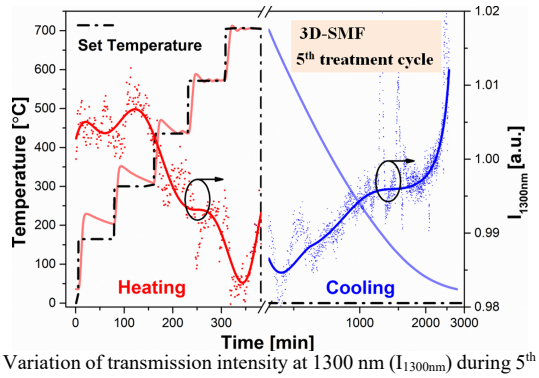

Fig. 5. Variation of transmission intensity at 1300 nm (I_{1300nm}) during 5th 700 ºC treatment cycle of 3D-SMF.

As can be seen from the Fig. 5, as the temperature gradually increases from room temperature to 700 ºC, the normalized transmission intensity at 1300 nm (I_{1300nm}) decreases to ~ 0.98, corresponding to ~ 0.22 dB/m loss growth. Then as the furnace slowly cooled down to room temperature, the I_{1300nm} gradually recovery to its initial level, confirming that the observed the sharp tip of loss growth in the 2nd, 3rd and the 4th treatment cycle is caused by the impact of high temperature. Such observed loss at high temperature could be associated with the changes of refractive index [16], and more research are needed to clarify above hypothesis.

IV. Discussion

To investigate the variation of 3D fiber structure before and after annealing, the Raman spectroscopy technique was applied. The Raman spectra of the samples were recorded at room temperature with a T64000 Jobin-Yvon-Horiba® spectrometer equipped with an Olympus® microscope. A confocal system and a 1024 Charge-Coupled Detector cooled by nitrogen were used, allowing a spatial resolution of 1-2 μm^2 with a ×100 objective. The spectral resolution is ~0.7 cm^{-1}. A Coherent® Argon laser is used with an excitation wavelength of 488.1 nm with 50 mW on the sample. All spectra were acquired in the frequency range 200-1300 cm^{-1} with the same experimental

conditions to minimize experimental errors. Fig. 6 below shows the shows Raman spectroscopy results of the 3D-SMF core before and 25 hr 800 °C annealing.

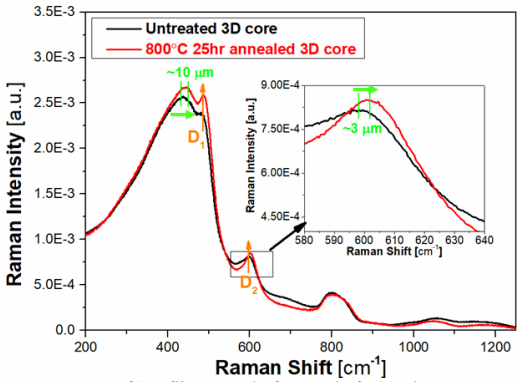

Fig. 6. Raman spectra of 3D fiber core before and after 25 hr 800 °C annealing. Inset: the detailed Raman spectra from 580 to 640 cm^{-1}.

From the Fig. 6 above, the principal Raman features of silica glass, peaking at around 440, ~ 490 (D1), and ~ 600 cm^{-1} (D2) [17, 18], are well observed in core of 3D-SMF. After 25 hr 800 °C annealing, the D1 and D2 peaks showing the characteristics of "dense" glass increase, indicating that the fiber core densification takes place after high temperature annealing [17]. The Raman spectra of 3D-SMF cladding before and after annealing were also measured, while the variation is not significant. Based on these results, we assumed that there are two primary mechanisms leading to the observed loss reduction. The first mechanism is that glass densification makes glass structure more homogeneous /less porous at the nanoscale, and thus less scattering loss. The second mechanism is that glass densification leads to the higher densification rate and a higher index of fiber core, and a strong index contrast between core and cladding is generated, leading to the higher mode confinement and thus less propagation loss. Based on the work revealing the relationship between Raman main band/D2 position and silica glass densification ratio [19], it is estimated that 3D SMF core demonstrates a ~ 2% to 3.5% densification increase after 25 hrs 800 ºC annealing since there is a ~ 10 cm^{-1} position shift of main band at 440 cm^{-1}, and a ~ 3 cm^{-1} position shift of D2 at 600 cm^{-1}. Assuming that there is no elastic response, the refractive index changes can be estimated from density changes using the differentiated Lorentz-Lorenz equation where the ratio of relative polarizability change to relative density change $\Omega = 0.22$ [20], and the refractive index of silica at 1300 nm n=1.45. It is estimated that core index can be increased by ~ 0.011 to ~ 0.019. These results indicate that inadequately densified structure could be main origin of loss of 3D fibers, and 3D fibers fabrication needs to be further optimized by prolonging the thermal processing and increasing the pressure.

V. Conclusion

In summary, the loss reduction of 3D silica lithography fibers by the post-draw annealing is reported. By successive annealing at 800 ºC, we have observed that the loss coefficient of fibers fabricated by 3D silica lithography techniques can be reduced. Meanwhile, we found that core densification takes place by measuring Raman spectrum. We assume that the observed loss reduction could be associated with more homogeneous structure and higher index contrast by the fiber core densification. We also observed an obvious temperature dependent loss as 3D silica lithography fibers heated to high temperature. We consider that further optimization is needed by prolonging thermal processing and increasing pressure.

Reference

[1] J. Ballato and P. Dragic, "Glass: the carrier of light - a brief history of optical fiber," *International Journal of Applied Glass Science,* vol. 7, no. 4, pp. 413-422, 2016.

[2] S. R. Nagel, J. B. MacChesney, and K. L. Walker, "An overview of the modified chemical vapor deposition (MCVD) process and performance," *IEEE Transactions on Microwave Theory and Techniques,* vol. 30, no. 4, pp. 305-322, 1982.

[3] G.-D. Peng, "3D silica lithography for Doped and Structured Optical Fibers," *Sixth International Workshop on Specialty Optical Fibers and Their Applications (WSOF 2019),* vol. 11206, 2019.

[4] K. Cook, S. Leon-Saval, J. Canning, Z. Reid, M. A. Hossain, and G.-D. Peng, "Air-structured optical fibre drawn from a 3D-printed preform," in *24th International Conference on Optical Fibre Sensors*, 2015, vol. 9634, p. 96343E: International Society for Optics and Photonics.

[5] F. Kotz *et al.*, "Three-dimensional printing of transparent fused silica glass," *Nature,* vol. 544, no. 7650, pp. 337-339, Apr 19 2017.

[6] Y. Luo, J. Canning, J. Zhang, and G.-D. Peng, "Toward optical fibre fabrication using 3D printing technology," *Optical Fiber Technology,* vol. 58, p. 102299, 2020.

[7] D. Zhang, X. Liu, and J. Qiu, "3D printing of glass by additive manufacturing techniques: a review," *Frontiers of Optoelectronics,* 2020/07/10 2020.

[8] D. T. Nguyen *et al.*, "3D - printed transparent glass," *Advanced Materials,* vol. 29, no. 26, p. 1701181, 2017.

[9] I. Cooperstein, E. Shukrun, O. Press, A. Kamyshny, and S. Magdassi, "Additive manufacturing of transparent silica glass from solutions," *ACS applied materials & interfaces,* vol. 10, no. 22, pp. 18879-18885, 2018.

[10] A. A. Al-Hasnawi and I. A. D. Al-Hydary, "The Effect of Sintering Temperature and Soaking Time on the Transparency of Silica Glass Prepared by Gel-Casting and Sintering," *International Journal of Applied Engineering Research,* vol. 12, no. 24, pp. 15257-15260, 2017.

[11] Y. Chu *et al.*, "Silica optical fiber drawn from 3D printed preforms," *Optics letters,* vol. 44, no. 21, pp. 5358-5361, 2019.

[12] J. CANNING, Y. WANG, M. LANCRY, Y. LUO, and G. PENG, "Helical Distributed Feedback Fibre Bragg Gratings & Rocking Filters in 3D Printed Preform-Drawn Fibre," 2019.

[13] Y. Wang *et al.*, "Thermal Stability of Type II Modifications Inscribed by Femtosecond Laser in a Fiber Drawn from a 3D Printed Preform," *Applied Sciences,* vol. 11, no. 2, p. 600, 2021.

[14] B. Zhang *et al.*, "Thermal bleaching of BACs in bismuth/erbium co-doped fiber fabricated through 3D silica lithography," *Optics Letters,* vol. 45, no. 13, pp. 3729-3732, 2020.

[15] A. Rose, "Devitrification in annealed optical fiber," *Journal of Lightwave Technology,* vol. 15, no. 5, pp. 808-814, 1997.

[16] D. P. Hawn, *The Effects of High Temperature and Nuclear Radiation on the Optical Transmission of Silica Optical Fibers*. The Ohio State University, 2012.

[17] Y. Wang, M. Cavillon, N. Ollier, B. Poumellec, and M. Lancry, "An Overview of the Thermal Erasure Mechanisms of Femtosecond Laser - Induced Nanogratings in Silica Glass," *physica status solidi (a),* p. 2100023, 2021.

[18] Y. Wang *et al.*, "Femtosecond laser direct writing in SiO2 - Al2O3 binary glasses and thermal stability of Type II permanent modifications," *Journal of the American Ceramic Society,* vol. 103, no. 8, pp. 4286-4294, 2020.

[19] C. Dereure, "Comportement mécanique des verres sous choc produit par interaction laser-matière: une approche expérimentale et numérique multi-échelles," Université Rennes 1, 2019.

[20] R. E. Schenker and W. G. Oldham, "Ultraviolet-induced densification in fused silica," *Journal of Applied Physics,* vol. 82, no. 3, pp. 1065-1071, 1997.

5.2 Thermal Stability of Type II Modifications Inscribed by Femtosecond Laser in a Fiber Drawn from a 3D Printed Preform

applied sciences

MDPI

Article

Thermal Stability of Type II Modifications Inscribed by Femtosecond Laser in a Fiber Drawn from a 3D Printed Preform

Yitao Wang [1], Shuen Wei [2,*], Maxime Cavillon [1], Benjamin Sapaly [1], Bertrand Poumellec [1], Gang-Ding Peng [2], John Canning [3] and Matthieu Lancry [1,*]

[1] French National Centre for Scientific Research, ICMMO (SP2M/MAP), Université Paris-Saclay, 91405 Orsay CEDEX, France; yitao.wang@universite-paris-saclay.fr (Y.W.); maxime.cavillon@universite-paris-saclay.fr (M.C.); benjamin.sapaly@universite-paris-saclay.fr (B.S.); bertrand.poumellec@gmail.com (B.P.)

[2] Photonics and Optical Communications, School of Electrical Engineering and Telecommunications, University of New South Wales, Sydney, NSW 2052, Australia; g.peng@unsw.edu.au

[3] Interdisciplinary Photonics Laboratories, Global Big Data Technologies Centre (GBDTC), School of Electrical & Data Engineering, University of Technology Sydney, Sydney, NSW 2007, Australia; john.canning@uts.edu.au

* Correspondence: shuen.wei@student.unsw.edu.au (S.W.); matthieu.lancry@universite-paris-saclay.fr (M.L.)

Abstract: Fiber drawing from a 3D printed perform was recently discussed to go beyond the limitations of conventional optical fiber manufacturing in terms of structure and materials. In this work, the photosensitivity of silica optical fibers to femtosecond laser light, and fabricated by 3D printing a preform, is investigated. The writing kinetics and the thermal performance of Type II modifications are studied by varying the laser pulse energy and investigating the birefringence response of the femtosecond (fs)-laser written structures. Compared with a conventional telecom single mode fiber (SMF28), the fiber made by 3D printing is found to have similar writing kinetics and thermal performance. Additionally, the thermal stability of the imprinted fs-laser induced nanostructures is investigated based on the Rayleigh–Plesset equation, describing a model of nanopores dissolution underpinning Type II modifications with thermal annealing.

Keywords: 3D printed preform; fibers; nanogratings; birefringence; femtosecond laser

check for updates

Citation: Wang, Y.; Wei, S.; Cavillon, M.; Sapaly, B.; Poumellec, B.; Peng, G.-D.; Canning, J.; Lancry, M. Thermal Stability of Type II Modifications Inscribed by Femtosecond Laser in a Fiber Drawn from a 3D Printed Preform. *Appl. Sci.* **2021**, *11*, 600. https://doi.org/10.3390/app11020600

Received: 23 November 2020
Accepted: 6 January 2021
Published: 9 January 2021

Publisher's Note: MDPI stays neutral with regard to jurisdictional claims in published maps and institutional affiliations.

Copyright: © 2021 by the authors. Licensee MDPI, Basel, Switzerland. This article is an open access article distributed under the terms and conditions of the Creative Commons Attribution (CC BY) license (https://creativecommons.org/licenses/by/4.0/).

1. Introduction

Silica optical fiber is the backbone of optical fiber communication networks, permitting signal transmission over long distances at high bandwidth. Since the 1970s numerous methods were explored in the development of low loss silica telecom fibers, most involving the fabrication of preforms from which fiber is subsequently drawn [1]. The most successful processes have been variations of chemical vapor deposition (CVD) [2]. With the development of optical fiber technology, the focus has gradually included increasing specialization of the fiber for components such as fiber Bragg grating (FBG) sensors, lasers, and amplifiers. Ideally optical fiber fabrication has to remain compatible with standard low-loss fiber as well as opening the door to novel functionalities. Nevertheless, conventional fabrication methods such as CVD and rod-in-tube stacking, have limited capability in both material and structure flexibility for diverse and custom-designed functionalities [3–5]. To address these limitations a new alternative is the use of additive manufacturing in the fabrication of preforms from which fiber is drawn [6,7].

The early work in this field was on 3D printing plastic fibers [6], followed by 3D printed silica-based fiber preform fabrication [7]. 3D silica printing allows greater freedom in both structure and material design and choice. This fabrication process will be a major disruption more broadly because it reduces the skill requirements typically required in CVD processes and reduces overall costs whilst enabling newer designs. Therefore, it is important to better understand and compare these new fibers against their equivalent

counterpart produced by conventional means. One important comparison that provides insights into the quality of glass in these fibers is assessing photosensitivity. This can be done by creating a refractive index grating in the core of an optical fiber using optical irradiation, a process that underpins fiber Bragg gratings (FBG) inscription and application, demonstrating both scientific and practical significance [8].

Among various types of FBGs, Type II-fs-IR-FBGs, inscribed by femtosecond near-infrared (fs-IR) irradiation, have drawn great attention, due to their notable thermal stability at T~1000 °C for at least several hours and even 100 h at this temperature after stabilization in SMF28(single mode fiber) fibers [9,10]. In addition, it has been shown that the thermal stability of these Type II modifications is affected by writing and fabrication conditions. For example, by increasing the writing speed, the reflectivity of Type II fs-IR FBGs is found to be more resistant to higher temperatures [11]. It has also been reported that the thermal performance of FBGs can be influenced by varying pulse energy or repetition rate [12]. Unlike Type I-fs-IR-FBGs where the refractive index changes are positive with respect to the non-irradiated region and could only be used up to T~800 °C [13], Type II fs-IR FBGs, associated with a high level of anisotropic index change, are attributed to the formation of self-organized nanogratings [14] made through glass oxide decomposition [15]. These nanostructures are composed of regularly spaced porous nanolayers with nanopores typically a few tens of nm in size [15,16]. Due to their periodic subwavelength nanostructure, the Type II modifications are birefringent, and therefore the optical retardance R can be monitored to investigate the thermal stability of our object.

Thus, to explore the photosensitivity of optical fibers fabricated from preforms produced by additive manufacture, an fs-IR laser was used to create changes within the fiber, henceforth termed "3D printed fiber". The laser-induced birefringence is measured at different pulse energies. Then the thermal stability of these fs-IR laser inscribed structures (Type II modifications) was evaluated through multiple isochronal annealing cycles. For comparison, similar experiments were performed on conventional silica SMF28 optical fiber (from Corning) and will serve as a reference throughout this work. Finally, the porous nanostructures, induced by Type II modifications in silica glass are stable at high temperatures (>1000 °C). To investigate their high-temperature stability behavior, isochronal annealing is performed on irradiated fiber samples, and the birefringent response is monitored. Following this, the Rayleigh–Plesset (R-P) equation is used to fit the data [16].

2. Experimental Setup

2.1. Fiber Manufacturing

A brief overview of the process for 3D printed fibers is shown in Figure 1. It can be divided into five steps, and are described in short. (1) First, a photocurable resin was fabricated by mixing 2-phenoxyethanol (POE), 2-hydroxyethyl methacrylate (HEMA), diphenyl(2,4,6-trimethylbenzoyl) phosphine oxide (DPO), tetra(ethylenglycol) diacrylate (TEGDA), and hydroquinone (Hyd), (all purchased from Sigma-Aldrich, Australia), which is a photoresin provided for use with digital light processing (DLP) 3D printer. Then, high purity silica glass nanoparticles (purchased from Evonik, Australia) were dispersed in the resin and sued in printing. (2) The optical fiber cladding preform was designed by Inventor CAD (the targeted cladding diameter was ϕ = 125 µm) and then fabricated using a DLP 3D printer (Asiga Freeform Pro 2 75 UV; x,y pixel resolution ~75 µm, Asiga, Sydney, Australia). (3) To make the preform core, germanium oxide (GeO_2) powder was added into the previously mixed resin. This increases the refractive index of the mix. The resin was subsequently injected into the cladding preform. (4) With high temperature heating, the preform undergoes thermal debinding above 300 °C to remove the polymer resin, leaving only a silica structure. (5) Finally, the preform is inserted into a supporting silica tube and placed inside a draw tower and drawn into fiber (L~2–3 km, cladding diameter ~125 µm) at a temperature T~1900 °C. More details of the fabrication process can be found in References [6,7,17].

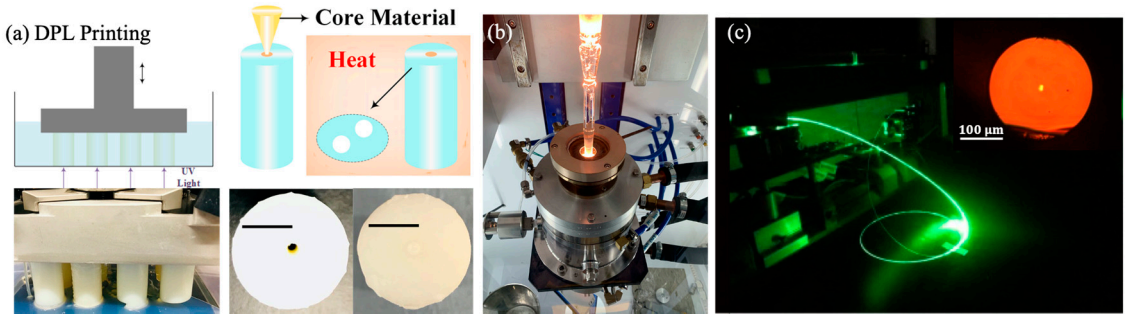

Figure 1. Overview of 3D printed fibers fabrication: (**a**) The preform is produced using additive manufacture and annealed to remove the binding agent. It is then (**b**) sintered on an optical fiber draw tower and drawn into (**c**) optical fiber.

2.2. Optical Fiber Characterization

After drawing, fiber segments are selected to investigate the core-cladding geometry, as well as the core radial distribution of the GeO_2 dopant. A highly asymmetric fiber core is observed in Figure 2 (inset), arising from core distortion during the drawing process where the outer support silica tube used required a temperature higher than optimal for the interior Fused Deposition Modeling (FDM) preform. The printed preform was not transversally uniform leading to stresses that distorted the softer germanosilicate core producing the observed twisted elliptical shape (long axis ϕ~4 µm, short axis ϕ~2 µm; they are not orthogonal suggesting elliptical birefringence). These were recorded using a ZEISS SUPRA 55 VP scanning electron microscope (SEM). This 3D printed preform drawn silica fiber has a germanosilicate core and silica cladding. Dopant distributions were measured with energy dispersive x-ray analysis (EDX) and shown in Figure 2 along one axis of the fiber. Compared to SMF28, the core size of the 3D printed fiber is smaller with (GeO_2) ~10 mol %, almost twice as much as SMF28, though less than commercial photosensitive fibers such as Nufern's GF1 ((GeO_2)~33 mol %). No evidence of polymer or water from the resin preform was detected using FTIR spectroscopy.

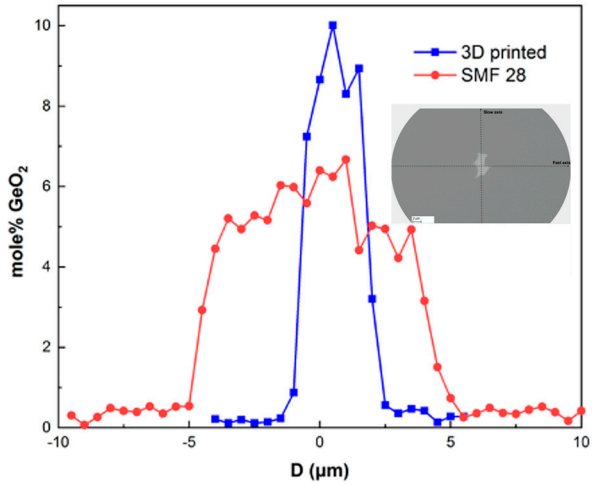

Figure 2. GeO_2 concentration profile across the core for two fibers: 3D printed fiber (squares) and SMF28 fiber (dots). D is the distance relative to the fiber core center. Inset: scanning electron micrograph of the 3D printed fiber core cross-section.

2.3. Laser Writing Experiments

Two fiber segments (one for 3D-printed and one for SMF28) were selected, each one having a length L~6–8 cm long. Their polymer coating was removed, and a high temperature adhesive was used to attach them onto a silica thin slide. A borosilicate glass

coverslip (170 µm thin) was placed on top of the fiber segments, with some index-matching oil (GN Nettest, n_D = 1.4580 at T = 25 °C) introduced between the silica and the borosilicate slides, to facilitate the observation of the core and subsequent laser irradiation. Each sample was then placed on an XYZ motorized translation stage and irradiated using a femtosecond laser (λ = 1030 nm, t = 250 fs). The laser repetition rate was fixed to rr = 100 kHz and the scanning speed to v = 100 µm/s. The laser beam was focused using a 0.6 NA aspheric lens. Geometry similar to a line-by-line FBG writing was performed to investigate the writing kinetics of Type II modifications. As represented in Figure 3a, several lines length L = 60 µm are written, traversing both the core and the cladding. They are written perpendicular to the direction of the fiber longitudinal axis with a linear laser polarization oriented either parallel (labeled Yy configuration,//) or perpendicular (labeled Yx configuration, ⊥) to the scanning direction. The spacing between each line is 5 µm, and the pulse energy E_p (in µJ/pulse) varies between each line in steps of ΔE~0.1 µJ, ranging from Ep = 0.1 to 1.5 µJ. To measure the optical retardance R, an Olympus BX51 polarizing optical microscope equipped with a quarter waveplate was used. The retardance is defined as R = B × L, where B is the birefringence and L is the length of the birefringent object being measured. In this work, the impact of pulse energy on the retardance response is investigated. This provides an indication of the kind of modifications (voids, nanogratings, densification) involved during the irradiation process. The impact of processing parameters such as repetition rate (rr), pulse duration (Δt) and writing speed (v) will be systematically studied in future work.

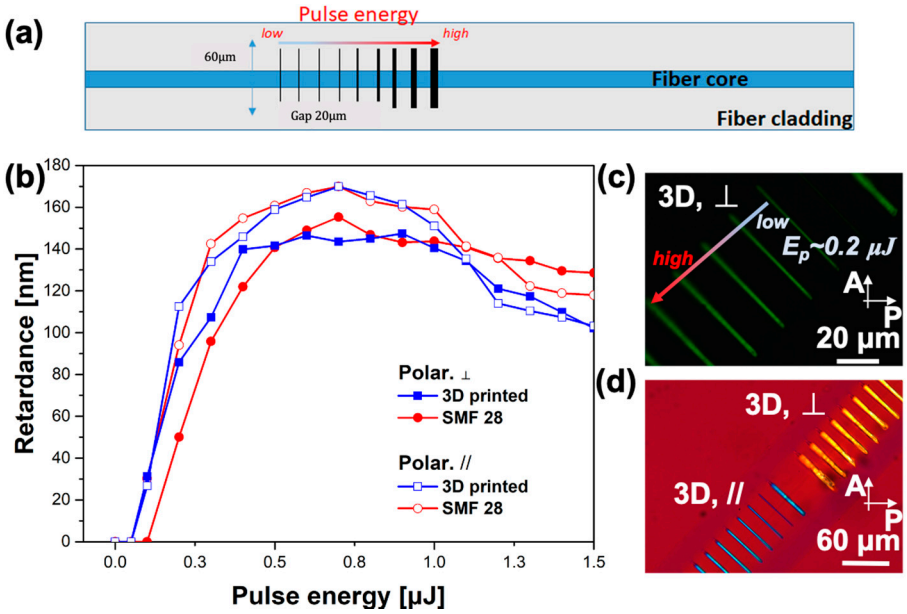

Figure 3. (**a**): Experimental laser writing design: irradiation of fs laser inside fiber core and cladding of an optical fiber using different pulse energies. (**b**) Retardance, R, as a function of pulse energy for 3D printed fiber (squares) and SMF28 fiber (circles). Experimental conditions are: λ = 1030 nm, rr = 100 kHz, v = 100 µm/s, NA = 0.6, t = 250 fs, laser polarization ⊥ and // to writing direction. (**c**) Optical microscope image of for 3D printed fiber using crossed polarizer and analyzer with the Yx configuration (⊥). (**d**) Optical microscope image of 3D printed fiber using crossed polarizer and analyzer and a full retardation waveplate inserted at 45° indicating the orientation of the slow axis.

3. Results

Figure 3b shows the measurements of the retardance, R, as a function of the laser pulse energy for both investigated fibers. We focused on the Type II fs-IR threshold where the optical properties of the irradiated regions are modified. A strong linear birefringence originating from the formation of nanogratings can be detected when the energy exceeds the threshold. Illustrated in Figure 3b, the 3D printed fiber shows a lower Type II threshold

than conventional fiber. A well-defined birefringence response appears when the pulse energy is above E_p~0.1 μJ for 3D-printed fiber. For the SMF 28 fiber, the Type II threshold is observed at a laser pulse energy E_p~0.2 μJ. Such variations in Type II threshold could be explained by the higher Ge concentration that leads to higher interface stresses and therefore lower thresholds. Under crossed polarizer and analyzer, the lines appear birefringent when E_p > 0.2 μJ for 3D printed fiber as shown in Figure 3c. Furthermore, the first order (full wave) plate technique [18] was used to detect the slow/fast axis orientation of the photo-induced birefringence (Figure 3d). When the inscribed line slow axis is parallel (perpendicular) to the slow axis of the full wave, the line appears blue (yellow). This is consistent with birefringence that we have observed previously that is related to the formation of nanogratings [19,20], and where the fast axis is oriented parallel to the laser polarization.

Although within error there are small differences between threshold values, R increases as a function of pulse energy in a similar way for both fibers (both in shape and magnitude) as shown in Figure 3b. R values rapidly increased after exceeding a threshold and began to plateau after E_p~0.4 μJ. It should be noted that the retardance is lower for the Yx configuration relative to the Yy configuration. Such polarization dependence is explained by boundary conditions and varying spatial–temporal properties of the ultrashort pulse laser beam. This was quantified with pulse front tilting, leading to anisotropic photosensitivity [21,22]. These results indicate that these 3D printed fibers exhibit analogous photosensitivity compared with SMF28, consistent with similar quality germanosilicate glass. They also suggest that similarly to conventional fibers, applications such as FBGs are possible using 3D printed preform derived optical fibers. This comparative study suggests material quality is comparable despite the large differences in initial preform fabrication. This is a promising result pointing towards a feasible disruption of conventional fiber fabrication using additive manufacturing.

In order to better understand and confirm the origin of the polarization dependent birefringence detected in Figure 3, the fiber segment was simply cleaved by the ceramic fiber scribe and the cross sectional area with the laser polarization ⊥ to the writing direction was directly investigated using an SEM (Field-Emission Gun Scanning Electron Microscope, ZEISS SUPRA 55 VP, 1 kV accelerating voltage, ZEISS, Jena, Germany). Figure 4c shows that the trajectory of the laser perfectly passes through the center of the fiber. As observed in Figure 4a,b, the formation of the nanogratings can be clearly identified in both the cladding and the core zone of the 3D printed fiber. In similar bulk compositions [15], such periodic array of porous nanoplanes separated by non-porous glass leads to the formation of form birefringence [15,20].

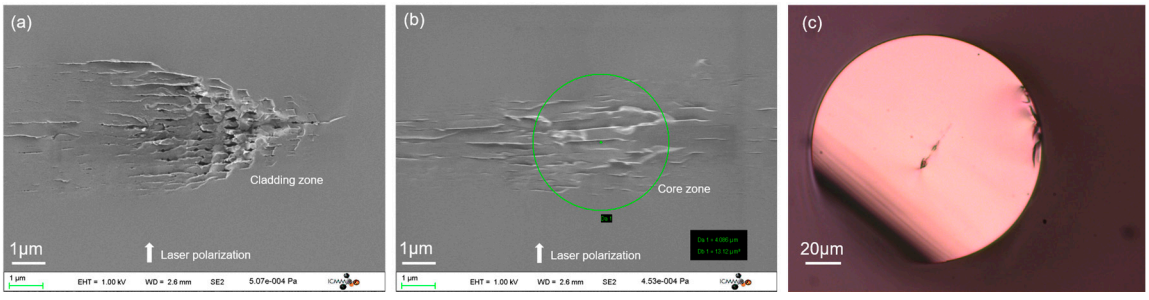

Figure 4. Scanning electron micrographs in the 3D printed fiber, both at the cladding (**a**) and the core (**b**) area, for orthogonal laser polarization direction with respect to the writing direction, which permits sideways visualization of the nanogratings. (**c**) Optical microscope image of the cross section of 3D printed fiber. Experimental conditions are: λ = 1030 nm, rr = 100 kHz, v = 100 μm/s, NA = 0.6, t = 250 fs, E = 0.7 μJ/pulse.

The thermal stability of the fibers was investigated using Δt = 30 min step isochronal annealing up to temperatures T = 1100 °C. In Figure 5, retardance values $R_{norm}(\Delta t, T)$ (normalized with respect to their initial room temperature values R(t = 0, and T = 20 °C)) as a function of annealing temperature for both SMF28 and the 3D printed fiber are

displayed. In this figure the comparison between the two samples is set for E = 1 μJ/pulse and//irradiation condition for which the measured R values are among the highest (see Figure 3). It is worth pointing out that in order for each data point to be independent to the other, the criterion $(\Delta t \times k_0)^{-(\Delta T/Tmax)} << 1$ must be fulfilled [23] (with k_0 estimated to be around 5×10^5 to 5×10^7 s^{-1} for nanogratings erasure in silica [24]). In this work, this criterion is not satisfied for T > 900 °C and therefore the thermal stability is slightly underestimated with respect to a stability curve having independent data points.

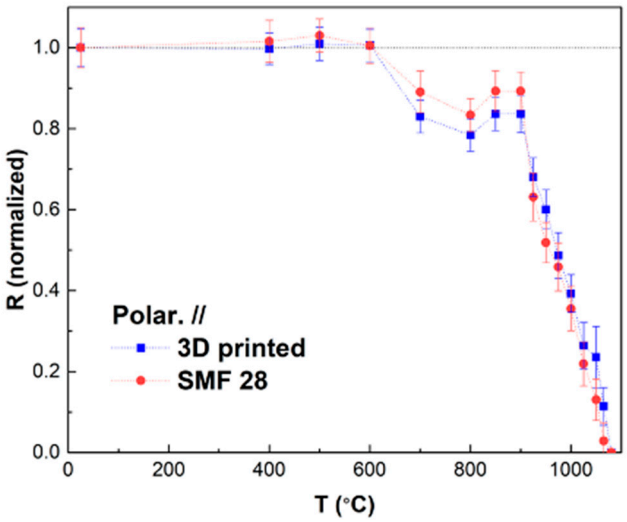

Figure 5. Thermal stability with normalized retardance, R_{norm}, as a function of annealing temperature, T, for drawn 3D printed fiber (in blue) and SMF 28 fiber (in red), for // configurations. The pulse energy is E = 1 μJ and the measurements were performed at room temperature after each annealing step (Δt = 30 min).

In Figure 5 some characteristic features are visible. These reveal different erasure mechanisms. First, in the low-temperature (T < 600 °C) range, compared with the initial value, the two fibers exhibit a similar trend, where R_{norm} slightly increases up to T = 600 °C. Such a feature could be attributed to central defects being erased at low temperatures (T < 600 °C) [20], resulting in an increase in nanogratings refractive index contrast (hence retardance). Beyond 600 °C, R_{norm} decreases up to T = 850 °C for both fibers, immediately followed by a very slight rise within T = 800 to 900 °C. This observed growth could be related to changes in the stress field. Isochronal annealing leads to an increase in residual stresses, resulting in an increase in the magnitude of birefringence. More details with respect to this can be found in References [19,25]. Turning to SiO_2 glass structure, it has been shown that changes in Si-O three and four-fold rings anneal out over T = 700–900 °C. They are well correlated with the structural relaxation of densified silica formed within the nanogratings regime [23]. As the annealing temperature increases, the induced stress relaxes gradually, lessening the birefringence and further decreasing retardance. Finally, above T = 925 °C, the normalized retardance, R_{norm}, for both fiber samples diminishes drastically. The latter could not be detected above T~1080 °C. Overall, the two fibers exhibit very similar thermal stability based on their performance during the isochronal annealing. It should be noted that the concentration of GeO_2 in the two fibers is different and the mode overlaps different. Hence, the results presented here are in agreement with Reference [11] where it was shown that the variation of GeO_2 concentration in the fiber core only has a minor impact on the overall thermal behavior.

To further investigate the thermal stability of the written Type II modifications in 3D-printed fibers at different pulse energies, and once again to compare them with conventional CVD fibers, we annealed the irradiated samples isochronously from T = 400 °C to 1100 °C, with a constant time increment of 30 min at each temperature step. Figure 6 shows the

evolution of normalized retardance (R_{norm}) as a function of T for lines irradiated with different energy (E).

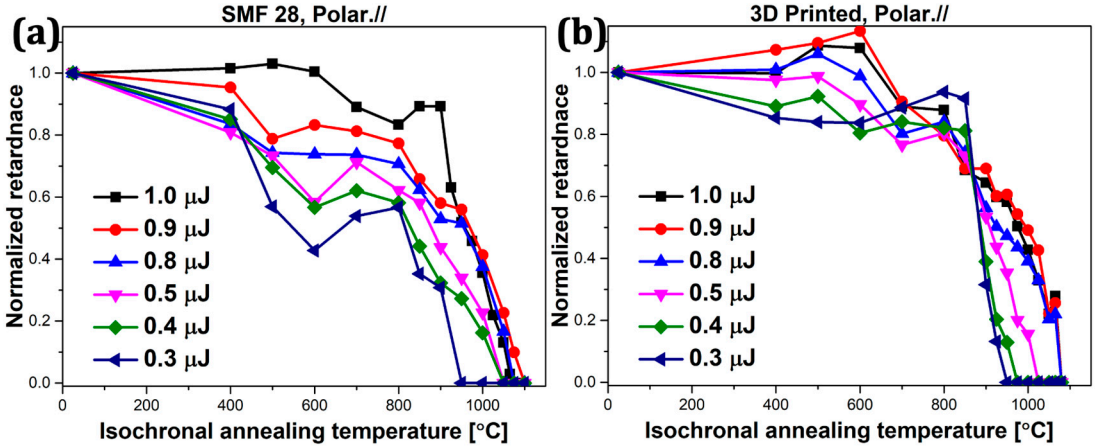

Figure 6. Normalized retardance (R_{norm}, relative to its initial value at room T) as a function of temperature for (**a**) SMF 28 fiber and (**b**) 3D printed fiber; different pulse energies were used. Experimental conditions are: λ = 1030 nm, rr = 100 kHz, v = 100 μm/s, 103 pulses/μm, NA = 0.6, pulse duration t = 250 fs, laser polarization // to writing direction (Yy). The measurements were performed at room temperature after each annealing step (Δt = 30 min) and the results are normalized by the initial value of the untreated sample R (t = 0, and T = 20 °C).

With different pulse energies, the two fibers exhibit similar trends during heat treatment. There are at least two distinct features in the retardance response, one at low temperature and one at high temperature. At low pulse energy (3D printed fibers $E_p \leq 0.7$ μJ and SMF 28 fiber $E_p \leq 0.9$ μJ) there is immediate retardance decay after the start of annealing. Typically, R_{norm} decreases until T = 600 °C corresponding to a 20–60% decrease in magnitude. This effect is more pronounced for the lowest pulse energies. Next, R increases in the range of T = (600–800) °C and is also more pronounced in the low energy regime. In the literature the appearance of this unusual increase in retardance can be related to annealing out of the residual part of the Type I modifications [26] between the nanolayer, that is mostly attributed to densification and related stress field (and thus stress-induced birefringence). This leaves a higher birefringence or FBG reflectivity [11]. Type I modifications require a lower deposited energy than Type II during the irradiation. This means the contribution of Type I response on the measured retardance is likely higher during lower energy Type II modification. The more significant increase in retardance R_{norm} of low energy Type II changes arise after the residual effects of Type I are "erased" or relaxed. This behavior has been observed across various conventional gratings written by UV (Type I, Type IA and Type II and Type IIA), with high temperature annealing, reflecting intrinsic amorphous material properties rather than laser writing [26].

As the annealing temperature increases beyond T = 800 °C, the R_{norm} for all lines and at any pulse energy starts to decline, likely due to gradual stress relaxation that takes place below the glass transition temperature (~0.9 T_g for 30 min). Finally, the erasure of the porous nanolayers is observed over T = (950–1080) °C range as a function of the laser pulse energy [16]. Indeed, the higher the laser pulse energy, the higher the annealing temperature needed to fully erase Type II modifications. This can be explained by noting that as the energy increases, the non-linear writing light dosage increases. As the energy increases in the Type II range, the thermal stability of the modification is enhanced for both the processed 3D printed fiber and the SMF28 fiber. This is a typical case described in Reference [23] where there is a link between writing and erasure. When the pulse energy increases, the demarcation energy increases and more stable sites, or deeper traps, are accessed, and more stable species produced. The subsequent modifications become more stable. The

process is reflective of the distribution of energies possible within amorphous materials; i.e., distribution of density states. More details will be discussed in the next section.

Given similar behaviors and stabilities between SMF-28 and the 3D silica printed fiber with respect to varying laser pulse energies, the thermal stability of Type II modifications and FBGs in all future 3D printed fibers can be similarly enhanced by optimizing the laser irradiation energy. The retardance values for the two types of fibers could not be reliably measured beyond the annealing temperature T = 1100 °C. We infer that mechanisms of Type II modifications erasure for both types of fiber are similar, and less affected by different fabrication techniques. This would imply that 3D-printed derived FBGs can also be used in high temperature environments. Furthermore, the 3D printed fiber appears to possess superior thermal stability in the low energy range. Various factors need consideration, however, including the higher GeO_2 content in 3D printed fiber, though its impact in femtosecond laser processing is said to be insignificant [19]. The second potential factor contributing to better thermal stability could be very large non-orthogonal anisotropy of the fiber structure, both form, and stress based, the role of which is unclear between low and high energy exposures. Exposure can lead to anisotropic relaxation and potential effects on optical rotation depending on the orientation of the fiber itself. Future work will explore these details to establish whether this is an orientation characteristic or something caused by the manufacturing process.

4. Discussion

Recently, our group has demonstrated that the form birefringence related to the so-called nanogratings is quantitatively correlated to the porosity-filling factor of these nanostructures [27]. Control of the porosity was achieved by adjusting the laser pulse energy and the number of pulses/micron; i.e., the overlapping rate [28]. To further explore the reason why thermal stability is improved when irradiated with higher pulse energy in 3D printed silica fiber, the Rayleigh–Plesset (R-P) equation was used to simulate the erasure of pores in the nanostructure during the annealing process, and taking into account the same conditions for a direct comparison between experiment and theory. The equation describes the evolution of a spherical bubble inside an incompressible Newtonian fluid, and it can be expressed as follows:

$$\frac{\Delta P}{\rho} = R_{pore}\frac{d^2R_{pore}}{dt^2} + \frac{3}{2}\left(\frac{dR_{pore}}{dt}\right)^2 + \frac{4\eta(T)}{\rho R_{pore}}\frac{dR_{pore}}{dt} + \frac{2S}{\rho R_{pore}} \quad (1)$$

Here, ΔP is the pressure difference (in Pa) between the inside of the nanopore (supposed spherical) and far away from it, ρ is the glass density (in kg/m^{-3}), R_{pore} the radius (in m) of the spherical nanopore, t the time (in s), $\eta(T)$ the viscosity (in Pas), and S is the surface energy (in J/m^{-2}). The viscosity and its dependence with respect to temperature can be injected into the model by using a Vogel–Tammann–Fulcher (VTF) law in the form $\log(\eta) = A + B/(T-T_0)$. Initial conditions are R_{pore} (at t = 0) = R_0 and dR_{pore}/dt (at t = 0) = 0.

The nanopore size diameter from the R-P equation needs to be converted into a normalized retardance (R) value and used to compare with the normalized R values obtained in the experiment. The Maxwell–Garnet equation [29] will be used first to calculate the average refractive index of the porous nanolayer (n_{pl}):

$$n_{pl} = \sqrt{n_G^2\frac{n_G^2 + \frac{(1+2FF)}{3}\left(n_{pore}^2 - n_G^2\right)}{n_G^2 + \frac{(1-FF)}{3}\left(n_{pore}^2 - n_G^2\right)}} \quad (2)$$

n_G is the fiber refractive index (taken as n_G = 1.484, estimated from the chemical composition of the fiber), n_{pore} is the nanopore refractive index (taken equal to 1). Another important factor is the filling factor (FF) which is defined as the proportion of the nanopores' volume

taken in a unit volume of porous nanolayer (V), so it is obviously related to the number of nanopores (N) with an averaged nanopore radius (R_{pore}) and can be calculated using:

$$FF = N\frac{4\pi R_{pore}^3}{3V} \quad (3)$$

The birefringence B can be determined by the difference between the refractive indices of the ordinary axis (n_o) and the extraordinary axis (n_e). The following equation illustrates the detail:

$$B = n_o - n_e = \sqrt{\left[1-\frac{\delta}{\Lambda}\right]n_G^2 + \frac{\delta}{\Lambda}n_{pl}^2} - \left[\sqrt{\frac{\left[1-\frac{\delta}{\Lambda}\right]}{n_G^2} + \frac{\frac{\delta}{\Lambda}}{n_{pl}^2}}\right]^{-1} \quad (4)$$

n_G represents the refractive index between the porous nanolayers [28], Λ is the average spacing between nanolayers, δ is the porous nanolayer thickness, and (Λ–δ) is the interlayer thickness. Finally, with the birefringence B calculated, the retardance R can be worked out by the expression R = B × L as we defined above. More details about the simulation are provided in our recent work [16]. The conditions used in the simulation were set as: the surface energy (S) = 0.3 J/m^{-2}; the viscosity η(T) fitted using a VTF (Vogel–Tamman–Fulcher) law for binary GeO_2-SiO_2 glass with (GeO_2)~10 mol % [30].

Measured annealing curves of the 3D silica printed fiber (pulse energies of 0.6 μJ and 0.4 μJ), and the predicted ones calculated based on the R-P, are shown in Figure 7. We suppose the total birefringence of the nanogratings is composed by the contributions additive and independent. Then, the measured data are normalized relative to the sharp retardance decrease at the highest annealing temperature values that we hypothesized here to be characteristic of the nanopore erasure. In this paper only the final erasure step of the measured retardance R(Δt,T) is investigated. Following the same experimental conditions as in the experiment, the R-P equation was used to simulate the nanopore erasure, and the evolution of the retardance was calculated based the nanopore diameter, the filling factor FF and using the form birefringence equations (Equations (2)–(4)) shown above.

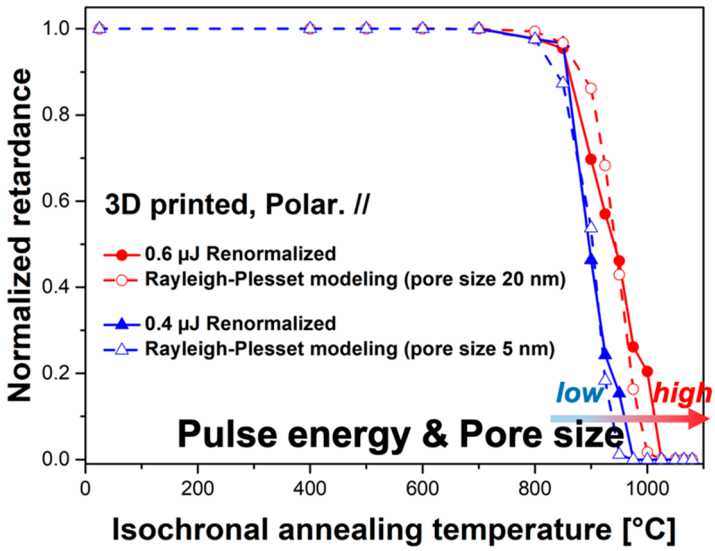

Figure 7. Evolution of the normalized retardance during step isochronal annealing experiments for 3D printed silica fiber in various pulse energies (taken from Figure 2b and re-normalized relative to the sharply decreased retardance value) compared with the Rayleigh–Plesset (R-P) equation used to simulate the nanopores' erasure.

As can be seen from experimental and simulation results in Figure 7, two pairs of curves are separated in the figure. The evolution in pulse energy corresponds to the increase in pore size, and each pair is consistent. Improved thermal stability can be observed as pulse energy or pore size increases. This work agrees with the previous simulation work carried out in glasses produced by mature fabrication technologies [16]. What this means is that similar to other glasses, the larger pore size induced by the higher laser pulse energy in the nanolayers can also play an extremely important role in the erasure of nanogratings and their associated birefringence in a high temperature regime for 3D printed silica glass.

5. Conclusions

The first study of the photosensitivity of the 3D printed silica fibers with fs-IR laser irradiation is reported. The results from the writing kinetics and isochronal annealing show that 3D printed fibers demonstrate similar, or slightly better, thermal stability in comparison with commercial single-mode fibers, which means that 3D printed fibers with complex configurations could be applied in high-temperature environments without the restriction of conventional fiber design and manufacturing.

Moreover, the thermal stability of these fs-IR laser inscribed structures in both 3D printed fiber and conventional fiber (Type II modifications) was studied and simulated with a Rayleigh–Plesset (R-P) model. Despite different fabrication routes, 3D printed fibers show comparable performance with SMF28 commercial single-mode fibers. Overall, 3D printed fibers are promising in FBG fabrication and high-temperature components for sensing applications. Regarding the laser-induced underlying porous nanostructure in silicate more generally, it can be treated as nanopores that slowly re-dissolve back into the glass with high temperature annealing. This dissolution is likely to be impacted by the surrounding environment that may account for some slight differences in response magnitude between the two fiber types.

Author Contributions: Conceptualization, Y.W., S.W., M.L., G.-D.P. and J.C.; methodology, Y.W., M.C. and M.L.; software, Y.W. and S.W.; validation, M.L., G.-D.P., J.C. and B.P.; formal analysis, Y.W. and S.W.; investigation, Y.W., S.W., M.C., B.S. and M.L.; resources, G.-D.P., J.C., B.P. and M.L.; data curation, Y.W., S.W. and B.S.; writing—original draft preparation, Y.W.; writing—review and editing, Y.W., S.W., M.C., J.C., B.P. and M.L.; visualization, M.L.; supervision, G.-D.P., J.C., M.L. and B.P.; project administration, M.L.; funding acquisition, M.L. All authors have read and agreed to the published version of the manuscript.

Funding: This research was funded by Agence Nationale pour la Recherche, FLAG/IR project, grant number ANR-18-CE08-0004-01 and CNRS Défi Instrumentation aux Limites, Ultrabragg project.

Institutional Review Board Statement: Not applicable.

Informed Consent Statement: Not applicable.

Data Availability Statement: The data presented in this study are available on request from the corresponding author.

Conflicts of Interest: The authors declare no conflict of interest.

References

1. Ballato, J.; Dragic, P. Glass: The carrier of light-a brief history of optical fiber. *Int. J. Appl. Glass Sci.* **2016**, *7*, 413–422. [CrossRef]
2. Geittner, P.; Küppers, D.; Lydtin, H. Low-loss optical fibers prepared by plasma-activated chemical vapor deposition (CVD). *Appl. Phys. Lett.* **1976**, *28*, 645–646. [CrossRef]
3. Luo, Y.; Wen, J.; Zhang, J.; Canning, J.; Peng, G.-D. Bismuth and erbium codoped optical fiber with ultrabroadband luminescence across O-, E-, S-, C-, and L-bands. *Opt. Lett.* **2012**, *37*, 3447–3449. [CrossRef] [PubMed]
4. Michie, A.; Canning, J.; Bassett, I.; Haywood, J.; Digweed, K.; Åslund, M.; Ashton, B.; Stevenson, M.; Digweed, J.; Lau, A.; et al. Spun elliptically birefringent photonic crystal fibre. *Opt. Express* **2007**, *15*, 1811–1816. [CrossRef] [PubMed]
5. Andreone, A. *Selected Topics in Photonic Crystals and Metamaterials*; World Scientific: Singapore, 2011.
6. Cook, K.; Leon-Saval, S.; Canning, J.; Reid, Z.; Hossain, M.A.; Peng, G.-D. Air-structured optical fibre drawn from a 3D-printed preform. In Proceedings of the 24th International Conference on Optical Fibre Sensors, Curitiba, Brazil, 28 September–2 October 2015; International Society for Optics and Photonics: Bellingham, WA, USA, 2015; Volume 9634, p. 96343E.

7. Chu, Y.; Fu, X.; Luo, Y.; Canning, J.; Tian, Y.; Cook, K.; Zhang, J.; Peng, G.-D. Silica optical fiber drawn from 3D printed preforms. *Opt. Lett.* **2019**, *44*, 5358–5361. [CrossRef] [PubMed]
8. Hill, K.; Malo, B.; Bilodeau, F.; Johnson, D. Photosensitivity in optical fibers. *Annu. Rev. Mater. Sci.* **1993**, *23*, 125–157.
9. Bricchi, E.; Kazansky, P.G. Extraordinary stability of anisotropic femtosecond direct-written structures embedded in silica glass. *Appl. Phys. Lett.* **2006**, *88*, 111119. [CrossRef]
10. Li, Y.; Yang, M.; Wang, D.; Lu, J.; Sun, T.; Grattan, K.T. Fiber Bragg gratings with enhanced thermal stability by residual stress relaxation. *Opt. Express* **2009**, *17*, 19785–19790. [CrossRef]
11. Wei, S.-E.; Wang, Y.; Yao, H.; Cavillon, M.; Poumellec, B.; Peng, G.-D.; Lancry, M. Thermal Stability of Type II Modifications by IR Femtosecond Laser in Silica-based Glasses. *Sensors (Basel)* **2020**, *20*, 762. [CrossRef]
12. Grobnic, D.; Hnatovsky, C.; Mihailov, S.J. Low loss Type II regenerative Bragg gratings made with ultrafast radiation. *Opt. Express* **2016**, *24*, 28704–28712. [CrossRef]
13. Mihailov, S.J.; Grobnic, D.; Hnatovsky, C.; Walker, R.B.; Lu, P.; Coulas, D.; Ding, H. Extreme environment sensing using femtosecond laser-inscribed fiber Bragg gratings. *Sensors* **2017**, *17*, 2909. [CrossRef] [PubMed]
14. Shimotsuma, Y.; Kazansky, P.G.; Qiu, J.; Hirao, K. Self-organized nanogratings in glass irradiated by ultrashort light pulses. *Phys. Rev. Lett.* **2003**, *91*, 247405. [CrossRef] [PubMed]
15. Lancry, M.; Poumellec, B.; Canning, J.; Cook, K.; Poulin, J.C.; Brisset, F. Ultrafast nanoporous silica formation driven by femtosecond laser irradiation. *Laser Photonics Rev.* **2013**, *7*, 953–962. [CrossRef]
16. Cavillon, M.; Wang, Y.; Poumellec, B.; Brisset, F.; Lancry, M. Erasure of nanopores in silicate glasses induced by femtosecond laser irradiation in the Type II regime. *Appl. Phys. A* **2020**, *126*, 1–9. [CrossRef]
17. Luo, Y.; Canning, J.; Zhang, J.; Peng, G.-D. Toward optical fibre fabrication using 3D printing technology. *Opt. Fiber Technol.* **2020**, *58*, 102299. [CrossRef]
18. Davidson, M. The First Order (Full Wave) Retardation Plate. 2019. Available online: https://www.olympus-lifescience.com/fr/microscope-resource/primer/techniques/polarized/firstorderplate/#:~{}:text=The%20first%20order%20retardation%20plate%20is%20designed%20to%20introduce%20a,polarized%20light%20at%20a%2045%2D (accessed on 9 January 2021).
19. Fedotov, S.S.; Drevinskas, R.; Lotarev, S.V.; Lipatiev, A.S.; Beresna, M.; Cerkauskaite, A.; Sigaev, V.N.; Kazansky, P.G. Direct writing of birefringent elements by ultrafast laser nanostructuring in multicomponent glass. *Appl. Phys. Lett.* **2016**, *108*, 071905. [CrossRef]
20. Bricchi, E.; Klappauf, B.G.; Kazansky, P.G. Form birefringence and negative index change created by femtosecond direct writing in transparent materials. *Opt. Lett.* **2004**, *29*, 119–121. [CrossRef]
21. Kazansky, P.G.; Shimotsuma, Y.; Sakakura, M.; Beresna, M.; Gecevičius, M.; Svirko, Y.; Akturk, S.; Qiu, J.; Miura, K.; Hirao, K. Photosensitivity control of an isotropic medium through polarization of light pulses with tilted intensity front. *Opt. Express* **2011**, *19*, 20657–20664. [CrossRef]
22. Patel, A.; Tikhonchuk, V.T.; Zhang, J.; Kazansky, P.G. Non-paraxial polarization spatio-temporal coupling in ultrafast laser material processing. *Laser Photonics Rev.* **2017**, *11*, 1600290. [CrossRef]
23. Poumellec, B.; Lancry, M. Kinetics of thermally activated physical processes in disordered media. *Fibers* **2015**, *3*, 206–252. [CrossRef]
24. Gecevičius, M. Polarization Sensitive Optical Elements by Ultrafast Laser Nanostructuring of Glass. Ph.D. Thesis, University of Southampton, Southampton, UK, 2015.
25. Canning, J.; Hossain, M.A.; Han, C.; Chartier, L.; Cook, K.; Athanaze, T. Drawing optical fibers from three-dimensional printers. *Opt. Lett.* **2016**, *41*, 5551–5554. [CrossRef] [PubMed]
26. Grobnic, D.; Smelser, C.W.; Mihailov, S.J.; Walker, R.B. Long-term thermal stability tests at 1000 °C of silica fibre Bragg gratings made with ultrafast laser radiation. *Meas. Sci. Technol.* **2006**, *17*, 1009. [CrossRef]
27. Lancry, M.; Canning, J.; Cook, K.; Heili, M.; Neuville, D.; Poumellec, B. Nanoscale femtosecond laser milling and control of nanoporosity in the normal and anomalous regimes of GeO 2-SiO 2 glasses. *Opt. Mater. Express* **2016**, *6*, 321–330. [CrossRef]
28. Desmarchelier, R.; Poumellec, B.; Brisset, F.; Mazerat, S.; Lancry, M. In the heart of femtosecond laser induced nanogratings: From porous nanoplanes to form birefringence. *World J. Nano Sci. Eng.* **2015**, *5*, 115. [CrossRef]
29. Markel, V.A. Introduction to the Maxwell Garnett approximation: Tutorial. *JOSA A* **2016**, *33*, 1244–1256. [CrossRef]
30. Birtch, E.M.; Shelby, J.E.; Whalen, J.M. Properties of binary GeO_2–SiO_2 glasses. *Phys. Chem. Glas. Eur. J. Glass Sci. Technol. B* **2006**, *47*, 182–185.

5.3 Helical distributed feedback fiber Bragg gratings and rocking filters in a 3D printed preform-drawn fiber

Optics Letters

Helical distributed feedback fiber Bragg gratings and rocking filters in a 3D printed preform-drawn fiber

John Canning,[1,*] Yitao Wang,[1,2] Matthieu Lancry,[2] Yanhua Luo,[3] and Gang-Ding Peng[3]

[1]Interdisciplinary Photonics Laboratories (iPL), School of Electrical & Data Engineering, Tech Lab, UTS, Ultimo, Sydney NSW 2007, Australia
[2]Institut de Chimie Molecuaire et des Materiaux d'Orsay, Universite Paris Sud, Université Paris Saclay, Paris, France
[3]National Fiber Facility (NFF), UNSW, Randwick, Sydney NSW 2052, Australia
*Corresponding author: John.Canning@uts.edu.au

Received 6 July 2020; revised 25 July 2020; accepted 21 August 2020; posted 24 August 2020 (Doc. ID 401081); published 25 September 2020

Using induced UV attenuation across a twisted fiber asymmetric core drawn from a 3D printed preform, linear fiber Bragg gratings (FBGs) are produced on one side of the core. By removing the twist, a helical grating with a period matching the twist rate is produced. Balancing the rate with the polarization beat length in a form birefringent fiber allows the production of a combined rocking filter and FBG device with tunable properties. Direct observation of the fiber grating dispersion within the rocking filter rejection band is possible. © 2020 Optical Society of America

https://doi.org/10.1364/OL.401081

By pre-twisting a birefringent fiber it is possible to balance and match optical losses of each polarization eigenstate creating an effective zero birefringence. In this way, phase-shifted gratings can in principle be written that have no intrinsic splitting, a method previously utilized to remove birefringence in conventional photosensitive rare-earth doped germanosilicate optical fibers optimized for distributed feedback (DFB) fiber lasers [1–3]. Notably, it was a simple method to remove polarization hole burning and subsequent laser instability that arises from intrinsic form birefringence existing in all fibers. Those results demonstrated the principle worked well with commercial-ready CW 244 nm laser writing of fiber Bragg gratings (FBGs). Despite weakly absorbed CW 244 nm light generally producing very little intrinsic birefringence ($\Delta n < 10^{-6}$, depending on $[GeO_2]$), it is commensurate with existing form birefringence in uniform low-loss fibers. The small but finite induced twisting is thought to arise predominantly from defect, and/or interfacial stress, anisotropy. It can be used to compensate for weak form birefringence directly. This allows permanent birefringence removal from grating devices with untwisting.

The method was instrumental in the successful demonstration of ultra-narrow linewidth DFB fiber lasers. In this work, we go further to demonstrate the novel production of helical gratings in fibers that have higher form birefringence arising from an initial strong core asymmetry combined with the greater induced index asymmetry from pulsed UV light.

Penetration across a germanosilicate core using pulsed 193 nm [4,5] is significantly less than at 244 nm for reasons that involve two-step excitation paths [6]. At higher intensities, these lead to localized index change at the core cladding interfaces that can generate, within a uniform fiber, significant form birefringence compared to UV CW light. This can be exploited by matching the twist rate with the induced birefringence beat length such that it makes both eigenstates degenerate through cross-coupling; then the twist period, Λ_τ ($\gg \Lambda_B$), will be superimposed and locked onto the grating with Bragg period, Λ_B, after the fiber twist is relaxed or removed. Under such a condition, it should be possible to produce a long period rocking filter [7,8] superimposed on the grating profile—its 1st order ($m = 1$) spectral position is then related to the wavelength, λ, dependent birefringence $B(\lambda)$:

$$\lambda = \Lambda_t B\,(\lambda)\,. \tag{1}$$

Figure 1 summarizes the concept. It can be greatly enhanced using a pre-existing high asymmetry in the fiber core profile.

The highly asymmetric core optical fiber (Fig. 2) was produced by additive manufacturing [9–11]. In short, this single-mode optical fiber was drawn from a preform prepared by 3D printing with a nanoparticle/photocurable resin preparation, subsequent core formation, thermal debinding to remove the polymer. Consolidation and drawing into a fiber was carried out on an optical fiber draw tower. It has a germanosilicate core and silica cladding, both dopant distributions shown in Fig. 2(a) along one axis of the fiber. These were measured by energy dispersive x-ray analysis (EDX) in a scanning electronic microscope (SEM—ZEISS SUPRA 55 VP). About 8 at. wt. % of Ge is found in the core; the rest is silica. No evidence of residual polymer or water from the resin preform is detected suggesting, within resolution, a pure germanosilicate fiber has been produced. The highly asymmetric fiber core arises from core distortion during drawing and is ideal for this work. The photosensitivity is as expected for a germanosilicate fiber, qualitatively

0146-9592/20/195444-04 Journal © 2020 Optical Society of America

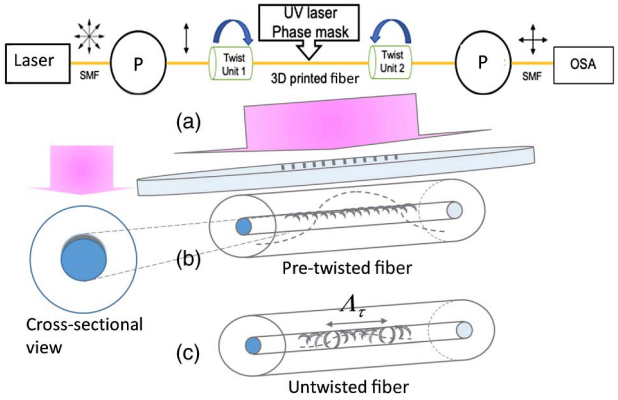

Fig. 1. Schematic of the grating writing (a) in twisted fiber with a twist period, Λ_τ. Closeup is shown in (b), along with the subsequent untwisting of the fiber (c). The untwisted grating has a period equal or close to Λ_τ. The cross-section shows the localized index change critical for efficient cross-coupling after twisting is removed (SMF, single-mode fiber; OSA, optical spectrum analyzer; P, polarizer).

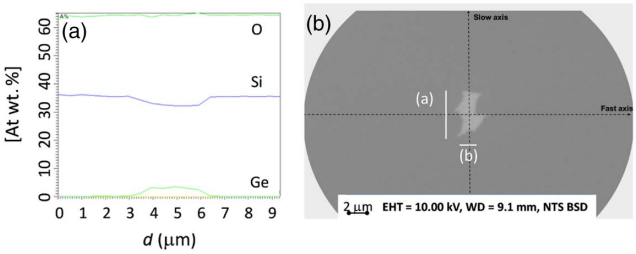

Fig. 2. Analysis of a highly asymmetric germanosilicate fiber drawn from a 3D printed preform: (a) x-ray analysis (EDX) of composition showing A% of O, Si, and Ge; (b) SEM micrograph showing approximate (a) long and (b) short axes. The fiber is treated like an elliptical fiber in the first instance, ignoring the jagged profile that gives rise to scattering loss.

similar to commercial fibers [12,13]. The printed preform was not uniform leading to stresses that distorted the softer germanosilicate core producing the observed twisted elliptical shape (long axis $\phi \sim 4$ μm, short axis $\phi \sim 1.3$ μm; they are not orthogonal). This shape was observed along the length of fiber and gives rise to scattering losses of $\alpha \sim 0.24$ dB/cm, measured by cutback. It is likely that there is also cross-polarization mixing occurring both from a frozen in twist variation and natural twisting of the fiber.

Two major axes are shown in Fig. 2(b). Assuming orthogonal eigenstates, the form or geometric birefringence is estimated from interference measurements to be $B_g \sim \Delta n_{a,b} \sim 4.5 \times 10^{-6}$. From this figure, if the core is approximated as an equivalent elliptical fiber core one can estimate the core/cladding index [14]. If the fiber axes ratio of $a/b \geq 3$, then $B_g \sim 0.32(\Delta n)^2$. Rearranging accordingly:

$$\Delta n \sim \sqrt{\frac{B_g}{0.32}} = 0.0038. \quad \textbf{(2)}$$

If the fiber eigenstates are twisted sufficiently, then further modal mixing and overlap will occur leading to degeneracy of the two eigenstates. Loss will also be degenerate, but further twisting will break that degeneracy. This in turn generates high-quality, narrower, and stronger spectral profiles since polarization eigenstates are overlapping. In previous work, phase-shifted gratings were used to demonstrate high finesse correction of the weak form birefringence within standard fibers, making it suitable for active DFB fiber lasers to remove polarization competition and mode beating [1–3]. Here, twisting the fiber is used to compensate for the form or shape induced birefringence caused by the high asymmetry of the fiber. By writing a highly localized uniform grating directly into this twisted fiber using the strong attenuation described above, the release of the fiber results in a unique twisted grating helix around the core over the grating length with twist period Λ_τ that counters the birefringence in that region. Uniform gratings ($L = 1$ cm) were produced by direct writing with 193 nm [15] are used (Ar F laser: $\lambda = 193$ nm, $w = 15$ ns, repetition rate $RR =$ 10 Hz, fluence $f_{\text{cum}} = 360\ \text{J/cm}^2$).

In physically twisting the grating, $\Lambda_\tau \gg \Lambda_B$. With appropriate selection to phase match the index difference between polarization eigenstates as described above, direct polarization coupling can be achieved such that one state is coupled into the other. The spectral bandwidth over which this occurs is determined by the period and length of interaction. This is effectively a rocking filter as described by Eq. (1) [7,8,16]. Since this is on top of the Bragg filter itself, the spectral filter of the rocking filter can be tuned to sit directly over the Bragg filter.

The combined rocking and Bragg grating filter produces an interesting function—whereas one polarization can be coupled into another across a spectral bandgap to generate a finite rejection filter function, within that filter bandgap there will be a direct transmission of a narrower Bragg resonance of the same polarization. The reason is that Bragg grating dispersion destroys the phase-matching condition of the rocking filter function around its bandgap. A similar phenomenon was exploited in novel integrated transmission pass photonic bandgap waveguides where the dispersion of a silicon-on-silica photonic crystal played a similar role [17] and in a tapered silica-on-silicon multimode waveguide [18].

The experimental setup shown in Fig. 1(a) was used to characterize twisting and polarization. Two rotational twist mounts were used to twist the fiber before grating writing. The polarization mixing between eigenstates occurs for one polarization over the fiber sample length [14,19]. During the test, the initial measurement is made for one parallel input polarization at 360° and then repeated for orthogonal input at 90° from the initial state. The shift in spectral fringes of the parallel and orthogonal polarizer shown in Fig. 3(a) measures the birefringence. The depth of the signal background reflects differences in the scattering loss for each eigenstate. The fiber is twisted in both directions [blue line shown in Fig. 3(a)]. When twisted $\theta \sim 130°$ in each fiber direction ($\Delta\theta \sim 5.2°$/cm), the polarization eigenstates are fully mixed and the response is a flat line. Assuming perfectly orthogonal eigenstates, the rocking filter bandwidth lies in the near IR window. Twisting separates the elliptical eigenstates and shifts the spectrum, demonstrating ready tunability. The twist is approaching 260°. The transmission spectra in Fig. 3(b) also show a similar result. After twisting, the maximum fiber signal coincides with the minimum signal.

The weaker undulating line in Fig. 3(a) demonstrates that the pretwist can permanently lock in a helical spiral of index change arising from the twisting of the photosensitive induced

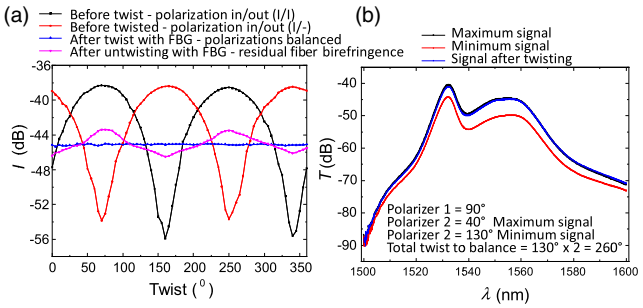

Fig. 3. (a) Polarized transmission with the rotation angle. Black is the case where the output and input polarizers are aligned, whereas red is the case where they are orthogonal; and (b) Er^{3+}-doped fiber amplifier transmission spectra through the 3D printed fiber. More information on fiber polarization can be found here [14,19].

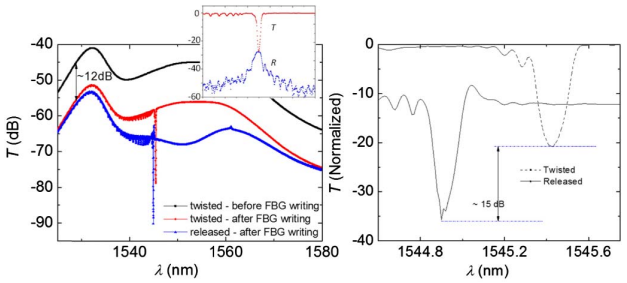

Fig. 4. (a) Transmission spectra of the 3D printed fiber with the FBG inscribed by an ArF exciplex laser; (b) comparison with and after removing applied twist. Inset shows transmission and reflection of a grating written with no polarizers and no twist [12,13] for comparison.

index changes when the fiber twist is removed. An estimate of the amount locked in, or reduced, after the twist is removed is $\Delta(\Delta B) \sim 85\%$; better optimization should lead to 100%. This points to substantial counter birefringence induced by the localized UV changes at the asymmetric core-cladding interface that are now helically distributed along the grating [Fig. 1(c)]. Importantly, this result shows that utilizing strong pulsed UV attenuation when grating writing within this fiber drawn from a bottom-up 3D printed preform has similar properties to standard commercial photosensitive fiber.

The spectral fringe has weakened sharply after the fiber twist was removed. It has not vanished completely suggesting the optimal twist has not been reached and/or some relaxation has occurred. The latter may be explained noting that the exposure itself, in addition to localized index changes, has altered the stress properties of the fiber, and these play a role in contributing to the overall deviation from degeneracy observed before irradiation and release—i.e., optimal twisting has to take into account these changes in iterative optimization. With an optimum twist angle, the grating is written with a UV laser. Once UV exposure is matched then the fiber can be relaxed and the asymmetry in the exposed region in theory lost.

Figure 4 shows the grating results in this fiber before and after the twist is released. An initial bulk exposure affects fiber transmission significantly with $\Delta\alpha \sim 20$ dB induced flat attenuation across the spectrum. This is attributed to enhanced Mie-like scattering of the grating out of the fiber because it is highly localized to one side, greatly exacerbating the losses arising from the nonadiabatic core shape. In uniform fibers, FBG attenuation due to scattering from off-center exposed regions can be as high as $\alpha \sim 0.1$ dB/cm with writing at $\lambda = 193$ nm [5]. When the fiber twist is released the FBG peak shifts to shorter wavelengths by $\Delta\lambda \geq -0.5$ nm, indicating the fiber was under a small tensile load during writing. The grating becomes stronger with a narrowing of the 3 dB bandwidth by $\Delta(\Delta\lambda) \sim 0.028$ nm or approximately a third.

A large induced attenuation around the grating spectrum reflects high core asymmetry so that when unwound, the localized UV induced changes introduce a broadband, flat loss around the grating. This is a combination of the grating asymmetry along with a grating twist as the fiber twist is relaxed, leading to a periodic coupling of the two polarization eigenstates—a rocking filter is superimposed on the Bragg grating. From Eq. (1), the central wavelength of this rocking filter is dependent on the twist period, Λ_τ, the coupling order, m, and the wavelength-dependent birefringence $B(\lambda)$:

$$\lambda_\tau = \frac{\Lambda_t}{m} B(\lambda). \tag{3}$$

However, those wavelengths that interact with the FBG experience resonance delays, or a dispersive time, and therefore a phase delay so the condition in Eq. (3) is not met over the grating bandgap. At the point where the rocking filter phase matching is no longer achieved, the rocking filter cross coupling from one polarization to the other is avoided and the signal not blocked by the inline polarizers. This leads to a transmission peak notch within the rocking filter bandwidth, shown in more detail in Fig. 5. Similarly, this behavior is observed at the shorter-wavelength Bragg cladding resonances. Further, it predicts that there should be no transmission peak in the center of the fiber grating and cladding resonances because there is no dispersion at that point—and this is observed as a narrow rejection notch within the transmission band. What this physically means is that there is a rocking filter induced broad rejection band of one polarization state and a narrower suppression of this polarization rejection in the center due to the fiber grating dispersion. An ultranarrow polarization notch within the bandgap is also present—quite a complicated polarization distribution in the spectra is created with a relatively simple grating combination. This can be extended by designing complex FBG functions such as chirped gratings, sample gratings, and more.

Figure 5(c) shows when the rocking filter spectrum exactly overlaps the FBG spectrum. Further optimization in both signal-to-noise and rocking filter bandwidth can be locked in once the ideal conditions are implemented initially. When the rocking filter and Bragg grating wavelengths, λ_τ, λ_B are equal, then

$$\lambda_\tau = \lambda_B = 2n\Lambda_B = \frac{\Lambda_t}{m} B(\lambda). \tag{4}$$

Rearranging for the lowest rocking filter order $m = 1$ and minimizing the twist over $\Lambda_\tau = 1$ cm to obtain full rotation, the minimum birefringence, $B(\lambda)$, can be estimated:

$$B(\lambda) = \frac{2\bar{n}\Lambda_B}{\Lambda_\tau} > 1.45 \times 10^{-4}. \tag{5}$$

Given the presence of cross-coupling increases with the twist before degeneracy, this figure is a measure of elliptical birefringence. As it approaches or exceeds the UV induced index

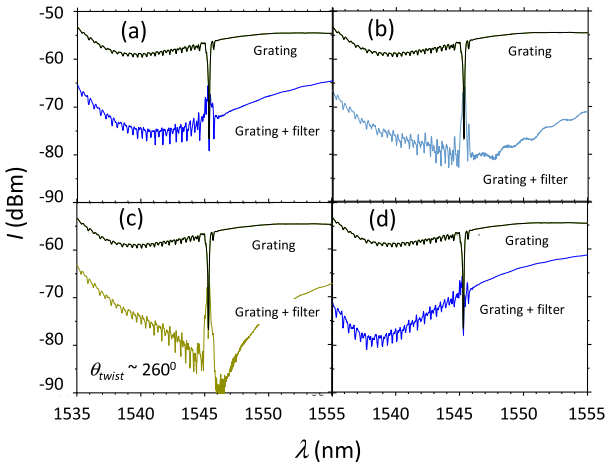

Fig. 5. By fine-tuning the degree of twist in the setup shown in Fig. 1, the rocking filter can be shifted over the fiber Bragg grating bandgap to optimize the notch transmission peak-to-floor signal within the rocking filter rejection band—(a) to (b) to (c) to (d). When overlapping spectrally, this improves polarization cross-coupling around the transmission notch, including the side-cladding-mode grating resonances at shorter wavelengths and demonstrates tunability. This is due to the phase spoiling the grating and side resonance dispersion profile introduces.

change for the fiber grating, elliptical birefringence will convert to circular birefringence. As well as form the twist, it combines localized UV-induced changes making it > 20 times the estimated untwisted fiber form birefringence. The value will also be larger than UV induced birefringence generated by 193 nm written gratings within uniform fibers [20].

The observed resonances are asymmetric reflecting the grating chirp and consequently the asymmetric time delay on the grating band edge. This resonant phenomenon is difficult to directly observe in spectra because of the presence of uncoupled background light. Coupling between polarization states with the rocking filter and using the Bragg grating dispersion to spoil that coupling has been used to generate a transmission notch within a high-loss polarization window. Combining these unique filter properties opens up interesting filter functions that offer narrowband fiber grating transmission and selective narrow and broadband polarization separation around the FBG bandgap. Such devices could be used in advanced polarization discrimination and polarization-based filtering applications in telecommunications and sensing. Further they offer a novel dispersion diagnostic because the information revealed by inline analysis of the resonance-impacted polarization states directly mirrors the fiber grating dispersion. By comparison, conventional approaches to measuring dispersion use a network analyzer while modulating a narrow linewidth source sufficiently fast to obtain high-resolution group delay measurements after signal processing. The current approach is also an alternative to direct bandgap resonance measurements from the side that rely on low levels of scattered light that limits resolution [21].

In conclusion, it has been shown within germanosilicate fibers produced from 3D-printed preforms that it is possible to overcome polarization splitting from form birefringence by twisting and to undo this permanently by as much as 85% with laser processing. Hybrid rocking filter and FBG devices where high-resolution selective spoiling of the rocking filter polarization coupling by the Bragg grating dispersion are demonstrated. This enables novel polarization and helical filter profiles to be tailored within the rejection band by directly tailoring the FBG. More localized multiphoton excitation of the glass band-edge with femtosecond near IR lasers [22,23], if needed, may permit additional degrees of processing and tunability.

Funding. French-Australia Science Innovation Collaboration.

Acknowledgment. Y. Wang acknowledges training and assistance with direct grating writing from Kevin Cook and support from the French-Australia Science Innovation Collaboration (PHC-FASIC) program enabling young researcher exchange and private funding. Private funds supporting this work are acknowledged.

Disclosures. The authors declare no conflicts of interest.

REFERENCES

1. A. Michie and J. Canning, Australian Conference on Optical Fibre Technology (ACOFT) Sydney, NSW, Australia, 2002.
2. J. Canning and A. Michie, "Helical feedback laser operation in a linear DFB laser," Australian Provisional Patent, PS2846 (2001).
3. J. Canning, G. L. Edvell, A. Michie, A. Graf, and M. Englund, "Helical feedback structure," Australian patent AU2003233252 (December 22, 2003).
4. A. M. Vengsarkar, Q. Zhong, D. Inniss, W. A. Reed, P. J. Lemaire, and S. G. Kosinski, Opt. Lett. **19**, 1260 (1994).
5. M. Janos, J. Canning, and M. G. Sceats, Opt. Lett. **21**, 1827 (1996).
6. J. Canning, Opt. Fiber Technol. **6**, 275 (2000).
7. R. H. Stolen, A. Ashkin, W. Pleibel, and J. M. Dziedzic, Opt. Lett. **9**, 300 (1984).
8. D. C. Johnson, F. Bilodeau, B. Malo, K. O. Hill, P. G. J. Wigley, and G. I. Stegeman, Opt. Lett. **17**, 1635 (1992).
9. Y. Chu, X. Fu, Y. Luo, J. Canning, Y. Tian, K. Cook, J. Zhang, and G.-D. Peng, Opt. Lett. **44**, 5358 (2019).
10. K. Cook, J. Canning, S. Leon-Saval, Z. Redi, Md. Hossain, J.-E. Comatti, Y. Luo, and G.-D. Peng, Opt. Lett. **40**, 3966 (2015).
11. K. Cook, G. Balle, J. Canning, L. Chartier, T. Athanze, M. A. Hossain, C. Han, J.-E. Comatti, Y. Luo, and G.-D. Peng, Opt. Lett. **41**, 4554 (2016).
12. K. Cook, J. Canning, Y. Luo, and G.-D. Peng, "Confirmation of 193 nm photosensitivity in germanosilicate fibre drawn from a 3D printed perform," (2019, unpublished).
13. J. Canning, *UTS Smart Sensing Research Showcase, NSW Smart Sensing Network (NSSN)* (2020).
14. A. Kumar and A. Ghatak, *Polarization of Light with Applications in Optical Fibers* (SPIE, 2011), Vol. **TT90**.
15. J. Canning, M. G. Sceats, H. G. Inglis, and P. Hill, Opt. Lett. **20**, 2189 (1995).
16. R. Kaul, Opt. Lett. **20**, 1000 (1995).
17. J. Canning, M. Kristensen, N. Skivesan, C. Martelli, A. Tetu, and L. H. Frandsen, J. Eur. Opt. Soc. **4**, 09019 (2009).
18. J. Canning and D. Moss, Opt. Lett. **23**, 174 (1998).
19. R. Hui and M. O'Sullivan, *Fiber Optic Measurement Techniques* (Academic Press, 2009).
20. T. Erdogan and V. Mizrahi, J. Opt. Soc. Am. B. **11**, 2100 (1994).
21. J. J. Canning, M. Janos, D. Stepanov, and M. G. Sceats, Electron. Lett. **32**, 1608 (1996).
22. A. Martinez, M. Dubov, I. Khrushchev, and I. Bennion, Electron. Lett. **40**, 1170 (2004).
23. "Technicasa White Paper," 2019, https://technicasa.com/technologies-high-temperature-fibre-bragg-grating-fbg-sensors/.

Conclusions

In this chapter, we investigate a recent method to fabricate optical fibers: drawing the fiber directly from the 3D printed silica-based preform. It is the first time that photosensitivity in both to UV and IR-fs laser light was investigated in such fibers. In particular, we compare writing kinetics and thermal stability of IR-fs modifications to conventional SMF28. Here are the main key results from this chapter:

- A ~ 3 dB/m (at 1300 nm) loss reduction of the 3D printed fiber could be archived by pre-annealing the fiber at 800 °C for 25h (initial attenuation loss before heat treatment: ~9.5 dB/m).
- From the aspect of fs laser writing kinetics and thermal performances during step isochronal annealing tests, the IR-fs Type II modifications written in 3D printed fiber exhibited a similar behavior as the conventional SMF-28 fiber.
- In both fibers (SMF-28 and 3D printed), the thermal stability of IR-fs Type II structures were highly dependent on the laser parameters, and particularly on the laser pulse energy: the higher the pulse energy, the higher the temperature of laser-induced structure erasure.
- SEM observation showed that higher laser pulse energies led to an increase in the averaged nanopores size, which could explain the higher thermal stability in this regime. This observation is in agreement with simulation using the Rayleigh-Plesset equation.
- A highly asymmetric fiber core of a 3D printed fiber could overcome polarization splitting from form birefringence as much as 85% after twisting and UV-laser processing.
- A helical fiber Bragg grating with a period matching the twist rate was written using UV laser.

Without the restrictions imposed by conventional fiber designs and manufacturing, 3D printed fibers with complex configurations could be applied to several industrial applications (e.g. sensing device). In the framework of fibers dedicated to high temperature operation, future work should be dedicated in the development of other glass core compositions with this technology, such as the ZrO_2-SiO_2 and Al_2O_3-SiO_2. We can also think about some others variants like core composition allowing fs-laser photo-precipitation of directionally solidified eutectics (such as perovskite phase $GdAlO_3$ or a garnet phase like $Y_3Al_5O_{12}$) in the fiber core, to further improve the high temperature performance of these fibers.

Chapter 6. Synthesis and discussion

Introduction 219

6.1 Discussion around silica densification: a general phenomenon observed in irradiated silica 220

6.1.1 Thermo-mechanical densification 221

6.1.2 Glass densification under irradiation 224

6.1.3 Silica glass densification under femtosecond laser irradiation 229

6.2 On the links between nanoporous layers and the birefringence thermal stability in silica glass 233

6.3 Going further about nanopores relationship with the ultimate thermal stability of the nanogratings and related birefringence 243

6.3.1 Influence of impurities (OH, Cl) in pure silica glasses 243

6.3.2 GeO_2-SiO_2 silica glasses with ultralow OH content 247

6.3.3 Al_2O_3-SiO_2 glasses (bulk or fibers) 249

6.3.4 Multi-components glasses (bulk or fibers) 252

6.4 Towards a computation of the lifetime prediction for IR-fs Type II modifications 255

Conclusions 260

References 261

Introduction

The purpose of this PhD thesis is to understand the origin and the transformation mechanisms of laser modifications to then allow the design of stable optical components at high temperatures via a materials approach. These optical components and devices are aimed to operate in a high temperature regime, e., typically above 800 °C and tentatively up to 1200 °C. Much of the answer is related to inherent glass structure and properties, particularly viscous flow/chemical migration and stress relaxation. Thermal stability may therefore be achieved by judicious application of glass preparation, annealing, and laser irradiation conditions.

In order to understand how what contributions impact the thermal stability of Type II modifications, we need to comprehend the origin of the anisotropic linear optical properties within the Type II regime. As we discussed in Chapters 1 and 3, there are different contributions to the total birefringence, including the form birefringence (LB_{form}) and stress-induced birefringence (LB_{stress}). In addition, there are additional phenomena that contribute to the total birefringence, namely densifications and point defects. The investigation of their thermal erasure kinetics has been presented in chapter 3. In short, whereas point defects can be neglected for high temperature operation since they are all bleached above 500°C, it is not the case for the densification that obviously contributed to LB_{stress} but also to LB_{form} (e.g., creating a refractive index increase between nanolayers). Thus, in section 6.1, we will focus on the densification phenomenon under various conditions and its thermal relaxation with a particular focus on fs laser-induced densification.

In section 6.2, the Rayleigh-Plesset (acronym R-P) equation is used to simulate the erasure process of the nanopores during the annealing. These nanopores have been identified as the origin of the form birefringence and dictates its ultimate thermal stability. Here, the relationships between changes in optical properties, structural relaxation, and viscous flow will be studied. Furthermore, we will also discuss how laser writing parameters (energy, speed) modify the averaged nanopore size in the irradiated area, and consequently alter the thermal stability of nanogratings.

In section 6.3, we summarize some key experimental results obtained along this PhD work and related to the thermal stability of Type II modifications. In particular, we will tentatively interpret the dependence of the thermal stability according to the material composition (fiber or bulk) which is another decisive factor for the thermal performance of sensors or optical data storage systems.

Finally, in section 6.4, accelerated aging experiments for Type II modifications in silica glass will be exploited and we will perform lifetime prediction of nanogratings in a reliable manner. The objective is to ensure long-term operation of IR-fs-Type II based sensors in high

temperature environment. In this view, we will build the master curve and determine the distribution of activation energy at the root of the measured optical retardance. Then we will predict the stabilization conditions for a dedicated environment. Finally, we will present additional ageing experiments carried out on stabilized modifications to check the validity of our predictions.

6.1 Discussion around silica densification: a general phenomenon observed in irradiated silica

Silica constitutes the backbone of many rapidly expanding applications, which opt for various fields such as communications, electronics, sensor technologies, materials processing, construction or even protection such as space vehicle windows. Since the 1950s and to this day, this model material has been extensively studied from a mechanical point of view under both quasi-static (under indentation or compression by diamond anvil cell) and dynamic loading conditions. From the 1960s, the effects of electron bombardment on glasses were studied with high-energy sources of the order of MeV. Silica glasses have subsequently been studied extensively since their discovery of their photosensitivity to ultraviolet laser radiation in the late 1970s in order to study the induced changes in volume and optical modifications. This has been accentuated since 1996 with the discovery of direct 3D writing by femtosecond laser where silica is subjected to strong thermo mechanical stresses depending on the regime studied. Whatever the type of irradiation, these changes are based on point defects and structural modifications (observable in vibrational spectroscopy for example) induced by the irradiation. In particular, a phenomenon observed from the first studies has captured a lot of attention because of its almost universal nature (under laser irradiation or in a radiative environment, under hydrostatic loading, under shock, etc.) but also because of its potential in the field of optics for guiding light or manufacturing optical functions. **This is a phenomenon of permanent densification of silica.** There is thus a very rich bibliography on the densification of silica in radiative medium (laser, ionizing, "ballistic") as well as in hydrostatic (cold or hot) compression and also about dynamic loading but at a much lower extend.

In the case of femtosecond laser irradiation of SiO_2, the resulting modifications range from isotropic refractive index changes (type I regime), birefringence due to self-organized oxide composition [1] (Type II regime) to microscopic voids with densified shell (also called Type III). In all of these regimes, there are experimental results that suggest the occurrence of densification, but the mechanisms are still unclear especially within type II regime. Thus, in this section we will review the different densification mechanisms and we will then analyze the case of femtosecond laser irradiation in the light of the literature.

6.1.1 Thermo-mechanical densification

A. Densification induced by high temperature treatment at ambient pressure

Glass is in a metastable state regarding parameters usually used in this case (Pressure, Temperature, and chemical composition) (P, T, c). It has been suggested [2, 3] that the glassy state could be characterized by completing this set of parameters with a quantity called fictive temperature. The *fictive temperature* T_f is the temperature at which the glass structure is frozen during its cooling down [4]. It is usually employed to describe glass order and could be altered by thermal treatments during a sufficient long time allowing the structural relaxation of glass [5]. It is worthwhile to note that the fictive temperature depends on the relaxation time, which varies locally according to the atomic arrangement specific to the vitreous state. This local variation appears with slower cooling rates, so we sought uniformity by applying a very fast cooling process. Usually for an oxide glass of a fixed composition, the density decreases with increasing fictive temperature, for a fixed temperature and pressure [5, 6]. On the other hand, unlike these oxide glasses, pure silica glass exhibits an anomalous behavior: the higher the fictive temperature, the higher the density [7, 8]. This behavior is known to be the "anomaly of silica".

B. Densification induced by high pressure treatment at ambient temperature

Pressure has been proven to greatly impact the macroscopic properties of glass such as density, viscosity, and mechanical properties [9-11]. These properties change stem from the process of adapting the atomic structure to the densification of the entire network. Therefore, we need to understand how pressure changes the atomic structure such as coordination number and degree of polymerization when compressing glass. In previous studies, pressure has been proven to bring the following changes to the structure: 1. the next-nearest neighbor (NNN) distributions and ring statistics [12, 13]; 2. the number of non-bridging oxygen (NBO) [14, 15]; 3. the atomic coordination number of network-former cations [16]; and 4. network-former/modifier-oxygen bond distances [13, 14]. We can then use various experimental and theoretical tools to study the structure of the densified glass. To identify and quantify the changes in the SRO in glasses, the Magic angle spinning (MAS) nuclear magnetic resonance (NMR) spectroscopy along with neutron and x-ray diffraction can be used to study [12, 17, 18]. On the other hand, Raman and IR spectroscopy are very sensitive to structural variations, thus, it is an optimal tool to follow the structural evolution of glasses upon compression, and to determine structural modifications both in the short- and medium-range order [19-22].

Mackenzie [23] used IR spectroscopy to investigate the influence of the compression on the glass structure (SiO_2, GeO_2, and B_2O_3 glasses). The experiment was running under the

condition of 8 GPa/848 K and observed an ~18% increase in glasses density. It should be point out that there is no sign of any structural changes through the analysis of IR spectrum. In many subsequent pressure-quenching experiments, compressing the glass at high temperatures usually brings about increasing the coordination number of cations in the glass network. The extent of this change depends on the composition of the glass, especially number of non-bridging oxygen (NBO) is considered as a crucial factor [24-27].

Specifically, in pure silica glasses a permanent increase of density (densification) occurs after compression, with the density of a SiO_2 glass approaching the one of the SiO_2 crystal, by increasing up to ~20-21% [28-30]. It has been experimentally verified that below 28 GPa, the densification is due to structural changes (intertetrahedral angles distribution and the ring statistic) without variations in Si-O coordinations [31-33]. Furthermore, molecular dynamics calculations also support these considerations ascribing the densification to modification of T-O-T angles and ring populations, rather than to an increase in coordination [34, 35].

C. Densification induced by high-pressure, impact of the temperature

Compressing the glass at room temperature or at a temperature significantly lower than T_g will bring elastic densification. For example, Deschamp et al. [33] studied SiO_2 glasses densified under hydrostatic pressures from 9.8 up to 26 GPa. The authors provided a Raman-density calibration curve, and also identified the elastic yield under hydrostatic pressure, at room temperature, to be around 9 GPa for a pure SiO_2 glass [33]. Thus the annealing at relatively low temperatures can successfully relax the glass to its pre-compressed state [23, 36]. In 1963, Mackenzie densified boron oxide glass with pressure at room temperature [37], then he observed the glass density keep decrease since the pressure was released.

In contrast, a permanent (plastic) densification can be caused if the glass is densified under a high-temperature environment (around or above T_g) as review recently by Kapoor et al. [38] concluded that Yamada et al. [39] and Østergaard et al. [40] performed pressure densification experiments on Mg-silicate glass and sodium borosilicate glass at different temperatures, respectively. *Figure 6-1* shows the results of the two experiments. Stage 1 is defined as the low-temperature region; the changes in density induced by the pressure are identified as elastic densification. With the temperature increases, stage 2 is the mid-temperature region. Under the same pressure applied, as the temperature increases, an abrupt increase in the degree of densification is observed, and the changes are found inelastic when the pressure is released. Finally, stage 3 corresponds to the high-temperature stage, the temperature keeps increasing and leads to the density to continue to rise, but compared with stage 2, the upward trend has gradually slowed down. It can be seen that although the types of glass are different, their experimental results have a high degree of similarity.

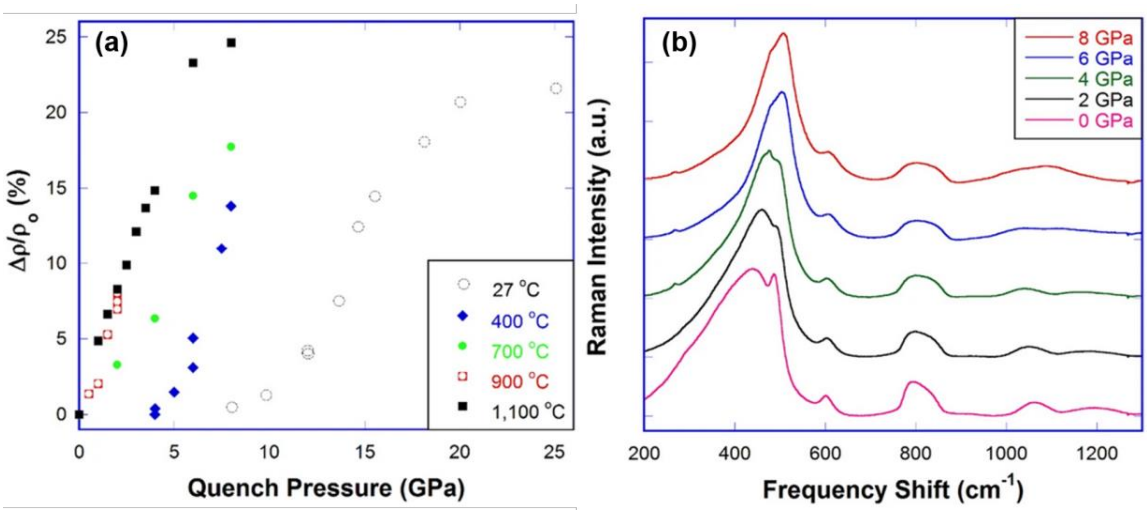

Figure 6-1. (a) Density increases of silica glass as a function of quench pressure at different temperatures. (b) The Raman spectra of silica glass hot-compressed structure under 2, 4, 6 and 8 GPa at 1100 °C, compared to that of pristine silica glass (0 GPa). (cited from [11])

Mackenzie's research in 1964 proved that when the temperature is lower than T_g, for a fixed pressure, the degree of glass densification increases as the temperature rises [41]. Uhlmann's research on alkali silicate glass in 1973 once again proved this point. He pointed out that as the temperature of the pressurization treatment approaches T_g, the relaxation time decreases, the degree of densification of alkali silicate glass is proportional to the applied temperature [42]. However, the permanent densification may still occur when the temperature is below T_g. The aluminosilicate glass was investigated this time by Smedskjaer et al. [43]. In an environment of 0,75T_g, when a pressure of 1 GPa is applied, permanent densification occurs, although the relaxation time at this temperature is about 500 years. Next, they continued to raise the temperature until T_g, a great increase of density was observed, and the relaxation time also plummeted to about 1 minute. Therefore, it can be inferred that high temperature can aggravate the kinetic process of densification. This phenomenon can be described as the rearrangement and combination of atoms through a viscous flow mechanism. On the other hand, the permanent densification at low temperatures tends to be caused by a non-viscous mechanism [43]. In addition, high-temperature densification can achieve different structural transformations, which also brings better thermal and mechanical stability to the glass [11]. Compared with the strain generated during the densification process at low temperature or room temperature, high temperature can promote the reorganization of the atomic structure and relax the stress therein, thereby greatly reducing the residual stress during the glass densification process, and making the treated structure more uniform and stable [44].

Conclusion

The thermo-mechanical densification in silica leads to the tuning of the interatomic distances and bonding patterns in a material. It can be achieved by the following methods: 1. the high-pressure treatment, which compresses the silica glass at room temperature, can bring high permanent densification on the glass. We also call this method cold compression. [33, 45]] had successfully obtained a densification rate of 21% by a 25 GPa pressure at room temperature. 2. High-temperature treatment, which can be divided into pressure quenching [12] and hot compression [43]. The former quench the glass-forming liquid under relative lower pressure and the latter heat the glass at elevated temperature (normally around the glass transition temperature T_g) under pressure.

6.1.2 Glass densification under irradiation

Silica glasses densification is also commonly observed under various kinds of irradiations employing neutrons, ions, electrons, γ rays, UV laser light and IR femtosecond laser irradiations, with energies ranging from keV to MeV [46-52]. Such kind of modification occurs also after sub-bandgap irradiations with UV [46, 53-55] or Vis-IR femtosecond lasers. The experimental fact that fused silica undergoes densification upon prolonged exposure to high-energy radiation is well documented in the literature. About 50 years ago, [47] reported permanent densification in SiO_2 under irradiation with neutron, electron, and γ-ray exposures. Therefore, there have been a number of experimental studies describing the permanent densification of silica or silica-based glasses under various kinds of irradiations and especially in glass fiber materials.

Apart from direct density measurements, the densification induced by the UV exposure was deduced from surface topography change. The measurements are usually performed on a flat irradiated sample and due to UV exposure; densification takes place and produces a surface depression. Then, from the measured surface topography the unconstrained strain was obtained with the help of a mechanical model and the densification can be deduced. Another common way is to follow the structural changes that indicate a density change using infrared or Raman spectroscopy. *Indeed, the spatial resolution and the high frequency resolutions achievable by Raman spectroscopy make it a very powerful and versatile tool to correlate macroscopic properties (density, mechanical behaviour) to variations down to the sub-nanoscale.* So one common way is to follow the structural changes that indicate a density change using Raman spectroscopy and particularly the so-called 'defect' bands. Historically, the D_1 and D_2 bands, located at 490 and 605 cm^{-1} respectively, have been first interpreted by Sharma et al., [56] and Galeener [57, 58] as being 'breathing' vibration modes of four and three-membered rings respectively in the material. As a first approximation, and for a given composition, a change in the intensity or the area of these bands indicates a modification in the rings statistics. For pure silica glass, it has been found for a long time that

the intensities of these bands increase with increasing macroscopic density ρ of glass [59-61]. As a result, many authors consider that the Raman D_1 and D_2 bands record matter densification in glass but there are some exceptions.

A. Glass densification induced by "nuclear radiations "

The knowledge of the glass structure in some simple systems before and after irradiation is a prerequisite for understanding the structural evolution of nuclear glasses under irradiation during long term storage but also to understand the behavior of glass fiber in some condition. Studies on irradiated glasses have been previously published on simple system like SiO_2 [62-64], or on multicomponent glasses like borosilicate glasses [65] and on some aluminosilicate [66]. In all sort of glasses, β-irradiation produces: -i) an increase of the network polymerization relative to the non-irradiated samples, -ii) an increase in concentration of molecular O_2, clearly visible at 1550 cm^{-1} and -iii) a decrease of the average Si-O-Si bond [65, 66]. For example, the *Figure 6-2* shows calcium aluminosilicate glasses before and after β-irradiation.

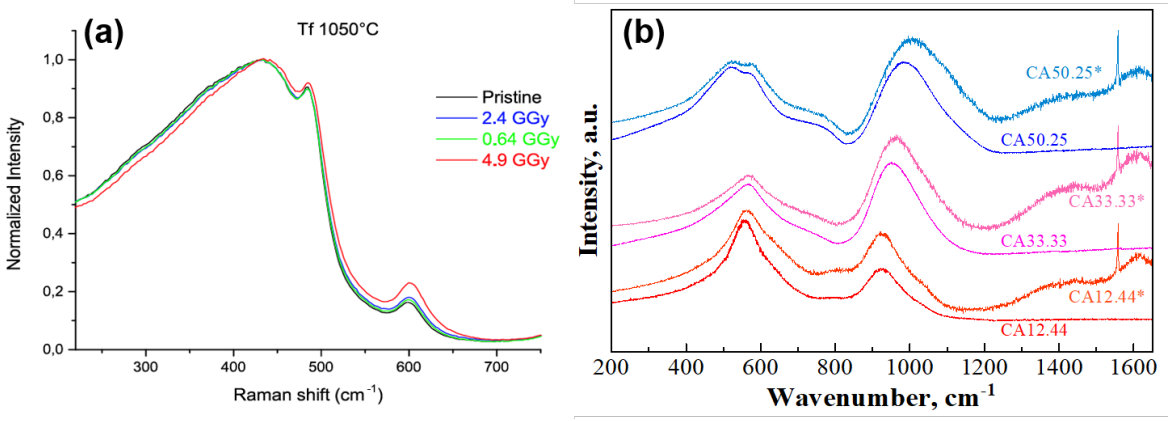

Figure 6-2. (a) Raman spectra evolution with the integrated dose of SiO_2 (T_f = 1050°C) samples; (b) Raman spectra of calcium aluminosilicate glasses before and after (*) irradiation. Samples were β-irradiated using 2.5 MeV electrons. The dose integrated in the CAx.y glasses is $3.8x10^9$ Gy where X is the content of SiO_2, Y the content of Al_2O_3 in mole % (CaO= 100-(X+Y)). (taken form [63, 66]).

All irradiated spectra, marked with *, show a shift in frequency for the prominent peak from 900 to 1050 cm^{-1}, as the silica content increases, which can be attributed to an increase of the network polymerization. The glass network becomes more connected as Si substitutes Al since the proportion of Q^3 and Q^4 species increases [67-69]. In the irradiated glasses, the shift of the Raman band at 520 cm^{-1} has been interpreted as a decrease of the average T-O-T bond angle [65].

This observation is similar to the effects induced by a glass densification and suggests a decrease of the average size of the TO_4 membered rings. Furthermore, the small shift of the large band around 900-1050 cm^{-1} indicates that the glass network becomes more

polymerized after irradiation. This is confirmed by an increase of the Q^3/Q^2 ratio after irradiation, as determined by the deconvolution of the Raman spectra. We also observed than the proportion of the Q^4 species increases. The migration of the calcium can be responsible for this structural change [65, 66].

The presence of the intense peak at 1550 cm^{-1} in the Raman spectra of irradiated glasses is characteristic of molecular O_2 and was also observed in irradiated borosilicate glasses [65]. The production of molecular O_2 is a consequence of the polymerization increase under irradiation because this process forms excess oxygen atoms within the glass structure. The proportion of O_2 does not seem to be dependent on the silica content.

B. Irradiation of "previously" densified silica

In a recent publication, the authors examined the "relaxation properties" of pre-densified synthetic fused silica glass under 2.5 MeV electron irradiation with high-integrated dose [63, 70]. The densification of the glass was obtained by hot compression (5 GPa-350 °C and 5 GPa-1000 °C). After irradiation of hot compressed silica, the Raman spectra display a significant increment of 4 and almost 3-membered rings whereas they exhibit a glass density reduction. In contrast, the wavenumber and the FWHM of the R band peaking at 440 cm^{-1} appears to remain correlated to the silica glass density for all investigated samples. In this work that the correlation between density and D_2 intensity remains valid until silica density remains lower than 2.26. This is consistent with many publications, which reports an increase of the D_2 band area with the dose [71] (for compaction rate < 3%, 5 keV electrons irradiation). Note that most of laser (IR-fs within Type I or even Type II regime or UV ns laser) related silica studies also mention a D_2 band increase that is assigned to a glass densification (where density variation is usually less than 1 %).

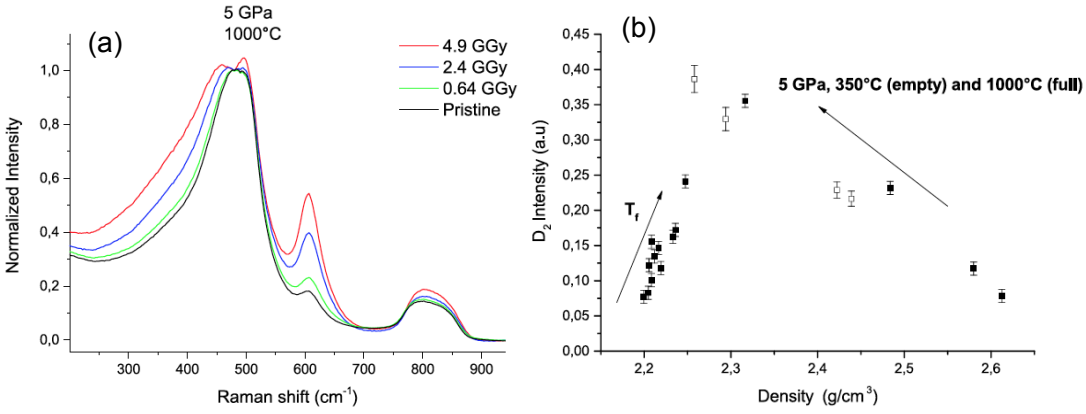

Figure 6-3. (a) Raman spectra evolution with the integrated dose of densified SiO_2 (5GPa, 1000°C) samples. (b) Raman D_2 band intensity as a function of density for HP-HT and T_f (heat-treated) SiO_2

samples. Irradiations were done with 2.5 MeV electrons at room temperature (taken from [63]).

Note that these measurements confirm that D_2 increase cannot be considered as an absolute marker of glass densification even in SiO_2. It remains only true in SiO_2 when the density is below its equilibrium value around 2.26. Up to date, the wavenumber and FWHM of the R-band around 440 cm^{-1} however seem to be a more relevant densification marker in a more general approach.

C. Glass densification induced by UV laser

Over the last two decades UV laser-induced Δn profiling in SiO_2 glasses was widely used for production of in-fiber/waveguide Bragg grating-based (BG) optical devices for photonics industry [72]. Irrespective of the type of irradiation, these changes are based on point defects and structural changes (observed in vibrational spectroscopy) induced by irradiation. In particular, the densification phenomenon observed from the first studies [73] received a lot of attention because of its potential in the field of optics for light guidance or the manufacture of integrated optical functions.

Fused silica could be densified under UV laser radiation as revealed by the surface topography (i.e. a valley formation) after irradiation [74]. The two-photons absorption process is considered as a crucial process to induce the compaction in the silica glass by UV lasers. Several experiments in the literature had proven that the compaction rate in the glass linearly depends on the laser intensity and the two-photon absorption coefficient [75-77]. A two-photons mechanism (193 nm UV laser) was reported for Fiber Bragg gratings photo-inscription in optical fibers [72] In order to understand the structure changes after the glass densification induced by UV laser radiation, using the x-ray diffraction [78] and neutron-diffraction [79] to investigate the compressed silica glass, the results indicate that the densification is induced by the changes of Si–O tetrahedra in an open three-dimensional corner-linked network. In fact, the SiO_4 tetrahedral unit keeps its composition and shape basically unchanged, except for the angle of the Si-O-Si bridging bond. The change of angle decides the glass structural densification and indicates the change of the structure [74].

D. Comparison of densification kinetics for silica according to the irradiation technique

Silica glass compaction can thus be reached under different types of radiations (ion, neutrons, electrons) but with a lower efficiency compared to High Pressure. Thus *Figure 6-4* exhibits the evolution of the different samples' density as a function of the irradiation dose expressed in eV/cm^3. The main purpose of this graph is to summarize the kinetics of density of silica under various irradiation conditions. This is for silica glass but also its crystalline polymorph Quartz.

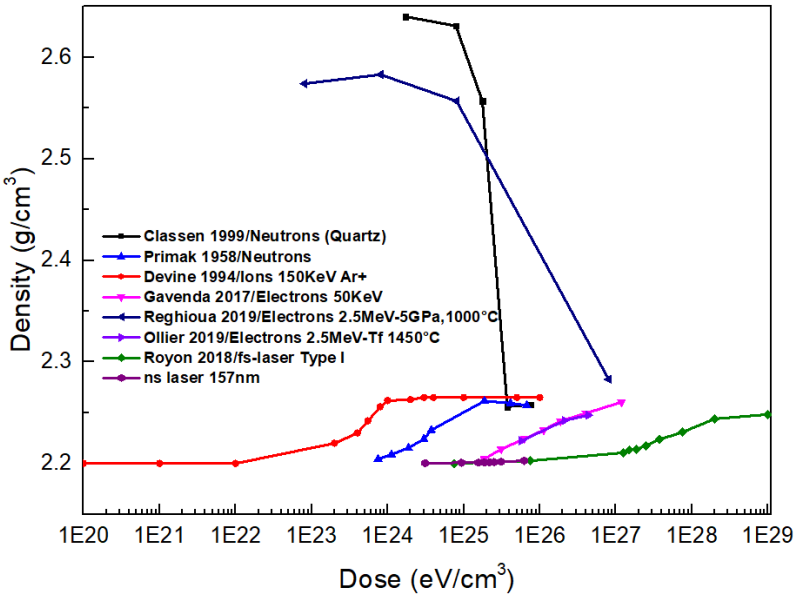

Figure 6-4. *The evolution of the density as a function of the irradiation dose for following samples: Neutrons (for quartz, black), Neutrons (for Suprasil, blue), Ions (red), Electrons (magenta), pre-treated sample by 5 GPa, 1000 °C (navy blue) and T_f treatment 1450 °C (violet), laser irradiation by fs-laser Type I modification (green) and UV ns-laser (deep purple).*

- We first compare the compaction of the glass achieved by Neutrons (for both vitreous silica and Quartz), Ions and Electrons radiation as we presented at the beginning of the Section 6.1. Despite the different nature of interaction mechanisms for neutrons and heavy ions (knock-on with atomic displacement) compared to electrons (bond breaking), the maximum of silica density variations are quite similar and does not exceed 3-4 % [80, 81]. The density was estimated to obey a power law as a function of the integrated dose D ($\alpha.D^{\beta}$ with β=1 for neutrons and 2/3 for ionizing irradiation) [82, 83].

- Then, the results of laser radiation include femtosecond laser Type I modifications regime and nanosecond UV laser (157 nm) are also inserted for sake of comparison. As it can be seen UV (cw or ns) [54, 74] or fs laser [84] irradiations lead to densify the silica glass with a quite similar kinetics. However, the compaction rate is below 1% for UV laser where it can reach around 3% under femtosecond laser irradiation (Type I regime).

- Finally, we add also two SiO_2 Suprasil samples that have been “pre-densified” before electrons irradiation. One has been strongly densified under 5 GPa hot compression at 1000 °C whereas the second one exhibits a slight densification by heat treatment (resulting in a fictive temperature T_f increases from 1000°C up to 1450 °C). Interestingly the densification of the hot-compressed sample relaxes (i.e. decreases)

under the 2.5 MeV electrons reaching a value around 2.26 g/cm^3 for a very high dose (typ. > 10GGy).

As a conclusion the compaction of silica glass can be done by ions, neutrons, electrons radiations (and likely also under X-ray or gammas rays provided we can reach dose that is high enough), the densification rate can hardly exceed 3-4%. Laser radiation is also known as an alternate method to densify the silica glass. Using UV laser [74] or femtosecond laser [84] to achieve the densification with the compaction rate lower than 3% had been reported. In this review we highlight that no matter the densification conditions and no matter the initial density of the silica sample (or even quartz under neutrons), the density of all of them reaches an equilibrium value around 2.26-2.27 g/cm^3 when the total dose is high enough (except the UV ns-laser irradiation where is dose is likely too small). This phase is defined as amorphous metamict silica by [64], which is a mineralogical term that describes the gradual and ultimately complete destruction of a crystal structure to yield an amorphous phase.

6.1.3 Silica glass densification under femtosecond laser irradiation

The femtosecond laser can generally induce several types of modifications in fused silica. As discussed in chapter 1, the type of modification is usually determined by different laser parameters, such as the laser pulse energy, duration, repetition rate, etc… Here, we will mostly focus on the densification process involved within these different regimes.

Within heat accumulation regime: When using high repetition rates the laser pulses act as a local heat source leading to temperatures well above the melting temperature of the glass [85]. After rapid cooling (typ. >10^6 K/s) the molten glass resolidifies allowing for the local bonding of glass interfaces but is also possible to crystallize glasses or to imprint permanent densification through local fictive temperature T_f changes [86], which can be further exploited for optical applications including fiber optics components and sensors. In chapter 1 an example IR femtosecond laser-induced modifications in silica inscribed with different repetition rates were analyzed by Raman spectroscopy to evaluate the consequences of increasing heat accumulation on the resulting T_f [5]. For all heat affected zones (HAZ) there is a significant T_f increase compared to pristine glass. Interestingly, T_f scales with the laser repetition rate and reaches values up to 1700 °C at 9.4 MHz. Based on the increase in fictive temperature it is also possible to evaluate the change in volume of the material within the focal volume. The relative free of stress volume change (opposite to material density - ρ) due to fictive temperature change is $-\frac{1}{\rho}\frac{\Delta\rho}{\Delta T_f} = -5.7 * 10^{-6}$ and is negative in case of silica [87]. For example, we obtain an increase ΔT_f of about 750 K for a repetition rate of 9.4 MHz within the heat-affected zone (HAZ) resulting in a free of stress densification of 5.10^{-3}.

Within Type I regime: Using a low pulse energy fs-laser, smoothly changing the structure and observing permanent refractive index changes in and around the area where the instantaneous power of the focus exceeds the intensity of Type I threshold [88]. Type I modification is mostly attributed the glass densification, often deduced from the silica refractive index increase and correlated to the increment of the D_1 and D_2 Raman bands [89-91], which corresponding to the increase of the number of 3-membered rings in silica [57]. Our group has published a model of an original physico-chemical mechanism to explain these observations for Type I modifications. We proposed that the first threshold, named T1, is based on the modification of the fictive temperature T_f of the glass when the duration of the heat pulse corresponding to the light energy is greater than the glass relaxation time $\eta(T)/G(T)$. However, considering this model can difficultly explain a densification rate higher than 1%. Recently, Molecular Dynamics by Shchleblanov and Povarnitsyn [92] modeled by bond-breaking mechanism by IR fs laser interaction accurately. The increase of 3 and 4 membered rings with a reduction of 6 and 7 fold rings fraction was proposed to explain the densification of vitreous silica under femtosecond laser irradiation [92].

What about fs laser irradiation within Type II regime? In this PhD thesis, the main kind of modification that we care about is the Type II modification. Type II is characterized by a high level of anisotropic index change [93] that is mostly attributed to the formation of nanogratings. In this case, the fs-laser induces in the glass a periodic arrangement of nanolayers that contain nanopores. In addition, the formation of these porous nanolayers creates a net volume expansion and further brings a static stress between these layers but also likely a high dynamical stress during their formation. The presence of these stresses could thus trigger a pressure-induced densification process within Type II regime but the presence of Type I like densification cannot be excluded as well. *So here, we wonder if its densification mechanism is the same as the Type I modification or not. Is it a defects-induced densification, a pure thermal densification or a pressure-induced densification with or without thermal effect (i.e., hot or cold compressed silica)?*

In chapter 3, we compare the Raman signature of fs-Type II to the one of various silica samples studied in Refs. [63, 64], and for which we have measured their macroscopic density. More specifically, *Figure 6-5 (a)* shows the Raman spectra of fs-Type II in comparison to high-energy electron irradiated pre-densified silica glasses obtained either from High Pressure-High Temperature (HP-HT) or from thermal treatment increasing their initial fictive temperature (T_f) [63]. From there, we can see that the Raman signature of fs-Type II mimics the one of HP-HT or high T_f samples that have been irradiated to high electron dose (5-11 GGy range). In particular Raman spectrum of fs-Type II silica is quite close to both T_f 1400 °C silica irradiated at 5 GGy, and sample irradiated at 11 GGy. The densities of latter samples are 2.248 and 2.244, respectively. This further confirms that the material between porous layers exhibits similar characteristics as Type I modification i.e. a denser structure accompanied by a higher Young's modulus compared to pristine silica as reported recently

by P. Vlugter [94].

In order to better quantify the observed variations to previously densified glasses (T_f and HP-HT) under irradiation (electrons vs femtosecond), the FWHM of the 440 cm^{-1} band and the D_2 intensity from [63] as a function of density were analyzed in chapter 3. From that we made a rough estimate of the average density to be around 2.25-2.27 after fs-irradiation. This corresponds to a refractive index change of around $+10^{-2}$ [63] in agreement with some anisotropic refractive index measurements early made by Bricchi et al. [95]. However, this is difficult to give a more reliable value at this step due to the composite nature of the probe volume: porous nanolayers (typ. 30 nm thickness) with densified interlayers (typ. 200-300 nm). In addition some potential volume changes might occur around the nanopores as well as suggested by Bellouard [96] and Poumellec [97].

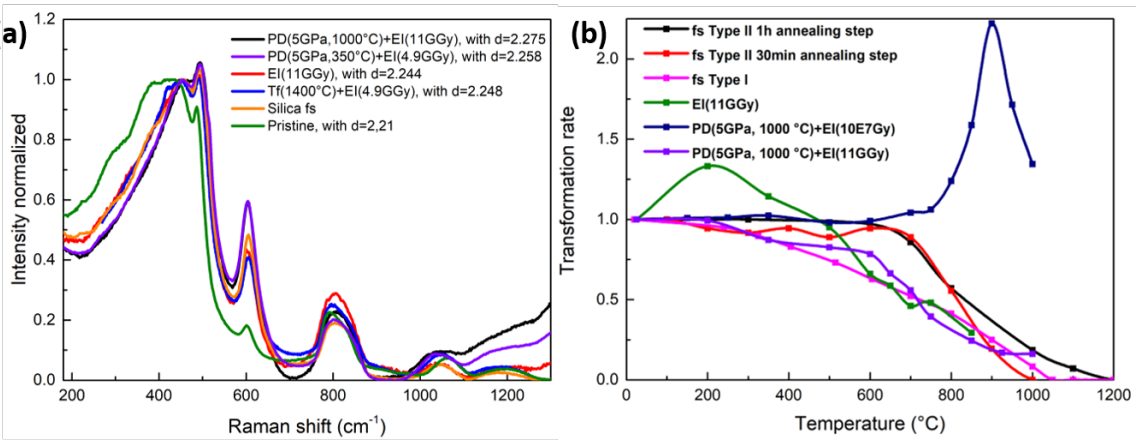

Figure 6-5**.** (a): Raman spectra of silica with following conditions: **black**, pre-densified (PD), (5 GPa, 1000 °C) + electron irradiation (EI), (11 GGy); **purple**, pre-densified (5 GPa, 350 °C) + electron irradiation (4.9 GGy); **red**, electron irradiation (11 GGy); **blue**, fictive temperature treated (1400 °C) + electron irradiation (4.9 GGy); the data are extracted from the literature [63, 64]. Silica irradiated by Femtosecond laser (**orange**) and the pristine sample (**green**) are also added for comparison; (b): Transformation rate (deduced from Raman spectra) as a function of annealing temperature for fs-laser irradiated silica glass (**red**: Type II, **magenta**: Type I). Data extracted from the literature : **black**, fs-laser irradiated silica glass follows 1h annealing step; **green**, electron irradiation (EI), (11 GGy); **violet**, pre-densified (PD), (5 GPa, 1000 °C) + electron irradiation (EI), (11 GGy); **navy**, pre-densified (PD), (5 GPa, 1000 °C) + electron irradiation (EI), (10E7 Gy), the data are extracted from the literature [63, 64, 86].

However, it is still unclear if the densification is due to defects accumulation or from a high pressure. For going a bit further in the analysis one can consider the effect of heat treatments.

- A first point is that, from our data and the literature [98] we reveal that densification and its related stress will be erased at a much lower temperature than the nanopores themselves. Hence, as the annealing temperature increases, densified regions will

gradually anneal away, causing a decrease of the refractive index within the porous nanolayers. More details can be found in the related publication in chapter 3.

- The second point is that each densification method exhibits more or less its own relaxation kinetics under thermal treatment. Following this view, we can analyse the literature to compare the thermal stability of Type II densification to the one of classical methods described above.

In this view, we performed a Raman spectroscopy analysis during step isochronal annealing. We used the principal Raman features of silica glass namely D_1 (490 cm^{-1}) and D_2 (606 cm^{-1}) peaks attributed to four-member and three-member siloxane rings respectively, are generally (but not always [63]) characteristics of a "dense" silica glass. The resulting comparison is displayed in *Figure 6-5 (b).* Here the amplitude of the D_2 band was normalized with respect to the value at room temperature. In addition, the D_2 strength of the pristine sample was also subtracted leading to a transformation rate from 1 down to 0, zero being for a pristine silica glass.

The behavior of fs Type II densification is stable up to 600 °C and starts to decay monotonously as the annealing temperature increases. This reduction could be interpreted by the fact that the densified silica network starts to relax at this range of temperature, which agrees with the observed stress relaxation. Through further T increase, the intensity went back to zero around 1000 °C - 1100 °C according to the laser parameters. Note that Type I curve (normalized index changes) start to decay earlier that is attributed to the defects contribution and the ultimate erasure temperature agrees with the one of Type II densification. Then, the sample pre-densified (5 GPa, 1000 °C) and subsequently irradiated with electrons (10^7 Gy) draws attention because of its non-monotonous evolution and superior thermal stability. As the annealing temperature increases, the transformation rate will expect to decrease monotonously. But in this sample, we observe a transient increase in the 700-900°C range while the glass density decreases. Then the transformation rate decreases monotonously at higher temperatures.

Interestingly, for the two pre-densified samples under the same conditions, we will get a completely different trend by increasing the dose to 11GGy. Note that this dose is high enough to relax the thermo-mechanical densification and thus this sample is close to the metamict phase. So this sample follows a quite classical trend during the isochronal annealing, both density (not shown here) and the Raman transformation rate are decreasing following a kinetics that is quite close to fs-Type I modifications.

Conclusion

Given the nature of the densification process, a pure thermal mechanism, i.e., melting followed by fast quenching, can be exclude since it would not relax at temperatures below T_g for such a short (30min) annealing time as we observed in Figure 6-5. Comparing to type I

modifications, it seems that type II densifications is a bit more stable and the estimated index changes is also quite higher. Interestingly, the estimated elastic properties of the densified interlayers are higher compared to a Type-I modification [94]. This suggests that the fs-Type II densification mechanism is more complex than the Regime-I modification. Then the Type II densification does not reveal the non-monotonous behavior that we observed during the relaxation of hot compressed silica and that was also observed by Cornet et al. [99]. Finally, it is still unclear if the densification is solely due do defects accumulation (such as for electrons irradiation or likely fs-Type I) or from a mixed mechanism including bath defects accumulation and high pressure-high temperature densification that develops during the nanogratings formation and party remains after as well [84].

6.2 On the links between nanoporous layers and the birefringence thermal stability in silica glass

As discuss in chapter 3 (in the paper *entitled "Overview of the thermal erasure mechanisms of femtosecond laser-induced nanogratings in silica glass"*), the main contribution to the fs-laser induced birefringence is the form birefringence, LB_{form}, due to the formation of nanogratings. The refractive index contrast along these nanogratings is due to the formation of nanopores inside the nanolayers whereas the interlayers are likely densified as discussed in the previous section. In addition, these nanopores formation is associated to a net volume expansion creating thus an elastic response and a stress-induced birefringence, LB_{stress}, whose orientation depends on the writing geometry (lines, circles, squares). In this PhD work, we observed there is a close connection between the thermal stability of the linear birefringence (or rather the associated optical retardance R) and the erasure of the nanopores. This agrees well with the porosity size and its filling factor (FF) that were observed to decrease during high temperature step isochronal annealing treatments. In this section, we will first introduce this topic through our recent publication that was published during this PhD work. In this publication, we chose the case of a commercial silica glass (SuprasilCG from Heraeus) and have presented the effect of the writing speed, pulse energy, and annealing temperature on the 2D porosity filling factor and the average nanopores size within nanogratings regime. The Rayleigh-Plesset equation was then proposed and uses to compute the collapse of the nanopores, and allow the simulation of nanopores erasure kinetics in a viscous fluid.

Applied Physics A (2020)126:876
https://doi.org/10.1007/s00339-020-04062-8

Applied Physics A
Materials Science & Processing

Erasure of nanopores in silicate glasses induced by femtosecond laser irradiation in the Type II regime

Maxime Cavillon[1] · Yitao Wang[1] · Bertrand Poumellec[1] · François Brisset[1] · Matthieu Lancry[1]

Received: 15 June 2020 / Accepted: 7 October 2020
© Springer-Verlag GmbH Germany, part of Springer Nature 2020

Abstract
Optical devices fabricated by femtosecond (fs) laser within the Type II regime are of interest for high temperature applications (> 800 °C). fs-Type II regime is characterized by the formation of self-organized nanogratings, which are composed of regularly spaced porous nanolayers with nanopores having a typical size of a few tens of nm. In this work, we first investigate the evolution of the nanopore size distribution as a function of fs-laser writing speed and pulse energy, as well as a function of annealing temperature after fs-laser irradiation. Then, the thermal stability of such nanopores is numerically investigated through the use of the Rayleigh–Plesset (R–P) equation, and is compared with experimental data. The R–P equation provides insights into the temperature range at which the nanopores would ultimately collapse, serving as a design tool for future high temperature fs-Type II based devices. The key role of glass viscosity and nanopore diameter on the overall thermal stability is also discussed.

Keywords Femtosecond laser · Nanogratings · Silicate glasses · Thermal stability

1 Introduction

Optical devices capable to withstand and operate at high temperatures (> 800 °C) for a long period of time (e.g., hundreds of hours) are attractive for many applications, including aircraft engine monitoring, fuel bed combustors, long lifetime optical data storage or fiber lasers [1–3]. Within the tools at one's disposal to fabricate devices in both fiber and bulk glass materials, femtosecond laser-direct writing (FLDW) is particularly interesting. Indeed, FLDW is a versatile technique that enables high peak powers to induce local three-dimensional (3D) modifications inside the glass subtract, due to the nonlinear absorption processes involved during the laser light–matter interaction. One of the unique features of FLDW is the possibility to induce self-organized nanogratings, within the so-called Type II regime [4]. In addition, nanogratings have been reported in a variety of glasses, including silica, germanates, silicates, borosilicates [5, 6].

In silica, these nanogratings can survive beyond 1000 °C for several hours [7], and are composed of regularly spaced porous nanolayers (typically few tens of nm thickness, with a period of about 300 nm). The latter are filled with nanopores having their size and number being a function of the laser parameters as well as the glass material [8]. Upon an increase in temperature, Type II regime laser-induced modifications would be accompanied by changes in the glass structure (e.g., point defects, stress, specific volume) and in the related physical properties (e.g., refractive index, birefringence, light absorption and scattering). Such modifications will ultimately dictate the response and the lifetime of a fabricated optical device (e.g., a grating used as a sensor [2] or a dot used for 5D optical data storage [3].

Thus, it is critical to understand what are the underlying mechanisms that drive the evolution of these aforementioned modifications at high temperatures. The annealing of fs-laser induced nanogratings yield to some modifications, at different temperature ranges, which have previously been investigated and reported. For instance, the presence of laser induced defects, such as non-bridging oxygen hole centers (NBOHC), fully erased at 600 °C within a few minutes [9]. Additionally, in silica the typically large amount of 3- and 4-membered rings, characteristic of densification and the presence of an intense compressive stress induced by Type

✉ Maxime Cavillon
maxime.cavillon@universite-paris-saclay.fr

[1] Institut de Chimie Moléculaire et des Matériaux d'Orsay (ICMMO/SP2M/MAP), Université Paris-Saclay, CNRS, 91405 Orsay Cedex, France

Published online: 20 October 2020

II laser irradiation, is found to decrease and to anneal away within the 800–900 °C temperature range [9, 10]. Moreover, the stress field associated with the formation of nanogratings (see for instance Ref. [11]) is typically relaxed slightly below or at the glass transition temperature (~1100 °C for silica) [10, 12, 13]. Ultimately, the fs-induced modifications correspond to a permanently decomposed glass with nanopores embedded inside it [14, 15]. As a note, the presence of defects in the glass, as discussed above, is partly associated with the dissociation of SiO_2 into $SiO_{2(1-x)}+xO_2$ [14]. The Raman peak intensity, centered at 1556 cm^{-1} in Ref. [14], is characteristic of free O_2 inside the glass nanopores [16]. Increasing the temperature in the 300–600 °C range causes bleaching of defects, which would yield a decrease of the O_2 pressure. The signature of free O_2 is detected up to ~ 600 °C using Raman spectroscopy (see Fig. 3.14 of Ref. [17]), and agrees well with the aforementioned defect bleaching.

In this work, we first investigate the nanopore size distribution, in silica glass, for different writing conditions (varying scanning speeds and pulse energies), as well as the erasure of the nanopores through heat treatments at different temperatures. Variations in the average nanopore diameter are observed [18]. Following this, the thermal stability of the laser induced nanopores is investigated using the Rayleigh–Plesset (R–P) equation [19], assuming the nanopores to have a spherical shape. In practice, the nanopores can take the form of ellipsoids or more complex shapes [20, 21]. However, this work intends to set the basis for future work to include these difficulties, and therefore, only spherical particles are considered herein.

The role played by both the glass material (including pure silica – Infrasil and PCVD types, Borofloat 33 – composition in mole%: 81%SiO_2–13%B_2O_3–4%Na_2O/K_2O–2%Al_2O_3, and ULE glass – Ultra Low Expansion and in mole%: 93%SiO_2–7%TiO_2) and the initial nanopore diameter on the overall thermal stability of the fs-induced nanogratings are modeled using the R–P equation, and compared with experimental data. This work is aimed to provide preliminary insights on the ultimate stability of the nanopores present in the glass. This may be used as a means to ease the selection of glass material and laser parameters to enhance thermal stability in future optical designs operating in a high temperature environment.

2 Materials and methods

First, the nanopore size distribution within the porous regions is investigated for three different pure silica glass samples (labeled S1, S2 and S3), which are reported in Table 1, along with the different laser irradiation conditions used. For S1 sample the writing speed is varied from 0.01 mm s^{-1} to 10 mm s^{-1}. For S2, the pulse energy is varied from 0.2 µJ to 1.0 µJ, and for S3 Type II laser-induced modifications are consecutively annealed for 30 min at 1000 °C, 1100 °C, and 1200 °C. To investigate the nanopores and their size distribution, each sample was cleaved perpendicularly to the laser light polarization direction (for instance see Ref. [1]) and imaged by a scanning electron microscope (FEG–SEM Zeiss Supra 55 VP).

Following the investigation of the nanopore sizes, a numerical approach, using the Rayleigh–Plesset (R–P) equation, is undertaken to simulate the erasure of the nanopores during the thermal annealing. The R–P equation is derived from the Navier–Stokes equation and physically describes the evolution of a spherical bubble inside an incompressible Newtonian fluid. The R–P equation takes the following form [19, 22, 23]:

Table 1 Glass samples and laser irradiation conditions investigated for nanopore size distribution characterization

Materials	Silica suprasilCG	Silica PCVD	Silica suprasilCG
Sample labelling	S1[1]	S2	S3
Pulse energy (µJ)	2.0	0.2; 0.4; and 1.0	1.0
Writing speed, v (mm s^{-1}) [2]	0.01; 0.1; 1; 10	0.1	1
Repetition rate, f (kHz)	100	100	100
Number of pulses per µm	10,000; 1,000; 100; 10	1,000	1,000
Wavelength (nm)	1030	1030	1030
Pulse duration (fs)	250	300	300
Numerical aperture, NA	0.6	0.6	0.6
Focusing depth (µm)	–	300	300
Configuration[3]	–	//	//

[1]This sample is the same as in Ref.[8]

[2]Varying the laser writing speed v with a constant repetition rate f is equivalent to changing the pulse density v/f, or the "number of pulses per µm" as defined in the table

[3] // or ⊥: Laser polarization parallel (//) or perpendicular (⊥) to the writing direction

$$\frac{\Delta P}{\rho} = R_{\text{pore}}\frac{d^2R_{\text{pore}}}{dt^2} + \frac{3}{2}\left(\frac{dR_{\text{pore}}}{dt}\right)^2 + \frac{4\eta(T)}{\rho R_{\text{pore}}}\frac{dR_{\text{pore}}}{dt} + \frac{2S}{\rho R_{\text{pore}}}. \quad (1)$$

In this equation, ΔP is the pressure difference (in Pa) between the inside of the nanopore (supposed spherical) and far away from it, ρ is the glass density (in kg m^{-3}), R_{pore} the radius (in m) of the spherical nanopore, t the time (in s), η(T) the glass viscosity (in Pa.s), and S is the surface energy (around 0.3 J m^{-2} for silica [24]). Both ρ and S are set independent to the temperature for sake of simplicity. The viscosity is extrapolated from glass manufacturer datasheets (Borofloat33, SuprasilCG, Infrasil and PCVD) and from Ref. [8] for ULE glass, using a Vogel–Tammann–Fulcher (VTF) law in the form $\log(\eta) = A + B/(T - T_0)$. Initial conditions are R_{pore} (at $t = 0$) $= R_0$ and dR_{pore}/dt (at $t = 0$) $= 0$. The equation is solved numerically using an ordinary differential equation (ODE) built-in solver from Matlab software. This work only intends to provide preliminary understandings on the ultimate stability of nanopores using the R–P equation. Therefore, several assumptions and simplifications are made. First, we set $\Delta P = 0$, as the decrease in O_2 concentration inside the nanopore, due to bleaching of defects as described in the introduction below 600 °C. Indeed, and as already described in the introduction section, the oxygen inside the nanopore is associated with formation of defects, and the oxygen is inserted back into the structure below 600 °C (and, therefore, without long distance diffusion). It would result in a rather small O_2 pressure, which will be subsequently neglected throughout the paper. The R–P equation is used to compute the nanopore size evolution for different glasses, including pure silica (PCVD, Infrasil301), Borofloat33 and ULE, which have been reported in Ref. [8]. In these experiments, the thermal stability of Type II nanostructures is investigated through step isochronal measurements ($\Delta t = 30$ min, ΔT typ. 25 °C or 50 °C) and by monitoring the retardance induced by the birefringent nanogratings. The Retardance (R) is defined as the product of the Birefringence (B) with the length (L) of the birefringent object ($R = B \times L$). In Ref. [8], the aforementioned $R(\Delta t, T)$ values measured at room temperature after each annealing step are normalized relative to the initial (not annealed) $R(t = 0, 20\ °C)$ value. In this work, the experimental data are normalized with respect to the R value at the temperature above which the retardance experiences a steep decay rate (e.g., $T = 1225$ °C for Infrasil301 in Fig. 5a in Ref. [8]). The latter normalization enables to investigate only the last step of nanograting erasure.

To compare the computed results from the R–P equation with the experimental normalized R values, the nanopore diameter (from R–P equation) is converted to a normalized retardance value following the procedure described below. First, we calculate the average refractive index of the porous nanolayer (n_{pl}) using the Maxwell–Garnet equation [25]:

$$n_{pl} = \sqrt{n_G^2\frac{n_G^2 + \frac{(1+2FF)}{3}\left(n_{\text{pore}}^2 - n_G^2\right)}{n_G^2 + \frac{(1-FF)}{3}\left(n_{\text{pore}}^2 - n_G^2\right)}}. \quad (2)$$

In the above equation, n_G is the glass refractive index (taken as 1.4599, i.e., index of silica at 551 nm), which is assumed independent of temperature (small dn/dT of ~ 10×10^{-6} K^{-1} [26]). This value is taken equal both inside the porous nanoplanes (i.e., around the nanopores) and between the porous nanoplanes. This simplification is acceptable in the conditions of this work, as we principally focus on the erasure of the nanopores for temperatures at, or above, the glass transition temperatures of the glass materials investigated. Therefore, the contributions to the refractive index due for instance to the presence of a stress field (see for example Fig. 5a in Ref. [13]), or a permanent densification of the glass, are annealed away (Refs. [17, 27]). FF is the filling factor, defined here as the relative volume taken by the nanopores per unit volume of porous nanolayer (labeled V), and n_{pore} is the nanopore refractive index, taken equal to 1. The filling factor is related to the averaged nanopore radius (R_{pore}) through the following equation:

$$\text{FF} = N\frac{4\pi R_{\text{pore}}^3}{3V}. \quad (3)$$

Here, N is the number of nanopores (with an averaged nanopore radius R_{pore}) per unit volume V of porous nanolayer. A 2D filling factor, corresponding to the area taken by the nanopores per unit surface of porous nanolayer, can be determined from SEM micrographs and is usually in the order of 20–40% [18]. The latter (labeled FF_{2D}) will be used in Sect. 3. When discussing the normalized retardance in Sect. 3.3, the FF defined in Eq. 3 is computed. Additionally, in this work, the refractive index of the glass between the porous nanolayers is set equal to n_G as in Ref.[18]. Hence, the birefringence $B = n_o - n_e$, where n_o and n_e are the refractive indices of the ordinary and extraordinary axes, respectively, is calculated from [7, 18]:

$$B = n_o - n_e = \sqrt{\left[1 - \frac{\delta}{\Lambda}\right]n_G^2 + \frac{\delta}{\Lambda}n_{pl}^2} - \left[\sqrt{\frac{\left[1 - \frac{\delta}{\Lambda}\right]}{n_G^2} + \frac{\frac{\delta}{\Lambda}}{n_{pl}^2}}\right]^{-1}. \quad (4)$$

Here, Λ is the average spacing between nanolayers, δ is the porous nanolayer thickness, and (Λ–δ) is the interlayer thickness. Finally, the linear retardance can be calculated using the expression $R = B \times L$ as defined above.

3 Results

3.1 Impact of laser writing conditions on the evolution of nanopore size and distribution

The impact of the writing speed in the nanopore morphology is depicted in Fig. 1, where SEM micrographs, nanopore size distribution, 2D filling factor and averaged nanopore diameter as a function of writing speed, are displayed (using Sample S1). We observed that the average nanopore diameter increases when writing speed increases (from 53 to 77 nm from 0.01 mm s^{-1} to 10 mm s^{-1}, respectively, corresponding to a ~ 45% increase). As the writing speed increases, the spread of the nanopore diameter distribution also becomes larger (e.g., standard deviation is increased from 13 to 34 nm between 0.01 mm s^{-1} and 10 mm s^{-1}). While the average nanopore size is increased when speed is increased, the 2D filling factor comparatively decreases. The evolution of FF_{2D} observed in Fig. 1 is qualitatively in agreement with retardance values reported in Ref. [8]. However, it is worth pointing out that other contributions factor into the measured retardance value, such as laser track length, porous nanolayer thickness or periodicity.

The evolution of the nanopore size and distribution, as presented in Fig. 1 with respect to varying writing speed conditions, is now investigated through the variation of the laser pulse energy, everything else being set constant (using Sample S2). The results are reported in Fig. 2. An increase

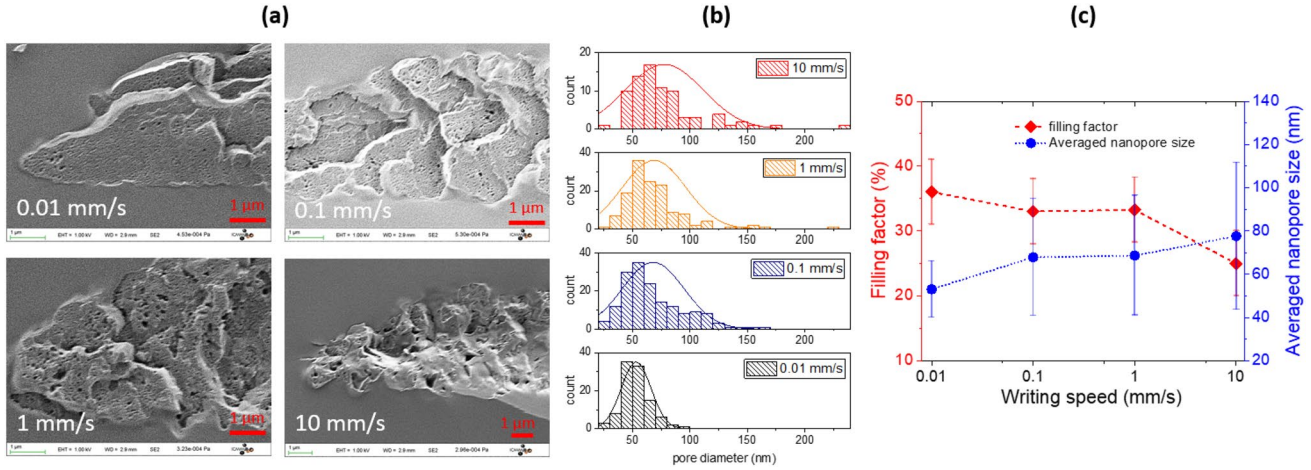

Fig. 1 Effect of the writing speed on nanopore size, distribution and filling factor, using Sample S1. **a** scanning electron micrographs of the porous regions for different writing speeds; **b** nanopore diameter distributions with respect to the writing speed; **c** evolution of the 2D porosity filling factor and the average nanopore diameter as a function of writing speed. The lines only serve as a guide-to-the-eye

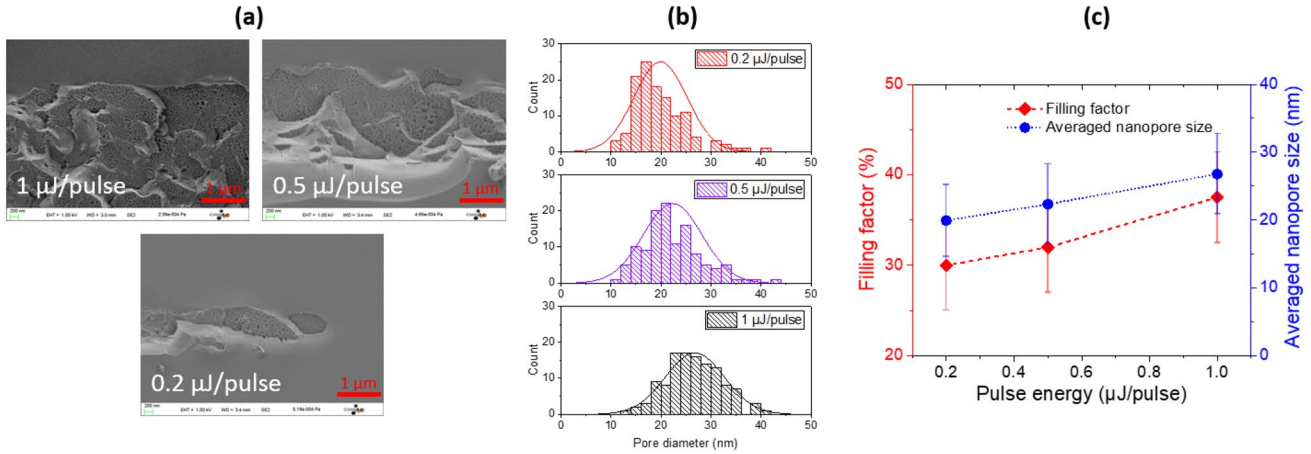

Fig. 2 Effect of the laser pulse energy on nanopore size, distribution and filling factor, using Sample S2. **a** scanning electron micrographs of the porous regions for different pulse energies; **b** nanopore diameter distributions with respect to pulse energy; **c** evolution of the 2D porosity filling factor and the average nanopore diameter as a function of pulse energy. The lines only serve as a guide-to-the-eye

of the pulse energy is associated with an increase in the nanopore diameter, which exhibits an almost linear rate within the investigated interval (~8.6 nm diameter increase per µJ). There is almost no evolution of the standard deviation (5.3 nm and 5.9 nm for 0.2 µJ and 1.0 µJ, respectively). However, as opposed to the results from Fig. 1a, the increase in energy is associated with an increase of the filling factor, and is in agreement with a higher retardance value (for instance in Ref. [28]).

3.2 Experimental observation of the decrease in nanopore size and distribution during annealing process

The evolution of the nanopore morphology and size distribution as a function of annealing temperature (for isochronal time steps Δt of 30 min, and using sample S3) is reported in Fig. 3. In this experiment, we observe that the nanopore diameter decreases first as the temperature increases, but appears to plateau at the highest temperature. This effect can be interpreted from the results obtained by the R–P equation, and is discussed in the following section. On the other hand, we observed a diminution of FF_{2D} that is characteristic of a decrease in the birefringence response (hence the measured retardance). Other SEM micrograph analysis, not presented here, also showed that both thickness of planes and spacing between planes were independent of temperature.

3.3 Simulation study of the decrease in nanopore size in annealing process by the Rayleigh–Plesset equation

Thermal stability of Type II nanogratings inscribed in various glasses (silica and silicate glasses) were investigated and reported in Ref. [8], using step isochronal annealing experiments ($\Delta t = 30$ min, $\Delta T = 25$ °C). These data are displayed in Fig. 4, but normalized relative to the sharp retardance decrease at the highest annealing temperature values that we hypothesized here to be characteristic of the nanopore erasure. It is worth pointing out that in order for each data point to be independent to the other, the criterion $(\Delta t \times k_0)^{-(\Delta T/T_{max})} << 1$ must be fulfilled [29] (with k_0 estimated to be around 5×10^5 to 5×10^7 s^{-1} for nanogratings erasure in silica [30]). In this work, this criterion is not satisfied, and therefore, the thermal stability in this condition is expected to be slightly underestimated with respect

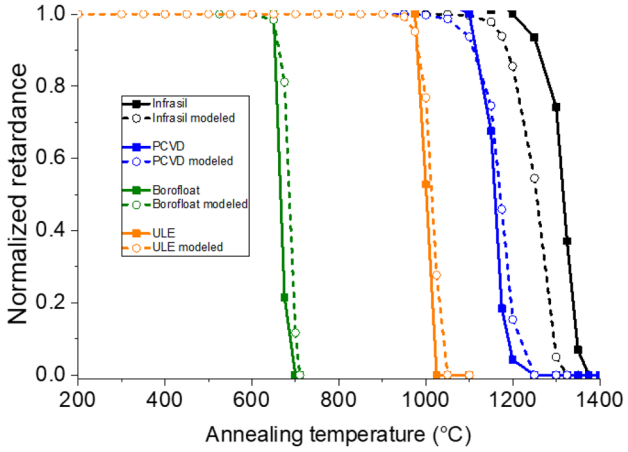

Fig. 4 Evolution of the normalized retardance during step isochronal annealing experiments for various glasses (taken and re-normalized from Ref. [8]) compared with the Rayleigh–Plesset (R–P) equation used to simulate the nanopores' erasure. Conditions used in the simulation: $\Delta P = 0$ Pa; $S = 0.3$ J m^{-2}; $\rho = 2200$ kg m^{-3}; Initial nanopore radius used during calculation: $R(t=0) = 25$ nm; η(T) fitted using a VTF law for each glass (Infrasil, PCVD, Borofloat33, and ULE)

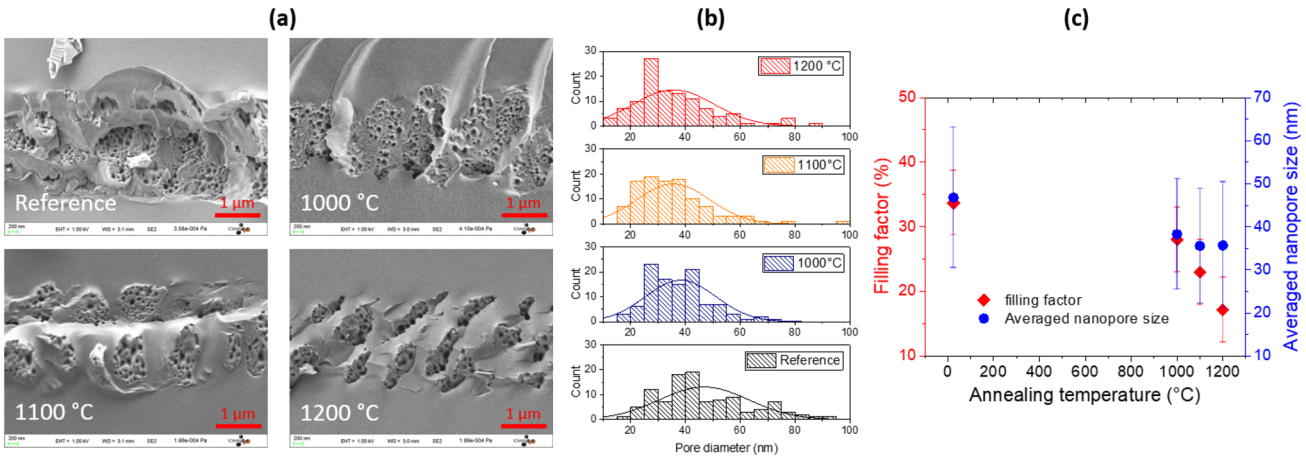

Fig. 3 Effect of thermal annealing on nanopore size, distribution and filling factor, using Sample S3. **a** scanning electron micrographs of the porous regions for different annealing temperatures ($\Delta t = 30$ min); **b** nanopore diameter distributions with respect to annealing temperature; **c** evolution of the 2D porosity filling factor and the average nanopore diameter as a function of annealing temperature

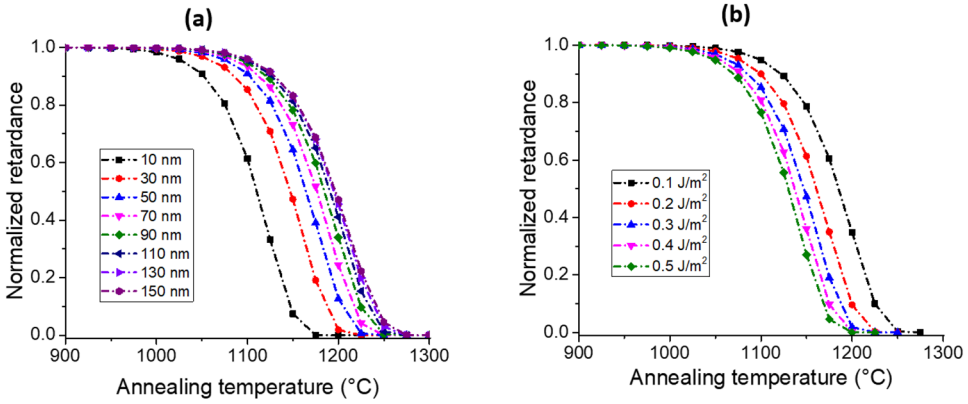

Fig. 5 Evolution of the Retardance (only taking into account the evolution of the nanopores) for step isochronal annealing experiments ($\Delta t = 30$ min, $\Delta T = 25$ °C) for SuprasilCG glass simulated by Rayleigh–Plesset (R–P) equations. **a** Effect of initial nanopore diameter (from 10 to 150 nm), with a constant value of $S = 0.3$ J m^{-2}. **b** Effect of surface energy S (from 0.1 to 0.5 J m^{-2}), with a constant value of $R(t=0) = 15$ nm

to a stability curve having independent data points. In this paper only the final erasure step of the measured retardance $R(\Delta t, T)$ is investigated. Following the same experimental conditions as in the experiment, the Rayleigh–Plesset (R–P) equation was used to simulate the nanopore erasure, and the evolution of the retardance was calculated based the nanopore diameter, the filling factor FF and using the form birefringence equations (Eqs. 2, 3, and 4) shown above. Here we assume that the nanolayers thickness (δ), the average spacing (Λ), and the interlayer thickness (Λ–δ), and the laser track length (L) did not change with the annealing steps. The comparison between experimental data and the simulated data (using R–P equation) are reported in Fig. 4. It is worth pointing out that the R–P equation computed here is for a single initial nanopore diameter. However, as was previously discussed, the nanopore diameter is distributed in a fairly wide interval, depending on the laser writing conditions but also with the chemical composition [6, 31]. However, as a first approximation, one can note that evolution of the simulated retardance, related to the erasure of the nanopores using the R–P equation, agrees rather well with the experimental data, even when the viscosity dynamics is found to vary by several order of magnitudes with respect to temperature for the studied glasses. This is indicative that viscosity (and its temperature dependence) is a first order property in the erasure mechanism of nanogratings and their associated form birefringence in a high temperature regime.

The effects of both nanopore diameter and surface energy S (from R–P equation) are investigated and reported in Fig. 5a and b. As the initial nanopore diameter is increased or the glass surface energy is decreased, the annealing curves shift to higher temperatures. With a 100 nm nanopore diameter change, thermal stability curve is expected to shift by ~100 °C (for a normalized retardance value of 0.5). In contrast, the surface energy plays a less significant role in the process, since a large change of surface energy ($\Delta S = 0.4$ J m^{-2}) shifts only by ~50 °C the annealing curves. The discrepancy between the experimental data and the model observed in Fig. 4 for the Infrasil301 could potentially be attributed to a variation of surface energy, although further investigations would be necessary to verify this hypothesis.

4 Discussion

In the previous section we have shown that the thermal stability of nanogratings (evaluated though optical retardance measurements) induced by IR fs-laser (so called Type II regime) is not only a function of the silicate glass chemical composition but also of the nanogratings morphology. The use of various laser-writing parameters, including writing speed (hence linear pulse density) and pulse energy, directly influence the distribution and the size of the nanopores within the porous nanolayers. A direct consequence of this is the change in the thermal stability of optical devices fabricated by Type II fs-laser writing. As an example, the average refractive index changes along the "fringes" of a Type II fiber Bragg grating (such as the ones in Ref. [2]) would be equal to $(n_e + n_o)/2$. In contrast polarizing based devices like radial–azimuthal polarization converter [32], achromatic polarization rotator [33], fs-laser-induced waveplates [13, 34] or 5D "eternal" optical memories [3] are based on the optical retardance amplitude and thus proportional to $(n_e - n_o)$. Hence, the optical response of these devices at high temperatures would be related to the magnitude of birefringence induced by the overall porous structure, and among which the nanopore size plays an important role.

In addition, the chemical composition of the glass material has a critical role in the erasure of the nanopores, as its viscosity behavior is found to principally dictate the overall nanopore erasure, as shown from the results using R–P equation. For instance, low OH and Cl impurity-containing materials, such as Infrasil301 silica, present high viscosity at high temperatures, which is expected to promote thermal stability of the nanopores. The differences observed in optical properties, here in term of linear birefringence, are in

fairly good agreement between experimental and simulated data using the R–P equation as shown in Fig. 4.

From Fig. 1, the average nanopore diameter increases from 53 to 77 nm between low and high writing speeds (0.01–10 mm s^{-1}), and the steep decay of the associated isochronal annealing curves is shifted by ~15 °C to higher temperatures (Ref. [8]). Using the R–P equation with the experimental conditions described in the same reference, a shift of ~ 15 °C is also predicted.

In Fig. 3c, we observe that, as the irradiated glass is progressively annealed, the nanogratings filling factor *FF* decreases, while the averaged nanopore size remains nearly constant. This can be explained on the basis of the R–P equation, where we observe that small nanopores being erased more quickly than the larger ones (see Fig. 5a). As a result, the fully erased small nanopores are not included in the counting to determine the average nanopore diameter. This has an effect of shifting up the average nanopore diameter to larger values. However, the filling factor still decreases as nanopores are progressively erased, which are in agreement with the observation of a decrease in retardance. On a more speculative note and based on results from Fig. 5a and 5b, a possible way to further promote thermal stability could be by minimizing the glass surface energy.

As was mentioned in the introduction, it is worth pointing out that the shape of the nanopore is more ellipsoidal than spherical, as was brought to evidence in Ref. [20] using small angle X-ray scattering (SAXS) measurements. In our conditions and to reveal the porosity of the nanopore layers, the sample are cleaved along the short axis direction and placed under an SEM for observation. But for such geometry (ellipsoid nanopores) the limiting factor of the erasure kinetic is controlled by the short axis of the nanopore. Although the shape of the annealing curve is expected to be slightly modified (and mostly at the highest temperatures), using an ellipsoidal geometry to model the dynamics of the nanopore erasure should not be drastically different with respect to a spherical geometry. Finally, on this matter is it possible to expect the ellipsoids to round up during the annealing to minimize their surface tension.

Type III regime, associated with the formation of nanovoids (typically in the 100 nm to 1 µm diameter range [35–37]), is known to be slightly more stable that type II nanogratings, provided that associated stress and densified shell surrounding the nanovoids can be stabilized. From this work, the larger size of the nanopores is expected to be a principal contributor to this higher thermal stability. Hence, in the realm of high thermal stability devices, one would want to maximize the nanopore diameter. Additionally, a single void structural modification induced by femtosecond laser may be advantageous over nanopores as one would not have to take into account a nanopore size distribution, which may ease thermal stability predictions. Finally, the viscous behavior of the glass material will ultimately set the upper limit of the thermal stability of the device. Hence the current interest is to develop high viscosity glasses and optical fibers [1, 38].

5 Conclusions

In this work, the effect of glass composition and laser parameters upon fs-laser direct writing in the Type II regime (formation of nanogratings), are reported in silica and silicate glasses. The evolution of nanopore diameter as a function of laser writing speed, pulse energy, and temperature (through step isochronal annealing) is investigated and discussed. The Rayleigh–Plesset (R–P) equation is then used to compute the collapse of such nanopores as a function of glass chemical composition and with varying initial nanopore diameters or surface energy values. The R–P equation shed light on the major role played by the temperature dependence of the glass viscosity on the thermal stability of fs-induced Type II modifications. Consequently, it is not only the glass annealing temperature (T_a) but rather the viscous behavior of the glass over a temperature range (between T_a and the softening temperature T_{soft}) that is the major parameter driving the erasure of the nanogratins and their related form birefringence. This viscous behavior is also expected to have an impact on nanogratings formation inside a glass. The initial nanopore diameter is also found to play a significant role in the overall thermal stability of the fs-laser induced modified region. On a final note, this work aims to serve as a roadmap for the development of components stable at high temperatures, by mean of both glass property tailoring (e.g., viscosity, surface energy) and the mastering of laser-induced structural modifications (such as the formation of large nanopores or voids). Future work will involve the implementation of ellipsoid nanopores in the model, along with a size distribution, as well as the injection of densified zones (together with their own thermal stability) within the interlayers.

Funding The authors would like to acknowledge the following institutions for funding their research: Agence Nationale pour la Recherche, FLAG/IR project, grant number ANR-18-CE08-0004-01 and CNRS Défi Instrumentation aux Limites, Ultrabragg project.

Data availability Not applicable.

Code availability Not applicable.

Compliance with ethical standards

Conflict of interest The authors declare no conflict of interest.

References

1. M. Cavillon, M. Lancry, B. Poumellec et al., Overview of high temperature fibre Bragg gratings and potential improvement using highly doped aluminosilicate glass optical fibres. J. Phys. Photonics **1**, 042001 (2019). https://doi.org/10.1088/2515-7647/ab382f
2. S.J. Mihailov, D. Grobnic, C. Hnatovsky et al., Extreme environment sensing using femtosecond laser-inscribed fiber bragg gratings. Sensors (2017). https://doi.org/10.3390/s17122909
3. J. Zhang, M. Gecevičius, M. Beresna, P.G. Kazansky, Seemingly unlimited lifetime data storage in nanostructured glass. Phys. Rev. Lett. **112**, 1–5 (2014). https://doi.org/10.1103/PhysRevLett.112.033901
4. Y. Shimotsuma, P.G. Kazansky, J. Qiu, K. Hirao, Self-organized nanogratings in glass irradiated by ultrashort light pulses. Phys. Rev. Lett. **91**, 247405 (2003). https://doi.org/10.1103/PhysRevLett.91.247405
5. S. Richter, C. Miese, S. Döring et al., Laser induced nanogratings beyond fused silica-periodic nanostructures in borosilicate glasses and ULE^{TM}. Opt. Mater. Express **3**, 1161–1166 (2013). https://doi.org/10.1364/OME.3.001161
6. M. Lancry, F. Zimmerman, R. Desmarchelier et al., Nanogratings formation in multicomponent silicate glasses. Appl. Phys. B Lasers Opt. **122**, 1–8 (2016). https://doi.org/10.1007/s00340-016-6337-8
7. E. Bricchi, P.G. Kazansky, Extraordinary stability of anisotropic femtosecond direct-written structures embedded in silica glass. Appl. Phys. Lett. **88**, 2–4 (2006). https://doi.org/10.1063/1.2185587
8. S.-E. Wei, Y. Wang, H. Yao et al., Thermal stability of type II modifications by IR femtosecond laser in silica-based glasses. Sensors **20**, 1–14 (2020). https://doi.org/10.3390/s20030762
9. J.J. Witcher, W.J. Reichman, L.B. Fletcher et al., Thermal annealing of femtosecond laser written structures in silica glass. Opt. Mater. Express **3**, 502–510 (2013). https://doi.org/10.1364/OME.3.000502
10. J. Lu, M. Yang, D.N. Wang et al., Fiber Bragg gratings with enhanced thermal stability by residual stress relaxation. Opt. Express **17**, 19785–19790 (2009). https://doi.org/10.1364/oe.17.019785
11. R.R. Thomson, P. Gillet, S. Mukherjee et al., Stress-state manipulation in fused silica via femtosecond laser irradiation. Optica **3**, 1285 (2016). https://doi.org/10.1364/optica.3.001285
12. V.R. Bhardwaj, P.B. Corkum, D.M. Rayner et al., Stress in femtosecond-laser-written waveguides in fused silica. Opt. Lett. **29**, 1312–1314 (2004). https://doi.org/10.1364/OL.29.001312
13. J. Tian, H. Yao, M. Cavillon et al., A comparison between nanogratings-based and stress-engineered waveplates written by femtosecond laser in silica. Micromachines **11**, 1–11 (2020). https://doi.org/10.3390/mi11020131
14. M. Lancry, B. Poumellec, J. Canning et al., Ultrafast nanoporous silica formation driven by femtosecond laser irradiation. Laser Photonics Rev. **7**, 953–962 (2013). https://doi.org/10.1002/lpor.201300043
15. J. Canning, M. Lancry, K. Cook et al., Anatomy of a femtosecond laser processed silica waveguide. Opt. Mater. Express **1**, 998–1008 (2011). https://doi.org/10.1364/ome.1.000998
16. A.J. Berger, Y. Wang, D.M. Sammeth et al., Aqueous dissolved gas measurements using near-infrared raman spectroscopy. Appl. Spectrosc. **49**, 1164–1169 (1995). https://doi.org/10.1366/0003702953965047
17. F. Zimmermann, *Ultrashort Pulse Induced Nanostructures in Transparent Materials* (Friedrich-Schiller-Universitat, Jena, 2017)
18. R. Desmarchelier, B. Poumellec, F. Brisset et al., In the heart of femtosecond laser induced nanogratings : From porous nanoplanes to form birefringence. World J. Nano Sci. Eng. **5**, 115–125 (2015). https://doi.org/10.4236/wjnse.2015.54014
19. A. Rudenko, J.P. Colombier, T.E. Itina, Nanopore-mediated ultrashort laser-induced formation and erasure of volume nanogratings in glass. Phys. Chem. Chem. Phys. **20**, 5887–5899 (2018). https://doi.org/10.1039/c7cp07603g
20. S. Richter, A. Plech, M. Steinert et al., On the fundamental structure of femtosecond laser-induced nanogratings. Laser Photonics Rev. **6**, 787–792 (2012). https://doi.org/10.1002/lpor.201200048
21. M. Sakakura, Y. Lei, L. Wang et al., Ultralow-loss geometric phase and polarization shaping by ultrafast laser writing in silica glass. Light Sci. Appl. **9**, 1–10 (2020). https://doi.org/10.1038/s41377-020-0250-y
22. M.S. Plesset, The dynamics of cavitation bubbles. J. Appl. Mech. **16**, 277–282 (1949). https://doi.org/10.1080/15435075.2018.1431546
23. C.E. Brennen, *Cavitation and Bubble Dynamics* (Oxford University Press, Oxford, 1995)
24. K. Boyd, H. Ebendorff-Heidepriem, T.M. Monro, J. Munch, Surface tension and viscosity measurement of optical glasses using a scanning CO2 laser. Opt. Mater. Express **2**, 1101–1110 (2012). https://doi.org/10.1364/ome.2.001101
25. V.A. Markel, Introduction to the Maxwell Garnett approximation: Tutorial. J. Opt. Soc. Am. A **33**, 1244–1256 (2016). https://doi.org/10.1364/JOSAA.33.001244
26. M.J. Weber, *Handbook of Optical Materials* (CRC Press, London, 2003)
27. F. Zhang, Y. Yu, C. Cheng et al., Wavelength response and thermal stability of embedded nanograting structure light attenuator fabricated by direct femtosecond laser writing. Appl. Phys. B Lasers Opt. **117**, 53–58 (2014). https://doi.org/10.1007/s00340-014-5797-y
28. M. Lancry, J. Canning, K. Cook et al., Nanoscale femtosecond laser milling and control of nanoporosity in the normal and anomalous regimes of GeO_2-SiO_2 glasses. Opt. Mater. Express **6**, 321 (2016). https://doi.org/10.1364/OME.6.000321
29. B. Poumellec, M. Lancry, Kinetics of thermally activated physical processes in disordered media. Fibers **3**, 206–252 (2015). https://doi.org/10.3390/fib3030206
30. M. Gecevičius, *Polarization Sensitive Optical Elements by Ultrafast Laser Nanostructuring of Glass* (University of Southampton, Southampton, 2015)
31. F. Zimmermann, M. Lancry, A. Plech et al., Femtosecond laser written nanostructures in Ge-doped glasses. Opt. Lett. **41**, 1161–1164 (2016). https://doi.org/10.1364/ol.41.001161
32. M. Beresna, M. Gecevičius, P.G. Kazansky, T. Gertus, Radially polarized optical vortex converter created by femtosecond laser nanostructuring of glass. Appl. Phys. Lett. **98**, 1–4 (2011). https://doi.org/10.1063/1.3590716
33. R. Desmarchelier, M. Lancry, M. Gecevicius et al., Achromatic polarization rotator imprinted by ultrafast laser nanostructuring in glass. Appl. Phys. Lett. **107**, 181111 (2015). https://doi.org/10.1063/1.4934866
34. M. Gecevičius, M. Beresna, P.G. Kazansky, Polarization sensitive camera by femtosecond laser nanostructuring. Opt. Lett. **38**, 4096–4099 (2013). https://doi.org/10.1364/ol.38.004096
35. R.J. Williams, R.G. Krämer, S. Nolte et al., Detuning in apodized point-by-point fiber Bragg gratings: insights into the grating morphology. Opt. Express **21**, 26854–26867 (2013). https://doi.org/10.1364/oe.21.026854
36. E.N. Glezer, M. Milosavljevic, L. Huang et al., 3-D optical storage inside transparent materials. Opt. Lett. **21**, 2023–2026 (1996)

37. E.G. Gamaly, S. Juodkazis, K. Nishimura et al., Laser-matter interaction in the bulk of a transparent solid: Confined micro-explosion and void formation. Phys. Rev. B Condens. Matter Mater. Phys. **73**, 1–15 (2006). https://doi.org/10.1103/PhysRevB.73.214101
38. Y. Wang, S. Wei, R.C. Yuta et al., Femtosecond laser direct writing in SiO_2 -Al_2O_3 binary glasses and thermal stability of Type II permanent modifications. J. Am. Ceram. Soc. (2020). https://doi.org/10.1111/jace.17164

Publisher's Note Springer Nature remains neutral with regard to jurisdictional claims in published maps and institutional affiliations.

6.3 Going further about nanopores relationship with the ultimate thermal stability of the nanogratings and related birefringence

Type II modifications induced by IR femtosecond laser pulses, characterized by birefringent self-induced nanogratings, present excellent thermal stability at high temperatures (typically > 800 °C for hours). The aggregate birefringent response of these structures arises from multiple contributions, including form birefringence, stress-induced birefringence but also densification, and point defects that factor into the refractive index contrast along these nanostructures. In the first paper from chapter 3 we have discussed and summarized these different erasure mechanisms again, and discriminated the effect of each contribution on the overall nanogratings thermal erasure kinetics. Having now a quite clear view of these phenomena and a model (developed in section 6.2) that is able to predict the nanopores erasure in silica, we are going a bit further into the analysis. Specifically, we will tentatively take into account the chemical composition and the dependence with the laser writing conditions (speed, energy) with a particular focus on the relationship between nanopores and the "ultimate" thermal stability of nanogratings.

6.3.1 Influence of impurities (OH, Cl) in pure silica glasses

Laser-writing process has been proved to be an important factor influencing the thermal performance of permanent optical modifications. It has been theoretically proven in the literature [100] that thermal stability of laser written index changes can be stronger by means of growing the writing time, whilst the impact of pulse intensity and repetition rate on the thermal performance of IR-fs Type II FBGs has been investigated in some other reference [101]. In addition to the laser parameters, as we all know for silica glass, at some stage in the incorporation of dopants or along the fabrication process, impurities such as chlorine (Cl) and hydroxyl groups (OH) are additionally inevitably introduced [102, 103]. All these intended incorporated elements or unintended contaminations would affect the formation of fs-Type II modifications and their thermal stability. In order to construct a more reliable model of the thermal stability of nanogratings, we still need to merge together the effect of laser writing parameters and glass composition on the overall thermal performance of the Type II modifications. This is done via step isochronal annealing experiments.

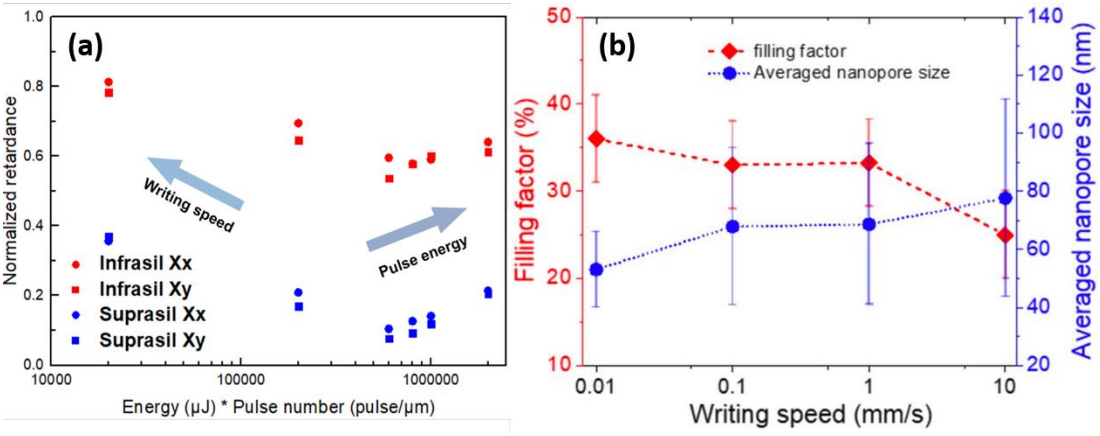

Figure 6-6. (a): Normalized retardance R_{norm} (with R_{norm}=R(6 h, 1100 °C)/R(0 h, 20 °C)) as a function of energy×pulse number (pulse number = repetition rate/writing speed) for SiO_2 (SuprasilCG and Infrasil) after pre-annealing at 1100 °C for 6 hours. Writing parameters: pulse energy E (0.6 µJ, 0.8 µJ, 1 µJ, and 2 µJ) and different writing speed (0.1mm/s, 1mm/s, and 10mm/s). The other laser parameters are: 1030 nm, 250 fs, 100 kHz, NA=0.6, laser polarization = // (Xx) or ⊥ (Xy) to the scanning direction. (b): Evolution of the 2D porosity filling factor and the average nanopores diameter measured by SEM as a function of writing speed.

In order to tentatively understand the impact of laser parameters on the thermal stability of Type II modifications in silica, the optical response (normalized retardance post annealing) as a function of writing speed and energy in two different silica glass namely Infrasil301 and SuprasilCG is investigated. All samples were annealed at 1100 °C for 6 hours, and the results are displayed in *Figure 6-6 (a)*. More specifically, in this figure, is displayed the evolution of the normalized retardance R_{norm}=R(6 h,1100 °C)/R(0,20 °C) as a function of the *E×p product* (i.e., pulse energy × pulse number). A higher value of the R_{norm} suggests an improved thermal stability. First let us discuss the influence of the writing speed: the smaller the *E×p*, the faster the writing speed. We easily find out that the R_{norm} value for both samples keep increasing with the increase of the writing speed. Moreover, and as can be observed in *Figure 6.6 (b),* the higher writing speed can effectively create a higher average nanopores size and will eventually lead to the formation of the nanostructures with better thermal stability as we discussed in section 6.2. Secondly, on the right side of the *Figure 6-6 (a),* the impact of the pulse energy on the R_{norm} (after annealing) also shows that the thermal stability is improved along with the use of higher pulse energies. We can then conclude that these two laser parameters have a decisive influence on thermal stability of Type II modifications. The reason behind these are as we know that the nanopore formation mechanism based on nano-cavitation which assisted by tensile stress with several important material parameters: thermal expansion coefficient, elastic modulus, Poisson coefficient, temperature, tensile stress, surface tension and viscosity. During the laser irradiation, in the very hot nanoplane, there is a rapid volume expansion in picosecond level and will create

the nanopores in the glass when it is in liquid state. With the higher laser pulse energy, the temperature, tensile stress and the surface tension will be higher, so the higher nanopores size can be achieved. In the case of higher writing speed, a single laser pulse leads to the voids regime. Then, by accumulating the number of pulses, there would be a transition from the void regime to the nanogratings regime. What is certain is that in this regime: for Voids formed by a single Pulse (which corresponds to a high speed) we formed a nanopore much larger than that of the nanogratings regime.

Here it is worth pointing out that we observed only a slight effect on the thermal stability with the different laser polarizations (in chapter 3, Figure 2 of the paper entitled "*an overview of the thermal erasure mechanisms of femtosecond laser-induced nanogratings in silica glass"*). Indeed, the R_{norm} value are higher for // configuration (Xx) relative to the ⊥ configuration (Xy) in most cases. We believe such polarization dependence can be explained by the boundary conditions [104] and spatial-temporal properties of the ultrashort pulse laser beam quantified by the pulse front tilt leading to anisotropic photosensitivity phenomena [105]. In the simplest explanation, we can put forward there is a higher energy deposited for x polarization (due to lower Fresnel losses), which translates into a higher thermal stability as per the above discussion.

Finally, although both samples are silica glass, there is still a noticeable difference (at least a factor of 2!) of their R_{norm} value after the pre-annealing treatment. This is attributed to their different impurities (like OH species, Cl content) and the resulting glass annealing temperature T_a; a detailed investigation about this factor is presented in *Figure 6-7*.

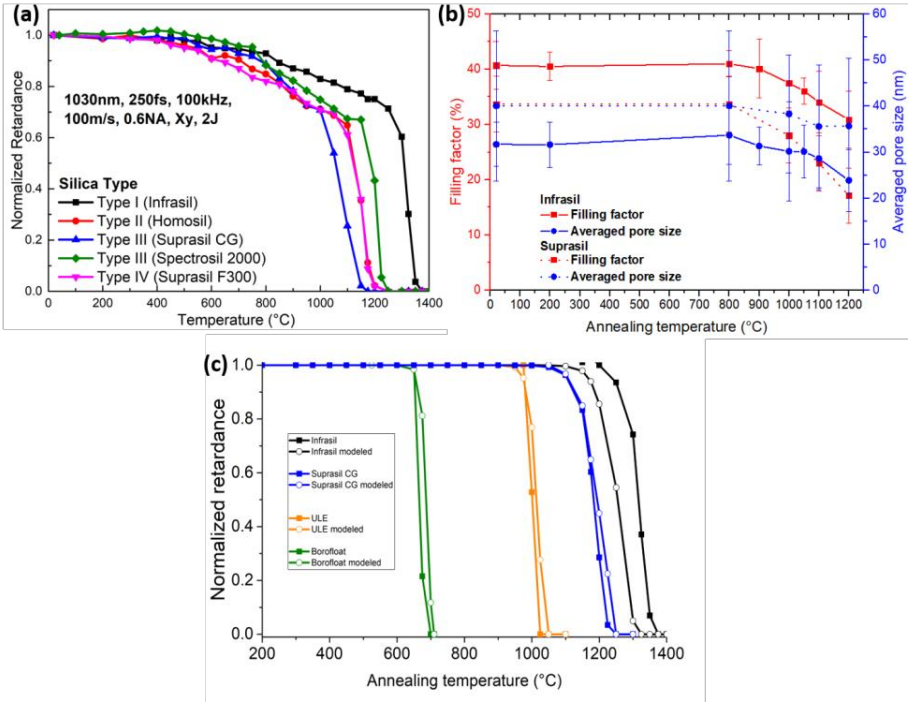

Figure 6-7. (a): Normalized retardance (R_{norm}) as a function of temperature for SiO_2 glasses: Type I (Infrasil 301), II (Homosil), III (Suprasil CG and Spectrosil 2000), and IV (Suprasil F300). The measurements were performed at room temperature. Laser parameters: 1030 nm, 250 fs, 2 μJ, 100 kHz, 100 μm/s, NA = 0.6, laser polarization ⊥ to writing direction; (b): Evolution of the 2D porosity filling factor and the average nanopores diameter as a function of annealing temperature for Infrasil and Suprasil; (c): Evolution of the normalized retardance during step isochronal annealing experiments for various glasses compared with the Rayleigh-Plesset (R-P) equation used to simulate the nanopores' erasure.

Five silica samples are chosen to reveal the impact of Cl and OH impurities on the thermal stability of Type II modifications. As described in the publication in chapter 3, they were fabricated by different processes, and categorized following the classification proposed by Brückner in 1970 [7]. By comparing their performances during the isochronal annealing, we can effectively reveal some typical characteristics. First, by keeping constant the OH impurity levels, we compare Type I (Infrasil 301) and Type IV (Suprasil F300) or compare Type III (Suprasil CG) and Type III (Spectrosil 2000). It is revealed that silica glasses produced with a lower Cl content all display higher thermal stability than the ones made from synthetics precursor. This suggests that a high Cl content would be one aspect to deteriorate the thermal stability of IR-fs-Type II modifications. On the other hand, if Cl content is kept at a similar level, dry glasses (e.g., Type I Infrasil 301) display greater thermal stability than wet glasses (e.g., Type III Spectrosil 2000). Finally, we can conclude that Type I silica (Infrasil) with lower levels of Cl and OH exhibit the best thermal stability.

In the paper inserted in section 6.2, we chose the case of SuprasilCG silica and have presented the effect of the writing speed, pulse energy, and annealing temperature on the 2D porosity filling factor and the average nanopores diameter in the IR-fs-Type II regime. To prove the generality of these results, different experimental conditions are selected to repeat similar tests. *Figure 6-7 (b)* adds the result of Infrasil301 with the same experimental conditions. The results illustrate that in the case of Infrasil, both the filling factor and the average nanopores diameter follows similar trends as the Suprasil. More specifically they remain stable until 800 °C, then decrease with the increasing annealing temperature. Of interest for applications, we can see that Infrasil has a higher filling factor but a lower nanopores size, which should result in high birefringence and lower scattering losses compared to SuprasilCG. There is an additional key point that should be noticed here: the measured average nanopore diameter is larger for Suprasil, but is less stable than Infrasil, as showed in *Figure 6-7 (a)*. So we suppose here that the main reason is related to the much higher viscosity of Infrasil. For going one step ahead, the nanopores erasure process of various glasses with different viscosity were thus simulated by Rayleigh-Plesset equation and exhibited in *Figure 6-7 (c)*. The viscosities $\eta(T)$ of each sample are applied in the simulation and all the other experimental parameters are kept constant. As we observed in the figure, the Infrasil glass showed a better thermal stability than the others, which is indicative that viscosity is a first order property in the erasure mechanism of nanogratings and their

associated form birefringence in a high temperature regime.

6.3.2 GeO_2-SiO_2 silicate glasses with ultralow OH content

Figure 6-8 displays the normalized retardance R_{norm}(t,T) of germanosilicate glasses as a function of annealing temperature T and shows some characteristic features. As the annealing temperature increases, the induced stress relaxes gradually and slowly decreasing the retardance. Finally, above 1100 °C, retardance diminishes dramatically, and no birefringence can be found after ~ 1200°C annealing. From the inset in *Figure 6-8*, it should be also noted that the "erasing slope" is inversely dependent on the GeO_2 concentration and increases from 1150 °C to 1200 °C as GeO_2 decreases from 16.9 mole% to 1.9 mole%.

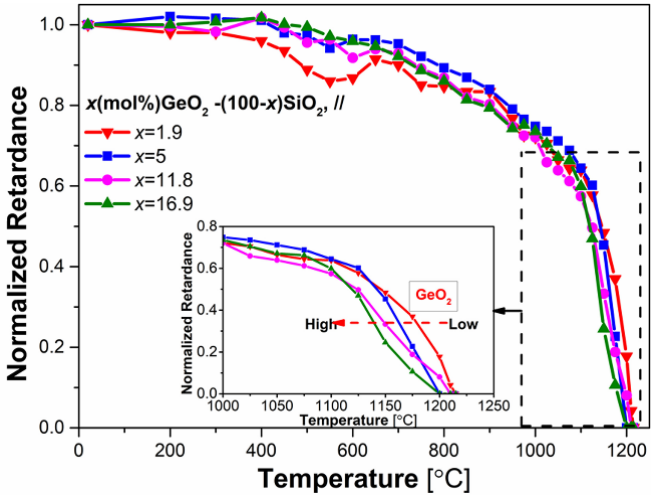

Figure 6-8. Normalized retardance, R_{norm}(t,T), as a function of temperature for *x* GeO_2-(1-*x*) SiO_2 glasses (*x* = 1.9 to 16.9 mole%). Pulse energy is 2 µJ/pulse. Laser parameters are: 1030 nm, 250 fs, 100 kHz, 100 µm/s, NA = 0.6, polarization // to writing direction.

It is also generally accepted that glass viscosity is reduced by OH concentration, which further reduces the glass annealing temperature (T_a). Therefore, due to the very fact that samples were fabricated with PCVD (thus ultralow OH content i.e., <10 ppb) and the fact that germanosilicate glasses are composed of an interpenetrated and interconnected structure of SiO_4 and GeO_4 tetrahedral units, viscosity is expected to change slowly as the concentration of GeO_2 varies from 1.9 mole% to 16.9 mole%. This is confirmed by viscosity measurements made using the Couette technique in all these samples shown in *Figure 6-9 (a).* This can explain why incorporating GeO_2 has less impact on overall thermal behavior in comparison with pure silica glasses (especially, Type II and IV silica) presented above in *Figure 6-9 (a).*

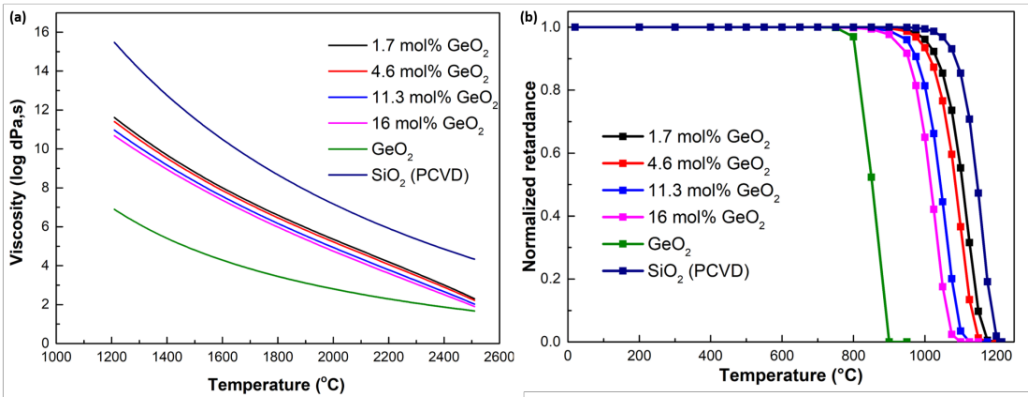

Figure 6-9. (a): Viscosities of GeO_2-SiO_2 with different GeO_2 amount as a function of temperature. The results of GeO_2 and PCVD (SiO_2) are also inserted for sake of comparison. Data above 1800°C have been extrapolated (b): Rayleigh-Plesset (R-P) equation used to simulate the nanopores' erasure for the glass with various concentration of GeO_2.

Observing the *Figure 6-9 (b),* excepted the pure GeO_2, all the other glass compositions showed a similar behavior Rayleigh-Plesset simulation. The PCVD (SiO_2) is found to be a little bit more stable than the GeO_2-doped glasses due to its higher viscosity as we can observe in *Figure 6-9 (a).* On the other hand, as the concentration of GeO_2 increases, the viscosity of the glass decreases, and the thermal stability decreases as well. Finally, the pure GeO_2 having the lowest viscosity also exhibits the lowest thermal performances both from the Rayleigh-Plesset simulation but also from experimental point of view [106].

As we mentioned before, another factor that can impact the thermal stability of IR-fs-Type II modifications is the porosity filling factor and average pore size of the nanoporous region. Here we have investigated this point of view within GeO_2 doped optical fibers namely SMF28, and with respect to SiO_2.

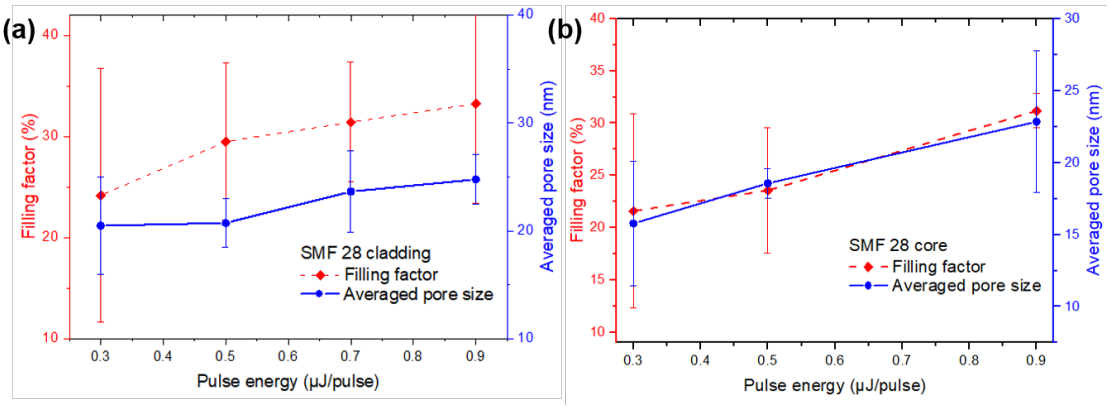

Figure 6-10. Evolution of the 2D porosity filling factor and the average nanopores diameter as a function of pulse energy for (a): SMF 28 fiber cladding area (i.e., pure silica); (b): SMF 28 fiber core area.

As can be seen from experimental results in *Figure 6-10*, two pairs of curves are

separated in the figure. The evolution in pulse energy corresponds to the increase in both the pore size and the filling factor. Improved thermal stability can be observed as pulse energy (see paper: *Erasure of nanopores in silicate glasses induced by femtosecond laser irradiation in the Type II regime*) and can be tentatively attributed to the pore size increase to the first order. This work agrees with the previous simulation work carried out in glasses produced by mature fabrication technologies [107]. What this means is that similar to other glasses, the larger pore size induced by the higher laser pulse energy in the nanolayers likely play an extremely important role in the erasure of nanogratings and their associated birefringence in a high temperature regime for 3D printed silica glass.

In addition, based on our publication (*Wang, Y.; Wei, S.; Cavillon, M.; Sapaly, B.; Poumellec, B.; Peng, G.-D.; Canning, J.; Lancry, M. Thermal Stability of Type II Modifications Inscribed by Femtosecond Laser in a Fiber Drawn from a 3D Printed Preform. Appl. Sci. 2021, 11, 600.)*, we observe similar behaviors (writing and erasure kinetics in SMF-28 and the 3D silica printed fiber with respect to varying laser pulse energies. The retardance values for the two types of fibers could not be reliably measured beyond the annealing temperature T = 1100 °C. Various factors need consideration, however, including the higher GeO_2 content in 3D printed fiber, though its impact in femtosecond laser processing is said to be insignificant [108]. So we infer that mechanisms of Type II modifications erasure for both types of fiber are similar, and less affected by the different fabrication techniques. We thus expect the thermal stability of Type II modifications (and likely FBGs) in the next generation of 3D printed fibers could be similarly enhanced by optimizing the laser writing parameters (speed, energy). This would imply that 3D-printed derived FBGs can also be used in high temperature environments.

6.3.3 Al_2O_3-SiO_2 glasses (bulk and optical fibers)

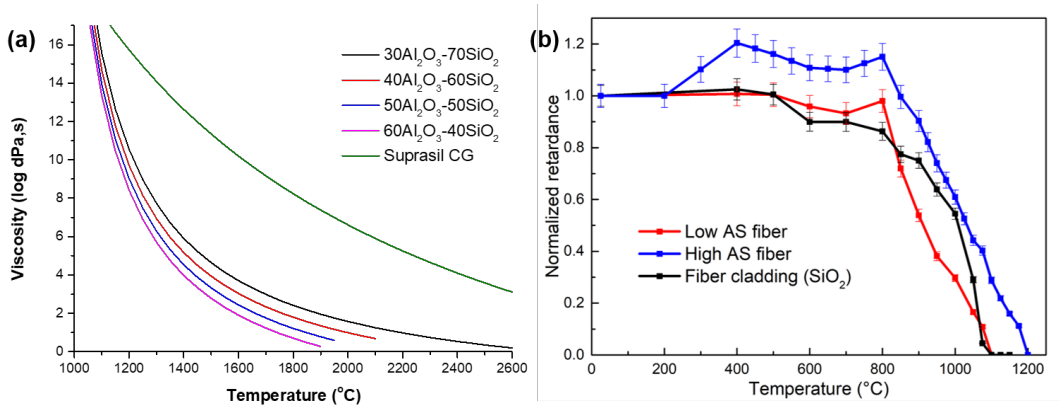

Figure 6-11. (a): Viscosities of Al_2O_3-SiO_2 with different concentration of Al_2O_3 as a function of temperature. These data were modeled using SciGlass. Suprasil CG is also inserted for sake of comparison.

(b): The heat treatment performance for both AS fibers and fiber cladding (pure SiO_2).

in this section, we summarize the findings about Al_2O_3-SiO_2 glasses in both bulk glass (fabricated by aerodynamic levitation) and optical fiber (fabricated by molten core method) samples. As discussed before, the glass viscosity (and its temperature dependence!) is one of the key factors that impact the thermal stability of IR-fs-Type II modifications: a higher viscosity can lead to a better thermal stability or more correctly a higher full erasure temperature. According to *Figure 6-11 (a),* as the concentration of Al_2O_3 increases, the viscosity of the aluminosilicate glass decreases. However, we have observed a contrasting situation from the results shown in *Figure 6-11 (b)* i.e., the High AS fiber (~52% Al_2O_3) performed better than the Low AS fiber (~42% Al_2O_3) and even than fiber SiO_2 cladding (SiO_2). We propose an interpretation based on oriented phase i.e., nanogratings in aluminosilicate samples are made of Al_2O_3-rich phase that separates from the SiO_2-rich matrix phase. In particular, the high thermal stability of this laser-induced phase separation is likely related to immiscibility. This immiscibility can be ascribed to the difference in the coordination number between oxygen ions bonded to Si and those bonded to Al. Indeed, when one Al^{3+} ions replace Si^{4+} in a tetrahedral coordination site, one oxygen ion must ideally tri-bridge three tetrahedral to maintain the charge balance, leading to a densification of the glass network. This could lead to nanoscale separation between Si and Al-rich glassy phases. Thus, immiscibility increases the structural connectivity in the "residual" Si-rich matrix whereas the separation of Al-rich phase might favor the formation of Mullite nuclei. Thus, it cannot be excluded that nanolayers are partly nano-crystallized in the form of Mullite, which would need further investigations with SEM-TKD (Transmission Kikuchi Diffraction) or TEM.

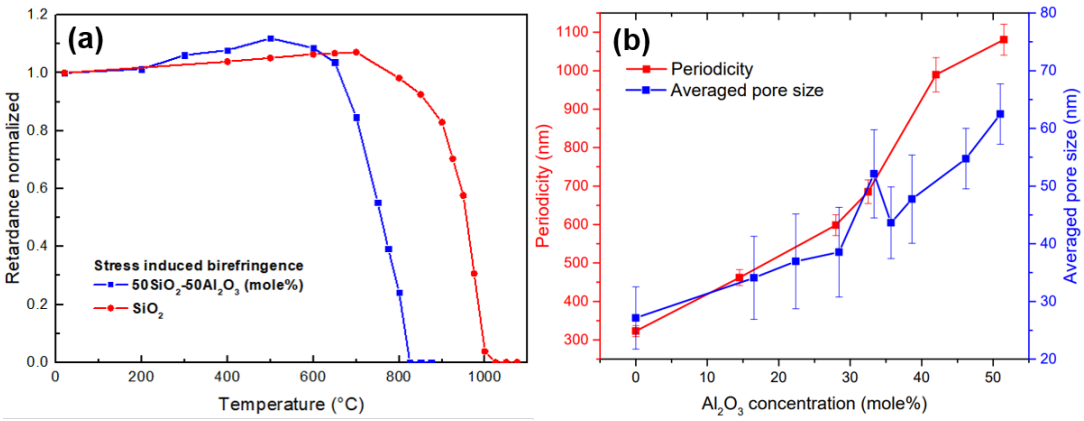

Figure 6-12. (a): The evolution of R_{norm}(t,T) related to the stress (measured between two irradiated area) as a function of isochronal annealing (30 minutes) temperature for both pure silica glass (Suprasil CG) and aluminosilicate binary glasses; (b): the evolution of nanoplans' periodicity and nanopores diameter as a function of Al_2O_3 concentration for AS fiber.

As we mentioned in Chapter 3, the regime of Type II modification induced by fs laser is

composed by the periodical nanolayers which are made of nanoporous structure, in the process of laser acting on sample, the SiO_2 is decomposed and many nanopores or nanocavities are created within these layers leading to a net glass volume expansion, therefore leads to a permanent strain $\varepsilon_p > 0$ in the irradiated area and thus an elastic response as well. In agreement with the literature we also confirm there exists an abnormal increase of the retardance during the isochronal annealing in silica that we attributed to the relaxation of stress-induced birefringence owning two different origins. To further verify this hypothesis, we compare two samples: pure silica glass (Suprasil CG) and aluminosilicate binary glasses (50 mol% Al_2O_3 doped) since both of them have shown an abnormal increase during the annealing in Chapter 3. *Figure 6-12 (a)* shows the evolution of their normalized retardance due to the stress-induced birefringence as a function of annealing temperature. As we can observe, both curves exhibit a similar trend that slightly increase from the beginning of the annealing and suddenly start to dramatically diminish to zero at high temperature (around 600 –800 °C).

Thus, we confirm that the stress-induced birefringence (LB_{stress}) is composed by a positive contribution, which arises from tensile stress and correlated to the densification, as well as a negative contribution, which plays a key role, and this time associated to a compressive stress due to net volume expansion of the nanolayers. The thermal relaxation of the densification happens during the annealing (normally within the 600-900 °C range) and leads to a higher net volume expansion, which effectively increases the compressive stress, thus the measured LB_{stress}. Then at higher temperature, the compressive stress is expected to relax plastically but before the complete erasure of nanopores themselves. This happens when approaching a temperature around $0.8 \times T_a$ for a few hours or $0.9 \times T_a$ for a few tens of minutes (T_a is the glass annealing temperature defined as the temperature for which the viscosity value is $\eta = 10^{13}$ Poise). This also explains why the LB_{stress} for aluminosilicate binary glasses with T_a = 830 °C is erased at a lower temperature than the Suprasil CG with T_a= 1100 °C.

Figure 6-12 (b) displays a selection of aluminosilicate optical fibers we studied in chapter 4. From the cladding to the core, the alumina concentration is increased, which promote higher averaged pore diameter (observed by SEM in the case of parallel configuration) and the nanolayers periodicity (measured for a perpendicular configuration) with respect to the silica cladding. As we presented in the paper dedicated to the Rayleigh-Plesset simulation, larger nanopores need more time (for a fixed T) or a higher temperature (for a fixed duration) to be fully erased. These results in *Figure 6-12 (b)* can explain why IR-fs-Type II nanostructures written in high aluminosilicate fibers exhibited a better thermal stability whereas these glasses do not own a higher T_a.

6.3.4 Multi-components glasses (bulk or fibers)

In order to finally achieve the objective of manufacturing laser written devices (for example FBG) with high thermal stability in optical fibers, we have to understand the dependence of IR-fs-Type II thermal stability with the glass composition to a large extent. However, it is not convenient to perform directly experiments on the fibers themselves because of their (usually) small core sizes along with the variety (but also the limitations in terms of doping and doping level) related to their fabrication processes. Therefore, it is more convenient to investigate the thermal performances of laser written modifications in bulks. Here we chose to review shortly main oxides usually used to manufacture optical fibers, such as germanium oxide (GeO_2), fluorine (F), aluminum oxide (Al_2O_3), boron oxide (B_2O_3), and titanium dioxide (TiO_2) incorporated into silica.

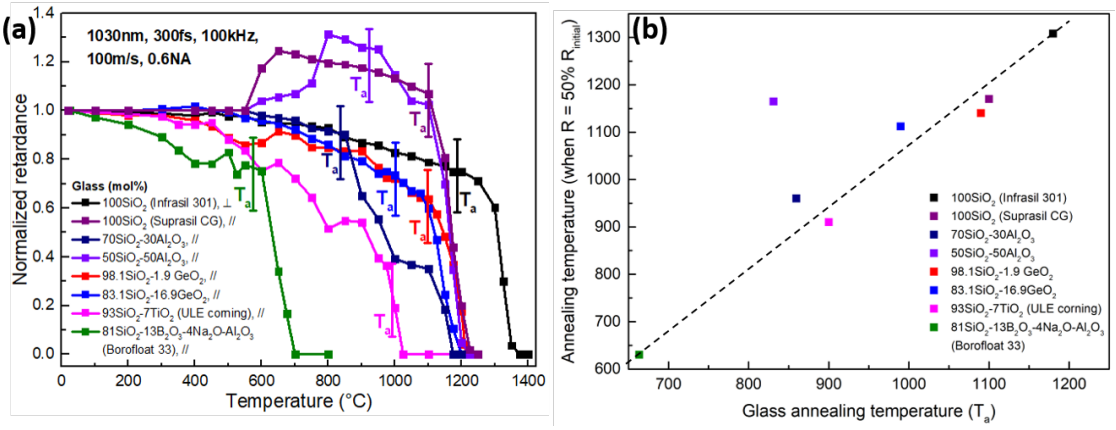

Figure 6-13. (a): Normalized retardance, $R_{norm}(t,T)$, as a function of annealing temperature T for SiO_2 (Infrasil 301 and Suprasil CG), $70SiO_2$-$30Al_2O_3$, $50SiO_2$-$50Al_2O_3$, $1.9GeO_2$-$98.1SiO_2$, $16.9GeO_2$-$83.1SiO_2$, $93SiO_2$-$7TiO_2$ (ULE®), and $81SiO_2$-$13B_2O_3$-$4Na_2O/K_2O$-$2Al_2O_3$ (Borofloat33®); (b): The annealing temperature (when R=50% $R_{initial}$) as a function of glass annealing temperature (T_a) for different compositions of glass.

Figure 6-13 (a) exhibits the evolution of the $R_{norm}(t,T)$ value as a function of annealing temperature for different bulk glasses. Only two samples exhibit a non-monotonous evolution namely Suprasil CG and $50\%Al_2O_3$-$50\%SiO_2$. We can observe the "abnormal increase" within 600-1000°C range because of the co-existence of Type I modifications (mostly densification and associated tensile stress) within nanogratings. All the other samples decrease smoothly with the annealing temperature.

- The retardance of the Borofloat33 (Schott) first disappears around 700 °C whereas the ULE (Corning), a TiO_2 doped SiO_2 follows a similar trend is fully erased around 1000 °C.
- Next, GeO_2-SiO_2 and $30Al_2O_3$-$70SiO_2$ samples exhibit quite similar trends i.e., all their

R_{norm} values become zero between 1075 °C – 1125 °C.

- We can also note that Suprasil CG and $50Al_2O_3$-$50SiO_2$ samples show slightly better thermal stability especially in the intermediate temperature range.
- Finally, the retardance of Infrasil 301 persists until 1400 °C.

Figure 6-13 (b) tentatively highlights the relationship between the glass annealing temperature T_a (thus the glass viscosity) and thermal stability. Here we choose the isochronal annealing temperature at which the retardance decays to 50% of its initial value. These results highlight a direct correlation, where the highest T_a values generally correspond to higher thermal stability. The one exception that deviates from the observed linear relationship is for the $50Al_2O_3$-$50SiO_2$ samples. This could be related to the phase separation or even the formation of Mullite nanocrystals as briefly discussed above.

About optical fibers

Finally, in order to identify and develop new fibers suitable as host for IR-fs laser written devices (like FBGs, Fabry-Pérot or Rayleigh amplified based sensors) for high temperature operation, we investigate a set of optical fiber candidates. In this view, we select a few different optical fibers made by various techniques namely conventional fibers like SMF28 (made by OVD), Ge-doped fibers made by 3D printing or aluminosilicate fibers made by the molten core method. We have inscribed all of them by Femtosecond laser irradiation (λ = 1030 nm, 250 fs) with the same laser writing process following geometry similar to line-by-line or point per point FBG but with a larger pitch (typ. 20 microns). For more information, please have a look to *Table 2-2* that summarizes the composition for all these fibers.

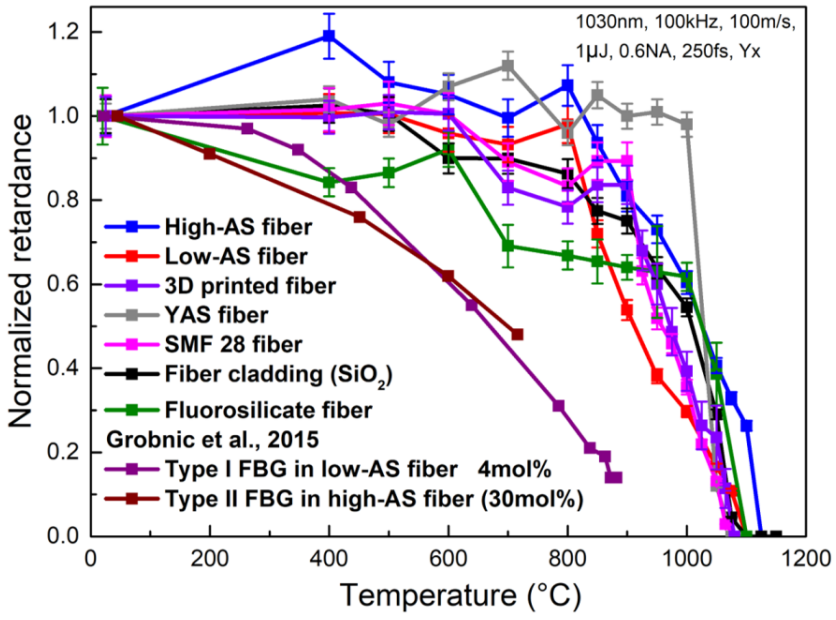

Figure 6-14. Normalized retardance $R_{norm}(t,T)$ as a function of temperature for aluminosilicate fibers High-AS (blue), Low-AS (red), SiO_2 cladding (black), 3D printed fiber (violet), yttrium aluminosilicate fiber YAS (grey), SMF-28 fiber (magenta) and Fluorosilicate fiber (green). Experimental conditions are: 1030 nm, 1 µJ/pulse, 100 kHz, 100 µm/s, 10^3 pulses/µm, NA=0.6, polarization ⊥ to writing direction (Yx). Data about Type I FBG in low content aluminosilicate fiber (4 mol%) and Type II FBG in high content aluminosilicate fiber (30 mol%) are extracted from [109] and inserted for comparison.

Figure 6-14 shows a comparison of the "thermal performance" of IR-fs Type II modifications written in each fiber during step isochronal annealing (Δt=30min). As a common trend, in most optical fibers Type II modifications exhibit similar thermal stability. First their $R_{norm}(\Delta t,T)$ value keeps stable until 600 °C and then a complex process with non-monotonous evolution happen between 600 °C - 900 °C. In a general scheme, this evolution is usually attributed to the co-existence of Type I modifications (densification and related tensile stress) in and around the nanogratings. Finally, the retardance starts to crush down to zero around 900-1100 °C.

The Fluorosilicate fiber presents something different, the decay starts from the beginning of heat-treatment, typically R_{norm} decreases smoothly until 400 °C corresponding to a 20% decay. Then, there is a slight increase in the R-value up to 500-600 °C compare with the initial value. Finally, there is a kind of double component decay: one around 700-800°C and the second one above 1000°C. In contrast, YAS fiber and High-AS fiber show more stable trends and own the highest thermal stability in terms of "area under the $R_{norm}(\Delta t,T)$ curve" and "full erasure temperature" respectively.

Conclusion

In this section, we have summarized some key experimental results obtained in this dissertation work. Aiming to investigate the thermal stability of IR-fs Type II modifications (i.e. nanogratings formation), we studied the impact of various parameters / properties: silica glass types and impurity nature / levels, laser writing parameters, glass chemical composition (addition of GeO_2, Al_2O_3, B_2O_3, TiO_2 in silica), and also a set of optical fibers. The investigated samples showed quite different trends (depending on laser writing parameters, writing geometry etc.) during the thermal annealing. The fundamental reason is that the birefringence measured in the nanogratings regime is composed of multiple factors, including the form birefringence, stress-induced birefringence, point defects, and densification. Since these contributions are essentially different from each sample, they may also exhibit some quite different thermal behaviors, which makes difficult to extract some general conclusions. However, we identify the porosity filling factor, averaged nanopores size and viscosity to be "key players" in the determination of the thermal stability of nanogratings. Using the Rayleigh-Plesset equation to simulate the evolution of pore size under the viscoelastic regime, we finally confirmed that they are responsible for the

measured form birefringence and they mostly dictate the ultimate thermal stability of nanogratings (i.e., the last birefringent contribution to survive at the highest temperatures).

This section provided a comprehensive view of the different mechanisms involved during thermal annealing of Type II modification. The discussion in this section can account for a wide range of results found both in this PhD thesis but also in the literature. In the next section, we build up on this work and conduct accelerated ageing experiments in order to develop a reliable lifetime model based on the VAREPA formalism and the Master Curve approach. Then we will exploit it to predict the lifetime of IR-fs Type II modifications at different temperatures.

6.4 Towards a computation of the lifetime prediction for IR-fs Type II modifications

Lifetime Prediction of Nanogratings Inscribed by Femtosecond Laser in Silica Glass

YITAO WANG[1], MATTHIEU LANCRY[1*], MAXIME CAVILLON[1], AND BERTRAND POUMELLEC[1]

[1] *Institut de Chimie Moléculaire et des Matériaux d'Orsay (ICMMO), Université Paris-Saclay, CNRS, Orsay 91405, France*
**Corresponding author: matthieu.lancry@universite.fr*

Received XX Month XXXX; revised XX Month, XXXX; accepted XX Month XXXX; posted XX Month XXXX (Doc. ID XXXXX); published XX Month XXXX

Abstract: This paper is dedicated to the lifetime prediction of IR-fs Type II modifications (i.e; nanogratings) written in silica glass. Here we report the thorough study of accelerated ageing of these nanogratings and their related linear birefringence. Based on the master curve formalism, we demonstrate that the laser induced structure can survive for 200 hours at 1100 °C. Under the reported processing conditions and after a dedicated passivation treatment, the estimated lifetime of the birefringent optical elements is beyond 10 years at 800 °C with a minor erasure of 7%.

The © 2021 Optical Society of America

http://dx.doi.org/10.1364/OL.99.099999

Introduction

Laser-induced self-organized nanogratings in silica glass were first discovered in 2003 [1]. They are composed of a quasi-periodic array of nanoporous silica layers, with elongated pore sizes of few tens of nm in diameter [2]. They have found numerous applications based on 2D or 3D space variant birefringence, as well as high temperature applications with Fiber Bragg Gratings (FBG) [3] for Structural Health Monitoring (SHM), or again 5D "eternal" optical data storage [4-6] with a potentially high densities reaching up to several petabits/mm^3. Most of these applications require long lifetime device and/or the possibility of forecasting potential spontaneous degradation of the photo-induced property change (e.g., birefringence). For example, securely storing large amounts of information over even relatively short time scales of 100 years, comparable to the human memory span, is a challenging problem. Therefore, accelerated aging measurements are mandatory to evaluate the stability of nanogratings in the working conditions (time/temperature couple). This has been previously investigated by Kazansky group in 2014 [7]. In these studies, the Authors concluded that nanogratings present a virtually unlimited lifetime (≈3×10^{20} years!) at room temperature (20 °C). The Authors approach this lifetime prediction problem by extrapolating from an Arrhenius law with a single activation energy (E_a) after pre-annealing at a temperature during a time t that erased the stress in silica. Although this approach is satisfying as a first approximation, it should be pointed out that glass is a disordered material that contains a distribution of activation energies, as opposed to a crystalline structure. This material specificity must be considered to strengthen lifetime prediction reliability. Considering that an E_a distribution was successfully done in the past but on UV-laser irradiated FBG [8], we propose here to apply this developed formalism in the lifetime prediction study of fs-laser induced nanograting modification.

Theoretical approach

Poumellec established in 1998 the VAREPA framework (Variable Reaction Pathways framework), which proposes a general approach to rationalize thermal stability of any optical property [9]. Feeding this framework using accelerated ageing data, this approach can be applied to predict the lifetime of nanogratings provided that several assumptions can be validated.

First group of assumptions:

- One limiting process. A<-B for which the measured quantity (here the optical retardance) is proportional to B. A and B are related to structural configurations of the glass linked by a reaction pathway.
- The process is Arrhenius type i.e. thermally activated with activation energy E_a that is the energy barrier between B and A. The reaction constant is $k(E_a)=k_0\exp(-E_a/k_BT)$.
- E_a is distributed following a function $g(E_a)$ which is not T or t dependent arising from the glass disorder.

Second group of assumptions (on the process type): the process is a first order kinetics like most reactions in solids. For any given T and t couple, a demarcation energy E_d (a Vand cutting energy [10]. E_d can be defined that is the boundary between achieved and non-achieved reactions. It has the expression $Ed=k_BTln(k_0t)$.

The consequence of these assumptions is that the total B content becomes only dependent on E_d and this defines a master curve whatever T or t [11, 12]. In particular, with a proper choice of k_0, several isotherms or several isochrones can be gathered. We can also show that the first derivative of this master curve yields a good approximation of the distribution function $g(E_a)$. It is important to note that several reasons may lead to the

impossibility to find a master curve: g is T or t dependent or if there are several types of reaction with different k_0 and $g(E_a)$.

In the following we thus suppose that the measured optical retardance R(t,T) response (that is proportional to the nanogratings birefringence) during an annealing treatment is proportional to one or several species B included in the nanogratings. In this erasure reaction (e.g. nanopores erasure in the viscous fluid) E_a is distributed, as it is the case for viscosity(T) or stress relaxation mechanisms.

Experiment and results

Femtosecond laser writing: The laser irradiation is achieved using a femtosecond laser system (Satsuma, Amplitude Systemes Ltd.) operating at 1030 nm, with a repetition rate of 100 kHz and delivering pulses of 250 fs. The Gaussian laser beam is focused 200 µm below the front face of a 1 mm thick Infrasil 301® silica glass sample (OH < 8 ppm; Cl < 0.15 ppm), using a 0.6 NA aspheric lens. Moving the sample along the X-axis at a scanning speed of 10 mm/s, lines are photo-induced with pulse energy of 2 µJ. Following these conditions, nanogratings are formed inside this glass.

Accelerated ageing: Accelerated aging measurements are required to evaluate the stability of nanogratings at room temperature and to estimate the E_a distribution during the porous nanogratings "erasure". This decay rate was evaluated using isochronal annealing experiments in the 20 °C to 1400 °C temperature range. Three different annealing times Δt: 30 min, 3 h and 18 h were chosen. After each annealing step (T-t), the sample was rapidly cooled and the retardance subsequently recorded at room temperature. Thus, any temperature-induced reversible effects that may occur above room temperature did not spoil the measurements.

Characterization techniques: The laser modification regions were observed using a polarized optical microscope in transmission mode, and to measure the amplitude of the linear retardance (R) response using the de Senarmont technique. R is defined as R=B×L, with B being the birefringence, and L the thickness of the birefringent object being measured. Moreover, the retardance is normalized (R_{norm}) relative to its initial value (before heat treatment).

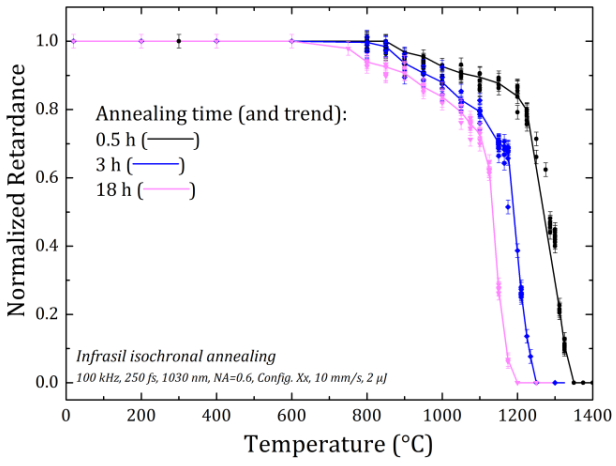

FIG. 1. Normalized retardance relative to the annealing temperature and for different annealing time conditions, Δt: 30 min (black), 3 h (blue) and 18 h (magenta). The trend curves are added for each annealing time as guides to the eye.

In order to tentatively determine a Master curve and k_0 value, annealing experiments with three different isochronal annealing times are used. Figure 1 shows the evolution of normalized retardance R_{norm} (t = 30 min; 3 h; 18 h, T) as a function of the annealing temperature. R_{norm}(t, T) with the different annealing time conditions follow a similar trend. From room temperature to about 800 °C, R_{norm} remains nearly constant. Then as the temperature continues to increase, R_{norm} correspondingly decreases smoothly up to 1100 °C - 1300 °C. The sample with Δt= 30 min annealing time exhibits the slowest decay rate. Finally, continuing to increase temperatures, R_{norm} rapidly reduced until it reaches zero at 1200 °C - 1350 °C, depending on the conditions.

Note that in our case, the curves in Figure 1 represent the "stability curve" provided that the criterion $(\delta t.k_0)^{-(\Delta T/T_{max})} \ll 1$ is fulfilled [13]. So, when this criterion is respected, each point can be considered independent of each other. If the criterion is not fulfilled this means that our measurements are slightly under-estimating the real thermal stability.

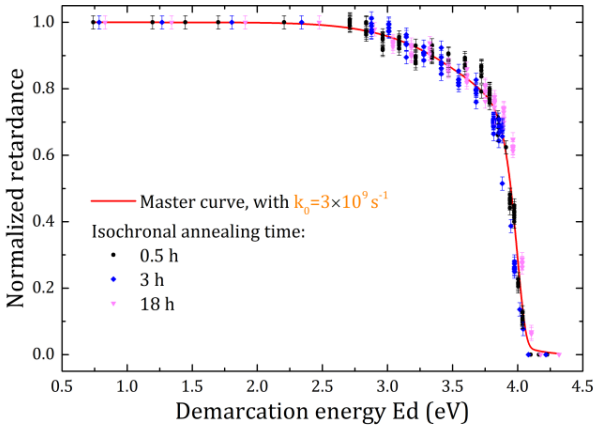

FIG. 2. Normalized retardance (R_{norm}) as a function of the demarcation energy $E_d = k_B.T.\ln(k_0t)$ (in eV), i.e., the master curve (red). k_0 is in s^{-1}. Inset: R_{norm} as a function of the demarcation energy $E_d = k_B.T.\ln(k_0t)$ (in eV), with k_0=1.

Now we will use E_d to tentatively derive the master curve $R(E_d)$. In Figure 2a we first consider the case where k_0 = 1. As visible from the figure, R_{norm} as a function of the intermediate variable $k_B.T.\ln(t)$ do not overlap. Now, in Figure 2b we searched for adjusting the value of k_0 (and its uncertainty) so that the R_{norm} curves as a function of the demarcation energy all merge into one single curve if possible, the so-called master curve. Here it is necessary to estimate the experimental uncertainties to derive confidence intervals for the estimates of the parameters. Least square optimization can be used to find the optimum value for k_0 and its confidence interval. This has been made in Figure 2 yielding $\ln(k_0$ in $s^{-1}) = 21.8 \pm 1.9$. It was thus possible to find a frequency factor (here $k_0 = 3\times10^9\ s^{-1}$., so that the earlier assumptions are reasonable.

For comparison in the literature, k_0 has been estimated to be around de 5×10^5 – $5\times10^7\ s^{-1}$ depending on the laser writing parameters in synthetic Type III silica (Viosil). The slightly different values of that we observe might be related to the use of Type I

silica (Infrasil) that exhibit a higher T_a (T_a is defined as the temperature at which the viscosity is 10^{13} dPa·s).

As observed in Figure 2b, the master curve shows two sections of declining trends with different slopes (emphasized in Figure 2). The first decay starts around 2.5 eV and slightly decreases around 20% - 25% of the R_{norm} value. The second decay starts from 3.75 eV and corresponds to a drastic decrease of R_{norm} down to zero. This double decay suggests that annealing is a bi-exponential decay process that is composed of at least two decay terms attributed to two additive contributions of the measured retardance. Therefore the following expression (1) can be used to fit the annealing decay rate: $R(E_d) = \alpha \times e^{-(a_1 \times E_d)^{b_1}} + (1-\alpha) \times e^{-(a_2 \times E_d)^{b_2}}$ **(1)** with α being the proportion of the contribution for the first decay. This fitting is a guide to the eye in Figure 3 but can also be employed as an engineering tool for prediction. Now the MC fit plot allows the user to predict the nanogratings lifetime, [14-16] providing that the anticipated conditions of use $E_d = f(t_{use}, T_{use})$ correspond to a point on the MC that has previously been sampled during the annealing experiment.

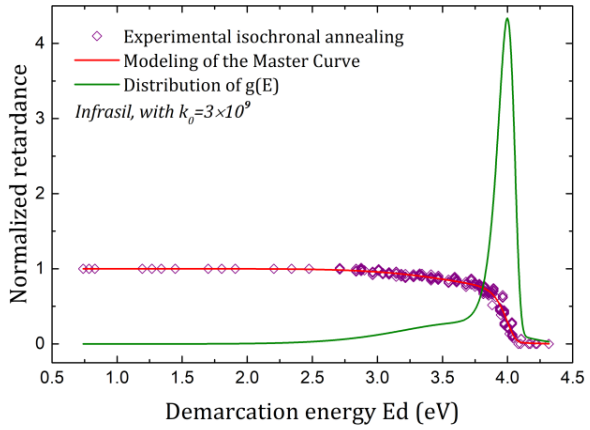

FIG. 3. Normalized retardance (R_{norm}) as a function of the demarcation energy $E_d = k_B.T.\ln(k_0 t)$ (in eV), i.e., the master curve (red). k_0 is in s^{-1}. The erasure reaction distribution g(E) is also inserted and calculated by deriving the master curve.

To further study the physicochemical reactions, which are responsible for the nanogratings birefringence, the erasure reaction distribution g(E) has been derived and is presented in Figure 3. There is no erasure reaction that can be found when the demarcation energy is lower than 2.5 eV. Then, a first "component" of the complex distribution occurs between 2.5 eV and 3.75 eV, and corresponds to the shoulder observed in the $R(E_d)$ curve. According to our recent research work [17], we linked the retardance (R) response, related to the birefringence, as an aggregate value of multiple contributions, including i) form birefringence (from porous nanolayers), ii) stress-induced birefringence due to permanent volume changes, iii) densification (whose contribution strongly depends on the writing conditions) and iv) a minor contribution of point defects.

Here, this process can be attributed to the plastic relaxation of the stress arising from volume expansion in the nanogratings, which arises in a temperature range of 800 °C – 1000 °C. Finally, the major part of the distribution g(E) is related to the main peak situated around 4 eV. This erasure requires high demarcation energies and is attributed to the erasure of nanopores within Type II regime [17]. In addition, we can notice that the main peak width is $2.6k_BT$ (0.18eV), which is close to a $2k_BT$ i.e. the signature of a single reaction pathway with single activation energy [18].

Lifetime mastering

Now complementary annealing experiments are needed to stabilize the nanogratings. The widespread method used for increasing the stability of a laser written component after its inscription consists in post-annealing for a time t_{anneal} at a temperature $T_{anneal} > T_{use}$. A coherent rationale of this method is formulated in [15]: the treatment wipes out the portion of the retardance (mostly defects and stress that occupies around 20% of the total retardance as we observed in Fig. 2) that would normally decay over the lifetime of the device and keeps only the stable portion of the retardance (mostly the nanopores). *Note this assumes that there is no other reaction pathway existing in the domain T,t out of the one investigated.*

From a practical point of view, the stabilization, also called passivation, is usually defined by a passivation ratio noted R0/R1 that is defined by the retardance R1 after a passivation time t_a at a given temperature T_a by the initial retardance R0. So if the end user imposes that after a given time t_{use} at a given temperature T_{use} (let us say 2 years at 800 °C for instance), the lifetime ratio Rf/R1 has to remain within a given range with ε < 2% for instance, we obtain the passivation ratio R0/R1 that should be 78%. From this we determine the passivation conditions to be t_a = 6 hours for a chosen temperature T_a = 1100 °C (equivalent to 5 years at 800 °C). After performing this passivation treatment experimentally, we found R_{norm} = 80.3%, which is very close from the predicted value.

In addition, predictions must be validated. From an industrial point of view, the principle is to compare the prediction established using the MC with accelerated ageing data typically during a few hundreds of hours at a temperature higher than the working temperature, i.e., to build some isotherms. Note that building a single isotherm cannot validate the prediction in a reliable manner but this is a first step and it allows the detection of potential failures in the lifetime prediction. Instead one could realize multiple isotherms or step isothermal annealing of passivated nanogratings and compared it to the MC.

In this view, the sample is annealed at 900 °C, 1000 °C, 1100 °C, for a total duration of 24 h at each temperature. Following this first step, the sample that was annealed at a temperature of 1100 °C was kept in the furnace until the nanogratings completely disappeared. It was only briefly and punctually taken out of the furnace to measure the retardance during the annealing program. Figure 4 presents the related decay of R_{norm} as a function of the E_d together with the MC itself. The experimental annealing results collapses on the master curve before the R_{norm} drops to 30%. This experiment validates the prediction methodology. Then for E_d>4eV, it should be pointed out that once the annealing temperature is close or above the glass annealing point (1180 °C for Infrasil), crystallization will appear on the glass substrate surface. In our case, the sample surface becomes blurry after few tens of hours at 1100 °C but the Type II modifications region was still clear for the measurement. Finally, for 264 hours at 1100 °C the sample was too much crystallized and no nanogratings could be observed.

Finally, we use the MC to predict the lifetime of these stabilized nanogratings in silica and for four temperature environments (800 °C, 900 °C, 1000 °C and 1100 °C). By computing a 10 years' lifetime prediction at these temperatures, Figure 4 inset exhibits the

evolution of R_{norm} as a function of annealing time. The results show that R_{norm} will stay stable for 10,000 hours and decrease only by 7% after 10 years of operation at 800 °C. For higher temperatures, Type II modifications can also survive without any damage for about 1000 hours, 100 hours and 10 hours at 900 °C, 1000 °C and 1100 °C respectively.

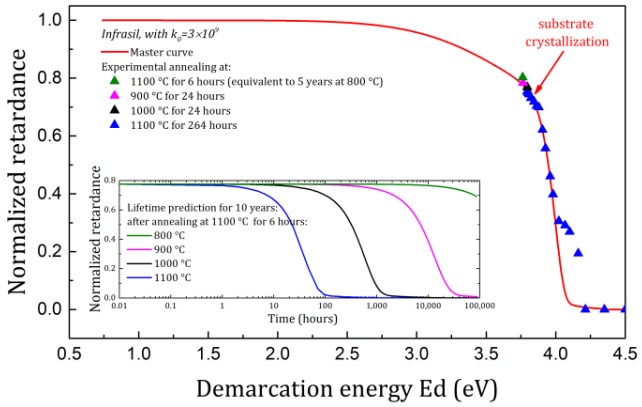

FIG. 4. R_{norm} as a function of the demarcation energy E_d, and the master curve is also inserted. Inset: 10 years' lifetime prediction for 800 °C (green), 900 °C (magenta), 1000 °C (black) and 1100 °C (blue) after the isothermal annealing at 1100 °C for 6 hours.

Conclusion

Based on the literature, VAREPA framework has been applied to of IR-fs type II modifications (so-called nanogratings) for prediction. The formalism is based on demarcation energy approximation and the existence of a master curve that we determined by accelerated ageing expriements. This master curve has been effectively obtained providing a clue that few assumptions are fulfilled: unicity of the reaction, thermally activated reaction, distribution of the activation energy and first order reaction.

However, in most cases, the lifetime is not large enough (e.g. to get a drift less devices), but due to the distributed nature of activation energies, it is possible to increase the nanogratings stability by erasing thermally the less stable part of the laser-induced birefrigence. Here we demonstrated that after a dedicated passivation treatment, the birefringence exhibits only a 7% erasure over 10 years at 800 °C. In addition, such annealing process allows controlling the retardance of printed elements and completely eliminating the stress-induced birefringence. This gives an additional degree of control and improves the readability of "eternal optical data storage" based on this laser direct wiring technique.

Funding. This research was funded by Agence Nationale pour la Recherche, FLAG/IR project, grant number ANR-18-CE08-0004-01 and CNRS Défi Instrumentation aux Limites, Ultrabragg project.

Disclosures. The authors declare no conflicts of interest

References

[1] Y. Shimotsuma, P. G. Kazansky, J. Qiu, and K. Hirao, "Self-organized nanogratings in glass irradiated by ultrashort light pulses," *Physical review letters,* vol. 91, no. 24, p. 247405, 2003.

[2] M. Lancry, B. Poumellec, A. Chahid-Erraji, M. Beresna, and P. Kazansky, "Dependence of the femtosecond laser refractive index change thresholds on the chemical composition of doped-silica glasses," *Optical Materials Express,* vol. 1, no. 4, pp. 711-723, 2011.

[3] G. C. Kahandawa, J. Epaarachchi, H. Wang, and K. Lau, "Use of FBG sensors for SHM in aerospace structures," *Photonic Sensors,* vol. 2, no. 3, pp. 203-214, 2012.

[4] M. Beresna, M. Gecevičius, and P. G. Kazansky, "Ultrafast laser direct writing and nanostructuring in transparent materials," *Advances in Optics Photonics,* vol. 6, no. 3, pp. 293-339, 2014.

[5] B. Zhang, X. Liu, and J. Qiu, "Single femtosecond laser beam induced nanogratings in transparent media-Mechanisms and applications," *Journal of Materiomics,* vol. 5, no. 1, pp. 1-14, 2019.

[6] Y. Shimotsuma *et al.*, "Ultrafast manipulation of self‐assembled form birefringence in glass," *Advanced materials,* vol. 22, no. 36, pp. 4039-4043, 2010.

[7] J. Zhang, M. Gecevičius, M. Beresna, and P. G. Kazansky, "Seemingly unlimited lifetime data storage in nanostructured glass," *Physical review letters,* vol. 112, no. 3, p. 033901, 2014.

[8] M. Lancry, B. Poumellec, S. Costes, and J. Magné, "Reliable lifetime prediction for passivated fiber bragg gratings for telecommunication applications," *Fibers,* vol. 2, no. 1, pp. 92-107, 2014.

[9] B. Poumellec and M. Lancry, "Kinetics of thermally activated physical processes in disordered media," *Fibers,* vol. 3, no. 3, pp. 206-252, 2015.

[10] V. Vand, "A theory of the irreversible electrical resistance changes of metallic films evaporated in vacuum," *Proceedings of the Physical Society,* vol. 55, no. 3, p. 222, 1943.

[11] J. P. van den Brink, "Master stress relaxation function of silica glasses," *Journal of Non-Crystalline Solids,* vol. 196, pp. 210-215, 1996.

[12] S. Kannan, P. Lemaire, J. Guo, and M. LuValle, "Reliability predictions on fiber gratings through alternate methods," *Proceedings of the Bragg Gratings Photosensitivity, Poling in Glass Fibers Waveguides: Applications Fundamentals, Williamsburg, VA, USA,* vol. 2628, 1997.

[13] S.-E. Wei *et al.*, "Thermal stability of type II modifications by IR femtosecond laser in silica-based glasses," *Sensors,* vol. 20, no. 3, p. 762, 2020.

[14] B. Poumellec, "Links between writing and erasure (or stability) of Bragg gratings in disordered media," *Journal of non-crystalline solids,* vol. 239, no. 1-3, pp. 108-115, 1998.

[15] T. Erdogan, V. Mizrahi, P. Lemaire, and D. Monroe, "Decay of ultraviolet‐induced fiber Bragg gratings," *Journal of applied physics,* vol. 76, no. 1, pp. 73-80, 1994.

[16] S. Kannan, J. Z. Guo, and P. J. Lemaire, "Thermal stability analysis of UV-induced fiber Bragg gratings," *Journal of lightwave technology,* vol. 15, no. 8, pp. 1478-1483, 1997.

[17] Y. Wang, M. Cavillon, N. Ollier, B. Poumellec, and M. Lancry, "An Overview of the Thermal Erasure Mechanisms of Femtosecond Laser‐Induced Nanogratings in Silica Glass," *physica status solidi,* p. 2100023, 2021.

[18] B. Poumellec, I. Riant, and C. Tessier-Lescourret, "Precise life-time prediction using demarcation energy approximation for distributed activation energy reaction," *Journal of Physics: Condensed Matter,* vol. 18, no. 7, p. 2199, 2006.

Conclusions

In this last chapter, we presented a roadmap for the development of high temperature devices, by providing a comprehensive study of the key parameters and effects that dictate the high temperature regime of IR-fs type II laser induced modifications in glass. Through analyzing and comparing our main experimental results; we clearly revealed that the laser parameters and the material chemical composition could effectively influence the thermal stability of IR-fs Type II modifications.

The different mechanisms of nanogratings formation explain the occurrence of polarization dependent linear optical properties is the presence of a strong linear birefringence, which owns multiple contributions: form birefringence due to self-organized nanogratings, stress-induced birefringence, densification, and point defects. Among them, the form birefringence caused by the formation of nanolayers (usually nanoporous in silica but that could be made of nanoscale phase separation as well) plays the key role in this study. We investigated and we tentatively rationalize its thermal stability through a simulation based on the Rayleigh–Plesset equation that matches with most experimental data. The Rayleigh–Plesset equation provides insights into the temperature range at which the nanopores would ultimately collapse, and eventually open the door to simulate the erasure process of the nanopores during any thermal annealing. Following this view, the origin of the better thermal stability of Type II modifications under different laser writing conditions (speed, energy, polarization) and different material compositions was tentatively interpreted. We proposed the former is led by the averaged nanopores diameter, while the viscosity temperature dependence of the materials is the main driver for the latter.

We use a framework to model erasure kinetics of thermally distributed activated processes that we can extended to IR-fs induced refractive index changes (or optical birefringence) both in bulks and fibers. This framework is based on a demarcation energy approximation and the existence of a Master Curve. From this modeling, it is possible to know the complete evolution in time of the system and thus the lifetime in operating conditions. It is also possible to determine the annealing conditions (also called passivation) for extending a lifetime of these laser-written optical modifications.

References

1. Lancry, M., et al., Ultrafast nanoporous silica formation driven by femtosecond laser irradiation. Laser Photonics Reviews, 2013. 7(6): p. 953-962.
2. Landau L.D. and Lifshitz E.M., Statistical physics. Pt. 1. Course of theoretical physics-Pergamon International Library of Science, Technology, Engineering and Social Studies, Oxford: Pergamon Press, and Reading: Addison-Wesley,| c1969, 2nd rev.-enlarg. ed. Vol. 1. 1969.
3. Lines M.E., Scattering losses in optic fiber materials. I. A new parametrization. Journal of applied physics, 1984. 55(11): p. 4052-4057.
4. Tool A.Q., Relation between inelastic deformability and thermal expansion of glass in its annealing range Journal of the American Ceramic Society, 1946. 29(9): p. 240-253.
5. Lancry M., Régnier E., and Poumellec B., Fictive temperature in silica-based glasses and its application to optical fiber manufacturing. Progress in Materials Science, 2011.
6. Gross T. M. and Tomozawa M., Fictive temperature of GeO2 glass: Its determination by IR method and its effects on density and refractive index. Journal of non-crystalline solids, 2007. 353(52–54): p. 4762-4766.
7. Bruckner R., Properties and structure of vitreous silica. I. Journal of non-crystalline solids, 1970. 5(2): p. 123-175.
8. Shelby J.E., Density of vitreous silica. Journal of non-crystalline solids, 2004. 349: p. 331-336.
9. YOSHIMOTO, M., et al., Effects of densification on mechanical properties of lead silicate glasses. Journal of the Ceramic Society of Japan, 1989. 97(1132): p. 1446-1450.
10. Toplis, M.J., et al., Viscosity, fragility, and configurational entropy of melts along the join SiO2-NaAlSiO4. American Mineralogist, 1997. 82(9-10): p. 979-990.
11. Guerette, M., et al., Structure and properties of silica glass densified in cold compression and hot compression. Scientific reports, 2015. 5(1): p. 1-10.
12. Lee, S.K., Effect of pressure on structure of oxide glasses at high pressure: Insights from solid-state NMR of quadrupolar nuclides. Solid state nuclear magnetic resonance, 2010. 38(2-3): p. 45-57.
13. Sonneville, C., et al., In situ Brillouin study of sodium alumino silicate glasses under pressure. The Journal of chemical physics, 2013. 139(7): p. 074501.
14. Xue, X. and J.F. Stebbins, 23 Na NMR chemical shifts and local Na coordination environments in silicate crystals, melts and glasses. Physics chemistry of minerals, 1993. 20(5): p. 297-307.
15. George, A. and J. Stebbins, Dynamics of Na in sodium aluminosilicate glasses and liquids. Physics Chemistry of Minerals, 1996. 23(8): p. 526-534.

16. Smedskjaer, M.M., et al., Irreversibility of pressure induced boron speciation change in glass. Scientific reports, 2014. 4(1): p. 1-6.
17. Salmon, P.S. and A. Zeidler, Networks under pressure: the development of in situ high-pressure neutron diffraction for glassy and liquid materials. Journal of Physics: Condensed Matter, 2015. 27(13): p. 133201.
18. Salmon, P.S., J.W. Drewitt, and A. Zeidler, Neutron diffraction as a probe of liquid and glass structures under extreme conditions. Neutron News, 2016. 27(3): p. 22-26.
19. Jin, W., et al., Structural transformation in densified silica glass: A molecular-dynamics study. Physical Review B, 1994. 50(1): p. 118.
20. Inamura, Y., et al., Intermediate range structure and low-energy dynamics of densified vitreous silica. Journal of non-crystalline solids, 2001. 293: p. 389-393.
21. Svenson, M.N., et al., Raman spectroscopy study of pressure-induced structural changes in sodium borate glass. Journal of Non-Crystalline Solids, 2016. 443: p. 130-135.
22. Mantisi, B., et al., Non-Debye normalization of the glass vibrational density of states in mildly densified silicate glasses. Journal of Physics: Condensed Matter, 2009. 22(2): p. 025402.
23. Mackenzie, J., High-pressure effects on oxide glasses: I, densification in rigid state. Journal of the American Ceramic Society, 1963. 46(10): p. 461-470.
24. Allwardt, J.R., B.C. Schmidt, and J.F. Stebbins, Structural mechanisms of compression and decompression in high-pressure K2Si4O9 glasses: an investigation utilizing Raman and NMR spectroscopy of glasses and crystalline materials. Chemical Geology, 2004. 213(1-3): p. 137-151.
25. Du, L.-S., et al., Pressure-induced structural changes in a borosilicate glass-forming liquid: boron coordination, non-bridging oxygens, and network ordering. Journal of Non-Crystalline Solids, 2004. 337(2): p. 196-200.
26. Lee, S.K., et al., Nature of polymerization and properties of silicate melts and glasses at high pressure. Geochimica et Cosmochimica Acta, 2004. 68(20): p. 4189-4200.
27. Chen, J., et al., Advances in high-pressure techniques for geophysical applications. 2005: Elsevier.
28. Bridgman, P. and I. Šimon, Effects of very high pressures on glass. Journal of applied physics, 1953. 24(4): p. 405-413.
29. Susman, S., et al., Structural changes in irreversibly densified fused silica: implications for the chemical resistance of high level nuclear waste glasses. Physics chemistry of glasses, 1990. 31(4): p. 144-150.
30. Cohen, H. and R. Roy, Effects of ultra high pressures on glass. Journal of the American Ceramic Society, 1961. 44(10): p. 523-524.
31. Meade, C., R.J. Hemley, and H. Mao, High-pressure X-ray diffraction of SiO 2 glass. Physical Review Letters, 1992. 69(9): p. 1387.

32. Sugiura, H., et al., Densified silica glass after shock compression. Journal of applied physics, 1997. 81(4): p. 1651-1655.
33. Deschamps, T., et al., Permanent densification of compressed silica glass: a Raman-density calibration curve. Journal of Physics: Condensed Matter, 2012. 25(2): p. 025402.
34. Jin, W., et al., Structural transformation, intermediate-range order, and dynamical behavior of sio 2 glass at high pressures. Physical review letters, 1993. 71(19): p. 3146.
35. Nomura, K.-i., et al., Defect migration and recombination in nanoindentation of silica glass. Applied Physics Letters, 2011. 99(11): p. 111906.
36. Sakka, S. and J. Mackenzie, High pressure effects on glass. J Journal of Non-Crystalline Solids, 1969. 1(2): p. 107-142.
37. Mackenzie, J., High-pressure effects on oxide glasses: II, Subsequent heat treatment. Journal of the American Ceramic Society, 1963. 46(10): p. 470-476.
38. Kapoor, S., L. Wondraczek, and M.M. Smedskjaer, Pressure-induced densification of oxide glasses at the glass transition. Frontiers in Materials, 2017. 4: p. 1.
39. Yamada, A., S. Gaudio, and C. Lesher. Densification of MgSiO3 glass with pressure and temperature. in Journal of Physics: Conference Series. 2010. IOP Publishing.
40. Østergaard, M.B., et al., Temperature-dependent densification of sodium borosilicate glass. RSC advances, 2015. 5(96): p. 78845-78851.
41. Mackenzie, J., High-pressure Effects on Oxide Glasses: III, Densification in Nonrigid State. Journal of the American Ceramic Society, 1964. 47(2): p. 76-80.
42. Uhlmann, D.R., Densification of alkali silicate glasses at high pressure. Journal of Non-Crystalline Solids, 1973. 13(1): p. 89-99.
43. Smedskjaer, M.M., et al., Mixed alkaline earth effect in the compressibility of aluminosilicate glasses. The Journal of chemical physics, 2014. 140(5): p. 054511.
44. Martinet, C., et al., Permanently densified SiO2 glasses: a structural approach. Journal of Physics: Condensed Matter, 2015. 27(32): p. 325401.
45. Polian, A. and M. Grimsditch, Room-temperature densification of a-SiO 2 versus pressure. Physical Review B, 1990. 41(9): p. 6086.
46. Seward III T.P., et al., Densification of synthetic fused silica under ultraviolet irradiation. Journal of non-crystalline solids, 1997. 222: p. 407-414.
47. Primak W. and Kampwirth R., The radiation compaction of vitreous silica. Journal of Applied Physics, 1968. 39(12): p. 5651-5658.
48. Kubota A., et al., Densification of fused silica due to shock waves and its implications for 351 nm laser induced damage. Opt. Express, 2001. 8(11): p. 611.
49. Spaargaren S.M.R. and Syms Richard R.A., Characterization of Defects in Waveguides Formed by Electron Irradiation of Silica-on-Silicon. Journal of lightwave technology, 2000. 18(4): p. 555.

50. Barbier D., Green M., and Madden S.J., Waveguide fabrication for integrated optics by electron beam irradiation of silica. Lightwave Technology, Journal of, 1991. 9(6): p. 715-720.
51. Syms R.R.A., Tate T.J., and Bellerby R., Low-loss near-infrared passive optical waveguide components formed by electron beam irradiation of silica-on-silicon. Lightwave Technology, Journal of, 1995. 13(8): p. 1745-1749.
52. Imai H., et al., Significant densification of sol-gel derived amorphous silica films by vacuum ultraviolet irradiation. Journal of applied physics, 1996. 79(11): p. 8304-8309.
53. Garcia Blanco S., et al., Electron-beam-induced densification of Ge-doped flame hydrolysis silica for waveguide fabrication. Applied Physics Letters, 2001. 79(18): p. 2889-2891.
54. Borrelli N.F., et al., Densification of fused silica under 193-nm excitation. JOSA B, 1997. 14(7): p. 1606-1615.
55. Poumellec B., et al., UV induced densification during Bragg grating inscription in Ge: SiO2 preforms. Optical Materials, 1995. 4(4): p. 441-449.
56. Sharma, S.K., J.F. Mammone, and M. Nicol, Raman investigation of ring configurations in vitreous silica. Nature, 1981. 292(5819): p. 140-141.
57. Galeener, F., Planar rings in glasses. Solid State Communications, 1982. 44(7): p. 1037-1040.
58. Galeener, F.L., Planar rings in vitreous silica. Journal of Non-Crystalline Solids, 1982. 49(1-3): p. 53-62.
59. Deschamps T., et al., Permanent densification of compressed silica glass: a Raman-density calibration curve. Journal of Physics: Condensed Matter, 2013. 25(2): p. 25402-25405.
60. Sugiura H. and Yamadaya T., Raman scattering in silica glass in the permanent densification region. Journal of Non-Crystalline Solids, 1992. 144(0): p. 151-158.
61. Vandembroucq D., et al., Density hardening plasticity and mechanical ageing of silica glass under pressure: A Raman spectroscopic study. Journal of Physics: Condensed Matter, 2008. 20(48): p. 485221.
62. Devine, R., Macroscopic and microscopic effects of radiation in amorphous SiO2. Nuclear Instruments Methods in Physics Research Section B: Beam Interactions with Materials Atoms
1994. 91(1-4): p. 378-390.
63. Ollier, N., et al., Relaxation study of pre-densified silica glasses under 2.5 MeV electron irradiation. Scientific reports, 2019. 9(1): p. 1-8.
64. Reghioua, I., et al., Unique silica polymorph obtained under electron irradiation. Applied Physics Letters, 2019. 115(25): p. 251101.
65. Boizot, B., et al., Raman study of β-irradiated glasses. Journal of non-crystalline

solids, 1999. 243(2-3): p. 268-272.
66. Neuville, D.R., et al., Structure of β-irradiated glasses studied by X-ray absorption and Raman spectroscopies. Journal of non-crystalline solids, 2003. 323(1-3): p. 207-213.
67. Neuville, D.R. and B.O. Mysen, Role of aluminium in the silicate network: In situ, high-temperature study of glasses and melts on the join SiO2-NaAlO2. Geochimica et Cosmochimica Acta, 1996. 60(10): p. 1727-1737.
68. Neuville, D.R., et al., Al speciation and Ca environment in calcium aluminosilicate glasses and crystals by Al and Ca K-edge X-ray absorption spectroscopy. Chemical Geology, 2004. 213(1-3): p. 153-163.
69. Neuville, D.R., L. Cormier, and D. Massiot, Al coordination and speciation in calcium aluminosilicate glasses: Effects of composition determined by 27Al MQ-MAS NMR and Raman spectroscopy. Chemical geology, 2006. 229(1-3): p. 173-185.
70. Ollier, N., et al., Impact of glass density on the green emission and NBOHC formation in silica glass: A combined high pressure and 2.5 áMeV electron irradiation. Journal of Non-Crystalline Solids, 2017. 476: p. 81-86.
71. Gavenda, T., O. Gedeon, and K. Jurek, Irradiation induced densification and its correlation with three-membered rings in vitreous silica. Journal of Non-Crystalline Solids, 2015. 425: p. 61-66.
72. Lancry, M. and B. Poumellec, UV laser processing and multiphoton absorption processes in optical telecommunication fiber materials. Physics Reports, 2013. 523(4): p. 207-229.
73. Allan, D.C., et al., 193-nm excimer-laser-induced densification of fused silica. Optics letters, 1996. 21(24): p. 1960-1962.
74. Piao, F., W.G. Oldham, and E.E. Haller, Ultraviolet-induced densification of fused silica. Journal of Applied Physics, 2000. 87(7): p. 3287-3293.
75. Schermerhorn, P.M. Excimer laser damage testing of optical materials. in Excimer Lasers: Applications, Beam Delivery Systems, and Laser Design. 1993. International Society for Optics and Photonics.
76. Schenker, R., P. Schermerhorn, and W. Oldham, Deep-ultraviolet damage to fused silica. Journal of Vacuum Science Technology B: Microelectronics Nanometer Structures Processing, Measurement, Phenomena, 1994. 12(6): p. 3275-3279.
77. Schenker, R.E., F. Piao, and W.G. Oldham. Material limitations to 193-nm lithographic system lifetimes. in Optical Microlithography IX. 1996. International Society for Optics and Photonics.
78. Susman, S., et al., Intermediate-range order in permanently densified vitreous SiO 2: A neutron-diffraction and molecular-dynamics study. Physical Review B, 1991. 43(1): p. 1194.
79. Simon, I., Structure of neutron-irradiated quartz and vitreous silica. Journal of the

American Ceramic Society, 1957. 40(5): p. 150-153.
80. Primak, W., Fast-neutron-induced changes in quartz and vitreous silica. Physical Review B, 1958. 110(6): p. 1240.
81. Devine, R., Macroscopic and microscopic effects of radiation in amorphous SiO2. Nuclear Instruments Methods in Physics Research Section B: Beam Interactions with Materials Atoms, 1994. 91(1-4): p. 378-390.
82. Piao, F., W.G. Oldham, and E.E. Haller, The mechanism of radiation-induced compaction in vitreous silica. Journal of non-crystalline solids, 2000. 276(1-3): p. 61-71.
83. Buscarino, G., et al., Polyamorphic transformation induced by electron irradiation in a-SiO 2 glass. Physical Review B, 2009. 80(9): p. 094202.
84. Bellouard, Y., et al., Stress-state manipulation in fused silica via femtosecond laser irradiation. Optica, 2016. 3(12): p. 1285-1293.
85. Eaton, S.M., et al., Heat accumulation effects in femtosecond laser-written waveguides with variable repetition rate. Optics Express, 2005. 13(12): p. 4708-4716.
86. Zimmermann, F., Ultrashort pulse induced nanostructures in transparent materials. 2017.
87. Le Parc, R., et al., Influence of fictive temperature and composition of silica glass on anomalous elastic behaviour. Journal of Physics: Condensed Matter, 2006. 18(32): p. 7507.
88. Miura, K., et al., Photowritten optical waveguides in various glasses with ultrashort pulse laser. Applied Physics Letters, 1997. 71(23): p. 3329-3331.
89. Bellouard, Y., et al., Nanoindentation and birefringence measurements on fused silica specimen exposed to low-energy femtosecond pulses. Optics express, 2006. 14(18): p. 8360-8366.
90. Royon, A., Structuration non-linéaire de verres oxydes par laser femtoseconde dans le proche infrarouge. 2009, Bordeaux 1.
91. Krol, D., Femtosecond laser modification of glass. Journal of Non-Crystalline Solids, 2008. 354(2-9): p. 416-424.
92. Shcheblanov, N.S. and M.E. Povarnitsyn, Bond-breaking mechanism of vitreous silica densification by IR femtosecond laser pulses. EPL, 2016. 114(2): p. 26004.
93. Bricchi, E., B.G. Klappauf, and P.G. Kazansky, Form birefringence and negative index change created by femtosecond direct writing in transparent materials. Optics letters, 2004. 29(1): p. 119-121.
94. Vlugter, P., E. Block, and Y. Bellouard, Local tuning of fused silica thermal expansion coefficient using femtosecond laser. Physical Review Materials, 2019. 3(5): p. 053802.
95. Bricchi, E. and P.G. Kazansky, Extraordinary stability of anisotropic femtosecond direct-written structures embedded in silica glass. Applied physics letters, 2006.

88(11): p. 111119.
96. Bellouard, Y., et al., Scanning thermal microscopy and Raman analysis of bulk fused silica exposed to low-energy femtosecond laser pulses. Opt. Express., 2008. 16(24): p. 19520-19534.
97. Poumellec, B., et al., Modification thresholds in femtosecond laser processing of pure silica: review of dependencies on laser parameters. Optical Materials Express, 2011. 1(4): p. 766-782.
98. Mihailov, S.J., et al., Extreme environment sensing using femtosecond laser-inscribed fiber Bragg gratings. Sensors, 2017. 17(12): p. 2909.
99. Cornet, A., et al., Relaxation processes of densified silica glass. The Journal of Chemical Physics, 2017. 146(9): p. 094504.
100. Poumellec, B., Links between writing and erasure (or stability) of Bragg gratings in disordered media. Journal of non-crystalline solids, 1998. 239(1-3): p. 108-115.
101. Grobnic, D., C. Hnatovsky, and S.J. Mihailov, Low loss Type II regenerative Bragg gratings made with ultrafast radiation. Optics express, 2016. 24(25): p. 28704-28712.
102. Shibata, S. and M. Nakahara, Fluorine and chlorine effects on radiation-induced loss for GeO 2-doped silica optical fibers. Journal of lightwave technology, 1985. 3(4): p. 860-863.
103. Ainslie, B., P. France, and G. Newns, Water impurity in low-loss silica fibre. Materials Research Bulletin, 1977. 12(5): p. 481-487.
104. Niziev, V. and A. Nesterov, Influence of beam polarization on laser cutting efficiency. Journal of Physics D: Applied Physics, 1999. 32(13): p. 1455.
105. Kazansky, P.G., et al., Photosensitivity control of an isotropic medium through polarization of light pulses with tilted intensity front. Optics express, 2011. 19(21): p. 20657-20664.
106. Zimmermann, F., et al., Femtosecond laser written nanostructures in Ge-doped glasses. Optics letters, 2016. 41(6): p. 1161-1164.
107. Cavillon, M., et al., Erasure of nanopores in silicate glasses induced by femtosecond laser irradiation in the Type II regime. Applied Physics A, 2020. 126(11): p. 1-9.
108. Fedotov, S., et al., Direct writing of birefringent elements by ultrafast laser nanostructuring in multicomponent glass. Applied Physics Letters, 2016. 108(7): p. 071905.
109. Grobnic, D., et al., Type I and II Bragg gratings made with infrared femtosecond radiation in high and low alumina content aluminosilicate optical fibers. Optica, 2015. 2(4): p. 313-322.

Conclusion and perspectives

Femtosecond laser direct writing (FLDW) enables to induce permanent modifications of structures and properties inside transparent solids, including glass materials such as silica. These modifications, which are dependent on the laser parameters, include among others refractive index variations, formation of porous nanogratings and related linear birefringence, but also voids, nanoscale phase separation or nanocrystals. For instance, it enables to induce strong refractive index changes (Δn from 10^{-3} to more than 10^{-2} in a large range of transparent glasses), in extremely well localized volumes (few μm^3) in the bulk due to strong non-linear effects. The processing of transparent glasses with low-energy femtosecond (fs) laser pulses (sometimes combined with chemical etching) defines a flexible 3D manufacturing platform suitable for technologies like optical data storage, optofluidics, optomechanics, marking but also photonics such as 3D optical waveguides and their combination, fiber Bragg gratings, and polarization devices. Controlling these modifications could potentially exceed the domain of current fs-laser applications. More specifically, the industrial demand for sophisticated all-optical integration is increasingly growing as the volume of exchanged data and information increases. This ultimately yields to demand in devices with an ever increase of “smartness” with enhanced performance(s), and therefore greater nuance and complexity of laser treatments are required. In this realm, there is a strong demand to realize 3D optical circuits, 3D geometric phase optics, 5D optical data storage systems or various optical sensors. This framework was the basis of this dissertation work.

The project started with the study of photo imprinting of anisotropic optical properties in transparent inorganic glasses using femtosecond laser light. In the first stage, we shed light on the importance of glass composition under laser irradiation, along with laser parameters associated. Among the findings to highlight, we determinate what parameter values are adequate to induce nanogratings in various silicate glasses. Then, in the second stage of this work, we studied fs-laser irradiation on several doped silica glasses and focused on investigating anisotropies in the physical properties (birefringence and its thermal stability). The initial objective was to provide a roadmap to produce optical sensors in a high-temperature regime by mastering 1/ nanogratings formation and 2/ their thermal stability and lifetime in operating conditions. The initial idea was to comprehend the interplay between the chemical composition (e.g., introduction of TiO_2, YAG or Al_2O_3 inside a silica glass) and the nanostructure itself (control of both shape, size and composition of nanogratings). In fact, this work systematically studies, through several approaches, the writing and erasing mechanisms of nanogratings as a function of pulse energy, polarization orientation, and silicate glasses chemical composition.

In Chapters 1 and 2, we start with the introduction of the background of the project, we present the state of art about the silica glass, the optical fibers, and femtosecond laser direct writing, nanogratings formation and the thermal stability of laser written optical modifications. Then, we also discuss experimental details processed in the entire

project in Chapter 2.

In Chapter 3 is presented the thermal stability of IR-fs Type II modifications in bulk silicate glasses, which included the different contributions of the nanogratings and their erasure mechanisms. This includes also the impact of laser parameters, glass impurities (OH, Cl) and glass composition to some extend (mostly GeO_2, Al_2O_3). In “pure” silica glass, and with respect to nanogratings stability contributions, the point defects centers are bleached under a fairly low-temperature thermal treatment (200-500 °C), and exhibit only a minor contribution, to the measured retardance. Moreover, the densification related tensile stress is progressively erased from 600 to 900 °C. In contrast the compressive stress field produced by the nanoporous layers disappears before the annihilation of the nanopores themselves, likely by plastic deformation around the nanopores. This happens in a temperature range between 800 °C and T_a (T_a = annealing temperature). Finally, the form birefringence, due to the self-organization of nanopores in a layered nanostructure, is found to play a key role in the ultimate thermal stability of the fs laser-induced nanogratings. Of interest as well, thermal stability of nanogratings depends on Cl and OH impurities and laser parameters: the lower the impurities (both Cl and OH), the higher the thermal stability. The higher are pulse energy or writing speed, the higher is the thermal stability. For other glass compositions, the viscosity (T) and T_a appears strongly related to the “ultimate” thermal stability of Type II modifications i.e., a higher viscosity = higher full erasure temperature. In the specific case of aluminosilicate glasses, the highly containing-Al_2O_3 silicate glasses promote enhanced annealing performance relative to pure silica that is potentially related to nanoscale separation between Si and Al-rich glassy phases. Furthermore, it is not excluded that nanolayers are partly nano-crystallized in the form of Mullite, which would need further investigations.

In chapter 4, we move from bulk glasses to optical fibers to study the photosensitivity of aluminosilicate fibers under femtosecond laser irradiation We pinpoint that an yttrium aluminosilicate fiber core (also labeled YAG-derived fiber) response to fs-laser irradiation globally resembles that of SiO_2, or commercial Ge-doped SiO_2 fibers (e.g., SMF-28). In contrast binary aluminosilicate fibers (also labeled sapphire-derived fibers) exhibit significantly lower birefringence amplitude. Compared with the conventional SMF-28, or Suprasil F300 cladding, the YAG-derived fiber has a better thermal stability around 800 °C – 1000 °C whereas Sapphire derived fiber (Al_2O_3 > 50 mol%) shows even better performance between 1000 °C – 1200 °C. We also found that the Rayleigh-scattering signature of Sapphire-derived fiber is more sensitive to the temperature compared to SMF-28 or its lower Al_2O_3 containing analog. Finally, in this chapter we emphasized the benefit of using non-conventional fiber fabrication techniques like the Molten Core Method to develop new materials in the fiber form and suitable for imprinting ultra-high temperature devices (e.g., FBGs) based on fs-laser direct writing, and overcoming the current performances of commercial fibers.

In chapter 5, a novel method to fabricate the optical fibers, by 3D printing the glass preform, was investigated. After describing the manufacturing process and some thermal post-treatment to achieve loss reduction, we investigated writing kinetics and thermal stability of IR-fs type II modifications. The results showed that the 3D printed

fibers presented a quite similar thermal behavior as SMF-28. With less restrictions than for conventional fiber in designs and manufacturing steps, it suggests that 3D printed fibers could offer a competitive advantage in fiber fabrication industry in the future namely low cost and high flexibility in the choice of materials and structures.

In the last chapter, we use the Rayleigh–Plesset (R–P) equation to simulate, and compare to experimental results, the thermal stability of Type II modifications. The R–P equation provides insights into the temperature range at which the nanopores would ultimately collapse, and eventually simulate the erasure process of the nanopores during the annealing. Finally, a framework for lifetime and passivation determination of standard type II modifications is presented. The formalism is based on demarcation energy approximation and the existence of a master curve. The MC is determined by accelerated aging experiments under specific conditions that correspond to operating conditions. Then due to the distributed nature of activation energies, it is possible to increase the nanogratings stability by erasing the less stable part to extend the lifetime.

Some key results are summarized as follow:

1) We described areas of compositions based on the presence of Cl, OH, GeO_2, TiO_2, Al_2O_3 and Y_2O_3. The landscape of nanogratings existence is evaluated, along with the laser parameter landscape that promote the best thermal stability;
2) We paved the way for the use of silica optical fibers manufactured by 3D printing for the development of flexible and low-cost optical fiber sensors;
3) We demonstrated the effects of laser writing parameters (energy, writing speed and polarization orientation) on the thermal stability of the photo-induced optical properties;
4) We revealed the underlying mechanisms at the origin of the observed linear birefringence and their entanglement: point defects, stress fields from several contributions, specific volume changes and nanostructures. Each of these contributions exhibits different thermal behaviors;
5) We developed a model allowing us to predict the erasure kinetic of nanogratings according to thermal treatments (laser or annealing) where there is a close dependence between the material parameters, and in particular the dependence of the viscosity with the temperature and the formation of nanogratings, hence associated anisotropic optical properties;
6) Finally, with the experimental results, we built a reliable lifetime model (following the Master Curve formalism) and used it to predict operation lifetime of Type II modifications under different time-temperature annealing conditions.

With these in hands, we can envision to develop glasses (bulk or fiber geometries) or select commercial ones dedicated to the creation of anisotropic optical properties in various spectral ranges, from UV to mid-IR but also for applications in a high-temperature regime where lifetime control is mandatory.

Perspectives

As many exciting key results were discovered throughout this Ph.D. project, we will continue to conduct more in-depth research on this topic. First of all, in this thesis, we always use the Retardance to quantify the effect of thermal stability, but for the actual sensing application, more other parameters need to be studied. For example, in the next step, we will use the femtosecond laser to write different structures in sapphire-derived fibers to make fiber Bragg grating sensors or distributed sensors based on Rayleigh scattering and monitor the Bragg wavelength and Rayleigh backscattering changes respectively during annealing, and to determine the thermal performance of these kinds of optical fibers in practical applications. In addition, we will continue to use the Rayleigh-Plesset model to study the process of formation of nanogratings, continue to further study the thermal stability of Type III modification, use Molten core and 3D printed method to manufacture optical fibers with other material components, etc. So in the following part, we will discuss the future potential of this project from different perspectives.

From a fundamental perspective

There are light forces that act on the plasma and its nanostructuring leading to the nucleation - growth of nanocavities or even nanocrystals depending on the chosen compositions. In particular, the Rayleigh-Plesset model provides insights into the temperature range at which the nanopores would ultimately collapse, serving as a design tool for future high-temperature IR-fs-Type II based devices. This discovery successfully inspired us, and we will use this model to simulate the nanopores generation process during the laser writing and related limits. In short, we keep the retardance calculation based on the R-P model as a function of (t, T), apply it with the "real" discretized cooling curve rather than the isochronal annealing procedure, then for the formation of nanopores, we can obtain:

- The nanopores relaxation time, which is defined as the function of nanopore size evolution over the time from 1 ns up to 10 µs; 1 µs is approximately the time needed for the heat to diffuse away from the laser focal point. Beyond this time the temperature is too "cold", the glass viscosity is too high, and the glass structure no longer evolves.
- The retardance evolution as a function of time from 1 ns up to 1 µs. We suppose that the structure of the glass is frozen when the curves of the glass relaxation time and cooling time intersect. Therefore, the generated nanopores structure can be conserved inside the glass. According to this idea, we can use Rayleigh-Plesset simulation to speculate on the possibility of different types of glass producing stable nanopores under the action of femtosecond lasers. For example, with an initial pore size of 50 nm, the size will be changed to 40 nm in SiO_2 after 1 µs following a 2µJ pulse, whereas it will fully erase in BK7 glass. This may help to explain why nobody detect nanogratings in BK7 glasses whereas we were able to generate some recently.

This work will pave the way for material selection in future femtosecond laser modification related industries and applications.

Towards a new paradigm – To go beyond a simple energy deposition mechanism to develop forces and torques

Understanding the nanoscale response of a material under intense laser excitation is underpinning future laser processing technologies. Mechanical, optical, structural and compositional-related properties of materials could be tailored for novel “alloy” formation, catalytic and sensor applications. Light polarization is an effective parameter to control the energy delivery in laser structuring of surfaces and volumes. But our objective is to go far beyond a simple deposition of laser energy in the matter. A classical effect of a light beam is a thermal effect (laser cutting, melting etc..) but we want to show that we can develop forces and torques, after non-linear energetic excitation of the transparent matter by intense laser light. What one can imagine with sub-picosecond laser nowadays can be also realized more clearly with a truly femtosecond one appearing on the market in the next years. The time for a half period in the IR at a wavelength of 1 µm is 1.7 fs. In that case, opposite charges can be more easily separated. At the end, we will unravel the materials science behind sub-cycle laser pulses irradiation. In the future we will use them to show that it is a general possibility in transparent materials. We intend 1) to challenge the proposed theory by simulation work i.e., to show that the forces and torques are large enough, to compute the electric field, and to compute the induced mechanical field, 2) to show we can twist the matter and to figure out the appropriate laser parameters to use, and 3) to show that precipitation and orientation of nanostructures (like nanocrystals or nanoscale phase separation) can be controlled using the laser beam only. These future works will increase our knowledge in non-linear action involving the interaction of intense and ultrashort laser light with matter. This new knowledge will be applicable to any structuring of optical functionalization of any dielectric materials in adjacent fields of integrated optics but also to solid-state chemistry in general.

Towards applications

Besides the fundamental interest in these nanogratings, which are the smallest structures that can be created by light in the volume of a transparent material, the ability to control the birefringence slow/fast axis and even to induce circular optical properties lead to the engineering of unique integrated optical devices with 3D spatially varying birefringence and more generally refractive index changes with ultrahigh thermal stability. However, to date, the intrinsic parameters (period, rotation in 3D, nanoporosity) of femtosecond laser induced nanogratings still are not fully controlled. To improve the device quality, an ongoing major problem is to quantitatively establish the role played by each one of the laser parameters. In addition, the light scattering losses and stress accumulation must be reduced. Again, in this thesis we have brought the understanding of the vectorial nature of light-matter interaction in the case of nanogratings formation/erasure understanding step further. The ability to manipulate them would

open possibilities for engineering optical properties of a given material. We will investigate the ability to induce high retardance of up λ/2 at 5 µm but also writing nanogratings at high speeds (Typ. > 10cm/s) to unlock the industrial potential of this laser direct writing technique. This will be one major objective of upcoming studies. As a result, we will be able to develop birefringent based devices operating in a broad spectral range including achromatic components that are very important for applications ranging from polarimetry, spectroscopy, attosecond pulse generation, THz, military and domestics applications. Furthermore, this will locally control the phase and polarization of the light that will substitute costly equipment such as spatial light modulators.

As one perspective, we propose to specifically apply this 3D manufacturing technique for the fabrication of compact, integrated and low cost optical components in visible and near-IR transparent materials like SiO_2 glasses. Additionally, we plan to extend our results in the UV range and towards the IR, i.e., mid-IR using heavy oxide glass materials and maybe later in the far IR using non-oxide glasses like fluorides and chalcogenides. Nanogratings formation inside polymers is another interesting area, which has not been explored yet. Indeed, in mid and far-IR instrumentation, there is a need for miniaturized, low weight and low cost optical systems for civil (smartphone, automobile) but also security and military applications (vehicles steering, survey, weapons guidance, unmasking, countermeasure identification). The constraints on size and weight of optical systems are so demanding that traditional optical systems with a single optical axis are reaching their limits. Therefore, new breakthroughs in optical design have been proposed that consist in developing bio-inspired multichannel architectures and integrating optical functions using planar optical components. In addition, the possibility of making 3D direct shaping by use of femtosecond lasers enlarges the panel of optical functions we could encode into a small device.

From Industry and sensors perspective

Harsh (or extreme) environments, whether they are furnaces, reactors, engines of various sorts, high temperature composites or high resistant optics for semiconductor fabrication for example, demand components that operate well outside the parameters of telecommunications. In particular, ultrahigh temperature sensing has attracted considerable attention with the development of new thermally resistant optical fiber components that can operate above 800 °C and even more for some applications.

FBG sensing technology using regenerated devices is proposed as a major innovation for the instrumentation of some critical parts of the Tokamak. For Plasma and Fusion studies, arrays of FBG sensors must operate at peak temperatures ranging from 1000 °C and even to 2000 °C depending on the plasma power. FBG sensors are foreseen to instrument tokamak's divertor and especially Plasma Facing Unit (PFU) made of graphite and/or Tungsten in the ultimate version to be installed in ITER facility. The arrays will be located several millimeters under the hottest surface of these PFUs and thermal inversion model is being developed to retrieve the surface temperature. Thus, FBG sensing arrays stable for years over a range of 800-1200 °C are required:

- Increased safety requirements and incredibly severe environments trigger the

developments of innovative instrumentations to monitor continuously and over their expected lifetime (40-60 years) the next-generation of nuclear reactors. The main need is to monitor the temperature within the liquid sodium zone. Thus FBG sensing technology need: i) operating temperature of 600 °C in average (and 800 °C peak values), ii) lifetime of several years without any maintenance (ideally same lifetime than the reactor), iii) thermally stable sensors or predictable wavelength drift over T and time, iv) mechanical reliability of the fiber sensors (in case of strain sensors but also to prevent breaks due to vibration and or crack propagation), v) preserved spectral purity of the Bragg peaks, vi) multiplexing capabilities (several tens of FBGs on a single fiber) and EM immunity and vii) lastly response time of the sensors in the order of several hundreds of milliseconds in order to detect early nuclear incidents (appearing as localized hot spots within the pool). Preliminary experiments have been recently conducted within a joined test campaign between CEA Saclay and PhLAM (Lille University) teams in order to embed FBG sensors into 3D-printed metallic structures (Inconel 316L).

- Not only proposing innovations for the research performed on fusion and fission area, but the industry has also clearly identified the need for such temperature resistant FBG arrays (or some variants like distributed Rayleigh sensors) in order to improve the monitoring of high temperature processes or to embed temperature resistant sensors into “hot” devices. As an example, the rapidly emerging and growing industry based on the Additive Layer Manufacturing techniques of metallic or ceramic structures will take benefit from such high temperature resistant FBGs. On the other hand, regenerated/fs FBGs will also provide an increased operating temperature and heat dissipation solutions through high temperature resistant coatings in order to support short-term exposure to the melt bath of the deposited powders. This will trigger their use as SHM-like sensors (Structure Health Monitoring) directly embedded into the 3D-printed metallic or ceramic devices during the laser deposition process. While at its early stage and requiring further technological developments, several FBG-based optical fiber sensors have recently been successfully embedded into 3D printed metallic specimens.

Appendix 1 – Fiber Bragg grating writing

Photosensitivity is a new non-elastic light-matter interaction that was discovered by Hill *et al.* in 1978 [1, 2]. These authors launched a 50 mW TEM_{00} beam from an Ar^+ single-mode laser at 514 nm into a 1 m long piece of a germano-silicate fiber (*internal writing technique*). They could observe that the optical power reflected from the input end of the fiber increased with exposure time until almost all the light was reflected. The effect was analyzed by assuming the photo-induced formation of a periodic refractive index change at the fiber core, i.e. a Bragg Grating (BG). The important features of the phenomenon lie in the facts that the narrow-band filters are persistent [3] and a two-photon absorption process mediates their formation [4]. However, the details of the mechanism behind the formation of the BG were the matter for some speculation. Indeed, two types of model were proposed to account for the refractive index changes: a local one, in which the modification of the index is a function only of the local intensity of light, assumes the photo-induced formation or bleaching of color centers [5, 6].

It was soon recognized that the *internal writing technique* suffered from two drawbacks for widespread applications of BG. Firstly, such grating can be used only close to the writing wavelength. Secondly, the photo-induced change in index proves to be too low ($< 5.10^{-5}$) to write short ($\approx$ mm) highly reflective grating. The *transverse holographic technique* proposed by G. Meltz and W.W. Morey helps in solving these issues [7]. Briefly the method consists in exposing a single-mode germano-silicate fiber, through the side of the cladding, to a coherent UV-two-beam interference pattern (which can be done using a phase mask or a Llpyd mirror for example) with a wavelength λ_p selected to lie in the Germanium Oxygen-vacancy Defect Center (GODC) absorption band near 244 nm. The UV exposure leads to the growth of a phase grating reflecting light around a Bragg wavelength λ_B given by *Equation 1*:

$$\lambda_B = 2n_{eff}\Lambda; \;\; \Lambda = \frac{\lambda_P}{2Sin\,(\frac{\alpha}{2})} \qquad \text{(Equation 1)}$$

In *Equation 1*, Λ is the fringe spacing ($\Lambda \approx 0.2\mu m$ in the experiment by G. Meltz et al.), α is the crossing angle between the interfering beams and n_{eff} is the effective index of the fundamental LP_{01} mode. Hence, by means of this technique and a proper choice for α and λ_p, one can now select the Bragg wavelength ($\lambda_B > n_{eff}\lambda_p$) almost anywhere in the transmission range of the fiber. Furthermore, the holographic technique proved to enhance the efficiency of the grating inscription [7].

As the Bragg gratings reflect part of the light, it is obvious that at the output of the fiber, there is less light at the wavelength of the Bragg peak: in transmission, the spectrum presents a peak of absorption as shown in *Figure 1*. Thus, Bragg gratings can be used as a spectral filter in transmission.

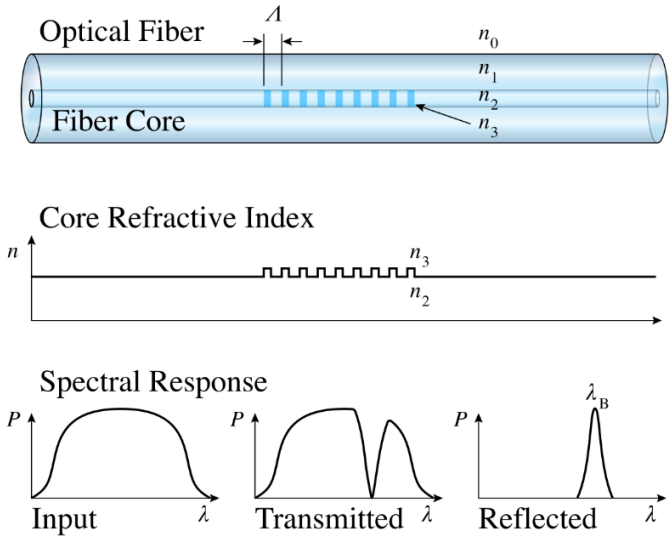

Figure 1. Diagram representing the reflection spectrum and the transmission spectrum induced by a Bragg grating in a single-mode optical fiber [8].

The usual length of Bragg gratings for sensors is between 1 and 20 mm. In a conventional optical fiber, the step of the grating is of the order of 535 nm for a Bragg grating having a Bragg wavelength close to 1548 nm.

About the temperature sensitivity of bragg gratings, when the fiber is subjected to a temperature variation, the glass undergoes expansion or contraction, resulting in a modification grating period. At the same time, the glass also undergoes a change in refractive index.

Suppose that the fiber is only subjected to a temperature variation, then the variation of Bragg wavelength $\Delta\lambda_B$ follows the following relation:

$$\frac{\Delta\lambda_B}{\lambda_B} = \frac{\Delta(n_e \times \Lambda)}{n_e \times \Lambda} = \left(\frac{1}{\Lambda} \times \frac{d\Lambda}{dT} \times \frac{1}{n_e} \times \frac{dn_e}{dT}\right) \times \Delta T = a \times \Delta T \qquad \text{(Equation 2)}$$

The first order coefficient of expansion of the silica glass $a = \frac{1}{\Lambda} \times \frac{d\Lambda}{dT} \approx 5 \times 10^{-7}/\circ C$, and the thermo-optical coefficient of silica $\frac{dn_e}{dT} \approx 10^{-5}/°C$, We deduce the theoretical coefficient which equals to $7.8 \times 10^{-6}/°C$ for a conventional optical fiber. Thus for a Bragg grating registered at 1550 nm, the thermal sensitivity $\frac{\Delta\lambda_B}{\Delta T}$ is approximately equal to 12.1 pm / °C [9].

Of course, this value serves as an example and only works over a small temperature range close to room temperature. The sensitivity coefficients of the Bragg grating must be adapted to the fiber used, to the reference state and to the variations in physical quantities undergone by the fiber. Therefore, the sensors must be calibrated before use.

Figure 2 illustrates the increase in the spectral position of the Bragg peak N°3 (Δλ) following the heating of the Bragg grating N°3 at a temperature T higher than the initial temperature T_0.

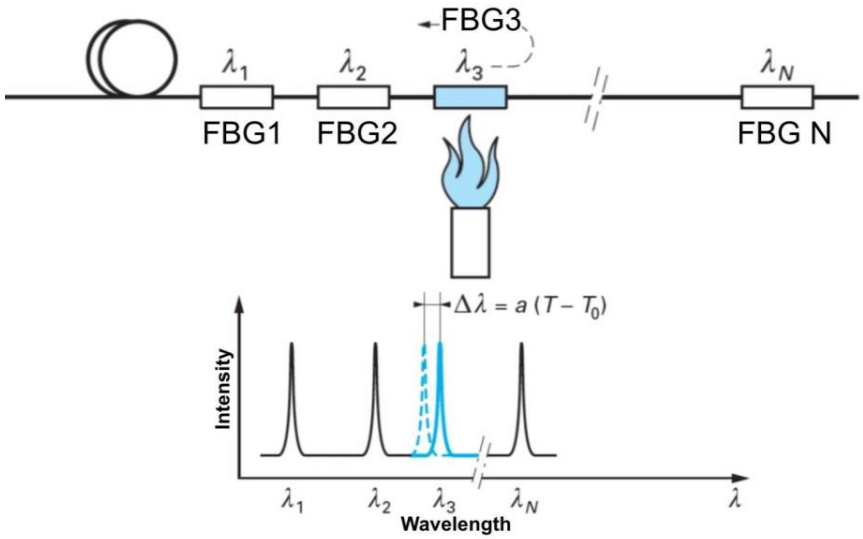

Figure 2. Diagram representing the response of a Bragg grating to an increase in temperature (taken from [9]).

A. Phase mask technique

The overall processes that have been used to produce the fringe patterns are reviewed in [10]. A typical experimental set-up involving a nulled zero-order phase-mask to make the fringe pattern is displayed in *Figure 2-2*. Here the UV laser is split into two beams, which are made to interfere with each other in the refractive index of a photosensitive fiber creating a periodic intensity distribution along the interference pattern. This interference pattern creates a corresponding periodic change in the refractive index of the optical fiber. Two types are differentiated -amplitude splitting and wave front splitting- depending on the splitting of the UV laser beam. As shown in *Figure 2-2,* the phase mask technique makes use of a mask (diffraction grating) for the inscription of the gratings in the fiber. The grating is designed such that diffraction orders m = +1 and m = -1 remains when illuminated with UV laser. These two orders interfere in the core of the optical fiber creating a periodic intensity distribution, which in turn induces a periodic refractive index change in the core of the fiber. Since 2006 this method has been extended to the use of IR femtosecond laser irradiation, usually with an 800nm Ti-Sa femtosecond laser.

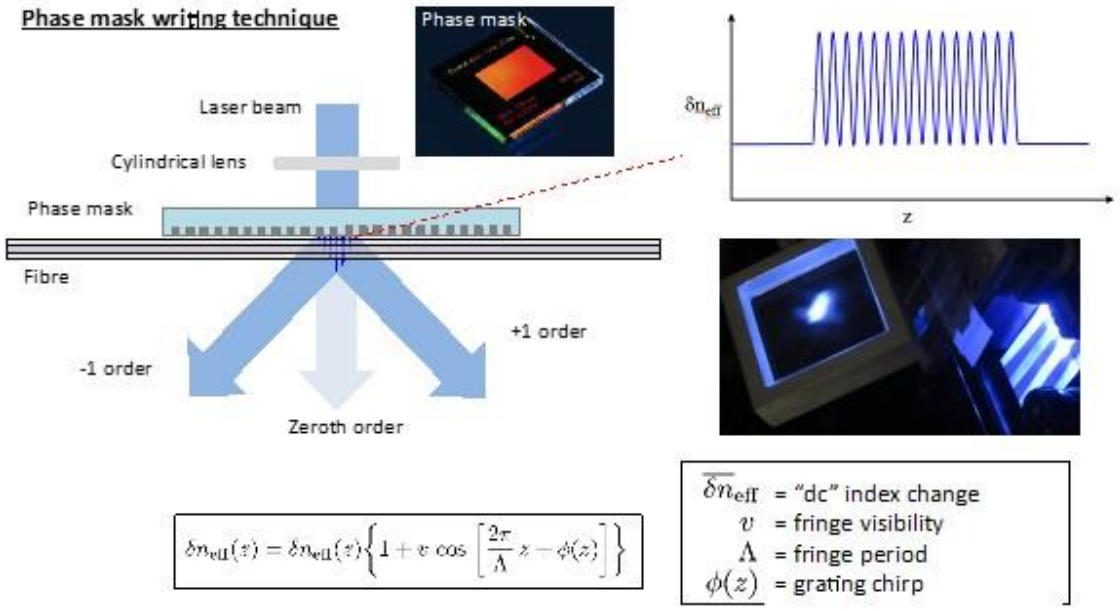

Figure 3: Fabrication the fiber bragg grating using the phase mask technique.[11]

By large, the BG pitch Λ is usually selected so that λ_B is located in a spectral range where the exposure-induced loss can be neglected (no absorption grating). As shown in this figure, the transmission T of the fiber near λ_B is measured by means of a tunable single-frequency laser and a power-meter. Thus, the changes in both the BG first-order reflection coefficient (R≈1-T), the grating width $\delta\lambda$ and the shift $\Delta\lambda$ in λ_B can be measured as a function of exposure time for various optical power densities at the fiber core.

B. Point-by-point inscription

K. O. Hill et al. took then rapidly benefit of the tensorial nature of the change in refractive index (UV-induced birefringence) to write polarization rocking filter within birefringent fiber using *the point by point side-writing technique* [12]. The method consists in periodically side-exposing a length W of the fiber core through an amplitude mask (W= Λ/2) in order to change the fiber birefringence with a grating period made equal to the fiber beat length ($\Lambda\approx$ 1 cm). *The point by point side-writing technique* was later implemented to write Long Period Gratings (LPG) that couple the fundamental guided mode to co-propagating cladding modes [13].

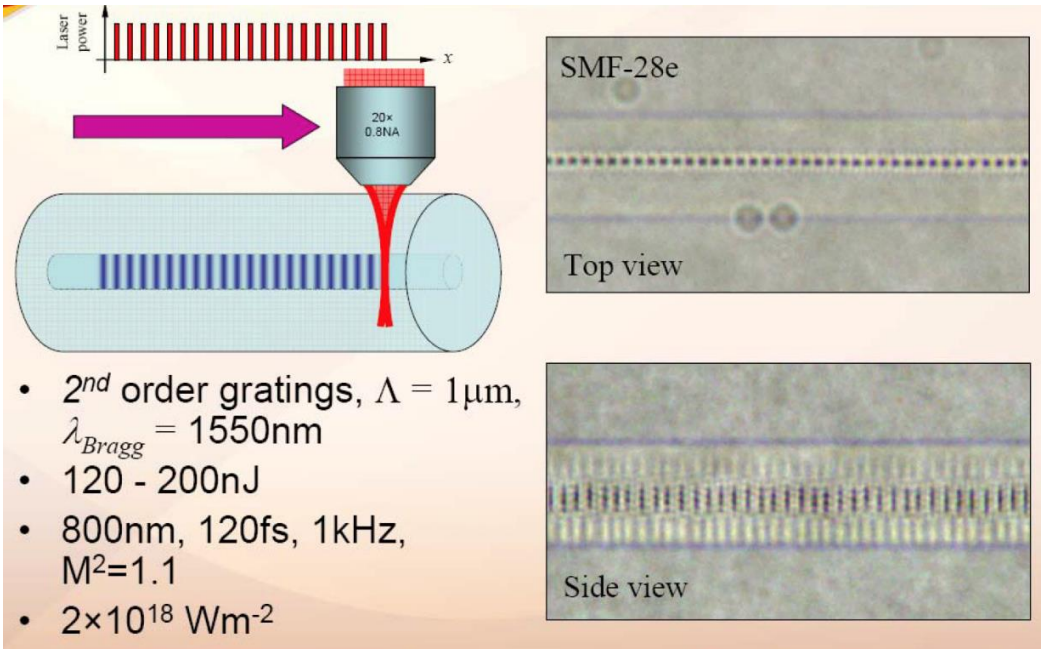

Figure 4: the schema of the point-by-point inscription method.

In 2006, Marshall et al. reported the first demonstration of a laser-written waveguide device integrated with a waveguide Bragg grating made by fs laser[14]. The fabrication process involved in creating the Bragg grating was based on the point-by-point (PbP) method more commonly applied to the inscription of FBGs [15-17]. In the PbP method, a single laser beam (a UV laser historically but it could be also IR femtosecond) is used to write the grating. As exhibited in *Figure 3*, a pinhole or focusing optics is used to narrow the beam and focus it on the fiber as it moves along a translation stage, each grating spatial perturbation (or voxel) is individually created by a single laser pulse of sufficient energy, typically close to or just above the damage threshold of the sample. In general, systems running at low repetition rates (< 500 kHz) are used to generate the pulse energies required to achieve single PbP modifications[18] . Here, the main difference with the previous method lies in the interaction between the laser radiation and the optical fiber. In the case of femtosecond inscribed gratings for example, multiphoton absorption is responsible for the refractive index change in the core.

The waveguide Bragg grating created by Marshall et al. used a sequential direct-write process that passed over the same region twice. The waveguide was written before the grating structure and the Bragg grating extended over the entire waveguide length. The reflection spectra of a typical waveguide and second-order Bragg grating using this two-step process. Although the region of material modified during the Bragg grating inscription process was smaller than the total volume of the waveguide, the guided mode overlap with the Bragg grating was sufficient to introduce a pronounced resonant reflection at the Bragg wavelength of 1550.63 nm.

References

1. Hill, K., et al., Photosensitivity in optical fiber waveguides: Application to reflection filter fabrication. Applied physics letters, 1978. 32(10): p. 647-649.
2. Kawasaki, B.S., et al., Narrow-band Bragg reflectors in optical fibers. Optics Letters, 1978. 3(2): p. 66-68.
3. Stone, J., Photorefractivity in GeO2-doped silica fibers. Journal of applied physics, 1987. 62(11): p. 4371-4374.
4. Lam, D. and B.K. Garside, Characterization of single-mode optical fiber filters. Applied Optics, 1981. 20(3): p. 440-445.
5. Payne, F., Photorefractive gratings in single-mode optical fibres. Electronics Letters, 1989. 25(8): p. 498-499.
6. Bernardin, J.P. and N. Lawandy, Dynamics of the formation of Bragg gratings in germanosilicate optical fibers. Optics communications, 1990. 79(3-4): p. 194-199.
7. Meltz, G., W.W. Morey, and W. Glenn, Formation of Bragg gratings in optical fibers by a transverse holographic method. Optics letters, 1989. 14(15): p. 823-825.
8. Fiber Bragg Grating. Available from: https://en.wikipedia.org/wiki/Fiber_Bragg_grating.
9. Ferdinand, P., Capteurs à fibres optiques à réseaux de Bragg. Techniques de l'ingénieur, 1999. 6735: p. 1-24.
10. Kashyap, R., Fiber bragg gratings. 2009: Academic press.
11. Al-Fakih, E.A., et al., The capability of fiber Bragg grating sensors to measure amputees' trans-tibial stump/socket interface pressures. Sensors, 2013. 13(8): p. 10348-10357.
12. Hill, K., et al., Birefringent photosensitivity in monomode optical fibre: application to external writing of rocking filters. Electronics Letters, 1991. 27(17): p. 1548-1550.
13. Vengsarkar, A.M., et al., Long-period fiber gratings as band-rejection filters. Journal of lightwave technology, 1996. 14(1): p. 58-65.
14. Marshall, G.D., M. Ams, and M.J. Withford, Direct laser written waveguide-Bragg gratings in bulk fused silica. Optics Letters, 2006. 31(18): p. 2690-2691.
15. Wikszak, E., et al. Recording of fiber Bragg gratings with femtosecond pulses using a "point by point" technique. in Conference on Lasers and Electro-Optics. 2004. Optical Society of America.
16. Malo, B., et al., Point-by-point fabrication of micro-Bragg gratings in photosensitive fibre using single excimer pulse refractive index modification techniques. Electronics Letters, 1993. 29(18): p. 1668-1669.
17. Martinez, A., et al., Direct writing of fibre Bragg gratings by femtosecond laser. Electronics Letters, 2004. 40(19): p. 1170-1172.
18. Ams, M., et al., Fabricating waveguide Bragg gratings (WBGs) in bulk materials using ultrashort laser pulses. Nanophotonics, 2017. 6(5): p. 743-763.

Appendix 2 – Fiber optic sensors

A. Fiber bragg gratings sensor

The straight-line Bragg gratings consist of a periodic and orthogonal modulation of the refractive index in the core of the optical fiber. This permanent modulation is induced by a laser that insulates the core of the optical fiber from the outside. The modulation period varies from a few hundred nanometers to a few micrometers. This modulation is responsible for the coupling between the guided fundamental mode and a counter-propagating fundamental mode (mode propagating in the opposite direction). This coupling induces the reflection of the main wavelength depending on the type of modification and the grating period.

The variations in environmental parameters (temperature, deformation) are measured by the variation in the wavelength of the light reflected by the Bragg grating. A temperature resolution of 0.01 °C and a deformation resolution of 0.1 με (1 μm / m = 1 με) can be detected with a Bragg grating [1]. The spatial resolution depends on the length of the grating and can be 2 mm. The maximum temperature of use of Bragg gratings registered by the femtosecond laser is 1000 °C for those who have not undergone heat treatments [2], and 1200 °C if the fiber has undergone a specific heat treatment before or after the inscription of the modulation [3, 4].

B. Interferometric sensors

Interferometric sensors work with an interferometric cavity intrinsic or extrinsic to optical fiber [5]. When this sensor is subjected to physical changes, the length of the interferometric cavity is modified. This change in length induces interference at the device output because of the difference in the phase of the light between the two waves of the interferometric cavity. The use of an interferometric method makes it possible to measure deformations less than 1 με.

There are many types of sensors employing different techniques (such as those with Mach-Zehnder interferometer or Sagnac interferometer), but this part will focus on those that are marketed: SOFO sensors and Fabry-Perot interferometric sensors.

SOFO sensors (Deformation Monitoring with Fiber Optic Sensors)

The SOFO sensors are weakly coherent interferometric sensors. They are inserted into structures (for example bridges, buildings, tunnels, oil pipelines) to detect the deformations there. These are long rod-shaped deformation gauges (25 cm to 10 m in length) containing a measuring fiber and a reference fiber with a reflecting surface at the end of the two fibers to reflect light and act as interferometry cavity. The deformation of the gauge induces a change in the length of the gauge and of the interferometric cavity. This change in length involves a modification of the interference pattern of the sensor, which is then "translated" into a variation in deformation. The reference fiber included

in the gauge makes the sensor insensitive to temperature, so there is no need to compensate for taking temperature into account when processing data.

SOFO sensors have a resolution of the order of micro-deformation (1 με) [5]. However, the deformation measurements are only made at low speeds (measurement frequency: 0.1 Hz - 1 Hz). In addition, these sensors cannot measure structural damage [5] and they are difficult to multiplex.

Fabry–Perot sensor

Fabry-Perot interferometric sensors are based on an internal cavity in the fiber: two partially reflecting faces are placed one after the other in the optical core. The light is reflected on these two surfaces separated by a certain distance. The reflections at the level of these two surfaces will interfere with each other. The reflection spectrum of the cavity presents several peaks separated by them by a wavelength characteristic of the length of the Fabry-Perot cavity. When the length of the cavity changes by variation in temperature or in deformation, the difference in length between two successive peaks changes.

Compared to SOFO sensors, Fabry-Perot sensors are compact and allow measurements to be made at one point. But they are also difficult to multiplex.

Fabry-Perot sensors have a maximum resolution of 0.15 με with a maximum deformation of 1000 με and can measure temperatures from -40 °C to 250 °C with a resolution of 0.1 °C [5]. Although lately, Yu et al. show the possibility of making measurements up to 1100 °C for 24 hours using a section of photonic crystal fiber as an interferometric cavity [6].

C. Distributed sensors

When light passes through a non-empty medium, incident photons can be scattered. The scattered photons can either conserve their energy (elastic scattering) or change the amount of energy and wavelength (inelastic scattering). There are three types of scattering of incident light in the matter: Rayleigh scattering, Brillouin scattering and Raman scattering [7]. The first is elastic, while the other two are inelastic. *Figure 1* illustrates the spectrum of light backscattered by Rayleigh, Raman and Brillouin scattering occurring in an optical fiber when the wavelength of the incident light is 1550 nm. The wavelength of the scattered photon depends on the scattering phenomenon taking place and the external parameters (temperature, deformation). While the probability that a diffusion phenomenon will occur depends on the environment and the external parameter.

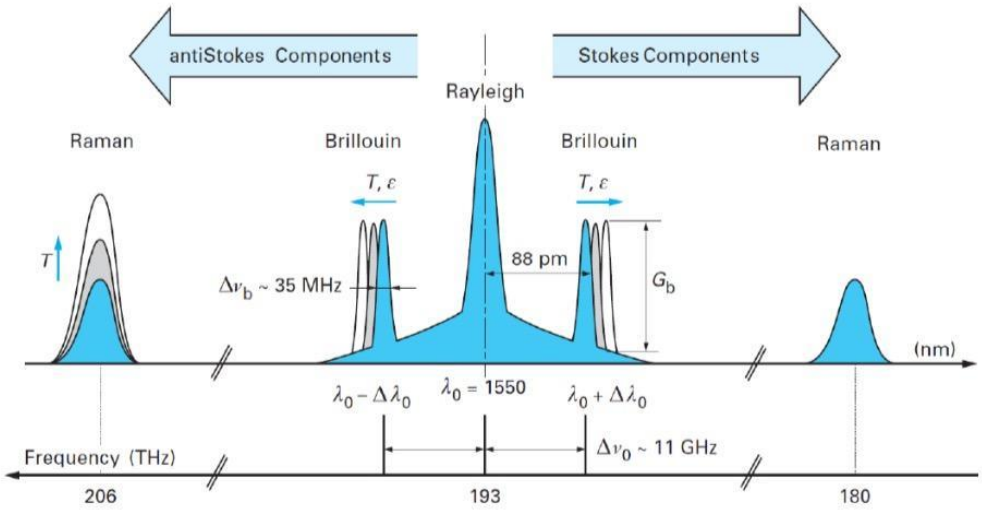

Figure 1. Diagram illustrating the spectrum of light backscattered by Rayleigh, Raman and Brillouin scattering phenomena in an optical fiber with the wavelength of incident light at 1550 nm (taken from [1]).

Distributed sensors rely on the scattering of light in matter. The light is inputted into the core of the optical fiber and the backscattered optical signal is characterized at the input of the fiber. The measurements are made in reflection since the light scattered by the material has no preferred direction.

Backscattered light has different characteristics depending on the environmental parameters to which the fiber is subjected. As the diffusion phenomena occur over the entire length of the optical fiber, it is possible to use the diffusion to quantify the variations in physical quantities as a function of the position on the whole of the fiber. As the measurements can be made on the fiber without discontinuity, the optical fiber sensors exploiting the light scattering are said to be distributed. Depending on the type of diffusion and the treatment method used, it is possible to make the measurements for the variation of temperature or deformation.

For each mode of diffusion, the measurement assembly is different and makes it possible to measure differently the variations of physical quantities to which the fiber is subjected.

Distributed sensors based on Raman scattering

Raman scattering is an inelastic scattering of photons with the modes of vibration of molecules of matter [7]. During this type of diffusion, atoms and molecules can:

- either absorb the photon and go to a higher energy level by emitting a photon of less energy and with a longer wavelength (Stokes shift);
- either absorb a photon to pass from a high vibrational level to the fundamental energy level, the emitted photon is then of higher energy and at a shorter wavelength.

When the temperature rises, there are more atoms in an excited state. As a result, the probability of anti-Stokes photon emissions increases. Temperature can be measured by measuring the ratio of the intensity of the anti-Stokes Raman backscatter to the intensity of the Stokes backscatter [8].

Raman Optical Time Domain Reflectometry systems (also called ROTDR) have a temperature resolution of approximately 0.1 °C with a spatial resolution of 1 m, for a range of 10 km [1, 5]. The range can reach 30 km with a spatial resolution of 17 meters and a temperature resolution of 5 °C [9]. The maximum temperature for use is around 700 °C [1].

Because of the long working length, ROTDR systems can be used to monitor the temperature of structures (tunnels, pipes, etc.).

Distributed sensors based on Brillouin scattering

The Brillouin scattering is an inelastic scattering of photons on acoustic phonons [7], according to a Stokes or anti-Stokes type interaction. The spectral shift of the Brillouin scattering depends on the index of the material n, the speed of sound in the material and the wavelength of the excitation light. When the fiber is subjected to the variation of temperature or deformation, the speed of sound in the material changes and the index of the fiber varies. On the other hand, the increase in the intensity of the anti-Stokes scattering with temperature is small, the Brillouin scattering is mainly used for deformation measurements.

The Brillouin Optical Time Domain Reflectometry (BOTDR) diffusion makes it possible to make temperature and deformation measurements over a hundred kilometers of fiber, with a temperature resolution of 1 K and a deformation resolution of 20 µm/m, when the spatial resolution is 1 m. The classical range of this method is between 20 km and 50 km, but it is possible to reach a hundred kilometers [8]. Thus, this method is used to monitor structural deformations.

Distributed sensors based on Rayleigh scattering

Rayleigh scattering is an elastic scattering of light by localized density fluctuations [7]. However, an optical fiber is not perfectly homogeneous: it has microscopic variations in density due to the raw material, the manufacturing procedure or the drawing process. It can also have contaminations or elements external in the glass to induce a local change in density. These fluctuations are responsible for Rayleigh scattering in optical fiber.

This effect is used for measurements distributed by frequency reflectometry, called "Optical Frequency Domain Reflectometry" (OFDR). This technique uses a Mach-Zehnder interferometer, one of the parts of which is used to connect the measurement fiber and the second part of which serves directly as the reference fiber. A frequency-modulated light signal is inputted into the interferometer. Rayleigh backscattering of the measurement fiber interferes with the reference part at the output of the interferometer. At the output of the interferometer, the intensity and the phase are measured as

a function of the wavelength and of the time. The signal obtained is compared to the previous measurement to quantify the variations in temperature and deformation.

The classic range of this device is between 30 m and 70 m with a gauge length of 2 cm for the temperature measurement resolution of 0.1 °C and for the deformation of 1 με [8]. A range of 2 km of fiber is achievable [10], the maximum temperature for using this technique is 775 °C for conventional optical fibers (SMF-28 fiber from Corning) [11].

References

1. Ferdinand, P. The evolution of optical fiber sensors technologies during the 35 last years and their applications in structure health monitoring. in EWSHM-7th European Workshop on Structural Health Monitoring. 2014.
2. Martinez, A., I. Khrushchev, and I. Bennion, Thermal properties of fibre Bragg gratings inscribed point-by-point by infrared femtosecond laser. Electronics letters, 2005. 41(4): p. 176-178.
3. Li, Y., et al., Fiber Bragg gratings with enhanced thermal stability by residual stress relaxation. Optics express, 2009. 17(22): p. 19785-19790.
4. Li, Y., et al., Prestressed fiber Bragg grating with high temperature stability. Journal of Lightwave Technology, 2011. 29(10): p. 1555-1559.
5. Guo, H., et al., Fiber optic sensors for structural health monitoring of air platforms. Sensors, 2011. 11(4): p. 3687-3705.
6. Yu, H., et al., Fabry-Perot interferometric high-temperature sensing up to 1200° C based on a silica glass photonic crystal fiber. Sensors, 2018. 18(1): p. 273.
7. Boyd, R.W., The nonlinear optical susceptibility. Nonlinear optics, 2008. 3: p. 1-67.
8. Boldyreva, E., Mesures réparties par réflectométrie fréquentielle sur fibre optique. 2016.
9. Bolognini, G., et al., Analysis of distributed temperature sensing based on Raman scattering using OTDR coding and discrete Raman amplification. Measurement Science Technology, 2007. 18(10): p. 3211.
10. Gifford, D., et al. Millimeter resolution otpical reflectometry over up to two kilometers of fiber length. in 2007 Ieee Avionics, Fiber-Optics and Photonics Technology Conference. 2007. IEEE.
11. Buric, M., et al. Distributed fiber-optic sensing in a high-temperature solid-oxide fuel cell. in Remote Sensing System Engineering VI. 2016. International Society for Optics and Photonics.

Publications list

Journal papers

1. Cavillon, M., Lancry, M., Poumellec, B., **Wang, Y**., Canning, J., Cook, K., Hawkins, T., Dragic, P. and Ballato, J., ''Overview of high temperature fibre Bragg gratings and potential improvement using highly doped aluminosilicate glass optical fibres.'' Journal of Physics: Photonics, 1(4), p.042001 (2019).
2. Wei, S., **Wang, Y**., Yao, H., Cavillon, M., Poumellec, B., Peng, G. and Lancry, M., ''Thermal Stability of Type II Modifications by IR Femtosecond Laser in Silica-based Glasses.'' Sensors, 20(3), p.762 (2020).
3. **Wang, Y**., Wei, S., Cicconi, M., Tsuji, Y., Shimizu, M., Shimotsuma, Y., Miura, K., Peng, G., Neuville, D., Poumellec, B. and Lancry, M., ''Femtosecond laser direct writing in SiO2-Al2O3 binary glasses and thermal stability of Type II permanent modifications.'' Journal of the American Ceramic Society, 103(8), pp.4286-4294 (2020).
4. Cavillon, M., **Wang, Y**., Poumellec, B., Brisset, F. and Lancry, M., ''Erasure of nanopores in silicate glasses induced by femtosecond laser irradiation in the Type II regime.'' Applied Physics A, 126(11) (2020).
5. Canning, J., **Wang, Y**., Lancry, M., Luo, Y. and Peng, G., ''Helical distributed feedback fiber Bragg gratings and rocking filters in a 3D printed preform-drawn fiber.'' Optics Letters, 45(19), p.5444 (2020).
6. Wei, S., Luo, Y., Zhang, B., Lu, M., Ding, M., **Wang, Y**., Lancry, M. and Peng, G., ''Impact of Al2O3 doping on Bi active center photobleaching in Bi/Er-codoped fibers.'' Optics Letters, 45(14), p.4016 (2020).
7. **Wang, Y**., Wei, S., Cavillon, M., Sapaly, B., Poumellec, B., Peng, G., Canning, J. and Lancry, M., ''Thermal Stability of Type II Modifications Inscribed by Femtosecond Laser in a Fiber Drawn from a 3D Printed Preform.'' Applied Sciences, 11(2), p.600 (2021).
8. **Wang, Y**., Cavillon, M., Ollier, N., Poumellec, B. and Lancry, M., ''An Overview of the Thermal Erasure Mechanisms of Femtosecond Laser-Induced Nanogratings in Silica Glass.'' physica status solidi (a), p.2100023 (2021).
9. **WANG, Y**., Cavillon, M., Ballato, J., Elsmann, T., Rothhardt, M., Desmarchelier, R., Laffont, G., Poumellec, B., and Lancry, M., ''3D laser engineering of molten core fibers: towards a new generation of harsh environment sensing devices.'' (in preparation).
10. **WANG, Y**., Cavillon, M., Poumellec, B., and Lancry, M., ''Lifetime prediction for Type II modifications inscribed by femtosecond laser in silica glass.'' (in preparation).
11. Wei, S., Lu, M., Luo, Y., Zhang, B., **Wang, Y.,** Lancry, M., Canning, J., and Peng, G., ''Loss reduction of 3D silica lithography fiber by post heat treatment.'' (under revision).

International conferences

1. 13th international symposium on SiO2, advanced dielectrics and related devices, https://sio2-2020.sciencesconf.org/ 14-15 June 2021, oral presentation "Femtosecond Laser Induced Nanogratings for Harsh Environment Operations using High Al2O3-containing Aluminosilicate

Fibers".

2. Conference on Lasers and Electro-Optics/Europe–European Quantum Electronics Conference (CLEO/Europe-EQEC 2021) https://www.cleoeurope.org/ 21-25 June 2021, oral presentation "Thermal Stability of Type II Modifications by IR Femtosecond Laser in Highly-Doped Aluminosilicate Glass Optical Fibers".

Synthèse en français

L'écriture directe par laser femtoseconde (FLDW) permet d'induire des modifications permanentes des structures et des propriétés à l'intérieur des solides transparents, y compris des matériaux verriers tels que la silice. Ces modifications, qui dépendent des paramètres laser, incluent entre autres des variations d'indice de réfraction, la formation de nanoréseaux poreux et la biréfringence linéaire associée, mais aussi des vides, une séparation de phase à l'échelle nanométrique ou des nanocristaux. Par exemple, il permet d'induire de fortes variations d'indice de réfraction (Δn de 10^{-3} à plus de 10^{-2} dans une large gamme de verres transparents), dans des volumes extrêmement bien localisés (quelques μm^3) dans la masse en raison de fortes non-linéaires effets. Le traitement de verres transparents avec des impulsions laser femtosecondes (fs) de faible énergie (parfois associées à une gravure chimique) définit une plateforme de fabrication 3D flexible adaptée aux technologies telles que le stockage de données optiques, l'optofluidique, l'optomécanique, le marquage mais aussi la photonique comme les guides d'ondes optiques 3D et leur combinaison, des réseaux de Bragg à fibre et des dispositifs de polarisation. Le contrôle de ces modifications pourrait potentiellement dépasser le domaine des applications fs-laser actuelles. Plus précisément, la demande industrielle pour une intégration tout optique sophistiquée augmente de plus en plus à mesure que le volume de données et d'informations échangées augmente. Cela cède finalement à la demande d'appareils avec une « intelligence » toujours croissante avec des performances améliorées, et donc une plus grande nuance et une plus grande complexité des traitements au laser sont nécessaires. Dans ce domaine, il existe une forte demande pour réaliser des circuits optiques 3D, des optiques de phase géométrique 3D, des systèmes de stockage de données optiques 5D ou divers capteurs optiques. Ce cadre a été la base de ce travail de thèse.

Le projet a commencé par l'étude de l'impression photo des propriétés optiques anisotropes dans des verres inorganiques transparents à l'aide de la lumière laser femtoseconde. Dans une première étape, nous avons mis en lumière l'importance de la composition du verre sous irradiation laser, ainsi que les paramètres laser associés. Parmi les résultats à mettre en évidence, nous déterminons quelles valeurs de paramètres sont adéquates pour induire des nanoréseaux dans divers verres de silicate. Ensuite, dans la deuxième étape de ce travail, nous avons étudié l'irradiation laser fs sur plusieurs verres de silice dopés et nous nous sommes concentrés sur l'étude des anisotropies dans les propriétés physiques (biréfringence et sa stabilité thermique). L'objectif initial était de fournir une feuille de route pour produire des capteurs optiques en régime haute température en maîtrisant 1/ la formation des nanoréseaux et 2/ leur stabilité thermique et leur durée de vie en conditions de fonctionnement. L'idée initiale était de comprendre l'interaction entre la composition chimique (par exemple, l'introduction de TiO_2, de YAG ou d'Al_2O_3 à l'intérieur d'un verre de silice) et la nanostructure elle-même (contrôle de la forme, de la taille et de la composition des nanoréseaux). En effet, ce travail étudie systématiquement, à travers plusieurs approches, les mécanismes d'écriture et d'effacement des nanoréseaux en fonction de l'énergie des impulsions, de l'orientation de polarisation et de la composition chimique des verres silicatés.

Dans les chapitres 1 et 2, nous commençons par l'introduction du contexte du projet, nous présentons l'état de l'art sur le verre de silice, les fibres optiques et l'écriture directe laser femtoseconde, la formation de nanoréseaux et la stabilité thermique des modifications optiques écrites au laser. Ensuite, nous discutons également des détails expérimentaux traités dans l'ensemble du projet au chapitre 2.

Dans le chapitre 3 est présentée la stabilité thermique des modifications IR-fs de type II dans les verres de silicate en vrac, qui incluaient les différentes contributions des nanoréseaux et leurs mécanismes d'effacement. Cela inclut également l'impact des paramètres laser, des impuretés du verre (OH, Cl) et de la composition du verre dans une certaine mesure (principalement GeO_2, Al_2O_3). Dans le

verre de silice « pur », et en ce qui concerne les contributions à la stabilité des nanoréseaux, les centres des défauts ponctuels sont blanchis sous un traitement thermique à assez basse température (200-500 °C) et ne présentent qu'une contribution mineure au retard mesuré. De plus, la contrainte de traction liée à la densification s'efface progressivement de 600 à 900 °C. En revanche, le champ de contrainte de compression produit par les couches nanoporeuses disparaît avant l'annihilation des nanopores eux-mêmes, vraisemblablement par déformation plastique autour des nanopores. Cela se produit dans une plage de température comprise entre 800 °C et T_a (T_a = température de recuit). Enfin, la forme biréfringence, due à l'auto-organisation des nanopores dans une nanostructure en couches, s'avère jouer un rôle clé dans la stabilité thermique ultime des nanoréseaux induits par laser fs. Il est également intéressant de noter que la stabilité thermique des nanoréseaux dépend des impuretés Cl et OH et des paramètres laser : plus les impuretés (à la fois Cl et OH) sont faibles, plus la stabilité thermique est élevée. Plus l'énergie d'impulsion ou la vitesse d'écriture sont élevées, plus la stabilité thermique est élevée. Pour d'autres compositions de verre, la viscosité (T) et Ta semblent fortement liées à la stabilité thermique « ultime » des modifications de type II, c'est-à-dire une viscosité plus élevée = une température d'effacement complet plus élevée. Dans le cas spécifique des verres d'aluminosilicate, les verres de silicate à haute teneur en Al_2O_3 favorisent une performance de recuit améliorée par rapport à la silice pure qui est potentiellement liée à la séparation à l'échelle nanométrique entre les phases vitreuses riches en Si et en Al. De plus, il n'est pas exclu que les nanocouches soient en partie nanocristallisées sous forme de Mullite, ce qui nécessiterait des investigations plus poussées.

Dans le chapitre 4, nous passons des verres massifs aux fibres optiques pour étudier la photosensibilité des fibres d'aluminosilicate, ou des fibres commerciales de SiO_2 dopées au Ge (par exemple, SMF-28) sous irradiation laser femtoseconde. En revanche, les fibres binaires d'aluminosilicate (également appelées fibres dérivées du saphir) présentent une amplitude de biréfringence significativement plus faible. Par rapport au revêtement conventionnel SMF-28 ou Suprasil F300, la fibre dérivée du YAG a une meilleure stabilité thermique autour de 800 °C à 1000 °C tandis que la fibre dérivée du saphir (Al_2O_3 > 50 % en moles) montre des performances encore meilleures entre 1000 °C – 1200 °C. Nous avons également constaté que la signature de diffusion Rayleigh de la fibre dérivée du saphir est plus sensible à la température par rapport au SMF-28 ou à son analogue contenant moins d'Al_2O_3. Enfin, dans ce chapitre, nous avons souligné l'avantage d'utiliser des techniques de fabrication de fibres non conventionnelles comme la méthode Molten Core pour développer de nouveaux matériaux sous forme de fibre et adaptés à l'impression de dispositifs à ultra-haute température (par exemple, FBG) basés sur fs-laser irradiation et surmonter les performances actuelles des fibres commerciales.

Dans le chapitre 5, une nouvelle méthode de fabrication des fibres optiques, par impression 3D de la préforme de verre, a été étudiée. Après avoir décrit le processus de fabrication et quelques post-traitements thermiques pour réduire les pertes, nous avons étudié la cinétique d'écriture et la stabilité thermique des modifications IR-fs de type II. Les résultats ont montré que les fibres imprimées en 3D présentaient un comportement thermique assez similaire à celui du SMF-28. Avec moins de restrictions que pour les fibres conventionnelles dans les étapes de conception et de fabrication, cela suggère que les fibres imprimées en 3D pourraient offrir un avantage concurrentiel dans l'industrie de la fabrication de fibres à l'avenir, à savoir un faible coût et une grande flexibilité dans le choix des matériaux et des structures.

Dans le dernier chapitre, nous utilisons l'équation de Rayleigh-Plesset (R-P) pour simuler la stabilité thermique des modifications de type II et comparer aux résultats expérimentaux. L'équation R-P donne un aperçu de la plage de températures à laquelle les nanopores finiraient par s'effondrer et simulerait éventuellement le processus d'effacement des nanopores pendant le recuit. Enfin, un cadre pour la détermination de la durée de vie et de la passivation des modifications standard de type II est

présenté. Le formalisme est basé sur l'approximation de l'énergie de démarcation et l'existence d'une courbe maîtresse (MC). Le MC est déterminé par des expériences de vieillissement accéléré dans des conditions spécifiques qui correspondent aux conditions opératoires. Ensuite, en raison de la nature distribuée des énergies d'activation, il est possible d'augmenter la stabilité des nanoréseaux en effaçant la partie moins stable pour prolonger la durée de vie.

Certains résultats clés sont résumés comme suit :

1) Nous avons décrit des zones de compositions basées sur la présence de Cl, OH, GeO_2, TiO_2, Al_2O_3 et Y_2O_3. Le paysage de l'existence des nanoréseaux est évalué, ainsi que le paysage des paramètres laser qui favorisent la meilleure stabilité thermique ;

2) Nous avons ouvert la voie à l'utilisation de fibres optiques en silice fabriquées par impression 3D pour le développement de capteurs à fibres optiques flexibles et à faible coût ;

3) Nous avons démontré les effets des paramètres d'écriture laser (énergie, vitesse d'écriture et orientation de polarisation) sur la stabilité thermique des propriétés optiques photo-induites ;

4) Nous avons mis en évidence les mécanismes sous-jacents à l'origine de la biréfringence linéaire observée et de leur intrication : défauts ponctuels, champs de contraintes de plusieurs contributions, changements de volume spécifiques et nanostructures. Chacune de ces contributions présente des comportements thermiques différents ;

5) Nous avons développé un modèle nous permettant de prédire la cinétique d'effacement des nanoréseaux selon des traitements thermiques (laser ou recuit) où il existe une étroite dépendance entre les paramètres du matériau, et en particulier la dépendance de la viscosité avec la température et la formation des nanoréseaux, donc les propriétés optiques anisotropes associées ;

6) Enfin, avec les résultats expérimentaux, nous avons construit un modèle de durée de vie fiable (suivant le formalisme de la courbe maîtresse) et l'avons utilisé pour prédire la durée de vie des modifications de type II dans différentes conditions de recuit temps-température.

Avec ceux-ci en main, nous pouvons envisager de développer des verres (verre massif ou fibre) ou sélectionner des verres commerciaux dédiés à la création de propriétés optiques anisotropes dans diverses gammes spectrales, de l'UV au moyen IR mais aussi pour des applications en régime haute température où le contrôle à vie est obligatoire.

université PARIS-SACLAY
ÉCOLE DOCTORALE
Sciences Chimiques: Molécules, Matériaux, Instrumentation et Biosystèmes (2MIB)

Titre : Une contribution aux applications à haute température utilisant l'écriture directe par laser femtoseconde dans des verres et des fibres optiques à base de silice

Mots clés : silice, silicates, verres, fibres optiques, laser femtoseconde, biréfringence, nanoréseaux, stabilité thermique, capteurs, impression 3D

Résumé : La détection environnementale hostile à l'aide de technologies optiques est un domaine de recherche en croissance rapide. Une nouvelle génération d'appareils fonctionnant dans des environnements extrêmes (en particulier ceux fonctionnant au-dessus de 700 °C et jusqu'à 1500 °C), y compris des environnements avec des défis supplémentaires tels que le rayonnement et les champs optiques intenses (par exemple, les lasers à haute puissance), doit être capable de résister au recuit et à la dégradation graduelle, ou au vieillissement, au fil du temps. Particulièrement pertinents, ces dispositifs incluent des diagnostics en direct avec des composites de capteurs optiques intégrés pour les avions, les hélicoptères et les infrastructures spatiales, la détection de température / pression dans des puits de pétrole de plus en plus profonds et chauds, ou encore la surveillance et la cartographie de la distribution de la température dans les centrales électriques, les fours et réacteurs chimiques.

Les principaux facteurs permettant de répondre à ces exigences sont liés à la nature intrinsèque du matériau en verre qui compose les dispositifs, et plus précisément à sa structure de verre et aux propriétés associées telles que l'écoulement visqueux, la migration chimique et la relaxation des contraintes. La stabilité thermique de ces dispositifs peut donc être obtenue par l'application judicieuse de la préparation du verre, du recuit du verre et des irradiations laser du verre.

D'un point de vue fondamental, l'écriture directe par laser femtoseconde permet de profiter des forces lumineuses qui agissent sur le plasma et sa nanostructuration conduisant à la nucléation-croissance de nanocavités voire de nanocristaux selon les compositions choisies. Ces modifications structurelles pourraient être un support idéal pour imprimer diverses fonctions optiques pouvant supporter un fonctionnement à haute température.

Dans ce contexte, les objectifs de cette thèse sont de comprendre les relations entre différents types de modifications induites par le laser fs dans les verres et les fibres (en particulier la silice et l'aluminosilicate) qui sont fabriqués par divers procédés, et de faire le lien entre la chimie des matériaux et transformations induites par laser fs. Nous cherchons à analyser l'effet de la composition chimique du verre et des paramètres d'écriture laser sur la stabilité thermique des propriétés optiques imprimées.

D'une part, nous révélons provisoirement les mécanismes sous-jacents à l'origine de la biréfringence observée et de leur intrication dans des verres silicatés massifs : défauts ponctuels orientés, champs de contraintes issus de plusieurs contributions, nanostructures et texturations, etc. des méthodes de fabrication de fibres telles que la technique du cœur fondu ou la préforme d'impression 3D sont également étudiées pour améliorer provisoirement la stabilité thermique des modifications imprimées au laser fs à travers l'aspect de la préparation du verre.

Ces découvertes ouvrent la voie à une nouvelle génération de dispositifs d'écriture laser à base de verre, à la fois sous forme de masse et de fibres, pour un fonctionnement à haute température, une propagation de puissance laser élevée ou des applications à longue durée de vie comme le stockage de données optiques, les capteurs pour la surveillance de la santé structurelle ou l'optique dans environnement hostile.

Université Paris-Saclay, CNRS
Institut de chimie moléculaire et des matériaux d'Orsay, 91405, Orsay, France.

université PARIS-SACLAY
ÉCOLE DOCTORALE
Sciences Chimiques: Molécules, Matériaux, Instrumentation et Biosystèmes (2MIB)

Title: A contribution to high temperature applications using femtosecond laser direct writing in silica-based glasses and optical fibers.

Keywords: silica, silicates, glasses, optical fibers, femtosecond laser processing, birefringence, nanogratings, harsh environment, thermal stability, sensors, 3D printing

Abstract: Harsh environmental sensing using optical technologies is a rapidly growing field of research. A new generation of devices that operate in extreme environments (particularly those operating above 700°C and up to 1500°C), including environments with additional challenges such as radiation and intense optical fields (e.g., high power lasers), must be capable of withstanding gradual annealing and degradation, or aging, over time. Of particular relevance, these devices include live diagnostics with embedded optical sensor composites for aircraft, helicopters, and space infrastructure, temperature / pressure sensing in increasingly deeper and hotter oil bores, or again monitoring and mapping of temperature distribution in power plants, furnaces, and chemical reactors.

The key enablers to meet these requirements are related to the intrinsic nature of the glass material that composes the devices, and more specifically its glass structure and associated properties such as viscous flow, chemical migration, and stress relaxation. Thermal stability of these devices may therefore be achieved by judicious application of glass preparation, glass annealing and glass laser irradiations.

From a fundamental point of view, femtosecond laser direct writing allows to take profit of light forces that act on the plasma and its nanostructuring leading to the nucleation - growth of nanocavities or even nanocrystals depending on the chosen compositions. These structural modifications could be an ideal support to imprint various optical functions that could withstand high temperature operation.

In this context, the objectives of this Ph.D. thesis is to figure out the relationship between different type of modifications induced by fs laser in glasses and fibers (particularly silica and aluminosilicate) that are fabricated by various methods, and make the link between chemistry of materials and femtosecond laser-induced transformations. We seek to analyze the effect of the glass chemical composition and the laser writing parameters on the thermal stability of the imprinted optical properties.

On the one hand, we tentatively reveal the underlying mechanisms at the origin of the observed birefringence and their entanglement in bulk silicate glasses: oriented point defects, stress fields from several contributions, nanostructures and texturation, etc. On the other hand, non-conventional fiber fabrication methods such as the molten core technique or 3D printing preform are also investigated to tentatively improve the thermal stability of fs-laser imprinted modifications through the aspect of glass preparation.

These discoveries pave the way towards a new generation of glass based laser written devices, both in bulk and fibers forms, for either high temperature operation, high laser power propagation or long lifetime applications like optical data storage, sensors for structural heath monitoring or optics in harsh environment.

Université Paris-Saclay, CNRS
Institut de chimie moléculaire et des matériaux d'Orsay, 91405, Orsay, France.